

# Seismic observation of the Earth's small-scale structure

Daniel Andrew Frost

Submitted in accordance with the requirements for the degree of  
Doctor of Philosophy

The University of Leeds

School of Earth and Environment

May 2014

*“In many of the more relaxed civilisations on the Outer Eastern Rim of the Galaxy, the Hitch Hiker’s Guide has already supplanted the great Encyclopedia Galactica as the standard repository of all knowledge and wisdom, for though it has many omissions and contains much that is apocryphal, or at least wildly inaccurate, it scores over the older, more pedestrian work in two important respects.*

*First, it is slightly cheaper; and secondly it has the words DON’T PANIC inscribed in large friendly letters on its cover.”*

*Adams [1979]*

The candidate confirms that the work submitted is his own, except where work which has formed part of jointly authored publications has been included. The contribution of the candidate and the other authors to this work has been explicitly indicated below. The candidate confirms that appropriate credit has been given within the thesis where reference has been made to the work of others.

Work from Chapter 2 has been published as Frost, Daniel A.; Rost, Sebastian; Selby, Neil D.; Stuart, Graham W., 2013. Detection of a tall ridge at the core-mantle boundary from scattered PKP energy, *Geophys. J. Int.*, 195, 558-574. Scientific and editorial guidance was provided by Dr. Rost and Dr Selby, and additional editorial guidance was provided by Prof. Stuart, all other work is that of the candidate.

Work from Chapter 4 has been accepted for publication and is in press as Frost, Daniel A.; Rost, Sebastian, 2014. The P-wave Boundary of the Large-Low Shear Velocity Province beneath the Pacific, *Earth planet. Sci. Lett.*. Scientific and editorial guidance was provided by Dr. Rost, all other work is that of the candidate.

This copy has been supplied on the understanding that it is copyright material and that no quotation from the thesis may be published without proper acknowledgement.

©2014 The University of Leeds and Daniel Andrew Frost.



# Acknowledgements

---

Firstly, I would like to express my gratitude to my primary supervisor, Sebastian Rost, for his friendship, enduring support, guidance with both my PhD and my academic career, and discussions about cycling during our meetings. Your constant expertise and enthusiasm have been invaluable. Additionally, my supervisors Neil Selby for getting me started with such a good idea, and his repeated visits to Leeds to check on my progress, and Graham Stuart for his help with publications and assistance throughout my project. I thank Jon Mound for being part of my post-graduate support group as well his as critical assistance with paper drafts. My project would not have been successful or so enjoyable without you all.

I thank NERC and my CASE partners, AWE, for funding my project and providing data access. I would also like to mention the people at AWE Blacknest who helped me throughout my project and during my visits, along with providing whatever codes or data I needed.

I am grateful to the general geophysics community for open access to so many useful codes that helped me to do things that I would never have been able to do alone.

The majority of the figures in Chapters 3 and 4 owe their existence to the Metropolis radio programme from KRCW which really helped when having to replot the same thing for the third time after finding mistakes at midnight.

Finally, I thank all of my friends both in the department and from outside for making my time in Leeds so enjoyable, and, my friends in 8.152 for putting up with sharing an office with me. I appreciated being a part of IGT, especially the cooking competition and the rivalries therein. Particular thanks to my house-mate, Tom, for distracting me with brewing and checking to make sure I was surviving my last few months of work, Dave and Sandra for their friendship and human pyramids from the start of the end of my PhD, Ben and Oli for reminding me of the necessity of being immature, and my family for their constant support.



# Abstract

---

The Earth's mantle is chemically and thermally heterogeneous varying in 3-dimensions and on many length-scales. Subduction introduces slabs into the mantle while interactions with the core may enrich the mantle in iron. The lower mantle demonstrates the strongest seismic anomalies outside of the crust. The Large Low Shear Velocity Provinces (LLSVPs), two volumes 1000s km across with seismic velocity reductions of 1-3 %, are likely thermally and chemically distinct from the surrounding mantle. Smaller velocity anomalies are detected close to the Core-Mantle Boundary (CMB) such as velocity increases  $\sim 100$  km thick often related to subducted slabs, and strong velocity decreases 10-100 km thick called Ultra Low Velocity Zones.

Array analysis of signals arriving before PKP demonstrates that they are waves scattered from volumes of anomalous material with 10 km scale-lengths in the lowermost mantle under South Africa. The data image a heterogeneous 80 km tall ridge at the CMB likely related to the edge of the African LLSVP. Scattering is likely caused by heterogeneities with strongly reduced velocities and increased densities probably elevated above the CMB by entrainment into the LLSVP.

Scattered PKKP waves (PK•KP) reveal heterogeneities irregularly distributed in the lowermost 300 km of the mantle. Scattering is also seen under South Africa, co-located with PKP observations. Anomalies are preferentially located towards the edges of the LLSVPs and regions of subducted material. The predisposition of small-scale anomalies towards the edge of the large-scale structure suggests control by dynamic processes.

$P(P_{diff})$ -travel-times are used to resolve the boundary of the Pacific LLSVP. The east of the LLSVP displays a sharp (60 km wide) transition and is traced steeply upwards sloping at  $70^\circ$ . The transition at the northern edge is broader (120 km wide) and shallower ( $30^\circ$  slope). The proximity to active subduction may sharpen and steepen the boundary of the LLSVP, providing insight into the dynamics of the lowermost mantle.



# Contents

---

<b>Acknowledgements</b>	<b>v</b>
<b>Abstract</b>	<b>vii</b>
<b>Contents</b>	<b>ix</b>
<b>List of Figures</b>	<b>xiii</b>
<b>List of Tables</b>	<b>xxxvii</b>
<b>1 Introduction</b>	<b>1</b>
1.1 Earth Structure . . . . .	1
1.1.1 Large-scale Mantle Structure . . . . .	2
1.1.2 Small-scale Heterogeneities . . . . .	8
1.2 Travel-times and Waveforms . . . . .	15
1.3 Scattered Waves . . . . .	17
1.4 Array Seismology . . . . .	22
1.4.1 Arrays . . . . .	22
1.4.2 Wave Characteristics . . . . .	24
1.4.3 Beamforming . . . . .	26
1.4.4 Fk Analysis . . . . .	28
1.4.5 Array Response Functions . . . . .	29
1.4.6 Other Coherence Measures . . . . .	31
1.4.7 Combined Methods . . . . .	32
1.5 Limitations . . . . .	34
1.5.1 Array Mislocation Vectors . . . . .	35
1.5.2 Attenuation . . . . .	35
1.5.3 Fresnel Zones . . . . .	36
1.6 Objectives and Thesis Outline . . . . .	36
<b>2 PKP Scattering</b>	<b>41</b>
2.1 Introduction . . . . .	41
2.2 PKP Probe . . . . .	41
2.3 Data . . . . .	48
2.4 PKP Scattering Coverage . . . . .	51
2.5 Method . . . . .	52
2.5.1 Array Processing . . . . .	52
2.5.2 Ray Tracing . . . . .	55
2.6 Results . . . . .	57
2.7 Error Analysis . . . . .	64
2.7.1 Azimuth and Slowness Estimation . . . . .	64

2.7.2	Location Uncertainty . . . . .	66
2.7.3	Stability of Detected Structure . . . . .	67
2.8	Modelling . . . . .	69
2.8.1	Modelling Process . . . . .	69
2.8.2	Modelling Results . . . . .	70
2.9	Discussion . . . . .	72
2.10	Summary . . . . .	78
<b>3</b>	<b>PKKP Scattering</b>	<b>79</b>
3.1	Introduction . . . . .	79
3.2	PK•KP Scattering Regions . . . . .	83
3.3	Data Collection . . . . .	86
3.4	PK•KP Scattering Coverage . . . . .	87
3.5	Data Processing . . . . .	89
3.6	Results . . . . .	93
3.7	Directivity Error Testing . . . . .	100
3.8	PK•KP Frequency Analysis . . . . .	106
3.9	Correlation With Large Scale Features . . . . .	109
3.9.1	Distribution Results . . . . .	116
3.9.1.1	Outside LLSVPs . . . . .	118
3.9.1.2	Inside LLSVPs . . . . .	123
3.9.1.3	Outside High Velocity Anomalies . . . . .	127
3.9.2	Considerations . . . . .	130
3.9.3	Summary of Distribution Results . . . . .	131
3.10	Discussion . . . . .	132
3.11	Summary . . . . .	136
<b>4</b>	<b>P-wave Travel Times</b>	<b>137</b>
4.1	Introduction . . . . .	137
4.2	Method . . . . .	139
4.3	Results . . . . .	144
4.4	Sources of Error . . . . .	153
4.5	Discussion . . . . .	155
4.6	Summary . . . . .	160
<b>5</b>	<b>Discussion</b>	<b>163</b>
5.1	Summary of Observations . . . . .	164
5.2	Integration of Observations . . . . .	166
5.3	Concluding Statement . . . . .	169
<b>A</b>	<b>Introduction Appendix</b>	<b>171</b>
A.1	Arrays . . . . .	171
<b>B</b>	<b>PKP Scattering Appendix</b>	<b>177</b>
B.1	Event Data . . . . .	177
B.2	Phonon Scattering Model Parameters . . . . .	180
<b>C</b>	<b>PKKP Scattering Appendix</b>	<b>183</b>
C.1	PK•KP Scattering Regions . . . . .	183
C.2	Scattering Results . . . . .	184
C.3	Directivity Error Testing . . . . .	188
C.3.1	Array Specific Errors . . . . .	188
C.3.2	Average Array Errors . . . . .	193

C.3.3 Correlation With Large Scale Features . . . . .	194
C.4 Event Data . . . . .	197
<b>D P-wave Travel Times Appendix</b>	<b>213</b>
D.1 Event Data . . . . .	213
D.2 Results . . . . .	216
<b>Bibliography</b>	<b>219</b>



# List of Figures

---

1.1	Tomographic images of the lower mantle. Lowermost mantle depth slices from P-wave tomography model GyPSuM [Simmons <i>et al.</i> , 2010] from the CMB to 2650 km (a and c) and S40RTS [Ritsema <i>et al.</i> , 2011] from the CMB to 2800 km (b and d). Slices are displayed centred on 0° (a and c) and 180° longitude (b and d). Contours are shown at 1 % velocity increments. Vertical slices centred on 0° longitude through the equator of (e) GyPSuM and (f) S40RTS tomography models from the CMB to the surface. Section line is shown by the black dashed line in Figures a-d. Colour scales and contouring as above. . . . .	4
1.2	$S_{diff}$ observed (upper) and synthetic (lower) waveforms sampling the edge of the south-eastern part of the African LLSVP, demonstrating multipathing along the boundary, thus exemplifying its sharpness. Traces are displayed as a function of azimuth from the source. From left to right, panels show the northern boundary, central region, and southern boundary of the LLSVP. Jumps in arrival time or changes in shape of $S_{diff}$ (marked by the grey line) demonstrate that the edge of the African anomaly can be sharply resolved, which points towards a thermo-chemical origin for the LLSVPs. From Ni <i>et al.</i> [2005] . . . . .	6
1.3	Mantle structures formed by subducting material interacting with an initial dense layer at the CMB. Subduction has an imposed plate history. The cross section demonstrates the thermal structure of the mantle where subducted material is cold (blue) and dense piles are hot (red). The 3-dimensional image displays the shapes into which the dense layer is forced by the subduction. The mantle dynamics generate both a steep-sided ridge structure under Africa and a more dome-like structure under the Pacific, separated by slabs. Plumes rising from the peaks of the dense piles could be the source of hotspots. Real hotspot locations and plate margins are marked by red circles and lines, respectively, on the top map surface. From McNamara & Zhong [2005]. . . . .	8
1.4	Amplitude of the global (vertical) short period wavefield processed using a 10 <sup>th</sup> root Vespa with an additional noise gate to suppress noise. Overlay indicates the arrival times of the major phases calculated with PREM. Major phases are represented by clear high amplitude arrivals while the additional lower amplitude signals following and preceding these are indicative of scattering generated by small-scale heterogeneities within the crust and mantle. From Rost <i>et al.</i> [2006b]. . . . .	9
1.5	Observations of D'' reflections (Scd) producing precursors to ScS from events sampling under the southern coast of Central America. The different residual time between Scd and ScS for the two events is indicative of topography on the D'' discontinuity. From Thomas <i>et al.</i> [2004a]. . . . .	10

1.6	Detections (red) and non-detections (blue) of ULVZs in studies up to 2010, overlaid onto S2ORTS [Ritsema <i>et al.</i> , 2011]. The majority of the ULVZ observations are in or around regions of slower than average seismic velocities, the LLSVPs (light red). By contrast, the non-observations are mainly in regions associated with subduction (light blue), such as the west coast of the Americas and the east coast of Asia. From <i>McNamara et al.</i> [2010]. . . . .	12
1.7	Dynamic model of dense convecting LLSVPs, the locations of which are forced by the subducting material, with an initial dense layer to simulate ULVZs. (a) Thermal structure of the whole mantle from the surface to the CMB. Cold material (blue) subducts to the CMB, is then heated from below, equilibrates with the ambient mantle, and rises back to the surface. Hot, dense piles (red) convect through viscous entrainment with the whole mantle convection. (b) Compositional and thermal structure in a section of the lowermost 289 km of the mantle (the area within the black box in in bottom left of Figure a). Subducted material, piles, and ULVZ material are indicated by blue, red, and dark red regions, respectively. The dense ULVZ material is partially entrained into the LLSVP convection and accumulates at the LLSVP edge. From <i>McNamara et al.</i> [2010]. . . . .	14
1.8	Core-Mantle Boundary topography from a joint tomographic and geodynamic inversion of P-wave travel-time data. The CMB is depressed (red colours) beneath regions of subduction, such as the edge of the Pacific, and upwarped (blue colours) beneath LLSVPs supporting observation that these structures are regions of upwelling. From <i>Soldati et al.</i> [2012]. . . . .	15
1.9	(a) Sketch of multiple rays ( $R_{1-4}$ ) and associated Fresnel Zones (dots and surrounding circles, respectively) sampling both ambient mantle, the boundary with an LLSVP, and the LLSVP itself. (b) Sketch seismograms of associated travel-time and waveform effects demonstrating multipathing as wavelet broadening ( $R_2$ ) and multiple arrivals ( $R_3$ ). These phenomena demonstrate varying degrees to which part of the wavefront is delayed before interfering with the main wavefront. . . . .	17
1.10	Scattering behaviour for various frequency/scatterer size ratios, and elastic parameter and density anomaly ratios. All patterns are for P•P scattering, are rotationally symmetric about the x-axis, and are generated by scattering of a wave propagating from left to right. Rayleigh scattering for (a) velocity and impedance type scattering and (b) for different scattering heterogeneity parameters (top) and frequency-size ratios (bottom) (Equation 1.1). (c) Volume factor for a Gaussian heterogeneity at a range of frequencies (see volume integral in Equation 1.4). The volume factor is independent of scatterer parameters and is only affected by frequency-size ratio and the way that parameters vary across the scatterer. (d) Mie scattering for a Gaussian heterogeneity at a range of frequencies for impedance type scattering (top) and velocity type scattering (bottom) (Equation 1.4). The Mie scattering pattern is the product of the Rayleigh scattering pattern (Figures 1.10a or 1.10b) and the volume factor (Figure 1.10c). After <i>Wu &amp; Aki</i> [1985a]. . . . .	20
1.11	Array apertures and number of stations of the dominant type (number of stations used displayed above the vertical bar). . . . .	23
1.12	Sketch array configuration of two crossing branches of seismometers (inverted pyramids) with interstation spacing $d$ . A wavefront (blue dashed line) is incident at the array along a ray (blue arrow) with back-azimuth $\theta$ and incidence angle $i$ . . . . .	24

1.13	Simplified arrays (stations shown by inverted triangles) with wavefronts (blue dashed lines) propagating with back azimuth (a) $\theta = 0^\circ$ and $\theta = 180^\circ$ and (b) $\theta = 90^\circ$ and $\theta = 270^\circ$ . Associated seismograms showing (c) no time delay, typical of situations such as (a), and (d) a time delay, $\Delta t$ , observed at each station, associated with situations such as (b). Red lines show moveout of the signal across the array. . . . .	25
1.14	Simplified arrays with wavefronts (blue dashed lines) propagating with back-azimuths $\theta = 90^\circ$ and incidence angles (a) $i = 90^\circ$ and (b) $i = 0^\circ$ . These situations are associated seismograms with Figure 1.13c for no time delay, and Figure 1.13d where the signal is delayed across the array, respectively. . . . .	26
1.15	Array processing for an event at 12:50:07 on 11/12/1996 in South Africa, recorded at YK, Canada. (a) Vespagram formed from beams, bandpass filtered between 1 and 2 Hz, for slownesses between 0.1 and 7.0 s/deg, at a back-azimuth of $54.4^\circ$ , showing PKP <sub>df</sub> arriving at $\sim 35$ s and two precursors arriving at $\sim 25$ and 28 s. The 90 % maximum amplitude region is marked by the green contour. (b) Beams formed on PKP <sub>df</sub> slowness (top) and precursor slowness (bottom), filtered between 1-2 Hz. . . . .	28
1.16	Array response functions computed for a 1 Hz wave with 0 s/deg slowness for two arrays, (a) Kurchatov in Kazakhstan and (b) Torodi in Niger. Due to the different array shapes, apertures, and station spacing the two arrays demonstrate different patterns of spatial aliasing over the slowness and back-azimuth range displayed (0 to 10 s/deg, 0 to $360^\circ$ ). Due to its much greater aperture, Kurchatov has a much narrower maximum, but significant side-lobes extending along the arms of the array. In comparison, Torodi has a much broader maximum but has no noticeable side-lobes as the stations are distributed in rings. For ARFs of other arrays see Figures in Appendix A. . . . .	31
1.17	The PKP <sub>df</sub> signal for an event at 22:19:36 on 22/04/1999 in South Africa recorded at YK in Canada processed using (a) linear beam-pack and (b) F-pack. Back-azimuth is on the azimuthal axis and slowness is on the radial axis, from 0 s/deg to 7 s/deg. Inner and outer blue rings mark inner and outer core slownesses, respectively. Contours are at 0.1 amplitude increments and the green contour marks the 90 % maximum amplitude region. The 90 % maximum amplitude region is reduced from $\sim 45^\circ$ and 1.7 s/deg wide ( $U_x=1.2$ s/deg, $U_y=1.2$ s/deg) in the beam-pack to $\sim 5^\circ$ and 0.3 s/deg ( $U_x=0.03$ s/deg, $U_y=0.3$ s/deg) by using the F-pack. . . . .	33
1.18	Frequency domain F-statistic showing PK•KP scattering time windows for an example event from the dataset used in Chapter 3. A magnitude 6.7 event recorded at Warramunga Array, Australia, on 15/10/2004. The time window displayed is from 1689 s to 1809 s. F-amplitude in (a) slowness and time and (b) back-azimuth and time space. Picked signals are shown as pink circles. Time, and slowness and back-azimuth limits are shown by vertical and horizontal blue lines, respectively. . . . .	34
2.1	Direct PKP <sub>df</sub> and PKP <sub>cd</sub> (solid lines) and source-side scattered P-to-PKP <sub>ab/bc</sub> and receiver-side scattered PKP <sub>ab/bc</sub> -to-P (dashed and dotted lines respectively) for an epicentral distance of $138^\circ$ . The direct paths PKP <sub>ab</sub> and PKP <sub>bc</sub> do not exist at this epicentral distance and are only possibly at distances greater than $144.6^\circ$ . PKP <sub>bc</sub> is shown at the minimum distance of $144.6^\circ$ (dashed-dotted line). The star, diamond, and inverted triangle represent source, scattering point, and receiver, respectively. . . . .	42

2.2	The range of slownesses and travel-times (relative to $PKP_{df}$ ) of waves scattered within the lowermost 200 km of the mantle at varying source-receiver distances ( $\Delta$ ) for along great-circle path scattering. Source- and receiver-side scattering are shown by red and blue lines, respectively. Source-side scattering typically generates waves with higher slownesses than receiver-side scattering. Source-receiver distance limits the amount of time by which scattered waves can precede $PKP_{df}$ , the earliest scattered energy is produced at source-receiver distances $\sim 130^\circ$ . The time by which the scattered wave precedes $PKP_{df}$ is independent of scattering side. After <i>Haddon &amp; Cleary</i> [1974]. . . . .	43
2.3	Global data stack showing time and distance dependence of precursors to $PKP$ calculated in $0.5^\circ$ distance bins. Data are aligned on $PKP_{df}$ and normalised to the maximum amplitude out of $PKP_{df}$ and $PKP_{cd}$ . White lines describe the earliest ray-theoretical precursor in each distance bin for scattering at different heights above the CMB. However, due to variable ray coverage, lateral variability of the prevalence of lower mantle scattering heterogeneities, and the small area that generates the earliest precursors (Figure 2.4a) the earliest scattered energy appears very weak in a global stack and is likely masked by high amplitude later arriving energy. From <i>Mancinelli &amp; Shearer</i> [2013]. . . . .	45
2.4	Areas in which scattering on the source side could generate precursors. This is shown for an event at $136.2^\circ$ distance from the receiver simulating ray paths typical of the dataset used in the remainder of the chapter. Earlier precursors scatter from the northern-most edge of the study region, furthest from the source, close to the CMB and the b-caustic (shown by the dashed black line). (a) Area at 40 km above the CMB in which scattering generates precursors. Arrival time of the precursor is shown relative to $PKP_{df}$ in seconds. The green line shows the great circle path from source to the receiver. (b) Slowness values (in s/deg) recorded at the array for scattering at different locations in the region that would generate precursors. The b-caustic is shown by the dashed black line. (c) Potential scattering areas at a range of heights from 0 km to 600 km above the CMB (depths of 2889 km to 2289 km). This shows the reduction in the area which can generate precursors and the reduction in the time by which scattered energy can precede $PKP_{df}$ with increasing height. Precursory times are contoured at 5 s intervals. All plots are created using a grid with spacing of $0.5^\circ$ in latitude and longitude. . . . .	47
2.5	(a) Yellowknife station configuration. YK contains 18 short-period stations with a minimum station spacing of 2.5 km and a maximum station separation (aperture) of 20 km along two perpendicular N-S; E-W oriented legs. Inset shows Yellowknife Array location in northern Canada. (b) Array response function computed at 1 Hz and 0 s/deg displayed for slownesses from 0 to 10 s/deg, in 2 s/deg steps, and back-azimuths from 0 to $360^\circ$ . Due to the aperture of the array the local maximum of the ARF is narrow but there is spatial aliasing along the arms of the array resulting from the cross shape. . . . .	49

2.6	(a) Source locations in southern Africa with category 1 and 2 events shown as filled circles (for category definitions see Chapter 2.5.1), category 3 as open triangles, and category 4 as open circles showing all events used and the mining region denoted by a black box. The minimum scattering distance, the b-caustic, of $116.5^\circ$ from YK is shown by the black curve. (b) The mining region with mine areas shaded dark grey and towns as white squares with event classifications as in (a). . . . .	50
2.7	Potential coverage by precursors to PKP for scattering at the CMB for all 153 source-receiver pair. The extent of the coverage, the zero-sampling contour, is shown by the green line. The blue contour indicates the extent of the scattering structure shown in Figure 2.12a (the 25 km height contour is shown). All 153 sources from all event categories are shown by yellow stars. Scattering could be observed outside of the region resolved to contain scattering heterogeneities (blue contour) suggesting that the detected scattering structure is real and constrained to the region shown. . . . .	51
2.8	Array processing for an event at 12:50:07.03 on 1996/12/11 in South Africa, recorded at YK, Canada, the same event shown in Figure 1.15. (a) F-Vespa formed from F-traces for slownesses between 0.0 and 7.0 s/deg. PKP <sub>df</sub> is seen arriving at $\sim 35$ s with slowness of $\sim 2.0$ s/deg, two precursors arriving at $\sim 25$ and 28 s with slownesses $\sim 4$ s/deg, and another arrival following PKP <sub>df</sub> which may be PKP <sub>cd</sub> (all pink circles). The 90 % maximum amplitude region is marked by the green contour. (b) F-traces formed on PKP <sub>df</sub> slowness (top) and precursor slowness (bottom), filtered between 1 and 2 Hz. The slowness (U) and back-azimuth (Baz) for which the F-traces are calculated are shown in the top left. . . . .	52
2.9	F-pack formed by creating beams for back-azimuths from $0^\circ$ to $360^\circ$ and slownesses of 0.0 s/deg to 7.0 s/deg and calculating the F-statistic for each beam, using data recorded at YK from an event at 22:19:36.77 on 22/04/1999 in South Africa. The F-traces are processed with a 4 pass, zero phase Butterworth bandpass filter with corner frequencies of 1.0 Hz and 2.0 Hz. The maximum F-statistic in a given time window is calculated and all amplitudes are normalised relative to the maximum. (a) Normalised F-statistic for a 60 s time window around PKP <sub>df</sub> with peaks identified as the first precursor (blue), second precursor (green), and PKP <sub>df</sub> (pink). Optimal slownesses (U) and back-azimuths ( $\theta$ ) used to form the (b) beams and (c) F-traces for the first precursor, second precursor, and PKP <sub>df</sub> (traces from top to bottom) are noted on each trace and on the F-pack as blue, green, and pink circles. Lines on the F-traces indicate the picked arrival time for each phase with the same colour code; energy arriving after these comprises the coda. . . . .	54
2.10	Spatial resolution of potential scatterer location for an event at $136.3^\circ$ distance. Slowness and time misfits are shown as solid and dashed contours, respectively. The grid of potential scatterers is aligned along the back-azimuth recorded at YK. The region to which the best fit scattering point (blue star) is constrained is shown as a green box, with distance uncertainties of $\pm 2^\circ$ and height uncertainties of $\pm 25$ km based on slowness errors of $\pm 0.25$ s/deg and time errors of $\pm 0.5$ s (calculated in Chapter 2.7). Source-to-scatterer distance is best constrained by slowness, and scatterer height is best constrained by travel-time. . . . .	57

2.11 Arrival-time and slowness deviations for precursors and PKP<sub>cd</sub> relative to PKP<sub>df</sub> (black diamond at 0,0. Average PKP<sub>df</sub> slowness is 2.1 s/deg and all time measurements are relative to this phase). (a) Arrivals for all category 1 and 2 events, with first precursors (blue circles), second precursors (red triangles), and PKP<sub>cd</sub> (green squares). Black diamonds show average arrivals with 1-standard deviation error bars for each phase. No time error bar is shown for PKP<sub>df</sub> as other times are measured relative to this. Precursors display distinctly different slownesses and arrival-times to PKP<sub>df</sub>. On an event by event basis, the slowness of the first precursor is generally greater than that of the second precursor (for example Figure 2.9a) although plotting all events together as in this figure makes this difficult to observe here, and there is a distinct time gap between the two arrivals. (b) Average arrivals for each phase, for each mining source region with 1 standard deviation error bars. Pink triangles, green circles, and brown squares represent events from Klerksdorp (NW), Welkom (SW), and Carletonville and Randfontein mines (NE) respectively. . . . . 58

2.12 Maps of scatterer locations beneath South Africa where circles and triangles represent the scattering location of first and second precursors, respectively. (a) Scattering heterogeneity height above the CMB overlaid on a surface of the same data contoured at 25 km intervals. (b) Precursor amplitudes relative to PKP<sub>df</sub> overlaid on a surface constructed from the same data contoured at 0.1 times PKP<sub>df</sub> amplitude intervals. Amplitudes are measured from the filtered beam formed on the phase of interest, while the F-amplitude is used to select the time window in which to pick the phase in the beam. (c) Scatterer height above the CMB and (d) precursor amplitude relative to PKP<sub>df</sub> only showing precursors with beamed SNR larger than 5 and with ray-tracing misfits less than 0.25 s/deg slowness and 1 s travel-time, leaving 41 data points. Outside the study region (-1° to 71° longitude, 1° to -26° latitude) the constructed surface is constrained to return to the CMB. . . . . 59

2.13 (a) Scattering heterogeneity height above the CMB showing scatterers as discrete volumes (cubes) forming a cluster of concentrated scattering. Cubes outlined in black satisfy the quality criteria used in Figures 2.12c and 2.12d (SNR>5, slowness misfit <0.25 s/deg and time misfit <1 s) and those outlined in red are of lower quality. The grid is viewed from 220° azimuth inclined at 35° to the plane. Cross-sections (b), from A to A' (-2.5° N, 11° E to -25° N, 20° E) through the scattering volume (red line shows the height of the scattering surface from Figure 2.12a along the same section), along the red line in the main figure (scattering points ±1° either side of this line are shown) with the b-caustic shown by the blue line, (c) from B to B' (-2.5° N, 21° E to -25° N, 30° E) through the scattering volume (scattering points within ±1° laterally of the cross-section shown), and (d) from C to C' (-22° N, 0° E to -2.5° N, 42° E), along the ridge (scattering points within ±0.5° laterally of the cross-section shown). . . . . 60

2.14 Number of scattering points per 2.5°×2.5° cell as symbol shading. Cells without scatterers are left blank. Sampling of the structure is good even towards the edges of the structure where scattering heights and amplitudes are lower (see Figure 2.12). . . . . 61

2.15	Precursor amplitudes relative to $PKP_{df}$ as in Figure 2.12 for the centre of the scattering ridge with the highest scattering point density. Contours are at 0.1 times $PKP_{df}$ amplitude intervals. Precursors are split into mine source regions with events from Welkom (south-west) shown as triangles, from Klerksdorp (north-east) shown as squares, and Randfontein and Carletonville (north-west) shown as circles. Arrows show the direction to the source in the south-east and the receiver in the north-west. . . . .	62
2.16	Beams filtered with a Butterworth bandpass between 1.0 Hz and 2.0 Hz formed on $PKP_{df}$ slowness and back-azimuth from seven category 1 events between $135.98^\circ$ and $136.06^\circ$ from YK. Traces are plotted with $PKP_{df}$ at the origin. All traces are normalised to the maximum amplitude within $\pm 15$ s of $PKP_{df}$ . Amplitude ratios of the precursor to $PKP_{df}$ vary significantly between events. . . . .	63
2.17	Spectrograms calculated using the unfiltered beam formed on $PKP_{df}$ slowness and back-azimuth for an event on 12/11/1997 with $m_b = 4.5$ . Spectrograms are created using (a) short-period, and (b) broad-band instrument recordings. The times at which the first precursor, second precursor, and $PKP_{df}$ are picked using the F-pack are shown by the red, green, and pink lines, respectively. Energy is seen arriving at 1 Hz throughout the period in which the first precursor is picked. A weak precursor can just be seen in the short-period spectrogram arriving at 2 Hz at the time of the first precursor. However, the dominant energy peak arrives at 0.2-0.4 Hz associated with the $PKP_{df}$ . Energy arriving after $PKP_{df}$ (visible as a distinct arrival in the broadband spectrogram), also at 0.2-0.4 Hz, may be related to $PKP_{cd}$ . The frequency of the precursors indicates scattering from heterogeneities of $\sim 6$ -13 km in size. . . . .	64
2.18	F-pack measurement errors for synthetic signals created at various Signal-to-Noise Ratios (SNR) for (a) slowness, (b) back-azimuth, (c) and time. Synthetic precursory signals (blue circles) have half the amplitude of synthetic $PKP_{df}$ signals (red squares). A SNR of 5 is found to be a suitable cut-off (red line), above which the F-pack is able to easily extract a signal from the noise with very low directivity errors. . . . .	66
2.19	Changes in scatterer locations determined by ray-tracing using systematically modified input data, varying slowness, back-azimuth, time, and source location to simulate errors in the dataset. Each scatterer location is plotted relative to that created with unmodified input parameters thus demonstrating the amount by which changes to each input parameter affect the scatterer location. Changes are made to the input event parameters: source latitude and longitude (triangles), signal arrival-time (stars), signal slowness (squares), signal back-azimuth (diamonds), and arrival-time, slowness, and back-azimuth simultaneously (circles). . . . .	67
2.20	Results of Bootstrap test using 300 realisations. (a) Average of the scatterer height differences between each bootstrap iteration and the original, unsampled grid (the same surface as the contours in Figure 2.12). (b) Original grid with the average difference subtracted. (c) original grid (before bootstrap sampling). The north-western face of the ridge dips at $\sim 11^\circ$ to the horizontal while the south-eastern face dips at $\sim 5^\circ$ . All surfaces are contoured at 25 km height increments. . . . .	68

2.21 Phonon scattering synthetics generated for a 1-D Earth model with scattering in the upper 200 km (lithosphere) and a variable lower mantle scattering layer, compared to data for beams formed on PKP<sub>df</sub> slowness (black line) and precursor slowness (grey line) from all category 1 events. Standard lower mantle layer parameters are 8 km heterogeneity scale length, 0.8 velocity/density scaling factor, 2 % RMS velocity perturbation, 50 km thickness, and layer lower surface at the CMB. Models maintain all other standard parameters and change (a) scale length, (b) RMS velocity perturbation, (c) layer thickness, and (d) layer lower surface height above the CMB. Density scaling factor is not shown as it does not affect the output envelope. (e) Models with two lower mantle scattering layers of varying thickness and RMS velocity perturbations, but a standard 8 km heterogeneity scale length. Layers in the models are described as L1 for the lower layer starting at the CMB, and L2 for the layer directly above this. Layer thickness is given in km and RMS velocity perturbation is in per cent. (f) Scattering models varying a combination of parameters based on previous models in an attempt to better fit the data. No single parameter or combination of parameters are able to model the data. Scattering is possible on both source and receiver sides of the core and both sides will contribute equally to the envelope. . . . . 71

2.22 Maps of (a) S-wave tomography, at 89 km above the CMB (2800 km depth) using S40RTS [*Ritsema et al.*, 2011], and of (b) P-wave tomography at 20 km above the CMB (2869 km depth) using MIT-P08 [*Li et al.*, 2008] with event locations (yellow stars), scattering points (green circles), and a great-circle path (purple) to YK (red triangle). Precursor amplitudes relative to PKP<sub>df</sub> are indicated by symbol size. (c) Local S-wave tomography structure, at 89 km above the CMB (2800 km depth) using S40RTS, with scatterer locations. The blue line indicates the eastern edge of the African LLSVP from *Wang & Wen* [2004]. (d) Cross-section through S40RTS from 20° S, 0° E to 50° E, 5° S for heights from the CMB to 1000 km above. Scattering points are projected onto the cross-section line and shown as green circles. Contours are at increments of 1 % velocity anomaly. . . . . 74

2.23 Possible structures in the lower mantle which may scatter (star) at different heights: (a) an LVZ comprising a collection of random heterogeneities likely included in LLSVP material (not shown), (b) an LVZ over the LLSVP, entrained by internal convection within the LLSVP (blue arrows), (c) or an LVZ with layered internal structure. . . . . 77

- 3.1 PKKP ray paths from source (yellow star) to receivers (red inverted triangles) showing (a) direct PKKP, (b) source-side scattered P•KKP, (c) receiver-side scattered PKK•P, (d) and CMB-scattered PK•KP. The scattering point can be at the CMB or above into the lower mantle on the antipodal side. The path is then effectively PKP•PKP but is still referred to as PK•KP. Scattering is caused by interaction of the incoming wavefield with small-scale heterogeneities in elastic properties or density. (e) Travel-time table showing all the variants of the PKKP path (in colour) and additional, unrelated paths that are observed in a similar time and distance range (in grey). The time and distance range used in this study to select PK•KP is shown by the blue box. The time window used is 100 s long following the PK•KP first arrival (at 1716 s) to limit analysis to signals from the lowermost 300 km of the mantle. PK•KP arrivals are possible at distances greater than  $60^\circ$  but may be contaminated by other phases and so are not used. After *Earle* [2002]. . . . . 81
- 3.2 Example PK•KP ray paths demonstrating how the probe scatters off great-circle path. Rays travel from the sources (yellow stars) A and D, avoiding the inner core, to the scattering point B', and to the receivers (red inverted pyramids) C and E. Despite having different source-receiver distances (A-C and D-E), it is possible for paths A-B'-C (purple path), and D-B'-E (green path) to have the same travel-time provided that the 1-dimensional paths travelled are the same (and have the same source-scatterer-receiver ray length). Point B shows the surface projection of the scattering point at B' which is significantly out of the diametral plane containing the sources and receivers. The same ray paths are also equally possible in the lower hemisphere. After *Chang & Cleary* [1981]. . . . . 82
- 3.3 Distance limits between which a KP path (or equivalently PK path) is possible for a range of scattering heights above the CMB.  $KP_{ab}$  path limits are shown in red and  $KP_{bc}$  path limits are in blue. All paths are calculated for IASP91 [*Kennett & Engdahl*, 1991]. . . . . 84
- 3.4 Regions of potential scattering for a surface focus event (yellow star) to a receiver (red inverted triangle) for scattering at 2689 km depth (200 km above the CMB) at (a)  $10^\circ$  and (b)  $45^\circ$  source-receiver distance (minor arc) and for scattering at 2889 km (at the CMB) (c)  $10^\circ$  and (d)  $45^\circ$  source-receiver distance. An example scatterer (purple circle) and ray path (purple line) are shown demonstrating the potentially asymmetric nature of the ray path. Travel-times are computed using IASP91. Colours indicate the travel-time of waves scattering at that point. The minimum whole path travel-time is 1716 s for a surface focus event, Scattering locations which would generate waves with travel-times longer than 1816 s are not shown, these limits are indicated by the black lines around the colour regions. Regions of potential scattering are much smaller for scattering above the CMB and at longer source-receiver (minor-arc) distances. At longer source-receiver distances there are two separate regions of sampling while at shorter distances ( $< 30^\circ$ ) there is a single continuous region centred at the antipode of the source-receiver mid-point. . . . . 86

3.5	Arrays used (inverted triangles) and events (stars) over magnitude 6.0, from 1985 to 1996 for GB and 01/01/1995 to 31/12/2011 for all other arrays. Closed stars indicate that scattered PK•KP waves were observed associated with the event, while open stars mark events that did not generate identifiable scattering. Out of 1097 events, 544 show scattering at at least one array. . . . .	87
3.6	Potential coverage by PK•KP for scattering at the CMB for all 2538 source-receiver pairs that could potentially sample each degree at the CMB. (a) Projection centred at 0° and (b) 180° longitude created using the scattering regions calculated for various source-receiver distances in Chapter 3.2. The extent of the coverage, the zero-sampling contour, is shown by the green line while blue and red contours indicate potential sampling at 150 and 50 count intervals, respectively. The maximum potential coverage of 717 hits per 1°×1° bin occurs off the coast of equatorial Africa. . . . .	88
3.7	Processing and results for a magnitude 7.9 event in the Banda Sea (7.14° S, 122.60° E) at 11:22 am on 17/06/1996 at 587 km depth recorded 49° away at Gauribidanur Array, India. Results of the fk F-statistic analysis displayed in (a) slowness-time space and (b) back-azimuth-time space from 0 to 6 s/deg and 1637 to 1757 s, and from -180 to 180° (about the great-circle back-azimuth of 112°) and 1637 to 1757 s, respectively. The lower time limit of 1652 s (for 587 km event depth) is shown by a vertical blue line and limits for slowness and back-azimuth are shown as horizontal blue lines (calculated in Chapter 3.2). Picked energy peaks are displayed as pink circles which are then ray-traced to the scattering points located in Figure c. The picked PK•KP energy peaks, from first to last, scatter at heights relative to the CMB of 0 km, 150 km, and 40 km, respectively. (c) Source (star) and receiver (inverted triangle) locations connected by the major-arc great-circle path (red line) showing the mid-point (purple dot). Potential scattering regions (grey wedges) are either side of the mid-point and the scattering points of 3 PK•KP signals located on different sides of the great-circle path, as is evident when viewed in back-azimuth-time space as in Figure b. The source-to-scatterer and scatterer-to-receiver paths are shown as purple dashed and purple solid lines, respectively. Scatterers are shown as green circles as they have slowness and time misfits lower than 1.5 s/deg and 2.5 s, respectively. Scattering points with misfits greater than this would be shown as red circles and disregarded from further processing. . . . .	90
3.8	Range of distances and depths possible for (a and b) KP <sub>bc</sub> and (c and d) KP <sub>ab</sub> and their influence on slowness and travel-time. When ray-tracing, the distance of the scattering point from the receiver is primarily controlled by slowness while scattering depth is dominantly controlled by travel-time. Red lines indicate the limit of each branch as in Figure 3.3. Labels for slowness and time are in s/deg and seconds, respectively. . . . .	93
3.9	Scattering heterogeneity heights above the CMB, centred at 0° (left) and 180° (right) longitude, displayed in 10° × 10° cells as (a and b) mean scattering height in each cell, (c and d) median scattering height, (e and f) maximum scattering height. The height of each cell is shown by the tile colour and the number of scattering locations in each cell is shown by the colour of the inset circle. The -0.4 % V <sub>S</sub> contour from S40RTS is displayed as the black line to represent the extent of the LLSVPs. For larger figures see Appendix Figure C.2 . . . . .	95

3.10	Distribution of scattering heights in $30^\circ \times 30^\circ$ cells (red) compared with the global scattering frequency (blue). The number of scattering points in the cell used to calculate the red histogram is shown red. Cells without any scattering points are left empty. Histograms are calculated from the CMB to 300 km above in 50 km width bins (x-axis), and displayed in frequency per cent (y-axis) from 0 to 100 per cent. Regions such as the west coast of Central America, the north coast of South America, South Africa, and Antarctica show considerably more scatterers at greater heights above the CMB than the global distribution while regions such as Australia, North Africa, and Europe tend to show more scatterers at lower heights, relative to the global distribution. . . . .	96
3.11	Number of scattering points located in each $10^\circ \times 10^\circ$ cells normalised by the number of times that cell is sampled and could show scattering (from Figure 3.6), centred at (a) $0^\circ$ and (b) $180^\circ$ longitude. The extent of the coverage, the zero-sampling contour, is shown by the green line while yellow and red contours show potential sampling at 150 and 50 count intervals, respectively. Most regions show low hit/sampling ratios due to the high level of sampling. However, South Africa, southern Australia, and southern South America are notable exceptions where more hits are recorded per potential sample than the global average. . . . .	97
3.12	Scattering points under South Africa shown as median height in each $5^\circ \times 5^\circ$ cell. (a) Scattering heterogeneities resolved by precursors to PKP from events in South Africa recorded at YK. (b) Scattering heterogeneities resolved by PK•KP from globally distributed events recorded at various IMS arrays. The edge of the African LLSVP defined by the $-0.4\% V_S$ contour from S40RTS [Ritsema <i>et al.</i> , 2011] is shown by the solid black line. Scattering heights and locations resolved by both PKP and PK•KP are similar in this region with a ridge of high scattering heights running roughly east-north-east west-south-west with lower scattering around. PK•KP energy is detected in the same region as high amplitude precursors to PKP <sub>df</sub> under the Comoros hotspot (dashed purple line) [Wen, 2000]. . . . .	98
3.13	Characteristics SNRs of the arrays used. Median SNRs calculated per trace (unbeamed) as: PK•KP signal against pre-event noise (green circles), PK•KP signal against PK•KP time window noise (blue triangles), and P wave against pre-event noise (red squares). PK•KP ratios are measured on the left axis and the P wave ratio is measured on the right axis. For each array, noise levels correlate between different signals. This consistency demonstrates that the SNR values are indicative of the noise at the array rather than the magnitudes of the events used to calculate the SNR, which differs for each array. The ratio of the PK•KP signal against PK•KP time window noise is used in subsequent calculations. Noise levels are independent of array size. . . . .	101

- 3.14 Array specific errors of signal direction and ray-traced locations for arrays AK (a and b) and BR (c and d) for a range of input directions. (a and c) Errors in directivity values measured using the fk F-statistic are shown at the input slowness and back-azimuth of the synthetic signal as deviations in back-azimuth measured from north (to indicate back-azimuth error) and arrow length (to indicate slowness error). Time errors are shown as coloured circles. (b and d) Scattering point mislocations resulting from ray-tracing shown at the input slowness and back-azimuth of the synthetic signal displayed in terms of direction and distance (green arrow angle and length) and depth (triangles). Triangles and inverted triangles indicate that the scattering point is moved shallower and deeper, respectively, by the directivity error. Measured slowness and back-azimuth errors and subsequent ray-traced mislocations are much larger at BR than AK, likely due to the smaller aperture and fewer stations at BR. Errors at AK are generally low except for the synthetic signal arriving with slowness of 3.0 s/deg and back-azimuth of 135°, respectively. For errors at other arrays see Figures in Appendix C.3.1. . . . . 103
- 3.15 Magnitude of errors of directivity values measured using the fk F-statistic (a and b) and the scattering point mislocations resulting from ray-tracing (c and d) for each array. Values are displayed as the mean (red) with 1-standard deviation error bars and the median (blue), the latter is considered more robust. Arrays are ordered by decreasing aperture from left to right. Measured (a) back-azimuth and (b) slowness errors for synthetic signals from a range of incoming directions with noise and noise levels typical of the array using values shown in Figure 3.13. Errors are dependent on incoming noise levels and the array configuration. (c) Lateral and (d) vertical mislocations for a typical scattering point ray-traced with the slowness and back-azimuth errors determined for that array. As depth changes can be positive or negative, the modulus is used to calculate the average error. Slowness errors primarily control depth mislocations and a combination of back-azimuth and slowness errors control lateral mislocations. Dashed horizontal lines indicate distance and depth errors of 2.5° and 30 km, respectively. Synthetic signals with slownesses of 2.0 s/deg are often poorly fit and result in large errors in depth as it is not possible for a PK path to have this slowness. For average and median mislocations where input slownesses of 2.0 s/deg are ignored see Appendix Figure C.18. . . . . 104
- 3.16 Parameters of events and stations from the 2009 GSN data used for measuring PK•KP signal frequency. All histograms are plotted in frequency per cent. Event (a) major-arc back-azimuth from station to source, (b) depth, (c) latitude, and (d) longitude. Station (e) distance from source, (f) altitude, (g) latitude, and (h) longitude. Details for all events for the year are shown by the coloured histograms while the data selected to contain PK•KP signals are shown by the black histograms. The locations of sources and receivers used does not dramatically change between the two set but the number of traces used decreases from 423 to 162. . . . . 107

- 3.17 Envelopes of stacked traces collected from GSN stations, bandpass filtered (order 2) between a range of frequencies in octaves for data from (a) 2008 and (b) 2009. These years show scattered energy most clearly. Data are picked to remove faulty channels and then picked to include only events that show energy arriving in the lower mantle PK $\bullet$ KP time window (red lines). These traces are then bandpass filtered between the frequency limits shown, enveloped, and stacked and then the logarithm is taken to emphasise the lower amplitude signals. Scattered energy is strongest in the 2-4 Hz frequency band, but is seen at all frequencies greater than 1 Hz. . . . . 108
- 3.18 Scattering heterogeneities relative to tomography models S40RTS (a-d) and SMEAN (e-h) [Ritsema *et al.*, 2011; Becker & Boschi, 2002]. Location and height of scattering points above the CMB compared with S40RTS for synthetic (a and b) and real (c and d) data. LLSVP iso-velocity contours (0.0, -0.4, and -0.8 %  $V_S$ ) and faster velocity contours (+0.9 %  $V_S$ ) at 2800 km from S40RTS [Ritsema *et al.*, 2011] are shown as purple and green lines, respectively. Location and height of scattering points above the CMB compared with SMEAN for synthetic (e and f) and real (g and h) data. LLSVP iso-velocity contours (0.0, -0.4, and -0.8 %  $V_S$ ) and faster velocity contours (+1.3 %  $V_S$ ) at 2850 km from SMEAN [Becker & Boschi, 2002] are shown as purple and green lines, respectively. The limit of the sampling area (from Figure 3.6) is shown by the black line. Within the sampled region synthetic data is distributed randomly with uniform probability laterally and with height from the CMB to 300 km above. For larger figures see Appendix Figure C.19. . . . . 111
- 3.19 Tomography models overlaid with the contours used to represent the low and high velocity anomalies to which distances from scatterers are measured for (a and b) S40RTS and (c and d) SMEAN. Low velocity anomalies, LLSVPs, are defined by the 0.0, -0.4, and -0.8 %  $V_S$  iso-velocity contours for both models (purple lines) and high velocity anomalies are defined by the +0.9 and +1.3 %  $V_S$  contours for S40RTS and SMEAN, respectively (green lines). All contours are taken from the lowermost depth slice of each model: 2800 km for S40RTS and 2850 km SMEAN. For larger figures see Appendix Figure C.20. . . . . 113
- 3.20 Empirically determined values of the standardised Anderson-Darling value,  $T_{akN}$ , and the associated probability values,  $P$  for (a) S40RTS and (b) SMEAN.  $P$  values can be directly compared with significance levels  $\alpha$ , shown by red lines. The points can be fit by a Gaussian curve for which  $\alpha$  values 0.05 and 0.01 are equivalent to  $T_{akN}$  values of 4.2 and 5.4 for S40RTS and 5.3 and 6.6 for SMEAN, respectively. The equation of the curve is  $f(x) = a \exp(-1((x-b)/c)^2)$  for which coefficients for S40RTS are  $a = 1.21$ ,  $b = 1.37$ ,  $c = 3.14$  and for SMEAN are  $a = 1.04$ ,  $b = 0.09$ ,  $c = 3.05$ . 116

3.21	Anderson-Darling test results for a range of scenarios calculated for different combinations of synthetic and real data samples for contours defined in S40RTS (a and b) and in SMEAN (c and d). Displayed is the mean value for 20 calculations using a specified number of synthetic and data samples (shown by the vertical position of circle for which labels are shown in the same order in the top right of each figure) randomly selected from the total 300 sample population for the (a and c) standardised Anderson Darling value, $T_{akN}$ , and (b and d) percentage of calculations shown to be statistically different, to $\alpha = 0.05$ . The larger the $T_{akN}$ and greater the percentage of calculations that are different, the more distinct the real and synthetic populations are for that scenario. For example, green or blue symbols in Figures a and c indicate that the real and synthetic populations are significantly different to greater than 99 % confidence (significance $\alpha=0.01$ ). Differences between the real and synthetic populations are most obvious for scenarios outside the -0.8 % LLSVP contour, inside the -0.4 and -0.8 % LLSVP contours, and outside the fast regions for all LLSVP contours. . . . .	118
3.22	Cumulative distribution curves for scattering heterogeneities measured away from the outside edge of various LLSVP contours in S40RTS. (a) Distribution of the non-bootstrapped original data (red lines) compared to the mean of all 300 samples of the synthetic data (blue lines) for scattering points between 0-300 km above the CMB measured relative to the 0.0 % $V_S$ contour (solid lines), -0.4 % $V_S$ contour (dashed lines), -0.8 % $V_S$ contour (dotted lines). Also shown are the number of scattering points used to construct each distribution and the AD-kS value calculated for 50 synthetic and 50 real samples. (b-d) Distribution of samples within the real and synthetic populations shown by the mean of all samples (orange and blue thick lines), standard error of the mean (dark red and dark blue regions), first standard deviation about the mean (dark red and dark blue shading) and second standard deviation about the mean (light red and light blue shading). For the real data, the actual scatterer distribution is plotted (thick red line) which often obscures the mean line (orange). Standard errors of the mean are often too small to be seen. Also shown, for each scenario, are the AD-kS values for a range of $k$ samples of synthetic and real data (values shown in Figures 3.21a and 3.21c). Scatterer distributions for (b) the 0.0 % contour, (c) the -0.4 % contour, and (d) the -0.8 % contour for heights from 0-300 km above the CMB. Relative to the outside of the -0.8 % contour, scatterers show a strong preference towards the edge when compared with the synthetic data. Around 40 % of the real scattering points are accounted for within $15^\circ$ of the LLSVP edge compared to less than 30 % of the synthetic data in the same distance range. The same pattern is just visible for heterogeneities measured relative to the -0.4 % contour but is not apparent when measured relative to the 0.0 % contour. . . . .	120

3.23	Cumulative distribution curves for scatterers measured away from the outside edge of various LLSVP contours in SMEAN. Lines and shading as in Figure 3.22. (a) Distribution of the non-bootstrapped original data (red lines) compared to the mean of all 300 samples of the synthetic data (blue lines) for scattering points between 0-300 km above the CMB measured relative to the 0.0 % $V_S$ contour (solid lines), -0.4 % $V_S$ contour (dashed lines), -0.8 % $V_S$ contour (dotted lines). Scatterer distributions for (b) the 0.0 % contour, (c) the -0.4 % contour, and (d) the -0.8 % contour for heights from 0-300 km above the CMB. Scattering heterogeneities cluster within $\sim 15^\circ$ (vertical dashed line) of the -0.4 % contour. A similar increase in scatterer concentration can be seen at slightly greater distances ( $\sim 19^\circ$ , vertical dashed line) when measured relative to the -0.8 % contour (which has smaller geographic extent). . . . .	121
3.24	Cumulative distribution curves for scatterers measured away from the outside edge of the -0.8 % LLSVP contour in S40RTS. Lines and shading as in Figure 3.22. (a) Data and means for scatterers from 0-100 km above the CMB (dashed lines) and 100-300 km above the CMB (dotted lines). Population distributions for scatterers (b) 0-100 km above the CMB and (c) 100-300 km above the CMB. Scattering points higher above the CMB associate less with the edge of the LLSVP than scattering points closer to the CMB (at heights less than 100 km above the CMB). This is especially visible at distances greater than $\sim 20^\circ$ from the edge of the LLSVP. The AD-kS values demonstrate that both distributions are statistically different from the random population but the pattern of scatterers at lower heights is more distinct. . . . .	122
3.25	Cumulative distribution curves for scatterers measured away from the outside edge of the -0.8 % LLSVP contour in SMEAN. Lines and shading as in Figure 3.22. (a) Data and means for scatterers from 0-100 km above the CMB (dashed lines) and 100-300 km above the CMB (dotted lines). Population distributions for scatterers (b) 0-100 km above the CMB and (c) 100-300 km above the CMB. Scattering points higher above the CMB associate less with the edge of the LLSVP (are more similar to the synthetic data) at distances greater than $\sim 25^\circ$ than scattering points closer to the CMB (at heights less than 100 km above the CMB). The AD-kS values indicate that the distribution of heterogeneities at greater heights cannot be reliably distinguished from random but distributions at lower heights are likely to be drawn from a different population (are distinct from the synthetics). . . . .	123

3.26 Cumulative distribution curves for scatterers measured from the inside edge of the various LLSVP contours in S40RTS. Lines and shading as in Figure 3.22. (a) Data and means for scatterers from 0-300 km above the CMB for distances measured relative to the 0.0 % contour (solid lines), the -0.4 % contour (dashed lines), and the -0.8 % contour (dotted lines). Population distributions for scatterers between 0-300 km above the CMB for the (b) 0.0 % contour (c) -0.4 % contour, and (d) the -0.8 % contour. Scattering points show a greater preference to be close to the inside of the 0.0 % contour than to be further away. This pattern is somewhat visible for the -0.4 % contour, but scatterer distribution relative to the -0.8 % is indistinguishable from the randomly distributed synthetic data. These observations are supported by the AD-kS test values. Despite all real distributions plotting below the synthetic data patterns are still apparent and statistically relevant; for the 0.0 % contour, scatterers still show preferential distribution towards the inside edge. . . . . 125

3.27 Cumulative distribution curves for scatterers measured from the inside edge of the various LLSVP contours in SMEAN. Lines and shading as in Figure 3.22. (a) Data and means for scatterers from 0-300 km above the CMB for distances measured relative to the 0.0 % contour (solid lines), the -0.4 % contour (dashed lines), and the -0.8 % contour (dotted lines). Population distributions for scatterers between 0-300 km above the CMB for the (b) 0.0 % contour (c) -0.4 % contour, and (d) the -0.8 % contour. Scattering heterogeneities are preferentially located close to inside of the larger contours. The pattern is most obvious for the 0.0 % contour, and partly visible for the -0.4 % contour, while relative to the -0.8 % contour scattering heterogeneities show no preference for being close to the edge. This result is also demonstrated by the AD-kS test values which are lower (populations are more similar) for smaller (more negative) LLSVP contours. . . . . 126

3.28 Cumulative distribution curves for scatterers measured away from the outside edge of the +0.9 % high velocity anomaly contours in S40RTS and up to the -0.8 % LLSVP contour. Lines and shading as in Figure 3.22. (a) Distributions of scattering points at 0-300 km (solid lines), 0-100 km (dashed lines), and 100-300 km above the CMB (dotted lines). The synthetic distributions (blue lines) for all heights overlap as the synthetic scattering point distribution is independent of height. Population distributions for scatterers outside the +0.9 % contour which defines the high velocity anomalies for (b) 0-300 km, (c) 0-100 km, and (d) 100-300 km above the CMB. Scattering points close to the CMB follow a similar distribution to the randomly distributed synthetic data up to  $\sim 22^\circ$ , followed by a slower increase in scatterer frequency with distance. At greater heights, scatterers are predominantly close to the edges of the high velocity anomalies; 50 % of the scattering points occur within  $\sim 13^\circ$  of the contours. The AD-kS values support the observations that the distribution of scatterers close to the CMB looks much more similar to random than the distribution for scatterers higher up. For all heights, scatterers within the high velocity anomalies are counted as having zero distance, hence why the cumulative distributions do not start at 0 % frequency. . . . . 128

- 3.29 Cumulative distribution curves for scatterers measured away from the outside edge of the +1.3 % high velocity anomaly contours in SMEAN and up to the -0.8 % LLSVP contour. Lines and shading as in Figure 3.22. (a) Distributions of scattering points at 0-300 km (solid lines), 0-50 km (dashed lines), and 50-300 km above the CMB (dotted lines). The synthetic distributions (blue lines) for all heights overlap as the synthetic scattering point distribution is independent of height. Population distributions for scatterers outside the +0.9 % contour defining the high velocity anomalies for (b) 0-300 km, (c) 0-50 km, and (d) 50-300 km. Scattering both close to the CMB (0-50 km) and above the CMB (50-300 km) follow different patterns from the synthetic data but scatterers above 50 km show a strong preference for the edge of the high velocity anomalies; 50 % of the heterogeneities above 50 km are accounted for within 12° of the contours while only 40 % of the scatterers below 50 km occur within this distance. The AD-kS values are similar for lower and higher scattering heterogeneities demonstrating that both patterns are significantly different from the synthetics. For all heights, scatterers within the high velocity anomalies are counted as having zero distance, hence why the cumulative distributions do not start at 0 % frequency. . . . . 129
- 3.30 Predicted mantle flow at 2685 km depth, calculated using density anomalies from models (a) TX2008 [*Simmons et al.*, 2009] and (b) GyPSuM [*Simmons et al.*, 2010]. Lateral flow (blue arrows) points towards many regions in which scattering is frequently observed at great heights above the CMB (Figure 3.18), such as South Africa and western Africa. These areas are also related to strong upwelling. Other concentrations of scattering points, for example, the west coast of Central America and the southern part of South America, are related to regions of strong downwelling. Areas in which few scatterers are seen or scattering heights are low (close to the CMB) appear to correlate with regions of weak vertical mantle flow, for example the Indian and South Atlantic Oceans. Red lines mark plate boundaries. From *Forte et al.* [2013]. . . . . 134
- 3.31 Cartoon showing mantle heterogeneities in relation to the large-scale structure. Subducting slabs depositing the basaltic crustal component into the mantle which separates from the slab and is mixed into increasingly small entities and is dispersed throughout the lower mantle. Heterogeneities are more concentrated higher in the mantle where the crust is more coherent and do not show preferential locations closer to the CMB. The slab is slowly assimilated into the ambient mantle. Heterogeneities at the margin of an LLSVP are entrained by the internal convection creating piles at the edge of the strongest velocity anomalies (dashed line). Not to scale. . . . . 135
- 4.1 Sketch of raypaths from source (star) to receivers (inverted triangles). Dotted paths are corrected for crust, upper and mid mantle structure (from travel-time anomalies predicted using the tomography and crustal models), leaving only travel-time residuals related to lower mantle structure, shown as solid paths. Background colours show broad mantle structure. . . . . 139

4.2 Events and stations used in this study. Events are denoted by stars with colour indicating source depth. A full listing of earthquakes used is shown in Appendix Table D.1. Stations are marked as inverted triangles with colour indicating year of deployment. Plate boundaries (red lines) from NUVEL-1 [*DeMets et al.*, 1990] are shown along with the area covered by the Pacific LLSVP, defined by the -0.4 %  $V_P$  contour in GyPSuM [*Simmons et al.*, 2010], shown as the purple contours and shaded areas. The LLSVP contours are drawn at 2350-2500 km depth (dotted line), 2500-2650 km (dashed line), and 2650-2900 km (solid line), defined by the depth slices in the tomography model. . . . . 140

4.3 Crustal structure taken from CRUST1.0 [*Laske et al.*, 2012]. (a) Crustal thickness and (b) travel time residuals resulting from the crustal structure in each  $1^\circ \times 1^\circ$  cell. The magnitude of the negative residual is roughly correlated with crustal thickness and, therefore, to some degree, topography, except in areas of high sediment thickness, e.g. the southern coast of USA, which are significantly slower than PREM. . . . . 142

4.4 Applied crustal and mantle travel-time corrections relative to PREM for (a) the whole path and (b) at each station in USArray. Crustal structure is determined from CRUST1.0 [*Laske et al.*, 2012] and mantle structure is determined from the P-wave component of the GyPSuM model [*Simmons et al.*, 2010]. The -0.4 %  $V_P$  contour at 2650-2900 km from GyPSuM is shown by the purple line. Circles display corrections for crustal structure at the source. Black circles indicate sources deeper than 24 km to which no source-side crustal correction is applied. Triangles show corrections for crustal structure at each station in USArray, averaged over all events which use the station. The background shows corrections for mantle structure along the raypath from the surface down to 1600 km, plotted at the turning point of each ray, averaged over all rays. Mantle corrections are applied for each source-receiver combination, receiver-side crustal corrections are applied for each station, and source-side crustal corrections are applied as a DC shift to all rays in an event, for events that are shallower than 24 km depth, the thickness of the crustal layer in PREM. Smearing of mantle heterogeneity along the ray-path is apparent in Figure a as significant negative corrections are applied at ray turning points outside the tomographic extent of the Pacific LLSVP. The crustal corrections applied for each station are directly related to the crustal structure in CRUST1.0 shown in Figure 4.3. . 142

4.5 Delay times shown at turning point location and depth for two separate events. Diamonds denote early, and circles show late arrivals (by up to 5 s) indicating fast and slow velocities in the lower mantle, respectively. Delay times are corrected for crust and mantle structure from the surface to 1600 km depth. Events occurring on (a) 28/02/2010 at  $34.97^\circ$  S,  $71.69^\circ$  W at  $46.5 \pm 4.5$  km depth, and (b) on 23/04/2010 at  $37.54^\circ$  S,  $72.92^\circ$  W at  $43.1 \pm 18.3$  km depth. The two events are closely located and sample the same region of the lower mantle. LLSVP contours from GyPSuM are shown as purple lines, as defined in Figure 4.2. No source-side crustal correction is applied as both events occur below the crust. Inset shows source location as a yellow star, and ray turning points as black circles. Very similar delay-time patterns are seen for both events suggesting that the signals observed are real and not dependent on the event used or on the processing. . . . . 144

- 4.6 Location of the P-wave LLSVP boundary determined using the zero transition of travel-time residuals and trends in residuals, overlaid on tomography for the lowermost mantle from 2650 km to the CMB from GyPSuM (left colour scale). (a) LLSVP boundary at various heights (right colour scale). Solid lines demarcate the observed zero transition and dashed lines indicate where a trend towards the boundary (increasing or decreasing delay times) is observed but the actual transition (as a clear zero delay time) is not seen. The boundary of the Pacific LLSVP determined with S-wave travel-time residuals by *He & Wen* [2012] is shown (grey line), along with the -0.4 and 0.0 %  $V_P$  contours in GyPSuM (purple and black dashed lines, respectively). Three subregions of the travel-time boundary, marked by dark green lines, are shown in greater detail: (b) north-west, (c) north-east, and (d) east. . . . . 146
- 4.7 Location of the P-wave LLSVP boundary (as in Figure 4.6) from delay-time gradients, overlaid on tomography for the lowermost mantle from 2650 km to the CMB from GyPSuM (left colour scale). (a) LLSVP boundary at various heights (right colour scale). Solid lines show where the boundary is observed, and dotted lines and the grey ellipse show the region of a suspected ULVZ characterised by very high velocity gradients. The boundary of the Pacific LLSVP determined with S-waves travel-times residuals by *He & Wen* [2012] is shown (grey line), along with the -0.4 and 0.0 %  $V_P$  contours in GyPSuM (purple and black dashed lines, respectively). Three subregions of the gradient boundary, marked by dark green lines, are shown in greater detail: (b) north-west, (c) north-east, and (d) east. . . . . 147
- 4.8 Best fitting P-wave LLSVP boundary determined using travel-time anomalies in the height bin from the CMB to 2800 km depth, taken from Figure 4.6. The LLSVP boundary determined using S-waves [*He & Wen*, 2012] and the -0.4 %  $V_P$  iso-velocity contour from GyPSuM are shown as dark grey and purple lines, respectively. The region of a suspected ULVZ, indicated by a high travel-time residual gradient in the height bin from the CMB to 2800 km depth, is marked by the dotted blue line and the resolved extent is displayed by the green ellipse, as in Figure 4.10. . . . . 148
- 4.9 Location of the determined P-wave LLSVP boundary, overlaid on S-wave tomography for the lowermost mantle from 2800 km to the CMB from S40RTS (left colour scale) [*Ritsema et al.*, 2011]. (a) LLSVP boundary drawn from travel-time residuals at various heights (right colour scale). Solid lines demarcate the observed zero transition and dashed lines indicate where a trend towards the boundary (increasing or decreasing delay times) is observed but the actual transition (as a clear zero delay time) is not seen (as in Figure 4.6). (b) LLSVP boundary determined from delay-time gradients (as in Figure 4.7). Solid lines show where the boundary is observed, and dotted lines show regions of a suspected ULVZ characterised by very high velocity gradients. The boundary of the Pacific LLSVP determined with S-waves travel-times residuals is shown (grey line) [*He & Wen*, 2012], along with the -0.4 % and 0 %  $V_S$  contours in S40RTS (purple and black line, respectively). . . . . 149

- 4.10 Residual travel-times shown at turning point location and depth. Diamonds denote early, and circles show late arrivals (by up to 5 s) indicating fast and slow velocities in the lower mantle, respectively. Events occurring on (a) 31/12/2006 at 37.97° S, 71.24° W at 47 ±17.1 km depth, and on (b) 28/06/2007 at 8.01° S, 154.52° E at 10 km depth. A region of travel-time residuals with varying sign is indicated by grey shading. A region of strong, negative travel-time residuals, interpreted as the location of a ULVZ, separated from the rest of the residuals by a large magnitude gradient of the travel-time residuals, is shown by a dotted line with green shading. The -0.4 %  $V_P$  iso-velocity contours from GyPSuM at 2500-2650 km and 2650-2900 km (representing the LLSVP boundary) are shown as purple contours and shaded areas, as defined in Figure 4.2. Inset shows source (star), ray turning points (circles), and cross-section end points (triangles). Cross-sections through turning points along the red section line shown in the maps for events on (c, e, g) 31/12/2006 and (d, f, h) on 28/06/2007. The vertical scale is exaggerated by a factor of 2.7. Figures (c) and (d) show travel-time residuals as symbol colour while figures (e), (f), (g), and (h) use more saturated colour scales to highlight the strongest travel-time variations and more clearly mark changes. Dotted lines separating the fast and slow regions are picked by following pronounced changes in magnitude and sign of the travel-time residuals. Travel-time residuals on the eastern edge of the LLSVP show a sharp transition from positive to negative residuals (c, e, g), whereas on the northern edge the transition is broader, especially close to the CMB, with a sharp and straight boundary on the northern side of the transition and a complex boundary on the southern side (d, f, h). Low travel-time residuals (-0.5 to +0.5 s, and -1 to +1 s, for figures (e) and (f), and (g) and (h), respectively) are shown as white squares. For larger versions of figures c-h see Appendix Figure D.1. . . . . 151
- 4.11 Residual travel-times plotted at the turning point distance along a profile transecting the east boundary of the Pacific LLSVP (red dashed line in Figure 4.10a for rays turning in 100 km thick height bins from 2500 km above down to the CMB. Diamonds denote early and circles show late arrivals while squares show low travel-time residuals (between -0.5 and +0.5 s, also indicated by the dashed line). In each height bin, the transition from positive to negative residual travel-time occurs over a short lateral distance demonstrating the sharpness of the eastern LLSVP boundary. The position of the transition only moves along the profile slightly with changing turning point height indicating the steepness of the boundary. . . . . 152
- 4.12 Residual travel-times plotted at the turning point distance along a profile transecting the northern boundary of the Pacific LLSVP (red dashed line in Figure 4.10b for rays turning in 50 km thick height bins from 2700 km above down to the CMB. Diamonds denote early and circles show late arrivals while squares show low travel-time residuals (between -0.5 to +0.5 s, also indicated by the dashed line). In each height bin, the transition from positive to negative residual travel-time occurs over a relatively large lateral distance indicating that the boundary of the LLSVP is broader than on the eastern side (Figure 4.11) while the position of the transition from positive to negative residuals moves along the profile with changing turning point height suggesting that the boundary is also less steep than the eastern side, dipping at a shallower angle. . . . . 153

4.13	Conceptual relationship between LLSVP structure and subduction processes. (a) The observed steep (70° dip), sharp (~40 km) LLSVP boundary in the east may be caused by recently subducted slab material increasing the thermal gradient and shaping the LLSVP. (b) The shallower (26°) and more diffuse (~120 km) northern boundary, by contrast, may be due to the absence of recent subduction. From <i>Frost &amp; Rost</i> [2014, in press]. . . . .	160
5.1	Lower mantle structures interacting on both large and small scales demonstrating features similar to those resolved in this study. Subducting slabs may introduce chemically anomalous basaltic crustal material to the lower mantle which can cause scattering, while also sharpening and steepening the edges of LLSVP (thin red line) on which they may impinge, similar to that observed under Central America and the Pacific LLSVP. Internal convection within LLSVPs may drive dense compositional anomalies to the margins (the region of strongest velocity contrast is shown by the dashed black line). Weak convection may be unable to entrain heterogeneities resulting in low piles of scatterers. In contrast, stronger internal convection may more fully entrain heterogeneities and create tall piles close to the edge of the LLSVP, similar to that seen under South Africa. Without interaction with subducting slabs, the margin of the LLSVP may be diffuse (region of dashed red lines) and shallowly sloping, similar to the northern edge of the Pacific LLSVP. Regions of the lower mantle without either LLSVPs or subducting slabs may contain relatively few scattering heterogeneities, such as under the Indian and southern Atlantic Oceans. Not to scale. . . . .	166
A.1	Array configuration and array response function computed at 1 Hz and 0 s/deg slowness for AK array in Ukraine. ARF is displayed between slownesses of 0 to 10 s/deg and back-azimuths of 0 to 360°. . . . .	171
A.2	Array configuration and array response function for AS array in Australia. Calculated as in Figure A.1. . . . .	171
A.3	Array configuration and array response function for BR array in Turkey. Calculated as in Figure A.3. . . . .	172
A.4	Array configuration and array response function for BV array in Kazakhstan. Calculated as in Figure A.4. . . . .	172
A.5	Array configuration and array response function for CM array in Thailand. Calculated as in Figure A.5. . . . .	172
A.6	Array configuration and array response function for EK array in Scotland. Calculated as in Figure A.6. . . . .	173
A.7	Array configuration and array response function for ES array in Spain. Calculated as in Figure A.7. . . . .	173
A.8	Array configuration and array response function for GB array in India. Calculated as in Figure A.8. . . . .	173
A.9	Array configuration and array response function for GE array in Germany. Calculated as in Figure A.9. . . . .	174
A.10	Array configuration and array response function for IL array in Canada. Calculated as in Figure A.10. . . . .	174
A.11	Array configuration and array response function for KS array in South Korea. Calculated as in Figure A.11. . . . .	174
A.12	Array configuration and array response function for MJ array in Japan. Calculated as in Figure A.12. . . . .	175
A.13	Array configuration and array response function for WR array in Australia. Calculated as in Figure A.13. . . . .	175

C.1	Regions of potential scattering for a surface focus event (yellow star) to a receiver (red triangle) for scattering at depths from 2889 km (at the CMB) to 2589 km (300 km above the CMB) in 100 km increments. As Figure 3.4.	183
C.2	Scattering heterogeneity heights above the CMB, centred at $0^\circ$ (left) and $180^\circ$ (right) longitude, displayed in $10$ by $10^\circ$ cells as (a and b) mean scattering height in each cell, (c and d) median scattering height, (e and f) maximum scattering height. The height of each cell is shown by the tile colour and the number of scattering locations in each cell is shown by the colour of the inset circle. The $-0.4\%$ $V_S$ contour from S40RTS is shown as the black line to represent the extent of the LLSVPs. . . . .	185
C.3	Scattering heterogeneity heights above the CMB as in Figure 3.9 but excluding scattering from arrays BV and BR, centred at $0^\circ$ (left) and $180^\circ$ (right) longitude, displayed in $10$ by $10^\circ$ cells as (a and b) mean scattering height in each bin, (c and d) median scattering height, (e and f) maximum scattering height. The height of each bin is shown by the tile colour and the number of scattering locations in each bin is shown by the colour of the inset circle. The $-0.4\%$ $V_S$ contour from S40RTS is shown as the black line to represent the extent of the LLSVPs. . . . .	187
C.4	Array specific errors of signal measurements and ray-traced locations for AS array for a range of input directions, as in Figure 3.14. (a) Errors in directivity values measured using the fk F-statistic are shown at the input slowness and back-azimuth of the synthetic signal as deviations in back-azimuth from north and arrow length. Time errors are shown as coloured circles. (b) Scattering point mislocations resulting from ray-tracing shown at the input slowness and back-azimuth of the synthetic signal displayed in terms of distance and direction (green arrow) and depth (triangles). Triangles and inverted triangles indicate the the scattering point is moved shallower and deeper, respectively, by the directivity error. . . . .	188
C.5	Array specific errors of signal measurements and ray-traced locations for BV array for a range of input directions as Figure C.4. . . . .	188
C.6	Array specific errors of signal measurements and ray-traced locations for CM array for a range of input directions as Figure C.4. . . . .	189
C.7	Array specific errors of signal measurements and ray-traced locations for EK array for a range of input directions as Figure C.4. . . . .	189
C.8	Array specific errors of signal measurements and ray-traced locations for ES array for a range of input directions as Figure C.4. . . . .	189
C.9	Array specific errors of signal measurements and ray-traced locations for GB array for a range of input directions as Figure C.4. . . . .	190
C.10	Array specific errors of signal measurements and ray-traced locations for GE array for a range of input directions as Figure C.4. . . . .	190
C.11	Array specific errors of signal measurements and ray-traced locations for IL array for a range of input directions as Figure C.4. . . . .	190
C.12	Array specific errors of signal measurements and ray-traced locations for KS array for a range of input directions as Figure C.4. . . . .	191
C.13	Array specific errors of signal measurements and ray-traced locations for KU array for a range of input directions as Figure C.4. . . . .	191
C.14	Array specific errors of signal measurements and ray-traced locations for MJ array for a range of input directions as Figure C.4. . . . .	191
C.15	Array specific errors of signal measurements and ray-traced locations for TO array for a range of input directions as Figure C.4. . . . .	192

C.16	Array specific errors of signal measurements and ray-traced locations for WR array for a range of input directions as Figure C.4. . . . .	192
C.17	Array specific errors of signal measurements and ray-traced locations for YK array for a range of input directions as Figure C.4. . . . .	192
C.18	Magnitude of errors of directivity values measured using the fk F-statistic (a and b) and the scattering point mislocations resulting from ray-tracing (c and d) for each array, as in Figure 3.15 but excluding errors calculated for signals with input slownesses of 2.0 s/deg. Values are displayed as the mean (red) with 1-standard deviation error bars and the median (blue), the latter is considered more robust. Arrays are ordered by decreasing aperture from left to right. Measured (a) back-azimuth and (b) slowness errors for synthetic signals from a range of incoming directions with noise and noise levels typical of the array using values in Figure 3.13. Errors are dependent on incoming noise levels and the array configuration. (c) Lateral and (d) vertical mislocations for a typical scattering point ray-traced with the slowness and back-azimuth errors determined for that array. . . . .	193
C.19	Scattering heterogeneities relative to tomography models S40RTS (a-d) and SMEAN (e-h) [Ritsema <i>et al.</i> , 2011; Becker & Boschi, 2002]. Location and height of scattering points above the CMB compared with S40RTS for synthetic (a and b) and real (c and d) data. LLSVP iso-velocity contours (0.0, -0.4, and -0.8 % $V_S$ ) and faster velocity contours (+0.9 % $V_S$ ) at 2800 km from S40RTS [Ritsema <i>et al.</i> , 2011] are shown as purple and green lines, respectively. Location and height of scattering points above the CMB compared with SMEAN for synthetic (e and f) and real (g and h) data. LLSVP iso-velocity contours (0.0, -0.4, and -0.8 % $V_S$ ) and faster velocity contours (+1.3 % $V_S$ ) at 2850 km from SMEAN [Becker & Boschi, 2002] are shown as purple and green lines, respectively. The limit of the sampling area (Figure 3.6) is shown by the black line. . . . .	195
C.20	Tomography models overlaid with the contours used to represent the low and high velocity anomalies to which distances from scatterers are measured for S40RTS (a and b) and SMEAN (c and d). Low velocity anomalies, LLSVPs, are defined by the 0.0, -0.4, and -0.8 % $V_S$ iso-velocity contours for both models (purple lines) and high velocity anomalies are defined by the +0.9 and +1.3 % $V_S$ contours for S40RTS and SMEAN, respectively (green lines). All contours are taken from the lowermost depth slice of each model: 2800 km for S40RTS and 2850 km SMEAN. . . . .	196
D.1	Cross sections through P-wave travel-time residuals sampling the (left) eastern and (right) northern edges of the Pacific LLSVP. Caption as Figure 4.10.217	



# List of Tables

---

1.1	IMS arrays used (including Gauribidanur which is not an IMS array). Arrays have been operating from the start dates given (in Year/Julian day) to present. . . . .	23
3.1	Noise characteristics for the IMS arrays used. All values stated are the median ratios calculated for all events that show PK•KP scattering and are not contaminated by other signals. . . . .	101
3.2	Interpolation coefficients for the Anderson-Darling test used in Equation 3.5. From <i>Scholz &amp; Stephens</i> [1987]. . . . .	115
B.1	Events in PKP dataset. Dates are given in day/month/year format. . . . .	177
B.2	Phonon scattering model parameters for single layer models. The height of the upper and lower bounds of the scattering layer above the CMB are shown in columns “Bottom” and “Top”. The velocity/density scaling factor is in column “Density scaling”, RMS velocity perturbation is in column “RMS %”, and scatterer length scale is in column “Scale (km)”. . . . .	180
B.3	Phonon scattering model parameters for double layer models. Parameters are listed as in Appendix Table B.2. The lower and upper of the two layers in the model are labelled “Layer 1” and “Layer 2”, respectively. . . . .	181
C.1	Events in PKKP dataset reported in the NEIC PDE catalogue. Dates are given in day/month/year format. . . . .	197
D.1	Events in dataset reported in the REB catalogue. Events at 0 km depth are assigned a depth of 10 km before being processed. Dates are given in day/month/year format. . . . .	213



# Chapter 1

---

## Introduction

---

### 1.1 Earth Structure

Seismology is our primary tool for determining the structure of the Earth's interior. Waves from earthquakes and other seismic sources can travel through the whole of the Earth, accumulating information throughout their passage. First order geophysical calculations using properties such as the Earth's size, moment of inertia, and gravity along with mineral physics experiments demonstrated that density and seismic velocities within the Earth generally increase with depth. Other observations of seismic "shadow zones", regions relative to an earthquake in which certain waves aren't observed, and triplications, where the same wave appears to arrive multiple times, were understood as evidence of interfaces and velocity drops within the Earth, most notably from the mantle to the outer core. Studies of seismic wave travel-times at different source-receiver distances [*Jeffreys & Bullen*, 1958] led to early models of Earth velocity structure, simplified to 1 dimension, such as PREM [*Dziewonski & Anderson*, 1981]. However, travel-times are observed to be dependent on sampling location thus demonstrating that the velocity structure is not radially 1-dimensional. Large-scale velocity structure, on the order of 1000s km, is evident from regional trends in seismic travel-times. Extended waves recorded following the known body waves, the coda, indicated that this variability was present on a range of length scales [*Aki*, 1969; *Wu & Aki*, 1988]. However, this small-scale velocity structure, from 10s to 100s of km, is more enigmatic as it is often more strongly laterally variable and has a weaker influence on travel-times than large-scale velocity variations. Nonetheless, heterogeneous Earth structure at all scales is significant as it is evidence of the dynamic history of a poorly mixed system, such as the Earth's mantle. To fully understand the Earth's evolution, from its formation to the present day, we must explore all levels of its structure.

Heterogeneous velocity structure has been observed throughout the mantle but is strongest in the uppermost mantle, from the surface down to  $\sim 700$  km depth, and lowermost mantle, from the CMB up to  $\sim 600$  km above [*Becker & Boschi*, 2002; *Schuberth et al.*, 2009; *Dziewonski et al.*, 2010]. In this work I will focus on the lower mantle, from the Core-Mantle Boundary (CMB) to around 1000 km above. Both the upper and lower boundary layers of the mantle, the crust and CMB, show great complexity in terms of structural and compositional observations [*Bullen*, 1942, 1949]. These layers serve as the

limits of mantle convection thus are the temporary resting places of buoyant and dense materials, before they become entrained and possibly mixed back into the mantle. The interface between the slowly convecting silicate mantle and rapidly, turbulently convecting liquid iron outer core, the CMB, has been observed seismically to be an extremely complicated region with potential for mechanical mixing, isostatic fluctuations of the interface, chemical contamination, and differential heating, possibly resulting in partial melting [for review of lower mantle structures see *Garnero, 2000; Garnero & McNamara, 2008*]. Fully understanding this section of the Earth will be difficult and require collaboration between various disciplines in Earth Science.

The various mantle features observed on all length scales show numerous and complicated indications of interaction and interconnection. Mechanical mixing, thermal effects, and chemical contamination are all important processes in generating structures that can be observed seismically. When studying mantle structures it is important to consider how one observation is connected with the different features on other scales. In this thesis I will demonstrate seismic observations of various anomalous mantle structures and compare them with observations from mineral physics, geochemistry, and geodynamics.

### 1.1.1 Large-scale Mantle Structure

The broad, global scale velocity structure of the lower mantle displays a dominant “degree 2” structure [*Dziewonski et al., 2010*] with faster material associated with subduction separating two, large, roughly antipodal regions of anomalously slow mantle material, one centred under the Pacific Ocean and the other under Africa (Figure 1.1). These features are most conspicuous in S-wave tomographic models showing  $\Delta V_S \sim -3\%$  [*Ritsema et al., 2011*] and so are called the Large Low Shear Velocity Provinces (LLSVPs). The large scale structure of the mantle is a good indication of the overall dynamic processes that are acting. These heterogeneities, which can be detected by their effect on seismic wave speed, are likely chemically or thermally anomalous, relative to the ambient mantle. Their chemical and physical properties control their dynamic behaviour within the mantle system. By tracking and understanding these anomalies, which act as tracers, we can determine a great deal about the gross history of the Earth.

The broad-scale 3-dimensional mantle structure is that which is best resolved (Figure 1.1). These structures are more obvious than smaller structures, due to being spatially extensive, and can be observed using a larger range of seismic methods and data. The majority of our knowledge about the large-scale Earth structure comes from tomographic studies [*Woodhouse & Dziewonski, 1984; Dziewonski, 1984*]. Using combinations of body-wave travel-times, surface waves, normal modes, and full waveforms we are able create 3-dimensional models of velocity and density variations within the mantle [e.g. *Masters et al., 2000; Becker & Boschi, 2002; Panning & Romanowicz, 2006; Simmons et al., 2010; Ritsema et al., 2011; Simmons et al., 2012*]. Subducted slabs display relatively fast seismic velocities while relatively slow seismic velocities are associated with dense piles (the LLSVPs). Fast and slow velocities are often interpreted as cold and hot material, respectively, but these approximations are complicated by other properties, such as composition, which also influence wave speed. Even relatively simple dynamic models with constraints of cooling from above and heating from below are capable of replicating Earth-like struc-

tures to first order [Fowler, 1993; Moresi & Solomatov, 1995]. More complex models using Earth-like controls, such as subduction history, can generate patterns very similar to those that we observe within the Earth with seismology [McNamara & Zhong, 2005; Li & McNamara, 2013].

Regions of faster than average velocities,  $>100$  km thick, are seen descending from the surface expressions of subduction zones [Creager & Jordan, 1986]. They are interpreted as cold, dense, and stiff lithospheric slabs which fall, under the influence of positive density, towards the CMB where they reside and are seen in tomography models to have S-wave velocity fluctuations of  $\Delta V_S \sim +2\%$  and P-wave velocity fluctuations of  $\Delta V_P \sim +1\%$  (Figure 1.1). Slab progress in the lower mantle is seen to be accelerated and decelerated, respectively, by the upper-mantle transitions at 440 and 660 km depth [Fukao *et al.*, 1992, 2001], most likely as phase changes take place in the slab and the surrounding mantle, thus changing the viscosity and density structure. The seismic signature of slabs broaden with depth as the slabs slowly heat up. Tomographic and body wave studies imply that slab material reaches all the way to the Core-Mantle Boundary [Dziewonski, 1984; Creager & Jordan, 1986], where it will be heated and will equilibrate with the ambient mantle through mixing.

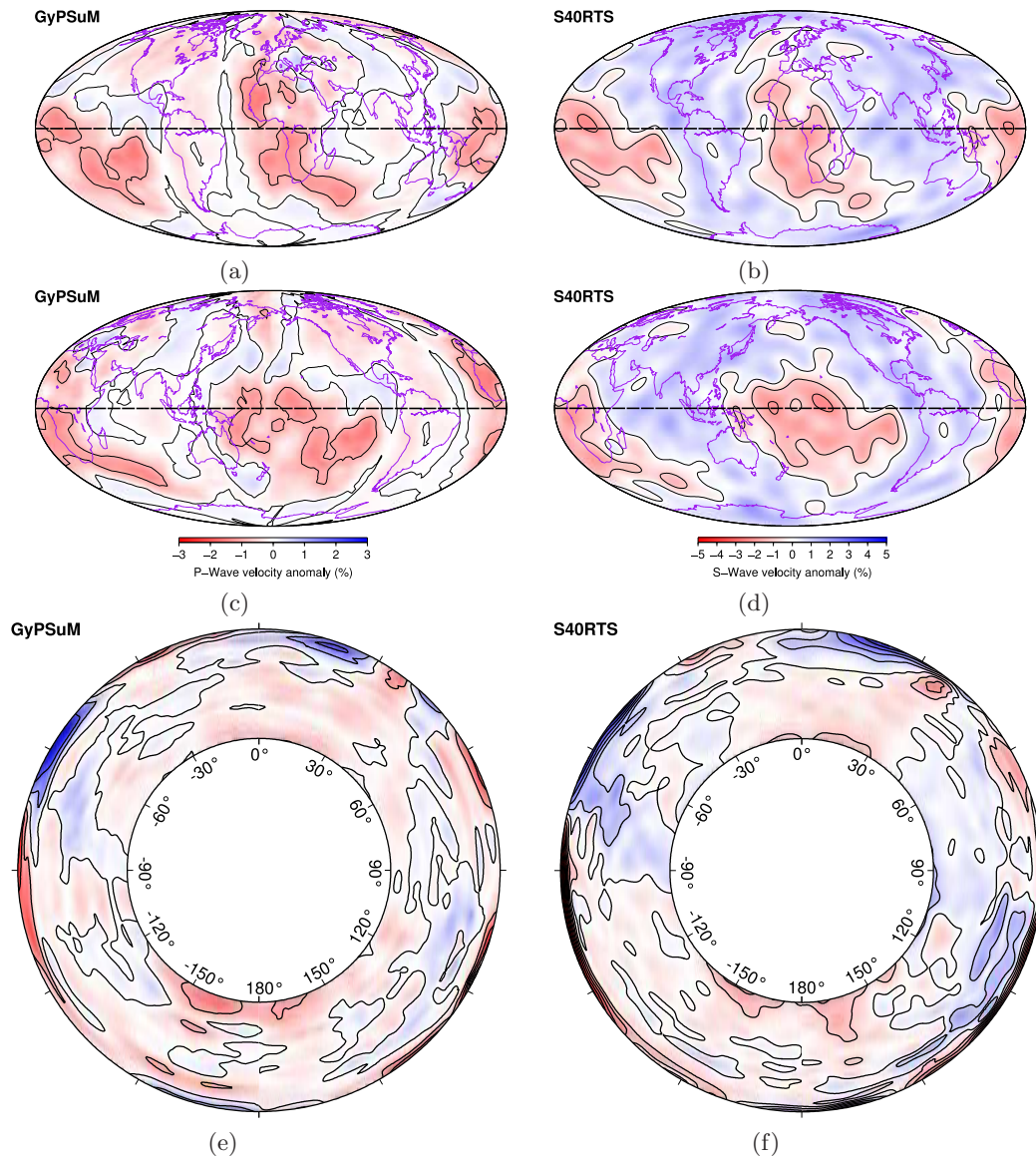


Figure 1.1: Tomographic images of the lower mantle. Lowermost mantle depth slices from P-wave tomography model GyPSuM [Simmons et al., 2010] from the CMB to 2650 km (a and c) and S40RTS [Ritsema et al., 2011] from the CMB to 2800 km (b and d). Slices are displayed centred on  $0^\circ$  (a and c) and  $180^\circ$  longitude (b and d). Contours are shown at 1 % velocity increments. Vertical slices centred on  $0^\circ$  longitude through the equator of (e) GyPSuM and (f) S40RTS tomography models from the CMB to the surface. Section line is shown by the black dashed line in Figures a-d. Colour scales and contouring as above.

Although the LLSVPs are most prominent in S-wave tomography models, they are also observed, but with a smaller velocity drop, in P-wave models with  $\Delta V_P \sim -1$  to  $-2$  % [Becker & Boschi, 2002; Simmons et al., 2011]. The lower amplitude P-wave signals of lower mantle anomalies may explain the discrepancies in the resolved structure between different P-wave models, while different S-wave models are more consistent with each other [Becker & Boschi, 2002; Lekic et al., 2012]. The two LLSVPs have different shapes; the Pacific anomaly is observed to be round with multiple peaks up to  $\sim 1000$  km above the CMB, while the African anomaly is seen to be ridge-shaped running North-South under Central Africa and East-West under Southern Africa with a dominant peak  $\sim 1500$  km above the CMB which may be connected with the Afar Rift [Becker & Boschi, 2002; Burke et al.,

2008]. One of the enigmatic features of LLSVPs is the apparent anti-correlation between S-wave and bulk-sound speed, as resolved in global tomographic images [Masters *et al.*, 2000]. Additional information from normal modes and gravity anomalies indicate that the LLSVPs are denser than the surrounding mantle [Ishii & Tromp, 1999] supporting dynamical models that also indicate increased density [Tan & Gurnis, 2005; McNamara *et al.*, 2010]. The reduced velocities, gravity anomalies, and shapes imply that these structures comprise hot and dense material. Modelling has indicated that the seismic character of these structures cannot be produced by increased temperature alone, suggesting a chemically anomalous component [Trampert *et al.*, 2004], although alternative models imply that they might be purely thermal [Schuberth *et al.*, 2009; Davies *et al.*, 2012]. Due to these observations, the LLSVPs are also referred to as Dense Thermo-Chemical Piles (DTP). I consider both descriptions valid, however, in this work I will refer to them as LLSVPs [for a review of lower mantle structures see Lay & Garnero, 2011].

More detailed seismic studies have given further evidence that these structures contain a chemically anomalous component [Ritsema *et al.*, 1997; Young & Lay, 1987; Ritsema *et al.*, 1998; Ni *et al.*, 2002; Ni & Helmberger, 2003a; Wang & Wen, 2004; Ni *et al.*, 2005; To *et al.*, 2005; Wang & Wen, 2007; He & Wen, 2012]. Body-wave studies, primarily using S-waves, have shown that the edges of the LLSVPs, where they contact the faster than average mantle, can be sharply resolved over  $\sim 50$  km from travel-time anomalies with some localised evidence for waveform effects due to the boundary (Figure 1.2) [Ritsema *et al.*, 1998; Wen, 2001; Wen *et al.*, 2001; Ni *et al.*, 2002; Wen, 2006; He & Wen, 2009, 2012]. However, the relatively low frequencies (0.008-1 Hz) that are used may limit the spatial resolution of these waves [Marquering *et al.*, 1998, 1999]. P-wave waveforms and travel-times are claimed to show little response to the African LLSVP [Helmberger & Ni, 2005], but in Chapter 4 I demonstrate that the Pacific LLSVP, at least, shows strongly varying P-wave velocity structure.

Measurements of the  $V_S$  to  $V_P$  ratio ( $R_{S,P}$ ) have been compared to equations of state from mineral physics calculations to determine the degree to which temperature and chemistry control the two different wave velocities [Robertson & Woodhouse, 1996a,b; Trampert *et al.*, 2004; Della Mora *et al.*, 2011]. The ratios observed in the lower mantle are  $>2.5$ , indicating that the velocity anomalies are at least partially the result of a compositional change, while a  $R_{S,P} < 2.5$  could be explained by a thermal change alone [Karato & Karki, 2001; Karato, 2003]. Associations with surface evidence of hot-spots and Large Igneous Provinces suggest that LLSVPs are hot, long-lived, and contribute to whole mantle dynamics [Williams *et al.*, 1998; Thorne *et al.*, 2004; Wen, 2006; Torsvik *et al.*, 2006]. Geochemical anomalies recorded in hot-spot lavas (Ocean Island Basalts) require a source region chemically distinct from that sampled at Mid-Ocean Ridges (by Mid-Ocean Ridge Basalts), referred to as the DUPAL anomaly, which is suggested to be related to the LLSVPs [Dupre & Allegre, 1983; Hart, 1984; Castillo, 1988].

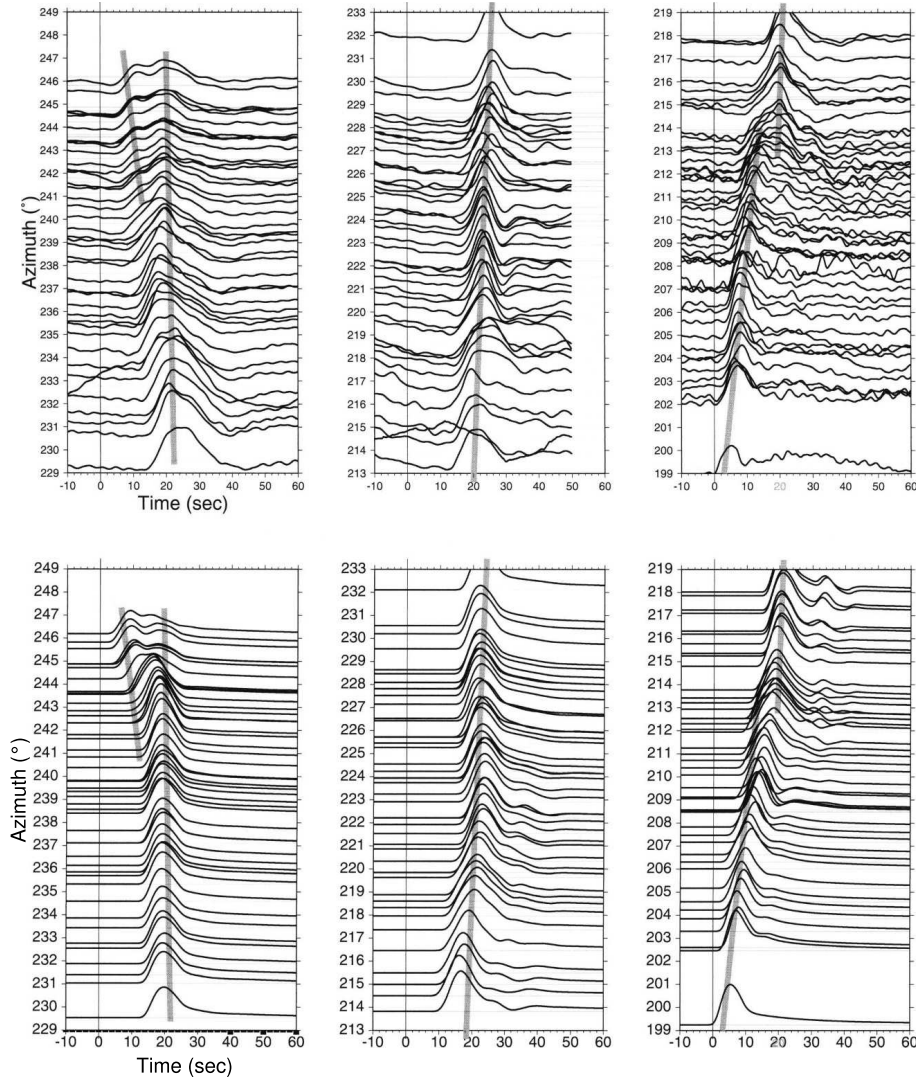


Figure 1.2:  $S_{diff}$  observed (upper) and synthetic (lower) waveforms sampling the edge of the south-eastern part of the African LLSVP, demonstrating multipathing along the boundary, thus exemplifying its sharpness. Traces are displayed as a function of azimuth from the source. From left to right, panels show the northern boundary, central region, and southern boundary of the LLSVP. Jumps in arrival time or changes in shape of  $S_{diff}$  (marked by the grey line) demonstrate that the edge of the African anomaly can be sharply resolved, which points towards a thermo-chemical origin for the LLSVPs. From *Ni et al. [2005]*

Results from waveform modelling demonstrate that the LLSVP edges show variations in slope dependent on location. For example, the African LLSVP is shown to have a steep western edge, claimed to be either overturned [*Ni et al., 2002*] or dipping at up to  $70^\circ$  but not overturned [*Wen, 2001; Wen et al., 2001; Wang & Wen, 2004; Helmburger & Ni, 2005; Wang & Wen, 2007; Helmburger et al., 2009*]. Other parts of the edge are reported to have a slope of  $\sim 28^\circ$  [*Wen, 2001; Wen et al., 2001*]. The Pacific LLSVP also shows boundaries with varying slopes, although actual values of the angle are not reported [*He & Wen, 2009, 2012*]. Geodynamic models are able to replicate the shape of the LLSVPs by modelling them as either buoyant plumes or dense piles bounded by subducting slabs. For example, the steepness and ridge-like shape of the African LLSVP can be modelled as a meta-stable plume with its density just preventing it from rising off

the CMB [Tan & Gurnis, 2005, 2007]. Other models demonstrate that the location and shape of LLSVPs can be replicated from an initial dense layer by imposing the subduction history for the past 120 Ma (Figure 1.3) [McNamara & Zhong, 2005; Tan *et al.*, 2011]. The steep sided profiles of the LLSVPs require variations in material properties: typical values stated are density and bulk-modulus increases of  $\sim 2$  and  $\sim 7$  %, respectively [Tan & Gurnis, 2005; McNamara & Zhong, 2005; Tan & Gurnis, 2007], which may fit the values determined for subducted oceanic crust [Hirose *et al.*, 1999; Kudo *et al.*, 2012]. Dynamic models have shown that subducted crustal material can accumulate to make LLSVP-like piles [Christensen & Hofmann, 1994; Brandenburg & van Keken, 2007; van Keken *et al.*, 2010]. However, this is challenged by calculations of seismic sensitivity to Mid-Ocean Ridge Basalt (MORB) in the lower mantle which indicate that it would increase seismic velocities, opposite to the pattern observed [Deschamps *et al.*, 2012], in addition to other dynamic models that claim that subducted basaltic crust would be too readily mixed and entrained to form the LLSVPs [Li & McNamara, 2013]. Alternatively, a “primordial” origin has been suggested for LLSVPs, whereby, during Earth accretion and differentiation, the mantle and core separated incompletely in a Basal Magma Ocean, leaving behind volumes of iron-enriched mantle [Becker *et al.*, 1999; Labrosse *et al.*, 2007; Lee *et al.*, 2010; Deschamps *et al.*, 2011, 2012]. Isotope studies require an untapped primordial reservoir that might have been formed as early as 400 to 500 Myr into Earth’s history [Boyet & Carlson, 2005; Carlson & Boyet, 2006] where as segregation of MORB as a source for lower mantle heterogeneities would be a continuous process [Christensen & Hofmann, 1994]. The primordial reservoir could have geochemical anomalies relative to the ambient mantle, sampling of which by hotspots would explain the geochemical deviations recorded in lavas of this type [Dupre & Allegre, 1983; Cabral *et al.*, 2013]. Incomplete separation of the iron and silicate components would also have provided a means to enrich the lower mantle in iron, a scenario suggested by some mineral physics models to also explain certain small-scale mantle structures (see Chapter 1.1.2) [Mao *et al.*, 2004, 2006; Wicks *et al.*, 2010].

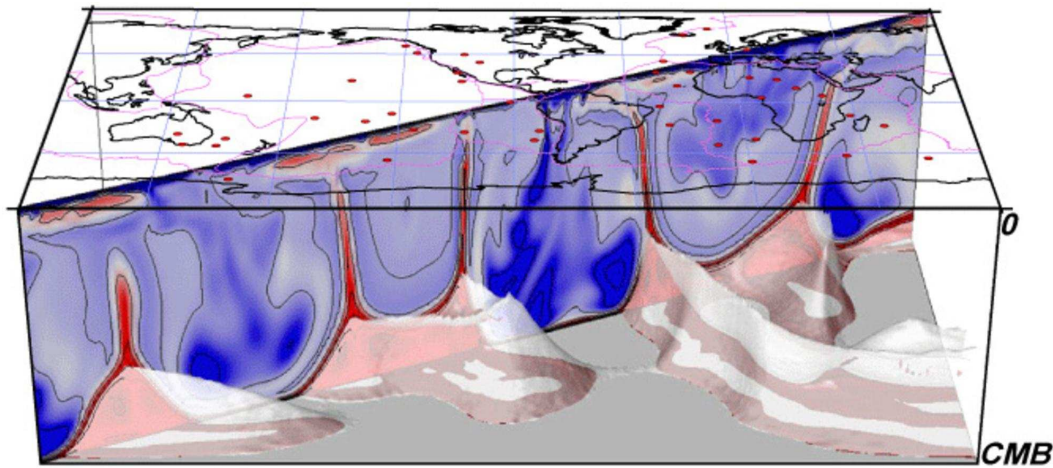


Figure 1.3: Mantle structures formed by subducting material interacting with an initial dense layer at the CMB. Subduction has an imposed plate history. The cross section demonstrates the thermal structure of the mantle where subducted material is cold (blue) and dense piles are hot (red). The 3-dimensional image displays the shapes into which the dense layer is forced by the subduction. The mantle dynamics generate both a steep-sided ridge structure under Africa and a more dome-like structure under the Pacific, separated by slabs. Plumes rising from the peaks of the dense piles could be the source of hotspots. Real hotspot locations and plate margins are marked by red circles and lines, respectively, on the top map surface. From McNamara & Zhong [2005].

Although there is much evidence and there are many geodynamical and mineral physics models which all suggest that LLSVPs are thermo-chemical structures, other sets of models are able to replicate the LLSVPs using thermally anomalous material alone [Schuberth *et al.*, 2009; Davies *et al.*, 2012]. I accept that it is necessary to test all possible hypotheses, but in this case I believe that, based on the seismological observations of a sharp LLSVP boundary, the magnitude of the velocity drops, and the spatial association with Ultra Low Velocity Zones (which are discussed fully in Chapter 1.1.2), as well as the additional observations of increased density and spatial association of LLSVPs with chemically anomalous geochemical measurements, the thermo-chemical hypothesis for the origin of LLSVPs is better supported than that of a purely thermal origin.

Tomographic studies are very effective at displaying the heterogeneities within the Earth on larger length scales. However, variable over- and underconstrained sampling, the reliance on long-period data, damping parameters, regularisation, and smoothing mean that these models are not able to accurately resolve scales smaller than  $\sim 1000$  km [Boschi & Dziewonski, 1999; Becker & Boschi, 2002]. Resolution can be improved by performing regional tomographic inversions, but again, these are limited by data availability and are often unable to resolve the lowermost mantle well. Heterogeneities of length scales smaller than  $\sim 1000$  km can be better resolved using other techniques discussed Chapter 1.4.

### 1.1.2 Small-scale Heterogeneities

Alongside the large scale velocity structures within the mantle, there is much evidence for smaller velocity anomalies on scales ranging from 100s to 10s km, and possibly smaller. Especially the smallest scale heterogeneities are unlikely to be thermal in origin as, given

the thermal diffusivity of mantle materials, small thermal anomalies would rapidly equilibrate in the mantle [Olson *et al.*, 1984; Manga & Jeanloz, 1996; Becker *et al.*, 1999; Turcotte & Schubert, 2002]. These smaller structures may be generated by mantle mixing or chemical exchange and so studying their physical nature and dynamic behaviour will elucidate larger scale processes as well.

The most obvious evidence for small heterogeneities within the Earth that is visible in the high frequency seismic wavefield ( $\sim 1$  Hz) are strong coda phases, additional energy following the direct arrivals [Aki, 1969; Earle & Shearer, 2001; Rost *et al.*, 2006b] (Figure 1.4). This energy is mainly generated by scattering of the direct seismic wavefront (the processes are explained in detail in Chapter 1.3). The relation between the size of the heterogeneity and the wavelength of the incoming wave controls the type of scattering. There is evidence for heterogeneities scattering waves of all wavelengths, to some degree, throughout the crust and entire mantle [Wu & Aki, 1988; Hedlin *et al.*, 1997]. Other more focussed studies using high frequency data have observed a range of small and laterally discontinuous velocity deviations from 1-dimensional Earth models, indicating both velocity increases and decreases.

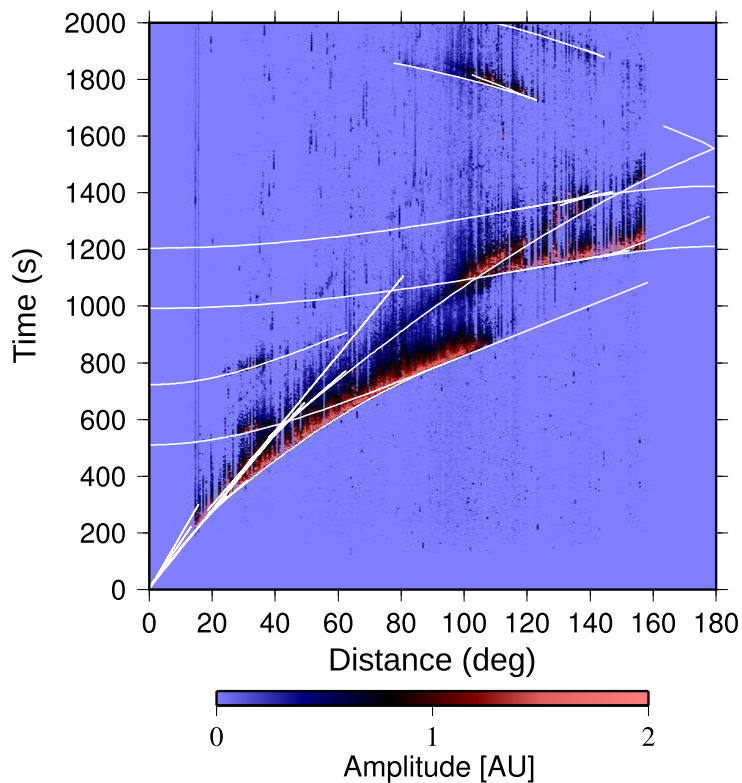


Figure 1.4: Amplitude of the global (vertical) short period wavefield processed using a 10<sup>th</sup> root Vespa with an additional noise gate to suppress noise. Overlay indicates the arrival times of the major phases calculated with PREM. Major phases are represented by clear high amplitude arrivals while the additional lower amplitude signals following and preceding these are indicative of scattering generated by small-scale heterogeneities within the crust and mantle. From Rost *et al.* [2006b].

Regional observations of a discontinuity  $\sim 100$  to  $\sim 300$  km above the CMB marking the top of a layer of increased seismic velocities have been associated with the relatively fast regions of the lowermost mantle between the LLSVPs [for review see Cobden & Thomas,

2013]. An additional arrival is sometimes seen to precede phases reflecting from the CMB (Figure 1.5). This phase is interpreted as a reflection from a shallower interface, indicative of a sharp increase in the velocity gradient which has been termed the  $D''$  discontinuity (a definition distinct from the  $D''$  region, a term often used to mean the lowermost 200 km of the mantle). The mantle beneath the discontinuity has also been seen to be anisotropic [Cormier, 1999; Thomas *et al.*, 2002; Ford *et al.*, 2006; Vanacore & Niu, 2011; Nowacki *et al.*, 2010, 2012]. The  $D''$  discontinuity is most often observed in seismically fast parts of lower mantle tomography models which are interpreted as being colder than the rest of the mantle. The discovery of a phase transition from perovskite (the most prevalent lower mantle mineral) to post-perovskite under high pressures and relatively low temperatures has provided a convenient physical explanation for this seismic phenomenon [Murakami *et al.*, 2004; Oganov & Ono, 2004] regarding both the velocity structure and the anisotropy. This mineral fits the required velocity increases and is also strongly anisotropic which may be able to match seismic observations of lowermost mantle anisotropy [Wookey *et al.*, 2005; Brodholt *et al.*, 2009; Nowacki *et al.*, 2010, 2012]. The Clapeyron slope measured for post-perovskite [Murakami *et al.*, 2004; Oganov & Ono, 2004; Catalli *et al.*, 2009] indicates that the transition occurs under relatively cold conditions and high pressures. The  $D''$  discontinuity is almost exclusively observed in faster regions of the mantle which are commonly associated with subduction, therefore, it is thought that depression of the lower mantle temperature gradient by slab material is required for the perovskite to post-perovskite phase transition to occur [Hernlund *et al.*, 2005; Lay & Garnero, 2007].

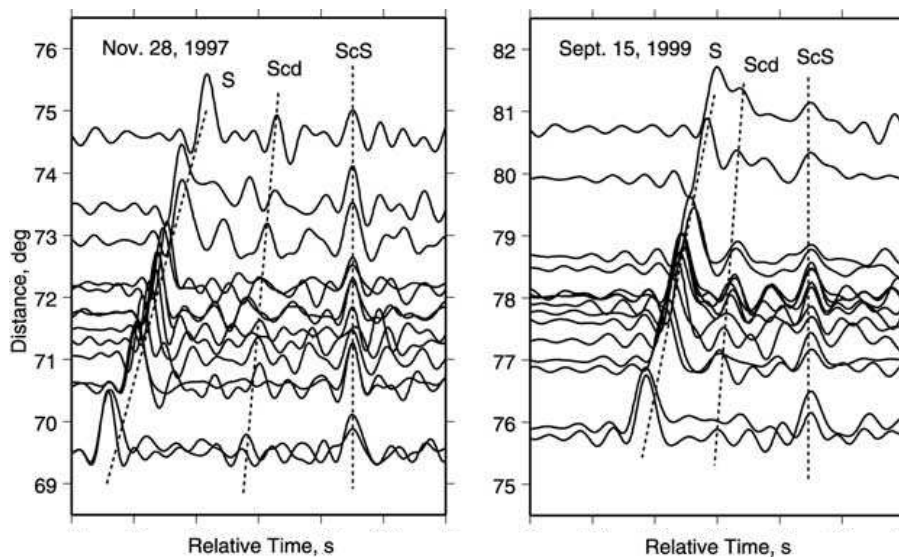


Figure 1.5: Observations of  $D''$  reflections ( $Scd$ ) producing precursors to  $ScS$  from events sampling under the southern coast of Central America. The different residual time between  $Scd$  and  $ScS$  for the two events is indicative of topography on the  $D''$  discontinuity. From Thomas *et al.* [2004a].

The discontinuity has been shown to vary in height laterally [Young & Lay, 1987; Wyssession *et al.*, 1998; Thomas, 2002; Thomas *et al.*, 2004a; Thorne *et al.*, 2007] and the mantle beneath shows velocity increases of  $\Delta V_S \sim 1$  to 3 % and smaller magnitude  $\Delta V_P \sim 1$  to 2 % [Weber, 1994; Thomas *et al.*, 2004a; Kito *et al.*, 2007]. Anti-correlation of  $\Delta V_P$  and  $\Delta V_S$  have also been observed ( $\Delta V_P$  decreases with  $\Delta V_S$  increases) [Chaloner *et al.*,

2009]. Often, further complexity is seen with velocity increases overlying velocity decreases [Thomas *et al.*, 2004b; Hernlund *et al.*, 2005; Hutko *et al.*, 2006; Lay *et al.*, 2006; Hutko *et al.*, 2009] and observations of the height of the discontinuity varying laterally within a single study region [Thomas *et al.*, 2002; Thomas, 2002; Thomas *et al.*, 2004b,a; Wallace & Thomas, 2005]. Observations of double-layered D'' discontinuities could be explained by cold material crossing the phase transition to post-perovskite and then again back into the perovskite stability field as the mantle temperature increases towards the CMB [Hernlund *et al.*, 2005], or by post-perovskite overlying chemically anomalous lower velocity material [Avants *et al.*, 2006b; Lay *et al.*, 2006]. Alternatively, the D'' discontinuity could be generated by a sharp change in anisotropy in the lowermost mantle [Brodholt *et al.*, 2009; Thomas *et al.*, 2011]. This anisotropic fabric has been suggested to be inherited from subducting slabs while the crystallographic changes occur in situ [Dobson *et al.*, 2013] and could be indicative of flow direction at the CMB.

Although observations of the D'' discontinuity are quite prevalent, there are distinct regions which do not show any evidence of velocity variations in the lower mantle [Weber, 1993; Krüger *et al.*, 1995]. These results indicate a process that is either thermally or compositionally controlled for both discontinuity magnitude and sharpness.

Seismic data give evidence for thin, regional low velocity layers known as Ultra Low Velocity Zones (ULVZs). The velocity drops are more drastic than the equivalent increases for the D'' discontinuity, reported as being up to  $\Delta V_S \sim -30\%$  [Revenaugh & Meyer, 1997; Helmberger *et al.*, 1998, 2000; Reasoner & Revenaugh, 2000; Ni & Helmberger, 2001; Rondenay & Fischer, 2003; Avants *et al.*, 2006a; Zhang *et al.*, 2009; Hutko *et al.*, 2009; Rost *et al.*, 2010a; Song *et al.*, 2010; Vanacore & Niu, 2011; To *et al.*, 2011; Cottaar & Romanowicz, 2012; Sun *et al.*, 2013] and  $\Delta V_P \sim -10\%$  [Garnero & Helmberger, 1995, 1996; Wen & Helmberger, 1998; Vidale & Hedlin, 1998; Garnero & Helmberger, 1998; Thomas *et al.*, 1999; Garnero & Jeanloz, 2000; Wen, 2001; Luo *et al.*, 2001; Niu & Wen, 2001; Thorne & Garnero, 2004; Rost & Garnero, 2004, 2006; Sun *et al.*, 2007b; Xu & Koper, 2009; Thomas *et al.*, 2009; Vanacore *et al.*, 2010; Thorne *et al.*, 2013b; Jensen *et al.*, 2013] with density increases of up to 10% [Havens & Revenaugh, 2001; Rost & Revenaugh, 2003; Rost *et al.*, 2005, 2006a; Thorne *et al.*, 2013a]. These values are consistently observed in the majority of studies with very few reporting other best fitting parameters. ULVZs are identified from observations of precursors to core reflected phases (ScS, PcP, ScP), and from strong travel-time delays of core diffracted phases ( $SP_{diff}KS$ ,  $S_{diff}$ ,  $P_{diff}$ ) (for discussion of  $P_{diff}$  see Chapter 4). Other studies, such as those using scattered waves, which are observed as precursors to PKP (see Chapter 2) and precursors to PKKP (see Chapter 3), are often unable to give specific velocity drops but indicate sharp, large magnitude velocity contrasts which are required to cause scattering (explained in Chapter 1.3) [Cleary & Haddon, 1972; Doornbos & Husebye, 1972; King *et al.*, 1973; Haddon & Cleary, 1974; Doornbos, 1974, 1976; Earle & Shearer, 1997; Earle, 2002; Miller & Niu, 2008; Rost & Earle, 2010; Ivan & Cormier, 2011; Frost *et al.*, 2013]. ULVZ thicknesses are reported between  $\sim 10$  to  $\sim 100$  km, and exceptionally up to 300 km, and lateral dimensions are small, on the order of 100s km [Helmberger *et al.*, 2000; Wen, 2001; To *et al.*, 2011; Sun *et al.*, 2013]. Thinner ULVZs have been resolved but are at the resolution limit for seismic studies of this type [Rost *et al.*, 2010a]. ULVZs may exist that are too thin to be

resolved, which might instead be detected by scattering studies. The frequencies involved in the scattering studies are indicative of individual heterogeneities on the order of 10 km and smaller (discussed in Chapters 2 and 3). Collections of these small heterogeneities may make up ULVZs.

Despite the prevalence of ULVZs, there are areas of the CMB where non-observations are reported, or areas where evidence for ULVZs is discontinuous and changes rapidly [Castle & van der Hilst, 2000; Castle *et al.*, 2000; Persh *et al.*, 2001; Rost & Thomas, 2010; Rost *et al.*, 2010b,a; Frost *et al.*, 2013]. It has been noted that ULVZs are predominantly detected in the vicinity of LLSVPs and often close to their edges [for overview see McNamara *et al.*, 2010], with few observations of ULVZs in regions that appear seismically fast in tomographic maps (Figure 1.6).

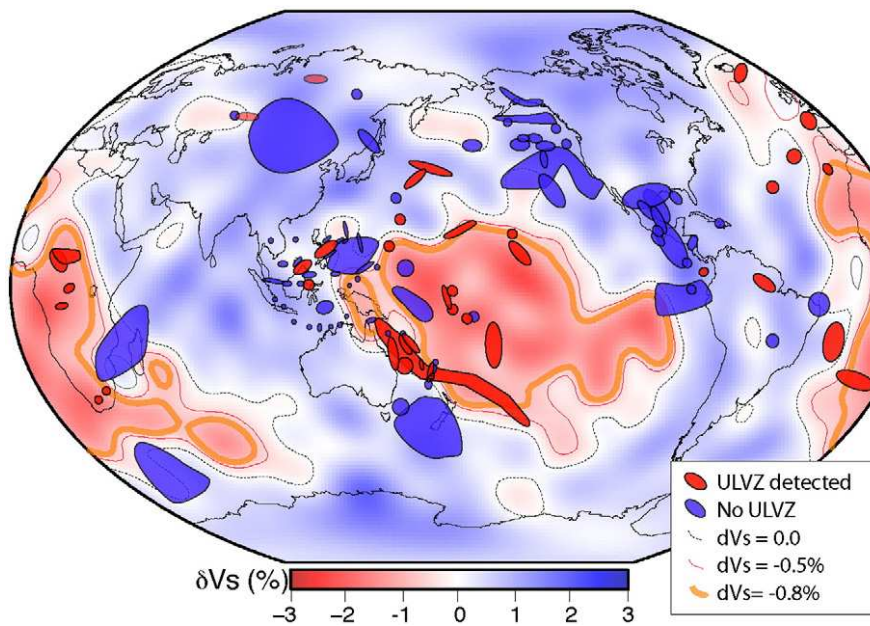


Figure 1.6: Detections (red) and non-detections (blue) of ULVZs in studies up to 2010, overlaid onto S20RTS [Ritsema *et al.*, 2011]. The majority of the ULVZ observations are in or around regions of slower than average seismic velocities, the LLSVPs (light red). By contrast, the non-observations are mainly in regions associated with subduction (light blue), such as the west coast of the Americas and the east coast of Asia. From McNamara *et al.* [2010].

The distribution of ULVZs, the observed  $\Delta V_S$  to  $\Delta V_P$  ratio on the order of 3:1, and the density increase have been used to infer the cause of the low seismic velocities. Two major competing theories exist: solid state enrichment of mantle perovskite with iron, and partial melt. The ratio of  $\Delta V_S$  to  $\Delta V_P$  is the main argument for ULVZs comprising partially molten mantle material and this ratio has been replicated in physical melting experiments [Williams & Garnero, 1996; Berryman, 2000; Lay *et al.*, 2004; Beuchert & Schmeling, 2013]. Given the association with LLSVPs, which are thought to likely be hotter regions of the mantle, partial melt seems like an attractive hypothesis. However, restricting a layer of fluid to a specific region of the CMB with the heights and steepnesses reported in some seismic studies would be difficult for both a positively or negatively buoyant melt, but it might be possible if melt only occurred at grain boundaries or was influenced by mantle convection [Rost *et al.*, 2005; Hernlund & Tackley, 2007; McNamara *et al.*,

2010; *Hernlund & Jellinek*, 2010; *Thomas et al.*, 2012; *Wimert & Hier-Majumder*, 2012]. Additionally, some mineral physics studies imply that partial melting of mantle peridotite would not correctly fit the  $\Delta V_S$  to  $\Delta V_P$  ratio [*Li & Weidner*, 2013]. Alternatively, solid state enrichment of (Mg,Fe)O with iron, possibly sourced from the outer core, is reported to match seismic observations of ULVZs [*Knittle & Jeanloz*, 1989, 1991; *Mao et al.*, 2006; *Wicks et al.*, 2010] and has the added advantage that the material would not flow away as rapidly. However, recent data imply that the degree of iron enrichment required may be so high as to cause partial melting (Wicks, unpublished). A purely thermal origin is not suggested for ULVZs as the temperature difference required would be unreasonably large ( $\sim 1000^\circ$  K) [*Wen*, 2001] and it is unlikely that such small structures would be able to maintain a large temperature anomaly [*Becker et al.*, 1999]. Chemical contamination of the mantle by assimilation of slab material has been proposed as a source of ULVZs and shown to be dynamically possible [*Tackley*, 2011], although this may not replicate the desired velocity drops [*Deschamps et al.*, 2012]. Solidification of the inner core may lead to expulsion of the contaminating light element, possibly silicon, which could rise and then be included into mantle rocks at the CMB changing their velocity [*Buffett et al.*, 2000], but there is little additional evidence for this.

ULVZs are often reported to be ridge- or dome-like in shape (Figures 1.7) [*Helmlberger et al.*, 2000; *Sun et al.*, 2013; *Frost et al.*, 2013] although resolution of the 3-dimensional shape is limited. From modelling density increases of the ULVZs relative to the lower mantle and their aspect ratios, it has been shown that the majority of ULVZs require dynamic support to maintain their heights [*Bower et al.*, 2011]. LLSVPs show internal convection due to viscous coupling to the external mantle convection and heat from the core [*McNamara et al.*, 2010]. The flow travels laterally along the CMB from the LLSVP centre to the margins, rises up the side, and descends back into the centre. This flow has been modelled to concentrate denser material at the edges and, dependent on the magnitude of the density contrast with the surrounding material, wholly or partially entrain the ULVZ into the upstream along the margin [*McNamara et al.*, 2010; *Hernlund & Jellinek*, 2010]. This dynamic support will help the dense material to achieve a greater height than possible through viscosity alone (Figure 1.7b). ULVZ height is also controlled by the amount of material available and so strong flow in areas of concentrated ULVZ material may allow even taller structures to be created [*Bower et al.*, 2011].

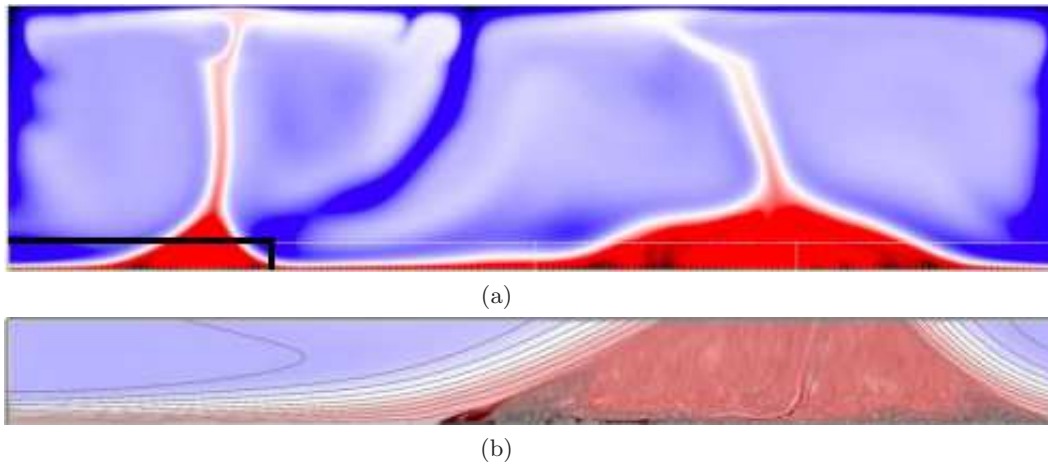


Figure 1.7: Dynamic model of dense convecting LLSVPs, the locations of which are forced by the subducting material, with an initial dense layer to simulate ULVZs. (a) Thermal structure of the whole mantle from the surface to the CMB. Cold material (blue) subducts to the CMB, is then heated from below, equilibrates with the ambient mantle, and rises back to the surface. Hot, dense piles (red) convect through viscous entrainment with the whole mantle convection. (b) Compositional and thermal structure in a section of the lowermost 289 km of the mantle (the area within the black box in in bottom left of Figure a). Subducted material, piles, and ULVZ material are indicated by blue, red, and dark red regions, respectively. The dense ULVZ material is partially entrained into the LLSVP convection and accumulates at the LLSVP edge. From McNamara et al. [2010].

Variations in travel-time measurements of a range of seismic phases (e.g. P, PcP, and PKP branches) have revealed undulations on the Core-Mantle Boundary. Although this has been studied in detail there is disagreement between results from different studies with a range of lateral and vertical length-scales resolved. This may be indicative of procedural errors or could be a real observation demonstrating that the interface has multiple scales of structure simultaneously. The most reported values are  $\pm 100$  to  $\pm 200$  m vertical variation over  $\sim 10$  km laterally [Doornbos, 1978, 1980; Menke, 1986; Vidale & Benz, 1992; Earle & Shearer, 1997], often described as CMB roughness, and  $\pm 5$  km vertically over 1000s km laterally [Poupinet et al., 1993; Sze & van der Hilst, 2003; Soldati et al., 2012], described as CMB topography. Dynamic modelling of distributions of dense material and variable upwelling and downwelling within the mantle also suggest CMB topography on a range of scales [Youngs & Houseman, 2007; Hernlund & Tackley, 2007; Lassak et al., 2010]. LLSVPs show broad upwarping of the CMB resulting from LLSVP material being hotter than ambient mantle, and localised downwarping at the boundary with the ambient mantle as a result of the very dense ULVZs predicted at these locations (Figure 1.8) [Lassak et al., 2010].

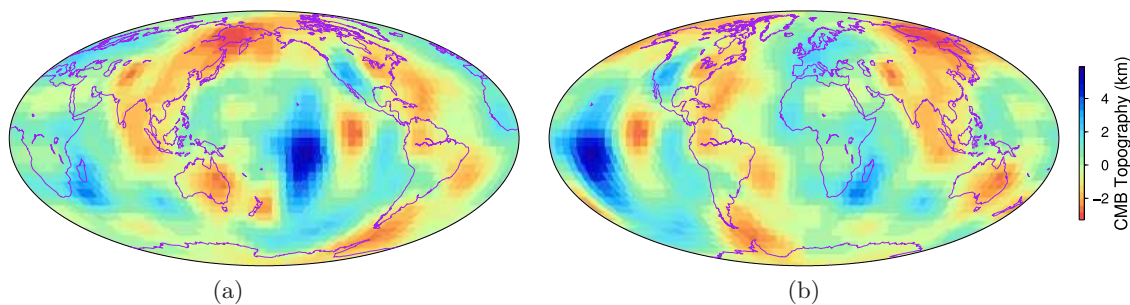


Figure 1.8: Core-Mantle Boundary topography from a joint tomographic and geodynamic inversion of P-wave travel-time data. The CMB is depressed (red colours) beneath regions of subduction, such as the edge of the Pacific, and upwarped (blue colours) beneath LLSVPs supporting observation that these structures are regions of upwelling. From Soldati et al. [2012].

## 1.2 Travel-times and Waveforms

The primary way that seismic waves can be used to study the Earth’s interior is by measuring variations in seismic travel-time, elucidating changes to the velocity structure along the wave path. Velocities are indicative of material properties in terms of bulk modulus  $K$ , shear modulus  $\mu$ , and density  $\rho$ , which are affected by the chemistry and temperature of the material. Materials whose properties are anisotropic will lead to travel-time variations which are dependent on the direction of wave propagation. The material properties affecting the seismic wavespeed, the bulk and shear moduli, can vary independently of each other. Therefore, a change in chemistry or temperature may affect the P- and S-wave velocities differently. The relationship between P and S wave velocities can be used to infer material properties. The seismic waveform is also dependent on the velocity of the material through which it travels. Varying velocity structure can lead to dispersion or convergence of the wavefront, the superposition of which affects the shape of the wave. By searching for these deviations of wave properties we can study the material through which it has passed.

Expected travel-times for waves can be easily predicted based on approximation of the wavefront to a ray (as discussed in Chapter 1.4.2) and application of Snell’s law to simple 1-dimensional models. Measurements of travel-times from seismic observations can then be compared with the predictions to determine whether the path being sampled through the Earth is faster or slower than the model. However, as it is already known that the Earth is laterally heterogeneous and 1-dimensional models are only approximations which fit a globally averaged structure, as is made clear in the definition of PREM [Dziewonski & Anderson, 1981], we can determine more information about the Earth by comparing measurements with tomography models which then reveals the difference between large and small scale velocity structure. Travel-time anomalies are representative of the velocity anomalies integrated along the ray path through the Earth. However, multipathing and the Fresnel zone (Equation 1.19) of the wave (discussed in more detail in Chapter 1.5.3) may mean that the travel-time anomaly includes the effects of structure away from the ray-theoretical path. Using higher frequency waves reduces the likelihood of either of these situations and restricts the sampling to a smaller volume around the ray-path [Marquering et al., 1998] so that delay times can be attributed to velocities in a specific region of the

Earth.

Measurements of travel-times have been used extensively to map some of the larger scale structure within the Earth, most notably the Large Low Shear Velocity Provinces (as in Chapter 4), as well as small scale structure close to the CMB (such as ULVZs) using diffracted paths. The large scale velocity anomalies such as LLSVPs may only have fairly small velocity reductions (compared to ULVZs) on the order of a few per cent [*Ritsema et al.*, 1998; *Ni & Helmberger*, 2003b; *Wang & Wen*, 2007] but are sufficiently large to significantly affect the passage of waves through them. Measuring travel-time anomalies associated with paths traversing the LLSVPs at various source-receiver distances has given information on how the velocity structure changes with height, from the slowest velocities near the CMB ( $-12\% \Delta V_S$ ) to relatively faster velocities ( $-3\% \Delta V_S$ ) at 700 km above the CMB [*Ritsema et al.*, 1998; *Wen*, 2001; *Ni & Helmberger*, 2003b; *He & Wen*, 2009, 2012; *Thorne et al.*, 2013b]. Core-diffracted paths, such as  $SP_{diff}KS$  and  $P_{diff}$ , are sensitive to structure at the CMB and just shallower and deeper, dependent on the wave frequency. The travel-time anomalies recorded by these phases are some of the best sources of high resolution information about the velocity structure of the lowermost mantle and have been used to study large-scale [*Wyssession et al.*, 1992; *Wyssession*, 1996] and small-scale structure [*Garnero & Helmberger*, 1995, 1998; *Wyssession et al.*, 1999; *Helmberger et al.*, 2000; *Ni & Helmberger*, 2001; *Rost*, 2003; *Rost & Garnero*, 2006; *Ford et al.*, 2006; *Rost et al.*, 2010b; *Cottaar & Romanowicz*, 2012; *Jensen et al.*, 2013]. By selecting specific paths and source-receiver distances we can restrict our analyses to a given phase of interest and use travel-time measurements to probe specific regions of Earth structure.

Although the ray approximation is valid for measuring travel-times, when considering the waveforms, the shape of the wave, the whole of the wavefield becomes important. The wavefield recorded at a single station is the integration of the effects of all velocity variations along and around the path from the source to the receiver, the area within the wave’s sensitivity kernel [*Liu & Tromp*, 2006]. Refraction by heterogeneities can cause focussing and defocussing of seismic waves, increasing and decreasing amplitudes, respectively [*Schweitzer et al.*, 2002].

Waves sampling inside the first Fresnel zone can arrive within half a cycle of the direct path and thus interfere with the signal (discussed in more detail in Chapter 1.5.3). For a ray that travels along a boundary between materials of differing velocities with its Fresnel zones sampling both inside and outside, the part of the wavefront propagating inside the slower region will be delayed. This energy, which under normal circumstances would be included in the main wavelet, will be delayed relative to the main wavelet and interfere with it, broadening the peak [*Schweitzer et al.*, 2002]. As this energy will not interfere constructively, the main wavelet will also have a lower amplitude than normal (Figure 1.9). Waves sampling further into or further out of the slower region will have a longer (slower) path which results in separation of the inside and outside waves, generating two distinct arrivals at the receiver. The process of a wave taking more than one route from source to receiver is known as “Multipathing” and is indicative of contrasts in seismic velocities.

The distance over which a wave shows multipathing can be used to indicate the sharpness of, and velocity contrasts across, the boundary. Models of appropriate lateral velocity structures can be created by calculating synthetic waveforms which are matched to the

data (Figure 1.2). This procedure has been used extensively to map the edge of the LLSVPs [Ritsema *et al.*, 1997; Wen, 2001; Wen *et al.*, 2001; Ni *et al.*, 2002; Wang & Wen, 2004; Ni *et al.*, 2005; To *et al.*, 2005; He & Wen, 2009, 2012; Thorne *et al.*, 2013b]. These studies indicate that the LLSVPs tend to have sharp boundaries on the order of 50-100 km wide as well as revealing the slope of the edges which vary between 28 and 70°, dependent on location.

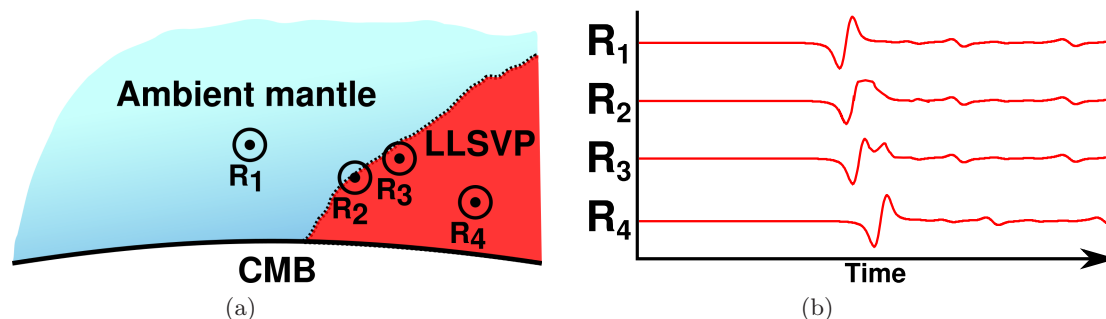


Figure 1.9: (a) Sketch of multiple rays ( $R_{1-4}$ ) and associated Fresnel Zones (dots and surrounding circles, respectively) sampling both ambient mantle, the boundary with an LLSVP, and the LLSVP itself. (b) Sketch seismograms of associated travel-time and waveform effects demonstrating multipathing as wavelet broadening ( $R_2$ ) and multiple arrivals ( $R_3$ ). These phenomena demonstrate varying degrees to which part of the wavefront is delayed before interfering with the main wavefront.

Techniques such as these which address the behaviour of wave travel-times are invaluable for studying the velocity structure of the Earth, particularly of larger scale anomalies with relatively small velocity contrasts and small-scale anomalies with large velocity contrasts. A wave has to travel at a different speed for a sufficient distance to accumulate a measurable travel time signature or waveform anomaly and so the magnitude of a structure that can be resolved is dependent on our ability to resolve travel-time. Nonetheless, in the case of larger seismic networks it becomes easier to observe regional trends in travel-time anomalies across the array. In Chapter 4 I analyse travel-time anomalies recorded in high frequency P- and  $P_{diff}$  waves to resolve the edge of the Pacific LLSVP.

### 1.3 Scattered Waves

Scattering, the process by which a wavefront is deflected and dispersed by a heterogeneity in its path, is observed in many physical systems. Waves will interfere with structures of a scale length comparable to the wavelength of the wave. Scattering within the Earth was first recognised by study of the coda following the direct P-wave [Aki, 1969], and of amplitude fluctuations of a wavefront across an array [Aki, 1973]. Scattering was further recognised through study of precursors to PKP, a phase in which a P-wave travels through the mantle, outer core, and again through the mantle back to the surface. These precursors could not be adequately fit by other hypotheses of: reflections from outer core discontinuities [Bolt, 1962], diffraction from the PKP caustic [Jeffreys, 1939], or dispersion within the F region [Gutenberg, 1958]. PKP precursors were instead explained by scattering from small heterogeneities close to the CMB on either the source or receiver side of the core [Cleary & Haddon, 1972; Doornbos & Husebye, 1972; King *et al.*, 1973; Doornbos & Vlaar, 1973; Haddon & Cleary, 1974; Wright, 1975]. PKP precursors are covered in greater detail

in Chapter 2. This model of lower mantle heterogeneities was then applied to precursors to PKKP, demonstrating further evidence for deep mantle scattering [Doornbos, 1974; Chang & Cleary, 1978; Doornbos, 1980; Chang & Cleary, 1981]. Precursors to PKKP are analysed in Chapter 3. Other observations have shown scattering due to downgoing slabs from the surface [Castle & van der Hilst, 2003; Rost *et al.*, 2008] and crustal material in the lower mantle [Miller & Niu, 2008; Vanacore *et al.*, 2010]. Study of the seismic wavefield has shown that scattering is strongest in the crust and upper mantle with an additional component of scattering from the lowermost mantle [Wu & Aki, 1988; Hedlin *et al.*, 1997; Shearer & Earle, 2004]. Scatterers can be treated as fluctuations of velocity and/or density (although in scattering literature the elastic parameters are often defined in terms of Lamé parameters) within the material through which the wave propagates [Chernov, 1960] and modelling of scattered seismic waves has been used to determine the elastic parameters, density, and size of the causative heterogeneities.

The scattering process can be treated as either a series of successive scattering events, known as multiple scattering [Chernov, 1960], or as a single scattering event, known as the Born approximation [Miles, 1960; Knopoff & Hudson, 1964]. The Born approximation is valid when the scattered wavefield is small compared to the incident field [Sato & Fehler, 2008]. Scattering media can be described as either a collection of random heterogeneities, generating stochastic scattering, or as a collection of discrete heterogeneities at specific locations, generating deterministic scattering. Array analysis (see Chapter 1.4) at various points throughout a P-wave coda has demonstrated the evolution of the wavefield [Sato & Fehler, 2008]. The direct P-wave is coherent with a single maximum direction and the early coda also has a similar single maximum direction, but the later coda is incoherent with no single maximum direction. This indicates that the early P-coda is dominated by single scattering and so the Born approximation is valid, and the later coda comprises multiply scattered waves and so the Born approximation is invalid [Sato, 1991]. Array processing of PKP precursor data shows that the energy has individual best fitting directions [Doornbos & Husebye, 1972; Doornbos & Vlaar, 1973; Doornbos, 1974; Haddon & Cleary, 1974; Wright, 1975; King *et al.*, 1976], indicating that it is likely generated by a single scattering event (deterministic scattering).

The scattered wavefield is dependent on the properties of both the incoming wave and the scattering heterogeneity. Scattering occurs for both incident P and S waves, and can generate both P and S waves. Phase conversions are, therefore, possible but discussion will be restricted to P to P scattering as this is of relevance here. Scattering of P to P can be written as  $P\bullet P$  where the  $\bullet$  indicates the location of scattering along the ray path. The total wavefield can be described as the sum of the incident plane wavefront and scattered wave. The scattering process is dependent on the ratio of the incident wavelength, often considered in terms of angular frequency,  $\omega$ , or wavenumber,  $k$ , to the radius of the scatterer,  $L$ , which is also written as the correlation distance,  $a$ . When the incident wavelength is much larger than the scattering heterogeneity ( $ka \ll 1$ ) scattering occurs in the Rayleigh regime [Wu & Aki, 1985a] in which the heterogeneity can be treated as a point source. When the incident wavelength is of similar size to the scattering heterogeneity ( $ka \approx 1$ ) scattering occurs in the Mie regime where the heterogeneity must then be considered a 3-dimensional volume. The spatial pattern of the radiation of scattered energy is depen-

dent on the elastic properties of the scattering heterogeneity, written as Lamé parameters  $\lambda$  and  $\mu$ , and density,  $\rho$ , relative to the overall medium with parameters  $\lambda_0$ ,  $\mu_0$ , and  $\rho_0$  and P-wave velocity  $\alpha_0$ . Discussion of scattering will be written in the notation used in *Wu* [1984] and *Wu & Aki* [1985a]. By knowing which type of scattering is occurring we can model the scattered wavefield and measure the frequencies involved to determine the properties of the causative heterogeneity.

The interaction of an incident plane wave with a heterogeneity is described by the equivalent body force, the displacement response of the medium to this is described by the Green's function [*Sato & Fehler*, 2008]. Convolution of the Green's function in the far-field with the equivalent body force gives the scattered P-waves in the far field. In the Rayleigh scattering regime, where the incident wavelength is much greater than the size of the scattering heterogeneity, the scattering from a heterogeneity of volume  $V$  can be approximated to a point source [*Wu & Aki*, 1985a] comprising a unidirectional force proportional to the density contrast and a moment tensor proportional to the elastic constant contrast with the surrounding medium. For a wave incident in direction  $x_1$  convolved with the Green's function, the scattered wave  $U^{PP}$  at distance  $r$  and time  $t$  from the origin can be written in polar co-ordinates with  $x_1$  as the polar axis and  $\theta$  as the angle relative to the incident direction as [*Wu & Aki*, 1985a]:

$$U_r^{PP} = \frac{V \omega^2}{4\pi \alpha_0^2} \left\{ \frac{\delta\rho}{\rho_0} \cos\theta - \frac{\overline{\delta\lambda}}{\lambda_0 + 2\mu_0} - \frac{\overline{2\delta\mu}}{\lambda_0 + 2\mu_0} \cos^2\theta \right\} \cdot \frac{1}{r} e^{i\omega(t-r/\alpha_0)} \quad (1.1)$$

The properties of the scattering heterogeneity,  $\rho$ ,  $\lambda$ , and  $\mu$  contribute differently to the shape of the scattered wavefield dependent on the direction relative to the direction of incidence (Figure 1.10 and Equation 1.1). The relationship between these parameters and the resultant scattered field can split Rayleigh scattering into two types with distinct special cases. For  $\delta\rho$ ,  $\delta\lambda$ , and  $\delta\mu$  all of the same sign, meaning a heterogeneity which is either denser and stiffer or less dense and softer, scattering is maximum in the backward direction. A special case is when the anomaly is proportionally denser and stiffer, where  $\frac{\delta\rho}{\rho_0} = \frac{\delta\lambda}{\lambda_0} = \frac{\delta\mu}{\mu_0}$ . This means that there is no velocity contrast between the medium and the inclusion (Equation 1.2), i.e.  $\frac{\delta\alpha}{\alpha_0} = 1$  where  $\delta\alpha$  and  $\alpha_0$  are the P-wave velocity perturbation and P-wave velocity of the medium, respectively.

$$\frac{\delta\alpha}{\alpha_0} = \frac{1}{2} \left[ -\frac{\delta\rho}{\rho_0} + \frac{(\delta\lambda + 2\delta\mu)}{(\lambda_0 + 2\mu_0)} \right] \quad (1.2)$$

The impedance (Equation 1.3) will be different, and so this is called impedance-type scattering [*Wu & Aki*, 1985a].

$$\frac{\delta(\rho\alpha)}{\rho_0\alpha_0} = \frac{\delta\alpha}{\alpha_0} + \frac{\delta\rho}{\rho_0} = \frac{\delta\rho}{\rho_0} + \frac{1}{2} \left( -\frac{\delta\rho}{\rho_0} + \frac{\delta\lambda + 2\delta\mu}{\lambda_0 + 2\mu_0} \right) \quad (1.3)$$

The scattering pattern is maximum in the backward direction with no scattering forwards (lower panel in Figure 1.10a).

Alternatively, for  $\delta\rho$  of a different sign to  $\delta\lambda$  and  $\delta\mu$ , meaning that a heterogeneity is either denser and softer or less dense and stiffer, scattering is maximum in the forward direction. The special case is when the anomaly is proportionally denser and softer, where  $-\frac{\delta\rho}{\rho_0} = \frac{\delta\lambda}{\lambda_0} = \frac{\delta\mu}{\mu_0}$ . In this situation there is no impedance contrast,  $\frac{\delta(\rho\alpha)}{\rho_0\alpha_0} = 1$ ,

although the velocity of the anomaly will be different from the surroundings, and so this is called velocity-type scattering (Equation 1.3). This pattern has scattering in the forward direction only (upper panel in Figure 1.10a). For two situations with equivalent anomaly magnitudes but different signs, the scattering patterns would be the same shape but opposite in direction.

If the deviation of the two elastic constants of the heterogeneity relative to the medium is proportional ( $\frac{\delta\lambda}{\lambda_0} = \frac{\delta\mu}{\mu_0}$ ) then the scattering field can be decomposed into contributions of impedance-type and velocity-type scattering. If the velocity and impedance contributions to the wavefield can be determined, such as by using the phase and amplitude fluctuations and coda excitation, respectively, then the elastic parameters and density can be independently determined, provided that they are correlated [Wu & Aki, 1985b]. Although in the Rayleigh regime scattering heterogeneities are approximated to point sources, the energy distribution pattern (Figure 1.10b) is still partially controlled by the frequency of the incoming wave.

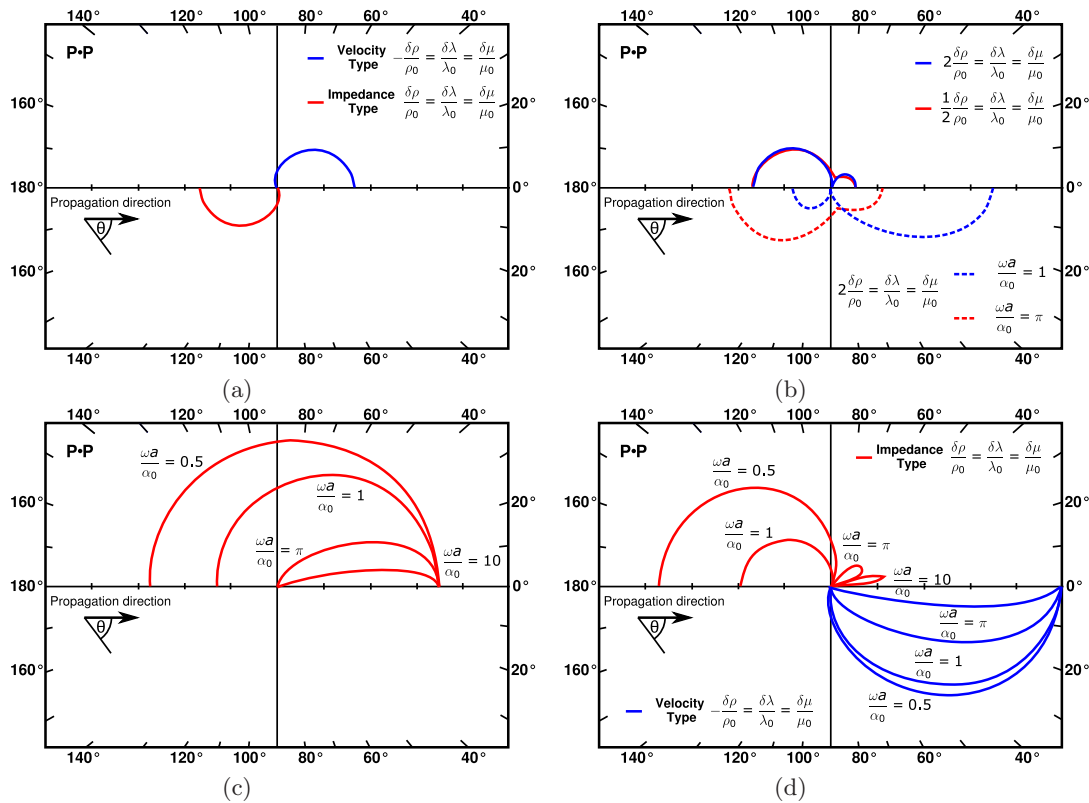


Figure 1.10: Scattering behaviour for various frequency/scatterer size ratios, and elastic parameter and density anomaly ratios. All patterns are for P•P scattering, are rotationally symmetric about the x-axis, and are generated by scattering of a wave propagating from left to right. Rayleigh scattering for (a) velocity and impedance type scattering and (b) for different scattering heterogeneity parameters (top) and frequency-size ratios (bottom) (Equation 1.1). (c) Volume factor for a Gaussian heterogeneity at a range of frequencies (see volume integral in Equation 1.4). The volume factor is independent of scatterer parameters and is only affected by frequency-size ratio and the way that parameters vary across the scatterer. (d) Mie scattering for a Gaussian heterogeneity at a range of frequencies for impedance type scattering (top) and velocity type scattering (bottom) (Equation 1.4). The Mie scattering pattern is the product of the Rayleigh scattering pattern (Figures 1.10a or 1.10b) and the volume factor (Figure 1.10c). After Wu & Aki [1985a].

For higher frequency waves, when the wavelength of the wave is similar to the radius of the scattering heterogeneity, the wave scatters in the Mie regime. In this case the scatterer can no longer be treated as a point source but instead the contribution from each volume element must be integrated together, multiplied by a volume factor [Wu & Aki, 1985a].

$$U_i^{PP}(\mathbf{x}) = \frac{V}{4\pi} \frac{\omega^2}{\alpha_0^2} \frac{1}{r} e^{i\omega(t-r/\alpha_0)} \left\{ \frac{\delta\rho}{\rho_0} \cos\theta - \frac{\delta\lambda}{\lambda_0 + 2\mu_0} - \frac{2\delta\mu}{\lambda_0 + 2\mu_0} \cos^2\theta \right\} \int_V P(\xi) \exp\left\{ i\frac{\omega}{\alpha_0} \xi_1 - i\frac{\omega}{\alpha_0} (\hat{\mathbf{x}} \cdot \xi) \right\} dV(\xi) \quad (1.4)$$

The description (Equation 1.4) is the same as the Rayleigh scattering (Equation 1.1) except that the volume,  $V$ , has been replaced by the volume factor integral (Figure 1.10c), as material parameters may vary with location,  $\xi$ , within the heterogeneity.  $P(\xi)$  is the parameter variation function which describes how material parameters vary throughout the scatterer, and  $\hat{\mathbf{x}}$  is the unit vector. For a uniform heterogeneity  $P(\xi) = 1$ .

Variation of incident wave frequency affects the shape of the scattering pattern (Figure 1.10d). For all forms of scattering, for values of  $\frac{\omega a}{\alpha_0} \sim 1$  scattering is roughly isotropic, but for values of  $\frac{\omega a}{\alpha_0} \sim \pi$  scattered energy is nearly entirely directed forwards, close to the axis, as forward scattering terms dominate [Wu & Aki, 1985a,b].

ULVZs have been demonstrated to cause scattering of high frequency waves ( $\sim 1$  Hz) which is often interpreted as evidence that they comprise heterogeneities with scale length of roughly 10 km [Ansell, 1973]. It is possible that ULVZs consist of multiple small heterogeneities clustered together which, when taken as a whole, are large enough to be detected by the other non-scattering probes which find ULVZs to be on the order of 10s to 100s km [Garnero & Helmberger, 1998; Rost & Revenaugh, 2003; Rost *et al.*, 2005; To *et al.*, 2011]. These non-scattering probes such as ScP and  $SP_{diff}$ KS suggest ULVZs to be dense and less stiff, therefore, scattering similar to velocity type scattering will likely be maximum in the forward direction with additional back-scattering for most frequencies. I will be able to observe small-scale mantle heterogeneities with both forward scattering probes, such as PKP (Chapter 2), and back-scattering probes, such as PKKP (Chapter 3). Separate determination of forward and back-scattering for the same region would allow me to independently calculate the elastic parameters and density of ULVZs. Detecting

scattered energy is an indication of heterogeneities on scales smaller than can easily be resolved by reflected waves. These heterogeneities must have anomalous density and/or elastic parameters to cause scattering. The size of the heterogeneity can be determined from the frequencies of waves that it scatters. In the high frequency ( $\sim 1$  Hz) wavefield these heterogeneities are likely to be so small (1s to 10s km) that, in order to remain for any appreciable amount of time, they must be chemically anomalous relative to the ambient mantle; thermal heterogeneities would rapidly equilibrate [*Manga & Jeanloz, 1996; Becker et al., 1999; Turcotte & Schubert, 2002*]. Scattering theory can be used to derive heterogeneity parameters from the observed scattered energy. By searching for the source of this energy through the use of arrays (for explanation of arrays see Chapter 1.4) I locate these anomalies within the Earth and try to understand their relationship with the rest of the dynamic mantle.

## 1.4 Array Seismology

### 1.4.1 Arrays

A group of multiple seismometers located in a well-defined configuration is known as an array. Arrays have two major advantages over single receivers: their ability to determine the direction of an incoming wave by measuring relative arrival times of a wave across the array, and noise suppression by constructive summation of coherent signals. The advantages of using multiple seismometers, or receivers, together to improve signal clarity were recognised in the late 1950s and arrays were adopted within forensic seismology [*Barber, 1957; Birtill & Whiteway, 1965; Husebye & Ruud, 1989*]. The configuration of the array in terms of number of receivers, inter-receiver spacing, and spatial relationships between the receivers i.e. the layout, affect the suitability of the array for detecting different kinds of waves [*Haubrich, 1968; Mykkeltveit et al., 1983*]. The inter-receiver spacing and the maximum horizontal receiver-to-receiver distance, the aperture, of an array dictate the frequencies of waves that can be best observed by it. In order for an array to successfully improve signal quality and characterise the signal terms of its incident direction (slowness and back-azimuth) the wave must be coherent across it. This means that the wavelength of the incoming wave can be up to the aperture of the array [*Schweitzer et al., 2002*]. For waves with wavelengths considerably greater than the aperture of the array, the phase difference at each station will be small and difficult to determine, and so the array will behave similarly to a single station [*Rost & Thomas, 2002*]. Small-scale lateral variations in the crust beneath the array will distort short wavelength waves, causing the wavefront to be incoherent across the array. It is for this reason that noise can be differentiated from signals at an array. The noise spectrum contains both high and low frequency signals from a range of sources [*Bormann, 2002; Koper et al., 2009, 2010*] and noise is often locally generated, thus the energy will not be the same at different stations and the noise signal will not be coherent across the array. Arrays can be optimised to reduce noise coherence and increase signal coherence making them more effective at extracting the signals from the noise (see Chapter 1.4.5).

Following the advent of the atmospheric Nuclear Test Ban in 1958, the first arrays were built in the USA, and then by groups such as the UKAEA (UK Atomic Energy Au-

thority), specifically to detect and locate the source of the high frequency seismic signals typical of underground nuclear tests [Birtill & Whiteway, 1965; Husebye & Ruud, 1989]. Consequently, many arrays were built with maximum apertures of  $\sim 10$ -25 km, best suited for 1 Hz waves [Selby, 2011]. In addition, this makes them ideal for detecting high frequency body waves associated with scattering within the deep Earth [Ansell, 1973]. The International Monitoring System (IMS) network includes arrays of a range of sizes with variable instrumentation (see Table 1.1 and Figure 1.11). The detection capabilities of an array vary with aperture, number of stations, and station spacing, and are also affected by the ambient noise and geology of the local environment [Bondár et al., 1999; Koper et al., 2010], the effects that these variables have on the signal processing power and resolution of the array will be covered in the subsequent sections.

Table 1.1: IMS arrays used (including Gauribidanur which is not an IMS array). Arrays have been operating from the start dates given (in Year/Julian day) to present.

Array	Location	Code	La.	Lo.	Start	Stat. #	Aper. (km)
Malin	Ukraine	GB	50.70	29.22	2002/067	24	27.6
Alice Springs	Australia	AK	-23.67	133.91	1987/001	19	9.8
Keskin	Turkey	WR	39.73	33.64	2003/041	11	3.0
Borovoye	Kazakhstan	KU	53.02	70.39	2002/187	9	3.4
Chiang Mai	Thailand	YK	18.46	98.94	1986/189	18	10.1
Eskdalemuir	Scotland	MJ	55.33	-3.16	1962/160	20	8.6
Sonsecu	Spain	IL	39.67	-3.96	1989/212	28	9.6
GERESS	Germany	KS	48.85	13.70	1990/067	19	30.8
Gauribidanur	India	CM	13.60	77.44	1965/300	25	3.9
Eielson	USA	AS	64.77	-146.89	1977/091	21	10.2
Wonju	South Korea	ES	37.44	127.88	1972/230	20	10.1
Kurchatov	Kazakhstan	EK	50.62	78.53	2006/263	21	22.5
Matsushiro	Japan	TO	36.52	138.25	1984/092	23	11.2
Torodi	Niger	GE	13.15	1.69	2005/270	16	6.1
Warramunga	Australia	BR	-19.94	134.34	1999/182	24	26.3
Yellowknife	Canada	BV	62.49	-114.61	1963/273	18	20.1

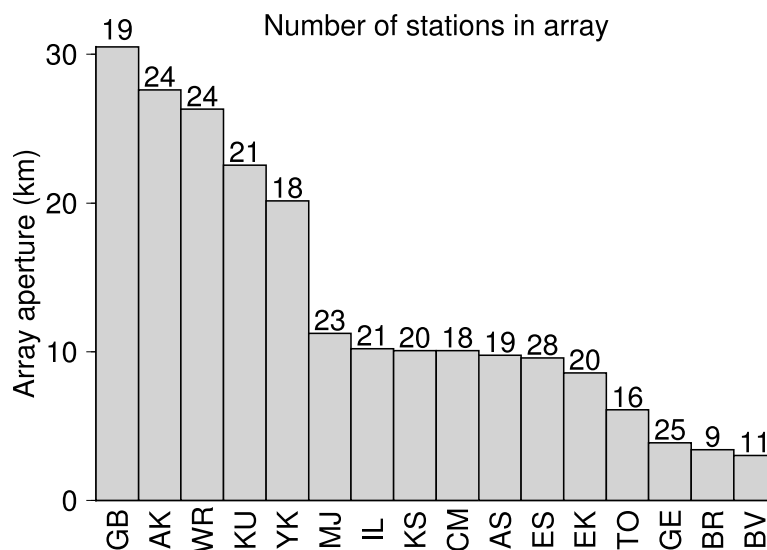


Figure 1.11: Array apertures and number of stations of the dominant type (number of stations used displayed above the vertical bar).

### 1.4.2 Wave Characteristics

Waves travelling through a medium as heterogeneous as the Earth are, as a result, complex. By using a few approximations of wave behaviour we can simplify waves and work out defining characteristics and extract usable signals from the surrounding noise. For waves received at larger distances, the wavefront can be approximated to be planar [Knott, 1899; Aki & Richards, 2002], where “larger” is a relative term based on the wave frequency and the number of wavelengths between the source and receiver. For infinite frequency waves, wavefronts can also be considered as rays, the infinitesimally thin path that is perpendicular to the wavefront (Figure 1.12). This assumption can be made for high frequencies, such as 1 Hz [Marquering *et al.*, 1998, 1999]. These simplifications make it considerably easier for us to use the relative arrival times of a wave at each receiver in the array, or moveout, to extract directivity information of the wave. The wave direction can be parameterised into the back-azimuth (angle from the receiver back to the source around from north),  $\theta$ , and incidence angle (steepness of the incoming wave away from vertical),  $i$  (Figure 1.12). In global seismology, the incidence angle and velocity beneath the array,  $v_0$ , are often converted into slowness,  $u$ , which is the reciprocal of the apparent velocity of the wave across the array observed at the surface,  $v_{app}$ :

$$u = \sin(i)/v_0 = 1/v_{app} \quad (1.5)$$

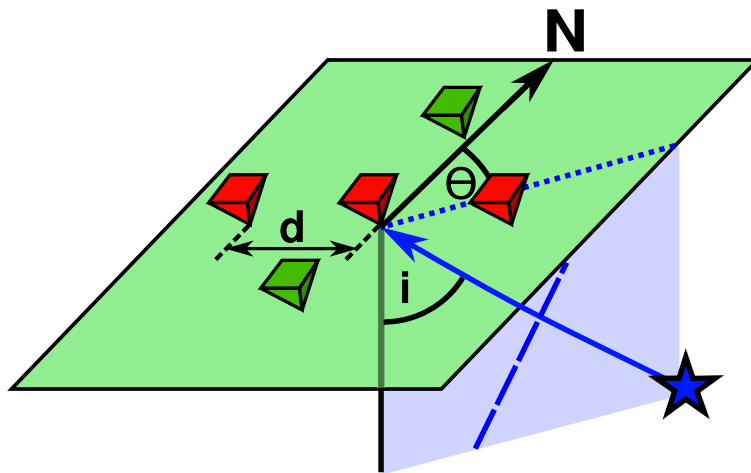


Figure 1.12: Sketch array configuration of two crossing branches of seismometers (inverted pyramids) with interstation spacing  $d$ . A wavefront (blue dashed line) is incident at the array along a ray (blue arrow) with back-azimuth  $\theta$  and incidence angle  $i$ .

The relative arrival times of a wavefront at each receiver in an array is characteristic of the propagation direction, but to determine this we must first understand how propagation direction effects the interaction of a wave with an array. Considering a simple 1-dimensional line array of seismometers oriented east-west, inter-station spacing  $d$ , and a wave known to be propagating along the surface of the Earth (incidence angle of  $90^\circ$ ) from north to south (back-azimuth of  $\theta = 0^\circ$ ) (Figures 1.13a and 1.13c), the wave front will arrive at all stations simultaneously. This is also true of a wave propagating from south to north (back-azimuth of  $\theta = 180^\circ$ ). From observing the seismograms, the wave can be

deduced to be coming from either of these directions. For the same array configuration and a wave travelling from east to west (back-azimuth of  $\theta = 90^\circ$ ), the wave will first be observed at the easternmost station, and then at each subsequent station in the direction of wave propagation (Figures 1.13b and 1.13d). Simple trigonometry can be used to determine the ray direction based on the delay-time and the distance,  $d$ . In this situation, east-west and west-east propagating waves can be distinguished.

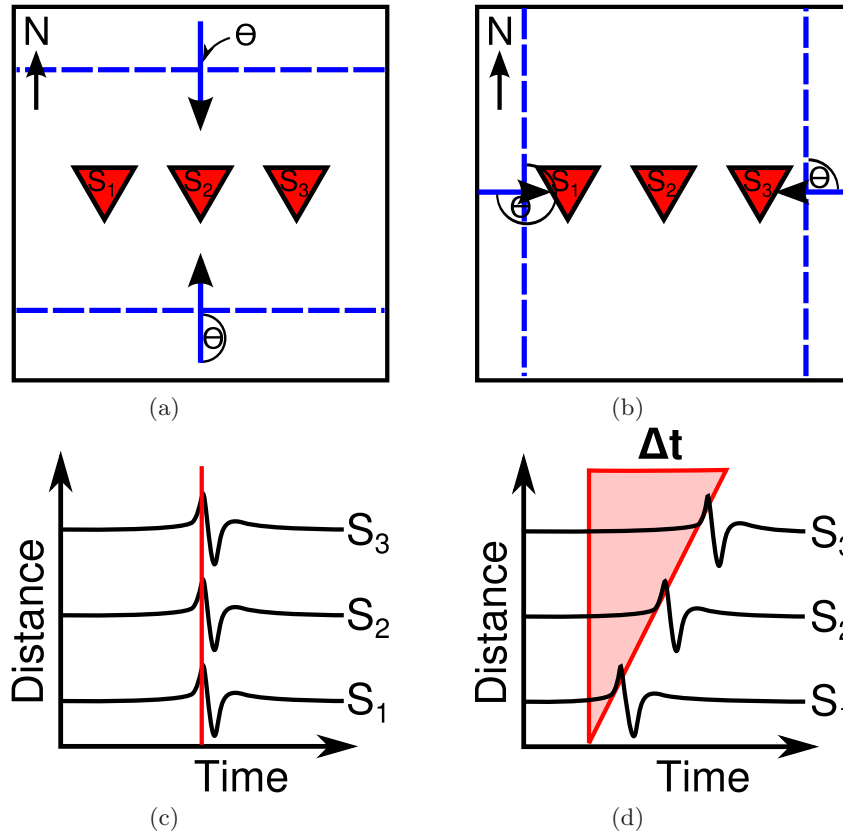


Figure 1.13: Simplified arrays (stations shown by inverted triangles) with wavefronts (blue dashed lines) propagating with back azimuth (a)  $\theta = 0^\circ$  and  $\theta = 180^\circ$  and (b)  $\theta = 90^\circ$  and  $\theta = 270^\circ$ . Associated seismograms showing (c) no time delay, typical of situations such as (a), and (d) a time delay,  $\Delta t$ , observed at each station, associated with situations such as (b). Red lines show moveout of the signal across the array.

Analysis of the delay times can also be used to determine the slowness of a wave. Again, considering a simple east-west oriented line array and a wave known to have a back-azimuth of  $\theta = 90^\circ$ , the delay times between stations in the array will depend on the slowness. A wavefront propagating vertically (incidence angle of  $i = 90^\circ$  equivalent to a slowness of  $u = 0$ ) will arrive at all stations simultaneously (Figures 1.14a and 1.13c). In contrast, a wavefront propagating along the surface (incidence angle of  $i = 0^\circ$  equivalent to a slowness of  $u \approx \infty$ ) will have a delay time of  $v_0/d$ , where  $v_0$  is the velocity immediately below the array (Figures 1.14b and 1.13d).

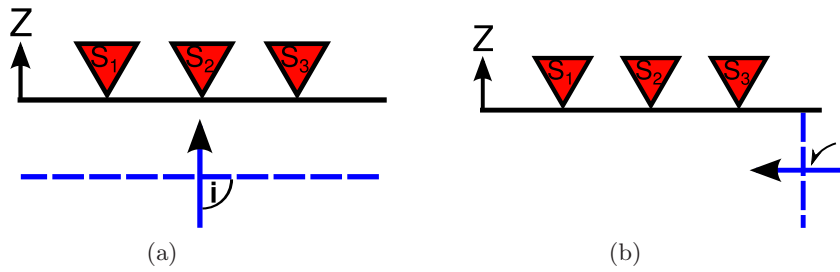


Figure 1.14: Simplified arrays with wavefronts (blue dashed lines) propagating with back-azimuths  $\theta = 90^\circ$  and incidence angles (a)  $i = 90^\circ$  and (b)  $i = 0^\circ$ . These situations are associated seismograms with Figure 1.13c for no time delay, and Figure 1.13d where the signal is delayed across the array, respectively.

These situations demonstrate the connection between slowness and back-azimuth. Indeed, slowness and back-azimuth can also be considered as a single vector in terms of horizontal and vertical slowness [Rost & Thomas, 2002] (see Chapter 1.4.4). By using a 2-dimensional array we are able to separate out the contributions of slowness and back-azimuth to the observed delay time. The degree to which wave directions can be separated from each other is dependent on the similarity of delay times between stations, and thus, the array configuration. This has led to different array designs optimised to best determine the slowness and back-azimuths for desired frequencies [Mykkeltveit *et al.*, 1983; Rost & Thomas, 2009] (discussed further in Chapter 1.4.5). By understanding how waves interact with arrays we can use them to both amplify signals and locate the source of the wave which makes them essential in studying small amplitude waves from points deep in the Earth.

### 1.4.3 Beamforming

Arrays can be used to suppress energy that is incoherent across an array by summing of traces together, also known as stacking. Stacking of the records from each receiver in an array will cause destructive interference of waves that are not in phase, and constructive interference of those that are. Therefore, this method can be used to increase the amplitude of a signal relative to the noise, i.e. to increase the signal-to-noise ratio (SNR). However, the delay of the signal of interest at each station, the moveout, must first be corrected for in order for it to stack constructively. Following the notation of Rost & Thomas [2002], an incident wave, that is coherent across the array and, hence, the waveform is not dependent on location, can be written as  $f(t)$ . This signal will be observed at each receiver in the array,  $i$ , at position  $\mathbf{r}_i$  from the centre of the array, plus some location dependent noise,  $n_i$ . If the noise is incoherent across the array then the signal can be separated from it. The signal,  $x$ , observed at station  $i$  is, therefore, described by the incident signal, delayed by an amount dependent on the distance from the reference point and the horizontal speed of the propagating wave, the slowness vector  $\mathbf{u}_{\text{hor}} = (u_x, u_y)$ , plus the noise:

$$x_i(t) = f(t - \mathbf{r}_i \cdot \mathbf{u}_{\text{hor}}) + n_i(t) \quad (1.6)$$

Once the delay time observed at each array location,  $\mathbf{r}_i \cdot \mathbf{u}_{\text{hor}}$ , which is dependent on the slowness value used, has been calculated and added back in, all  $N$  traces in the array can be summed to create a beam,  $b(t)$ :

$$b(t) = \frac{1}{N} \sum_{i=1}^N x_i(t + \mathbf{r}_i \cdot \mathbf{u}_{\text{hor}}) = f(t) + \frac{1}{N} \sum_{i=1}^N n_i(t + \mathbf{r}_i \cdot \mathbf{u}_{\text{hor}}) \quad (1.7)$$

This process enhances the signals that are in phase ( $f(t)$ ) and helps to cancel out the noise ( $n_i$ ), where the amount of improvement is dependent on the number of the stations in the array. The signal-to-noise ratio of the beam relative to an individual record scales as  $\sqrt{N}$ , assuming ideal correlation of the signal across the array and uncorrelated noise [Harjes & Henger, 1973; Rost & Thomas, 2002], although in practical terms due to real signals and noise this scaling is often only an approximation. Thus, as long as the wave is coherent across the whole array, arrays with more stations tend to produce better quality beams than those with fewer stations. As this process involves removing the delay observed at each station and then summing all records together, this process is also known as Delay-and-Sum, or, as it creates a beam, beamforming.

This process relies on knowing the directivity of the wavefront in order to calculate the delay times at each station. When this is not known, beamforming is often done on a grid-search basis to find the best fitting values. A range of slowness are used and the associated delays are calculated. The slowness that gives the best summation of a signal is assumed to be representative of that particular wave. This procedure also allows for identification of otherwise unpredicted signals, which is of particular importance for scattered waves. It was first applied by choosing a fixed back-azimuth along the ray and varying the slowness (the reciprocal of the velocity) and, as such, is known as Velocity Spectral Analysis (Vespa) processing and creates Vespagrams (Figure 1.15) [Davies *et al.*, 1971]. On application to data observed at the Large Aperture Seismic Array (LASA), a 350 station, 200 km wide array in Montana which operated between 1968 and 1978, deviations in the slowness of some rays from those predicted by travel-time models were used to indicate lateral heterogeneities within the Earth [Davies & Sheppard, 1972]. The Vespa process can also be applied to back-azimuth, for a fixed slowness [Husebye *et al.*, 1976]. The processing can be extended by performing a grid search over slowness and back-azimuth space and calculating beams for each combination, thus calculating the best fitting values of both parameters for a signal in time, known as beam packing (Figure 1.17a) [Schweitzer *et al.*, 2002; Rost & Thomas, 2002]. The BEAMAN process is very similar as it also involves forming beams for a range of slownesses and back azimuths, differing only in the way the result is displayed [King *et al.*, 1976; Weber & Wicks, 1996].

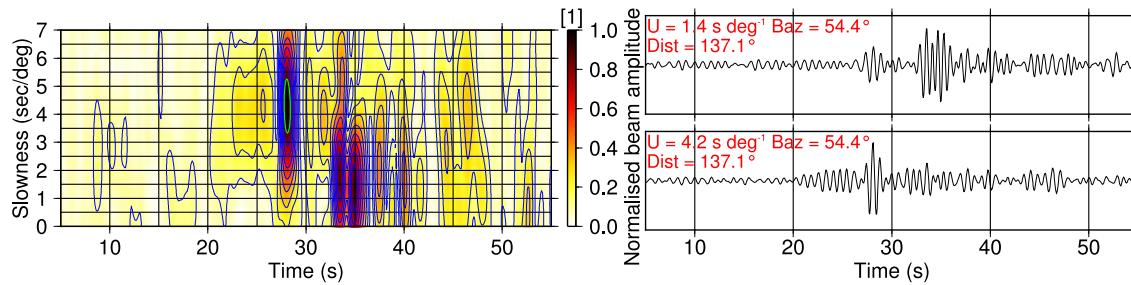


Figure 1.15: Array processing for an event at 12:50:07 on 11/12/1996 in South Africa, recorded at YK, Canada. (a) Vespagram formed from beams, bandpass filtered between 1 and 2 Hz, for slownesses between 0.1 and 7.0 s/deg, at a back-azimuth of  $54.4^\circ$ , showing  $\text{PKP}_{df}$  arriving at  $\sim 35$  s and two precursors arriving at  $\sim 25$  and 28 s. The 90 % maximum amplitude region is marked by the green contour. (b) Beams formed on  $\text{PKP}_{df}$  slowness (top) and precursor slowness (bottom), filtered between 1-2 Hz.

Other methods of determining the directivity of a wavefront also exist. The  $N^{\text{th}}$  root process further enhances small amplitude coherent signals by taking the  $N^{\text{th}}$  root of each trace, prior to stacking, and then raising the beam to the  $N^{\text{th}}$  power [Kanasewich *et al.*, 1973]. This reduces the amplitude difference of the samples and so is effective at exposing small amplitude coherent signals hidden amongst noise. Phase-weight stacking (PWS) involves measuring both the amplitude and “instantaneous phase” of a signal, and measuring the coherence of this and a reference wavelet [Schimmel & Paulssen, 1997; Schimmel, 1999]. Although I do not use such methods it is important to note the range of techniques that have previously been used to study the deep Earth to extract directivity information from the wavefield. Here I apply extensions of some of these methods, discussed below.

#### 1.4.4 Fk Analysis

Frequency-wavenumber analysis (fk) is able to simultaneously determine the best fitting slowness and back-azimuth for a signal [Capon *et al.*, 1967; Capon, 1969; Rost & Thomas, 2002]. Like beam-forming, the fk process seeks to account for the delay time observed at each station location,  $\mathbf{r}_n$ , characteristic of the direction of the wave,  $\mathbf{u}_0$ , thus increasing the amplitude of the sum,  $y(t)$ :

$$y(t) = \frac{1}{N} \sum_{n=1}^N x_n(t + \mathbf{u}_0 \cdot \mathbf{r}_n) \quad (1.8)$$

The time series for each trace in the array (Equation 1.6) is converted to the frequency domain via a Fourier transform, in order to save computation time. The slowness and back azimuth are then defined by a single vector in the frequency domain, the wave number vector  $\mathbf{k}$ , where  $\omega$  represents angular frequency:

$$\mathbf{k} = \omega \cdot \mathbf{u} = \frac{\omega}{v_0} (\cos\theta, \sin\theta) \quad (1.9)$$

The transform of  $y$  is the power spectral density of the signal in the frequency domain,  $S(\omega)$ , combined with the array response function,  $A$ , as a function of slowness and back-azimuth, for the input time window:

$$E(\mathbf{k} - \mathbf{k}_0) = \frac{1}{2\pi} \int_{-\infty}^{\infty} |S(\omega)|^2 |A(\mathbf{k} - \mathbf{k}_0)|^2 d\omega \quad (1.10)$$

Where the array response function (discussed in Chapter 1.4.5) is a measure of the power of a specific array to resolve different directions, or wave number vectors,  $\mathbf{k}$ . This can be represented by:

$$|A(\mathbf{k} - \mathbf{k}_0)|^2 = \left| \frac{1}{N} \sum_{n=1}^N e^{(2\pi i(\mathbf{k} - \mathbf{k}_0) \cdot \mathbf{r}_n)} \right|^2 \quad (1.11)$$

For each slowness and back-azimuth value, all energy is summed over the number of samples taken from the trace. Signals from different directions arriving at the same time will not be able to be distinguished. Therefore, to determine the variation of wave direction with time, the location of the time window in the trace must be varied, sliding it along and performing fk analysis at a different time, a sliding-window fk [Rost & Weber, 2001, 2002]. This makes the fk another very useful technique for determining signal directivity with the advantage of reduced computational expense.

### 1.4.5 Array Response Functions

The ability of an array to distinguish between waves coming from different directions, i.e. with different wave number vectors, is described by the Array Response Function (ARF) (Equation 1.11) [Rost & Thomas, 2002]. The ARF is a measure of how the amplitude of beams for a given wave varies between the signal direction and other directions. The ability of an array to differentiate between different slowness and back-azimuths is dependent on the shape of the array, the direction from which a wave arrives, and also the frequency of the wave. The most desirable ARF is that of a 2-dimensional delta spike whereby a given slowness and back-azimuth cannot be misidentified as any other. When beam amplitude varies rapidly with slowness and back-azimuth, the ARF will be a narrow, delta-like peak. When the beam amplitude variation is small between different beamforming directions then the ARF will be broad. The ARF also shows directional dependence, where, due to the array configuration, some directions can be separated from each other better than others. Local maxima of the ARF are known as side-lobes and can lead to spatial aliasing whereby signals from different directions cannot be distinguished (Figure 1.16 and Figures in Appendix A).

The way in which the configuration of an array affects the ARF can be simplified to a few general rules [Schweitzer *et al.*, 2002]. The slowness and back-azimuth resolution are dependent on the array aperture and geometry. When the incident wavelength is greater than the array aperture it acts like a single station. The number of stations in the array controls the precision of the slowness and back-azimuth resolved, where more stations allow distinguishing of smaller differences in direction. The relative distances of the stations in an array control both the location of side lobes and the limit of the wavelengths that can be resolved. Smaller distances allow smaller wavelengths (higher frequencies) to be differentiated. These guides are considered when an array is being designed to tune it to signals of a particular type and can also be used to indicate the possible resolution of an extant array.

Local noise levels and frequency contents show spatial variation relating to the distance from various noise sources. Short period noise in the 0.5 Hz to 4 Hz frequency band dominantly comprises surface waves ( $L_g$ ) generated by wave action in shallow water, body waves (P) generated in deeper water distant from the coast, and a minor Rayleigh wave component ( $R_g$ ) of cultural origin [Koper *et al.*, 2010]. Noise levels, particularly those created by water motion, show seasonal patterns [Koper *et al.*, 2009]. Noise cannot be controlled, but arrays can be optimised to minimise it and increase the Signal-to-Noise ratio. As discussed in Chapter 1.4.3, the scaling relation for SNR improvement requires correlated signals and uncorrelated noise. Optimisation, therefore, focusses on the best station placement to achieve this. An experimental array can be used to collect information about the local wavefield. By cross-correlating noise windows, filtered for specific frequency bands, between each station pair in the experimental array the station separation distance at which that frequency of noise becomes uncorrelated can be established [Mykkeltveit *et al.*, 1983]. This can then be compared against the separation distance at which signals in the wavefield become correlated. To determine the rate of signal improvement with number of sensors,  $N$ , or the SNR gain,  $G$ , the average noise correlation,  $\bar{\rho}$ , is compared with the average signal correlation after the moveout has been corrected for,  $\bar{c}$ :

$$G = \frac{1 + (N - 1)\bar{c}}{1 + (N - 1)\bar{\rho}} \quad (1.12)$$

By adhering to these various criteria the array geometry, spacing, and number of stations can be selected to both reduce spatial aliasing and increase  $G$ .

Arrays are constructed following the guidelines but different array configurations are still used resulting in different ARFs. For example; considering an array comprising two straight, crossing arms (e.g. YK and the other “UK-style” arrays), the array has poorest resolution if a wave has back-azimuth along the arms, and best resolution if a wave travels between the arms (Figure 1.16a). The ARF will, therefore, have a “cross”-shape, like the array, with lobes of high amplitude (local maxima) projecting out along the arms. These “side-lobes” will radiate out from the maximum of the ARF, the width of which is controlled by the aperture of the array. Sidelobes indicate spatial aliasing where one signal direction can be indistinguishable from another. Directional resolution is best for arrays comprising rings of stations as these have no side lobes (Figure 1.16b). However, the circular IMS arrays are often small, giving limited resolution overall and a broad peak in the ARF. As mentioned previously, the wavelength of the incoming wave and the inter-station spacing affects the coherency of the observations across the array and, thus, the shape of the ARF changes with frequency. Additional processing methods, such as applying the coherence measures described above to a linear beam (see Chapter 1.4.3), can be used to mitigate the effects of the ARF.

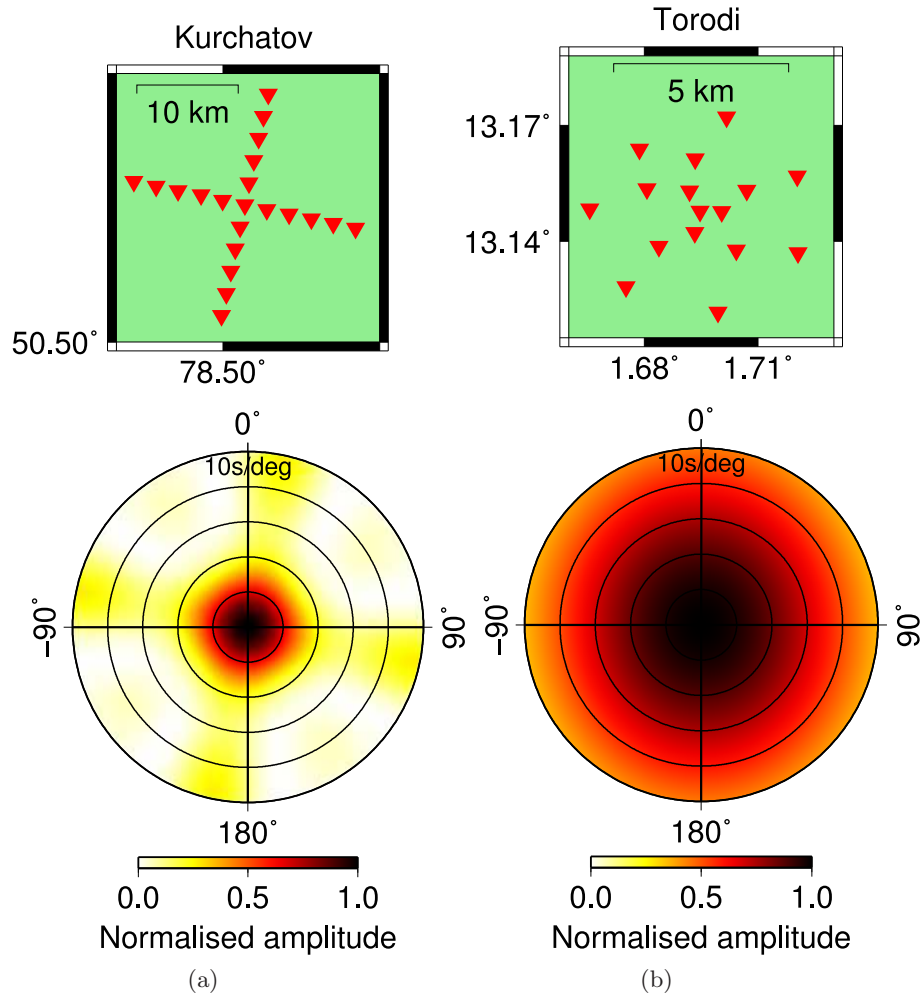


Figure 1.16: Array response functions computed for a 1 Hz wave with 0 s/deg slowness for two arrays, (a) Kurchatov in Kazakhstan and (b) Torodi in Niger. Due to the different array shapes, apertures, and station spacing the two arrays demonstrate different patterns of spatial aliasing over the slowness and back-azimuth range displayed (0 to 10 s/deg, 0 to 360°). Due to its much greater aperture, Kurchatov has a much narrower maximum, but significant side-lobes extending along the arms of the array. In comparison, Torodi has a much broader maximum but has no noticeable side-lobes as the stations are distributed in rings. For ARFs of other arrays see Figures in Appendix A.

#### 1.4.6 Other Coherence Measures

Beamforming and beam packing can be improved by using measures of signal coherence, often used in forensic seismology. Semblance,  $S$ , is a measure of the ratio of the output energy to the input energy, where these represent the amplitude of the beam (output) and the average amplitude of the un-beamed traces (input), respectively, in some number of samples,  $M$ , i.e. the power of the beam compared with the average power of the traces used to form it [Neidell & Turhan Taner, 1971]:

$$S = \frac{\sum_{t=1}^M \left[ \sum_{i=1}^N x_i(t) \right]^2}{N \sum_{t=1}^M \sum_{i=1}^N x_i(t)^2} \quad (1.13)$$

Larger semblance values thereby indicate that the beam has been efficient at enhancing

a signal relative to the noise.

The F-statistic is more effective than beamforming and semblance at suppressing waves not travelling along the beam direction [Melton & Bailey, 1957; Blandford, 1974; Bowers, 2000]. It calculates the time-average of the signal strength,  $F$ , by taking the ratio of the beam  $b(t)$  and the difference between the beam and each trace in the beam  $x_i$ , summed over  $M$  samples (typically a few times larger than the desired signal length), and weighted by the number of traces  $N$ :

$$F = \frac{N - 1}{N} \frac{\sum_{t=1}^M b(t)^2}{\sum_{t=1}^M \sum_{i=1}^N (x_i(t) - b(t))^2} \quad (1.14)$$

Creating a beam for a slowness and back-azimuth that is not correct for the recorded signal will result in a beam which is very different from each individual trace, thus, the denominator will be much larger than the numerator, leading to a small  $F$  value. Alternatively, a well formed beam will be representative of the signal observed in each trace, and the only remaining difference between the traces and the beam is the receiver-dependent noise, therefore,  $F$  will be large. As the F-statistic penalises off beam energy, the improvement in slowness and back-azimuth resolution relative to a standard beam is dramatic, (Figure 1.17) allowing more precise determination of the direction of an incoming wave. This greater precision means that smaller amplitude signals can be resolved than would be possible with a standard beam, thus it is ideal for analysis of scattered signals (see Chapter 2 and 3). The F-statistic can be applied through time, changing the position of  $M$  in the trace, giving an F-trace. It has been used effectively to detect low amplitude teleseismic signals at small aperture arrays [Blandford, 1974; Bowers, 2000; Heyburn & Bowers, 2008; Selby, 2008, 2011; Frost *et al.*, 2013]. The power of the F-statistic is demonstrated further in the subsequent section.

### 1.4.7 Combined Methods

Beam packing is used to test the amplitude of the energy arriving from different directions while coherence measures are designed to penalise energy arriving away from the direction for which the measure is being calculated. A combination of coherence measures and beam packing can be used together to improve directivity resolution over a standard beam pack.

$$F_{(\theta,u)} = (N - 1) \frac{N \sum_{t=1}^M b_{\theta,u}(t)^2}{\sum_{t=1}^M \sum_{i=1}^N (x_i(t) - b_{\theta,u}(t))^2} \Bigg|_{u=S_2}^{u=S_1} \Bigg|_{\theta=A_2}^{\theta=A_1} \quad (1.15)$$

This can be incredibly effective and allows more precise location of the source of the incoming energy. In Chapter 2 I apply the F-statistic to beams in a beam pack (for slowness between  $S_1$  and  $S_2$ , and back-azimuth between  $A_1$  and  $A_2$ ) to create an ‘‘F pack’’ (Equation 1.15). I can then use the output of the F pack to pick points of the highest F-value (Equation 1.14) to select the best fitting slowness and back-azimuth. The resolution improvement is dramatic. To illustrate this I use a data example from the study in Chapter 2. This signal is processed using both a beam pack and an F pack. Between the beam pack and the F pack the region of 90 % maximum amplitude (normalised) is reduced from  $\sim 45^\circ$  and 1.7 s/deg wide ( $U_x=1.2$  s/deg,  $U_y=1.2$  s/deg) to  $\sim 5^\circ$  and 0.3

s/deg ( $U_x=0.03$  s/deg,  $U_y=0.3$  s/deg) (Figure 1.17), an improvement which can then be carried into subsequent ray-tracing to more precisely determine the source of the energy.

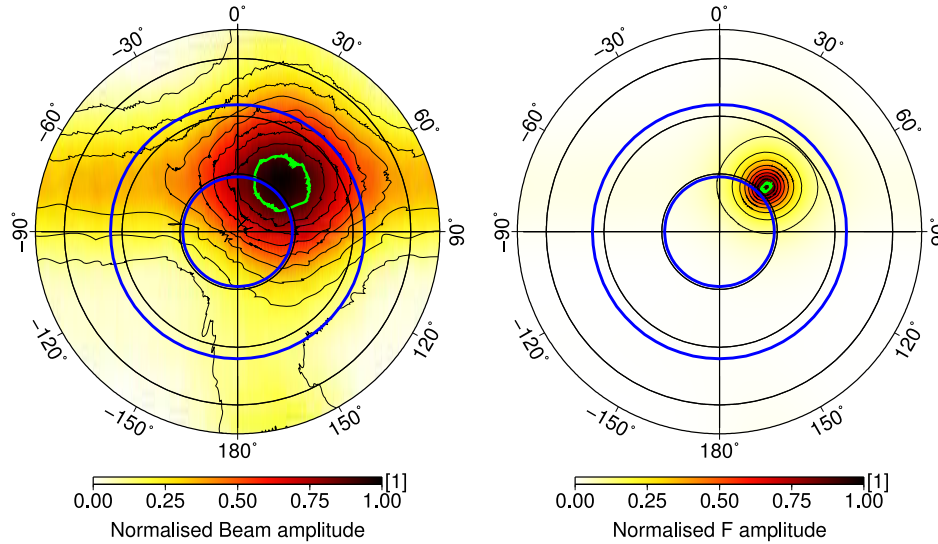


Figure 1.17: The  $PKP_{dj}$  signal for an event at 22:19:36 on 22/04/1999 in South Africa recorded at YK in Canada processed using (a) linear beam-pack and (b) F-pack. Back-azimuth is on the azimuthal axis and slowness is on the radial axis, from 0 s/deg to 7 s/deg. Inner and outer blue rings mark inner and outer core slownesses, respectively. Contours are at 0.1 amplitude increments and the green contour marks the 90% maximum amplitude region. The 90% maximum amplitude region is reduced from  $\sim 45^\circ$  and 1.7 s/deg wide ( $U_x=1.2$  s/deg,  $U_y=1.2$  s/deg) in the beam-pack to  $\sim 5^\circ$  and 0.3 s/deg ( $U_x=0.03$  s/deg,  $U_y=0.3$  s/deg) by using the F-pack.

To assess changes in amplitudes and dominant directions of energy through time, I could calculate the F-statistic for long traces for a range of directions. However, in the code used, when calculating the F-trace for a given beam direction all  $N$  channels in the array are Fast-Fourier transformed (FFT) and then Inverse Fast-Fourier transformed before the F-statistic calculation (Equation 1.14) is performed (although this process does involve conversion to the frequency domain I will continue to refer to it as the time-domain F-statistic as the majority of the calculation occurs in the time-domain). Each FFT requires  $X \log X$  calculations (where  $X$  is the number of points), thus for  $B$  beams the time taken to create the F-pack scales as  $2NB \cdot X \log X$ . Therefore, as computing the F-statistic for many directions would be computationally expensive, exacerbated by using long traces, I use a combination of the F-statistic and a sliding-window fk analysis to reduce processing time. I choose short time windows within longer traces and apply a formulation of the F-statistic to traces transformed into the frequency domain [Selby, pers. comm.]. The process returns the signal amplitude at different slownesses and back-azimuths for the total length of the time window. Time information within this window is, therefore, lost and so small time steps must be used to allow precise determination of the changing signal through time. In the fk-F-statistic, each of the  $N$  channels is Fast-Fourier transformed once per time window  $T$  (where each FFT requires  $\frac{X}{T} \log(\frac{X}{T})$  calculations) and then the F-statistic is applied in the frequency domain. The time taken for this process, therefore, scales as  $NX \cdot (\log X - \log T)$ , making it considerably faster

than the equivalent time-domain F-statistic. Thus this approach allows for relatively fast, precise determination of slowness and back-azimuth of long traces. In later processing (see Chapter 3) I apply this sliding-window frequency F-statistic to 120 s long samples of array data to pick precursors to PKKP (Figures 1.18).

Applying the F-statistic in the frequency domain reduces computational time by a factor of 5 relative to performing an equivalent process using the time domain F-statistic but still dramatically increases slowness, back-azimuth, and time resolution relative to a standard sliding-window fk. By using a sliding window I can separate out signals arriving from different directions through time without the need for pre-selecting specific time windows around incoming phases. The window length and time-step chosen affect processing time as well as time and directivity resolution and so various combinations are tested to find the optimal values. Subsequent processing uses windows 10 s long with a 1 s time step (creating a 90 % overlap). If multiple coherent signals arrive within the same time window then selecting the correct directivity information will be more complicated. Using short time windows and viewing the signal amplitude in slowness-time space (Figure 1.18a), and back-azimuth-time space (Figure 1.18b) can help to reduce these complications and allow separate signals to be identified. Using this sliding window process allows for more signal information than would be possible performing the frequency domain F-trace using a single long time window and allows me to track the evolution of energy throughout the window of interest.

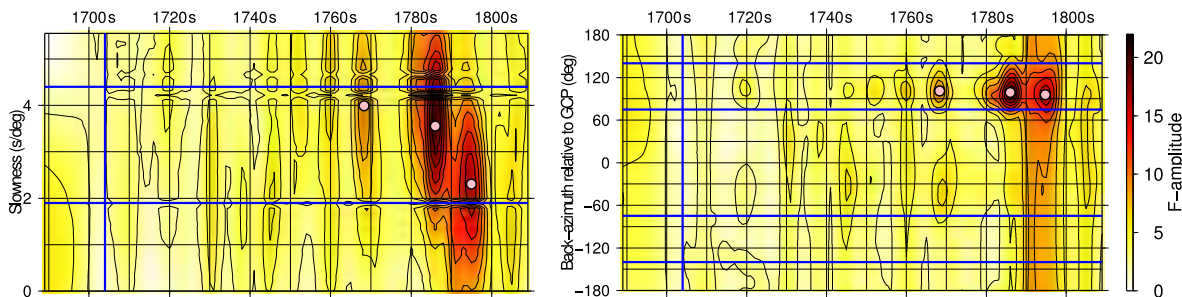


Figure 1.18: Frequency domain F-statistic showing PK•KP scattering time windows for an example event from the dataset used in Chapter 3. A magnitude 6.7 event recorded at Warramunga Array, Australia, on 15/10/2004. The time window displayed is from 1689 s to 1809 s. F-amplitude in (a) slowness and time and (b) back-azimuth and time space. Picked signals are shown as pink circles. Time, and slowness and back-azimuth limits are shown by vertical and horizontal blue lines, respectively.

## 1.5 Limitations

While array processing techniques are theoretically very good at improving signal clarity and suppressing noise, the real data to which they are applied have additional complications due to the non-ideal Earth and the simplifications made to aid processing. These limitations are important while analysing the data to prevent over-interpretation or mis-interpreting noise as signals.

### 1.5.1 Array Mislocation Vectors

As the wavefield travels through the crust, the geological structure beneath an array can lead to reflections and refractions which distort the wavefront. In a laterally isotropic Earth, the direction of an arriving wave can be predicted, assuming that the location of the source and radial velocity structure of the Earth are well constrained. Measurements of slowness and back-azimuth of waves arriving at IMS arrays have been compared to those predicted with a 1-dimensional velocity model [Wright & Cleary, 1974; Bondár *et al.*, 1999]. It is shown that there are consistent patterns of directivity residuals, the amount by which the array mis-determines the slowness and back-azimuth, at each array. Certain arrays, for example Yellowknife in Canada, demonstrate very small directivity residuals, in this case due to the array being sited on flat-lying Canadian Precambrian Shield [Weichert & Whitham, 1969]. Arrays such as PD (Pindale, USA) and TX (Texas, US) show strong directivity deviations, consistent for all directions, most likely due to varying Moho depth beneath the array [Bondár *et al.*, 1999]. Detailed study of the local geology, borehole measurements, and refraction surveys led to a model of the local crustal structure beneath Gräfenberg Array, Germany, that accounted for the direction and magnitude of directivity residuals observed in beams at this array [Krüger & Weber, 1992]. These effects make siting of an array crucial to being able to accurately resolve the true direction of incoming signals.

### 1.5.2 Attenuation

Wave amplitudes are affected by the medium through which the wave is propagating. Energy is lost from the wave by attenuation through various dissipative mechanisms [Aki & Richards, 2002]: intrinsic attenuation,  $Q_a$ , which is due to all Earth materials being anelastic, and extrinsic or scattering attenuation,  $Q_s$ , caused by heterogeneities interfering with the wave (see Chapter 1.3). Anelastic attenuation,  $Q_a$ , has been shown to vary laterally and with depth [Bhattacharyya *et al.*, 1996]. Energy is lost from the wave with each successive cycle, and so attenuation is a frequency dependent process. Higher frequency waves, therefore, are more rapidly attenuated in both time,  $t$ , and distance,  $x$ , than lower frequencies:

$$A(t) = A_0 \exp \left[ \frac{-\omega t}{2Q_a} \right] \quad (1.16)$$

Where  $A(t)$  is the wave amplitude at a given time in comparison to a starting amplitude,  $A_0$ , for a wave propagating through a medium with phase velocity  $c$ .

$$A(x) = A_0 \exp \left[ \frac{-\omega x}{2cQ_a} \right] \quad (1.17)$$

Scattering attenuation,  $Q_s$ , is also locally variable, both in intensity and the frequencies at which it most strongly operates [Aki, 1969; Aki & Chouet, 1975; Korn, 1997; Hock *et al.*, 2004].

Wave amplitude,  $A_D(t)$ , therefore, is affected by the losses through anelastic attenuation and scattering attenuation through time as a function of frequency,  $\omega$ , [Korn, 1997]:

$$A_D(t) = A_0 \exp \left[ \omega t (Q_s^{-1} + Q_a^{-1}) \right] \quad (1.18)$$

Given the lateral variability of both anelastic and scattering attenuation within the mantle, amplitudes of rays taking considerably different paths will not be easily comparable. Therefore amplitude measurements can only be compared for rays travelling similar paths, for example those related to PKP scattering (see Chapter 2).

### 1.5.3 Fresnel Zones

Ray theory is an infinite frequency approximation for a wave. Realistic waves of finite frequency are sensitive to off-ray path structure [Marquering *et al.*, 1998] and the velocity variations sampled by the whole wavefront can lead to focussing and defocussing (also discussed in Chapter 1.2). Focussing may cause energy interacting with other parts of Earth structure to interfere be incorporated into the main signal. The region of sensitivity, the Fresnel zone, is dependent on wavelength,  $\lambda$ , and the distance along the path between the source and receiver at which the Fresnel zone is measured,  $Z$ . The first Fresnel volume is the 3-dimensional region around the ray path where energy arrives within half a cycle of the first arrival and interferes constructively.

$$F = \frac{\sqrt{\lambda Z}}{2} \quad (1.19)$$

For example; for direct P-waves sampling the lower mantle with a dominant frequency of 1 Hz the first Fresnel zone is  $\sim 100$ -140 km wide at its greatest [Sato & Fehler, 2008] and velocity variations detected with these waves can be attributed to any point within the Fresnel zone. The size of the Fresnel zone must be considered when interpreting results to avoid overstating the precision to which source of a velocity variation is known. The ray theory approximation is only valid if the scale length of the velocity heterogeneity is much greater than the wavelength of the wave. Seismic travel-time measurements are, therefore, only valid when studying relatively large structures.

## 1.6 Objectives and Thesis Outline

A variety of studies have shown that the Earth is variable on a range of length scales, from Large Low Shear Velocity Provinces 1000s km wide, to Ultra Low Velocity Zones 10s km thick, and smaller anomalies responsible for high frequency coda waves. This structure is a result of the Earth's dynamic history from formation to present and it is important to observe and understand all scales of heterogeneity to be able to unravel past and present global processes. The seismic wavefield samples the whole of the Earth and so contains information about the Earth's interior in the form of travel-time, waveform, and directivity variations. A combination of different seismological techniques is available to extract this information from the wavefield and help us to resolve Earth's structure.

The lower mantle, as the lower thermal boundary layer of the mantle, and the termination of mantle convection containing the core-mantle boundary, is likely a region of great structural complexity. Within the range of scales of mantle structure the smaller length scales are the least studied. The link between the different scale-lengths is rarely

addressed and so the relationship between velocity structures of different sizes is not well known. The P-wavefield is less utilised than the S-wavefield. This is likely because P-waves are of lower amplitude than S-waves, and often are less sensitive than S-waves to mantle structures, resulting in smaller velocity anomalies. Although models of the Earth's large scale structure are now very coherent and indicate similar structures, much less is known about the Earth's small-scale structure. Throughout this thesis I will address this gap in knowledge by using high frequency P-waves to explore the smaller length-scales of mantle structures and will compare these observations to the known large scale structure. I will also include results from other disciplines, such as mineral physics, and geochemistry, to give possible explanations of these features. In this thesis I will:

1. Demonstrate new processing techniques.

Novel processing techniques adopted from other branches of seismology can help to improve seismologists' ability to resolve global-scale structure. Improving resolution of signals at arrays helps to better determine the direction of incoming seismic waves, allowing the source of the energy to be located more accurately. Increased resolution also means that smaller amplitude signals can be analysed. Testing new techniques will reveal their resolution limit. This can be used to increase the size of the dataset that can be used to study Earth structures.

2. Resolve small-scale heterogeneities of the lowermost mantle and their properties.

Small-scale anomalies have been observed throughout the lowermost mantle using a range of probes (as discussed in Chapter 1.1.2). These structures are most likely compositionally distinct from their surroundings. The seismically resolvable characteristics of these structures in terms of their size, velocity contrasts, and density contrasts may help to reveal their physical properties. The physical distribution of these anomalies may indicate their sources and the processes involved in their formation.

3. Resolve fine aspects of known large-scale structures.

Many of the large scale structures of the mantle are resolved by low frequency data, or from relatively low resolution studies, such as global tomography. Fine scale complexities of the character of these structures may demonstrate other scales of mantle dynamic processes and indicate greater detail of their physical properties, for example, rapid changes in temperature or chemistry which may be related to small-scale mantle processes.

4. Link observations of different scales of mantle structure.

There have been many studies attempting to map mantle structures of the different length scales and understand their causes. However, this information can be better used to study the whole processes of the mantle when analysed together. The interconnection between observations of small and large scale mantle anomalies and their causes will help to reveal how the mantle operates, and how Earth has evolved since its formation.

In Chapter 1 (this chapter) I discussed our present level of knowledge about the Earth's mantle and introduced a range of seismic methods that have been used previously and

some that will be used in this study. This will be followed by three individual case studies, each of which employs a different seismic probe and dataset. Each case study includes an overview of the problem and the progress of past studies, a description of the methods used and the results, discussion of sources of error and the limits of the techniques, and an individual discussion which relates the new observations to the existing knowledge. The thesis ends with a short summary of results and a discussion to link the observations of each of the previous chapters into a coherent image of the thermal, chemical, and dynamic interplay within the Earth.

In Chapter 2 I use data from a small region of South Africa to reveal localised extreme small-scale lower mantle structure using PKP waves scattered by small, volumetric heterogeneities. I apply the F-statistic, a method from forensic seismology, to the beam pack, a technique often used in global seismology, to improve resolution limits (Objective 1). I test the resolution limits of the new F-pack process and demonstrate the lower limit of event magnitudes that can be used. I attempt to use 1-dimensional modelling and calculations from mantle dynamic models to characterise the physical properties of the observed anomalous mantle structures (Objective 2) but discount this method as inadequate due to its simplicity and inability to model 3-D structure. I then discuss how the observation of a  $\sim 80$  km tall heterogeneous ridge at the CMB is related to the larger mantle structure, dynamic convection processes, and composition (Objective 4).

In Chapter 3 I use globally recorded data to study the global distribution of lower mantle heterogeneities using scattered PKKP waves. I apply the same method from forensic seismology to improve resolution limits and processing speed (Objective 1). I observe scattering at a range of heights above the CMB with strong patterns in the distribution in terms of height and lateral location. Scattering is frequently detected at great heights ( $\sim 250$  km) above the CMB beneath Central America and Southern Africa. The location of scattering below South Africa is similar to that observed in Chapter 2. Using another, separate global dataset I study the size of lower mantle structures and find that they have a maximum scale-length of  $\sim 13$  km but are dominantly  $\sim 6$  km or smaller (Objective 2). I then employ statistical methods to study the spatial link between small and large scale structures and compare these observations to global convection and smaller-scale dynamic mixing processes (Objective 4). The small-scale heterogeneities detected with PKKP show correlation with the inside edge of the LLSVPs and also regions of subduction.

In Chapter 4 I employ a single regional array (USArray) and a few specific source regions to study large scale lower mantle structures (LLSVPs). I make new and novel observations of P and  $P_{diff}$  wave residual travel-time patterns at a range of locations and heights which are vital for understanding the influence of composition and temperature on mantle structure. I use high frequency data to improve resolution limits on the location of the boundary of the Pacific LLSVP (Objective 3). I observe differences in the shape and sharpness of the LLSVP boundary: the Eastern edge is seismically sharp and steep ( $\sim 40$  km wide dipping at  $\sim 70^\circ$ ), while the Northern edge is seismically diffuse and shallow ( $\sim 120$  km wide dipping at  $\sim 26^\circ$ ). In addition, I observe strong seismic travel-time delays within a thin, spatially limited region close to the CMB on the northern edge of the Pacific LLSVP which I identify as an Ultra-Low Velocity Zone. I then consider the cause of these spatial complexities and how mantle dynamics and convection may influence lower mantle

structure (Objective 4).

Chapter 5 is the final discussion in which I compare the results of each of the three previous studies. I use these and existing observations to hypothesise about mantle processes and the links and dynamic processes operating within the mantle.



## Chapter 2

---

# PKP Scattering

---

### 2.1 Introduction

Some of the earliest evidence of lower mantle scattering came from observations of precursors to the core phase PKP<sub>df</sub> [Cleary & Haddon, 1972; Doornbos & Husebye, 1972; King et al., 1973; Doornbos & Vlaar, 1973; Haddon & Cleary, 1974; Wright, 1975]. Since then, further observations of precursors to PKP<sub>df</sub> were made and now this phase is routinely used for studying the small-scale structure of the lowermost mantle [Wen & Helmberger, 1998; Shearer et al., 1998; Thomas et al., 1999; Hedlin & Shearer, 2000; Niu & Wen, 2001; Margerin, 2003; Cao & Romanowicz, 2007; Miller & Niu, 2008; Thomas et al., 2009; Vanacore et al., 2010; Frost et al., 2013; Mancinelli & Shearer, 2013]. Precursors to PKP<sub>df</sub> are typically of low amplitudes and so arrays are useful for separating these small signals from the noise, and subsequently locating the source of the energy, the scattering heterogeneity within the lowermost mantle. I use small magnitude events from South Africa, in particular rockbursts in gold mines, combined with the high resolution F-statistic (discussed in Chapter 1.4.6) to resolve scattering heterogeneities. These form a ridge structure  $\sim 80$  km tall located at the CMB under South Africa close to the eastern edge of the African LLSVP. The results of 1-dimensional scattering modelling are inconclusive in determining the contrast in properties of these heterogeneities, although the high amplitude of the scattered wave relative to PKP<sub>df</sub> implies that there is a strong variation. I conclude that these scatterers represent a low velocity and high density material entrained by viscous coupling into the LLSVP convection creating a sharp, tall ridge, which correlates with other observations of ULVZs close to the edges of LLSVPs. The material shown in this Chapter, except for Chapter 2.8, has been published: Frost, Rost, Selby, and Stuart; Detection of a tall ridge at the core-mantle boundary from scattered PKP energy, GJI, 2013.

### 2.2 PKP Probe

PKP waves travel as P-waves through the mantle and outer core, and in the case of PKP<sub>df</sub> through the inner core as well (Figure 2.1). The PKP<sub>ab</sub> and PKP<sub>bc</sub> branches of PKP travel only through the mantle and outer core, while PKP<sub>cd</sub> reflects from the Inner Core Boundary (ICB). Like all waves, PKP can be scattered by velocity anomalies along its path

(explained in Chapter 1.3). Following from observations of additional energy associated with direct P generated by scattering [Aki, 1969], complexities associated with the core phase PKP<sub>df</sub> were the first recognised evidence of scattering of seismic energy within the deep Earth [Cleary & Haddon, 1972]. Low amplitude, high frequency waves arriving before the predicted arrival time of the direct PKP<sub>df</sub> wave at distances between  $\sim 118^\circ$  and  $\sim 145^\circ$  were determined to be generated by scattering from small-scale heterogeneities within the lowest few 100 km of the mantle [Hedlin *et al.*, 1997; Hedlin & Shearer, 2000]. In this distance range PKP<sub>ab</sub> and PKP<sub>bc</sub> waves are not possible. Direct waves possible at this distance, such as PKP<sub>df</sub> and PKP<sub>cd</sub>, will travel deeply into the outer core (and in the case of PKP<sub>df</sub> through the upper inner core), travelling slowly until they emerge back into the mantle. However, due to the velocity drop from the mantle to the outer core, PKP<sub>ab</sub> and PKP<sub>bc</sub> waves scattered in the lower mantle will penetrate less deeply into the outer core and, therefore, arrive at the surface at a shorter distance than possible otherwise and earlier than the direct PKP<sub>df</sub> wave by up to 17 s (Figure 2.2).

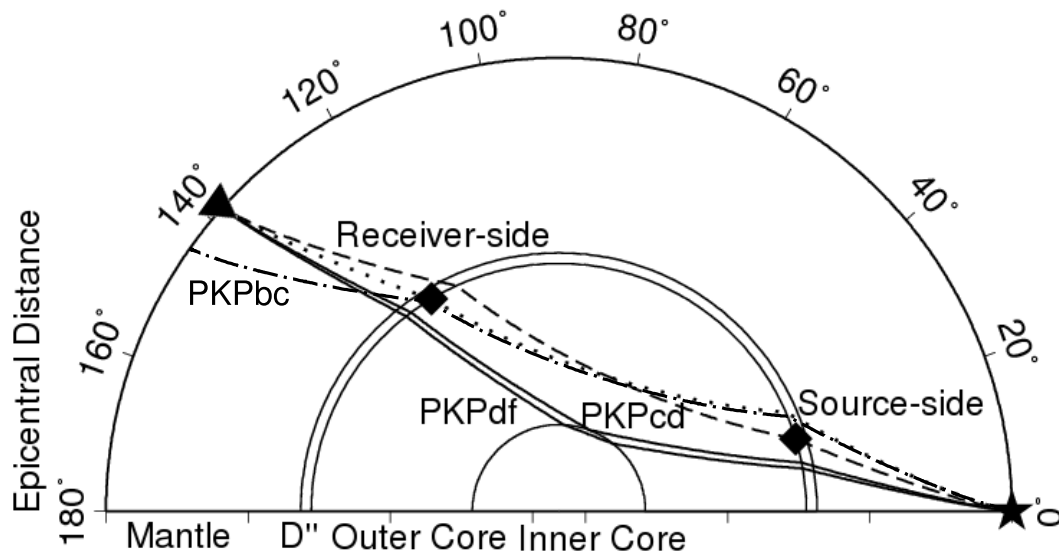


Figure 2.1: Direct PKP<sub>df</sub> and PKP<sub>cd</sub> (solid lines) and source-side scattered P-to-PKP<sub>ab/bc</sub> and receiver-side scattered PKP<sub>ab/bc</sub>-to-P (dashed and dotted lines respectively) for an epicentral distance of  $138^\circ$ . The direct paths PKP<sub>ab</sub> and PKP<sub>bc</sub> do not exist at this epicentral distance and are only possible at distances greater than  $144.6^\circ$ . PKP<sub>bc</sub> is shown at the minimum distance of  $144.6^\circ$  (dashed-dotted line). The star, diamond, and inverted triangle represent source, scattering point, and receiver, respectively.

Calculations demonstrate that, theoretically, these scattered waves can be generated on either the source side (P•KP, where • is the location of scattering along the ray path) or receiver side of the mantle (PK•P) [Haddon & Cleary, 1974], which has since been verified by observations [King *et al.*, 1974; Bataille & Flatte, 1988; Wen & Helmberger, 1998; Wen, 2000; Cao & Romanowicz, 2007; Vanacore *et al.*, 2010; Frost *et al.*, 2013]. When PKP precursors are recorded at arrays, if single scattering is assumed which is shown to be an acceptable approximation from array analysis [Haddon & Cleary, 1974; King *et al.*, 1976], the slowness (incidence angle) can be used to distinguish between scattering from either side of the core. For scattering in the deep mantle, source-side scattered energy will arrive at the receiver with higher slownesses than receiver-side scattered energy (Figure

2.2). For example, at a distance of  $135^\circ$ , source-side scattered waves will have slownesses from 2.7 to 4.4 s/deg, whereas receiver-side scattered energy will arrive with slownesses between 1.0 and 3.0 s/deg [Haddon & Cleary, 1974]. Precursors to PKP have not shown evidence of being scattered in the outer core, based on slowness. While it is often assumed that the outer core is convecting so rapidly as to mix heterogeneities and remain roughly homogeneous, there is some evidence of outer core complexity: either chemical anomalies or stratification in the upper outer core [Garnero & Jeanloz, 2000; Rost & Revenaugh, 2001; Kaneshima & Helffrich, 2013; Helffrich, 2014]. The strongest evidence is derived from phases with multiple CMB underside bounces, known as SmKS, which indicate a 300 km thick slow layer at the top of the outer core. However, these studies do not account for any topography or roughness on the CMB which would substantially influence the inferred velocity structure. Another study utilising the path of PKKP which includes a CMB underside bounce did not find any evidence for outer core structure [Niu *et al.*, 2012]. I consider this problem unresolved but use the evidence of scattered wave slowness to indicate that scattering is restricted to the mantle.

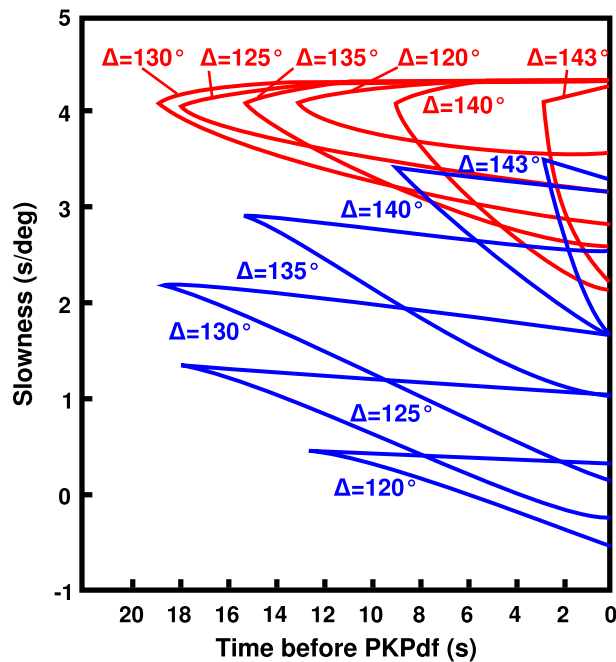


Figure 2.2: The range of slownesses and travel-times (relative to  $PKP_{df}$ ) of waves scattered within the lowermost 200 km of the mantle at varying source-receiver distances ( $\Delta$ ) for along great-circle path scattering. Source- and receiver-side scattering are shown by red and blue lines, respectively. Source-side scattering typically generates waves with higher slownesses than receiver-side scattering. Source-receiver distance limits the amount of time by which scattered waves can precede  $PKP_{df}$ , the earliest scattered energy is produced at source-receiver distances  $\sim 130^\circ$ . The time by which the scattered wave precedes  $PKP_{df}$  is independent of scattering side. After Haddon & Cleary [1974].

The amount of time by which the scattered phase precedes the direct arrival depends on the height above the CMB at which it scattered, the distance along the path at which the scattering occurs, and the angle off the Great Circle Path (GCP) from source to receiver at which it scattered. Scattering off the GCP can also generate precursors, albeit often later arriving waves than on GCP scattering. The earliest scattered wave can arrive 17 s before

the direct wave, for scattering at the CMB with the longest possible P section of the P•KP or PK•P path, along the GCP. PKP paths with long pre or post scattering P segments have shorter paths in the outer core than PKP paths with short P segments. Scattering higher into the lower mantle (above the CMB) and with a shorter P section will arrive closer to PKP<sub>df</sub> as, after scattering, these waves have to traverse the lower mantle at a low angle to reach the CMB and then will travel for longer in the outer core, extending their path length in regions of relatively low velocities (Figure 2.3). Scattering higher than  $\sim 900$  km above the CMB will generate precursors to PKP<sub>df</sub> which will likely be hidden by the coda of the direct wave [Hedlin *et al.*, 1997; Mancinelli & Shearer, 2013]. The scattered coda of PKP<sub>df</sub> has been used in a stochastic sense to study mid-mantle anomalies, but as distinct precursors are obscured in the rest of the coda, the energy cannot be easily characterised in slowness and back-azimuth to locate deterministic scatterers [Hedlin & Shearer, 2002]. Scattering off the GCP extends the path length leading to later arrival of precursors. The volume of the mantle that will generate precursors to PKP<sub>df</sub> can be mapped out by ray-tracing (Figure 2.4) [Thomas *et al.*, 1999] and the shape is limited by the b-caustic at  $\sim 116.5^\circ$  (exact distance dependent on the velocity model used), the shortest distance that PK or KP can travel. The caustic surface is a focal region of PKP energy, therefore, scattering within this area will produce larger amplitude precursors than at other distances [Thomas *et al.*, 2009]. All of the mantle within the scattering volume could potentially contribute energy to precursors to PKP<sub>df</sub>. If a wave travelling in this region is scattered by a heterogeneity it will generate secondary waves which will precede the direct wave.

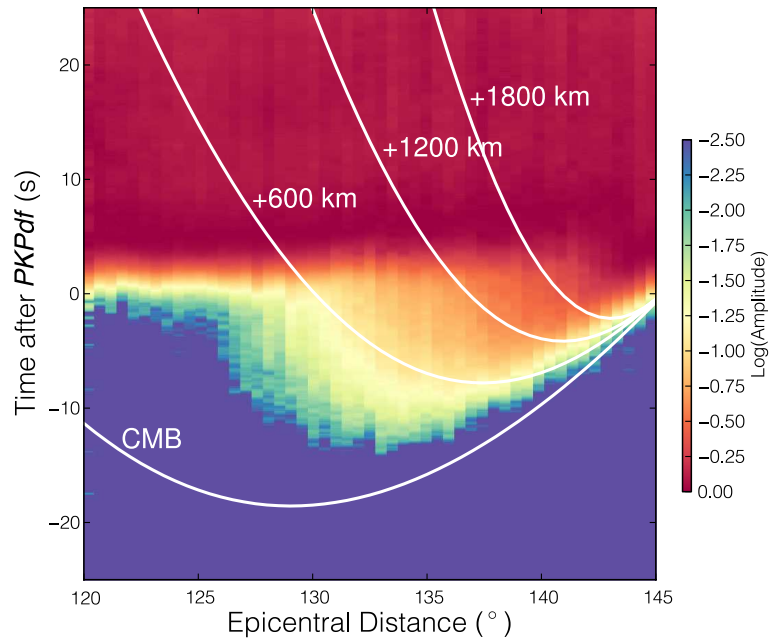


Figure 2.3: Global data stack showing time and distance dependence of precursors to PKP calculated in  $0.5^\circ$  distance bins. Data are aligned on  $PKP_{df}$  and normalised to the maximum amplitude out of  $PKP_{df}$  and  $PKP_{cd}$ . White lines describe the earliest ray-theoretical precursor in each distance bin for scattering at different heights above the CMB. However, due to variable ray coverage, lateral variability of the prevalence of lower mantle scattering heterogeneities, and the small area that generates the earliest precursors (Figure 2.4a) the earliest scattered energy appears very weak in a global stack and is likely masked by high amplitude later arriving energy. From Mancinelli & Shearer [2013].

When precursors to  $PKP_{df}$  are recorded at arrays, the Vespa process (introduced in Chapter 1.4.3) and ray-tracing can be utilised to determine precise location of scatterers in the deep mantle. The Vespa technique shows the evolution of the precursory wavetrain through time and the dominant slowness at each point. Studies have shown individual pulses of energy with distinct slowness values which supports interpreting this energy as singly scattered [King *et al.*, 1974]. Using combined array processing techniques, such as beam packing (discussed in Chapter 1.4.7), allows the determination of slowness and back-azimuth simultaneously, thus identifying off-azimuth scatterers. In this chapter I apply the F-statistic, a method to improve directivity resolution, to beam packing to create F-packs. This improves slowness and back-azimuth resolution and allows use of smaller amplitude events than would be possible with traditional beam forming.

Other techniques can be used to determine scatterer location when precursors are recorded at single stations. Although I do not use these methods I discuss them to explain how non-array observations of precursors to  $PKP_{df}$  can be located. Single stations cannot accurately resolve the direction of incoming waves (although some insight can be gained by using particle motions at 3-component stations). However, the knowledge of the travel-time for a certain scatterer location (as in Figure 2.4c) can be used to overcome the source-receiver ambiguity. For a given source-receiver distance, the region of scattering at a distinct height can be calculated. The area that could possibly generate a precursor with a given arrival time before  $PKP_{df}$  is defined by a line or “iso-time scatterer arc” within

the whole scattering region [Wen, 2000]. By measuring the arrival times of precursors for numerous detections in a similar region, the isotime scatterer arcs can be overlaid and the location at which the most of these lines intersect is taken to be the position of the scatterer [Wen, 2000; Niu & Wen, 2001]. This relies on multiple observations and resolving a dominant scattering location. To prevent mislocation, these studies tend to focus on the source of only the first precursor meaning that some of the later information about scattering at greater heights is missed. This method provides additional observations of precursors to PKP and thus helps to locate lower mantle heterogeneities but is less precise than using arrays to locate scatterers as I do in this chapter.

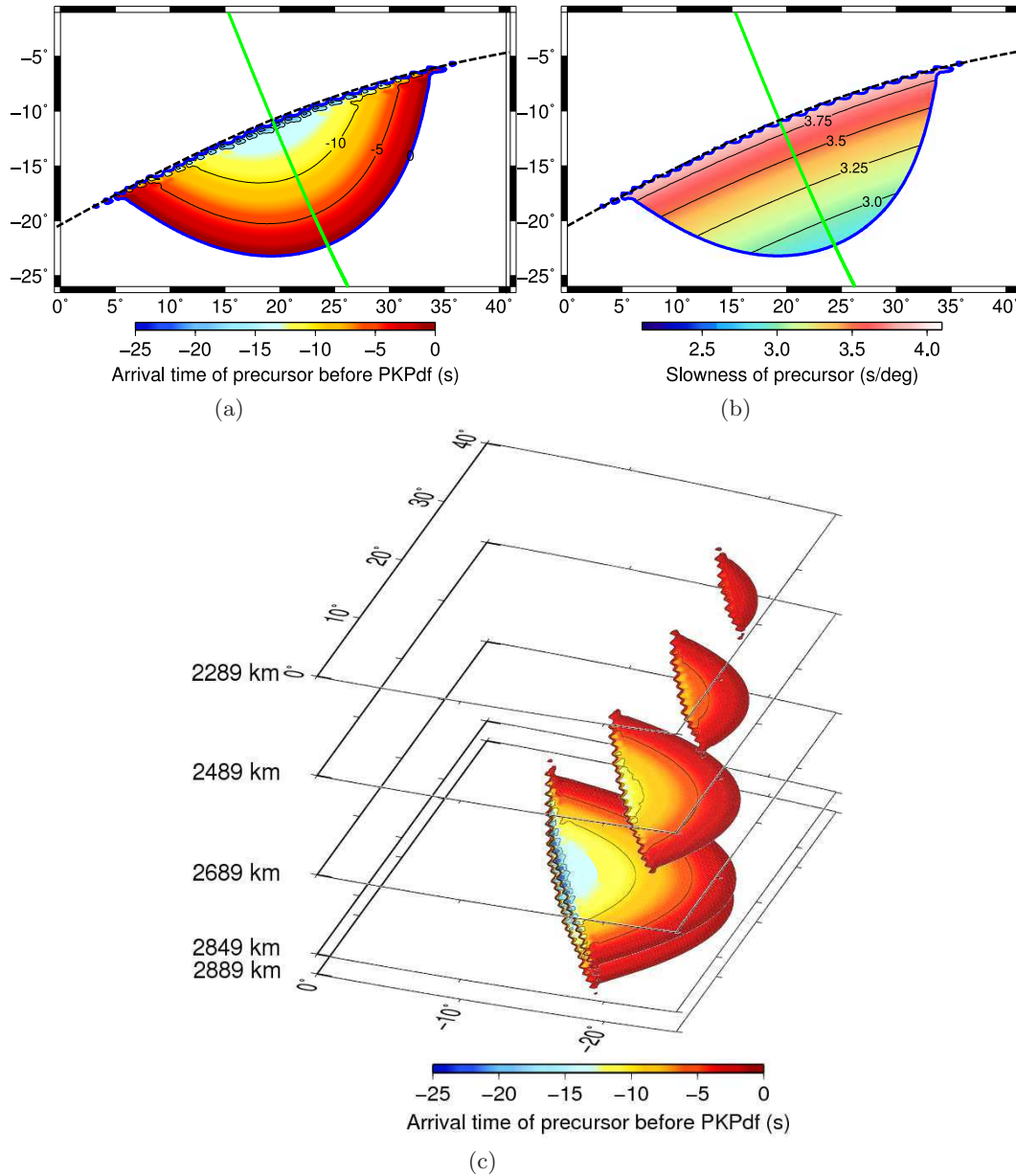


Figure 2.4: Areas in which scattering on the source side could generate precursors. This is shown for an event at  $136.2^\circ$  distance from the receiver simulating ray paths typical of the dataset used in the remainder of the chapter. Earlier precursors scatter from the northern-most edge of the study region, furthest from the source, close to the CMB and the  $b$ -caustic (shown by the dashed black line). (a) Area at 40 km above the CMB in which scattering generates precursors. Arrival time of the precursor is shown relative to  $PKP_{df}$  in seconds. The green line shows the great circle path from source to the receiver. (b) Slowness values (in s/deg) recorded at the array for scattering at different locations in the region that would generate precursors. The  $b$ -caustic is shown by the dashed black line. (c) Potential scattering areas at a range of heights from 0 km to 600 km above the CMB (depths of 2889 km to 2289 km). This shows the reduction in the area which can generate precursors and the reduction in the time by which scattered energy can precede  $PKP_{df}$  with increasing height. Precursory times are contoured at 5 s intervals. All plots are created using a grid with spacing of  $0.5^\circ$  in latitude and longitude.

Single station observations of PKP precursors at global networks have been used to calculate a global average scattering structure. Modelling of stacks of precursor envelopes

has suggested heterogeneities of scales on the order of 10 km with a 0.1-1 % RMS velocity perturbation distributed throughout the whole mantle [Hedlin *et al.*, 1997; Mancinelli & Shearer, 2013]. These data have also been used to calculate lateral variation in scattering strength, although this is complicated by the source-receiver ambiguity which cannot easily be resolved with single stations. Studies demonstrate strong regional dependence of scattering, which primarily originates in the lowermost mantle [Hedlin & Shearer, 2000]. This suggests a bimodal structure with ubiquitous low level scattering and additional, localised, higher amplitude scattering.

## 2.3 Data

Yellowknife Array (YK) is a  $\sim 20$  km aperture, UK-style (cross-shaped) array on the northern coast of the Great Slave Lake (Figure 2.5a). It comprises 18 short-period vertical seismometers in two perpendicular branches, oriented North-South and East-West, with an inter-station spacing of 2.5 km [Weichert & Whitham, 1969], plus 4 additional broadband stations. The aperture of the array results in good slowness and back-azimuth resolution, although there is significant aliasing along the array arms owing to the cross shape (Figure 2.5b and for further discussion about Array Response Functions see Chapter 1.4.5). The remote location of this array and the simple crustal structure of the underlying Canadian Precambrian Shield result in extremely low ambient noise conditions and small mislocation vectors [Bondár *et al.*, 1999]. It is, therefore, well suited to studying high frequency, low amplitude P-waves.

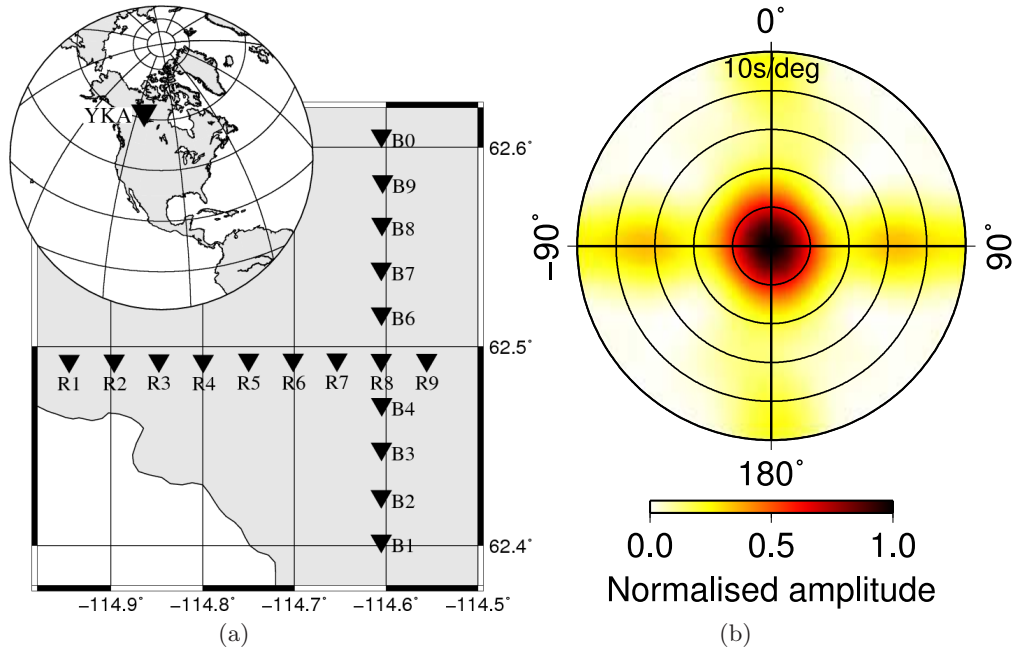


Figure 2.5: (a) Yellowknife station configuration. YK contains 18 short-period stations with a minimum station spacing of 2.5 km and a maximum station separation (aperture) of 20 km along two perpendicular N-S; E-W oriented legs. Inset shows Yellowknife Array location in northern Canada. (b) Array response function computed at 1 Hz and 0 s/deg displayed for slownesses from 0 to 10 s/deg, in 2 s/deg steps, and back-azimuths from 0 to 360°. Due to the aperture of the array the local maximum of the ARF is narrow but there is spatial aliasing along the arms of the array resulting from the cross shape.

Intraplate earthquakes from southern Africa (between 30° S to 7° S, and 15° E to 35° E) over the time period from 1978 to 2011 recorded at YK are selected from the data holdings of the Atomic Weapons Establishment (AWE) Blacknest (Figure 2.6a). Data from 1978 to 1990, without magnitude restriction, are taken from analogue tapes recently digitised by AWE Blacknest. Although 4 broadband stations were operating from 1990 onwards, only short-period data are used. I select 153 events from the International Seismological Centre (ISC) catalogues and Comprehensive Nuclear Test Ban Treaty Organisation Reviewed Event Bulletins (REB) with the smallest magnitude ( $m_b$ ) used being 3.2 and the largest being 6.0. Events are between 119.3° and 138.8° epicentral distance from YK with back-azimuths ranging between 38.1° and 64.8° (from North). The majority of the events are related to four deep gold mining regions: the Free State Gold Mines near Welkom, Klerksdorp Gold Mines near Klerksdorp, the Far West Rand Gold Mines near Carletonville, and the West and Central Rand Gold Mines near Randfontein (Figure 2.6b; see Appendix Table B.1 for source location details). Waveform modelling of some of these events has previously shown that they are likely mining induced seismicity [Bowers, 1997]. Depths listed in the catalogue for nearly all events are either very shallow ( $\leq 2$  km), poorly constrained, or are unconstrained. Given their association with the gold mines, I assume a surface source depth for subsequent processing. The seismicity from the South-African mining region is subdivided into 3 groups dependent on the association with the Welkom (SW), Klerksdorp (NW), or Carletonville and Randfontein mining regions (NE).

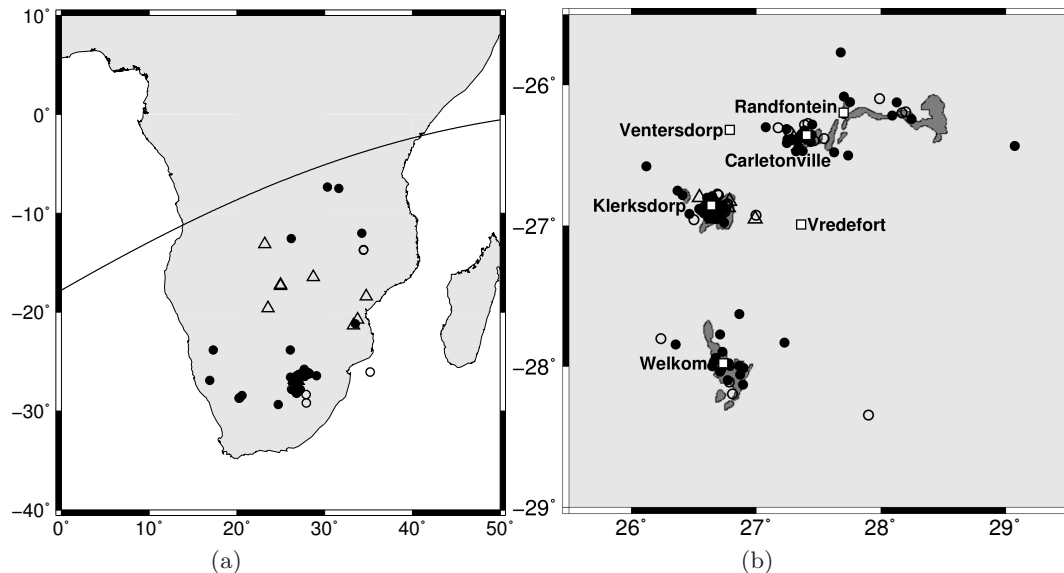


Figure 2.6: (a) Source locations in southern Africa with category 1 and 2 events shown as filled circles (for category definitions see Chapter 2.5.1), category 3 as open triangles, and category 4 as open circles showing all events used and the mining region denoted by a black box. The minimum scattering distance, the  $b$ -caustic, of  $116.5^\circ$  from YK is shown by the black curve. (b) The mining region with mine areas shaded dark grey and towns as white squares with event classifications as in (a).

Waveform modelling of both regional and teleseismic waves from mining events in a range of settings have been used to determine source parameters for induced seismicity. Additional information from witness accounts of events in mines have helped to describe the ways in which mining events occur. Gold mines in South Africa are generally  $\sim 2$  km deep, although the Western Deep Levels mine in the Carletonville region is up to 4 km deep. The majority of mining induced seismicity has been shown to generate events with primarily implosive source mechanisms with dilational first motions and simple source mechanisms [Hasegawa & Gendzwil, 1989; Julian et al., 1998; Miller et al., 1998]. For example, events in the Carletonville region have been modelled as having a strong implosive component [Julia et al., 2009] and some events in the Klerksdorp region have also been shown to be implosive [McGarr, 1992]. However, the Klerksdorp and Welkom regions contain pervasive, pre-existing normal faults. Some mining related events in these regions, particularly the large events with  $M_b \geq 5$ , are demonstrated to result from slip on these faults, complemented by the existing ambient stress field, adding an implosive (dilational) component [McGarr et al., 1989; Bennett et al., 1996; Bowers, 1997]. Event depths for all mines used in this study are mostly  $\leq 2$  km. The source spectrum is reported to be broader at Klerksdorp than Carletonville, however, this is based on analysis of only two events [McGarr et al., 1989]. An extensive study of seismic disturbances in South African mines demonstrated that nearly all events were shallow and related to mining and were not standard earthquakes [Bowers, 2000]. Although it is not appropriate to assume that all mining events are implosive and isotropic, as the difference in take-off angle between the  $PKP_{df}$  and precursor waves is  $\leq 5^\circ$  for all distances in this study it is unlikely that there will be any significant differences in amplitude between these two paths due to source radiation pattern. Therefore, wave amplitudes from all 3 mining regions can be

calculated in the same way without any corrections for the take-off angle relative to the radiation pattern. Previous studies of precursors to PKP<sub>df</sub> have typically used events with magnitudes of  $\geq 5.5$  [Wen & Helmberger, 1998; Thomas et al., 1999; Niu & Wen, 2001; Cao & Romanowicz, 2007; Thomas et al., 2009], whereas in this study the average event magnitude is 4.5. To accurately observe scattered waves associated with these low magnitude events and measure their slowness and back-azimuth I employ higher resolution processing methods than have previously been used to study precursors to PKP<sub>df</sub>.

## 2.4 PKP Scattering Coverage

To determine the area of the CMB from which scattering from the 153 events in the data set could generate precursors and be identified in the seismograms, I calculate potential source-side scattering regions for PKP at the CMB, similar to Figure 2.4. Potential scattering regions are created for different source-receiver distances from  $120^\circ$  to  $140^\circ$  in  $5^\circ$  increments. I select the scattering region created for the distance closest to the exact source-receiver distance for each source, I then rotate this to align with the great-circle path and move it according to the source location of the event, thus indicating the region at the CMB that precursors from this event could sample. These scattering regions are stacked for all 153 events and the number of hits per  $0.5^\circ \times 0.5^\circ$  bin is calculated (Figure 2.7). The overall region of sampling is limited by the b-caustic at  $116.5^\circ$ . Although there is a clear region of dominant sampling, there is additional sampling outside of this area, therefore, small-scale structure of the lower-most mantle in this region should be well resolved.

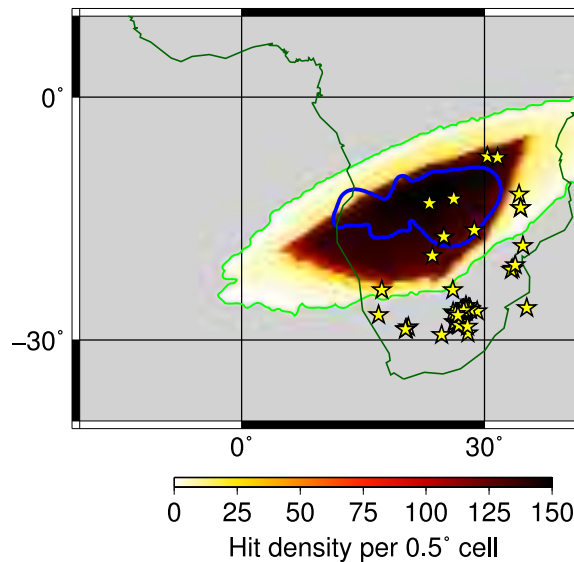


Figure 2.7: Potential coverage by precursors to PKP for scattering at the CMB for all 153 source-receiver pair. The extent of the coverage, the zero-sampling contour, is shown by the green line. The blue contour indicates the extent of the scattering structure shown in Figure 2.12a (the 25 km height contour is shown). All 153 sources from all event categories are shown by yellow stars. Scattering could be observed outside of the region resolved to contain scattering heterogeneities (blue contour) suggesting that the detected scattering structure is real and constrained to the region shown.

## 2.5 Method

### 2.5.1 Array Processing

I apply the F-trace to the time window surrounding  $\text{PKP}_{df}$  to resolve scattered precursors to the main phase. Initially, I use an F-Vespa to identify events that show scattering (introduced in Chapter 1.4.3). The events used are low magnitude (average  $m_b = 4.5$ ) and so precursory signals will be very small. This technique is significantly more precise at resolving the directivity information of a signal than a standard Vespa (demonstrated in Chapter 1.4.3 and 1.4.6). For each event I select a 120 s long time window which includes the arrival time predicted for  $\text{PKP}_{df}$  using IASP91 [Kennett & Engdahl, 1991]. Data are Butterworth bandpass filtered between 1.0 and 2.0 Hz with 4 poles, from which I create beams for slownesses from 0 s/deg to 7 s/deg in 0.1 s/deg increments and then apply the F-trace to improve slowness resolution. For a typical event in the dataset, when processed using a standard Vespa, the 90 % maximum amplitude region around the highest amplitude signal (which in the case of the event in Figure 2.8 is a precursor to  $\text{PKP}_{df}$ ) is 1.9 s/deg wide (Figure 1.15a). By contrast, for the same event processed using the F-Vespa the 90 % maximum amplitude region of the same signal is only 0.5 s/deg wide (Figure 2.8a). The  $\text{PKP}_{df}$  arrival is picked from the processed data as the maximum F-trace amplitude within 1.5 s of the predicted IASP91 time with a slowness of  $\sim 2$  s/deg. This arrival time is then adjusted to ensure the strongest arrival is selected, thus accounting for travel-time variations due to 3D velocity variations. The number and arrival times of peaks preceding and following  $\text{PKP}_{df}$  are noted for later processing. There is no specific F-amplitude which defines a peak, only that it is obvious in the normalised F-Vespa, is shorter than  $\sim 5$  s, and has a single, clear slowness maximum in that time window.

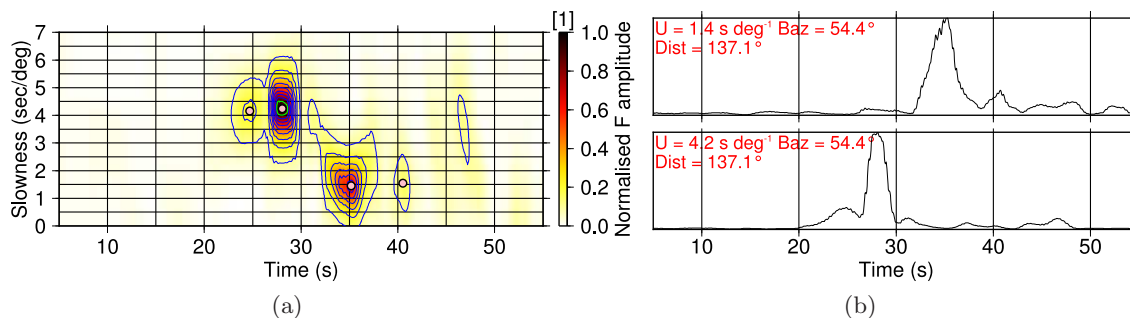


Figure 2.8: Array processing for an event at 12:50:07.03 on 1996/12/11 in South Africa, recorded at YK, Canada, the same event shown in Figure 1.15. (a) F-Vespa formed from F-traces for slownesses between 0.0 and 7.0 s/deg.  $\text{PKP}_{df}$  is seen arriving at  $\sim 35$  s with slowness of  $\sim 2.0$  s/deg, two precursors arriving at  $\sim 25$  and  $28$  s with slownesses  $\sim 4$  s/deg, and another arrival following  $\text{PKP}_{df}$  which may be  $\text{PKP}_{cd}$  (all pink circles). The 90 % maximum amplitude region is marked by the green contour. (b) F-traces formed on  $\text{PKP}_{df}$  slowness (top) and precursor slowness (bottom), filtered between 1 and 2 Hz. The slowness ( $U$ ) and back-azimuth ( $Baz$ ) for which the F-traces are calculated are shown in the top left.

From the results of the F-Vespa, each event is categorised based on the occurrence and clarity of precursors and direct phases. Category 1 events show both  $\text{PKP}_{df}$  and  $\text{PKP}_{cd}$  along with two precursors (56 events in this category, 37 % of all events). Category 2

events show  $\text{PKP}_{df}$ , and one precursor (42 events, 27 %). Category 3 contains events in which only  $\text{PKP}_{df}$  can be observed (18 events, 12 %). Category 4 contains events in which there are no identifiable arrivals (37 events, 24 %). In the following I use only arrivals from category 1 and 2 events, leaving 98 events (64 % of the original population) with 157 precursor detections to be analysed. Some events have 3 or more visible precursors, and as many as 5 in one case. However, I limit analysis to a maximum of 2 precursors. Events with greater than 2 precursors make up the minority of the dataset ( $\sim 11$  %) and so I choose not to adapt my processing to study them. It is interesting to note that there is a positive correlation between the number of precursors and event magnitude, and between the number of precursors and SNR, which become more prominent for more than 2 precursors, although the number of events used in this calculation is very low and the result is likely not statistically robust.

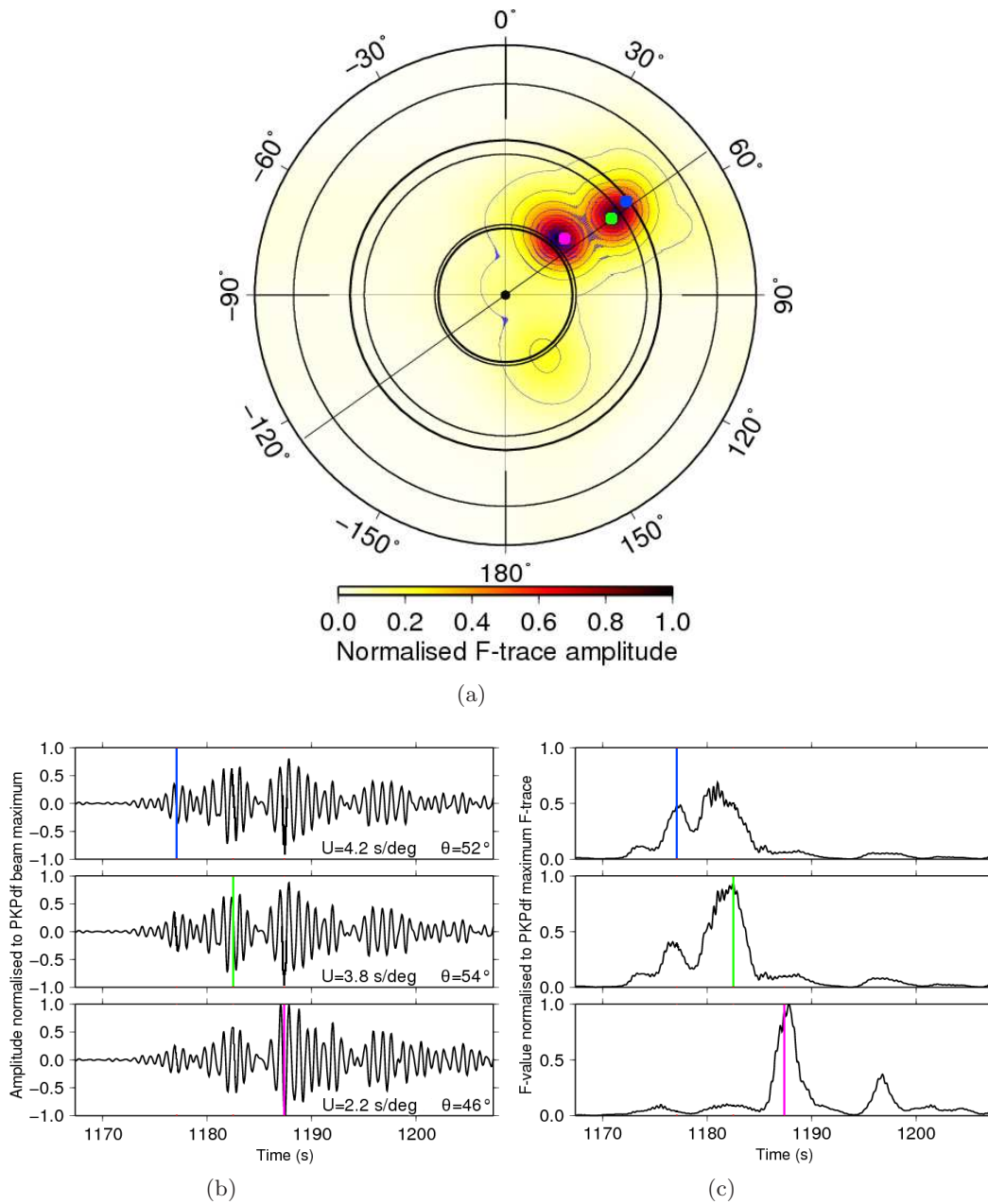


Figure 2.9: F-pack formed by creating beams for back-azimuths from  $0^\circ$  to  $360^\circ$  and slownesses of  $0.0$  s/deg to  $7.0$  s/deg and calculating the F-statistic for each beam, using data recorded at YK from an event at  $22:19:36.77$  on  $22/04/1999$  in South Africa. The F-traces are processed with a 4 pass, zero phase Butterworth bandpass filter with corner frequencies of  $1.0$  Hz and  $2.0$  Hz. The maximum F-statistic in a given time window is calculated and all amplitudes are normalised relative to the maximum. (a) Normalised F-statistic for a  $60$  s time window around PKP<sub>df</sub> with peaks identified as the first precursor (blue), second precursor (green), and PKP<sub>df</sub> (pink). Optimal slownesses ( $U$ ) and back-azimuths ( $\theta$ ) used to form the (b) beams and (c) F-traces for the first precursor, second precursor, and PKP<sub>df</sub> (traces from top to bottom) are noted on each trace and on the F-pack as blue, green, and pink circles. Lines on the F-traces indicate the picked arrival time for each phase with the same colour code; energy arriving after these comprises the coda.

To reduce processing time, a new, shorter,  $60$  s time window is selected around PKP<sub>df</sub>. Traces are analysed in slowness and back-azimuth space with the F-pack (see Chapter 1.4.7). The F-pack is applied for slownesses between  $0.0$  to  $7$  s/deg in  $0.1$  s/deg incre-

ments and back-azimuths between  $1^\circ$  and  $360^\circ$  in  $1^\circ$  increments, giving F-amplitude for all directions through time (Figure 2.9). The arrival times picked in the F-Vespas are used to select the time window for the F-pack for each precursor, from which the best fitting slowness and back-azimuth are then determined. The best fitting values are selected by finding the maximum F-trace amplitude between 16 s to 11 s and 8 s to 3 s prior to  $\text{PKP}_{df}$  to allow picking of distinct first and second precursory phases, respectively. A 3 s separation between phases is introduced to ensure that discrete signals are used and individual scattering anomalies can be located. Travel-times are picked on the maximum F-statistic and are computed relative to  $\text{PKP}_{df}$  travel-time to minimize errors due to 3D velocity structure. A phase arriving, on average, 4.7 s after  $\text{PKP}_{df}$  can be identified which is potentially  $\text{PKP}_{cd}$ , the PKP reflection off the inner core boundary. Despite matching the slowness predicted by IASP91 [Kennett & Engdahl, 1991] to within, on average, 0.3 s/deg, this phase arrives, on average, 2.5 s later than predicted for this distance. This delayed phase may be the result of heterogeneous Earth structure; it will be referred to as  $\text{PKP}_{cd}$  but is not used in the following analysis and therefore I do not explore its origin further.

### 2.5.2 Ray Tracing

I use the slowness, back-azimuth and travel-time values of each precursory signal measured with the F-pack to locate volumetric scatterers within the lowermost mantle. Based on ray-path calculations which indicate that the range of slownesses possible from scattering on the source side is significantly higher than on the receiver side (Figure 2.2) and the relatively high slownesses of the precursors I conclude that scattering occurs on the source side under South Africa. A previous study [Cao & Romanowicz, 2007] observed scattered PKP precursors in YK records from earthquakes in South America. The scattered signals had slownesses lower than those seen in my study and thus were attributed to receiver-side scattering. The core exit points of the events are located beneath central Canada [Cao & Romanowicz, 2007] compared to north-east Canada (close to Greenland) in my study. Therefore, the sampling of the CMB region is sufficiently different to explain the different results and so I am unlikely to be sampling the same scattering structures. It is possible that source-side scattering may mask receiver-side scattering. However, receiver-side scattering has characteristically different slownesses from source-side scattering (Figure 2.2) and the resolution of the F-pack is sufficient to resolve these differences.

To determine scattering location I construct a 2-dimensional grid under South Africa along the back-azimuth recorded at YK. The grid extends from  $110^\circ$  from the receiver along the back-azimuth back towards the source to  $1^\circ$  past the source location, with a lateral grid spacing of  $0.5^\circ$ . The grid then extends vertically from the CMB to 200 km above, with grid-points every 5 km (Figure 2.10). As I am assuming that these events are mining related or mining induced (discussed in Chapter 2.3) and the source depths reported in the catalogue are either 0 or are unconstrained, I use the surface as the source depth. For the velocity model used (IASP91) for a PKP path, a 3 km difference in source depth would result in a travel-time difference of 0.5 s, which is negligible, compared to the sensitivity limits (calculated in Chapter 2.7). Travel-times are calculated by raytracing through IASP91 from the source at the surface to each scattering point in the grid, and

then from the scattering point to the receiver. Some scatterer-receiver combinations are not possible, subsequently, these scattering points are discarded. The cumulative travel-time and slowness recorded at the receiver for each point in the grid is calculated and then compared to the values measured with the F-pack. The best fitting scattering grid point is found by minimizing the misfit between the observed and traced slowness and travel-time. Thirty-nine scatterers (25 % of the 157 precursors) cannot be located with sufficiently low misfits (below 1 s/deg slowness and 1.5 s travel-time). These events are potentially multiple scattered arrivals or mis-identifications and are discarded from further analysis. Scattering strength for each scattering point is measured by taking the ratio of the maximum filtered beam amplitude of the precursor relative to that of PKP<sub>df</sub>, for beams formed on the slowness and back-azimuth of the phase of interest. The F-amplitude information is used only to identify the time window in which to pick the precursor and PKP<sub>df</sub> beam amplitudes and the directivity information on which to form the beam. Given that the paths of the two waves through the mantle are likely to be very similar they will most probably encounter similar attenuation structure, and so the amplitudes can be compared to obtain an estimate of heterogeneity strength without correcting for attenuation. However, there is evidence for regional variation of the attenuation structure of the inner core with notable differences between the east and west hemispheres [Tanaka & Hamaguchi, 1997; Ouzounis & Creager, 2001]. When comparing the relative precursor strengths for waves sampling different regions of the Earth, the amplitudes ratios of PKP precursors to PKP<sub>df</sub> would, therefore, have to be corrected for variation in attenuation structure.

Ray tracing is repeated with scattering grids located on the receiver side. However, much higher misfits are recorded than for scattering on the source side, even for the precursors that are poorly fit on the source side. Tests with a few events are ray-traced for grids extending up to 1200 km above the CMB, however, no scatterers could be found above 200 km and so subsequent processing is limited to heights from the CMB to 2689 km depth.

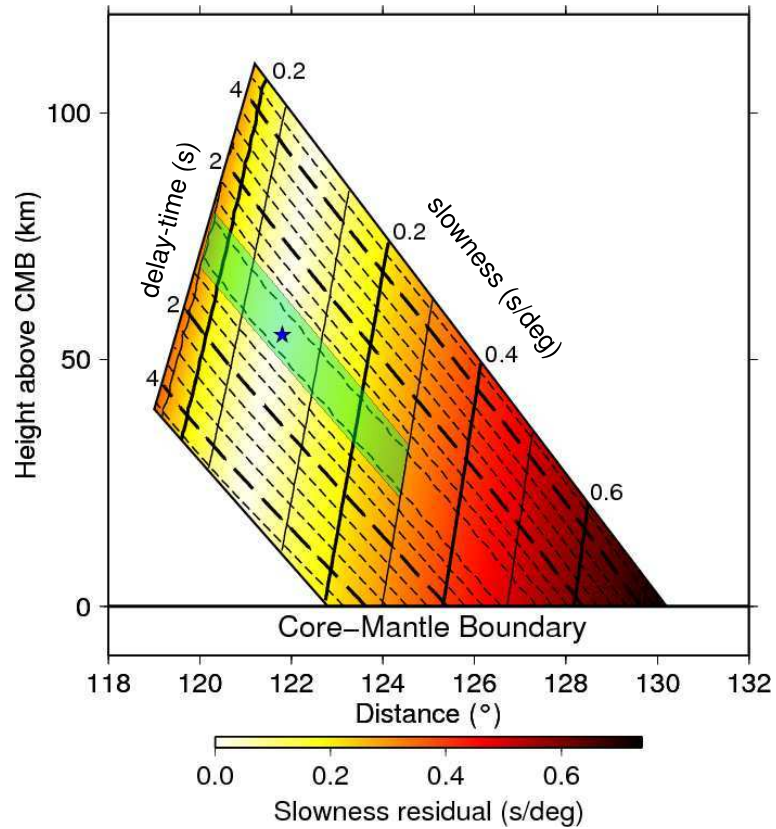


Figure 2.10: Spatial resolution of potential scatterer location for an event at  $136.3^\circ$  distance. Slowness and time misfits are shown as solid and dashed contours, respectively. The grid of potential scatterers is aligned along the back-azimuth recorded at YK. The region to which the best fit scattering point (blue star) is constrained is shown as a green box, with distance uncertainties of  $\pm 2^\circ$  and height uncertainties of  $\pm 25$  km based on slowness errors of  $\pm 0.25$  s/deg and time errors of  $\pm 0.5$  s (calculated in Chapter 2.7). Source-to-scatterer distance is best constrained by slowness, and scatterer height is best constrained by travel-time.

## 2.6 Results

The waveforms of the precursors are similar to that of  $\text{PKP}_{df}$  (Figure 2.9b), indicating that these signals are of related origin and, therefore, can be compared. Unrelated signals coincidentally arriving at YK in the precursory time window would, most likely, have considerably different back-azimuths, as well as waveforms and so could be differentiated. The major phase,  $\text{PKP}_{df}$ , arrives within  $\sim 5$  s of the time and 0.3 s/deg of the slowness (with a standard deviation of  $\pm 0.4$  s/deg) predicted by the IASP91 model (Figure 2.11) [Kennett & Engdahl, 1991].  $\text{PKP}_{df}$  is preceded by several high slowness phases arriving 3-15 s prior to  $\text{PKP}_{df}$ . Most events (37 % of the total dataset and 57 % of all the events that have precursors) show two distinct, time separated precursors with slownesses 1.8-2.0 s/deg higher than  $\text{PKP}_{df}$ . The earlier precursor generally has a higher slowness than the second which arrives closer to  $\text{PKP}_{df}$ , and likely originates closer to the CMB and closer to the b-caustic (Figure 2.4a). These precursors have clearly defined amplitude peaks and are often separated by a period of incoherent, low amplitude energy, probably noise (Figure 2.8). Precursors arrive off great-circle path by up to  $\pm 30^\circ$  (average of  $7.4^\circ$  with a standard deviation of  $6.7^\circ$ ) for the first (early) precursor and up to  $\pm 30^\circ$  (average of

$6.0^\circ$  with a standard deviation of  $6.0^\circ$ ) for the second (later) precursor. As they are not constrained to the GCP, the precursors sample a wider region of the CMB than  $\text{PKP}_{df}$ . Although these back-azimuth deviations are large, theoretical calculations of the back-azimuths from the outermost points of the scattering zone (Figure 2.4) show that these values are in agreement with the extent of the b-caustic and other scattering limits.

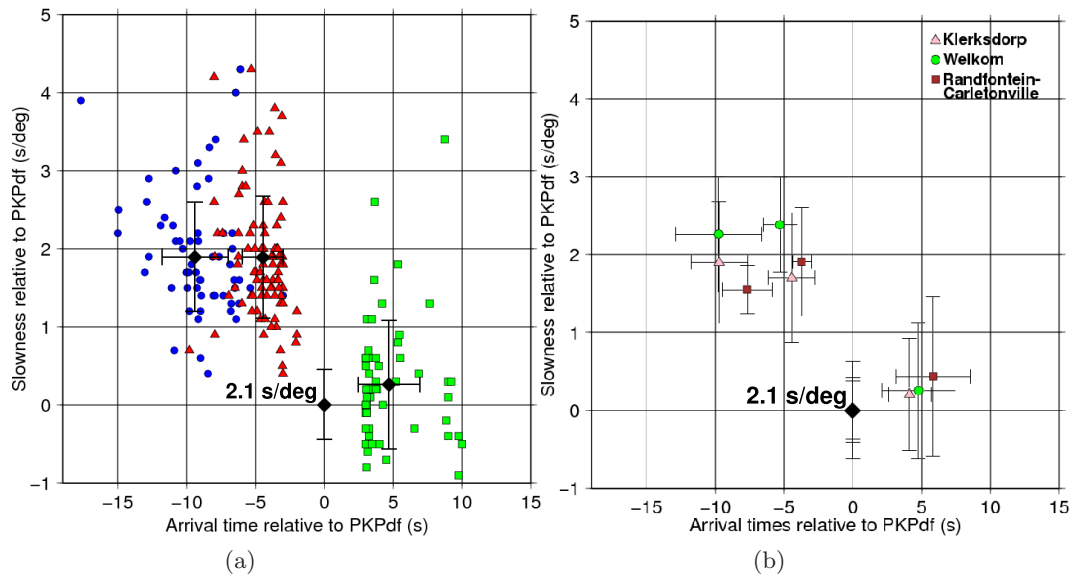


Figure 2.11: Arrival-time and slowness deviations for precursors and  $\text{PKP}_{cd}$  relative to  $\text{PKP}_{df}$  (black diamond at 0,0. Average  $\text{PKP}_{df}$  slowness is 2.1 s/deg and all time measurements are relative to this phase). (a) Arrivals for all category 1 and 2 events, with first precursors (blue circles), second precursors (red triangles), and  $\text{PKP}_{cd}$  (green squares). Black diamonds show average arrivals with 1-standard deviation error bars for each phase. No time error bar is shown for  $\text{PKP}_{df}$  as other times are measured relative to this. Precursors display distinctly different slownesses and arrival-times to  $\text{PKP}_{df}$ . On an event by event basis, the slowness of the first precursor is generally greater than that of the second precursor (for example Figure 2.9a) although plotting all events together as in this figure makes this difficult to observe here, and there is a distinct time gap between the two arrivals. (b) Average arrivals for each phase, for each mining source region with 1 standard deviation error bars. Pink triangles, green circles, and brown squares represent events from Klerksdorp (NW), Welkom (SW), and Carletonville and Randfontein mines (NE) respectively.

The ray-tracing results indicate that discrete scatterers reside at heights ranging from the CMB to approximately 80 km above the CMB, with a few outlying scattering points up to 150 km above the CMB (Figures 2.12a and 2.12c). The scattering points detected define a ridge  $\sim 1200$  km long by  $\sim 300$  km wide, trending East-North-East, West-South-West, with modal heights of 80 km above the CMB (Figure 2.13). The north-western face of the ridge is steeper and dips at  $\sim 11^\circ$  to the horizontal while the shallower south-eastern face dips at  $\sim 5^\circ$  (Figure 2.13). The most elevated scattering points correlate with larger precursor amplitudes relative to  $\text{PKP}_{df}$ , whereas scatterers closer to the CMB tend to have lower precursor amplitudes (Figure 2.12). The region of most and strongest scattering is surrounded by weak scattering located on, and just above, the CMB (up to 10 km). There is no evidence of scattering significantly above the CMB in areas other than the ridge indicating strong scattering from this region and less from the surrounding region.

Precursor amplitudes relative to  $PKP_{df}$  are very high; the average precursor to  $PKP_{df}$  amplitude ratio of the first arriving precursors is 0.44 (ranging from 0.1 to 1.90, standard deviation of 0.29), whereas the average second precursor to  $PKP_{df}$  amplitude ratio is 0.79 (ranging from 0.20 to 2.50, standard deviation of 0.49). Early first precursors locate closer to the CMB than later second precursors; this agrees with ray-tracing results indicating that energy with the largest differential travel-time relative to  $PKP_{df}$  originates from those rays which scatter closest to the CMB (Figures 2.3 and 2.4). Scatterer distribution is uneven across the study region; however, the centre of the structure is sampled by most source-receiver combinations (Figure 2.7) and also is the region in which most scattering is observed (Figure 2.14). This structure is, therefore, well constrained with multiple data points supporting the resolved features. Nonetheless, the areas at the periphery of the scattering structure, although containing fewer observed scatterers, are still supported by multiple data points.

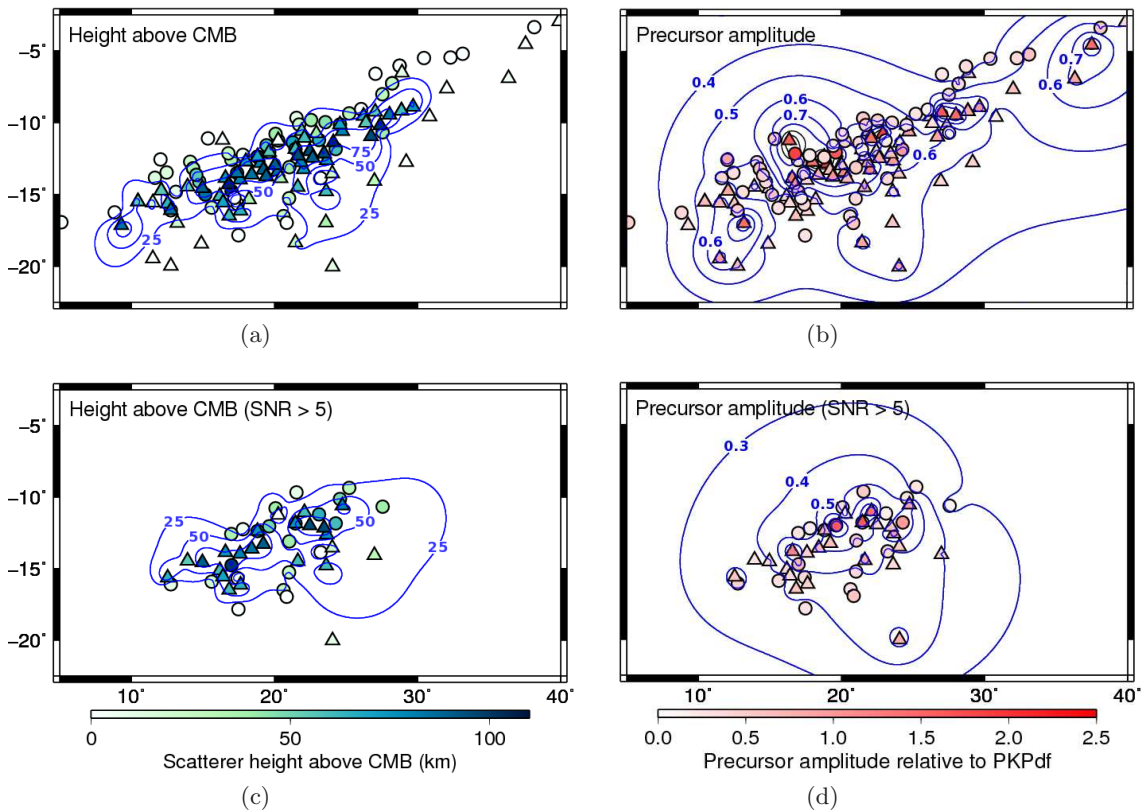


Figure 2.12: Maps of scatterer locations beneath South Africa where circles and triangles represent the scattering location of first and second precursors, respectively. (a) Scattering heterogeneity height above the CMB overlaid on a surface of the same data contoured at 25 km intervals. (b) Precursor amplitudes relative to  $PKP_{df}$  overlaid on a surface constructed from the same data contoured at 0.1 times  $PKP_{df}$  amplitude intervals. Amplitudes are measured from the filtered beam formed on the phase of interest, while the  $F$ -amplitude is used to select the time window in which to pick the phase in the beam. (c) Scatterer height above the CMB and (d) precursor amplitude relative to  $PKP_{df}$  only showing precursors with beamed SNR larger than 5 and with ray-tracing misfits less than 0.25 s/deg slowness and 1 s travel-time, leaving 41 data points. Outside the study region ( $-1^\circ$  to  $71^\circ$  longitude,  $1^\circ$  to  $-26^\circ$  latitude) the constructed surface is constrained to return to the CMB.

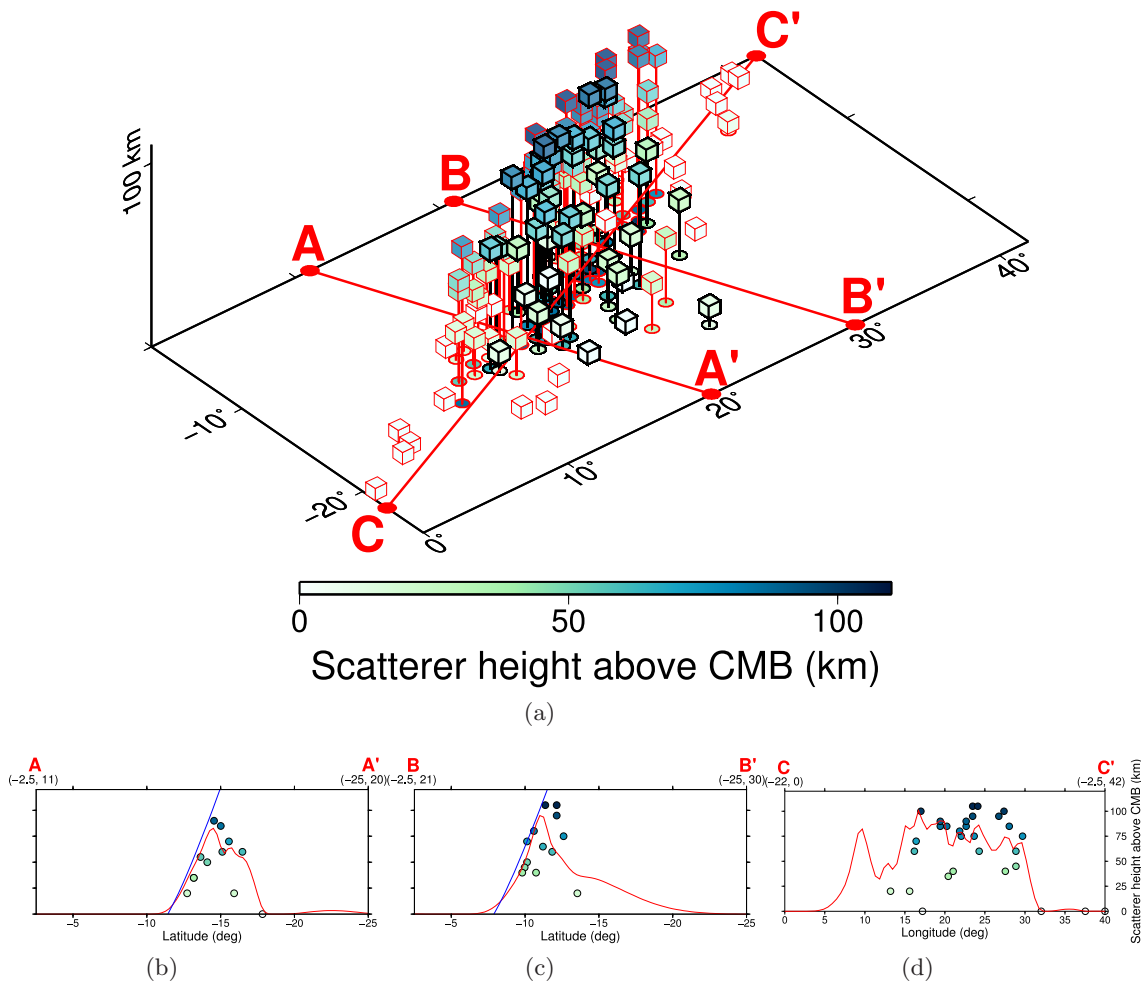


Figure 2.13: (a) Scattering heterogeneity height above the CMB showing scatterers as discrete volumes (cubes) forming a cluster of concentrated scattering. Cubes outlined in black satisfy the quality criteria used in Figures 2.12c and 2.12d ( $\text{SNR} > 5$ , slowness misfit  $< 0.25$  s/deg and time misfit  $< 1$  s) and those outlined in red are of lower quality. The grid is viewed from  $220^\circ$  azimuth inclined at  $35^\circ$  to the plane. Cross-sections (b), from A to A' ( $-2.5^\circ$  N,  $11^\circ$  E to  $-25^\circ$  N,  $20^\circ$  E) through the scattering volume (red line shows the height of the scattering surface from Figure 2.12a along the same section), along the red line in the main figure (scattering points  $\pm 1^\circ$  either side of this line are shown) with the b-caustic shown by the blue line, (c) from B to B' ( $-2.5^\circ$  N,  $21^\circ$  E to  $-25^\circ$  N,  $30^\circ$  E) through the scattering volume (scattering points within  $\pm 1^\circ$  laterally of the cross-section shown), and (d) from C to C' ( $-22^\circ$  N,  $0^\circ$  E to  $-2.5^\circ$  N,  $42^\circ$  E), along the ridge (scattering points within  $\pm 0.5^\circ$  laterally of the cross-section shown).

Scattering at the CMB in the north-east, south, and south-west constrain that the scattering volume returns to the CMB at these edges (flattens out). However, the northern edge of the scattering structure is not well constrained as the northern extent of the study area is limited by the PKP raypath and the location of the PKP b-caustic which marks the lower distance limit at which scattering can occur (Figure 2.4). Inside the sampled region, the scattering ridge height begins to decrease towards the north; however, there are no scatterers recorded at the CMB on this side of the structure. The northern slope of the scattering ridge follows the vertical continuation of the PKP b-caustic up from the CMB, hence it is possible that the ridge structure may continue in this direction but cannot be detected with this dataset (Figure 2.13). Although scattering from topography,

for example undulations on the CMB, is possible and has been suggested as a source of PKP precursors, 1 Hz waves would only detect variations of the CMB up to 1 km in height and  $\sim 10$  km wide [Doornbos, 1978, 1980; Bataille & Flatte, 1988; Bataille et al., 1990]. Therefore, it is likely that the waves observed are not caused by the shape of the ridge. An alternative explanation for stronger scattering at greater heights above the CMB may be related to material properties. Hotter material would have a lower density and be more likely to be entrained into upwards convection. The increased temperature would also decrease the stiffness increasing the elastic parameter contrast between the heterogeneity and the ambient mantle. Therefore, the spatial correlation between the elevated scatterers and high amplitude precursors in the centre of the structure suggests that it is a volumetric heterogeneity with a large velocity and/or density contrast with the surrounding mantle.

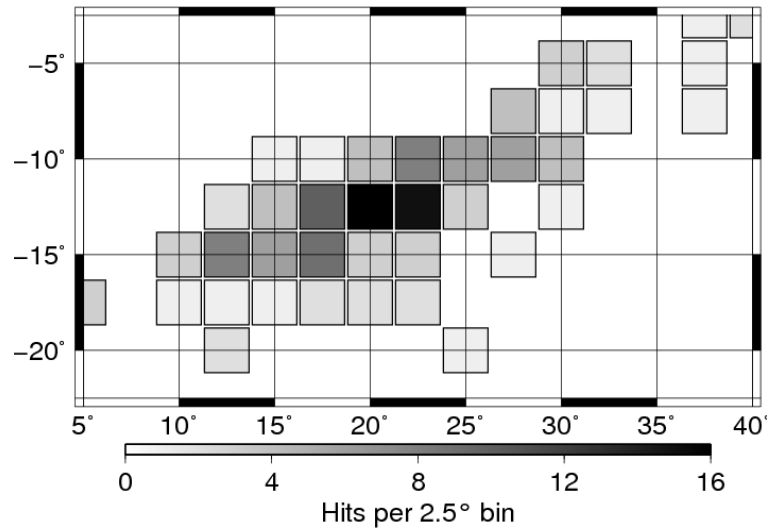


Figure 2.14: Number of scattering points per  $2.5^\circ \times 2.5^\circ$  cell as symbol shading. Cells without scatterers are left blank. Sampling of the structure is good even towards the edges of the structure where scattering heights and amplitudes are lower (see Figure 2.12).

To check the robustness of the detected structure against lower quality results I discard all data with SNR (of PKP against background noise before PKP) in the beam less than 5 as synthetic tests show that this is a reasonable noise limit for the F-packing process (calculated in Chapter 2.7). Furthermore, to reduce uncertainty in scattering location based on velocity model inaccuracies or picking errors, I remove any scattering points for which the ray-tracing process shows misfits in terms of slowness and travel-time of greater than 0.25 s/deg and 1 s, respectively. The strict quality criteria relate to scatterer mislocations of  $\pm 2^\circ$  and 60 km (horizontal and vertical, respectively) and can be seen as a stringent test of the reliability of the results. Despite leaving only 41 of the original 157 data points the overall structure of the detected ridge remains very similar (Figures 2.12c and 2.12d).

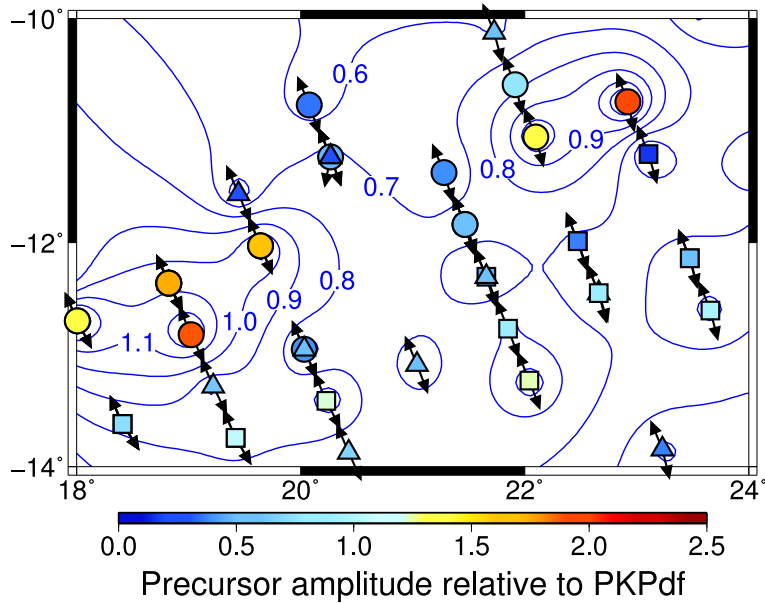


Figure 2.15: Precursor amplitudes relative to  $PKP_{df}$  as in Figure 2.12 for the centre of the scattering ridge with the highest scattering point density. Contours are at 0.1 times  $PKP_{df}$  amplitude intervals. Precursors are split into mine source regions with events from Welkom (south-west) shown as triangles, from Klerksdorp (north-east) shown as squares, and Randfontein and Carletonville (north-west) shown as circles. Arrows show the direction to the source in the south-east and the receiver in the north-west.

Some insight into the scattering mechanism of the ridge comes from the study of the different earthquake (mining) regions of the dataset. Comparison of scattering between the mining areas displays the differences in scattering strength caused by the location of the source, whereas comparison between sources in each mining area images the overall variation in scattering strength across the ridge. Despite all three mining source areas having similar event magnitudes, source-to-scatterer, and source-to-receiver distances, the scattering strength recorded varies between them significantly (Figure 2.15). On average, the (filtered beam) amplitude ratio of the second precursor to  $PKP_{df}$  ranges from 1.30 for the Welkom events (SW region), to 0.90 for the Carletonville and Randfontein events (NE region), and 0.50 for the Klerksdorp events (NW region). Events from the SW region tend to scatter on the northern edge of the ridge, the NE region events scatter in the middle of the ridge, and the NW region events scatter from the northern and southern edges of the ridge. On the other hand, events from the same source region sampling the same area of the CMB have similar relative precursor amplitudes with rapid systematic variation with location. Three scattering points from events in the SW region are separated by  $< 1^\circ$  and have an average precursor to  $PKP_{df}$  amplitude ratio of 0.40, with a standard deviation of 0.06. Two pairs of scattering points from the NE region, separated roughly east-west by  $< 1^\circ$ , both show an increase in amplitude ratio of  $\sim 0.40$  from NW to SW (Figures 2.16 and 2.15). In order to eliminate any effects due to scattering angle or source variation, I analyse events from the SW region with similar back-azimuths. Scattering amplitude ratio increases with distance from 0.40 amplitude in the south-east to 1.60 before decreasing to 1.40 towards the north-north-west over less than  $2^\circ$  distance. This variation is too large to be explained by geometric spreading alone and requires an anomaly which focusses energy

differently from SE to NW along the detected ridge [Wright, 1975].

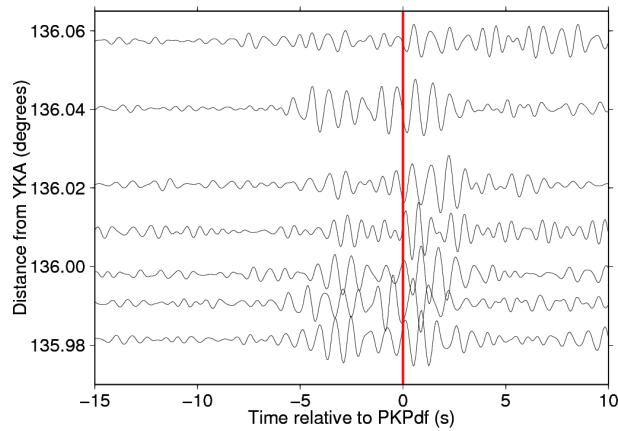


Figure 2.16: Beams filtered with a Butterworth bandpass between 1.0 Hz and 2.0 Hz formed on  $PKP_{df}$  slowness and back-azimuth from seven category 1 events between  $135.98^\circ$  and  $136.06^\circ$  from YK. Traces are plotted with  $PKP_{df}$  at the origin. All traces are normalised to the maximum amplitude within  $\pm 15$  s of  $PKP_{df}$ . Amplitude ratios of the precursor to  $PKP_{df}$  vary significantly between events.

Spectral analysis of the processed beams created using short period and long period instruments at YK give additional information on the size of the scattering heterogeneities (Figure 2.17). In the high frequency data the two precursors can clearly be seen at around 1 and 2 Hz, although lateral smearing makes the actual timing difficult to determine. Broadband data also shows evidence for precursory energy at  $\sim 0.5$  Hz which appears distinct from the high frequency precursors. This suggests two scales of scattering heterogeneity, as has previously been observed with PKP precursors originating from the western Pacific [Wen & Helmberger, 1998]. This study modelled the two different frequency precursors as being generated by peaks of heterogeneities of different sizes around 100 to 300 km wide and 60 to 80 km tall. Although the frequencies used in the study [Wen & Helmberger, 1998] are not published and so a direct comparison with my data is not possible, it could be that the long-period precursors in the spectrogram are scattering from the whole ridge, i.e. at the topographic anomaly, while short-period precursors are scattering from individual anomalies.

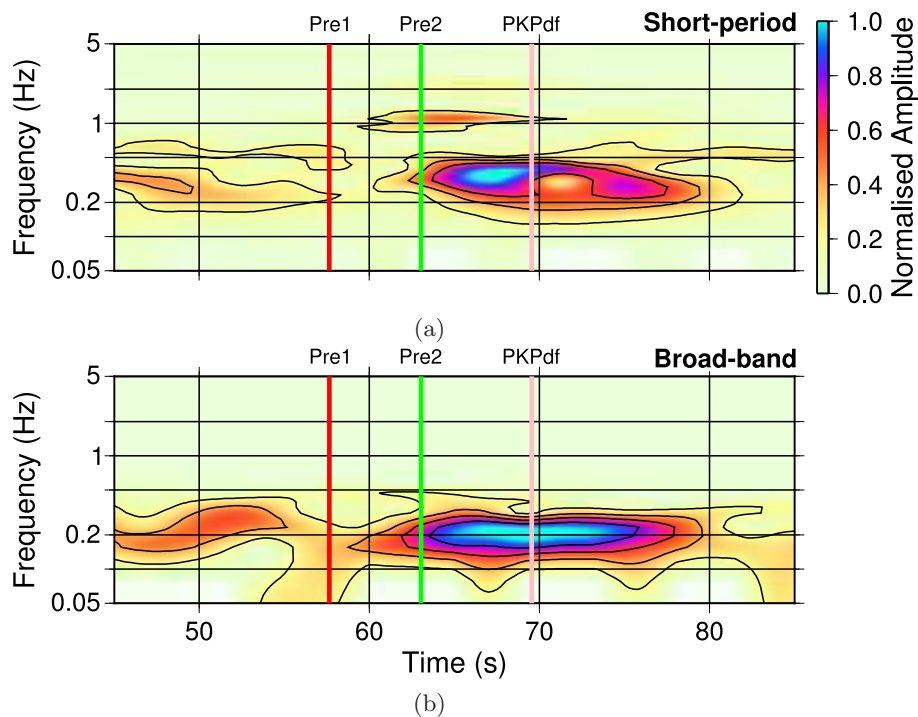


Figure 2.17: Spectrograms calculated using the unfiltered beam formed on  $PKP_{df}$  slowness and back-azimuth for an event on 12/11/1997 with  $m_b = 4.5$ . Spectrograms are created using (a) short-period, and (b) broad-band instrument recordings. The times at which the first precursor, second precursor, and  $PKP_{df}$  are picked using the F-pack are shown by the red, green, and pink lines, respectively. Energy is seen arriving at 1 Hz throughout the period in which the first precursor is picked. A weak precursor can just be seen in the short-period spectrogram arriving at 2 Hz at the time of the first precursor. However, the dominant energy peak arrives at 0.2-0.4 Hz associated with the  $PKP_{df}$ . Energy arriving after  $PKP_{df}$  (visible as a distinct arrival in the broadband spectrogram), also at 0.2-0.4 Hz, may be related to  $PKP_{cd}$ . The frequency of the precursors indicates scattering from heterogeneities of  $\sim 6$ -13 km in size.

## 2.7 Error Analysis

### 2.7.1 Azimuth and Slowness Estimation

To quantify the uncertainties inherent in the F-packing process in determining the slowness and back-azimuth for each arrival, synthetic seismograms with varying noise levels are generated and processed. To simulate YK ambient noise conditions, a trace is taken from YK for all stations for a time at which no phases arrive according to the catalogues, and no arrivals can be detected when the data are filtered at a range of frequencies (bandpass filters, 0.5 Hz wide, in increments of 0.5 Hz from 0.1 Hz to 3 Hz). Four cosine tapered, 1 Hz sine wavelets, each 2.5 s long, are added to the noise with moveouts (time delays across the array. See Figure 1.13) that would be recorded at YK for slownesses and back-azimuths typical of the PKP wavetrain. Phases are modelled to simulate first and second precursors,  $PKP_{df}$ , and  $PKP_{cd}$  and have slownesses of 4.21 s/deg, 3.97 s/deg, 2.17 s/deg, and 2.27 s/deg, respectively, and all have back-azimuths of  $54^\circ$ , values which are typical for many events in the dataset. As the first and second arrivals represent precursors they are modelled as having half the amplitude of the third and fourth

arrivals, which represent  $\text{PKP}_{df}$  and  $\text{PKP}_{cd}$ . Signal to Noise Ratio (SNR) is calculated for each unbeamed trace by creating the envelope and then taking the maximum amplitude in a 3 s time window around the  $\text{PKP}_{df}$  arrival relative to the maximum amplitude over a 3 s time window before the precursor arrivals. The SNR of the unbeamed traces is varied between 0.005 and 0.5. These are then beamed, filtered, and enveloped and the SNR of the resulting filtered envelope is calculated and is found to vary between 1.9 and 19. To test the accuracy of the F-packing approach, the difference between the slowness, back-azimuth, and travel-time of the synthetic waveforms, measured with the F-pack in the same way as for the data, is compared to known input values. The misfit between the slowness, back-azimuth, and arrival-time of the input synthetic signals and the measured values is used to indicate the precision of the F-pack with varying signal strength.

SNR values are calculated for all  $\text{PKP}_{df}$  event recordings in the same way as for the synthetic data. Each event category is analysed individually, and category 1, 2, and 3 events are seen to have, on average, SNR values of 10.4, 5.1, and 7.8, respectively. Using synthetics, for a beamed SNR value of 4.6, slowness and back-azimuth can be picked to within  $\pm 0.43$  s/deg and  $\pm 7^\circ$  back-azimuth. Below this beamed SNR, both slowness and back-azimuth picking errors become much larger (Figure 2.18). For a beamed SNR of 12, errors are as low as 0.07 s/deg in slowness and  $0^\circ$  in back-azimuth. Arrival time residuals for all SNR values and for all phases are up to 1 s, most likely due to the emergent onset of the wavelet, which takes this long to reach its maximum amplitude. This test demonstrates that the F-packing approach is highly accurate at picking the correct slowness, back-azimuth, and travel time despite noisy data. Given the SNR values of the data, the majority of the phases used can be picked to within  $\sim 0.3$  s/deg slowness, 0.75 s arrival time, and  $2^\circ$  back-azimuth.

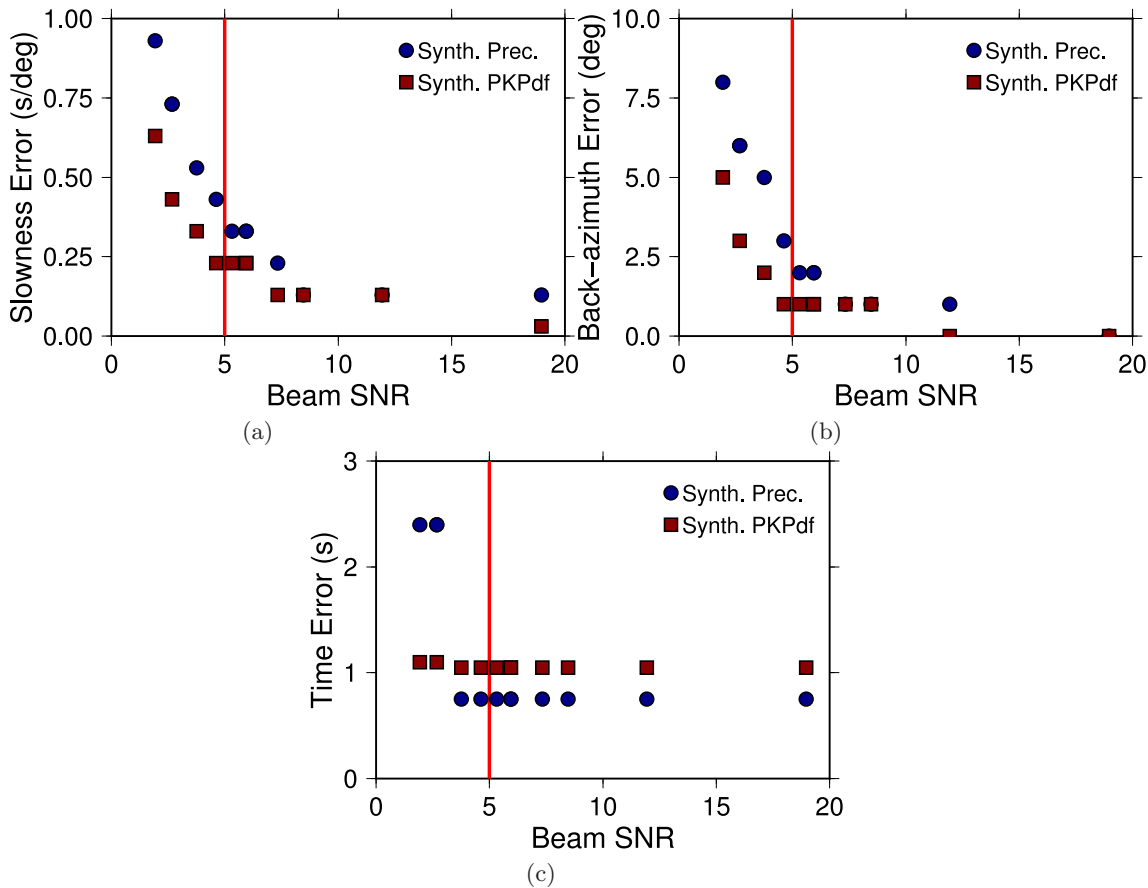


Figure 2.18: *F*-pack measurement errors for synthetic signals created at various Signal-to-Noise Ratios (SNR) for (a) slowness, (b) back-azimuth, (c) and time. Synthetic precursory signals (blue circles) have half the amplitude of synthetic PKP<sub>df</sub> signals (red squares). A SNR of 5 is found to be a suitable cut-off (red line), above which the *F*-pack is able to easily extract a signal from the noise with very low directivity errors.

## 2.7.2 Location Uncertainty

To estimate the location error related to the ray-tracing approach I use an example event and change the input parameters and measure the change in the output location. I vary input slowness, back-azimuth, and travel-time by up to  $\pm 1$  s/deg,  $\pm 5^\circ$ , and  $\pm 2$  s, respectively, (Figure 2.19) according to the maximum errors measured using the *F*-trace for a good signal, as determined in Chapter 2.7.1. Changing the signal arrival time by  $\pm 2$  s primarily moves the scatterer vertically by up to 20 km, with later signals making the scatterer shallower, and earlier signals making the scatterer deeper. Scatterer location is almost insensitive to changes in slowness of up to  $\pm 0.5$  s/deg. However, scatterer location is most strongly affected by back-azimuth modifications, with  $\pm 5^\circ$  changes in back-azimuth moving the scatterer location by up to  $\sim 4.5^\circ$  horizontally and 5 km vertically. Hence back-azimuth is the parameter which must be best determined for good scatterer relocation.

Another source of error is the uncertainty in the published source locations. Published error ellipses for the events used are up to 136 km long and up to 70 km wide, but on average 13.7 km long (with a standard deviation of 20.7 km) and 8.5 km wide (with a standard deviation of 9.0 km). To test the effect that the worst possible errors would

have on the ray-tracing results I vary the source locations from those published by  $\pm 2^\circ$  in longitude and latitude, deviations greater than the size of the largest stated error ellipse of the REB source locations. Source longitude and latitude variations result in the scatterer location shifting by up to  $1.5^\circ$  horizontally and 35 km vertically.

Further testing combines slowness, back-azimuth, and arrival-time errors of the same size as found in the synthetic tests for an event with SNR  $\sim 5$ , and the scatterer location deviations were calculated. Using all permutations of  $\pm 0.5$  s/deg,  $\pm 2^\circ$ , and  $\pm 1$  s, the scatterer mislocation area was found to be  $\sim 4^\circ$  latitude and longitude wide ( $\sim 240$  km) and 25 km in height (Figure 2.10). Overall, the F-trace and ray-tracing are excellent tools which very accurately determine scatterer location in latitude, longitude, and height.

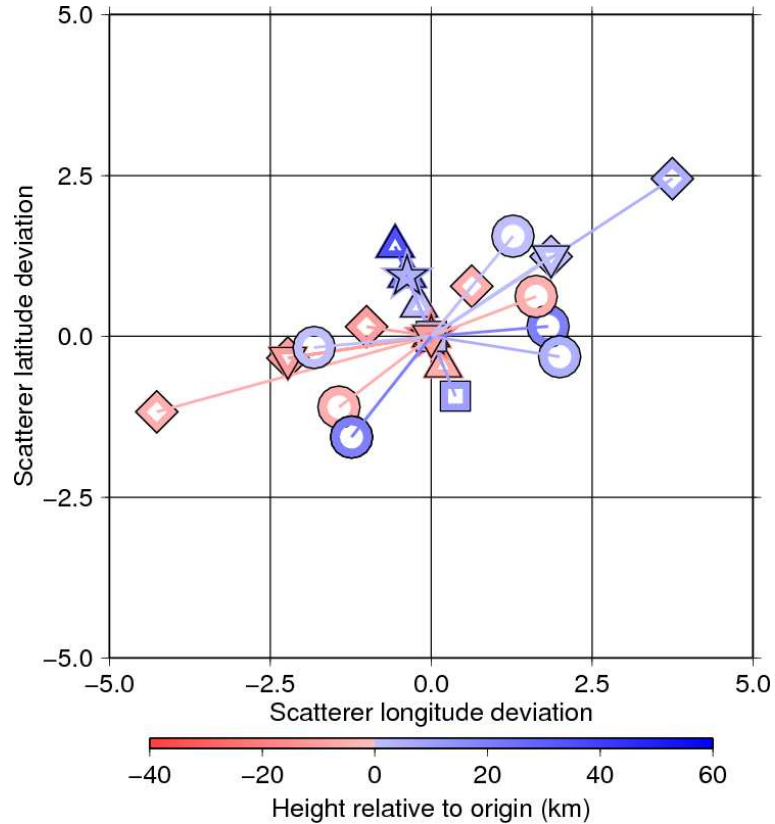


Figure 2.19: Changes in scatterer locations determined by ray-tracing using systematically modified input data, varying slowness, back-azimuth, time, and source location to simulate errors in the dataset. Each scatterer location is plotted relative to that created with unmodified input parameters thus demonstrating the amount by which changes to each input parameter affect the scatterer location. Changes are made to the input event parameters: source latitude and longitude (triangles), signal arrival-time (stars), signal slowness (squares), signal back-azimuth (diamonds), and arrival-time, slowness, and back-azimuth simultaneously (circles).

### 2.7.3 Stability of Detected Structure

The robustness of the shape of the scattering structure is assessed by applying a bootstrapping technique to the scattering locations [Efron & Tibshirani, 1991]. Using all scattering locations I calculate a best fit surface to resolve the ridge structure. Three-hundred bootstrap realisations are created by randomly sampling 157 scattering points, including duplicates, from the original 157 scattering points in the data (i.e. the new realisation may

contain all 157 of the original points, or will, more likely, contain fewer unique points but include duplicates totalling to 157). A surface is created for each bootstrap realisation. The height difference between the bootstrapped surface and the original surface is calculated and averaged over all the realisations to determine the change caused by resampling data, and allows me to test the sensitivity of the scattering structure to individual data points (Figure 2.20a). This surface of bootstrapped differences is then subtracted from the original surface thus removing the influence of the least stable elements to reveal the remaining, most stable part of the structure (Figure 2.20b). On average the bootstrapped surface is 1.9 km higher than the original, unsampled surface with 2 outliers decreasing in height by 68 km and 41 km respectively; these points are likely unreliable. The maximum height of the new surface of the structure is 95 km, defining peaks, above a stable plateau approximately 75 km high; this tapers to the CMB over 120 km laterally to the north and 200 km to the south, and over 750 km to the east and west of the peak. There is no appreciable change in the lateral extent of the structure caused by the bootstrapping process. The bootstrapping process smooths the structure which still remains stable with substantial relief even for the limited dataset, thus indicating that the structure is robust and is supported by the majority of the data, and not the result of isolated points.

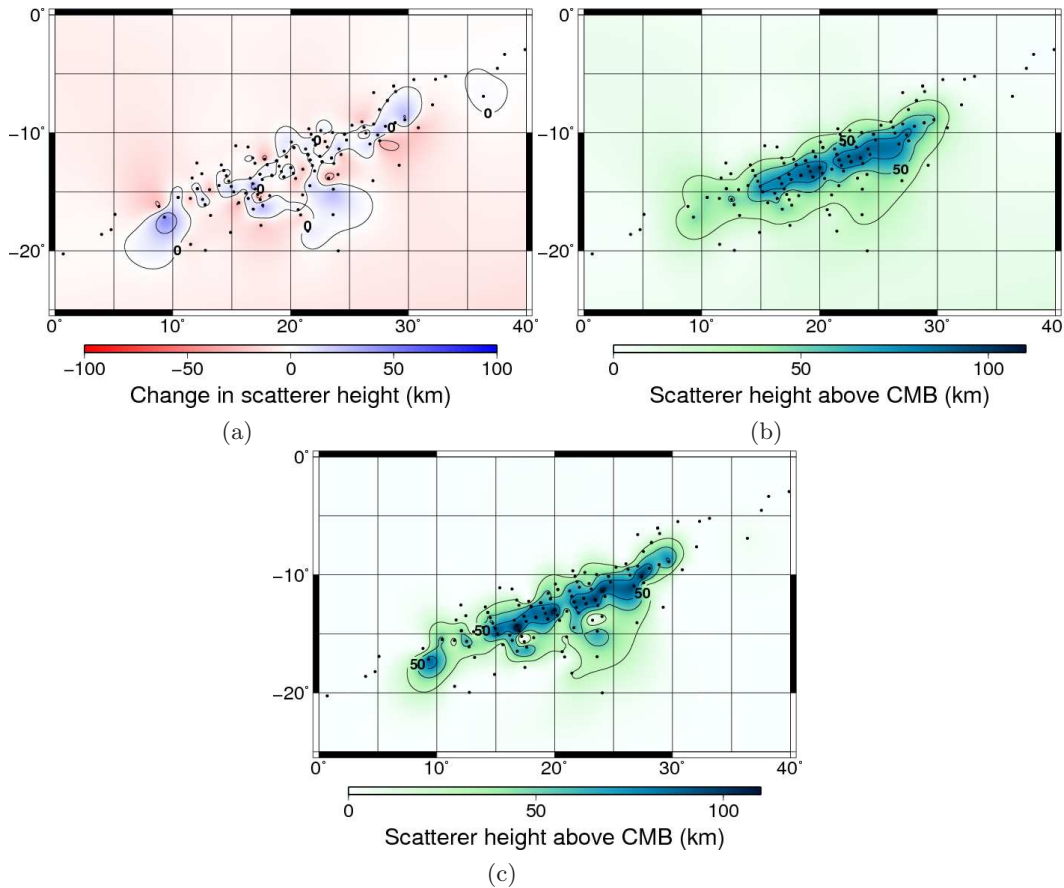


Figure 2.20: Results of Bootstrap test using 300 realisations. (a) Average of the scatterer height differences between each bootstrap iteration and the original, unsampled grid (the same surface as the contours in Figure 2.12). (b) Original grid with the average difference subtracted. (c) original grid (before bootstrap sampling). The north-western face of the ridge dips at  $\sim 11^\circ$  to the horizontal while the south-eastern face dips at  $\sim 5^\circ$ . All surfaces are contoured at 25 km height increments.

## 2.8 Modelling

### 2.8.1 Modelling Process

To quantify the magnitude of the velocity and/or density contrast of heterogeneities required to generate precursors of the observed amplitudes and as an independent measure of the scattering volume thickness, I model the scattering structure using a Monte Carlo, Phonon Scattering code [Shearer & Earle, 2004]. This approach treats energy as particles, or phonons, which are fired from a source along a range of ray parameters and their travel-times, slownesses, and back-azimuths are recorded. A large number of phonons is required to simulate a full wavefield and so this code must be run for a long time to reach a stable solution. Phonons are traced through a 1-dimensional velocity structure, here chosen to be IASP91 [Kennett & Engdahl, 1991], which can be modified in layers to contain additional small-scale heterogeneities while not affecting the gross velocity structure. Although the Earth model is only 1-dimensional, the code allows for 3-dimensional scattering with phonons able to travel off the Great Circle Path, yet still scatter back to the receiver. The code calculates scattering for both P- and S-waves and conversions between P- and S-waves, and S- and P-waves are possible. This code is an effective way to model random scattering within the Earth.

Global layers containing scattering heterogeneities are defined by an upper and lower depth, P- and S-wave velocities, a RMS velocity perturbation, a density to velocity fluctuation scaling factor, and heterogeneity scale length. Multiple scattering layers are permitted. Scattering follows the theory described in Wu & Aki [1985a] and Sato & Fehler [2008] (summarised in Chapter 1.3) and scattering patterns are, therefore, like those shown in Figure 1.10. Phonons have a chosen frequency which affects how their energy attenuates and the way in which they interact with the heterogeneities, given the scale length. Phonons follow the predetermined ray-parameters along paths defined by Snell's Law, but can be scattered from these paths when travelling through a scattering layer if they encounter heterogeneities. As this is a stochastic code, whether a phonon encounters a heterogeneity within a scattering layer is determined by an exponentially distributed random probability assigned to the phonon on entering the scattering layer. If a phonon is scattered, another randomly assigned probability specifies if the phonon will convert from P to S or S to P. The scattered phonon then continues along a new path where the scattering angle is randomly assigned but controlled by the scattering pattern. The code also allows for multiple scattering and the energy of the phonon decays due to attenuation and geometrical spreading. The phonon will continue travelling, and potentially scattering, until a maximum time limit is reached. The code runs until it is manually ended. I use a cut-off of  $2 \times 10^8$  phonons, after which the process is stopped. Given a number of scattering layers with specified heterogeneity parameters, the code generates a trace of amplitude with time for a given distance, equivalent to an amplitude envelope. I then normalise this to the maximum amplitude in the PKP<sub>df</sub> time window to account for differences in the number of phonons used between models.

In order to compare the model output with observations, I create a data envelope, taking only category 1 events, in which PKP<sub>df</sub> and at least two precursors are visible. I align filtered beams on PKP<sub>df</sub>, take the envelope of each trace, linearly sum the traces,

and normalise by the maximum value ( $\text{PKP}_{df}$ ). Within the initially selected 120 s long data window (explained in Chapter 2.5.1)  $\text{PKP}_{df}$  can occur at any time. When traces are aligned on  $\text{PKP}_{df}$  to create the data envelope I cut all traces to ensure that start and end times for all traces match. Due to the differences in the time of  $\text{PKP}_{df}$  relative to the start and end of traces, the longest possible time window for which I can create the data envelope is 40 s long, cut 20 s either side of  $\text{PKP}_{df}$ . The average source-receiver distance of the data is  $136.2^\circ$  and so I compare the data with synthetic results generated for distances between  $136^\circ$  and  $137^\circ$ . When comparing real data with the synthetic traces, I shift the real data using the predicted arrival time of  $\text{PKP}_{df}$  at  $136.2^\circ$  so that the main phase is aligned with the synthetics.

Starting from the assumption that precursors to 1 Hz  $\text{PKP}_{df}$  are generated by scattering in the lowermost mantle, as indicated by ray-tracing, I test a range of layer parameters (see Appendix Tables B.2 and B.3). I alter the scattering layer in terms of: thickness, height above the CMB, number of scattering layers, RMS velocity perturbation of the heterogeneities, density scaling factor, and heterogeneity scale length in an attempt to match the shape of data envelopes.

### 2.8.2 Modelling Results

After testing a range of models I find that changes to all of the above parameters significantly affect the shape, amplitude, and duration of both the precursor and coda wavetrain (Figure 2.21), with the exception of the density scaling factor. It is apparent that the same precursor envelope amplitude can be created by altering either the RMS velocity perturbation or the scattering layer thickness or, to a lesser degree, scale-length. These different models can be distinguished by small differences in coda shape but this is somewhat ambiguous. This illustrates the trade-off between thickness and scattering strength that is encountered when modelling heterogeneities based on wave amplitude alone [e.g. *Husebye et al.*, 1976; *Garnero & Helmberger*, 1998; *Jensen et al.*, 2013]. Ray-tracing gives an independent method to determine scattering height. None of the models tested are able to replicate the data envelope. Further models using two scattering layers either stacked on top of each other or separated by a non-scattering volume of various thicknesses are equally inadequate at matching the data (Figure 2.21e). I then attempt to fit the data by varying a combination of parameters, taking the values that match small parts of the data envelope and using them in a single model (Figure 2.21f). However, these models are also insufficient to fit the precursory wavetrain, although coda amplitudes can be matched.

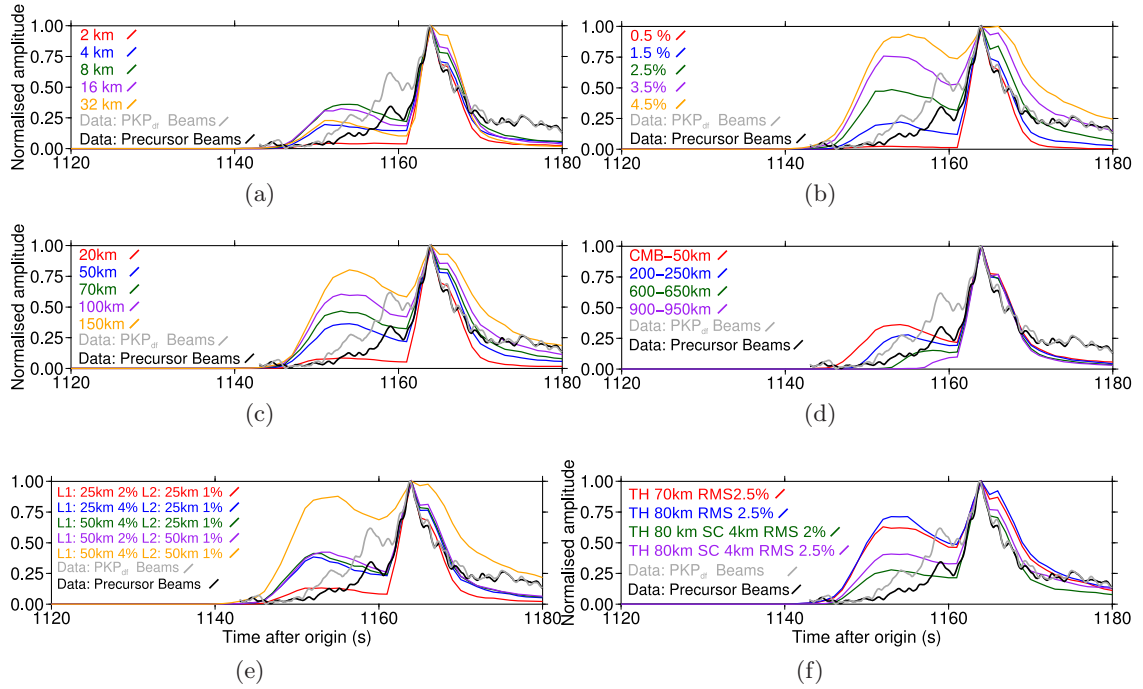


Figure 2.21: Phonon scattering synthetics generated for a 1-D Earth model with scattering in the upper 200 km (lithosphere) and a variable lower mantle scattering layer, compared to data for beams formed on  $PKP_{ab}$  slowness (black line) and precursor slowness (grey line) from all category 1 events. Standard lower mantle layer parameters are 8 km heterogeneity scale length, 0.8 velocity/density scaling factor, 2 % RMS velocity perturbation, 50 km thickness, and layer lower surface at the CMB. Models maintain all other standard parameters and change (a) scale length, (b) RMS velocity perturbation, (c) layer thickness, and (d) layer lower surface height above the CMB. Density scaling factor is not shown as it does not affect the output envelope. (e) Models with two lower mantle scattering layers of varying thickness and RMS velocity perturbations, but a standard 8 km heterogeneity scale length. Layers in the models are described as L1 for the lower layer starting at the CMB, and L2 for the layer directly above this. Layer thickness is given in km and RMS velocity perturbation is in per cent. (f) Scattering models varying a combination of parameters based on previous models in an attempt to better fit the data. No single parameter or combination of parameters are able to model the data. Scattering is possible on both source and receiver sides of the core and both sides will contribute equally to the envelope.

The difference between the synthetics and the data is likely due to limitations in the model and because this type of simulation is inappropriate for modelling volumetric scattering structures. The primary limitation is that the code uses a 1-dimensional scattering structure meaning that there is no source-receiver difference, or topographic variation. Phonons entering the heterogeneous layer on the source-side may be scattered from  $PKP_{ab}$  or  $PKP_{bc}$  paths to the PKP precursor path. Energy still on  $PKP_{ab}$  or  $PKP_{bc}$  paths when leaving the mantle will also be able to scatter to the PKP precursor path, thus there are two points on the ray-path at which energy can be scattered and contribute to the PKP precursor envelope. Scattering on either the source or receiver side will contribute an equal amount of energy to the resulting envelope. A thin or weakly scattering layer scattering on both sides of the mantle would be able to replicate the effects of a thicker or strongly scattering layer on one side of the mantle. Modelling using a 1-dimensional structure will lead

to under estimation of velocity RMS and/or thickness. Secondly, the layer is continuous and stochastic where as the scattering volume is discontinuous and deterministic. In the discontinuous case, the sampling region of the waves (Figure 2.4) may not entirely overlap the scattering volume, therefore, some ray geometries (travel-times, slownesses, and back-azimuths) will not be able to be generated by scattering. For example, if the scattering ridge only interacts with the rear-most part of the sampling region (e.g. south-eastern part of the region in Figure 2.4a) then there will be no early precursors. As a result, the precursor time window of the data is likely not evenly represented and so I cannot expect to be able to match the data envelope using 1-dimensional scattering synthetics. It is not possible to replicate the amplitude and shape of the precursory energy envelope with scattering from a continuous layer causing scattering on both the source and receiver sides of the path. More sophisticated techniques with velocity structure varying in more than 1-dimension are necessary to accurately model this laterally heterogeneous scattering structure and derive appropriate material parameters.

## 2.9 Discussion

The data indicate laterally discontinuous velocity structure within the lowermost mantle deviating from standard 1-dimensional Earth models. Many mechanisms for the generation of PKP precursors have been suggested, such as scattering of  $P_{diff}$  [Bataille & Lund, 1996; Thomas *et al.*, 2009], scattering of PKP by topography on the CMB [Wright, 1975], and scattering of PKP by volumetric heterogeneity [Doornbos & Husebye, 1972]. In this chapter I demonstrate scattering from volumetric heterogeneities near the CMB.

Energy may be scattered from  $P_{diff}$  at the PKP b-caustic by heterogeneities in the lowermost mantle [Bataille & Lund, 1996; Thomas *et al.*, 2009]. However, 1 Hz waves attenuate to about 1 % of their original amplitude within  $3^\circ$  from the b-caustic at  $143^\circ$  [Doornbos & Husebye, 1972]. Diffracted waves could be channelled from the b-caustic to the receiver at different distances by a wave-guide structure such as a low velocity zone [Thomas *et al.*, 2009]. Diffracted precursory waves would then be of a lower frequency than direct  $PKP_{df}$ , the reverse of which is seen in these data (Figure 2.17), therefore diffraction is unlikely to explain the precursors in this study.

CMB topography has been proposed as a cause of scattering [Wright, 1975]. CMB undulations are reported to have two scales, one with a maximum peak-to-peak amplitude of 3 km and wavelengths  $\geq 300$  km [Menke, 1986; Morelli & Dziewonski, 1987; Sze & van der Hilst, 2003], and the second with a root-mean squared amplitude of only  $\sim 300$  m and wavelengths of  $\sim 10$  km, often described as “roughness” (Figure 1.8) [Menke, 1986; Earle & Shearer, 1997]. Structures of this wavelength would generate waves with frequencies above 2 Hz [Vanacore *et al.*, 2010] which is greater than the 1-2 Hz dominant frequency of the precursors seen in the data (Figure 2.17) hence this is an unlikely source of the PKP scattering and cannot explain scattering up to 80 km above the CMB, the height of which is well constrained through the array processing. However, positive CMB topography is thought to be indicative of mantle upwellings [Sze & van der Hilst, 2003] and the scattering structure matches the location of a 2 to 3 km tall upwarping of the CMB, about 1000 km wide, and a -1 % velocity decrease [Sze & van der Hilst, 2003; Soldati *et al.*, 2012]. Positive CMB topography may imply that this region of the mantle is upwelling which

could dynamically support anomalous mantle material.

The most likely explanation for the anomalous observations in this dataset is scattering of PKP at volumetric heterogeneities, i.e. at discrete bodies in the lower mantle with strong velocity and/or density contrasts, where the scatterer spacing is greater than the incident wavelength [Cao & Romanowicz, 2007]. As anomalies scatter waves of similar wavelengths to their size (explained in Chapter 1.3), the precursor frequencies imply that scattering is caused by individual anomalies  $\sim 10$  km in size [Ansell, 1973]. The precursory wave-train observed here is similar to that of other studies of PKP scattering where multiple coherent packets of energy, of increasing amplitude, precede PKP<sub>df</sub> [Doornbos & Husebye, 1972; Wen & Helmberger, 1998; Hedlin & Shearer, 2000; Cao & Romanowicz, 2007]. This differs from other studies [Hedlin & Shearer, 2000], which model scatterers as statistically distributed throughout a mantle volume, i.e. scatterers represent statistical scattering volumes generating precursors along the whole ray-path. For the source-receiver distances of this dataset, according to the minimum time curve, the earliest precursors scattering from the b-caustic should precede PKP<sub>df</sub> by 17-13 s depending on epicentral distance (Figure 2.3). The recorded precursors arrive later than this, implying that they do not scatter from the b-caustic, either because there is no heterogeneity along this path, or because the scattered energy is small and below the noise level. Instead they must be scattering above the CMB, off-azimuth, or from larger scatterer-to-receiver distances (Figure 2.12a).

Recorded slownesses for the direct PKP<sub>df</sub> and PKP<sub>cd</sub> waves are consistently  $\sim 0.2$  s/deg higher than predicted by IASP91 [Kennett & Engdahl, 1991] with back-azimuths deviating from the great-circle path by on average approximately  $-5^\circ$  and  $12^\circ$ , respectively. Slowness deviations are in line with those previously observed at YK [Bondár *et al.*, 1999] which were attributed to local receiver structure. However, the back-azimuth deviation of the data is larger and consistently in a different direction than previously determined. The different sign of the PKP<sub>df</sub> and PKP<sub>cd</sub> azimuth deviations imply that this is likely to be due to 3-D velocity structure within the sampling area while the slowness deviation is probably due to local receiver structure.

The precursor slownesses indicate that the waves are scattered on the source-side before they enter the core (Figure 2.11a). However, this does not preclude receiver-side scattering which may still occur [Thomas *et al.*, 1999], but these waves, although they are predicted to be of similar amplitudes to source-side energy, may be masked by the source-side waves which are known to appear up to three times larger than receiver-side waves at certain arrays due to amplification by the array [Haddon & Cleary, 1974]. Given the dominance of energy with slownesses indicative of source-side scattering in these data, it implies that the heterogeneities within the scattering volume are much stronger on the source-side than on the receiver-side. The ridge structure scatters waves more effectively than the surrounding mantle likely due to a combination of topography and velocity/density heterogeneity. The scattering structure correlates well with a region of the African LLSVP showing a steep velocity gradient, as defined in tomographic images, indicating a link between the large-scale LLSVP and the small-scale mantle structure creating scattering (Figure 2.22). However, the apparent strike of the ridge is perpendicular to the sharp eastern boundary of the African LLSVP (Figure 2.22c) which has been resolved with

SKS waveform modelling [Ni *et al.*, 2002; Wang & Wen, 2004; Helmberger & Ni, 2005]. There are several interpretations of the exact location of this boundary, and the scattering structure is in general agreement with proposed models. The difference in strike may be an indication that the resolved structure is only the southernmost end of a larger body which runs further north, parallel with the boundary of the African LLSVP, but this cannot be resolved due to lack of data coverage in this direction in this study.

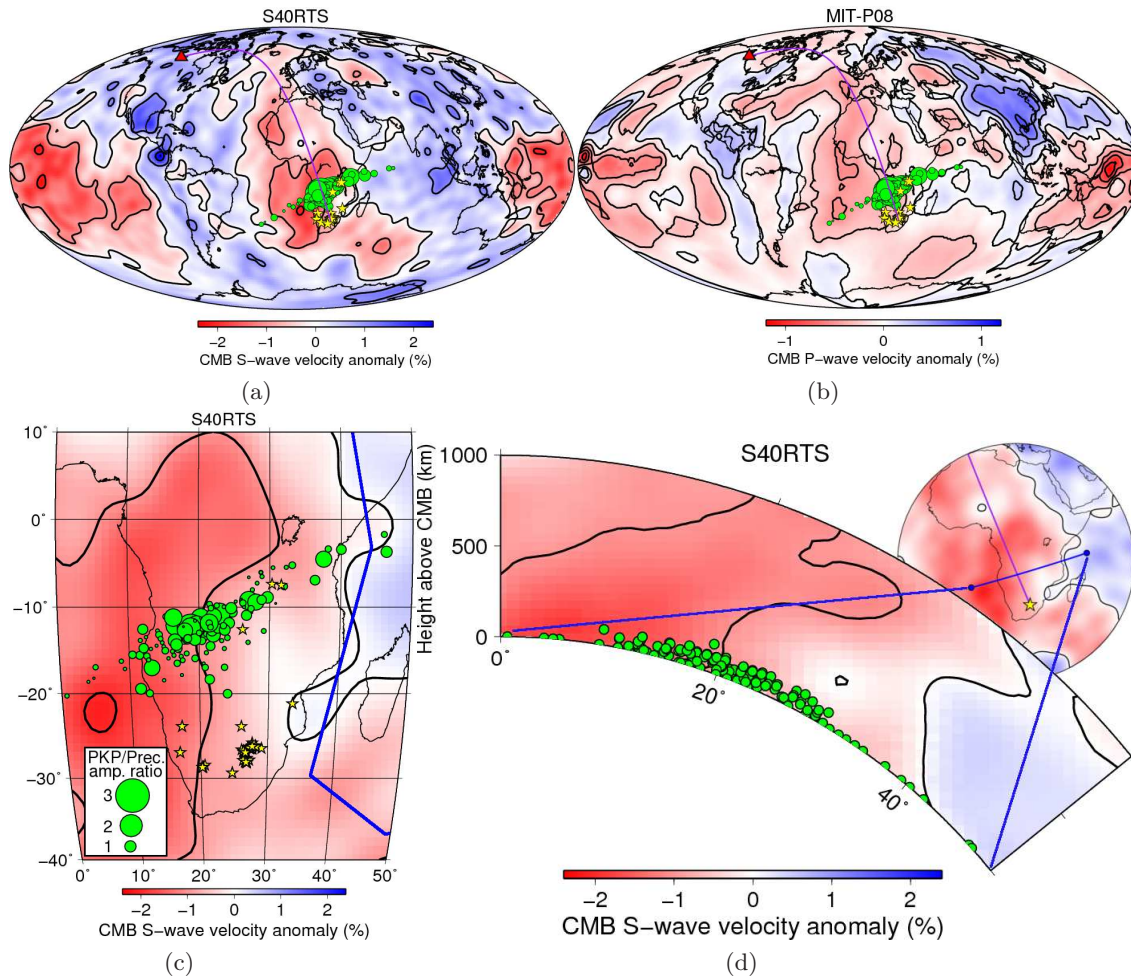


Figure 2.22: Maps of (a) S-wave tomography, at 89 km above the CMB (2800 km depth) using S40RTS [Ritsema *et al.*, 2011], and of (b) P-wave tomography at 20 km above the CMB (2869 km depth) using MIT-P08 [Li *et al.*, 2008] with event locations (yellow stars), scattering points (green circles), and a great-circle path (purple) to YK (red triangle). Precursor amplitudes relative to PKP<sub>af</sub> are indicated by symbol size. (c) Local S-wave tomography structure, at 89 km above the CMB (2800 km depth) using S40RTS, with scatterer locations. The blue line indicates the eastern edge of the African LLSVP from Wang & Wen [2004]. (d) Cross-section through S40RTS from 20° S, 0° E to 50° E, 5° S for heights from the CMB to 1000 km above. Scattering points are projected onto the cross-section line and shown as green circles. Contours are at increments of 1 % velocity anomaly.

Back-projection of the location of Large Igneous Provinces, kimberlites, and hotspot volcanism to the CMB, corrected for plate motion, implies that they originate close to the -1 %  $\Delta V_S$  contour in the SMEAN tomography model [Becker & Boschi, 2002], hence close to the edge of the LLSVPs [Torsvik *et al.*, 2006, 2010; Tan *et al.*, 2011]. S-wave

travel-time and waveform studies [He & Wen, 2012] locate the boundary of the Pacific LLSVP in good agreement with the  $-0.4\%$   $\Delta V_S$  contours in the S40RTS tomography model [Ritsema *et al.*, 2011]. The best fit for the data seems to be the  $-0.5\%$  to  $-1\%$   $\Delta V_S$  region, in good agreement with previous studies mapping the edge of the LLSVP (Figures 2.22c and 2.22d). LLSVPs have been shown in geodynamic models (see Figure 1.7) to internally convect driving denser residual material to their edges [McNamara *et al.*, 2010]. Hotspots could be the surface expression of entrained dense material caused by the convecting LLSVP which could draw the heterogeneities upwards where it would be supported by the material beneath. Alternatively, tall heterogeneous piles at the CMB could be produced by dense material carried upwards within the LLSVP, which percolates down along the edges.

Although my model tests were inconclusive (see Chapter 2.8), past studies have modelled precursors to PKP<sub>df</sub> using Chernov’s theory for random elastic media or by numerical solution of the acoustic wave equation [Chernov, 1960; Vidale & Hedlin, 1998; Thomas *et al.*, 2000]. These studies indicate that a heterogeneous layer with a 5-15%  $V_P$  velocity decrease with 100-300 km thickness at the base of the mantle is required to generate scattered energy as observed in their data. Modelled velocity parameters are similar to those determined for ULVZs [Williams & Garnero, 1996; Revenaugh & Meyer, 1997; Rost *et al.*, 2005]. However, as seen in 1-dimensional synthetics tests (see Chapter 2.8), there is a trade-off between anomaly thickness and velocity anomaly within the body where the same scattering and waveform results can be generated by a small volume with a large velocity/density variation or a large volume with a smaller heterogeneity [Husebye *et al.*, 1976]. Thus thicker layers may actually represent Low Velocity Zones (LVZs), bodies with lesser velocity and density contrasts than ULVZs, but significantly thicker than ULVZs [Avants *et al.*, 2006a]. Both structures might be of similar origin. In the data, the height of the scatterers is constrained by the slowness and back-azimuth recorded at the array leaving the magnitude of the velocity and/or density anomaly as the only variables in the modelling. ULVZs have been seen within other parts of the African LLSVP, most often near the margins [Helmberger *et al.*, 2000; Ni & Helmberger, 2001; Sun *et al.*, 2009], and scatterers were detected using a different probe to small-scale structure (PKKP) in a similar location to those in this study [Rost & Earle, 2010] (see Chapter 3). That these two studies agree so well despite using an entirely separate set of events processed with different techniques is very suggestive that this location of the lowermost mantle is strongly heterogeneous. However, my study goes further than previous studies of this area as the slowness and back-azimuth resolution is improved by using F-packs compared to beam packs and utilises the time information to determine the height of the scattering heterogeneity above the CMB. In Chapter 3 I use the same probe as Rost & Earle [2010], PKKP, with a different process that determines heterogeneity height. I locate scattering in the same location as with using the PKP probe at comparable heights, further strengthening the hypothesis that this region of the mantle is highly anomalous.

Geodynamic modelling [McNamara *et al.*, 2010; Bower *et al.*, 2011] shows that ULVZs might form elongate structures with varying heights along the margins of LLSVPs. These models indicate that dense material will be transported to the edges of LLSVPs during convection and may pool close to the CMB [McNamara *et al.*, 2010; Li *et al.*, 2014].

Modelling also suggests that traction dominant flow would generate steep-sided and flat-topped isolated patches of dense material starting from an initially ubiquitous, thin sheet of dense material ( $\Delta\rho = +1$  to  $+3$  %) underlying the mantle, matching ULVZ observations [Wen, 2001; Youngs & Houseman, 2007, 2009]. If the scattering volume in this study is composed of mantle material with a density more than 10 % greater than ambient mantle as derived in ULVZ studies [Garnero & Helmberger, 1998; Rost & Revenaugh, 2003; Rost *et al.*, 2005] then it is unlikely that it could maintain a height of 80 km above the CMB without some kind of dynamic support through convection or buoyant support through contrasting densities [McNamara *et al.*, 2010]. The aspect ratio of the scattering ridge (height/half-width) implies a Buoyancy Number (the ratio of chemical to thermal buoyancy) of  $\sim 1$ -2 [McNamara *et al.*, 2010; Bower *et al.*, 2011]. Using the Buoyancy Number and parameters controlling mantle convection used in recent models [McNamara *et al.*, 2010] gives a density contrast for the ridge of between  $+2.5$  % and  $+10$  % relative to the ambient mantle. However, the results of this model are strongly dependent on the chosen viscosity structure as well as the relative densities of the materials. Models suggest that a density anomaly of  $\geq 5$  % is required to prevent entrainment of LVZ material into the LLSVP convection [McNamara *et al.*, 2010]. If the scattering volume had a density close to or just below this threshold it may be drawn up along the LLSVP margin but avoid complete destruction by entrainment, explaining the height found here. Despite the smaller density anomaly and, most likely, smaller velocity contrast, the thick nature of the body would result in stronger scattering, equivalent to a thinner, denser layer [Wu & Aki, 1985a]. As scattering is caused by discrete velocity anomalies, this implies that the causative structure comprises individual bodies, possibly small pockets of iron-enriched mantle material as has been proposed as the origin for ULVZs [Mao *et al.*, 2006; Wicks *et al.*, 2010; Bower *et al.*, 2011] or partial melt [Williams & Garnero, 1996; Vidale & Hedlin, 1998]. Waveform studies have found ULVZs 40 km to 300 km tall in association with the edges of LLSVPs demonstrating that this is not the only occurrence of tall low velocity anomalies [Helmberger *et al.*, 2000; Wen, 2001; To *et al.*, 2011; Sun *et al.*, 2013].

Velocity-type scattering mainly directs scattered energy forwards whereas impedance-type scattering mainly directs scattered energy backwards (explained in detail in Chapter 1.3) [Wu & Aki, 1985a, 1988]. These scattering styles are controlled by changes to the elastic parameters and density, respectively [Sato & Fehler, 2008]. Precursors to PKP require scattering in the forward direction, through the outer core, hence may be generated by velocity-type scattering when the changes in elastic parameters and density are proportional and of different sign [Wu & Aki, 1985a] meaning that the scattering body is either stiffer (therefore faster) and less dense or less stiff (therefore slower) and more dense. This agrees well with either a partially molten ULVZ or a solid state iron-enriched ULVZ [Williams & Garnero, 1996; Wicks *et al.*, 2010]. Alternatively, other combinations of changes of elastic parameters and density would also direct scattered energy forwards, along the direction of propagation. Comparing the forward scattered amplitude recorded with PKP with the back scattered amplitude from a back-scattering probe (see Chapter 3) for a given scattering location would allow determination of the relative influence of elastic parameters and density, thus indicating the material properties of the scattering heterogeneity. However, material properties cannot be determined from PKP precursors

alone. The frequency of the scattered energy is indicative of the size of the scattering heterogeneity. The observed PKP precursors have frequencies of  $\sim 1\text{-}2$  Hz (Figure 2.17), indicative of scattering from heterogeneities  $\sim 6\text{-}13$  km in size.

Some events have a clear time window before  $\text{PKP}_{df}$  (open triangles in Figure 2.6a) yet do not show scattering despite being at a similar distance from YK as events which do show scattering. These events have distances greater than the b-caustic (black curve in Figure 2.6a) so theoretically could produce PKP precursors through scattering. This implies that the scattering structure is laterally discontinuous, like that seen in other studies [Thomas *et al.*, 1999; Wen, 2000], and strong scattering is not a ubiquitous feature within the lowermost mantle. This is supported by the noticeable grouping of the non-scattering events implying that scattering heterogeneities are less prevalent in the area of the mantle sampled by these events than in other regions.

As the first and second precursors, for the same event, apparently scatter at different heights above the CMB, several scenarios are likely: (1) multiple distinct layers of heterogeneities at different heights, or random heterogeneities may be locally concentrated at the edge of the LLSVP (Figures 2.23a and 2.13). (2) LVZs with scatterers could overlie the LLSVP, and sharp transitions between layers from the mantle to the LVZ and then the LVZ to the LLSVP could cause scattering at two heights (Figure 2.23b). (3) Alternatively, if the LVZ contains a large percentage of melt, below the percolation threshold, then gravitational settling or cumulate precipitation may generate a velocity contrast from mantle to melt, then melt to cumulate (Figure 2.23c) [Rost *et al.*, 2005]. The range of scatterer heights favours distributed scatterers as there are no specific heights at which scattering of either the first or second precursor seem to cluster, except that the maximum scattering height of around 80-100 km above the CMB is nearly entirely defined by second precursors, and so I favour a combination of the models (1) and (2) (Figures 2.23a and 2.23b) with heterogeneities located inside of the LLSVP and being concentrated towards the edge of the larger scale structure. This could indicate that the earlier precursors are produced by scattering from heterogeneities near the CMB and the later, larger amplitude precursors are generated by scattering from the strong topography formed by the pile of heterogeneities at the boundary of the LLSVP.

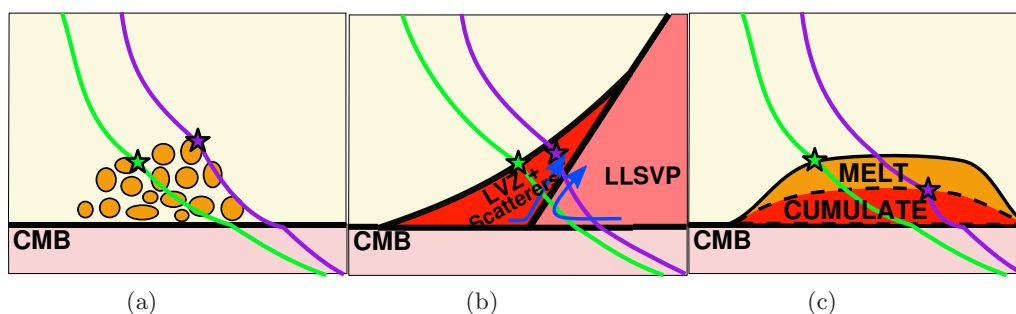


Figure 2.23: Possible structures in the lower mantle which may scatter (star) at different heights: (a) an LVZ comprising a collection of random heterogeneities likely included in LLSVP material (not shown), (b) an LVZ over the LLSVP, entrained by internal convection within the LLSVP (blue arrows), (c) or an LVZ with layered internal structure.

## 2.10 Summary

Precursors to  $\text{PKP}_{df}$  from events in South Africa are found to originate from scattering on the source side close to the CMB beneath southern Africa at the edge of the LLSVP in a region of strong seismic velocity gradients. The scattering volume is identified as an 80 km tall ridge trending east-north-east, west-south-west, although some of the boundaries are not well defined and likely the full structure is not being sampled by the dataset.

## Chapter 3

---

# PKKP Scattering

---

### 3.1 Introduction

The link between anomalous, high-frequency waves and small-scale structure was first shown by identification of precursors to PKP, which were explained as waves scattered at, or close to, the CMB. Following from the identification of deep mantle scattering of PKP [Cleary & Haddon, 1972; Doornbos & Husebye, 1972] (shown in Chapter 2) high frequency precursors to other phases were also observed and identified as the result of lower mantle scattering. Precursors to PKKP were first observed in beams of NORSAR data [Doornbos, 1974] at distances greater than  $125^\circ$ . These waves were attributed to scattering of P to KKP (P•KKP where the • denotes the point of scattering along the ray path. Figure 3.1) based on the observed energy preceding the main PKKP arrival, but arriving along the great-circle path with a slowness indicative of a path travelling through the outer core. Later array studies [Chang & Cleary, 1978, 1981] found off great-circle path scattering arriving at distances around  $60^\circ$ . At this distance only PKKP<sub>df</sub> (also written as PKIKKIKP) is theoretically possible however, due to the attenuation structure of the inner core and the steepness of the wave's incidence at the reflection point, it is expected that this would never practically be observed [Chang & Cleary, 1978]. The other branches of the PKKP phase (PKKP<sub>ab</sub> and PKKP<sub>bc</sub>) can only be observed at (minor-arc) distances greater than  $72.1^\circ$  (for IASP91 [Kennett & Engdahl, 1991]). The slowness of the observed precursors was also indicative of paths through the outer core and typical of PKKP<sub>bc</sub>. The energy was thus explained as PK<sub>bc</sub> waves that were travelling off great-circle path being scattered back (back-scattered) from the underside of the CMB to the receiver as PK•KP (Figure 3.2), travelling outside the diametral plane, the plane through the centre of the Earth containing both the source and receiver [Chang & Cleary, 1978]. Through the use of spherical trigonometry and a reference Earth model, it was determined that the PK•KP path would have a minimum travel time (1716 s in IASP91), regardless of the source-receiver great-circle distance. Further analysis of PKKP and its related scattered paths have determined the distance ranges in which these waves can be observed and their predicted travel times (Figure 3.1e). Many PK•KP waves are observed coming in from the "back" of the array, travelling further than  $\Delta = 180^\circ$  (along the major arc, the long segment of the path), but it is also possible for waves to arrive from the front of the array and from directly beneath, travelling through  $\Delta = 0^\circ$  (minor-arc distance, the short

segment of the path). At distances less than  $\Delta \sim 70^\circ$ , as the direct PKKP is not possible, scattered waves are not technically precursors as there is no main phase to precede, hence I refer to these waves as PK•KP.

It was originally proposed that PK•KP was generated by CMB topography (roughness) on the order of 100 m radial variation [*Chang & Cleary, 1978*]. Mathematical modelling of this problem indicated that scattering from CMB irregularities would create 1 Hz waves [*Doornbos, 1980*], equivalent to the frequencies of the scattered waves observed. However, subsequent more detailed studies have revealed that PK•KP comprises long trains of energy lasting over 100 s, which is better explained by scattering from volumetric heterogeneities higher above the CMB, into the lower mantle on the antipodal side [*Earle & Shearer, 1998; Earle, 2002; Rost & Earle, 2010*]. When scattering above the CMB, the ray path is technically PKP•PKP as the wave travels as a P-wave in the lower mantle on the antipodal side before scattering. However, the path is still referred to as PK•KP. The causative scattering heterogeneities are likely similar to the volumetric anomalies identified with PKP precursors [*Wen & Helmberger, 1998; Cao & Romanowicz, 2007; Thomas et al., 2009; Frost et al., 2013*], with similar velocity and/or density contrasts (explained in Chapters 1.3 and 2).

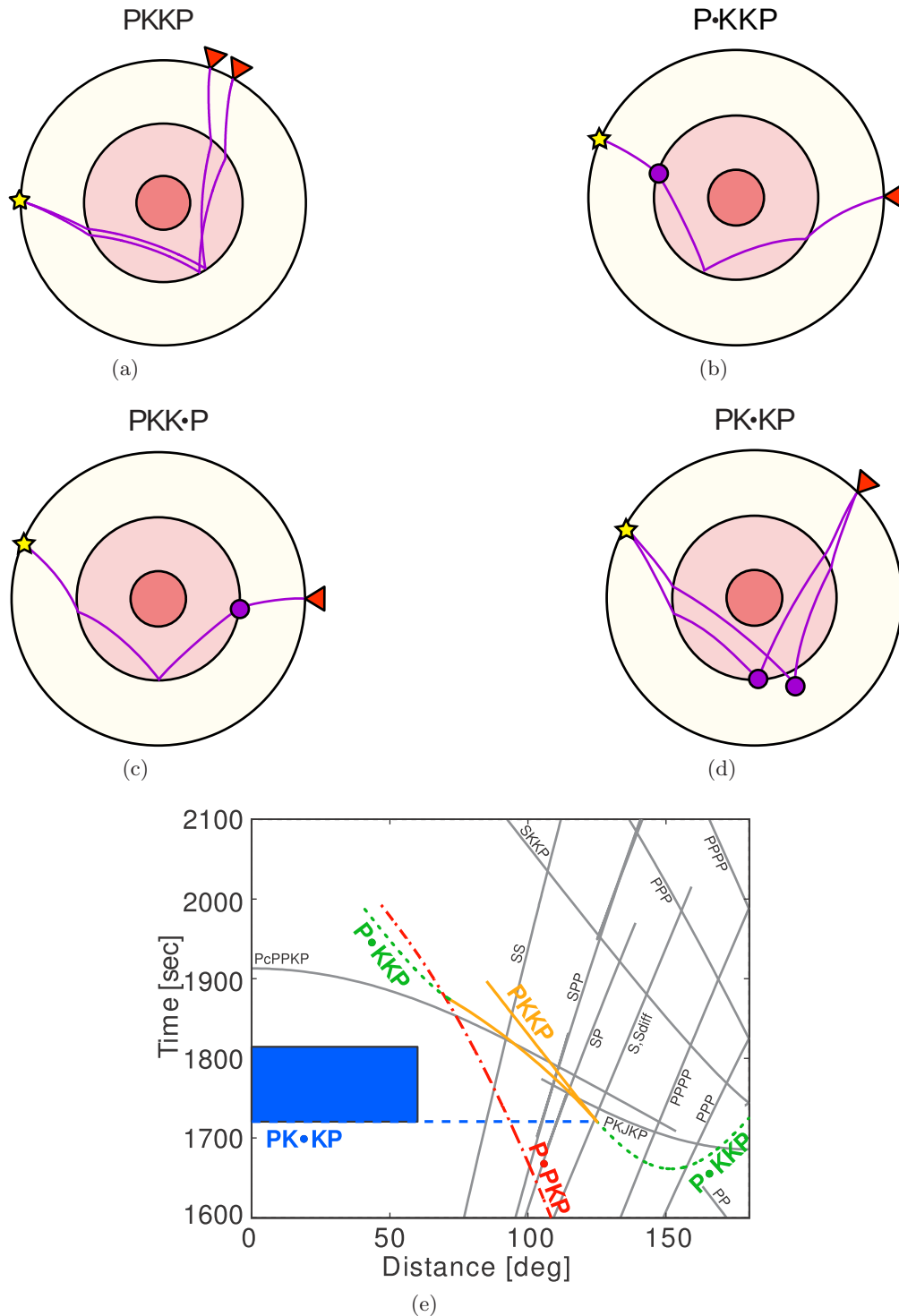


Figure 3.1: PKKP ray paths from source (yellow star) to receivers (red inverted triangles) showing (a) direct PKKP, (b) source-side scattered P•KKP, (c) receiver-side scattered PKK•P, (d) and CMB-scattered PK•KP. The scattering point can be at the CMB or above into the lower mantle on the antipodal side. The path is then effectively PKP•PKP but is still referred to as PK•KP. Scattering is caused by interaction of the incoming wavefield with small-scale heterogeneities in elastic properties or density. (e) Travel-time table showing all the variants of the PKKP path (in colour) and additional, unrelated paths that are observed in a similar time and distance range (in grey). The time and distance range used in this study to select PK•KP is shown by the blue box. The time window used is 100 s long following the PK•KP first arrival (at 1716 s) to limit analysis to signals from the lowermost 300 km of the mantle. PK•KP arrivals are possible at distances greater than 60° but may be contaminated by other phases and so are not used. After Earle [2002].

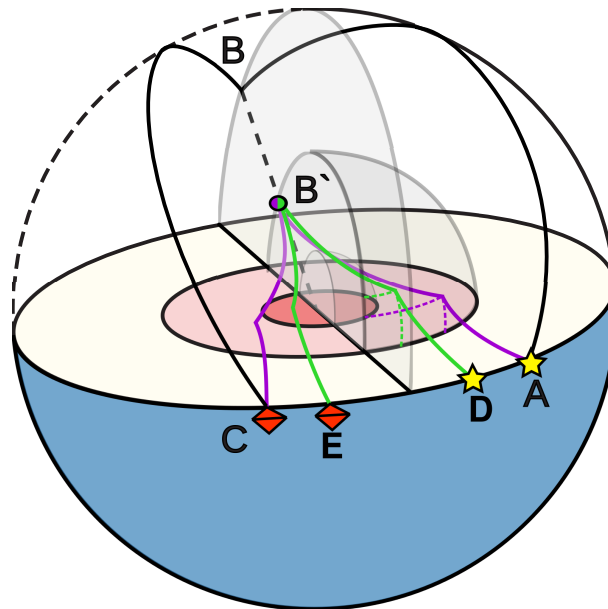


Figure 3.2: Example PK•KP ray paths demonstrating how the probe scatters off great-circle path. Rays travel from the sources (yellow stars) A and D, avoiding the inner core, to the scattering point B', and to the receivers (red inverted pyramids) C and E. Despite having different source-receiver distances (A-C and D-E), it is possible for paths A-B'-C (purple path), and D-B'-E (green path) to have the same travel-time provided that the 1-dimensional paths travelled are the same (and have the same source-scatterer-receiver ray length). Point B shows the surface projection of the scattering point at B' which is significantly out of the diametral plane containing the sources and receivers. The same ray paths are also equally possible in the lower hemisphere. After Chang & Cleary [1981].

The PK•KP path can be extended upwards to include scattering in the mid and upper mantle, where the phase is better known as P'P' [King & Cleary, 1974; Earle et al., 2011] [Rost et al., 2014, in press]. The later the arrival time of the scattered energy following the minimum value (1716 s in IASP91), the higher into the mantle on the opposite side from the source the scattering occurs. Thus, the time window used can be limited in order to focus on certain parts of the mantle. Selecting the first 100 s following the minimum time allows study of just the lowermost mantle. Past studies have used the slowness and back-azimuth values of PK•KP waves to determine the location of scattering within the earth [Rost & Earle, 2010]. However, previously the whole of the 100 s time window was used at once, averaging all the signals over this time window thus recording the dominant scattered energy and giving only one source location within the mantle. In this study, I analyse the scattered energy through the scattering time window to observe the evolution of the energy arriving at the array in terms of slowness and back-azimuth. In doing so, I find multiple separate signals in the time window indicating several discrete inhomogeneities are sampled by, and scatter, the PKKP wavefield. Therefore, the PK•KP probe is incredibly effective for sampling and locating heterogeneities from large areas of the lowermost mantle.

The knowledge that scattering heterogeneities are chemically distinct volumes within the mantle means that they can be used to track convection and also chemical processes [McNamara et al., 2010]. Scatterers are often found in areas containing Ultra Low Velocity

Zones (ULVZs) which show extreme, sharp, localised velocity drops and density increases, and extend a few 100s km laterally and a few 10s km vertically [Vidale & Hedlin, 1998; Thomas *et al.*, 1999; Wen, 2000; Rost *et al.*, 2010a,b; Frost *et al.*, 2013]. These features are thought to comprise either partially molten mantle material [Williams & Garnero, 1996; Vidale & Hedlin, 1998; Reasoner & Revenaugh, 2000; Lay *et al.*, 2004], plume related activity [Williams *et al.*, 1998; Wen, 2000; Rost *et al.*, 2005; Cottaar & Romanowicz, 2012], or solid-state enrichment of mantle perovskite with iron [Garnero & Jeanloz, 2000; Rost *et al.*, 2006a; Mao *et al.*, 2006; Wicks *et al.*, 2010] either from above [Dobson & Brodtholt, 2005] or below [Garnero & Jeanloz, 2000]. ULVZs tend to be spatially associated with the edges of larger-scale mantle features such as the Large Low Shear Velocity Provinces (LLSVPs) [McNamara *et al.*, 2010]. This spatial correlation may be due to convection within the LLSVPs, which themselves show evidence for being thermo-chemical anomalies [Hart, 1984; Castillo, 1988; Ritsema *et al.*, 1998; Ni & Helmberger, 2003b; Wang & Wen, 2007; Deschamps *et al.*, 2012]. Concentrated chemical anomalies, especially those with positive density anomalies, could fall out of convection and pond at the edges of LLSVPs in areas of stagnant flow [McNamara *et al.*, 2010]. Scattering outside of ULVZ regions may instead be due to slab remnants breaking up in the mantle [Cao & Romanowicz, 2007; Rost *et al.*, 2008; Miller & Niu, 2008]. Through dynamic models, LLSVP structure has been shown to be affected by the subduction history with the LLSVPs interacting with slabs [McNamara & Zhong, 2005]. Subduction could, therefore, carry chemically, and thus seismically, anomalous oceanic crust into the lower mantle where it could be disaggregated, potentially piling at the LLSVP margins [Christensen & Hofmann, 1994; Tackley, 2011]. Therefore, there are mechanisms by which small-scale heterogeneities could be found in both the LLSVPs, or within the surrounding (on average faster) mantle material. Dynamic models suggest that anomalies would be concentrated close to the edges of the LLSVPs [McNamara *et al.*, 2010], but could still occur at any other point in the mantle [van Keken *et al.*, 2002; Stixrude & Lithgow-Bertelloni, 2012].

I use the PK•KP probe with a near global distribution of earthquakes and arrays to locate small-scale scattering heterogeneities within the Earth, both laterally and in depth. I find that the number and height of scattering points varies strongly with location and I observe patterns which I relate to large-scale mantle structures. I use a global set of broadband records of PK•KP to determine the dominant frequency of scattered waves, and thus calculate the range of sizes of scattering heterogeneities. I determine similar distributions and scale-lengths of scattering heterogeneities to those calculated in other studies using a range of probes but using a single probe allows direct comparison between observations.

## 3.2 PK•KP Scattering Regions

The PK•KP wave has a versatile but complex path, Therefore, to effectively utilise this probe it is important to understand how the component paths involved behave and where the source-receiver combination allows sampling. The total path comprises any combination of a down-going PK<sub>ab</sub> or PK<sub>bc</sub> leg, and an up-going KP<sub>ab</sub> or KP<sub>bc</sub> leg. The paths of the PK and KP legs are opposite but equivalent hence the following constraints are true for both. The minimum and maximum distance range of each of the *ab* and *bc*

branches is dependent upon the depth above the core at which the scattering occurs and the velocity model used (Figure 3.3), which in this case is IASP91 [Kennett & Engdahl, 1991]. For the  $ab$  branch, the distance of scattering at the CMB received at the surface ranges from  $\Delta = 116.5^\circ$  to  $\Delta = 124.1^\circ$  and, for the  $bc$  branch, from  $\Delta = 116.5^\circ$  to  $\Delta = 144.1^\circ$ . For scattering at 2589 km depth, for the  $ab$  branch, permissible distances range from  $\Delta = 125.6^\circ$  to  $\Delta = 144.9^\circ$  and, for the  $bc$  branch, from  $\Delta = 124.4^\circ$  to  $\Delta = 146.5^\circ$ . These limits are shifted to shorter distances for deeper sources. For example, a 500 km deep source scattering at the CMB has a range with upper and lower bounds  $\sim 1.5^\circ$  shorter (i.e. closer to the source for a PK path) for the  $ab$  branch and  $\sim 1^\circ$  shorter for the  $bc$  branch. Knowing these limits not only allows me to limit the distances tested when ray-tracing, thus saving time, but also demonstrates what paths are feasible and where can be sampled by PK•KP. The area sampled by PK•KP is greatest at the CMB.

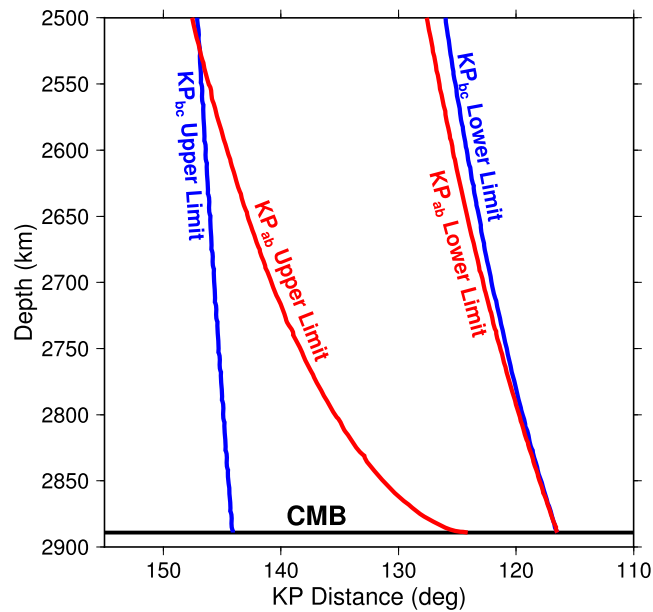


Figure 3.3: Distance limits between which a KP path (or equivalently PK path) is possible for a range of scattering heights above the CMB.  $KP_{ab}$  path limits are shown in red and  $KP_{bc}$  path limits are in blue. All paths are calculated for IASP91 [Kennett & Engdahl, 1991].

The off great-circle path nature of the PK•KP phase results in a unique geometry which, for a single event, samples the CMB at multiple distinct, and often separate, locations. For longer source-receiver distances (minor arc), there are two possible regions of scattering, either side of the inner core (Figure 3.4). At shorter source-receiver distances, the area of possible scattering becomes a ring around the antipode. Each source-receiver pair samples a large area of the lowermost mantle making the probe extremely effective, although precise array processing is required to locate individual scattering heterogeneities within these regions.

To explore the flexibility of this probe, and as a constraint on subsequent selection of scattered energy (in terms of possible back-azimuths, slownesses, and times), regions of potential PK•KP scattering at the CMB are determined for distances from  $\Delta = 0^\circ$  to  $\Delta = 60^\circ$  in  $5^\circ$  increments. For a given source-receiver distance (minor arc), rays are traced (through IASP91) along the major arc from a source at the surface to a point in a

grid representing possible scattering points located around the mid-point at the CMB, and then from the scattering point to the receiver at the surface. All possible complete paths where both down-going and up-going legs are possible (as either  $bc$  or  $ab$  branches), are calculated indicating where scattering could occur and be observed at the receiver. For each point, the travel-time of the whole path and the back-azimuth and slowness of the upward leg are measured (Figure 3.4). The possible ranges of back-azimuths and travel times for each source-receiver distance are then calculated. Only rays with total travel-times over 1716 s (the minimum travel time for PK•KP in IASP91) and under 1816 s are considered (Figure 3.1e). After this time the wave sample above the lower 300 km of the mantle and other phases can arrive which may interfere with a scattered wave.

It is found that for source-receiver distances of  $\Delta \leq 25^\circ$  all back-azimuths are permissible (Figures 3.4a and 3.4c), thus energy can arrive along the minor arc path, as well as arriving along the major arc path. The scattering region forms a continuous ring around the antipode on the opposite side of the Earth. However, for source-receiver distances of  $\Delta \geq 30^\circ$  the potential scattering region separates into two "wedge" shapes either side of the major arc great-circle path (Figures 3.4b and 3.4d). With increasing source-receiver distance, the range of back-azimuths from which scattered energy can be received decreases, thus less of the CMB is sampled. Additionally, potential scattering areas decrease in size with increasing height of scattering above the CMB (Figures 3.4a and 3.4b and Appendix Figure C.1), and scattered arrivals become later. For example, when scattering occurs at 200 km above the CMB, the earliest possible arrival is at 1778 s, close to the end of the time window used here and the permissible scattering area is  $\sim 6$  times smaller than that at the CMB. At 300 km above the CMB the scattering region is 40 times smaller. However, the region of permissible scattering would be larger if scattered energy arriving after 1816 s were accepted.

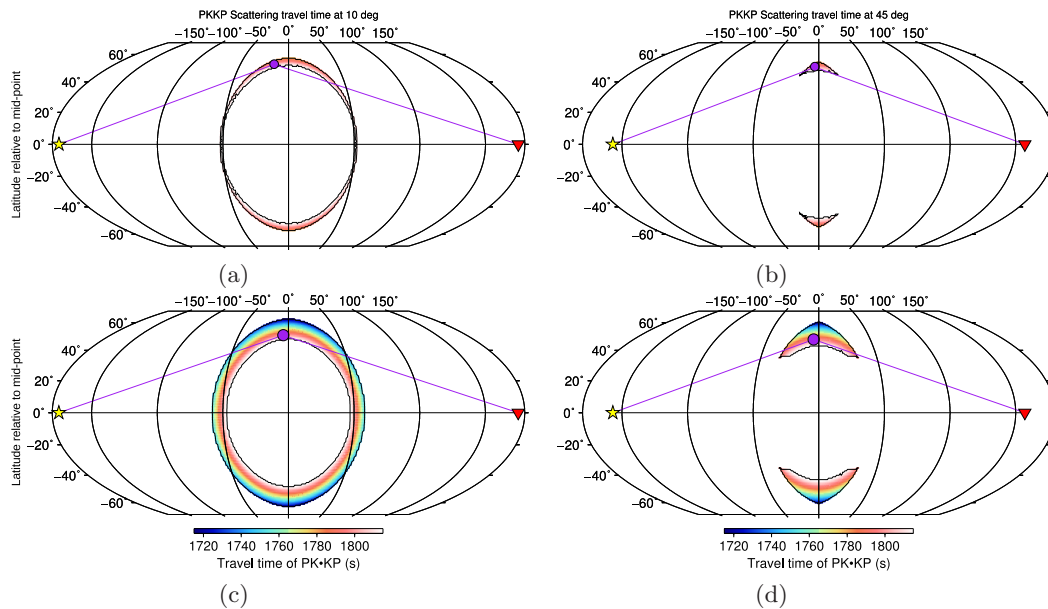


Figure 3.4: Regions of potential scattering for a surface focus event (yellow star) to a receiver (red inverted triangle) for scattering at 2689 km depth (200 km above the CMB) at (a)  $10^\circ$  and (b)  $45^\circ$  source-receiver distance (minor arc) and for scattering at 2889 km (at the CMB) (c)  $10^\circ$  and (d)  $45^\circ$  source-receiver distance. An example scatterer (purple circle) and ray path (purple line) are shown demonstrating the potentially asymmetric nature of the ray path. Travel-times are computed using IASP91. Colours indicate the travel-time of waves scattering at that point. The minimum whole path travel-time is 1716 s for a surface focus event, Scattering locations which would generate waves with travel-times longer than 1816 s are not shown, these limits are indicated by the black lines around the colour regions. Regions of potential scattering are much smaller for scattering above the CMB and at longer source-receiver (minor-arc) distances. At longer source-receiver distances there are two separate regions of sampling while at shorter distances ( $< 30^\circ$ ) there is a single continuous region centred at the antipode of the source-receiver mid-point.

Using the observations of where scattered waves can be received for a given source-receiver distance I am able to predict the expected range of slownesses, back-azimuths, and travel-times for PK•KP waves. This knowledge helps to prevent falsely identifying other signals in the data as scattered arrivals.

### 3.3 Data Collection

I use data recorded at 16 small to medium aperture International Monitoring System (IMS) arrays from around the world (Table 1.1). The majority of the arrays used became operational around 1995 or afterwards, with the exception of GB (which is not IMS) and the UKAEA arrays (which includes AS, EK, WR, YK). The NEIC PDE catalogue is searched for earthquakes over magnitude 6.0 from 01/01/1995 to 31/12/2011 and from 1985 to 1996 for GB due to limited access; 1512 events are found (Figure 3.5). This catalogue is chosen for its consistency throughout this time period in reporting depth information which is critical in matching arrival times in the ray-tracing process. For each array, from its operational date onwards, for each event within  $0^\circ \leq \Delta \leq 60^\circ$ , seismograms from all stations in the array are retrieved from the CTBTO collection. A total of 2538 event-receiver pairs are collected from 1097 events (see Appendix Table C.1). The events

that are not used (out of the initial 1512) are either outside the cut-off dates, inside the cut-off date but with a limited number of stations operating, had corrupted data, or data are otherwise unavailable.

Data for each event-receiver pair are de-spiked, and the trend and mean are removed. To avoid potential problems with different instrument responses, channels other than the prevailing type in an array are removed, ie. as Yellowknife array has 18 short-period stations and 4 broad-band stations, the broad-band stations are removed. The remaining traces are visually inspected and erroneous channels are removed. If more than half of the total number of channels in the array are removed then the whole event recording is discarded to avoid creating a low quality beam.

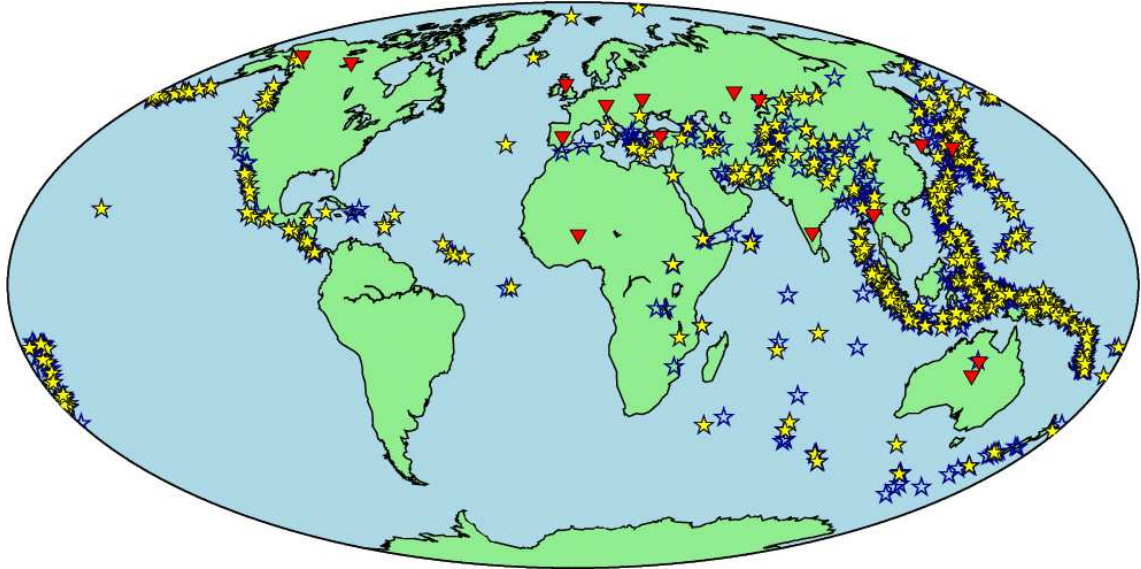


*Figure 3.5: Arrays used (inverted triangles) and events (stars) over magnitude 6.0, from 1985 to 1996 for GB and 01/01/1995 to 31/12/2011 for all other arrays. Closed stars indicate that scattered PK•KP waves were observed associated with the event, while open stars mark events that did not generate identifiable scattering. Out of 1097 events, 544 show scattering at at least one array.*

### 3.4 PK•KP Scattering Coverage

Using the potential scattering regions calculated previously (see Chapter 3.2 and Figure 3.4) and the events available (Figure 3.5 and Appendix Table C.1), a map of potential scattering coverage is generated. For each source-receiver pair for which data could be retrieved from the CTBTO, the minor-arc distance is used to select the most appropriate scattering region at the CMB from the  $5^\circ$  bins (e.g. Figure 3.4). This scattering region is then rotated by the great-circle path back-azimuth and centred at the mid-point of the path, thus demarcating the one or two potential PK•KP scattering regions either side of the major arc path for this source-receiver combination. The scattering regions for all 2538 source-receiver pairs are stacked and the number of hits per  $1^\circ \times 1^\circ$  bin is calculated (Figure 3.6). I observe a range of concentrations of scattering coverage ranging from areas with theoretically no sampling at all (primarily under the Asia, Arabia, and north-western North America) to regions potentially sampled by up to 717 source-receiver pairs (under the southern and mid-Atlantic, Central America, and the South Pole regions).

Although this calculation demonstrates where coverage by PK•KP is most likely, it is not completely accurate as it uses sampling regions created for  $5^\circ$  distance increments for each source-receiver pair, rather than creating sampling regions for each specific source-receiver distance. Therefore, the scattering region may be a slight over or under estimation of the true extent of the area. Additionally, scattering wedges are only calculated for surface focus events, regardless of the actual event depth. There is, therefore, a negligible error in the size of the regions used and, as scattering wedges are only calculated at the CMB (where scattering regions are largest), this an upper bound for scattering coverage. Nevertheless, this map is a useful approximation of where the data are able to sample the Earth's small scale structure.

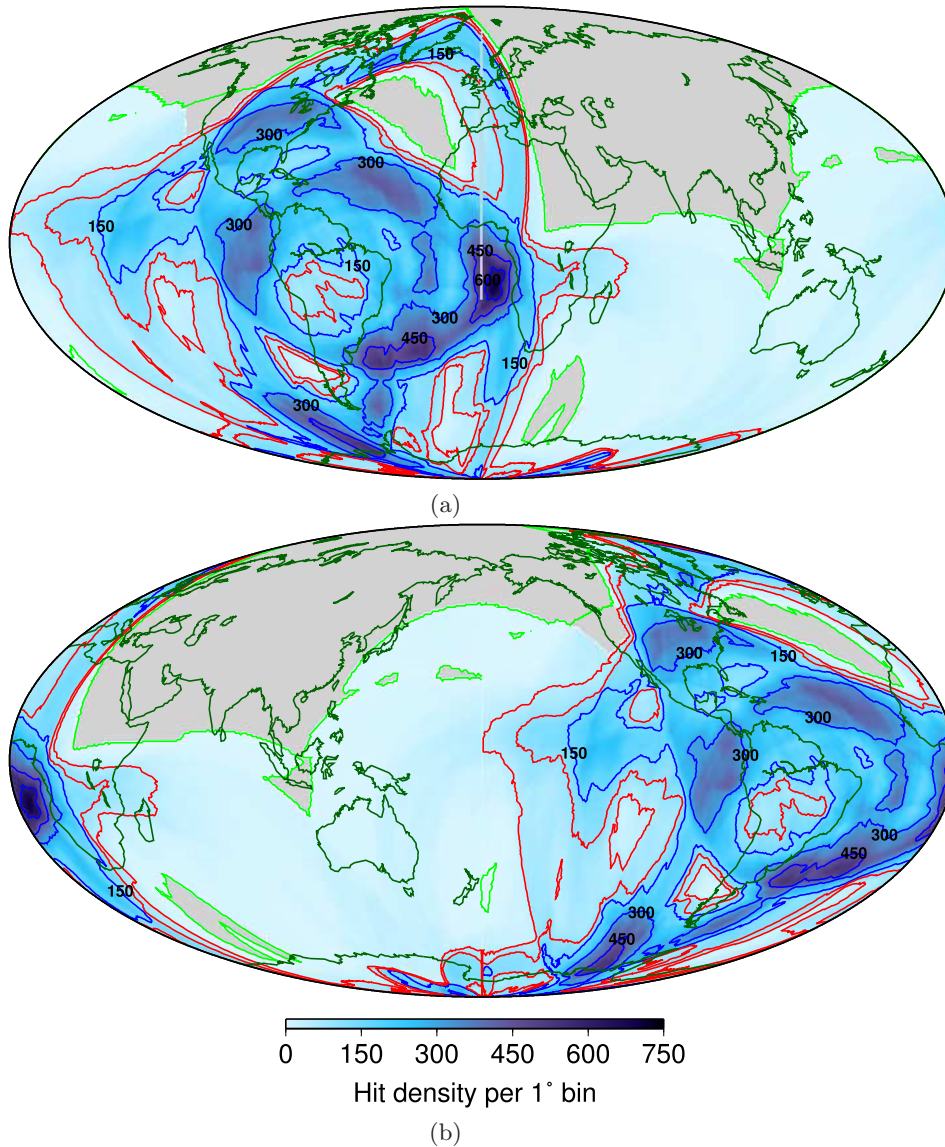


Figure 3.6: Potential coverage by PK•KP for scattering at the CMB for all 2538 source-receiver pairs that could potentially sample each degree at the CMB. (a) Projection centred at  $0^\circ$  and (b)  $180^\circ$  longitude created using the scattering regions calculated for various source-receiver distances in Chapter 3.2. The extent of the coverage, the zero-sampling contour, is shown by the green line while blue and red contours indicate potential sampling at 150 and 300 count intervals, respectively. The maximum potential coverage of 717 hits per  $1^\circ \times 1^\circ$  bin occurs off the coast of equatorial Africa.

### 3.5 Data Processing

The PK•KP time window of each event is analysed using the F-trace (explained in Chapter 1.4.6) to extract high-resolution directivity information. The arrival time, slowness, and back-azimuth limits calculated above for a range of source-receiver distances (see Chapter 3.2) are used to mark out the time window and slowness-back-azimuth space in which scattered waves are able to arrive. I use the directivity information measured by the F-trace to locate the source of the scattered energy, the scattering heterogeneity, in latitude-longitude, and depth so that global patterns of scattering can be studied.

For each event, using the source depth information given in the catalogue, the fastest possible PK•KP path is calculated by ray-tracing through IASP91 from the focus to the CMB at  $\Delta = 116.5^\circ$ , and from the CMB to the surface at  $\Delta = 116.5^\circ$  and taking the sum of the travel time for the two legs. The total travel-time ranges from 1716 s for a surface focus event to 1642 s for a 688 km focus event (the deepest event in the dataset). The arrival-time of the first possible PK•KP wave is then predicted by using the sum of the calculated travel-time and the origin time in the NEIC PDE catalogue. Seismograms are sampled in a 125 s time window starting 25 s prior to the predicted first arrival to account for discrepancies in the Earth model and to observe the pre-signal noise level (which aids signal identification). To reduce processing time, the whole 125 s seismograms are sampled in a 10 s sliding window with a 1 s time step (90 % overlap). These parameters are found to best extract short discrete signals typical of PK•KP from the noise, while preventing smearing of the signal through time. Each event is converted to the frequency domain, bandpass filtered between 0.5 Hz and 2.0 Hz (frequencies are tested and this range is found to best reveal PK•KP energy) and then is processed with the sliding window F-statistic [Blandford, 1974; Bowers, 2000] in the frequency domain (introduced in Chapter 1.4.7) to create a fk F-statistic. This process determines the signal strength at different slownesses and back-azimuths for the sampled time window. It is important to note that although the filtering limits are similar to those used in the PKP study (see Chapter 2) [Frost *et al.*, 2013], the shape of the filter is different due to it being applied in the frequency domain rather than the time domain. The fk is calculated for slownesses from 0 to 11.11 s/deg in 0.27 s/deg increments, and back-azimuths from  $-180^\circ$  to  $180^\circ$  in  $2^\circ$  increments. This is repeated using a finer slowness spacing of 0.111 s/deg, between 0 and 6 s/deg and the same back-azimuth spacing and range. This parameter space was chosen to maximise the directivity resolution in the range of importance to these signals. The fk result is shown as a beam power map in slowness-time and back-azimuth-time space for visual inspection (Figure 3.7). Scattering is visually identified, guided by the back-azimuth and travel-time ranges determined in Chapter 3.2, and lower and upper slowness limits of 2.1 s/deg and 4.4 s/deg, corresponding to waves turning between the ICB and CMB, respectively.

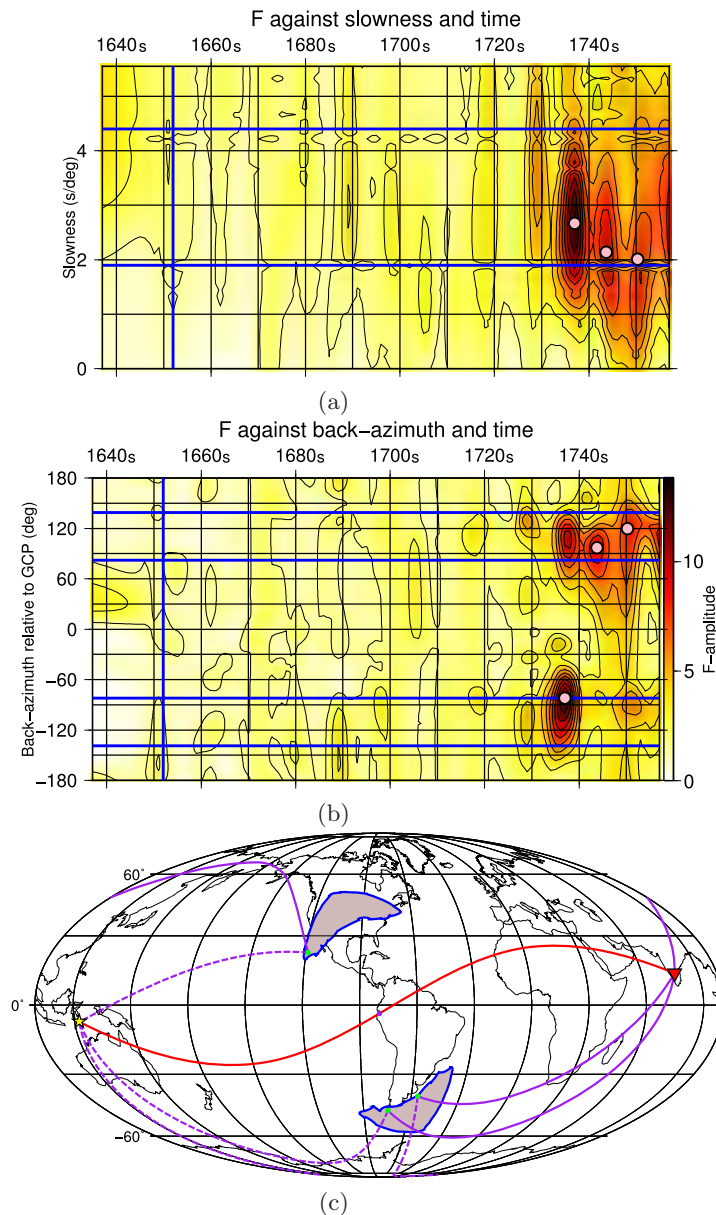


Figure 3.7: Processing and results for a magnitude 7.9 event in the Banda Sea ( $7.14^{\circ}$  S,  $122.60^{\circ}$  E) at 11:22 am on 17/06/1996 at 587 km depth recorded  $49^{\circ}$  away at Gauribidanur Array, India. Results of the  $f_k$   $F$ -statistic analysis displayed in (a) slowness-time space and (b) back-azimuth-time space from 0 to 6 s/deg and 1637 to 1757 s, and from  $-180$  to  $180^{\circ}$  (about the great-circle back-azimuth of  $112^{\circ}$ ) and 1637 to 1757 s, respectively. The lower time limit of 1652 s (for 587 km event depth) is shown by a vertical blue line and limits for slowness and back-azimuth are shown as horizontal blue lines (calculated in Chapter 3.2). Picked energy peaks are displayed as pink circles which are then ray-traced to the scattering points located in Figure c. The picked PK•KP energy peaks, from first to last, scatter at heights relative to the CMB of 0 km, 150 km, and 40 km, respectively. (c) Source (star) and receiver (inverted triangle) locations connected by the major-arc great-circle path (red line) showing the mid-point (purple dot). Potential scattering regions (grey wedges) are either side of the mid-point and the scattering points of 3 PK•KP signals located on different sides of the great-circle path, as is evident when viewed in back-azimuth-time space as in Figure b. The source-to-scatterer and scatterer-to-receiver paths are shown as purple dashed and purple solid lines, respectively. Scatterers are shown as green circles as they have slowness and time misfits lower than 1.5 s/deg and 2.5 s, respectively. Scattering points with misfits greater than this would be shown as red circles and disregarded from further processing.

The amplitude of the F-trace is displayed in slowness-time (Figure 3.7a) and back-azimuth-time space (Figure 3.7b) for simultaneous analysis of how the two parameters vary through time. For events showing energy within the directivity limits mentioned above, each individual packet of scattered energy is selected and the corresponding slowness, back-azimuth, and travel-time are recorded. Signals arriving outside of the slowness, back-azimuth, and travel-time limits calculated for a given source depth and source-receiver distance are ignored as it is not possible that they originated from single scattering of PK•KP energy from the event being considered. I select between 0 and 8 scattered arrivals for a single event. Signals are picked if they are clear relative to the noise, arrive within the directivity limits, appear as separate signals, and are not obviously erroneous. The sharpness of the signal (extent of smearing in slowness, back-azimuth, and time space) affects the accuracy to which the signal can be picked. This is dependent on the array used and will be discussed in more detail in Chapter 3.7.

Doublet earthquakes, a pair of events closely located in space and time, foreshocks, or aftershocks would introduce difficulty into linking scattered energy with its origin. Associating PK•KP energy with the wrong event in an doublet would lead to an incorrect location when ray-tracing. Given the similar source locations, the directivity and time information would not be sufficient to distinguish which source a scattered signal is related to. As there is no additional information about the scattered signals, discretion must be used when picking scattered signals from events shown in the catalogue to do be closely related to other earthquakes.

For each event, the source of each packet of scattered energy is determined in terms of latitude, longitude, and depth, by ray tracing through a 1-dimensional Earth model (IASP91) using the slowness, back-azimuth, and time observed for each signal to find the best fitting location of the scattering heterogeneity. A 2-dimensional grid representing possible scattering locations is constructed along the back-azimuth recorded at the array, in terms of epicentral distance from the array, between the maximum limits of the PK<sub>ab</sub> and PK<sub>bc</sub> paths (Figure 3.3), and height above the CMB, from the CMB to 300 km above. As mentioned in Chapter 3.2, the *ab* and *bc* branches of the PK and KP ray-paths have different distance ranges dependent on scattering depth. For each distance and each scattering depth in the grid, all permissible combinations of down-going PK<sub>ab</sub> or PK<sub>bc</sub> legs and up-going KP<sub>ab</sub> or KP<sub>bc</sub> legs are constructed. Each complete path from each point in the scattering grid is then associated with a travel-time (the sum of the down-going and up-going legs) and a slowness (that of the up-going leg). From amongst this range of points the distance, depth, and complete path branch combination which best fits the recorded slowness and travel-time is selected by minimising residuals. The selection is weighted in favour of picking scattering points with the smallest possible slowness residual given that a 1 s/deg slowness deviation is much more significant than a 1 s travel-time deviation. To maximise processing speed, and accuracy, the grid is searched twice with different depth and distance spacing. In the first search, a coarse grid is constructed with 40 km depth intervals and 4° distance intervals. Scattered energy packets that cannot be fit by any scattering location are discarded while for those signals that can, the search is repeated using a finer grid. This new grid is 100 km tall and 10° wide, centred on the best-fitting point found in the first search, with scatterers at 10 km depth intervals and

0.5° distance intervals. The best fitting scattering point is then updated using the results of this second processing step. The misfits between the traced slowness and travel-time and those measured in the data with the fk F-statistic are calculated and used to assess the quality of the match. Energy packets are disregarded if either the slowness misfit is greater than 1.5 s/deg, the travel-time misfit is greater than 2.5 s, or the F-amplitude of the scattered signal is more than twice that of the P-wave signal for the same event (on the assumption that the direct P-wave measured on the minor arc should be considerably stronger than the scattered PK•KP energy). This processing results in 952 scattering points, each with well fitting latitude, longitude, and depth (e.g. Figure 3.7c).

The coarse and fine grid extents and spacings are selected by testing a few events using this two step method against a single step method using a grid with scatterers at 10 km depth intervals and 0.5° distance intervals (the fine grid spacing). The fastest combination of two step grid parameters that matches the results of the single step process are used in subsequent processing. Scattered energy packets that cannot be satisfactorily fit by any scatterer location are considered either multiple scattering, interference of two coincident scattered waves from different directions or, more likely, mis-identified noise, and not processed further.

The ray-tracer balances the influence of the travel-time and slowness misfits. Although slowness and back-azimuth both influence distance and depth of the scattering point, slowness primarily controls the position in terms of distance, while travel-time is the main control on the depth (Figure 3.8). The two branches, *ab* and *bc*, have different slowness and travel-time ranges. The ray-tracer selects the branches for each leg which best fit the measured parameters of the whole path.

Although ideally the amplitude of the scattered wave would be used to indicate the degree of heterogeneity of the scatterer i.e. the density and elastic parameter contrasts with the surrounding mantle [*Wu & Aki, 1985a*] (discussed in Chapter 1.3), this is considered infeasible as there is no suitable reference phase to measure the amplitude relative to. In the case of PKP (see Chapter 2) [*Frost et al., 2013*], precursor amplitude can be compared to the direct PKP<sub>df</sub> phase as these waves have similar propagation paths and, crucially, take-off angles from the source. Waves travelling along both the direct and scattered paths will, therefore, originate from a similar part of the focal mechanism with similar amplitudes. The paths through the mantle will also be similar, hence the two waves will sample roughly the same attenuation structure (see Chapter 1.5.2) and so differences in amplitude between the direct and scattered waves will likely only result from the scattering process. However, possible reference phases for PK•KP, such as P and PcP, travel the minor arc rather than the major arc. These phases, therefore, will leave the source from a different part of the focal mechanism and so have a different amplitude at the start. This is true for any focal mechanism other than a pure explosion or implosion, which is unlikely for these events. Regardless of focal mechanism, rays travelling in different directions will sample disparate parts of the mantle, thus experience contrasting attenuation. P'P' could possibly be used as this travels the major-arc path and would have a similar take-off angle from the source to PK•KP, but this phase is rarely observed in my data. I conclude that without in-depth ray-tracing through a 3-dimensional velocity and attenuation model of both the PK•KP and P waves using well studied CMT solutions, extracting any useful

information from the amplitude of the scattered waves is impractical.

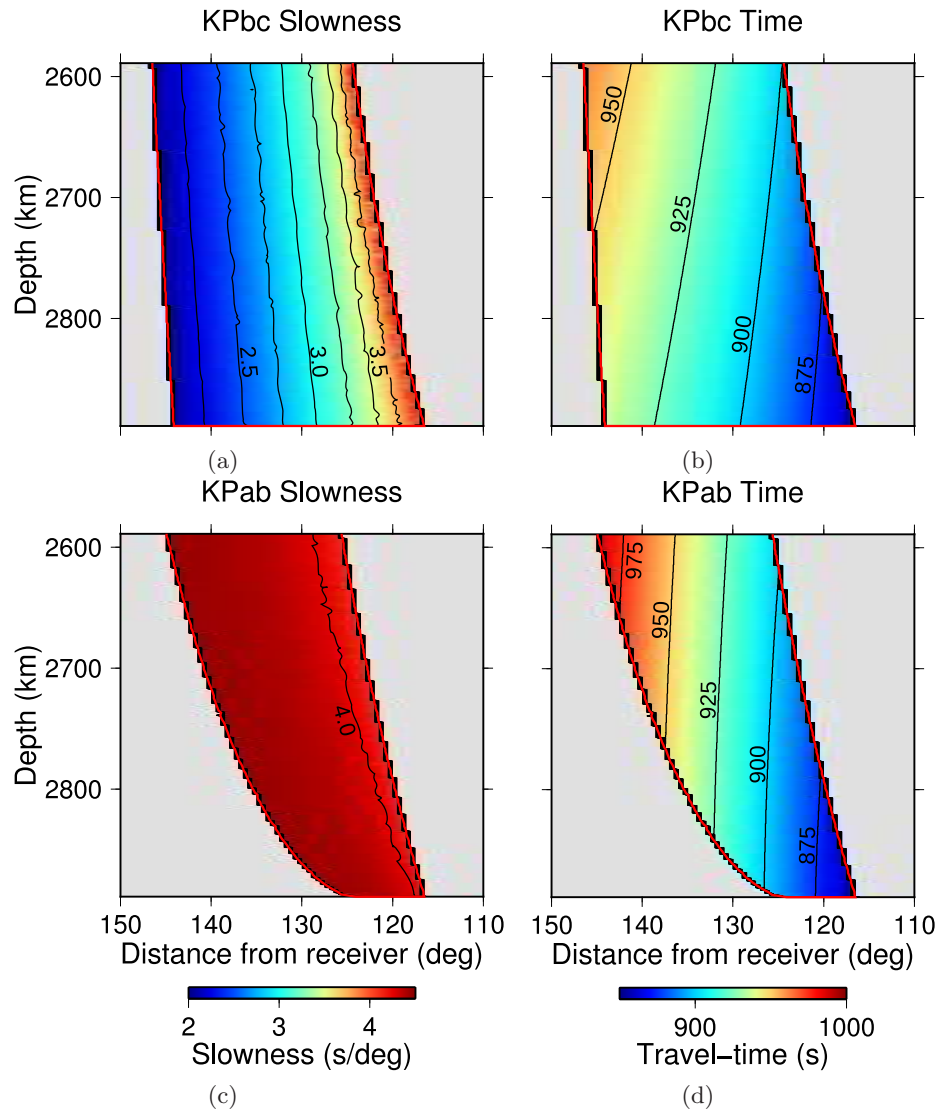


Figure 3.8: Range of distances and depths possible for (a and b)  $KP_{bc}$  and (c and d)  $KP_{ab}$  and their influence on slowness and travel-time. When ray-tracing, the distance of the scattering point from the receiver is primarily controlled by slowness while scattering depth is dominantly controlled by travel-time. Red lines indicate the limit of each branch as in Figure 3.3. Labels for slowness and time are in s/deg and seconds, respectively.

### 3.6 Results

Of the 1097 events used, 544 are found to show at least one scattered arrival detected at one or more of the 16 arrays used. A total of 942 event-receiver pairs show scattering at least once. Scattering heterogeneities are located between the CMB and 320 km above the CMB (although the initial coarse grid in the ray-tracing process only runs to 300 km above the CMB, the second fine grid can extend this maximum height by an additional 50 km). Following ray-tracing, the results are collated and plotted to create maps of scattering height above the CMB. Due to the amount of scattering points in similar regions, I group scattering points into  $10^\circ \times 10^\circ$  cells. An important measure of the credibility of

the scattering patterns is the reproducibility. As such, I also show the number of scatterers observed in each cell alongside the scattering height (Figure 3.9). Additionally, I analyse the distribution of scattering points with height in larger  $30^\circ \times 30^\circ$  cells, compared with the global distribution of scattering points (Figure 3.10).

I find that there is strong lateral variation in scattering height above the CMB with regional patterns visible. Many areas show scattering close to the CMB but scattering away from the CMB is less common. Scattering heterogeneities higher above the CMB are often grouped, and adjacent  $10^\circ$  cells are seen to contain similar heights. Cells with the scatterers located highest above the CMB often also show a range of scatterers at varying heights, down to the CMB (Figure 3.10). However, cells often only contain scatterers at the CMB. Although the maps of maximum scattering heights are most striking (Figures 3.9e and 3.9f), the maps of median scattering heights (Figures 3.9c and 3.9d) are likely the most useful as they show regions that have scattering consistently above the CMB. Mean scattering heights (Figures 3.9a and 3.9b) can easily be distorted by a single high scattering point due to the relatively small number of scatterers per cell. Cells in which many scattering heterogeneities are observed often contain higher maximum scattering heights.

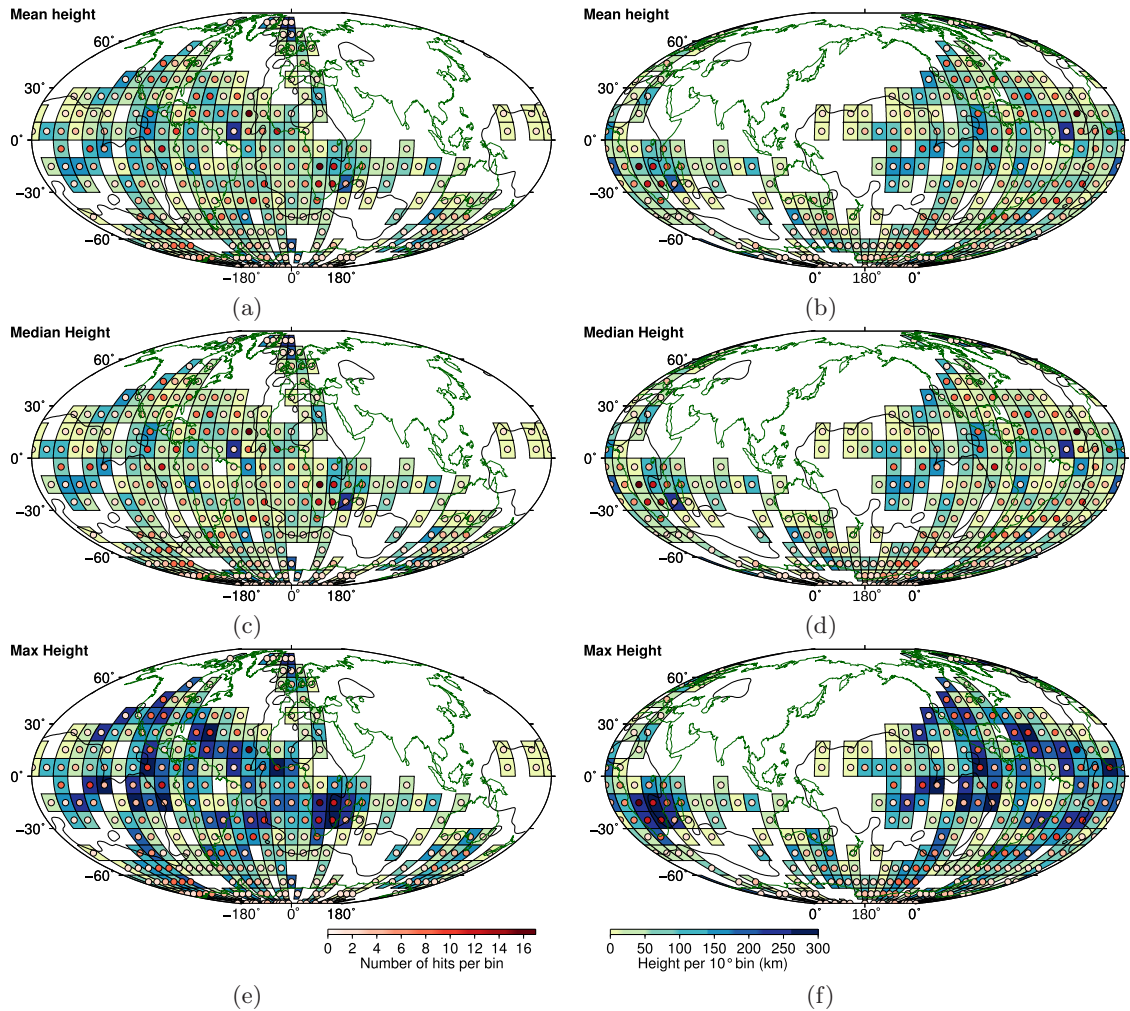


Figure 3.9: Scattering heterogeneity heights above the CMB, centred at  $0^\circ$  (left) and  $180^\circ$  (right) longitude, displayed in  $10^\circ \times 10^\circ$  cells as (a and b) mean scattering height in each cell, (c and d) median scattering height, (e and f) maximum scattering height. The height of each cell is shown by the tile colour and the number of scattering locations in each cell is shown by the colour of the inset circle. The  $-0.4\%$   $V_S$  contour from S40RTS is displayed as the black line to represent the extent of the LLSVPs. For larger figures see Appendix Figure C.2

High scattering heights and high concentrations of scatterers are observed in many regions (Figure 3.10), some of which have previously been reported to show lower mantle seismic anomalies: the Caribbean arc [Rost & Earle, 2010], the west coast of Central America [Weber & Körnig, 1990, 1992; Niu & Wen, 2001; Sun et al., 2007b; Hutko et al., 2009; Ford et al., 2012], the northern coast of South America [Miller & Niu, 2008; Rost & Earle, 2010], the Galapagos [Vanacore & Niu, 2011], the east coast of Greenland [Weber & Davis, 1990], the middle [Rost & Earle, 2010; Thorne et al., 2013a] and north-east of the Pacific LLSVP [Liu et al., 2011], the south coast of West Africa, and all of South Africa [Wen, 2000; Song et al., 2010; Rost & Earle, 2010; Frost et al., 2013]. These regions appear to be either areas related to subduction or close to the edges of the LLSVPs, a relationship which is analysed quantitatively in Chapter 3.9. Regions in which scattering is concentrated and dominantly above the CMB could be indicative of mantle flow collecting heterogeneities in certain locations and producing piles of chemical anomalies which overlie and support each other. This will be discussed further in Chapter 3.10.

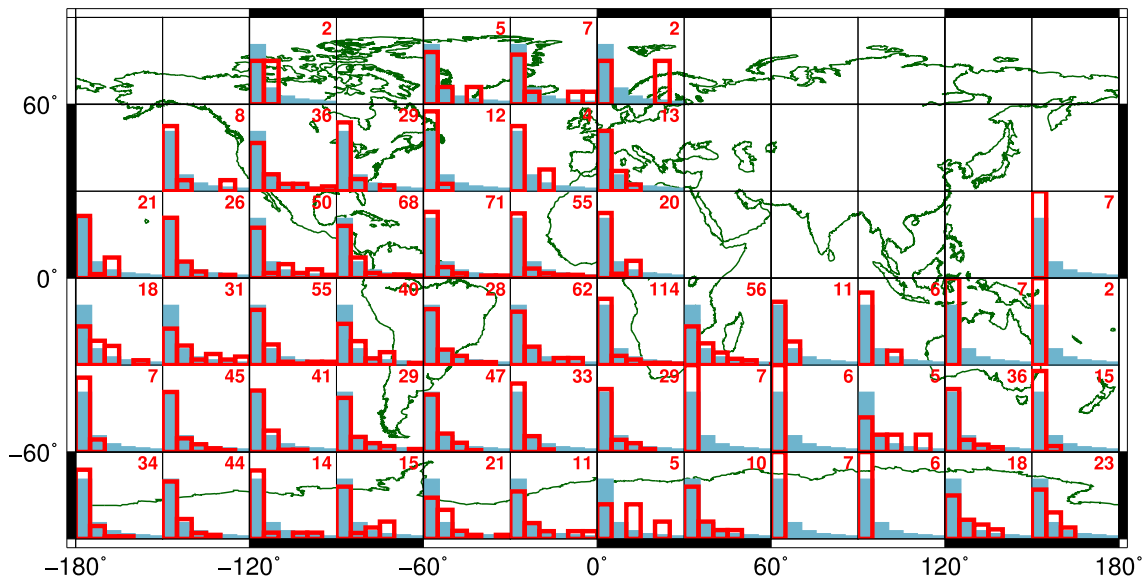


Figure 3.10: Distribution of scattering heights in  $30^\circ \times 30^\circ$  cells (red) compared with the global scattering frequency (blue). The number of scattering points in the cell used to calculate the red histogram is shown red. Cells without any scattering points are left empty. Histograms are calculated from the CMB to 300 km above in 50 km width bins (x-axis), and displayed in frequency per cent (y-axis) from 0 to 100 per cent. Regions such as the west coast of Central America, the north coast of South America, South Africa, and Antarctica show considerably more scatterers at greater heights above the CMB than the global distribution while regions such as Australia, North Africa, and Europe tend to show more scatterers are lower heights, relative to the global distribution.

Although the number of scattering heterogeneities within a certain region may be indicative of the degree to which chemical heterogeneities are concentrated in it, a better measure may be the ratio between the number of heterogeneities located in a cell and the number of times that cell is sampled and could show scattering (Figure 3.11) (sampling is discussed in Chapter 3.4). The Americas and the Atlantic show very good coverage but relatively few scatterers, except for the southern tip of South America which shows more scattering that is close to the CMB. This agrees with another study which shows scattering in a similar area [Rost & Earle, 2010] derived from an independent dataset. South Africa and the region off the eastern coast of South Africa demonstrate low sampling but also relatively many scatterers at greater heights. This region correlates well with other lowermost mantle studies in similar areas using different datasets and probes [Wen, 2000; Song *et al.*, 2010; Frost *et al.*, 2013]. Scattering is also relatively prevalent under southern Australia. Scattering in this area is close to the CMB. In this area it is likely that few scattering points are made more prominent by the very low sampling. This is also especially true of the region under the Mediterranean. Generally, although the ratio is effective at highlighting some scattering regions, in others it only demonstrates how little a region is sampled.

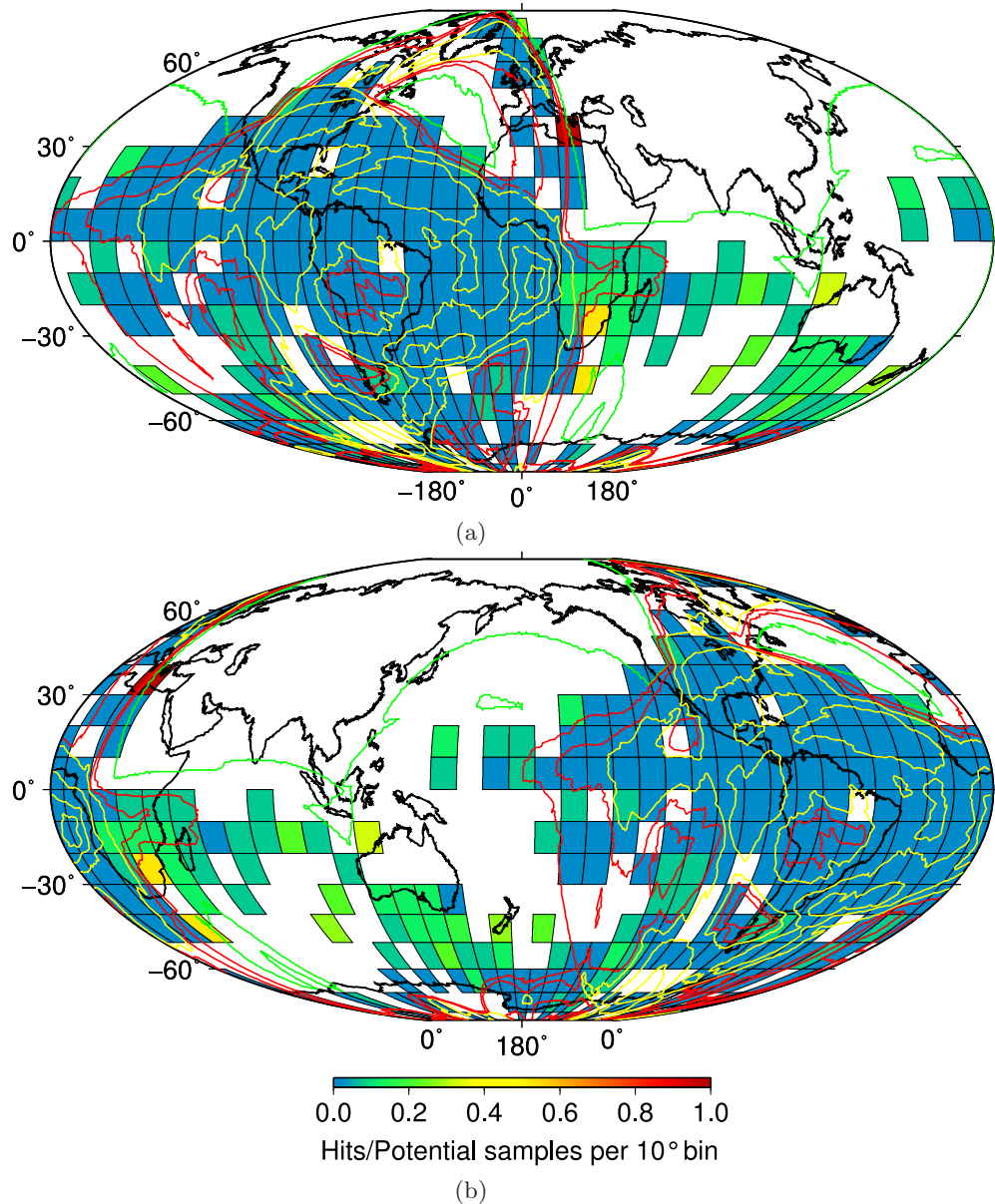


Figure 3.11: Number of scattering points located in each  $10^\circ \times 10^\circ$  cells normalised by the number of times that cell is sampled and could show scattering (from Figure 3.6), centred at (a)  $0^\circ$  and (b)  $180^\circ$  longitude. The extent of the coverage, the zero-sampling contour, is shown by the green line while yellow and red contours show potential sampling at 150 and 50 count intervals, respectively. Most regions show low hit/sampling ratios due to the high level of sampling. However, South Africa, southern Australia, and southern South America are notable exceptions where more hits are recorded per potential sample than the global average.

It is interesting to note that there are few areas that are sampled by more than about 150 source-receiver pairs (first and largest yellow contour in Figure 3.11) and do not show some scattering. This implies that scattering is prevalent almost globally, but is either a rare occurrence or is rarely strong enough to be detected since generally these areas are characterised by low sampling-to-scattering ratios. This is supported by other near-global studies of lower mantle scattering that report low levels of scattering heterogeneities world-wide with some localised patches of stronger scattering [Hedlin *et al.*, 1997; Hedlin & Shearer, 2000; Mancinelli & Shearer, 2013].

Precursors to  $PKP_{df}$  (discussed in Chapter 2) in the frequency range of 1 to 2 Hz are observed to result from scattering by heterogeneities  $\sim 10$  km in size at heights up to  $\sim 100$  km above the CMB, and mostly  $\sim 80$  km above the CMB under South Africa (Figure 2.22). Other studies also demonstrate PKP scattering from a similar region [Wen, 2000; Hedlin & Shearer, 2000]. The  $PK\bullet KP$  probe can be used to sample the same region of the lower mantle and also shows evidence of concentrated scattering heterogeneities at heights up to 320 km above the CMB, but mainly up to  $\sim 110$  km above the CMB (Figure 3.9). The PKP study has limited areal coverage but much greater sampling of this region of the CMB due to using densely located sources (Figure 2.6) whereas the  $PK\bullet KP$  study has much greater areal coverage due to the wider range of source locations (Figure 3.5) but has generally poorer sampling. The heights of scattering heterogeneities resolved by the two probes are very similar (Figure 3.12). Although the exact locations differ slightly, the pattern of a small area of tall scattering reaching heights up to 150 km, surrounded by much lower scattering is visually consistent throughout both studies, although further quantitative comparison would be preferable to fully confirm this correlation. The densely sampled PKP data resolve a ridge trending east-north-east west-south-west (Figure 3.12a). The more sparsely sampled  $PK\bullet KP$  data also resolve a tall structure with a similar trend (Figure 3.12b). The level of agreement of these two studies is indicative of strong structure in the region.

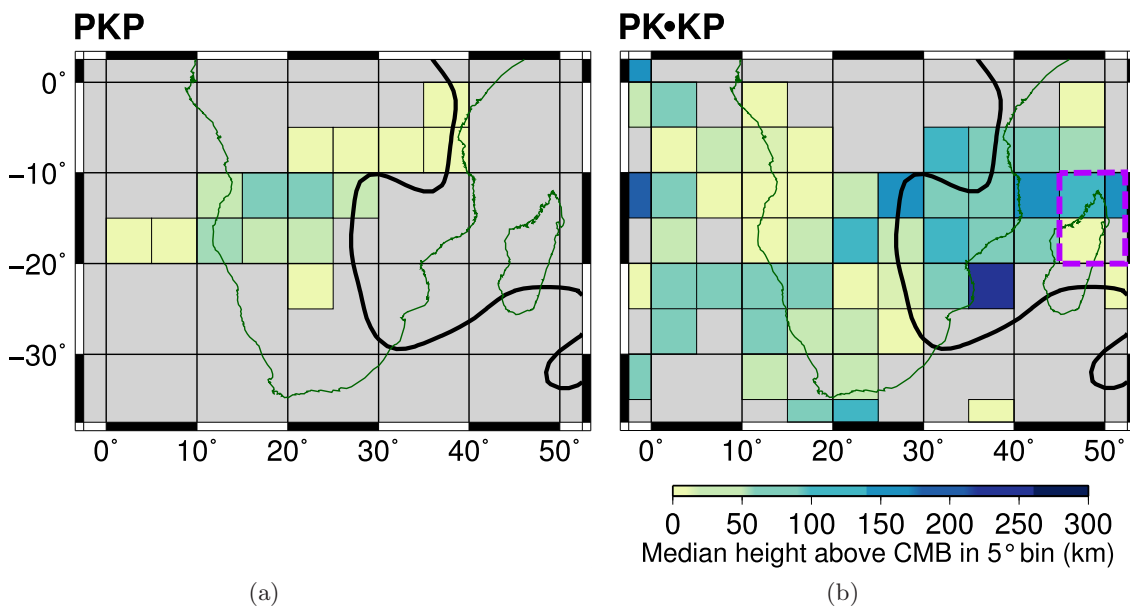


Figure 3.12: Scattering points under South Africa shown as median height in each  $5^\circ \times 5^\circ$  cell. (a) Scattering heterogeneities resolved by precursors to PKP from events in South Africa recorded at YK. (b) Scattering heterogeneities resolved by  $PK\bullet KP$  from globally distributed events recorded at various IMS arrays. The edge of the African LLSVP defined by the  $-0.4\%$   $V_S$  contour from S40RTS [Ritsema et al., 2011] is shown by the solid black line. Scattering heights and locations resolved by both PKP and  $PK\bullet KP$  are similar in this region with a ridge of high scattering heights running roughly east-north-east west-south-west with lower scattering around.  $PK\bullet KP$  energy is detected in the same region as high amplitude precursors to  $PKP_{df}$  under the Comoros hotspot (dashed purple line) [Wen, 2000].

In Chapter 2.6 it is noted that as PKP scattering points are not observed at the CMB

on the north-western side of the ridge it may continue further in this direction. The PK•KP results are also unable to resolve the extent of the ridge in the north-west as the ray paths are again limited by the b-caustic. However, the PK•KP scattering is observed much further to the north-east, east, and south-west of the ridge than seen by PKP, thus the ridge is possibly longer than the  $\sim 1200$  km stated in Chapter 2.6 and *Frost et al.* [2013]. Scattering on the southern and south-eastern edges of the ridge is constrained to the CMB by both the PKP and PK•KP studies. Further east of the ridge, in a region not resolved by PKP, frequent scattering is consistently observed at about 100 km above the CMB. This has previously been reported as showing strong PKP<sub>df</sub> precursors recorded at single stations generated by scattering from the Comoros hotspot [*Wen, 2000*] (purple region in Figure 3.12). The consistency between the results in all these studies implies that they are robust observations and that the small scale structure of the lower mantle beneath South Africa is highly anomalous.

The discrepancies between the two studies are related to the different data, and processing techniques and their respective levels of error and uncertainty. The PKP study uses only data recorded at YK while the PK•KP data in this area consists of roughly half traces recorded at YK and half from other stations. Although the PK•KP data recorded at YK matches the PKP data best, there is still agreement between the PK•KP data recorded at other arrays. Source location error ellipses for PKP data are, on average, 13.7 km long and 8.5 km wide, and for PK•KP data are both 3.1 km wide and long. Thus, the sources used in the PK•KP study are better constrained laterally than the PKP sources. However, depth errors for the PK•KP data, when reported, are  $\pm 7.3$  km, whereas for PKP I assume a surface depth given the association of these events with deep gold mines. Source depth is an important parameter for accurately determining depth of scattering. PKP sources are, therefore, better constrained in depth than the PK•KP sources, likely meaning that the scattering depths reported in the PKP study are more reliable. Lateral and vertical errors resulting from processing errors are comparable between these two studies, around  $\pm 2^\circ$  laterally and  $\pm 25$  km in depth for PKP (calculated in Chapter 2.7) and  $\pm 2.5^\circ$  and  $\pm 30$  km for PK•KP, dependent on the array used (calculated in Chapter 3.7). Therefore, although the exact locations of the scattering heterogeneities resolved in the two studies are not identical, the uncertainties are low enough that the general patterns in scattering location and height are comparable.

In general, scattering in the lower mantle is strongly heterogeneous with scattering points found between the CMB and up to 320 km above the CMB. Heterogeneities also show strong spatial patterns with clustering in certain areas, sometimes contrary to the level of sampling by the PK•KP probe. Many areas in which scattering is prevalent contain scatterers at a range of heights, seemingly forming a pile which may imply some support or viscous entrainment by the mantle convection cycle. This is supported by the spatial correlation (at least visually) between regions of concentrated scattering or high scattering heights and the LLSVPs or areas known to be associated with subduction. This relationship is investigated further in Chapter 3.9.

### 3.7 Directivity Error Testing

To determine the accuracy of the scattering heterogeneity locations calculated by ray-tracing, I use synthetic waves designed to be typical of the real signals in the dataset and apply the same processing steps as for the real data. I calculate errors for each array individually as the ambient noise field and signal resolution is dependent on array location, size, and configuration (discussed in Chapter 1.4.5). For each array, I create synthetic PK•KP signals with known slownesses, back-azimuths, and arrival-times, to which I add real noise traces at the SNR typical of the array, and apply the fk F-statistic. Slowness, back-azimuth and time residuals associated with each synthetic signal from each test direction are calculated. These errors are then added to the input parameters (slowness, back-azimuth, and travel-time) of a test signal typical of a known PK•KP scattering point, which is then ray-traced. The location errors resulting from these measured errors are characteristic of signals arriving from different directions recorded at a given array.

To characterise the noise levels at each array I measure the Signal-to-Noise Ratio (SNR) of observed PK•KP signals. For events in which scattered signals are previously detected using the fk F-statistic, for each individual (unbeamed) trace of the array, I measure the SNR of each scattered PK•KP signal compared to pre-event noise (after the origin but before the P arrival), and also compared to noise typical of the PK•KP time window (ensuring that no scattered signals are measured as noise). I then calculate the mean PK•KP SNR for the event across all traces. Using the mean values from all events I calculate the median SNR for the array. The median is used as the mean values are easily skewed by outliers with unreasonably high SNRs. I repeat this for all events for each array. To ensure that I am calculating the PK•KP SNR typical of the ambient noise at the array, events where there is a possibility of contamination of signals, for example, by aftershocks, which could disturb the wavefield, are disregarded. The SNR calculated with the PK•KP time window noise is used for further processing as this is representative of the noise field from which the fk F-statistic must extract the scattering signal.

The calculated SNR values are very low, often between 1 to 1.2 with some outliers (Figure 3.13 and Table 3.1). This exemplifies how weak the PK•KP signal is and why arrays are necessary to effectively analyse these waves. These SNR values are independent of the array configuration and only represent the noise field at each array.

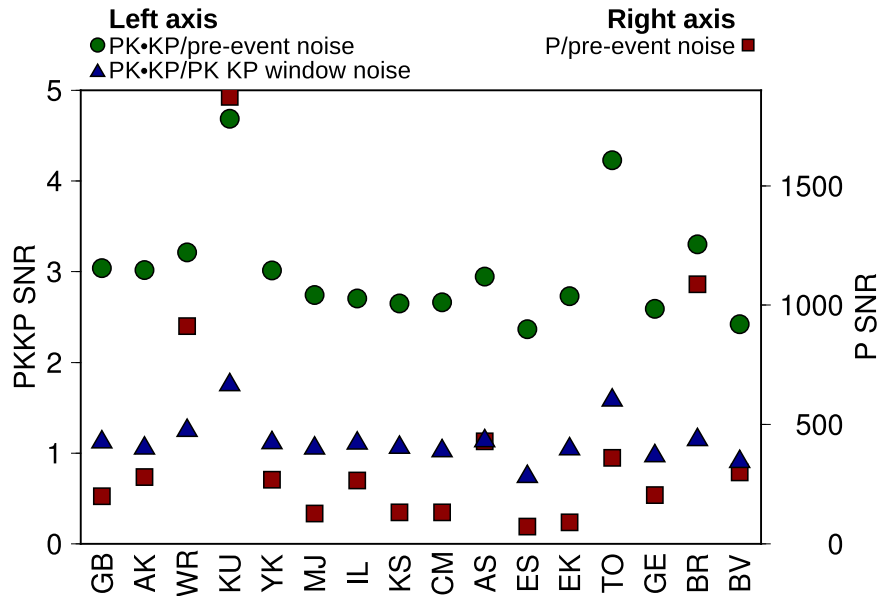


Figure 3.13: Characteristics SNRs of the arrays used. Median SNRs calculated per trace (unbeamed) as: PK•KP signal against pre-event noise (green circles), PK•KP signal against PK•KP time window noise (blue triangles), and P wave against pre-event noise (red squares). PK•KP ratios are measured on the left axis and the P wave ratio is measured on the right axis. For each array, noise levels correlate between different signals. This consistency demonstrates that the SNR values are indicative of the noise at the array rather than the magnitudes of the events used to calculate the SNR, which differs for each array. The ratio of the PK•KP signal against PK•KP time window noise is used in subsequent calculations. Noise levels are independent of array size.

Table 3.1: Noise characteristics for the IMS arrays used. All values stated are the median ratios calculated for all events that show PK•KP scattering and are not contaminated by other signals.

Code	P/pre noise	PK•KP/pre noise	PK•KP/PK•KP noise
GB	199.3	3.04	1.12
AK	279.4	3.02	1.05
WR	911.7	3.21	1.25
KU	1872.8	4.68	1.75
YK	269.1	3.02	1.11
MJ	127.0	2.74	1.05
IL	264.8	2.71	1.11
KS	132.5	2.65	1.06
CM	131.6	2.66	1.02
AS	429.6	2.95	1.14
ES	72.9	2.37	0.74
EK	89.4	2.73	1.04
TO	359.8	4.23	1.58
GE	204.9	2.59	0.97
BR	1087.8	3.30	1.15
BV	298.5	2.42	0.91

These SNR values are used to simulate PK•KP waves typical of those observed at each array. For each array, real noise at each station in the array is sampled for an event clear of any coherent signals. Although variation of the noise field across the array is

likely to be fairly small, it is most realistic to use the actual noise from each station. As real PK•KP signals are so small relative to the noise (Figure 3.13) it is not possible to analyse the real scattered wavelet shape. Therefore, a 2.5 s long, 1 Hz, cosine tapered sine wave is used as the synthetic signal. This wavelet was seen to match the shape of the scattered precursors in the PKP study (shown in Chapter 2.7.1) and so is assumed to be appropriate to simulate PK•KP. The synthetic wavelet is delayed by times characteristic of the moveouts (see Figure 1.13) related to the slownesses and back-azimuths from which PK•KP can arrive. Slowness is varied between 2.0 and 4.0 s/deg in 0.5 s/deg increments and back-azimuth is varied between 0 and 325° in 45° increments. The real array noise is applied to the delayed wavelets at the SNR calculated for that array. These noisy synthetic signals are processed with the sliding-window fk F-statistic using the same time window, time step, and filter parameters as in Chapter 3.5. The best fitting back-azimuth, slowness, and arrival-time are then picked i.e. the direction that gives the highest F-value.

The slowness and back-azimuth residuals (the difference between the synthetic signal input and the calculated output) recorded at an array vary in magnitude and direction both between different synthetic input directions and also between arrays (Figure 3.14). These differences are related to the local noise field and the Array Response Function of each array (see Chapter 3.5 and see Figures in Appendix A) and, therefore, the array aperture, number of stations, and configuration. Considering all arrays, time errors are commonly zero, and rarely as large as  $\pm 1$  s. Time errors appear to be independent of array aperture, number of stations, and configuration. Directivity errors for the larger arrays are generally small with back-azimuth and slowness errors of  $< 2^\circ$  and  $< 0.4$  s/deg, respectively (Figures 3.15a and 3.15b). However, for smaller arrays, such as BR and BV, directivity errors are much larger,  $> 30^\circ$  and 1.2 s/deg. There appears to be a trade-off between SNR and both array aperture and number of stations whereby a noisy array of a similar size with many stations can have lower directivity errors than a less noisy array with fewer stations; for example, ES (noisy, 28 stations, small directivity errors) compared with EK (quiet, 20 stations, larger directivity errors) (Figures 3.13 and 3.15). Arrays comprising clusters or rings of stations are more accurate at determining directivity information than cross-shaped arrays of comparable size, such as AK (ellipse shaped) compared with KU (cross-shaped), and IL (rings) compared with EK (cross-shaped), most likely due to less spatial aliasing. Large directivity errors typical of smaller array apertures can apparently be compensated for by using more stations; for example BV (few stations, large errors) and GE (similar aperture, many stations, lower errors). Despite its relatively large aperture, high number of stations, and relatively low noise levels, AS behaves anomalously resulting in large directivity errors. This may be related to the character of the noise at this array compared to others. The power spectrum of typical noise traces at AS is considerably different from that at the other arrays with peaks within the 2-3 and 8-9 Hz bands, in addition to the broad range of noise below  $\sim 1.5$  Hz seen at most other arrays. However, as the arrays in the dataset have multiple varying factors (e.g. the size, number of stations, configuration, and local noise field) it is difficult to determine the degree of control each aspect has on the array's ability to resolve incoming energy. Following this analysis, I conclude that the arrays worst at accurately extracting a PK•KP signal from the local noise are: BV, BR, GE, and AS. All other arrays perform well at identifying the signal

and its incoming direction.

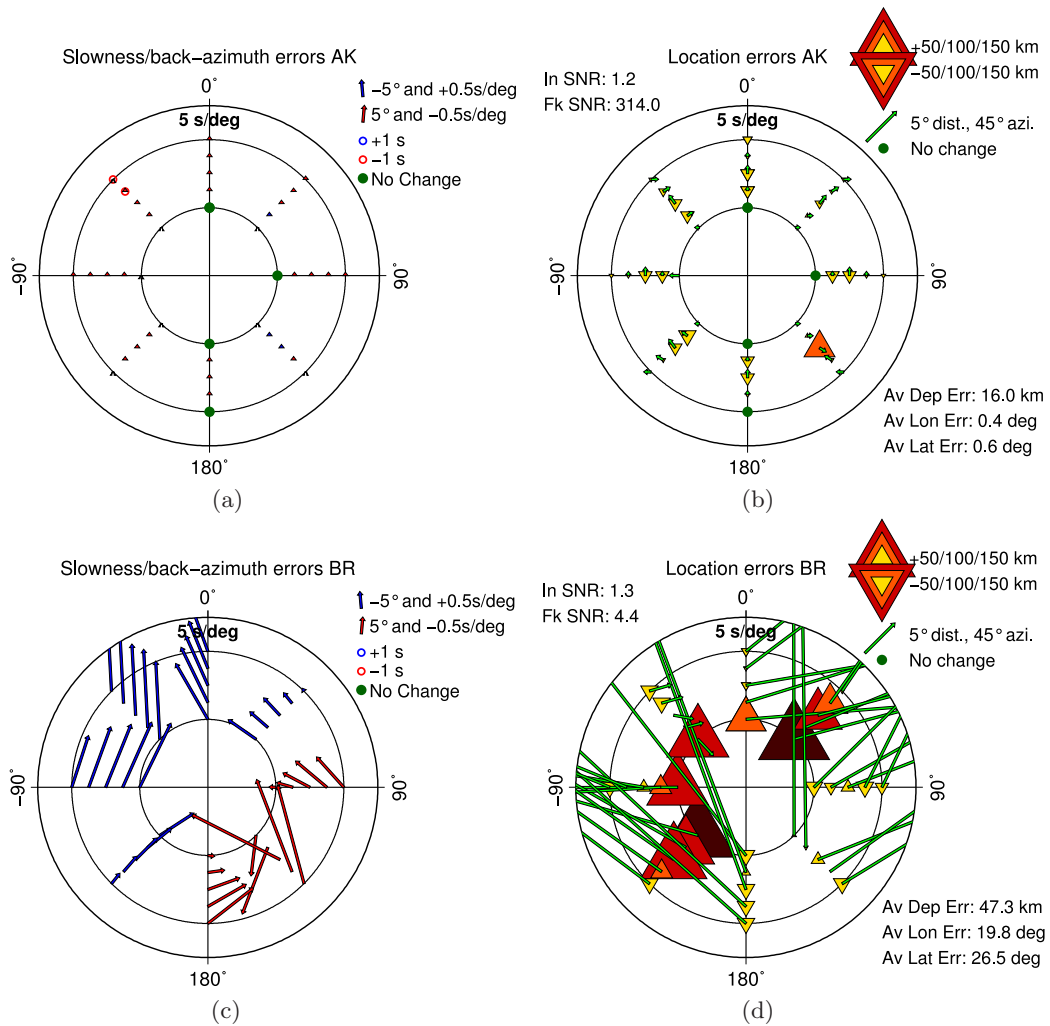


Figure 3.14: Array specific errors of signal direction and ray-traced locations for arrays AK (a and b) and BR (c and d) for a range of input directions. (a and c) Errors in directivity values measured using the  $f_k$  F-statistic are shown at the input slowness and back-azimuth of the synthetic signal as deviations in back-azimuth measured from north (to indicate back-azimuth error) and arrow length (to indicate slowness error). Time errors are shown as coloured circles. (b and d) Scattering point mislocations resulting from ray-tracing shown at the input slowness and back-azimuth of the synthetic signal displayed in terms of direction and distance (green arrow angle and length) and depth (triangles). Triangles and inverted triangles indicate that the scattering point is moved shallower and deeper, respectively, by the directivity error. Measured slowness and back-azimuth errors and subsequent ray-traced mislocations are much larger at BR than AK, likely due to the smaller aperture and fewer stations at BR. Errors at AK are generally low except for the synthetic signal arriving with slowness of 3.0 s/deg and back-azimuth of  $135^\circ$ , respectively. For errors at other arrays see Figures in Appendix C.3.1.

The effect of these typical directivity errors on the ray-tracing process is then measured. A test point is created by ray-tracing along a specified back-azimuth to a specified depth (2849 km for all directions) and the slowness and PK•KP travel-time calculated for a scatterer at this position is recorded. These slowness, back-azimuth, and travel-time values are then perturbed by each of the combinations of slowness, back-azimuth, and

time residuals measured with the fk F-statistic for the different input directions. Given this modified directivity information the ray-tracer then fits a new scattering point. The amount by which the output scatterer location differs in latitude, longitude, and depth from the test location, the mislocation, is measured. This process calculates the amount by which the scattering location may change for typical directivity and time residuals calculated by the fk F-statistic when using real noise applied to signals that simulate PK•KP in terms of SNR and input direction.

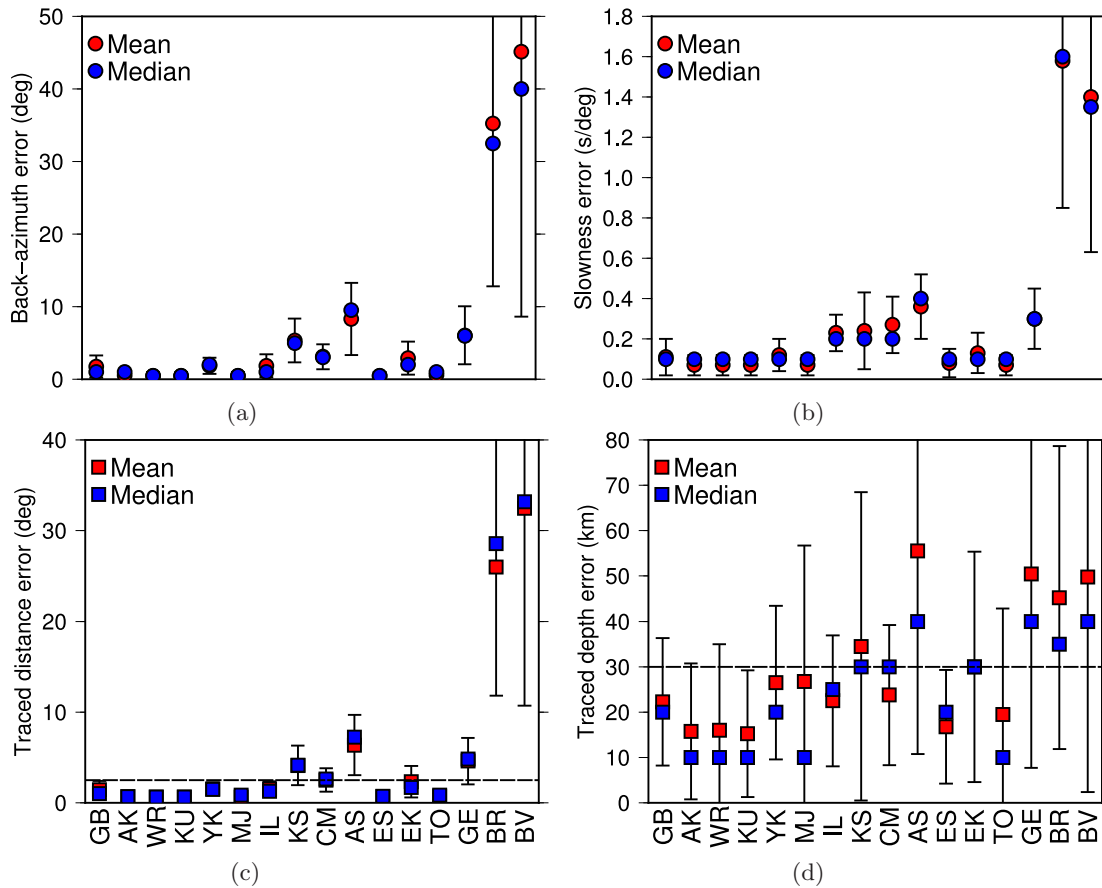


Figure 3.15: Magnitude of errors of directivity values measured using the fk F-statistic (a and b) and the scattering point mislocations resulting from ray-tracing (c and d) for each array. Values are displayed as the mean (red) with 1-standard deviation error bars and the median (blue), the latter is considered more robust. Arrays are ordered by decreasing aperture from left to right. Measured (a) back-azimuth and (b) slowness errors for synthetic signals from a range of incoming directions with noise and noise levels typical of the array using values shown in Figure 3.13. Errors are dependent on incoming noise levels and the array configuration. (c) Lateral and (d) vertical mislocations for a typical scattering point ray-traced with the slowness and back-azimuth errors determined for that array. As depth changes can be positive or negative, the modulus is used to calculate the average error. Slowness errors primarily control depth mislocations and a combination of back-azimuth and slowness errors control lateral mislocations. Dashed horizontal lines indicate distance and depth errors of  $2.5^\circ$  and 30 km, respectively. Synthetic signals with slownesses of 2.0 s/deg are often poorly fit and result in large errors in depth as it is not possible for a PK path to have this slowness. For average and median mislocations where input slownesses of 2.0 s/deg are ignored see Appendix Figure C.18.

Applying the slowness, back-azimuth, and time residuals relative to the ray-tracer

input, determined for each array using the fk F-statistic, the likely scattering point mislocations for that array are calculated (Figures 3.15c and 3.15d). Lateral mislocations are generally small (less than  $\pm 2.5^\circ$ ) at all arrays except BR and BV where mislocations are relatively large ( $> \pm 25^\circ$ ). Depth mislocations are smallest for the denser arrays such as AK, GB, WR, KU, ES, TO, and MJ, and largest for the smaller arrays with fewer stations, for example, BV, BR, and GE. The majority of arrays have depths errors less than  $\pm 30$  km. Some arrays with generally low mislocations have larger mislocations for certain directions (Figure 3.14 and Figures in Appendix C.3.1). For example, the majority of the depth errors at AK are less than 30 km but for a signal arriving with slowness 3.0 s/deg and back-azimuth  $135^\circ$  the ray-tracer computes a depth error of 70 km, despite the small slowness, back-azimuth, and time errors used in ray-tracing. This will be discussed in later paragraphs. Overall, scattering point mislocations are too small to significantly affect the results and recognition of spatial patterns, except for BR and BV. However, these arrays contribute only 20 scattering points to the final dataset and so have negligible influence on the distribution of scattering (for scattering results without data from BV and BR see Appendix Figure C.3).

Contributions from the measured slowness, back-azimuth, and time errors affect the ray-traced location differently. Slowness errors primarily affect the depth of the scattering point. Positive residuals, where the fk F-statistic resolves a slowness higher than the synthetic input, result in shallower scattering locations, and negative residuals result in deeper scattering locations. The back-azimuth residual controls the lateral location of the scattering point. When the back-azimuth residual is zero and the slowness residual is non-zero, the scattering point will only mislocate along the great-circle path. However, when both the back-azimuth and slowness residuals are non-zero the scattering point will move both laterally and in depth. For non-zero back-azimuth residuals and zero slowness residuals the scattering point may change vertically as well as laterally to account for the change in path length for the same PK•KP travel-time. Travel-time errors of the magnitude used here have minimal control on scattering point mislocation.

The magnitude of the input slowness and back-azimuth errors is related to the magnitude of the resulting change in ray-traced location. However, ray-tracing of some input directions (in terms of the slowness and back-azimuth of the synthetic signal) is particularly sensitive to change and small directivity residuals can result in relatively large scattering point mislocations. For example, for an input slowness of 3.0 s/deg, small directivity residuals, when ray-traced, move the scattering point by a greater distance than the same residual for a different input slowness. This is likely due to the nature of the PK (or KP) path, as slowness does not change linearly with distance and depth and, therefore, some slownesses are less common than others (Figure 3.8). Depth errors are large for an input slowness of 2.0 s/deg. This slowness cannot be successfully fit as the minimum KP slowness is 2.1 s/deg. If an input slowness of 2.0 s/deg is precisely resolved by the fk F-statistic then the ray-tracer will likely mislocate the scattering point. Positive depth mislocations, i.e. the scattering point moving deeper, are limited by the CMB to a maximum of 40 km (given that the unperturbed scattering point is at 2849 km depth, 40 km above the CMB).

The resulting location errors are only an estimation of the true errors of the process.

In order to measure the change in scattering location a standard set of slowness, back-azimuth, and time parameters is required that can then be perturbed; this is the test scattering point at a set depth. However, given the range of slownesses used (2.0 to 4.0 s/deg), this scattering location may not always be appropriate (Figure 3.8). This is accounted for by changing the source-receiver distance and back-azimuth to maximise the range of slownesses available around the input slowness. The ray-tracer is then more likely able to produce appropriate slownesses. Real signals observed in the data will follow ray-theory while synthetic signals are not inherently bound by this, as they comprise two separate paths added together rather than a single continuous path, and so these further controls are necessary. Despite these limitations, the ray-tracing process provides some useful constraints on the reliability of the ray-traced locations.

Synthetic signals with real noise at the SNR typical of each array are used to determine how well the fk F-statistic can resolve the slowness, back-azimuth, and arrival time of signals arriving from different directions. These directivity residuals are then used to calculate the size of the change in scatterer location, the mislocation, typical of a given incoming direction at a given array. Scattering points for all arrays except BV, BR, AS, and GE, for most input directions can be located to within  $\pm 30$  km depth and  $2.5^\circ$  laterally (horizontal dashed lines in Figures 3.15c and 3.15d), equivalent to a region  $\sim 300$  km wide at the CMB. This region is just larger than that determined for errors associated with PKP scattering (calculated in Chapter 2.5.2). While scattering points from BV and BR are likely poorly located and should be ignored (shown in Appendix Figure C.3), scattering points for the most arrays are accurately located.

### 3.8 PK•KP Frequency Analysis

As discussed in Chapter 1.3, waves are scattered by heterogeneities of a similar size to dominant wavelength. By assessing the seismic wavefield at a range of frequencies, the bands in which PK•KP scattered energy is most prevalent will suggest the dominant sizes of the scattering heterogeneities. The prior analysis of PK•KP uses IMS arrays that are predominantly short-period instruments optimally configured to detect the 1 Hz waves associated with nuclear explosions [Mykkeltveit *et al.*, 1983]. The filtering applied also best brings out 1-2 Hz waves which are indicative of scattering from anomalies with scale-length  $\sim 10$  km. However, this isn't necessarily the only size of mantle heterogeneity that exists, as is evident in global stacks [Hedlin & Shearer, 2000; Mancinelli & Shearer, 2013], local studies [Wu & Aki, 1988], and mantle dynamic models [McNamara *et al.*, 2010; Tackley, 2011]. The spectrum of mantle anomaly sizes and dominant scale-length will elucidate mixing processes and, potentially, the source of the scatterers. For example, a range of heterogeneity sizes from 10s km down to single km could imply progressive slab break-up, or else chaotic mixing and interaction between the lower mantle and core.

Analysis of PK•KP energy using arrays gives a localised image of the scattering heterogeneities as the technique selects energy only from certain directions. Using envelopes from single stations includes the whole of the wavefield recorded at that station and so displays the global character of the scattered signal. I assess the spectrum of PK•KP waves using the Global Seismic Network (GSN). I collect data for all events over magnitude 6.0 recorded from 01/01/2004 to 31/12/2010 at all stations within  $60^\circ$  of the source.

Despite these stations being 3-component broadbands, I use only the vertical component, given the steep incidence angle of PK•KP waves. I initially apply a Butterworth bandpass filter between 0.3 and 4 Hz, order 2, and then remove traces that appear faulty. Taking the original unfiltered traces, I discard those identified in the filtered traces as faulty, leaving only working, unfiltered traces. Traces are then aligned on their respective origin time, enveloped to account for phase differences, and stacked linearly. This results in a diffuse P-wave arrival as source-receiver distance is not corrected for, however, PK•KP will sum constructively due to the arrival time not being dependent on distance (Figure 3.1e) [Chang & Cleary, 1981]. I then repeat the stacking procedure for a series of filter frequencies in octaves. I apply the bandpass filter, take the envelope, then stack the traces and take the logarithm of the amplitude to emphasise the lower amplitude PK•KP signal. Comparison of the amplitude of the PK•KP energy in these final filtered, stacked traces indicates the dominant frequency range of scattering globally, or as far as is allowed by the global distribution of sources and receivers.

When analysing the stacks on a year-by-year basis, for some years I find energy arriving within the PK•KP time window. However, in other years there is no clear signal within the PK•KP time window. This suggests that the scattering signal depends strongly on sources and receivers used, and perhaps also low noise levels, and so the causative heterogeneities are spatially variable. When all years are stacked together the PK•KP signals previously observed in the single year data are obscured, possibly being “stacked out” by noise.

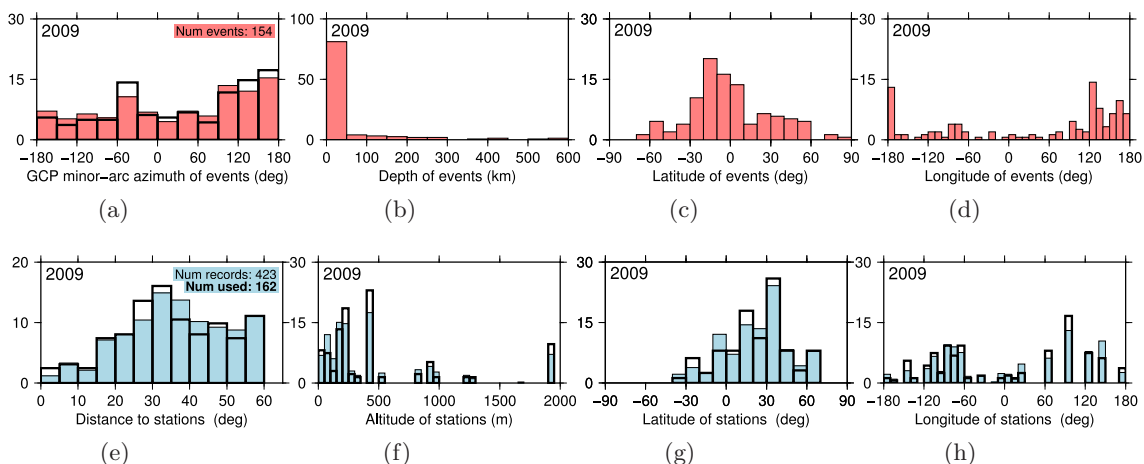


Figure 3.16: Parameters of events and stations from the 2009 GSN data used for measuring PK•KP signal frequency. All histograms are plotted in frequency per cent. Event (a) major-arc back-azimuth from station to source, (b) depth, (c) latitude, and (d) longitude. Station (e) distance from source, (f) altitude, (g) latitude, and (h) longitude. Details for all events for the year are shown by the coloured histograms while the data selected to contain PK•KP signals are shown by the black histograms. The locations of sources and receivers used does not dramatically change between the two set but the number of traces used decreases from 423 to 162.

To maximise the clarity of the PK•KP signal I choose two years in which the scattered energy is most obvious and analyse the traces again only selecting those that clearly show energy arriving in the PK•KP time window. This imposes a strong bias and means that the resulting stacks are no longer global representations of the scattering structure. I

consider how locations of the sources and receivers used change between the first stack and the second more selective stack, a systematic change which might suggest regional scattering structure (Figure 3.16). However, there is no obvious pattern in the differences but the reduction in the number of traces used to create the stack is significant. This implies that the PK•KP signal is very weak and liable to being obscured by noise in other traces. PK•KP appears especially weak when compared with PKP scattered energy which is obvious in global stacks (Figure 1.4) [Hedlin *et al.*, 1997; Hedlin & Shearer, 2000; Mancinelli & Shearer, 2013].

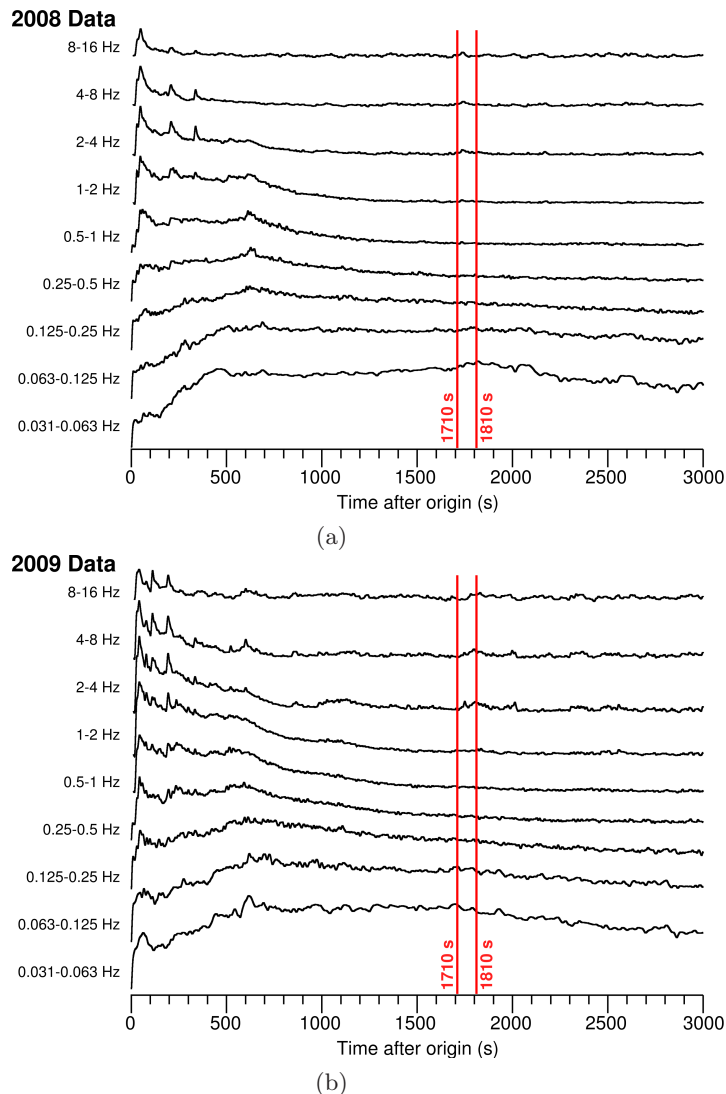


Figure 3.17: Envelopes of stacked traces collected from GSN stations, bandpass filtered (order 2) between a range of frequencies in octaves for data from (a) 2008 and (b) 2009. These years show scattered energy most clearly. Data are picked to remove faulty channels and then picked to include only events that show energy arriving in the lower mantle PK•KP time window (red lines). These traces are then bandpass filtered between the frequency limits shown, enveloped, and stacked and then the logarithm is taken to emphasise the lower amplitude signals. Scattered energy is strongest in the 2-4 Hz frequency band, but is seen at all frequencies greater than 1 Hz.

Energy is observed arriving in the PK•KP time window in envelopes created using traces filtered at frequencies of 1 Hz and higher (Figure 3.17). Although some energy is

seen in the 1-2 Hz frequency range (close to the frequency range used in the array analysis), the strongest signals arrive at the same time in the 2-4 and 4-8 Hz ranges. A signal is still visible in the 8-16 Hz frequency range although at this point it is little stronger than other peaks at different times which aren't observed in the lower frequency bands and might be noise. The lack of scattering at frequencies lower than  $\sim 1$  Hz (a process which is theoretically possible) suggests that coherent chemical anomalies of greater than  $\sim 10$  km do not exist, or do not have appropriate properties to cause scattering. Thermal anomalies may also cause scattering, but they would likely be larger than chemical heterogeneities, due to the rapid equilibration of small thermal anomalies in the mantle [Olson *et al.*, 1984], and so contribute to the lower frequency PK•KP signal. The PK•KP signal appears to increase in amplitude fairly rapidly, and then decay more slowly. Energy arriving later in the PK•KP time window is indicative of scattering higher up into the mantle, possibly indicating more prevalent scattering close to the CMB, as is observed in the array data (Figure 3.10).

The frequencies observed demonstrate scattering from heterogeneities of sizes between  $\sim 13$  km for 1 Hz energy and  $\sim 1$  km for 8 Hz energy, and dominantly  $\sim 6$  km for 2 Hz energy. Lower mantle heterogeneities of these sizes have been observed in previous scattering studies [Wen & Helmberger, 1998; Thomas *et al.*, 1999; Wen, 2000; Braña & Helffrich, 2004; Thomas *et al.*, 2009; Rost & Earle, 2010; Ivan & Cormier, 2011; Frost *et al.*, 2013]. These scales are suggestive of chemical heterogeneities due to the thermal diffusivity of the lower mantle meaning that purely thermal anomalies would dissipate rapidly compared to chemical anomalies [Turcotte & Schubert, 2002]. Turbulent mixing of the mantle is modelled to operate as a “cascade process” whereby a range of heterogeneities sizes are produced by the break up of large anomalies [Olson *et al.*, 1984]. The range of anomaly sizes observed may indicate break-up of larger chemical heterogeneities, or accumulation of smaller heterogeneities. For example, basaltic crust is typically on the order of 7 km in thickness and is found to have chemical and physical properties that are distinct from the ambient lower mantle when it is subducted [Hirose *et al.*, 1999, 2005; Kudo *et al.*, 2012]. Alternatively, reaction products from the interaction across the CMB between the core and the lowermost mantle [Mao *et al.*, 2006] may introduce small chemical heterogeneities which could be the cause of this scattering. Although the results of the frequency analysis are not conclusive in determining the cause of scattering in the lowermost mantle, they do suggest that only small scale products are involved.

### 3.9 Correlation With Large Scale Features

Small scale features within the lower mantle are often spatially associated with large scale structures. For example; ULVZs are frequently observed close to the margins of LLSVPs [McNamara *et al.*, 2010] and detections of small scale velocity increases, the D'' discontinuity, are almost exclusively outside of the LLSVPs, and often close to regions of subduction. Dynamic models demonstrate that subducted slabs can separate into smaller chemical heterogeneities in the lower mantle [Tackley, 2011; Li & McNamara, 2013] and dense material within the LLSVPs will be concentrated at the edges by internal convection [McNamara *et al.*, 2010]. I observe clustering of the located PK•KP scattering points in certain locations which may be related to other mantle structures (Figure 3.18). To

determine if small-scale mantle structures are related to, and therefore, possibly influenced by, larger scale anomalies, I compare the spatial distribution of scattering heterogeneities with tomographic models which I use as representations of the broad structure of the lowermost mantle.

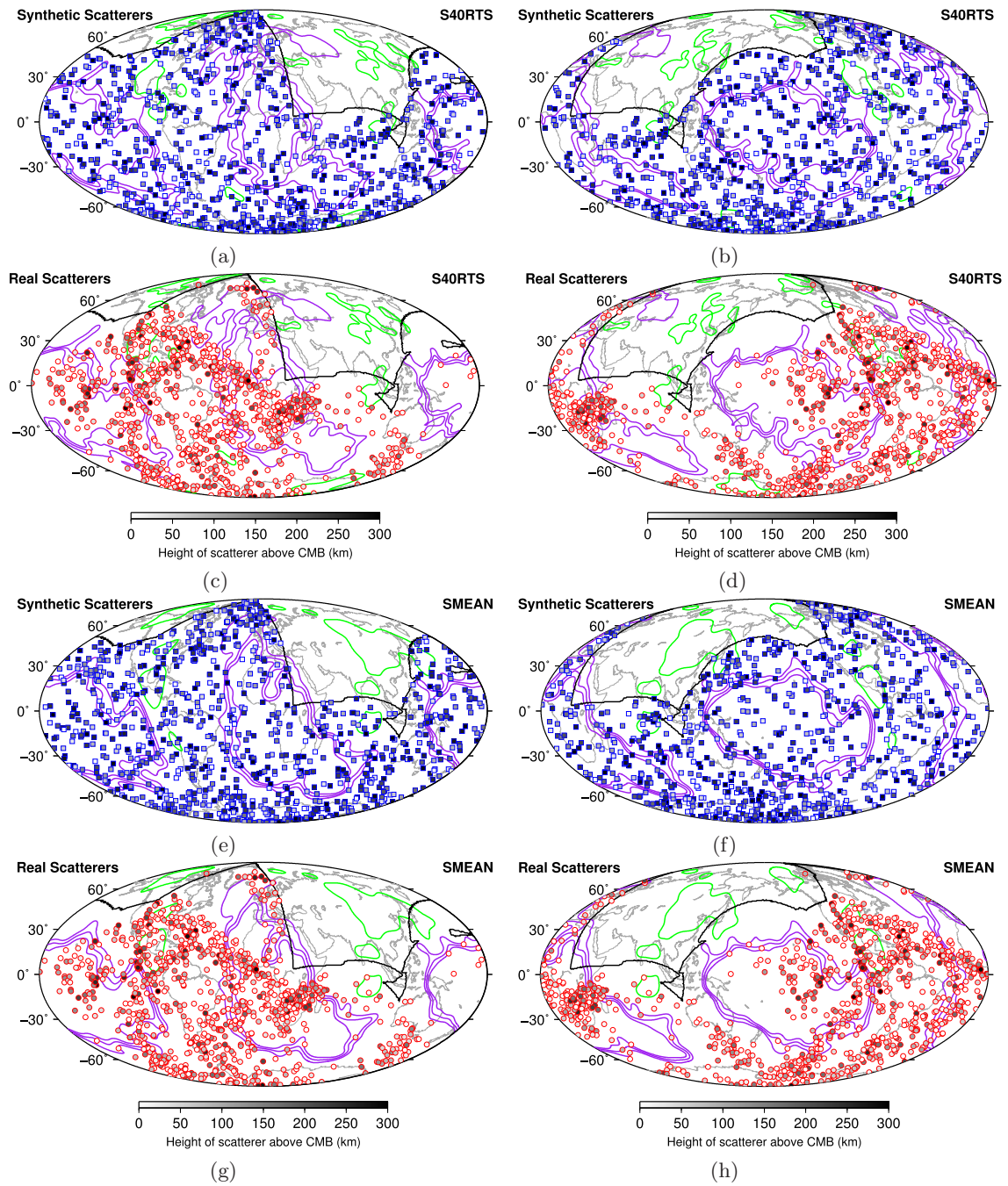


Figure 3.18: Scattering heterogeneities relative to tomography models *S40RTS* (a-d) and *SMEAN* (e-h) [Ritsema et al., 2011; Becker & Boschi, 2002]. Location and height of scattering points above the CMB compared with *S40RTS* for synthetic (a and b) and real (c and d) data. LLSVP iso-velocity contours (0.0, -0.4, and -0.8 %  $V_S$ ) and faster velocity contours (+0.9 %  $V_S$ ) at 2800 km from *S40RTS* [Ritsema et al., 2011] are shown as purple and green lines, respectively. Location and height of scattering points above the CMB compared with *SMEAN* for synthetic (e and f) and real (g and h) data. LLSVP iso-velocity contours (0.0, -0.4, and -0.8 %  $V_S$ ) and faster velocity contours (+1.3 %  $V_S$ ) at 2850 km from *SMEAN* [Becker & Boschi, 2002] are shown as purple and green lines, respectively. The limit of the sampling area (from Figure 3.6) is shown by the black line. Within the sampled region synthetic data is distributed randomly with uniform probability laterally and with height from the CMB to 300 km above. For larger figures see Appendix Figure C.19.

To test for correlation between scattering heterogeneities and large scale mantle structure I use S40RTS [Ritsema *et al.*, 2011] and SMEAN [Becker & Boschi, 2002] as examples of recent and stable S-wave tomography models, respectively, and measure the shortest distance from each scatterer to the edge of either slow or fast velocity structures in the lower mantle by testing each combination of scattering point and each node within the contour. I simplify the models into low velocity anomalies, the two LLSVPs, and high velocity anomalies, multiple smaller patches which are likely related to subducted slab material. On the basis that internal convection patterns within the LLSVPs may affect the location of volumetric heterogeneities and that subduction zones may supply anomalous material to the lower mantle [Li & McNamara, 2013], I choose to test distance from the outside and inside of the LLSVPs, and from the outside high velocity anomalies but not the inside as these are too small to show any internal pattern. Given the uncertainty in the exact edge of the LLSVP, multiple definitions are used for both models: the 0.0 %  $V_S$  iso-velocity contour, the -0.4 % contour, and the -0.8 % contour (Figure 3.19). The high velocity anomalies are defined by the +0.9 %  $V_S$  iso-velocity contour in S40RTS and the +1.3 %  $V_S$  contour in SMEAN. However, as the fast regions in both models are more diffuse and numerous than the slow regions I use only the more significant contours and those that best follow the subduction zone pattern as this is the structure for which I am testing. I then measure the minimum point-to-point distance of each scattering location from the nearest contour in the structure of interest. The height of the scatterer above the CMB is also considered in order to test if the dynamic processes which may be acting on the heterogeneities entrain them, and thus influence their vertical position in the mantle, as well as their lateral location. Therefore, I separate scatterers into different height bins to determine if lateral scatterer distribution varies systematically with height. When measuring distance from the inside of the LLSVP, scattering points outside the LLSVP are disregarded. Likewise, when measuring the distance away from the outside of the LLSVP, scattering points inside the LLSVP are disregarded. When measuring the distance from the fast regions, scatterers inside the fast region are counted as having a distance of 0° as proximity of these scattering points implies that they are related. When measuring relative to the fast regions, scatterers in the LLSVPs are not included, therefore, changing the LLSVP velocity contour (0.0 %, -0.4 %, or -0.8 %) affects the number of scattering points that are considered (larger LLSVP contours will include more scattering points which will then not be included in the measurements).

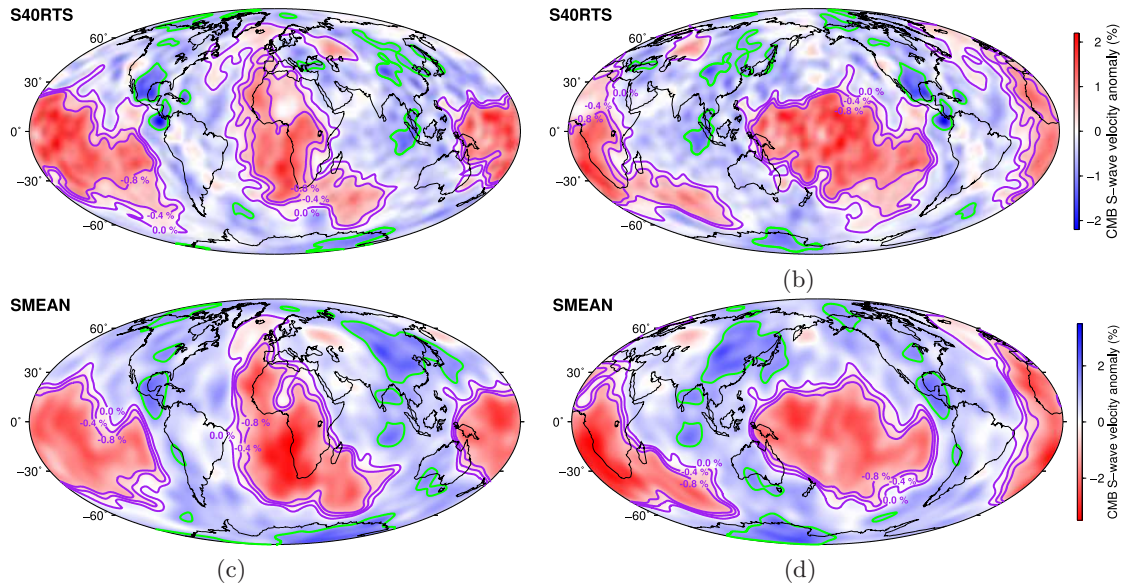


Figure 3.19: Tomography models overlaid with the contours used to represent the low and high velocity anomalies to which distances from scatterers are measured for (a and b) S40RTS and (c and d) SMEAN. Low velocity anomalies, LLSVPs, are defined by the 0.0, -0.4, and -0.8 %  $V_S$  iso-velocity contours for both models (purple lines) and high velocity anomalies are defined by the +0.9 and +1.3 %  $V_S$  contours for S40RTS and SMEAN, respectively (green lines). All contours are taken from the lowermost depth slice of each model: 2800 km for S40RTS and 2850 km SMEAN. For larger figures see Appendix Figure C.20.

I calculate the distribution of scattering points with distance from the slow and fast anomalies. The distance from the anomaly is calculated by minimising the distance on a sphere between a given scattering point and every node of all the contours that describe the anomaly. The distribution of distances is calculated cumulatively as the number of heterogeneities within a particular distance range is of importance, rather than the number of heterogeneities at a specific distance. Patterns of preferential location are apparent in the data. However, I observe that when measuring distances from a given point, or number of points, there will always be an underlying pattern to the distribution as the area of a region around a point increases with distance away from that point. When considering scatterers, the likelihood that scatterers will be within a certain distance from a contour will increase with distance away from that contour. Additionally, the limits of observations imposed by the distribution of sources and receivers which defines the region of potential PK•KP sampling (see Chapter 3.4 and Figure 3.6) will impart a pattern on the scatterer distribution with distance. To identify the “null” distribution, where scattering locations are controlled only by observation limits, I create synthetic scattering points. I generate multiple synthetic realisations (each realisation will from here-on be referred to as a sample) of randomly located data (laterally and vertically) of the same number of points as the real data, constrained by the same observation limits as the data (black line in Figure 3.18). The “null” distribution has uniform probability in terms of lateral distribution, within the observation limits imposed by the data sampling, and vertical distribution, from the CMB to 300 km above. To account for variability in the synthetic data, 300 samples are created and the distance from each structure is measured in the same way as the data. Similarly, to develop a numerical estimate of the full data population

[Efron, 1979; Efron & Tibshirani, 1991], I bootstrap (i.e resample with replacements) the real scatterer location sample to create 300 bootstrap samples. Each sample has its own cumulative distribution. Therefore, the synthetic samples demonstrate the distribution that would result from the observational limits and increasing area with distance from a point without any external pattern, while the bootstrapped data samples will be controlled by those limits but may show additional evidence of preferential distribution which may be attributed to mantle processes.

I compare the synthetic data and real samples both visually and numerically looking for deviations of the data distribution from the “null” distribution. Initially, the Shapiro-Wilk test (Equation 3.1) [Shapiro *et al.*, 1965] is applied to assess the normality of all the samples of each population (synthetic and real) at each distance point. For a given distance along the distribution, the cumulative scatterer frequencies of all samples in the population are analysed. The test determines whether data can be considered normally distributed (the null hypothesis), or not, to a given significance level:

$$W = \frac{(\sum_{i=1}^n a_i x_{(i)})^2}{\sum_{i=1}^n (x_i - \bar{x})^2} \quad (3.1)$$

Where  $x_{(i)}$  is the  $i$ th order statistic,  $\bar{x}$  is the sample mean, and the constants  $a_i$  are given by the expected values of the order statistics of independent and identically distributed random variables, and the covariance matrix of the order statistics, also known as the normalised ‘best linear unbiased’ coefficients [Shapiro *et al.*, 1965]. Results show that to 0.05 significance (95 % confidence) the cumulative frequency for a given distance for all samples in each population can be considered normally distributed. Consequently, I make the two populations of samples (synthetic and real) easier to compare by reducing each to the mean and standard deviation at each distance. Error bars of 1 and 2 standard deviations about the mean account for 68 and 95 % of the set, respectively. I also consider the standard error of the mean to show its reliability in representing the whole population.

Despite demonstrating the distribution of the majority of samples within the two datasets, comparing the standard deviations alone is not sufficient to establish whether the two populations are statistically different. To test for statistical significance I apply the Anderson-Darling Test (equation 3.2) [Anderson, 1962; Pettitt, 1976], a non-parametric test which determines whether a random sample  $X_1 \cdots X_m$ , described by the empirical distribution function (EDF)  $F_m(x)$ , can be said to come from a continuous population with the distribution specified by  $F_0(x)$ . For example, when comparing the distribution of the real data with that of the synthetic data these could be considered  $F_m(x)$  and  $F_0(x)$ , respectively.

$$A_m^2 = m \int_{-\infty}^{\infty} \frac{\{F_m(x) - F_0(x)\}^2}{F_0(x)\{1 - F_0(x)\}} dF_0(x) \quad (3.2)$$

The Anderson-Darling Test was generalised to the  $k$ -sample case (equation 3.3) [Scholz & Stephens, 1987] allowing the comparison of multiple ( $k$ ) samples.

$$A_{kN}^2 = \sum_{i=1}^k \int_{B_N} \frac{\{F_{in_i}(x) - H_N(x)\}^2}{H_N(x)\{1 - H_N(x)\}} dH_N(x) \quad (3.3)$$

Where  $F_{in_i}(x)$  is the EDF of the  $i$ th sample,  $H_N(x)$  is the EDF of the pooled sample  $N = n_1 + \dots + n_k$ , and  $B_N = \{x \in R : H_N(x) < 1\}$ . The  $k$ -sample Anderson-Darling (A-D) Test compares the squared rank difference between the  $n$  points in each sample,  $k$ , and the overall population, comprising  $N$  data points, summed over  $k$  samples. The null hypothesis states that all  $k$  samples are drawn from a population with the same distribution. The test is similar to the Kolmogorov-Smirnov and Cramer-von Mises test, except that it is more robust against distributions which cross, and weights towards the tails of the distribution where differences tend to be most significant [Babu & Feigelson, 2006; Engmann & Cousineau, 2011; Razali et al., 2011]. The differences from the population of each sample in the population is weighted for the sample size, is summed over all samples, and the resulting value is “standardised” by dividing it by the empirically calculated variance,  $\sigma_N$ .

$$T_{akN} = \frac{A_{akN}^2 - (k - 1)}{\sigma_N} \quad (3.4)$$

The variance accounts for the number of samples,  $k$ , the size of each sample,  $n$ , and the overall number of data points in the population,  $N$ . The standardised Anderson-Darling value,  $T_{akN}$  (Equation 3.4) also later referred to as AD-kS, is, therefore, more resistant to changes in the number of samples than the unmodified Anderson-Darling value,  $A_{akN}^2$ , although some changes with  $k$  still occur (see Chapter 3.9.1). As with other rank statistics, tied values, numbers with the same value and hence the same rank, are important and are corrected for. The standardised Anderson-Darling value can then be compared with critical values,  $t_m$  (equation 3.5), for different significance levels,  $\alpha$ , interpolated for the number of samples used,  $m$  where  $m = k - 1$ , based on values given in Scholz & Stephens [1987], which were determined using Monte-Carlo simulation.

$$t_m(\alpha) = b_0 + \frac{b_1}{\sqrt{(m)}} + \frac{b_2}{m} \quad (3.5)$$

Where coefficients  $b_0, b_1$ , and  $b_2$  are taken from Scholz & Stephens [1987] (Table 3.2). The standardised A-D value,  $T_{akN}$ , has an associated probability value,  $P$ , which, when it is less than the test significance level,  $\alpha$ , can be used to reject the null hypothesis thus demonstrating that the samples are not drawn from a population with the same distribution. Lower  $P$  values indicate an increased probability that the populations tested are different. I use this test to determine whether the real and synthetic samples can be said to be drawn from the same population or are significantly different.

Table 3.2: Interpolation coefficients for the Anderson-Darling test used in Equation 3.5. From Scholz & Stephens [1987].

$\alpha$	$b_0$	$b_1$	$b_2$
0.25	0.675	-0.245	-0.105
0.10	1.281	0.250	-0.305
0.05	1.645	0.678	-0.362
0.025	1.960	1.149	-0.391
0.01	2.326	1.822	-0.396

The value  $P$  indicates the significance (or the probability) of the similarity or difference

of the samples whereas the standardised A-D value,  $T_{akN}$  or AD-kS, can be seen as a measure of the degree of difference of the samples in the population, where more disparate samples result in greater  $T_{akN}$  values. By calculating the  $P$  and AD-kS values for a range of scenarios (where “scenario” is used to mean which large scale structure the scattering points are being compared with, the contour used (in terms of  $\Delta V_S$ ), and the height above the CMB of the scatterers used), numbers of synthetic samples, numbers of real samples, and which samples are drawn from the random and bootstrap population, I plot and fit a curve from which the values of the critical points for different significance levels,  $t_m(\alpha)$ , can be measured (Figure 3.20), analogous to Equation 3.5. For significance levels of  $\alpha=0.05$  and  $\alpha=0.01$ , for S40RTS, the AD-kS values must be 4.1 or greater, or 5.32 or greater, respectively, to reject the null hypothesis. For SMEAN the thresholds for the significance levels of  $\alpha=0.05$  and  $\alpha=0.01$  are 5.3 and 6.6, respectively. These values can be used when analysing the results of the A-D test to identify the statistically significant distributions using the probability  $P$ , and then quantify how different they are with  $T_{akN}$ .

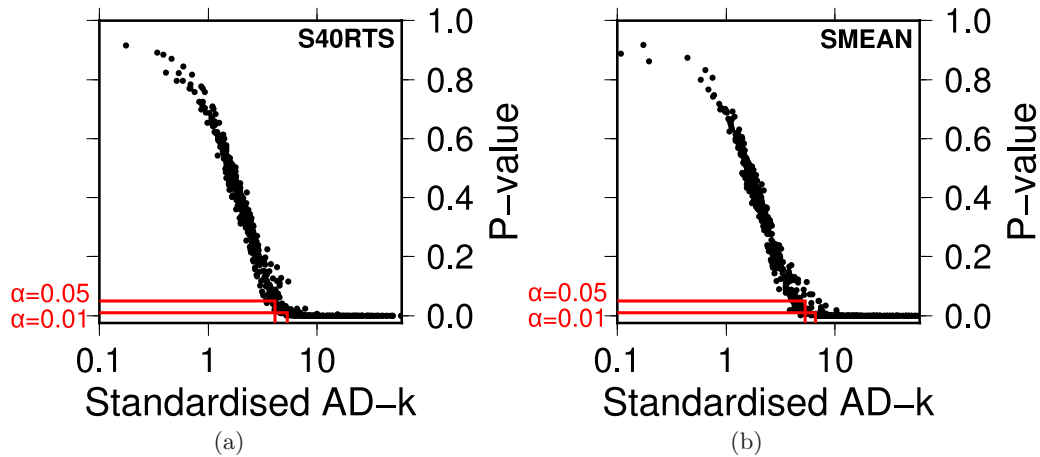


Figure 3.20: Empirically determined values of the standardised Anderson-Darling value,  $T_{akN}$ , and the associated probability values,  $P$  for (a) S40RTS and (b) SMEAN.  $P$  values can be directly compared with significance levels  $\alpha$ , shown by red lines. The points can be fit by a Gaussian curve for which  $\alpha$  values 0.05 and 0.01 are equivalent to  $T_{akN}$  values of 4.2 and 5.4 for S40RTS and 5.3 and 6.6 for SMEAN, respectively. The equation of the curve is  $f(x) = a \exp(-1((x-b)/c)^2)$  for which coefficients for S40RTS are  $a = 1.21$ ,  $b = 1.37$ ,  $c = 3.14$  and for SMEAN are  $a = 1.04$ ,  $b = 0.09$ ,  $c = 3.05$ .

### 3.9.1 Distribution Results

I compare real and synthetic data visually and apply the  $k$ -sample Anderson-Darling test to empirical distribution functions of scatterer distances measured relative to the inside and outside of the LLSVPs (for 0.0, -0.4, and -0.8 %  $V_S$  contours), and the outside of the high velocity anomalies (+0.9 and +1.3 %  $V_s$  contours for S40RTS and SMEAN, respectively) for scatterers at depths of 0-300 km, 50-300 km, 100-300 km, 0-50 km, and 0-100 km above the CMB for S40RTS and SMEAN. I find that distributions vary considerably dependent on the scenario: considering the LLSVPs or high velocity anomalies, measuring from the inside or outside of the structure, and the range of heights of scatterers used. In certain scenarios the real and synthetic distributions look visually very similar but the A-D test can determine a significant difference between the two popula-

tions, either implying subtle discrepancies between the two data sets or that the range of variability within the population (shown by the standard deviation of the samples in the population) does not significantly overlap (e.g. Figure 3.22). Both visual comparisons and the results of the A-D test are important in observing if patterns exist or not and if they are statistically significant.

To measure the degree of difference between the two populations, I apply the A-D test for a range of numbers of real and synthetic samples (Figure 3.21). The A-D test requires fewer real samples compared to the number of synthetic samples to be able to identify more disparate populations. I run A-D tests where 1 sample is drawn from the synthetic population and 1 sample from the real (bootstrapped) population. I also run this test using various combinations of synthetic and real samples: 50/1, 50/5, 50/10, 50/50, and 150/150. I also test 300 synthetic samples and no real samples to measure the variability within the synthetic population. I run these calculation 20 times, each time selecting a number of synthetic and real samples, which are drawn at random from the whole 300 samples. Therefore, each run of the calculation for a specific number of samples of each population will be different. I calculate the mean AD-kS ( $T_{akN}$ ) and P value for all 20 calculations. Standard deviations are small, demonstrating that although there is variability between the samples within the whole population of 300 samples, it is low. For tests containing only real or only synthetic data the A-D test P-value indicates that all samples were drawn from the same population (triangles in Figures 3.21b and 3.21d), and the low AD-kS values demonstrate that the natural variability between samples resulting from the the random location (generation of randomly located synthetic points) or random selection (bootstrap sampling of real data) process is low (Figures 3.21a and 3.21c). Also, this null result, even when using large  $k$ , demonstrates that the A-D test is resistant to false positives resulting from small differences being interpreted as statistically significant. For other numbers of real and synthetic samples the  $T_{akN}$  and P values vary.

The real and synthetic populations are most easily distinguished for scenarios outside the -0.8 % LLSVP contour, inside the -0.4 and -0.8 % LLSVP contours, and outside the fast regions for all LLSVP contours (green and blue symbols in Figure 3.21). The lower the number of real samples relative to synthetic samples required for the A-D test to determine a significant difference within the population the more disparate the two data sets are. An alternative interpretation is that outliers in the real data cause the two populations to look more similar than the majority of the data are and the bootstrapping process effectively suppresses outlying points and so a larger number of bootstraps amplifies the most representative parts of the data which, if it is significantly different from the random data, leads to an increased AD-kS value. Using an equal number of real and synthetic samples is likely the most robust way of determining a statistically significant difference. Variability within the synthetic and bootstrap populations may mean that for low  $k$  the two populations look similar while at higher  $k$  the populations are calculated to be distinct.

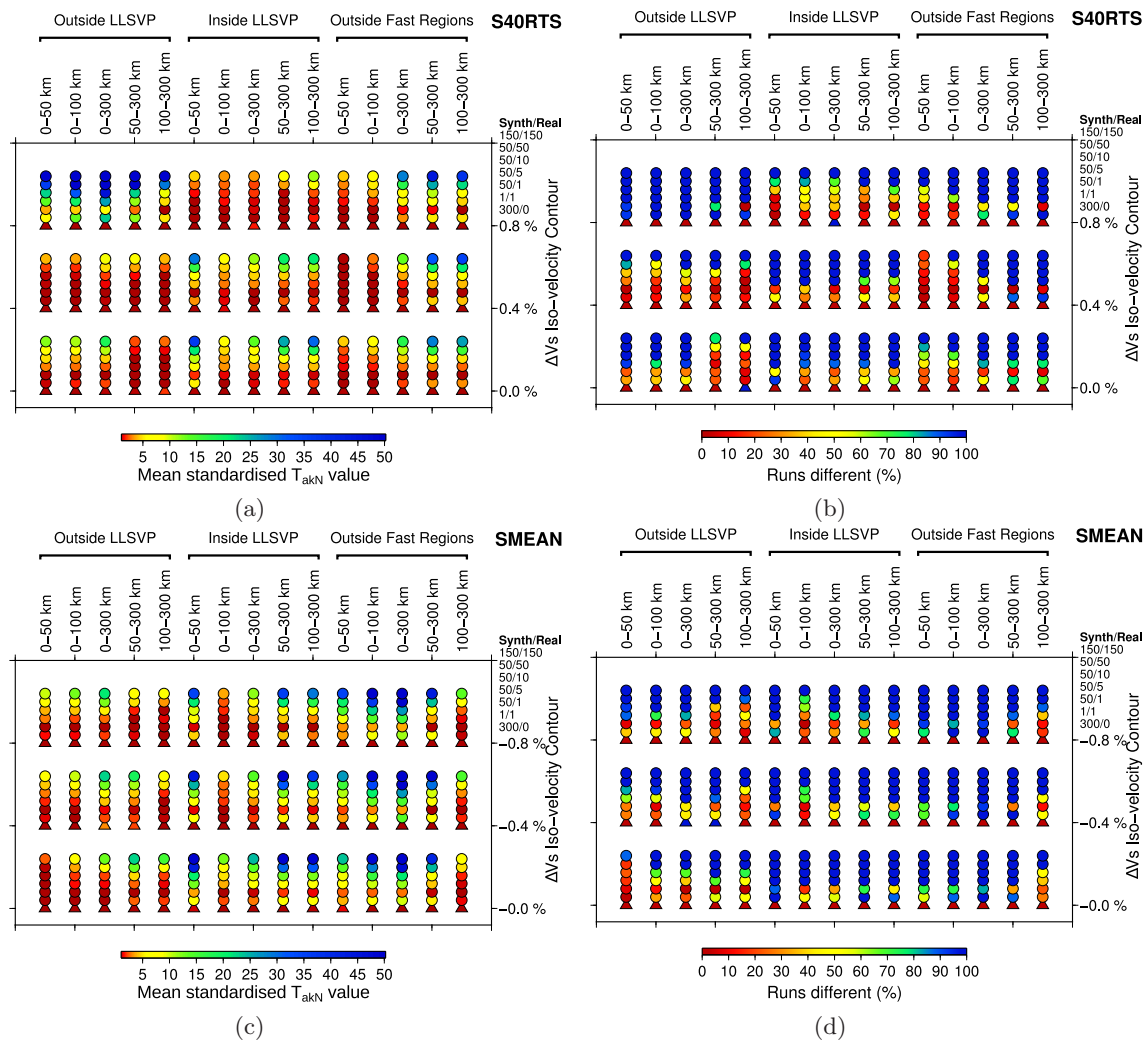


Figure 3.21: Anderson-Darling test results for a range of scenarios calculated for different combinations of synthetic and real data samples for contours defined in S40RTS (a and b) and in SMEAN (c and d). Displayed is the mean value for 20 calculations using a specified number of synthetic and data samples (shown by the vertical position of circle for which labels are shown in the same order in the top right of each figure) randomly selected from the total 300 sample population for the (a and c) standardised Anderson Darling value,  $T_{akN}$ , and (b and d) percentage of calculations shown to be statistically different, to  $\alpha = 0.05$ . The larger the  $T_{akN}$  and greater the percentage of calculations that are different, the more distinct the real and synthetic populations are for that scenario. For example, green or blue symbols in Figures a and c indicate that the real and synthetic populations are significantly different to greater than 99 % confidence (significance  $\alpha=0.01$ ). Differences between the real and synthetic populations are most obvious for scenarios outside the -0.8 % LLSVP contour, inside the -0.4 and -0.8 % LLSVP contours, and outside the fast regions for all LLSVP contours.

### 3.9.1.1 Outside LLSVPs

Scattering heterogeneities are first measured relative to the outside of the LLSVP (Figure 3.22 and 3.23). For both S40RTS and SMEAN, the scattering points are preferentially distributed close to the outside edge of the -0.8 % contour. Initially, frequency of heterogeneities increases rapidly, levels slightly at  $\sim 20^\circ$  away from the contour, and then increases again. This pattern is apparent, but weaker, for scatterers relative to the -0.4

% contour, but is not visible when the 0.0 % contour is used. Therefore, the scattering points show an affinity for the region between the -0.8 and 0.0 % contours, close to the inside edge of the LLSVP. The AD-kS ( $T_{akN}$ ) values demonstrate that, for the -0.8 % contour at least, the real and synthetic populations are statistically distinct and so this pattern is not a result of underlying distribution of scattering points. The AD-kS values also suggest that the real and data populations are more different when only scatterers within 100 km of the CMB are considered (Figures 3.21a and 3.21c). Figures 3.24 and 3.25 (and the AD-kS values therein) demonstrate that this pattern is not easily apparent visually and possibly may be a result of the greater variability between real samples at higher heights (wider standard deviations at higher heights). An alternative interpretation is that scatterer distribution outside the LLSVPs is distinct from the synthetic data, but at higher heights above the CMB and at distances greater than  $\sim 25^\circ$ , the scatterer locations are less controlled by external processes and begin to return to the underlying distribution demonstrated by the synthetics i.e. at higher heights and further from the contour the distribution is more similar to random. Scattering heterogeneities appear to show little correlation with the outer edge of the larger LLSVP contours (-0.4 and 0.0 %) but lie closer to the edge of the core of the LLSVPs (the -0.8 % contour) than would be expected from a random distribution.

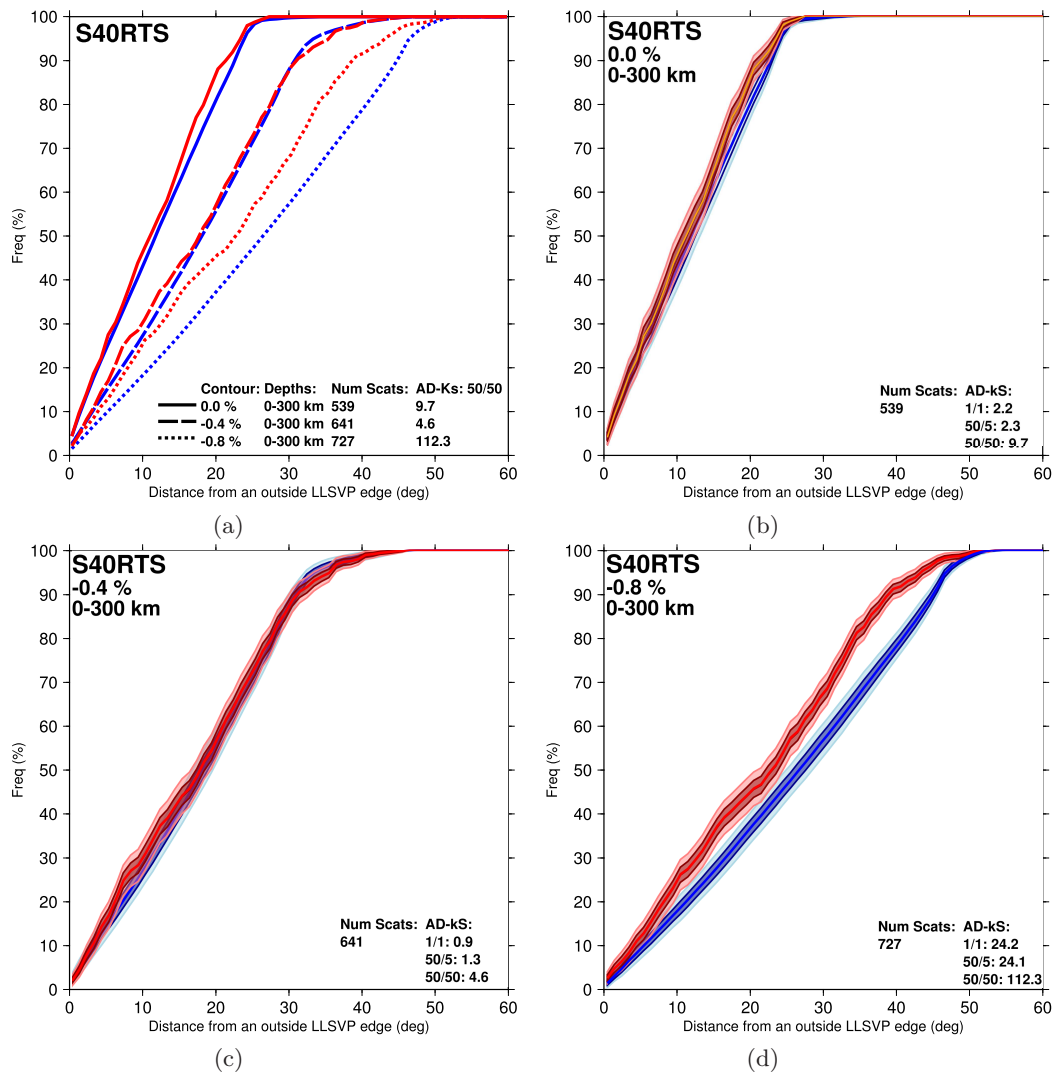


Figure 3.22: Cumulative distribution curves for scattering heterogeneities measured away from the outside edge of various LLSVP contours in S40RTS. (a) Distribution of the non-bootstrapped original data (red lines) compared to the mean of all 300 samples of the synthetic data (blue lines) for scattering points between 0-300 km above the CMB measured relative to the 0.0 %  $V_S$  contour (solid lines), -0.4 %  $V_S$  contour (dashed lines), -0.8 %  $V_S$  contour (dotted lines). Also shown are the number of scattering points used to construct each distribution and the AD-kS value calculated for 50 synthetic and 50 real samples. (b-d) Distribution of samples within the real and synthetic populations shown by the mean of all samples (orange and blue thick lines), standard error of the mean (dark red and dark blue regions), first standard deviation about the mean (dark red and dark blue shading) and second standard deviation about the mean (light red and light blue shading). For the real data, the actual scatterer distribution is plotted (thick red line) which often obscures the mean line (orange). Standard errors of the mean are often too small to be seen. Also shown, for each scenario, are the AD-kS values for a range of  $k$  samples of synthetic and real data (values shown in Figures 3.21a and 3.21c). Scatterer distributions for (b) the 0.0 % contour, (c) the -0.4 % contour, and (d) the -0.8 % contour for heights from 0-300 km above the CMB. Relative to the outside of the -0.8 % contour, scatterers show a strong preference towards the edge when compared with the synthetic data. Around 40 % of the real scattering points are accounted for within  $15^\circ$  of the LLSVP edge compared to less than 30 % of the synthetic data in the same distance range. The same pattern is just visible for heterogeneities measured relative to the -0.4 % contour but is not apparent when measured relative to the 0.0 % contour.

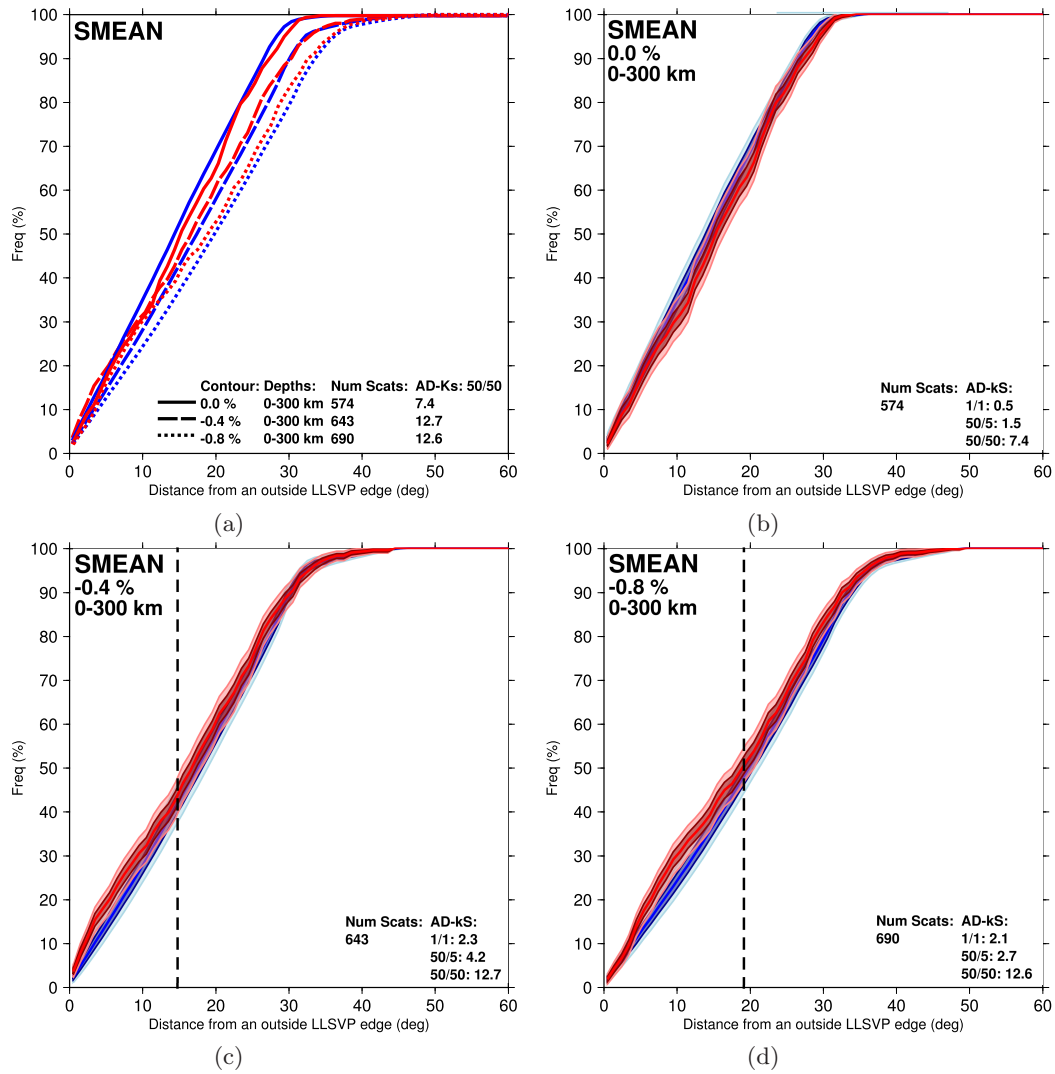


Figure 3.23: Cumulative distribution curves for scatterers measured away from the outside edge of various LLSVP contours in SMEAN. Lines and shading as in Figure 3.22. (a) Distribution of the non-bootstrapped original data (red lines) compared to the mean of all 300 samples of the synthetic data (blue lines) for scattering points between 0-300 km above the CMB measured relative to the 0.0 %  $V_S$  contour (solid lines), -0.4 %  $V_S$  contour (dashed lines), -0.8 %  $V_S$  contour (dotted lines). Scatterer distributions for (b) the 0.0 % contour, (c) the -0.4 % contour, and (d) the -0.8 % contour for heights from 0-300 km above the CMB. Scattering heterogeneities cluster within  $\sim 15^\circ$  (vertical dashed line) of the -0.4 % contour. A similar increase in scatterer concentration can be seen at slightly greater distances ( $\sim 19^\circ$ , vertical dashed line) when measured relative to the -0.8 % contour (which has smaller geographic extent).

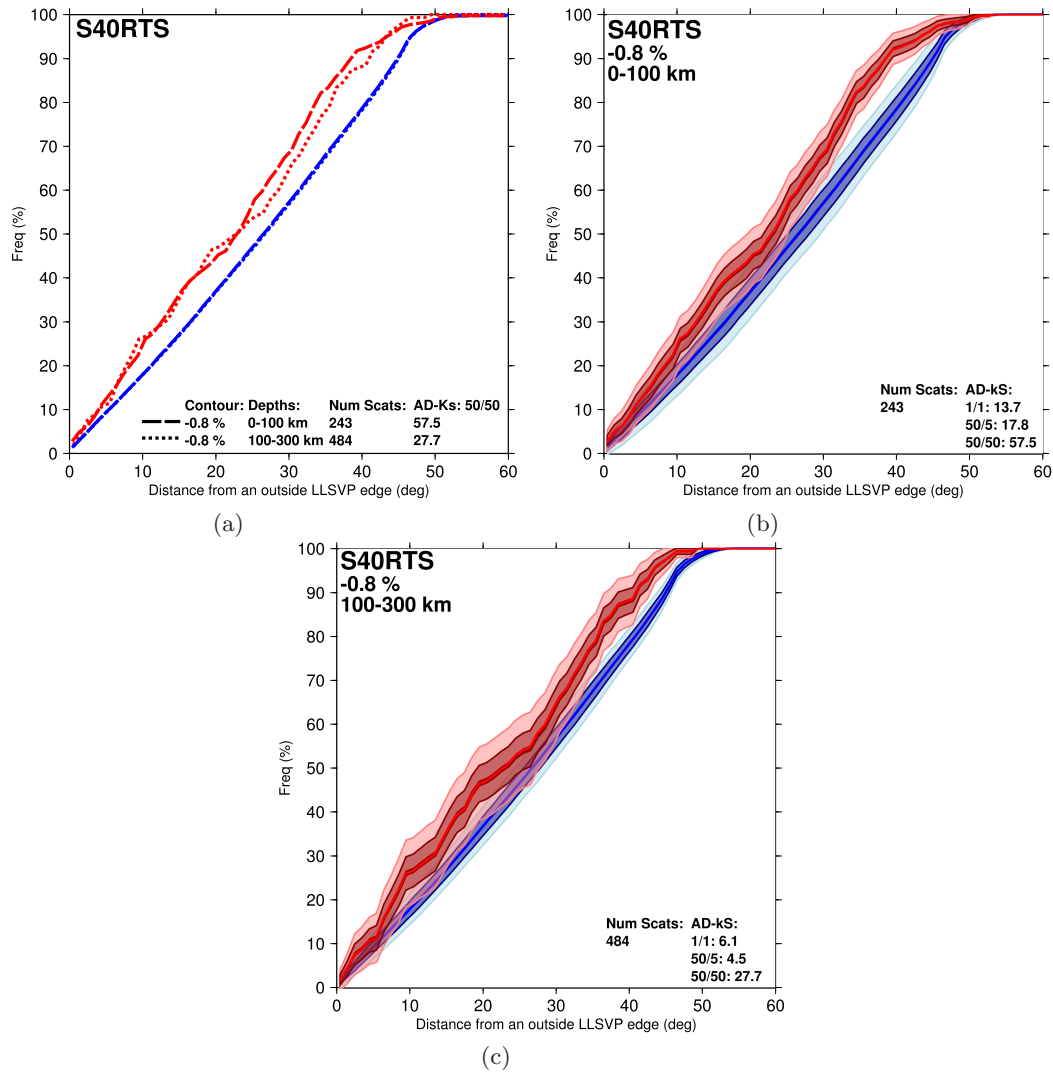


Figure 3.24: Cumulative distribution curves for scatterers measured away from the outside edge of the  $-0.8\%$  LLSVP contour in S40RTS. Lines and shading as in Figure 3.22. (a) Data and means for scatterers from 0-100 km above the CMB (dashed lines) and 100-300 km above the CMB (dotted lines). Population distributions for scatterers (b) 0-100 km above the CMB and (c) 100-300 km above the CMB. Scattering points higher above the CMB associate less with the edge of the LLSVP than scattering points closer to the CMB (at heights less than 100 km above the CMB). This is especially visible at distances greater than  $\sim 20^\circ$  from the edge of the LLSVP. The AD-kS values demonstrate that both distributions are statistically different from the random population but the pattern of scatterers at lower heights is more distinct.

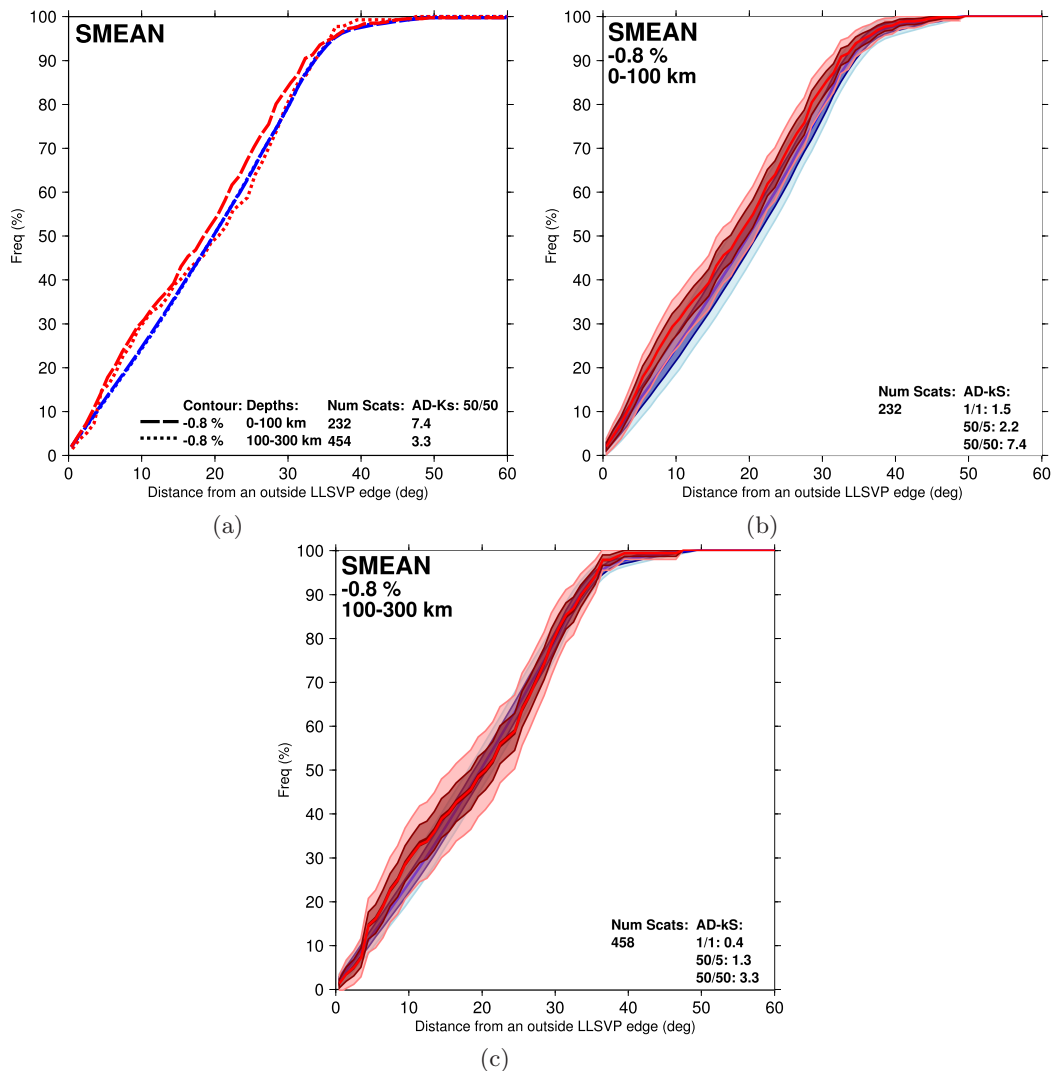


Figure 3.25: Cumulative distribution curves for scatterers measured away from the outside edge of the  $-0.8\%$  LLSVP contour in SMEAN. Lines and shading as in Figure 3.22. (a) Data and means for scatterers from 0-100 km above the CMB (dashed lines) and 100-300 km above the CMB (dotted lines). Population distributions for scatterers (b) 0-100 km above the CMB and (c) 100-300 km above the CMB. Scattering points higher above the CMB associate less with the edge of the LLSVP (are more similar to the synthetic data) at distances greater than  $\sim 25^\circ$  than scattering points closer to the CMB (at heights less than 100 km above the CMB). The AD-kS values indicate that the distribution of heterogeneities at greater heights cannot be reliably distinguished from random but distributions at lower heights are likely to be drawn from a different population (are distinct from the synthetics).

### 3.9.1.2 Inside LLSVPs

Within the LLSVPs the opposite patterns appear present (as seen in Figure 3.26 and 3.27) scatterers are more closely related to the inside edge of the  $0.0\%$  contour, show some preference for the  $-0.4\%$  contour, and real data are indistinguishable from randomly distributed data inside the  $-0.8\%$  contour. Similar to the distribution relative to the outside of the  $-0.8\%$  contour, when measured relative to the inside edge of the  $0.0\%$  contour the frequency of scattering points increases quickly up to  $\sim 10^\circ$  away and then increases more gradually i.e. most scattering heterogeneities ( $>50\%$ ) sit within  $10^\circ$  of the boundary. The same is true, but to a lesser extent, for the  $-0.4\%$  contour. The pattern

does not appear particularly strong (not visually very different from the synthetic data) for either the 0.0 % or -0.4 % contour but this may be primarily due to the small area within the LLSVP in which the scatterers can be distributed. Secondly the comparatively weak pattern for these contours may be due to the relatively low number of scattering points considered. However, the A-D test demonstrates that this pattern is statistically robust for the 0.0 and -0.4 % contours (Figures 3.21a and 3.21c) and that there is little difference between the distribution relative to the -0.8 % contour and the randomly distributed synthetics. I accept that the 0.0 % contour likely over-estimates the areal extent of the LLSVPs, but it does give an outermost constraint on their shape and so I use it as an upper limit of their size.

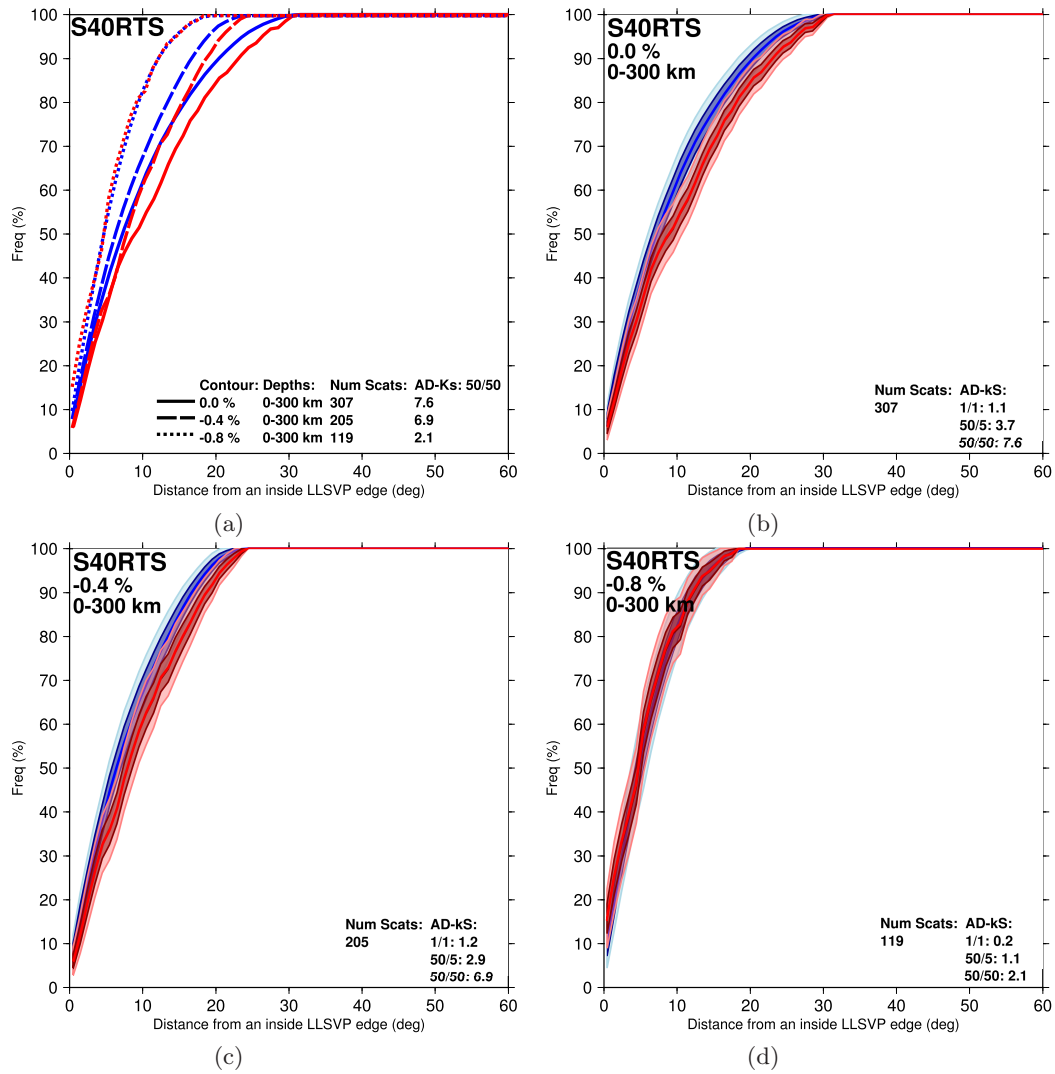


Figure 3.26: Cumulative distribution curves for scatterers measured from the inside edge of the various LLSVP contours in S40RTS. Lines and shading as in Figure 3.22. (a) Data and means for scatterers from 0-300 km above the CMB for distances measured relative to the 0.0 % contour (solid lines), the -0.4 % contour (dashed lines), and the -0.8 % contour (dotted lines). Population distributions for scatterers between 0-300 km above the CMB for the (b) 0.0 % contour (c) -0.4 % contour, and (d) the -0.8 % contour. Scattering points show a greater preference to be close to the inside of the 0.0 % contour than to be further away. This pattern is somewhat visible for the -0.4 % contour, but scatterer distribution relative to the -0.8 % is indistinguishable from the randomly distributed synthetic data. These observations are supported by the AD-kS test values. Despite all real distributions plotting below the synthetic data patterns are still apparent and statistically relevant; for the 0.0 % contour, scatterers still show preferential distribution towards the inside edge.

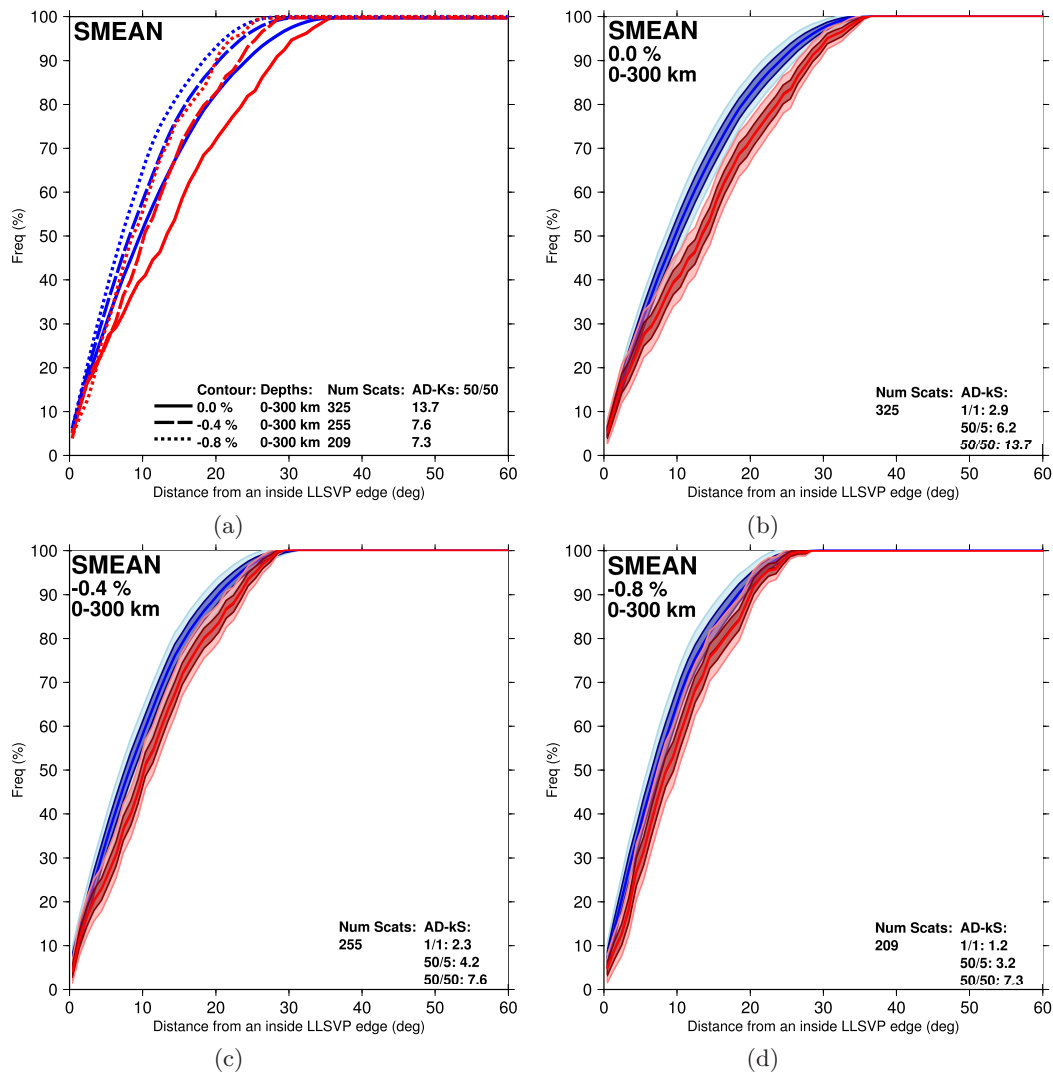


Figure 3.27: Cumulative distribution curves for scatterers measured from the inside edge of the various LLSVP contours in SMEAN. Lines and shading as in Figure 3.22. (a) Data and means for scatterers from 0-300 km above the CMB for distances measured relative to the 0.0 % contour (solid lines), the -0.4 % contour (dashed lines), and the -0.8 % contour (dotted lines). Population distributions for scatterers between 0-300 km above the CMB for the (b) 0.0 % contour (c) -0.4 % contour, and (d) the -0.8 % contour. Scattering heterogeneities are preferentially located close to inside of the larger contours. The pattern is most obvious for the 0.0 % contour, and partly visible for the -0.4 % contour, while relative to the -0.8 % contour scattering heterogeneities show no preference for being close to the edge. This result is also demonstrated by the AD-kS test values which are lower (populations are more similar) for smaller (more negative) LLSVP contours.

The observations of increased scatterer frequency away from the outside edge of the LLSVP core (the -0.8 % contour) and inside of the upper-most estimate of the LLSVP extent (the 0.0 % contour), and slightly more concentrated scatterers relative to both the inside and outside of the -0.4 % contour, taken together imply that scatterers tend to fall between the -0.8 % and 0.0 % contours. This preference can also be seen when looking at the spatial distribution of scatterers (Figures 3.9 and 3.18) with scattering points clustering between these two contours. There are other notable regions in which scattering points appear more concentrated; for example under the east side of South Africa where the south

eastern and northern extensions of the African LLSVP connect, the western edge of the African LLSVP under west Africa, the north-eastern edge of the Pacific LLSVP, and the south-eastern edge of the Pacific LLSVP. Dynamic models have demonstrated that flow in the lower mantle can concentrate dense compositional anomalies close to the edges of, or just inside, internally convecting LLSVPs (Figure 1.7) [McNamara *et al.*, 2010; Li & McNamara, 2013]. It is likely that the scattering heterogeneities are compositionally distinct, given their ability to scatter seismic waves, and so may be acted upon by mantle flow, concentrating them in regions of stagnant flow. If scattering heterogeneities are related to ULVZs, as has been suggested [Wen & Helmberger, 1998; Thomas *et al.*, 1999, 2000; Wen, 2000; Ni & Helmberger, 2001; Thomas *et al.*, 2009; Rost & Earle, 2010], and comprise material  $\sim 10$  % denser than the ambient mantle, as has been determined for scatterers and for ULVZs using other probes [Garnero & Helmberger, 1998; Rost & Revenaugh, 2003; Rost *et al.*, 2005], then it would be possible for these heterogeneities to become partially entrained in the internal convection of LLSVPs [McNamara *et al.*, 2010; Bower *et al.*, 2011]. Embayments within an LLSVP structure (such as along the south-eastern edge of the African LLSVP or the north-eastern edge of the Pacific LLSVP) may cause regions of stagnant flow, further concentrating scattering heterogeneities. These mechanisms could account for the strong patterns observed in scatterer distribution relative to the LLSVPs.

### 3.9.1.3 Outside High Velocity Anomalies

Outside the high velocity anomalies (Figures 3.28 and 3.29) scattering points show a strong preference to be close to the edge, particular when the  $-0.8$  % LLSVP contour is used. When measuring relative to the high velocity anomalies which LLSVP contour is used only affects the number of scattering points and maximum distance of scatterers as scattering points inside the LLSVP are disregarded. Using a large contour (e.g.  $0.0$  %) means that fewer scattering points will be considered. Scatterers show the strongest preference for being close to the high velocity anomalies at heights greater than  $100$  km (although the pattern is also apparent but weaker for heights greater than  $50$  km). For the scattering points higher above the CMB, more than  $40$  % of the points are accounted for within  $10^\circ$  of the edge of the high velocity anomalies, and half of the scattering points are within  $\sim 13^\circ$  of the high fast anomalies, for S40RTS. By comparison, scatterers between the CMB and  $100$  km above appear to initially follow the trend of the synthetic points up to  $\sim 22^\circ$  and then scatterer frequency increases more slowly. This is also demonstrated by the AD-kS values which indicate that the distribution of scattering points higher than  $100$  km above the CMB is significantly different from the synthetic population and show a stronger difference than the distribution of scattering points below  $100$  km.

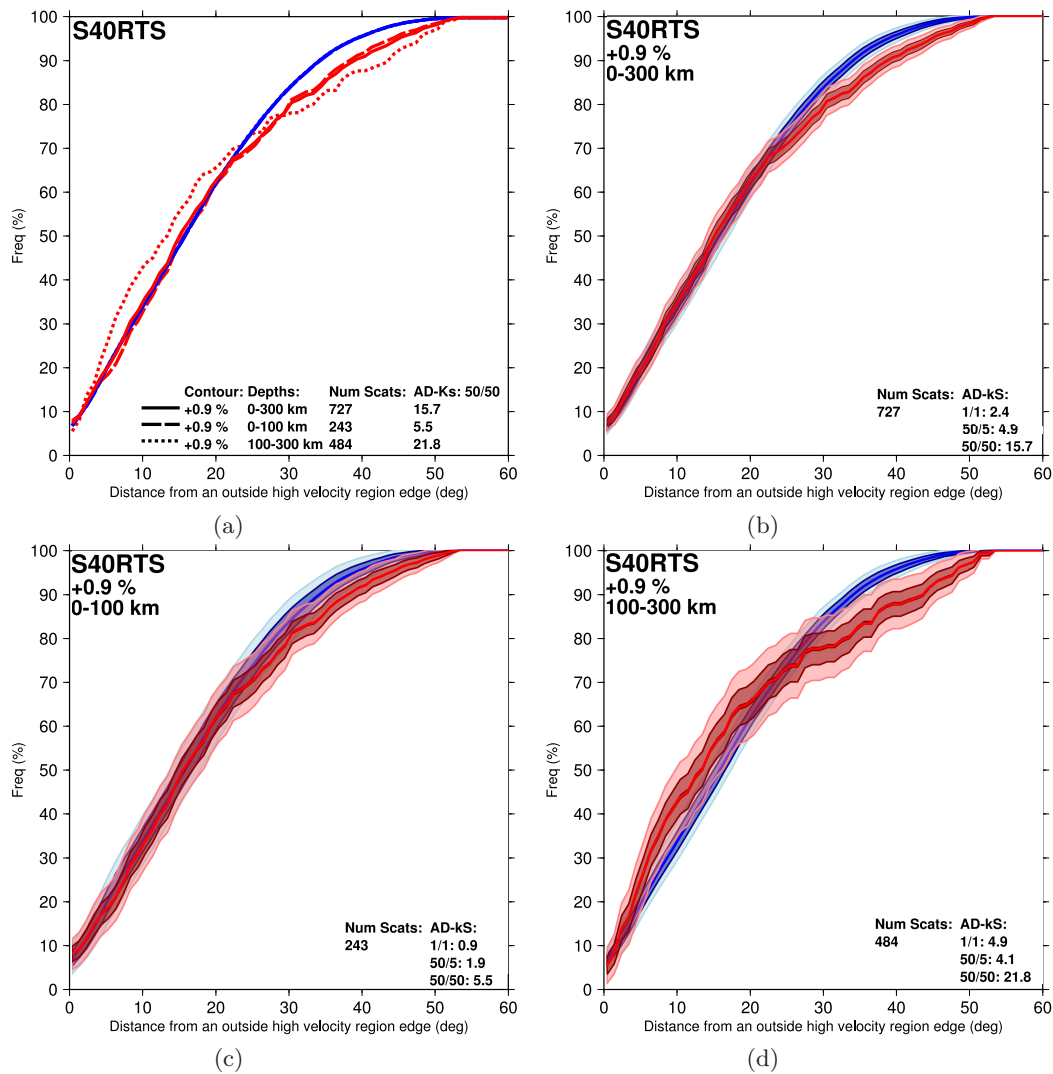


Figure 3.28: Cumulative distribution curves for scatterers measured away from the outside edge of the +0.9% high velocity anomaly contours in S40RTS and up to the -0.8% LLSVP contour. Lines and shading as in Figure 3.22. (a) Distributions of scattering points at 0-300 km (solid lines), 0-100 km (dashed lines), and 100-300 km above the CMB (dotted lines). The synthetic distributions (blue lines) for all heights overlap as the synthetic scattering point distribution is independent of height. Population distributions for scatterers outside the +0.9% contour which defines the high velocity anomalies for (b) 0-300 km, (c) 0-100 km, and (d) 100-300 km above the CMB. Scattering points close to the CMB follow a similar distribution to the randomly distributed synthetic data up to  $\sim 22^\circ$ , followed by a slower increase in scatterer frequency with distance. At greater heights, scatterers are predominantly close to the edges of the high velocity anomalies; 50% of the scattering points occur within  $\sim 13^\circ$  of the contours. The AD-kS values support the observations that the distribution of scatterers close to the CMB looks much more similar to random than the distribution for scatterers higher up. For all heights, scatterers within the high velocity anomalies are counted as having zero distance, hence why the cumulative distributions do not start at 0% frequency.

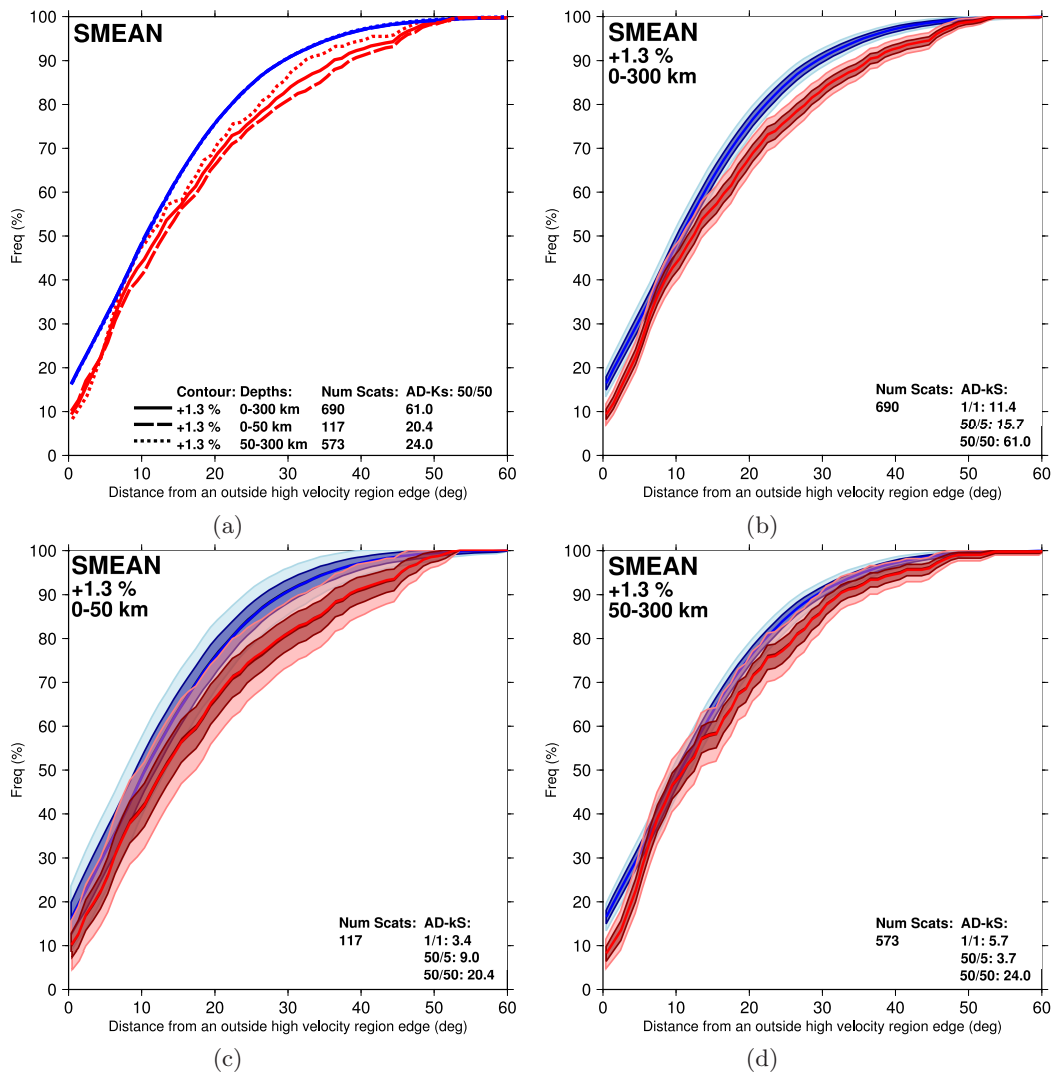


Figure 3.29: Cumulative distribution curves for scatterers measured away from the outside edge of the +1.3 % high velocity anomaly contours in SMEAN and up to the -0.8 % LLSVP contour. Lines and shading as in Figure 3.22. (a) Distributions of scattering points at 0-300 km (solid lines), 0-50 km (dashed lines), and 50-300 km above the CMB (dotted lines). The synthetic distributions (blue lines) for all heights overlap as the synthetic scattering point distribution is independent of height. Population distributions for scatterers outside the +0.9 % contour defining the high velocity anomalies for (b) 0-300 km, (c) 0-50 km, and (d) 50-300 km. Scattering both close to the CMB (0-50 km) and above the CMB (50-300 km) follow different patterns from the synthetic data but scatterers above 50 km show a strong preference for the edge of the high velocity anomalies; 50 % of the heterogeneities above 50 km are accounted for within  $12^\circ$  of the contours while only 40 % of the scatterers below 50 km occur within this distance. The AD-kS values are similar for lower and higher scattering heterogeneities demonstrating that both patterns are significantly different from the synthetics. For all heights, scatterers within the high velocity anomalies are counted as having zero distance, hence why the cumulative distributions do not start at 0 % frequency.

The high velocity anomalies likely represent the points at which subducted material reaches the CMB. Anomalous structures have previously been imaged at the CMB under the Cocos plate suggesting that slab products are seismically visible in the lower mantle [Thomas *et al.*, 2004a; Hutko *et al.*, 2006; Miller & Niu, 2008]. Slabs are often modelled as

physically and thermally distinct from the ambient lower mantle and a source of chemical heterogeneities, particularly the basaltic crust component [McNamara *et al.*, 2010; Tackley, 2011; Stixrude & Lithgow-Bertelloni, 2012; Li & McNamara, 2013]. The pattern of greater scattering closer to the slabs at greater heights is suggestive of either mixing processes or changes in the scattering potential of the heterogeneities, i.e. how likely they are to scatter waves that can be observed using this probe. I speculate as to mechanisms that could produce this pattern. A downgoing slab may be acted upon by viscous forces within the mantle causing mechanical mixing and progressive break-up of the slab material as well as small scale density driven convection within the slab [e.g. Tackley, 2011]. As the slab descends deeper into the mantle heating will reduce the viscosity, possibly making it more susceptible to separation and entrainment into the whole mantle convection cycle. In this situation an initially coherent slab, which would be too large to be detectable by scattering probes at these frequencies, would be broken into increasingly small segments as it travels deeper, separating into objects of appropriate scale length to cause scattering. Closer to the CMB, dispersion of heterogeneities by the “mantle wind” [e.g. Thorne *et al.*, 2004] may make the scattering signature of the slab broader. Alternatively, deeper in the mantle mechanical mixing may have progressed to such a degree that heterogeneities become too small to generate observable scattering. However, without dynamic modelling of slab mixing and detailed spectral analysis of PK•KP waves compared to the height of the located scatterer I don’t feel that these situations are testable.

### 3.9.2 Considerations

In the tests above the number of data points,  $n$ , that fit the scenario (e.g. are inside/outside the LLSVP/high velocity anomalies) varies for each sample due to the variation in the data set. To determine the robustness of the A-D test to samples of different sizes, I repeat A-D calculations with the same combinations of different numbers of synthetic and real samples as before (as in Figure 3.21), but limit the samples to the same length ( $n$ ) of both synthetic and real data. The results show negligible difference from the tests with variable  $n$  and no systematic trend even when using scenarios where the sizes of samples from the two populations are most different. The standardisation of the A-D test is, therefore, effective at accounting for differing sample sizes.

The distribution away from the outside edge of the LLSVPs may be expected to be similar to the pattern outside of the fast regions as the same scattering points are being considered. However, this is not the case as there are many more high velocity regions than there are LLSVPs. This means that at increasing distances away from a contour, the “regions of interest” (or area a certain distance away from the contour) around a high velocity contour will overlap with another much sooner than when considering the LLSVPs. Therefore, the underlying distribution of scatterers (demonstrated by the synthetic data) will be different when measuring distances away from the outside LLSVPs and away from the outside of high velocity anomalies. Inside the LLSVPs, the lack of a clear difference between the real and synthetic data might result from the real data having no preferential distribution, or because the range of distances available is too small for a pattern to be observable.

Overall, scatterers show a strong preference to be within  $30^\circ$  of the LLSVPs and

15° of the fast regions, when compared with randomly distributed synthetic data. This matches observations of other scattering structures and ULVZs close to the edge of the LLSVPs [McNamara *et al.*, 2010], and of small-scale seismic velocity increases close to subducted slabs at the CMB [Thomas *et al.*, 2004a; Hutko *et al.*, 2006; Cobden & Thomas, 2013]. Within LLSVPs, scatterer distributions are only slightly different from random and differences are strongest for the larger contours.

It is likely that none of the three contours I use to represent the LLSVPs (0.0 %, -0.4 %, and -0.8 %) are correct depictions of the extent of the structure. A high resolution S-wave determination of the Pacific LLSVP boundary [He & Wen, 2012] is best matched by the -0.4 % contour. However, no equivalent high resolution study is available for the whole of African LLSVP which instead has only been partially mapped [Wang & Wen, 2004, 2007]. Therefore, I assume that the -0.8 % and 0.0 % contours are minimum and maximum estimates of the extent of the LLSVPs, respectively. Although contours of different velocity anomalies are of roughly similar shapes, in places there are large deviations (Figure 3.19). This is true for both SMEAN and S40RTS but is most notable for S40RTS around the north and south-east of the African LLSVP and south-east of the Pacific LLSVP. These discrepancies likely contribute to why the distributions vary so significantly when measured relative to different contours, and additionally why the distribution of scatterers away from the inside of a larger contour does not mirror the distribution away from the outside of a smaller contour.

Although there are strong apparent spatial associations between the scattering heterogeneities and the large-scale structures defined in the tomography models, it is not certain that these patterns are the result of mantle processes. Dynamic models suggest that mantle processes would concentrate heterogeneities but it is quite speculative to infer that the dominant factor controlling the distributions resolved in this study is the motion of the mantle. Nonetheless, the patterns in the data are visually obvious and determined to be statistically different from random distributions.

### 3.9.3 Summary of Distribution Results

Cumulative distributions of scatterer frequency with distance relative to large-scale lower mantle features are measured at various heights above the CMB. The distribution of scattering points varies dependent on whether they are measured relative to LLSVPs (depicted by the 0.0 %, -0.4 %, and -0.8 %  $V_S$  contours in S40RTS and SMEAN) or high velocity anomalies which are linked to subduction zones (depicted by the +0.9 % contour in S40RTS and the +1.3 % contour in SMEAN). Using randomly distributed synthetic data to display how distribution curves would look if there were no controls on scatterer location, I demonstrate that patterns observed in the real data are distinctly non-random. I use the  $k$ -sample Anderson-Darling Test, a non-parametric rank test, to compare synthetic and real distributions to determine if, to 95 or 99 % significance, the two sets could come from one population or if they are more likely to be drawn from two independent populations, thus indicating the non-randomness of the real data.

I find that there is a preference for real scatterers to lie close to the outside of the -0.8 % LLSVP contour and close to the inside of the 0.0 % LLSVP contour implying that scattering points are concentrated between these two contours, which likely mark

the inside and outside edges of the LLSVPs, respectively. From this I speculate that heterogeneities close to the inside edge of the LLSVPs are entrained into the internal convection but are concentrated at the edge by their above-average density. Outside of the LLSVPs, scattering heterogeneities above the CMB (either greater than 50 or 100 km height, dependent on the tomography model) show a strong preference to be close to the outside edge of high velocity anomalies indicating a distinct flow and possibly the beginning of entrainment of slab material into ambient mantle. Close to the CMB, heterogeneities are randomly distributed suggesting strong mixing. Heterogeneities associated with the high velocity anomalies may be introduced from above by subducting slabs and are then progressively laterally dispersed by mechanical mixing as the slab reaches the CMB. Lower viscosity in the thermal boundary layer at the base of the mantle may aid mixing close to the CMB, while mixing may be more sluggish at greater heights. Overall, scattering heterogeneities appear to show spatial links with the large-scale structures in the lower mantle.

### 3.10 Discussion

This near-global study of PK•KP scattering is the first to utilise such a large dataset recorded at arrays to precisely locate the scattering heterogeneities within the Earth. Further information from the broadband GSN stations reveals scatterer size. The locations and sizes of scattering heterogeneities and their relation to the other structures in the mantle may be indicative of the geodynamics in the lower mantle and could therefore be used as tracers of flow. Combining observations of patterns in the prevalence and height of heterogeneities with measurements of their size and physical properties may help further modelling efforts to elucidate processes on all scales acting in the mantle.

Scattering heterogeneities are observed to be near globally, yet unevenly, distributed throughout the lowermost 300 km of the mantle (Figure 3.10). Heterogeneities are often clustered in areas associated with large-scale mantle structures (Figure 3.18 and larger Appendix Figure C.2), the LLSVPs and high-velocity anomalies (which are likely related to subducted slabs). These groupings tend to contain scattering heterogeneities at the greatest recorded heights of up to 320 km above the CMB (Figure 3.9), and also the most heterogeneities at moderate heights of  $\sim 100$  km above the CMB (the greatest median heights). Lower mantle velocity anomalies of similar heights have previously been detected using other probes [Helmberger *et al.*, 2000; Wen, 2001; To *et al.*, 2011; Sun *et al.*, 2013]. Scattering heterogeneities close to the CMB are more prevalent in areas far from the margins of large-scale mantle structures. These patterns are shown by the Anderson-Darling Test to be statistically robust (Figure 3.21). In the majority of cases, the errors associated with the ray-traced locations of scattered points are likely too small to significantly affect the spatial relationships (Figure 3.15). The spatial association implies that the large scale structures are influencing the heterogeneities, perhaps by concentrating them in lateral location, or supporting them in height. Areas without any scattering heterogeneities are observed, despite being able to be sampled by the source-receiver combinations in this study. It is possible that in these areas scattering is too weak to be detected by this probe, or it is such a rare occurrence that, given the number of times the area is sampled, scattering is not likely to be observed, or else that there are no hetero-

geneities present. Either way, this observation indicates lateral variation in heterogeneity structure. Many of these regions without scattering are also either distant from both the LLSVPs and the high velocity anomalies, or are within the centre of the LLSVPs. This suggests that the edges of the LLSVPs and the high velocity anomalies are either sources or sinks of heterogeneities, leaving other areas bare. Previous studies have also reported non-observations [Persh *et al.*, 2001; Rost *et al.*, 2010b; McNamara *et al.*, 2010, and references therein] demonstrating that while scattering and other lower mantle heterogeneities are widely observed, they are not ubiquitous in the lower mantle.

Many of the regions which consistently scatter PK•KP at large heights above the CMB have previously been seen to be seismically anomalous using a range of techniques. The two most obvious areas of strong PK•KP scattering, under South Africa and off the west coast of Central America, have been demonstrated to contain anomalies of different types. The CMB under South Africa has been linked to strong scattering at up to  $\sim 100$  km above the CMB associated with the edge of the African LLSVP (see Chapter 2 and Figure 3.12) [Rost & Earle, 2010; Frost *et al.*, 2013] and the Comoros Hotspot [Wen, 2000]. This is likely a low velocity region comprising small, dense chemical anomalies with negative velocity deviations. In contrast, the area close to Central America and the north of South America has been linked to subduction zones processes, observed as reflections from the D'' discontinuity [Weber & Körnig, 1990, 1992; Niu & Wen, 2001; Sun *et al.*, 2007b; Hutko *et al.*, 2009; Ford *et al.*, 2012] and reflection or scattering from whole or disaggregated subducted crust [Miller & Niu, 2008; Kito *et al.*, 2008; Rost & Earle, 2010]. These structures are reported to show increased seismic velocities of a few per cent. Scattering of PK•KP, therefore, is indicative of only a change in the elastic parameters and/or density, but not specifically a velocity drop or increase.

PK•KP is a back-scattering probe and theory indicates that back-scattering is strongest when density and elastic parameter deviations are of the same sign (explained in detail in Chapter 1.3), and therefore, when scattering is caused by an anomaly that is both stiffer and denser. In spite of this, back-scattering is still possible from anomalies with different parameters, but is not dominant (Figures 1.10). This implies that scattering from high velocity subducted oceanic crust, which is reported to be denser and stiffer than the ambient lower mantle [Hirose *et al.*, 1999; Karato & Karki, 2001; Hirose *et al.*, 2005], would be stronger than scattering from low velocity ULVZ material, which is often reported to be denser and less stiff [Mao *et al.*, 2006; Wicks *et al.*, 2010]. However, the lack of any way to calibrate amplitude measurements of scattered signals with reference phases means that this cannot be tested here. Analysis of PK•KP scattering recorded in broadband data (Figure 3.17) demonstrates that, globally, heterogeneities are on the order of 1-10 km in size, with a dominant size of  $\sim 6$  km. This size range is similar to the thickness of the oceanic crust, which has been shown to be faster and denser than the ambient material at lower mantle pressures [Kudo *et al.*, 2012]. Scattering heterogeneities may also be caused by other means, such as partial melt [Williams & Garnero, 1996; Berryman, 2000; Lay *et al.*, 2004; Beuchert & Schmeling, 2013] or iron-enriched mantle material [Knittle & Jeanloz, 1989, 1991; Mao *et al.*, 2006; Wicks *et al.*, 2010; Bower *et al.*, 2011]. Given that scattering is observed in regions associated with both LLSVPs and subduction, structures which are thought to have contrasting compositions [Deschamps *et al.*,

2012], the scattering heterogeneities sampled in these regions may be of differing compositions. Seismic modelling of PK•KP using a radial velocity structure was not conclusive in determining the nature of the scattering heterogeneities as this approach is inappropriate for modelling laterally strongly variable scattering structures (shown for PKP in Chapter 2.8). Detailed seismic modelling that operates in more than 1-dimension could be used to calculate contrasts in the elastic parameters and density of the material.

The spatial relationship between scattering heterogeneities in the lower mantle and both the high velocity anomalies (likely related to subduction) and the inside edge of the LLSVPs (the region outside of the  $-0.8\%$   $V_S$  contour and inside the  $0.0\%$   $V_S$  contour in both S40RTS and SMEAN) is suggestive of dynamic processes that may be generating or concentrating chemical anomalies in these regions (see Chapter 3.9). Maps of lower mantle flow have been created from analysing density anomalies in joint tomography inversions and plate motions [Forte *et al.*, 2013]. Regions of concentrated scattering heterogeneities at high heights above the CMB (Figure 3.9) appear to correlate well with regions of strong upwelling or downwelling within the flow models (Figure 3.30). For example, South Africa and western Africa show frequent scattering high above the CMB scattering and correlate with upwellings while Central America, southern South America, and northern South America also show common scattering at great heights and agree with locations of strong downwelling. Similarly, regions in which few scattering points are observed or scattering is dominantly close to the CMB (such as the Indian and south Atlantic oceans) are co-located with areas in which vertical flow is weak in the models. This provides strong support that the locations of small-scale volumetric heterogeneities in the lower mantle are influenced by mantle flow.

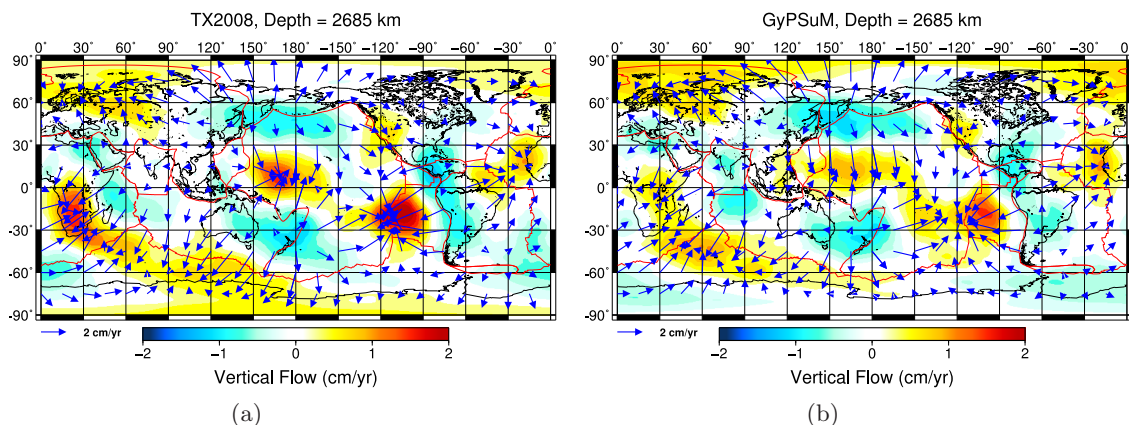


Figure 3.30: Predicted mantle flow at 2685 km depth, calculated using density anomalies from models (a) TX2008 [Simmons *et al.*, 2009] and (b) GyPSuM [Simmons *et al.*, 2010]. Lateral flow (blue arrows) points towards many regions in which scattering is frequently observed at great heights above the CMB (Figure 3.18), such as South Africa and western Africa. These areas are also related to strong upwelling. Other concentrations of scattering points, for example, the west coast of Central America and the southern part of South America, are related to regions of strong downwelling. Areas in which few scatterers are seen or scattering heights are low (close to the CMB) appear to correlate with regions of weak vertical mantle flow, for example the Indian and South Atlantic Oceans. Red lines mark plate boundaries. From Forte *et al.* [2013].

Scattering heterogeneities have previously been observed to be denser than the sur-

rounding mantle by  $\sim 10\%$  based on seismological observations [Wen & Helmberger, 1998; Cao & Romanowicz, 2007; Thomas *et al.*, 2009] and 2.5-10% based on aspect ratio measurements of lower mantle structures (calculated from the PKP ridge in Chapter 2.9) [McNamara *et al.*, 2010; Bower *et al.*, 2011]. Other studies of ULVZ structures using non-scattering probes report similar density increases of 10% relative to the ambient mantle [Garnero & Helmberger, 1998; Rost & Revenaugh, 2003; Rost *et al.*, 2005]. Experimental studies demonstrate that subducted oceanic crust would also be more dense than the ambient lower mantle [Hirose *et al.*, 1999; Karato & Karki, 2001]. Subduction zones may be supplying chemically heterogeneous material to the lower mantle which breaks up into volumes of scale lengths of 1-10 km and collects close to the CMB. This material may then be swept laterally by mantle convection. Material with density contrasts  $\geq 5\%$  is likely too dense to be entrained into mantle convection [McNamara *et al.*, 2010] and this may remain at the CMB and possibly be incorporated into the LLSVPs. Alternatively, the dense anomalous material associated with LLSVPs may come from iron-enrichment, partial melt, or be primordial. Convection within the LLSVPs would also be unable to entrain material with a large density anomaly, although viscous coupling may succeed in partially elevating these anomalies above the CMB (Figure 3.31). Partial entrainment and convection of dense anomalies within the LLSVPs is modelled to concentrate these heterogeneities at the margins [McNamara *et al.*, 2010], providing a suitable mechanism to explain the observed association of large heterogeneity heights close to the LLSVPs (Figure 3.28a). Dynamic models of the lower mantle suggest that these processes are likely to be operating [Li *et al.*, 2014] and so the patterns of scattering sampled with PK•KP may be the result of the action of lower mantle dynamic processes on dense chemical anomalies.

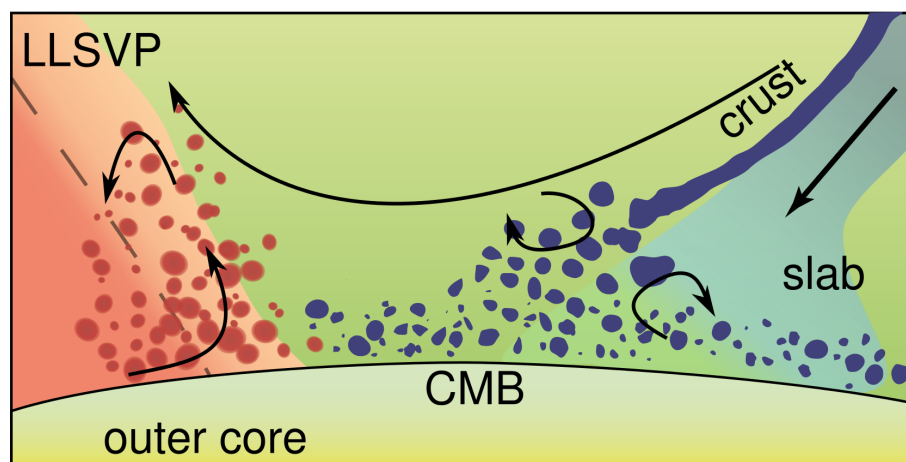


Figure 3.31: Cartoon showing mantle heterogeneities in relation to the large-scale structure. Subducting slabs depositing the basaltic crustal component into the mantle which separates from the slab and is mixed into increasingly small entities and is dispersed throughout the lower mantle. Heterogeneities are more concentrated higher in the mantle where the crust is more coherent and do not show preferential locations closer to the CMB. The slab is slowly assimilated into the ambient mantle. Heterogeneities at the margin of an LLSVP are entrained by the internal convection creating piles at the edge of the strongest velocity anomalies (dashed line). Not to scale.

### 3.11 Summary

Anomalies in the lower mantle on scales of 1-10 km are observed with PK•KP energy generated by scattering. The sources of the scattered energy are likely chemical heterogeneities, unevenly distributed throughout the lower mantle. Localised patches of high heterogeneity concentrations are often correlated with high heterogeneity heights above the CMB. In other regions, scattering heterogeneities frequently lie at, or close to the CMB. Analysis of the spatial distribution of scattering heterogeneities reveals that they preferentially occur close to large patches of high seismic velocities and the edges of the LLSVPs resolved in lower mantle tomography models. I propose that dense chemical anomalies enter the lower mantle in subduction zone regions, are mechanically mixed and broken into a range of scale-lengths suitable to be observed seismically, and then are distributed throughout the lower mantle. Other chemical anomalies may arise from iron-enrichment of lower mantle rocks or partial melting. Convection within LLSVPs may concentrate these dense anomalies at their edges building piles of heterogeneities or drawing them up above the CMB by viscous coupling. This study demonstrates the global interplay between large-scale mantle structure and small-scale heterogeneities.

## Chapter 4

---

# P-wave Travel Times

---

### 4.1 Introduction

The Large Low Shear Velocity Provinces (LLSVPs) in the lower mantle represent volumetrically significant thermal, chemical, or thermo-chemical heterogeneities (see Chapter 1.1.1). Their structure and boundaries have been widely studied (see Chapter 1.2), mainly using S-waves, but much less is known about their signature in the P-wavefield. These anomalous regions are characterised by a shear-wave (S-wave) velocity drop of about 2 % in tomography models and 3-5 % in high-resolution S-wave studies [Ritsema *et al.*, 1997, 1998; Ni & Helmberger, 2003b; Wang & Wen, 2007; Lay & Garnero, 2011] relative to 1D Earth models [e.g. Dziewonski & Anderson, 1981; Kennett & Engdahl, 1991] and extend from the Core Mantle Boundary (CMB) to  $\sim 1000$  km above [Burke *et al.*, 2008; Helmberger *et al.*, 2009]. Models suggest that the location of the LLSVPs is a consequence of the overall dynamics of the Earth's mantle [McNamara & Zhong, 2005; Trønnes, 2010] and that the steepness of the edges may be controlled by the viscosity of the material and the convective support of the structure [Tan & Gurnis, 2005; McNamara & Zhong, 2005; Tan & Gurnis, 2007]. The cause of these velocity anomalies is debated [Christensen & Hofmann, 1994; Robertson & Woodhouse, 1996a,b; Becker *et al.*, 1999; Karato, 2003; Trampert *et al.*, 2004; Labrosse *et al.*, 2007; Brandenburg & van Keken, 2007; Schubert *et al.*, 2009; van Keken *et al.*, 2010; Della Mora *et al.*, 2011; Davies *et al.*, 2012; Deschamps *et al.*, 2012; Li & McNamara, 2013]. The two primary theories are that LLSVPs are the result of purely thermal variation within the mantle, or that they are thermo-chemical structures comprising currently unknown material. The argument whether they are chemically or thermally dominated is based on observations of the magnitude of the velocity reductions, the sharpness of the transition between fast and slow velocities across their boundaries, the ratio of  $V_S$  to  $V_P$  within them ( $R_{S,P}$ ), the anti-correlation of bulk sound velocity and  $V_S$ , observations of increased density, and evidence from Ocean Island Basalts (OIBs) of a geochemically distinct source region in the lower mantle. By studying the Pacific LLSVP using high frequency P( $P_{diff}$ )-waves recorded at USArray, I intend to add observations of the P-wave boundary location, sharpness, and steepness, and P-wave velocity drop to the debate. The material in this chapter has been accepted for publication pending minor revision as Frost, Daniel A.; Rost, Sebastian, 2014. The P-wave Boundary of the Large-Low Shear Velocity Province beneath the Pacific, *Earth and Planetary Science Letters*.

The location of LLSVPs at the CMB is well resolved using S-wave tomographic techniques [for the consistency between different S-wave models see *Lekic et al., 2012*], although resolution of the precise boundaries is poor close to the CMB [*Panning & Romanowicz, 2006; Lay & Garnero, 2011*]. The boundaries can instead be determined with high-resolution travel-time and waveform studies [*To et al., 2005; Ford et al., 2006; He & Wen, 2009, 2012*]. Nonetheless, the shape of the LLSVPs above the D'' region is less well resolved due to a decay of resolution in tomographic images. Despite wide ranging agreement for S-waves, P-wave tomography models fail to agree on the location of the LLSVPs, and no attempt has been made for a high resolution determination of the boundaries of the Pacific LLSVP using P-wave travel times and waveforms, as has been done with S-waves [*He & Wen, 2012*].

Existing studies of travel-time and waveform anomalies associated with LLSVPs have focussed on relatively low frequency S-waves (0.008-1 Hz). They have resolved the precise location of the edge of the Pacific [*He & Wen, 2009, 2012*] and, to a lesser extent, the African LLSVP [*Ritsema et al., 1997, 1998; Wen, 2001; Wen et al., 2001; Ni et al., 2002; Ni & Helmberger, 2003a; Wang & Wen, 2004; Ni et al., 2005; Wang & Wen, 2007*]. Many studies report sharp lateral changes in seismic velocity across the LLSVP boundaries on the order of a few per cent  $\Delta V_S$  over 50-200 km width [*Ritsema et al., 1998; Ni et al., 2002; Ni & Helmberger, 2003b*]. Additionally, strong vertical velocity gradients are found, the most extreme being a change from -12 to -2 %  $V_S$  from the CMB to 300 km above [*Wen, 2001; Wen et al., 2001*]. Waveform modelling has been used to determine the slope of the boundaries of LLSVPs with reports of relatively shallowly dipping edges at  $\sim 28^\circ$  [*Wen, 2001; Wen et al., 2001; He & Wen, 2012*], steeply dipping overturned edges [*Ni et al., 2002*], and edges with slopes of  $\sim 70^\circ$  [*Wang & Wen, 2004, 2007; Helmberger et al., 2009; He & Wen, 2012*]. Where raypaths are available, the S-wave structure of the LLSVPs is fairly well resolved.

Despite the extent to which S-waves have been utilised, P-waves have been little exploited for studying the LLSVPs with limited reports of small (1 to 3 %) velocity drops [*Wyssession et al., 1992; Wyssession, 1996; Wyssession et al., 1999; Wang & Wen, 2007; Sun et al., 2007a*] and even some studies reporting no velocity drops at all [*Helmberger & Ni, 2005; Helmberger et al., 2005*]. Given that boundary sharpness and the relationship between P- and S-wave structure are observations used in the thermal/chemical debate it seems clear that more study is required. USArray [*Meltzer et al., 1999*] offers an excellent opportunity to study velocity anomalies related to the Pacific LLSVP, especially in the north and east of the LLSVP. This extensive array (discussed in Chapter 4.2) is ideally located to observe events in South America and the Western Pacific and its size allows for regional travel-time patterns to be studied. Using the lateral extent of USArray I am able to map the precise location of some boundaries of the Pacific LLSVP. I use travel-times of lower mantle turning and core-grazing P-waves to, for the first time, determine the P-wave LLSVP boundary location. I utilise a wide range of epicentral distances and back azimuths to track the vertical and lateral extent of the LLSVP, respectively. I correct for both upper and mid mantle structure (down to depths of 1600 km) and for crustal structure in the receiver region using the combined P-wave geodynamic tomography model GyPSuM [*Simmons et al., 2010*] and the crustal structure model CRUST1.0 [*Laske et al.,*

2012]. I resolve the P-wave boundary of the LLSVP as the transition from positive to negative travel time anomalies, the zero transition. The observed boundary tracks the 0 % contour of GyPSuM well, but only partially agrees with the S-wave velocity structure.

## 4.2 Method

By measuring variation in travel-times between different paths through the Earth I observe lateral variations in velocity structure. The travel-times of rays traversing different distances and back-azimuths can be measured to resolve changes in velocity with depth and laterally, respectively. Although tomography models involve many paths sampling a plethora of depths and back-azimuths, the smoothing, regularisation, and damping procedures used mean that their spatial resolution of velocity variations is low [Boschi & Dziewonski, 1999; Becker & Boschi, 2002]. Large regional arrays sample similar, but marginally different, paths through the Earth and so variation in travel-times across the array can be used to resolve changes in seismic properties over short distances laterally and vertically.

The travel-time of a wave results from the integrated velocity structure along the whole of its path. By comparing travel-times for paths sampling different regions of the Earth with those predicted by velocity models it is possible to determine local variation in velocity structure. The travel-time difference between the measured and predicted times, the residual, indicates the velocity structure along the whole path relative to the velocity model. It is possible that a path sampling material with both faster and slower seismic velocities (relative to the model) could have the same residual as a path sampling material whose velocity does not deviate from the model. If tomography models are assumed to be accurate representations of mantle velocity anomalies then, using information in the model, the travel-time anomaly can be calculated to correct for structure in a specific depth-range, meaning that the residual is due only to velocity anomalies along the uncorrected part of the path (Figure 4.1). With this method, travel-times can be used to study the velocity anomalies associated with the LLSVPs in the lower mantle.

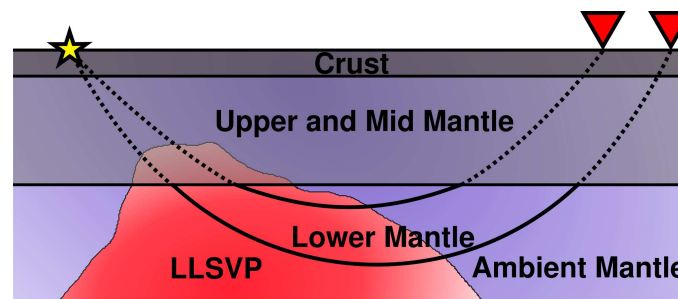


Figure 4.1: Sketch of raypaths from source (star) to receivers (inverted triangles). Dotted paths are corrected for crust, upper and mid mantle structure (from travel-time anomalies predicted using the tomography and crustal models), leaving only travel-time residuals related to lower mantle structure, shown as solid paths. Background colours show broad mantle structure.

The crust arguably shows the strongest lateral velocity variations in the entire Earth. Crustal thickness varies significantly, between  $\sim 7$  and 70 km, along with the material it comprises which, in places, has seismic velocities as low as half that of the upper mantle.

The crust, therefore, must also be accounted for when assessing travel-times for lower mantle structure. Global tomography models often do not have detailed information of crustal thickness and structure and so, by correcting for delay times using a tomography model alone, large residual times can be attributed to the wrong part of the path. Recent models of crustal structure have been compiled using data from receiver function and active source studies, along with constraints from gravity data [Laske *et al.*, 2013]. Applying travel-time corrections for crustal velocity variations at the source and receiver sides of the path (if the source is within the crust) further constrain the origin of travel-time anomalies to the uncorrected part of the ray-path. The remaining travel-time anomaly is representative of the velocity anomaly integrated along the uncorrected path (Figure 4.1). However, multipathing and the Fresnel zone of the wave (described in Chapter 1.5.3) may mean that the travel-time anomaly includes the effects of structure off the raypath. Using higher frequency waves restricts the sampling to closer to the ray-path [Marquering *et al.*, 1998] so that delay times can be attributed to velocities in a finite region of the Earth.

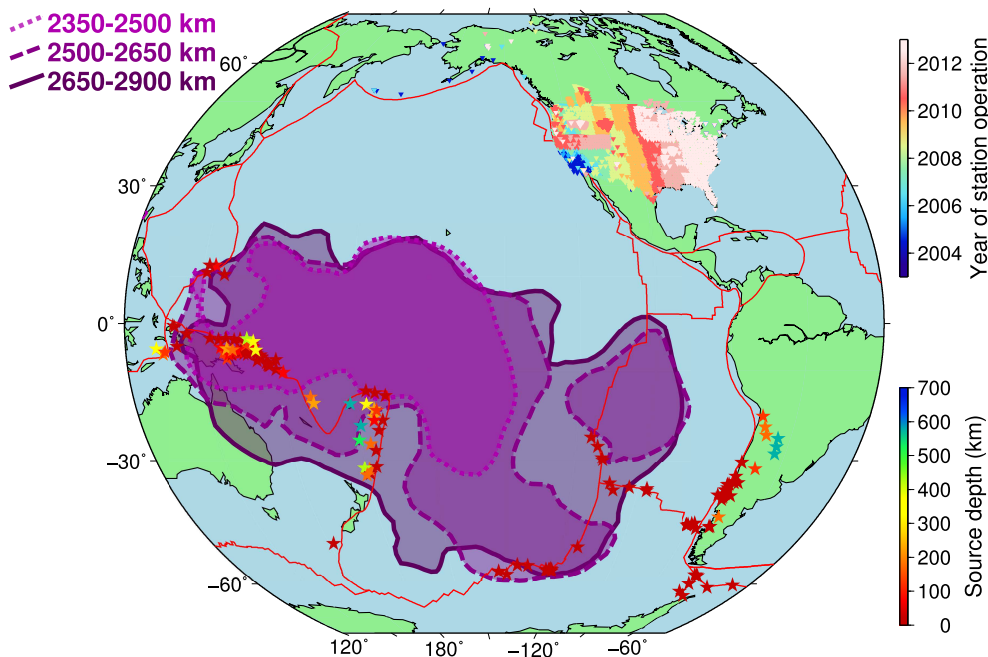


Figure 4.2: Events and stations used in this study. Events are denoted by stars with colour indicating source depth. A full listing of earthquakes used is shown in Appendix Table D.1. Stations are marked as inverted triangles with colour indicating year of deployment. Plate boundaries (red lines) from NUVEL-1 [DeMets *et al.*, 1990] are shown along with the area covered by the Pacific LLSVP, defined by the  $-0.4\%$   $V_P$  contour in GyPSuM [Simmons *et al.*, 2010], shown as the purple contours and shaded areas. The LLSVP contours are drawn at 2350-2500 km depth (dotted line), 2500-2650 km (dashed line), and 2650-2900 km (solid line), defined by the depth slices in the tomography model.

I employ data from USArray, mainly the Transportable Array (TA) with additional permanent “backbone” stations. USArray has an approximate station spacing of 70 km and is deployed on a grid system (Figure 4.2). The array has been operational between 2004 and 2014, moving across the USA with stations being relocated roughly every two years. At any one time, there have been between 300 and 600 operational stations. Using this network configuration allows for a wide sampling of the lowermost mantle, both laterally

and vertically, due to the large distance and azimuthal range covered by the stations.

I search the Reviewed Events Bulletin (REB) for events with magnitudes of 5.0 and above and select those that are between  $\sim 85^\circ$  to  $\sim 95^\circ$  from the centre-point of the array, thus limiting the study to waves sensitive to the lowermost mantle. Although this range of event to centre-point distances is narrow, the extent of USArray means that within these events there are stations that sample a greater range of distances. I concentrate on events from the Indonesian Arc, Tonga Trench, south-eastern Pacific, and South-American Trench. The great-circle paths of these events to USArray are best suited to sampling the northern and eastern edges of the Pacific LLSVP. Although events at any depth, including crustal events, are used in areas with low seismicity, I preferentially use events with depths  $\geq 30$  km due to their simpler source mechanisms (resulting in simpler first arrivals that are easier to pick) and to reduce travel-time anomalies from crustal and uppermost mantle heterogeneities in the source region. The selected events and stations are shown in Figure 4.2 (and Appendix Table D.1).

For each event, data are de-spiked, re-sampled at 40 samples/s, and bandpass filtered. I filter data between 0.5 and 1.6 Hz, order 2, as this was found to be best to extract P and  $P_{diff}$  arrivals from the noise, where the order controls the rate of decay of energy at frequencies outside of the pass-band. Noisier events, where the P-wave is less clear relative to the noise, are filtered with order 3 or 4, defining a sharper frequency cut-off. To retain as much waveform information as possible, I use the lowest possible order filter that clearly reveals the first arrivals. I only consider traces at distances between  $60^\circ$  and  $120^\circ$  to restrict analysis to raypaths turning in the lower mantle. I then visually inspect each trace to decide whether to include it in further processing, based on the P-wave arrival being obvious above the noise.

I use an adaptive stacking routine [Rawlinson & Kennett, 2004] to find the best alignment of an ensemble of network stations and to determine travel-time deviations from a 1-dimensional Earth model. The adaptive stacking first applies a move-out correction based on distance through a 1-dimensional Earth model (PREM [Dziewonski & Anderson, 1981]) and iterates to minimise residual travel-times by maximising the amplitude and coherence of a stack of all traces. I correct for crustal structure on both the source and receiver side and topography on the receiver side by applying travel-time corrections determined from CRUST1.0 [Laske *et al.*, 2012], and for upper mantle structure from the underside of the crust down to 1600 km depth (the shallowest turning depth in the collection) by ray-tracing through the P-wave component of GyPSuM [Simmons *et al.*, 2010] (Figures 4.3 and 4.4). All travel-time deviations are calculated relative to PREM. The source side correction applied is static and is only used for events shallower than 24 km as this is the thickness of the crustal layer in PREM. Using the crustal thickness and velocities from PREM would, particularly in oceanic regions, be inappropriate for waves travelling through the lithosphere which is often a very different velocity to that in PREM. The crustal and mantle corrections allow me to attribute the remaining travel-time residual to structure at depths greater than 1600 km. Travel-time residuals are plotted at the location and depth of the turning point of the ray as this represents the region in which the ray spends the most time and so has the potential to accumulate the largest delay time (Figure 4.5).

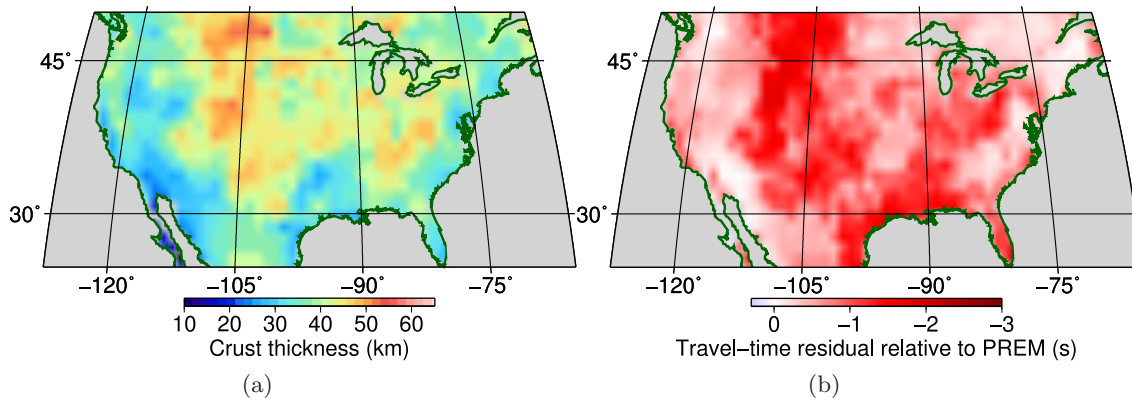


Figure 4.3: Crustal structure taken from CRUST1.0 [Laske et al., 2012]. (a) Crustal thickness and (b) travel time residuals resulting from the crustal structure in each  $1^\circ \times 1^\circ$  cell. The magnitude of the negative residual is roughly correlated with crustal thickness and, therefore, to some degree, topography, except in areas of high sediment thickness, e.g. the southern coast of USA, which are significantly slower than PREM.

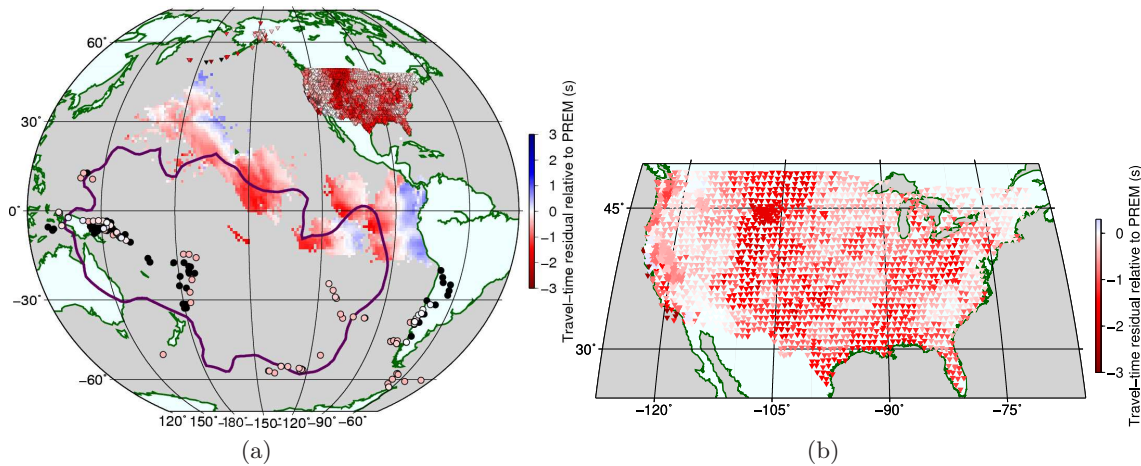


Figure 4.4: Applied crustal and mantle travel-time corrections relative to PREM for (a) the whole path and (b) at each station in USArray. Crustal structure is determined from CRUST1.0 [Laske et al., 2012] and mantle structure is determined from the *P*-wave component of the GyPSuM model [Simmons et al., 2010]. The  $-0.4\%$   $V_P$  contour at 2650-2900 km from GyPSuM is shown by the purple line. Circles display corrections for crustal structure at the source. Black circles indicate sources deeper than 24 km to which no source-side crustal correction is applied. Triangles show corrections for crustal structure at each station in USArray, averaged over all events which use the station. The background shows corrections for mantle structure along the raypath from the surface down to 1600 km, plotted at the turning point of each ray, averaged over all rays. Mantle corrections are applied for each source-receiver combination, receiver-side crustal corrections are applied for each station, and source-side crustal corrections are applied as a DC shift to all rays in an event, for events that are shallower than 24 km depth, the thickness of the crustal layer in PREM. Smearing of mantle heterogeneity along the ray-path is apparent in Figure a as significant negative corrections are applied at ray turning points outside the tomographic extent of the Pacific LLSVP. The crustal corrections applied for each station are directly related to the crustal structure in CRUST1.0 shown in Figure 4.3.

The boundary of the LLSVP is defined by obvious trends in the travel-time residuals.

I distinguish between cases where the transition can be clearly identified, i.e. where both positive and negative residuals are separated by zero residual, and where a trend towards the transition is observed, i.e. where decreasing or increasing residuals are seen but no change in sign is observed. As the boundary location changes with height, I consider each event individually and partition turning points into a series of 100 km thick radial bins from the CMB upwards. Events with too few turning-points in a height bin to show either the boundary or a trend towards the boundary are disregarded. For each event, I trace the LLSVP boundary in each height bin, with extent controlled by the ray coverage. For each height bin, I then consider the boundaries of all events together and define a single boundary which best fits all the individual measurements (Figure 4.6).

As an additional measure of the LLSVP boundary, I calculate the magnitude of the gradient of travel-time residuals. Data are partitioned into  $0.5^\circ \times 0.5^\circ$  (lateral) cells and the average residual in the cells is calculated. Where data fill adjacent cells, the gradient of the travel-time residuals is calculated and I choose a boundary defined by a line of highest gradient, indicating the sharpest transition (Figure 4.7). Although this method is more robust as it analyses only the pattern of residual travel-times, rather than the absolute value which can be affected by source depth errors (discussed in Chapter 4.4), it is only applicable in regions of dense sampling (adjacent cells must be filled to be able to calculate a gradient). In comparison, the absolute travel-time residuals can be used to locate the boundary when sampling is poor, but the location will be more sensitive to errors in travel-time. In general, in well sampled regions the results of both methods agree well (Figures 4.6 and 4.7).

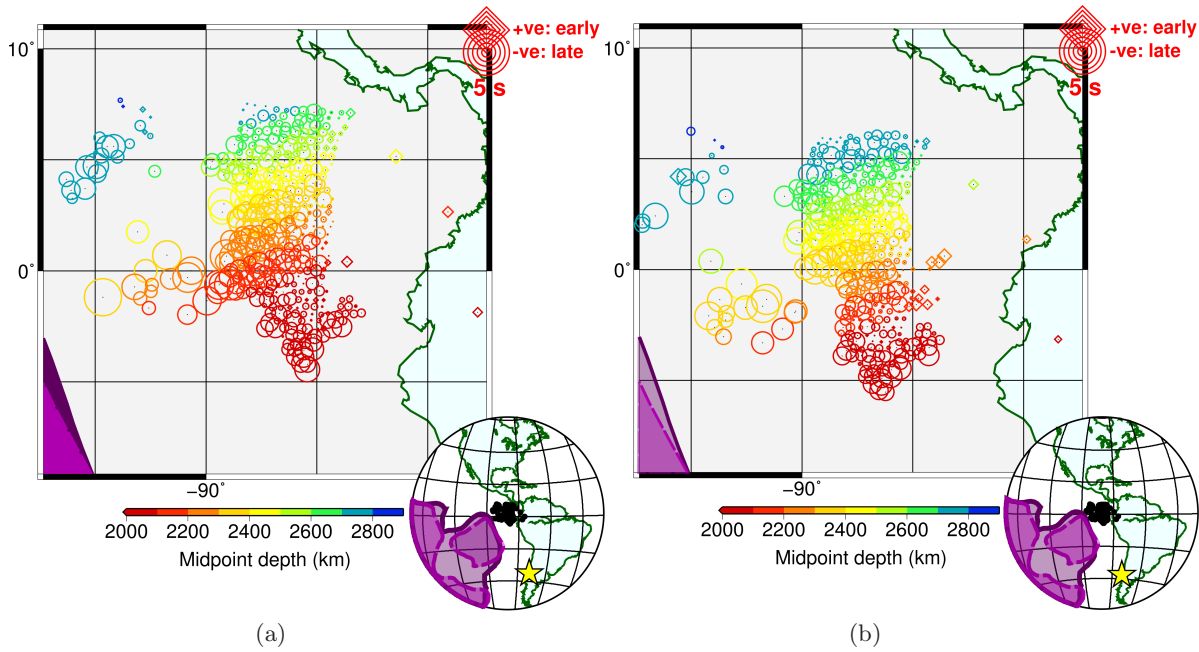


Figure 4.5: Delay times shown at turning point location and depth for two separate events. Diamonds denote early, and circles show late arrivals (by up to 5 s) indicating fast and slow velocities in the lower mantle, respectively. Delay times are corrected for crust and mantle structure from the surface to 1600 km depth. Events occurring on (a) 28/02/2010 at  $34.97^\circ$  S,  $71.69^\circ$  W at  $46.5 \pm 4.5$  km depth, and (b) on 23/04/2010 at  $37.54^\circ$  S,  $72.92^\circ$  W at  $43.1 \pm 18.3$  km depth. The two events are closely located and sample the same region of the lower mantle. LLSVP contours from GyPSuM are shown as purple lines, as defined in Figure 4.2. No source-side crustal correction is applied as both events occur below the crust. Inset shows source location as a yellow star, and ray turning points as black circles. Very similar delay-time patterns are seen for both events suggesting that the signals observed are real and not dependent on the event used or on the processing.

### 4.3 Results

I find laterally varying delay times at all depths greater than 2000 km with some of the largest deviations observed in the lowermost 300 km of the mantle. I detect patterns of the delay times that are consistent between different source-receiver combinations sampling comparable regions of the lowermost mantle (Figure 4.5), showing that the method is robust and the delay times are the result of the mantle structure and not artefacts of the processing. The segments of the LLSVP boundary resolved by individual events show very good agreement and excellent continuity between events, allowing the construction of a continuous boundary. The boundary is complex with small scale variations. The resolved P-wave LLSVP boundary is broadly consistent with the shape of the LLSVP boundary as defined in both P- and S-wave tomography models (Figures 4.6, 4.8, and 4.9a), nevertheless, there are deviations from the tomographically defined structure. The boundary can also be followed in height up from the CMB, dependent on ray coverage.

By calculating the gradient of the travel-time residuals and considering both the magnitude (trend of changing travel-time residuals) and its direction, I am better able to observe structure within regions of predominantly fast or slow delay-times in which transitions be-

tween positive and negative delay times cannot be observed. I detect sharp increases in gradient around large negative travel-time residuals within the lower 200 km of the mantle, which are consistently observed in all events sampling the same region. In particular, along the northern edge of the LLSVP at  $\sim 20^\circ$  N,  $\sim 164^\circ$  W (dotted line in Figures 4.7a and 4.7b, and the southern-most points highlighted in Figure 4.10b). These sharply defined regions are up to  $5^\circ$  wide and show travel-time delays of up to 4 s, among the highest detected in this study, relative to the corrected model. Due to the large travel-time anomaly, their small size, and sharp boundaries I interpret these areas as ULVZs.

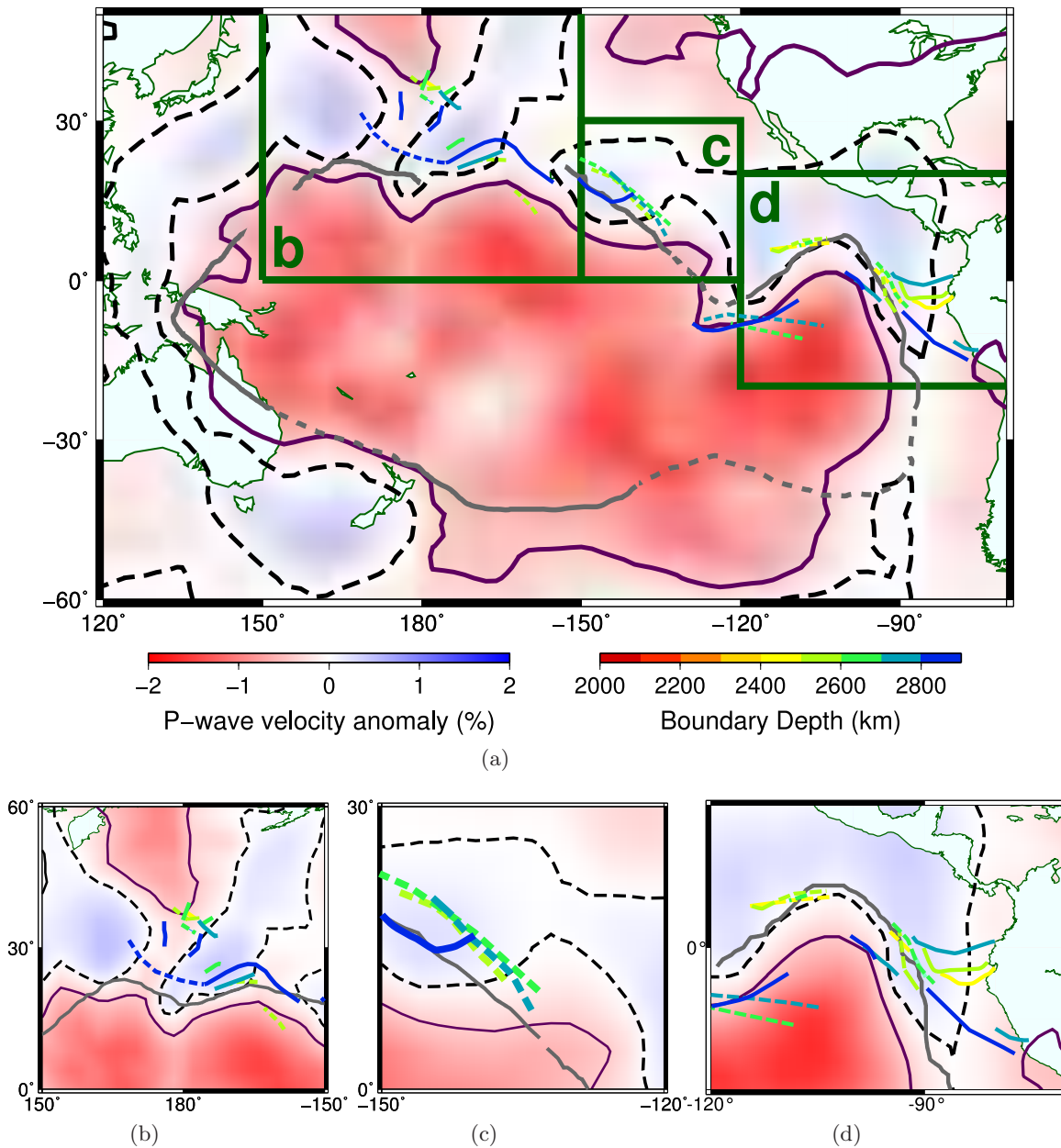


Figure 4.6: Location of the P-wave LLSVP boundary determined using the zero transition of travel-time residuals and trends in residuals, overlaid on tomography for the lowermost mantle from 2650 km to the CMB from GyPSuM (left colour scale). (a) LLSVP boundary at various heights (right colour scale). Solid lines demarcate the observed zero transition and dashed lines indicate where a trend towards the boundary (increasing or decreasing delay times) is observed but the actual transition (as a clear zero delay time) is not seen. The boundary of the Pacific LLSVP determined with S-wave travel-time residuals by He & Wen [2012] is shown (grey line), along with the  $-0.4$  and  $0.0$  %  $V_P$  contours in GyPSuM (purple and black dashed lines, respectively). Three subregions of the travel-time boundary, marked by dark green lines, are shown in greater detail: (b) north-west, (c) north-east, and (d) east.

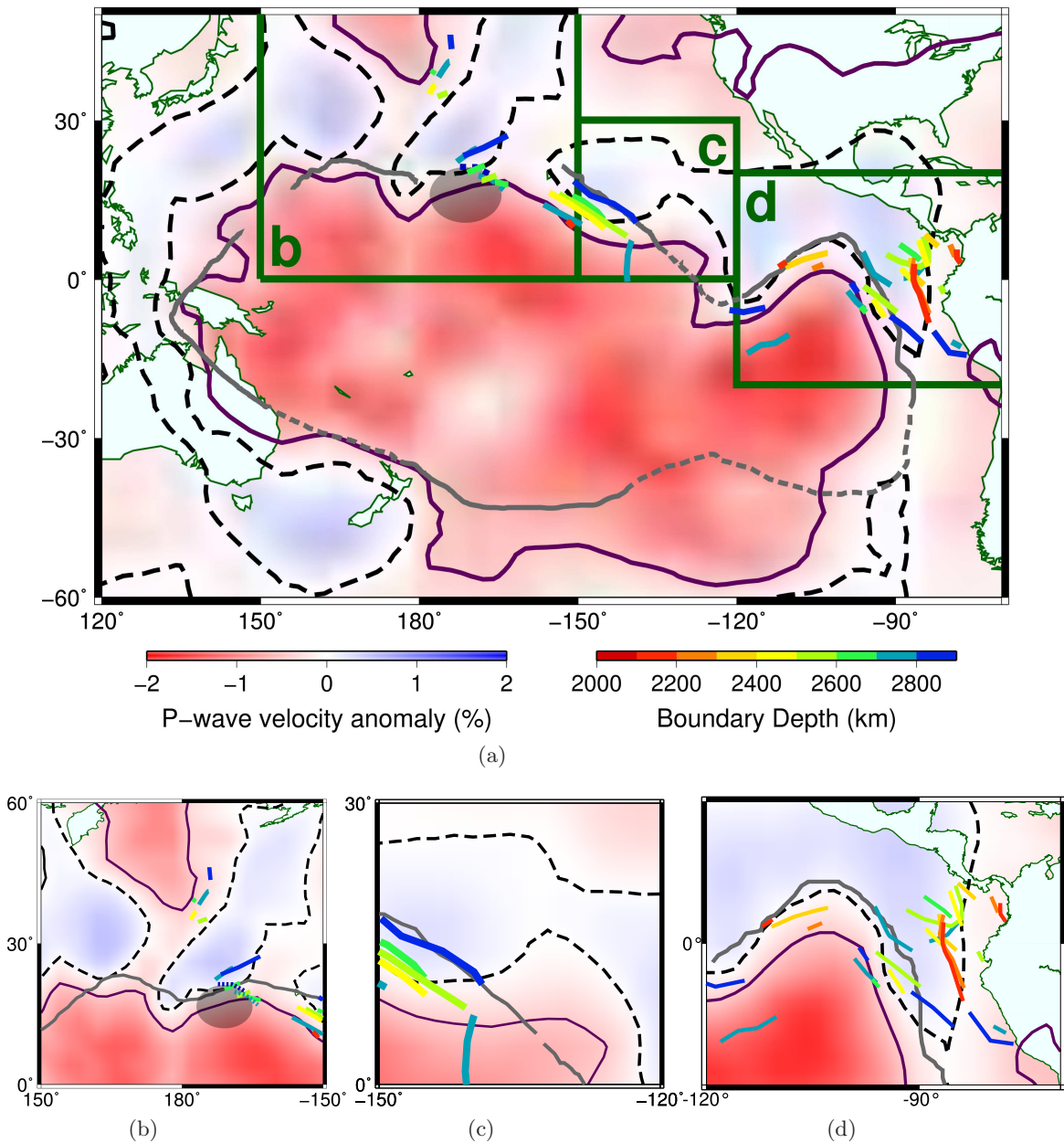


Figure 4.7: Location of the *P*-wave LLSVP boundary (as in Figure 4.6) from delay-time gradients, overlaid on tomography for the lowermost mantle from 2650 km to the CMB from GyPSuM (left colour scale). (a) LLSVP boundary at various heights (right colour scale). Solid lines show where the boundary is observed, and dotted lines and the grey ellipse show the region of a suspected ULVZ characterised by very high velocity gradients. The boundary of the Pacific LLSVP determined with *S*-waves travel-times residuals by He & Wen [2012] is shown (grey line), along with the  $-0.4$  and  $0.0$  %  $V_P$  contours in GyPSuM (purple and black dashed lines, respectively). Three subregions of the gradient boundary, marked by dark green lines, are shown in greater detail: (b) north-west, (c) north-east, and (d) east.

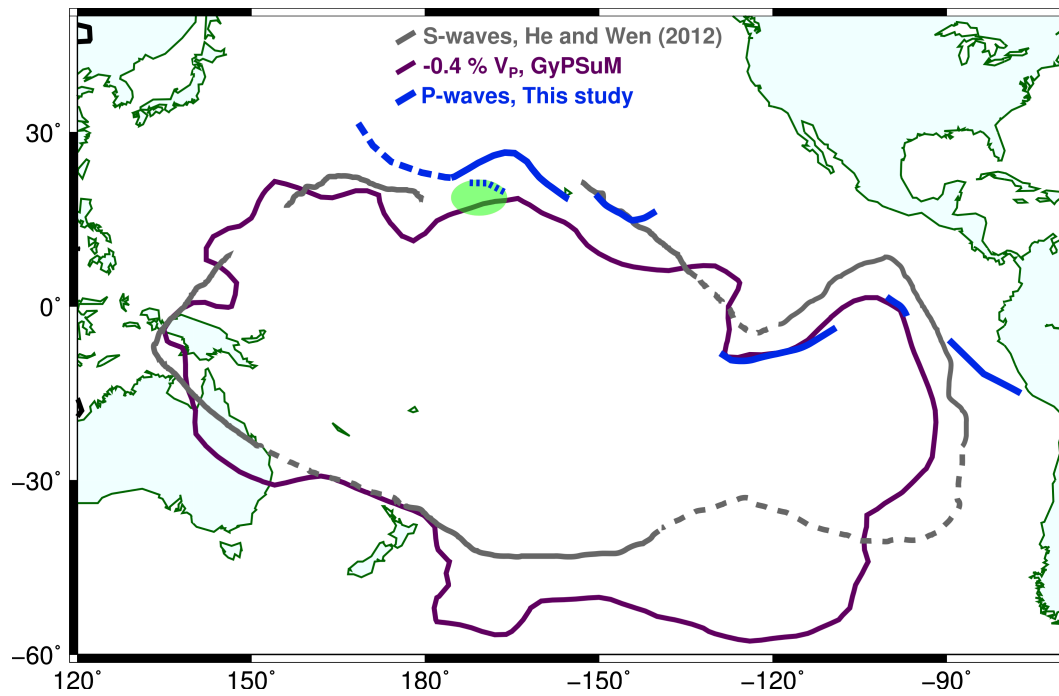


Figure 4.8: Best fitting P-wave LLSVP boundary determined using travel-time anomalies in the height bin from the CMB to 2800 km depth, taken from Figure 4.6. The LLSVP boundary determined using S-waves [He & Wen, 2012] and the  $-0.4\% V_P$  iso-velocity contour from GyPSuM are shown as dark grey and purple lines, respectively. The region of a suspected ULVZ, indicated by a high travel-time residual gradient in the height bin from the CMB to 2800 km depth, is marked by the dotted blue line and the resolved extent is displayed by the green ellipse, as in Figure 4.10.

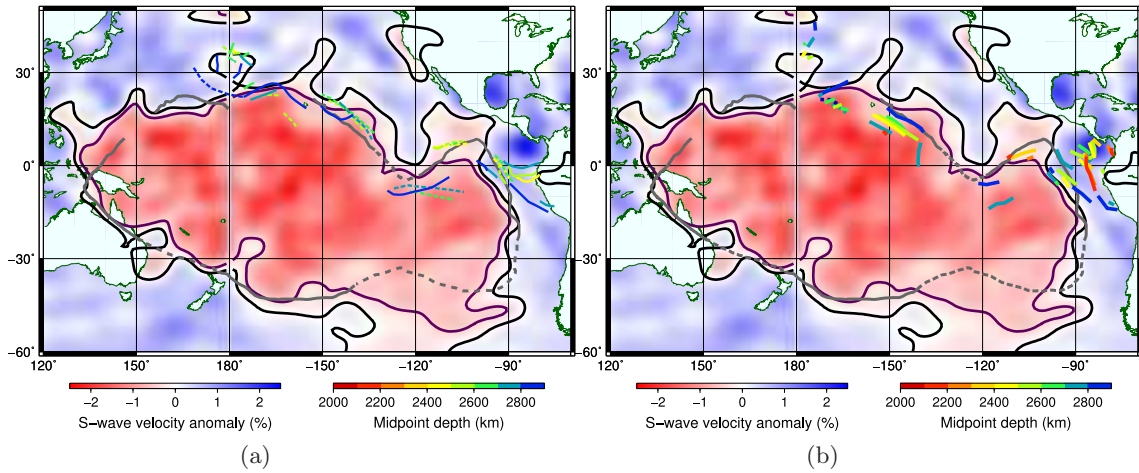


Figure 4.9: Location of the determined *P*-wave LLSVP boundary, overlaid on *S*-wave tomography for the lowermost mantle from 2800 km to the CMB from *S40RTS* (left colour scale) [Ritsema et al., 2011]. (a) LLSVP boundary drawn from travel-time residuals at various heights (right colour scale). Solid lines demarcate the observed zero transition and dashed lines indicate where a trend towards the boundary (increasing or decreasing delay times) is observed but the actual transition (as a clear zero delay time) is not seen (as in Figure 4.6). (b) LLSVP boundary determined from delay-time gradients (as in Figure 4.7). Solid lines show where the boundary is observed, and dotted lines show regions of a suspected ULVZ characterised by very high velocity gradients. The boundary of the Pacific LLSVP determined with *S*-waves travel-times residuals is shown (grey line) [He & Wen, 2012], along with the  $-0.4\%$  and  $0\%$   $V_S$  contours in *S40RTS* (purple and black line, respectively).

I use two methods to define the *P*-wave LLSVP boundary: (1) the area of transition between positive and negative travel-time residuals (the “travel-time residual method”), (2) the largest magnitude of the gradient of the travel-time residuals (“the gradient method”). Often the boundary appears to be very sharp, with the transition occurring between two turning points, over as little as 40 km at the eastern edge of the LLSVP (Figures 4.10a, c, e, g, and 4.11). This is consistent with the results from *S*-wave studies for the African LLSVP which shows similar sharpness [Ni et al., 2002]. However, the assumption of a sharp boundary may be inappropriate in some locations; for example, the northern edge of the LLSVP where the boundary appears to be more diffuse (Figures 4.10b, d, f, h, and 4.12). The regions of dominantly positive residuals and dominantly negative residuals appear to be separated by as much as  $\sim 2^\circ$  (120 km) of small, mixed positive and negative residual travel-times. This transitional region is broader at the CMB and narrows upwards. To the north of the transitional boundary I detect a rapid change in residual time to positive residuals, which appears almost linear (dashed line in Figures 4.10d, f, h) while south of the transitional region the change to negative residuals is more gradual and complex in shape. Although I do not assess the waveforms further, I note that there is evidence for wavelet broadening along the northern edge of the LLSVP which is not observed for events sampling the eastern edge. However, this could be due to a smaller range of azimuths available for the eastern side. Nonetheless, the boundary is clearly evident in the travel-time residuals. Alternatively, this region of mixed positive and negative travel-time residuals could be the result of the ray geometry relative to the edge of the LLSVP causing

rays to travel through both slower and faster material away from the turning point of the ray. On the eastern side of the LLSVP rays are more likely to travel either outside or inside the LLSVP, but due to the small Fresnel zone of the data are unlikely to travel through both, and so do not show a broad variable region.

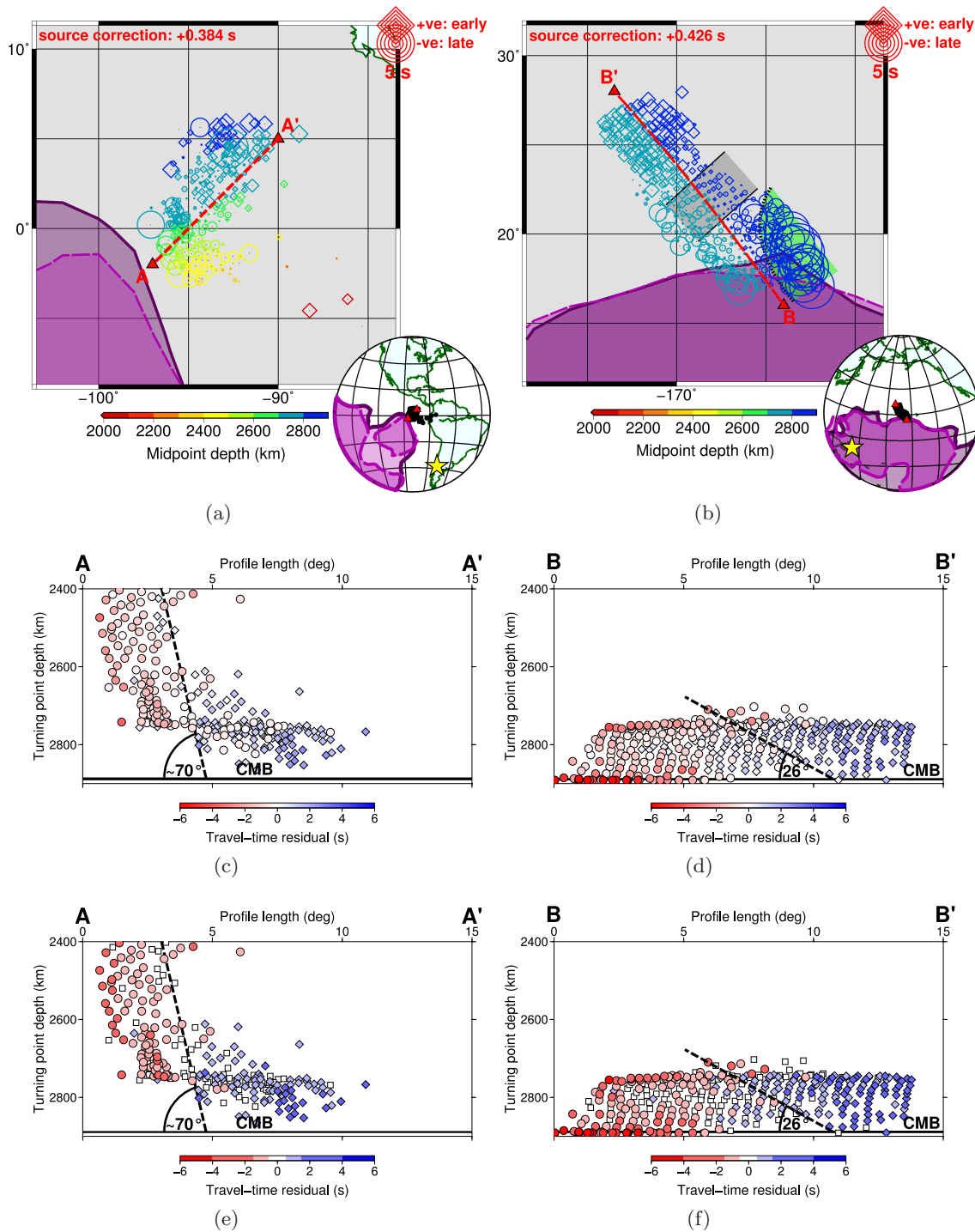


Figure 4.10: Continues on to next page.

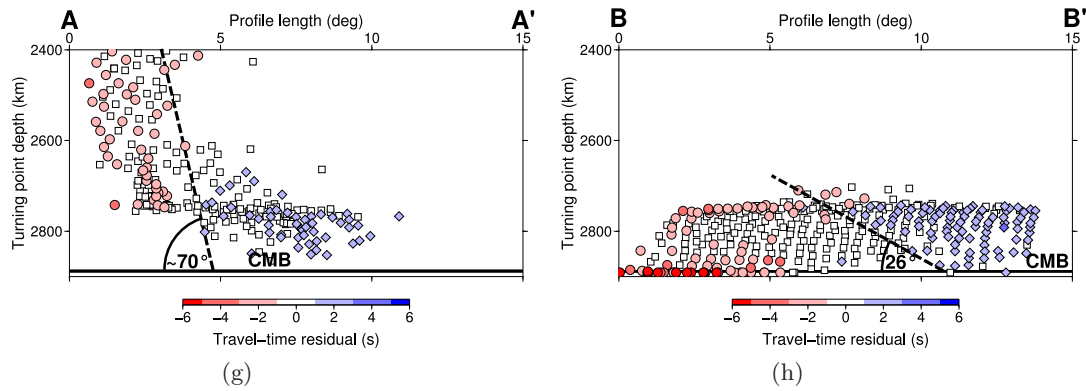


Figure 4.10: Residual travel-times shown at turning point location and depth. Diamonds denote early, and circles show late arrivals (by up to 5 s) indicating fast and slow velocities in the lower mantle, respectively. Events occurring on (a) 31/12/2006 at  $37.9^\circ$  S,  $71.24^\circ$  W at  $47 \pm 17.1$  km depth, and on (b) 28/06/2007 at  $8.01^\circ$  S,  $154.52^\circ$  E at 10 km depth. A region of travel-time residuals with varying sign is indicated by grey shading. A region of strong, negative travel-time residuals, interpreted as the location of a ULVZ, separated from the rest of the residuals by a large magnitude gradient of the travel-time residuals, is shown by a dotted line with green shading. The  $-0.4\%$   $V_P$  iso-velocity contours from GyPSuM at 2500-2650 km and 2650-2900 km (representing the LLSVP boundary) are shown as purple contours and shaded areas, as defined in Figure 4.2. Inset shows source (star), ray turning points (circles), and cross-section end points (triangles). Cross-sections through turning points along the red section line shown in the maps for events on (c, e, g) 31/12/2006 and (d, f, h) on 28/06/2007. The vertical scale is exaggerated by a factor of 2.7. Figures (c) and (d) show travel-time residuals as symbol colour while figures (e), (f), (g), and (h) use more saturated colour scales to highlight the strongest travel-time variations and more clearly mark changes. Dotted lines separating the fast and slow regions are picked by following pronounced changes in magnitude and sign of the travel-time residuals. Travel-time residuals on the eastern edge of the LLSVP show a sharp transition from positive to negative residuals (c, e, g), whereas on the northern edge the transition is broader, especially close to the CMB, with a sharp and straight boundary on the northern side of the transition and a complex boundary on the southern side (d, f, h). Low travel-time residuals ( $-0.5$  to  $+0.5$  s, and  $-1$  to  $+1$  s, for figures (e) and (f), and (g) and (h), respectively) are shown as white squares. For larger versions of figures c-h see Appendix Figure D.1.

Using residual travel-times determined at different heights, I trace the boundary of the LLSVP from the CMB up to  $\sim 500$  km above the CMB (up to  $\sim 700$  km in some regions) (Figures 4.6 and 4.7). I observe variations in the steepness of the detected boundary between the east, and the north-west and north-east sides of the LLSVP, the regions best resolved by the data. Using cross sections through the travel-time residuals at the turning points, I visually define the boundary and estimate the slope. I find that the eastern edge is steep at  $\sim 70^\circ$  (relative to the horizontal) dipping roughly to the north-east, while the northern edge is shallower at  $\sim 26^\circ$ , dipping north-west (Figures 4.10c and 4.10d).

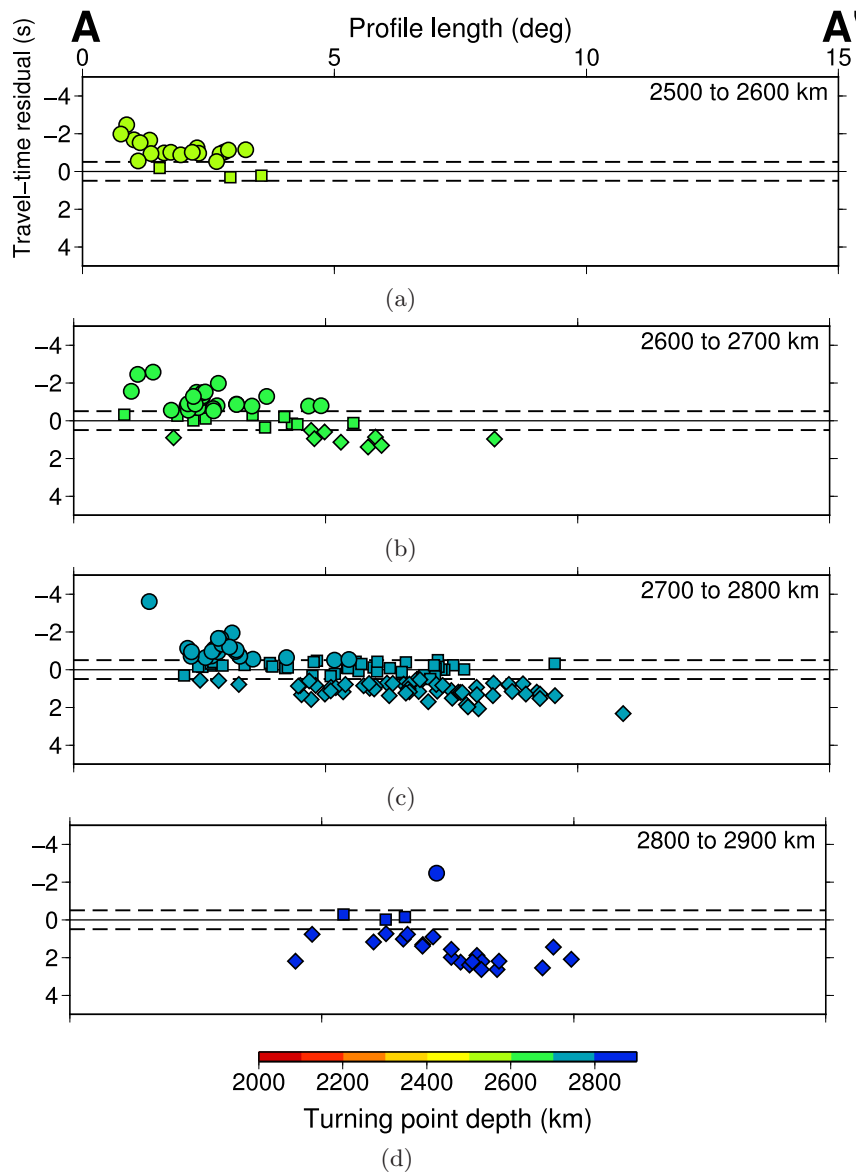


Figure 4.11: Residual travel-times plotted at the turning point distance along a profile transecting the east boundary of the Pacific LLSVP (red dashed line in Figure 4.10a) for rays turning in 100 km thick height bins from 2500 km above down to the CMB. Diamonds denote early and circles show late arrivals while squares show low travel-time residuals (between  $-0.5$  and  $+0.5$  s, also indicated by the dashed line). In each height bin, the transition from positive to negative residual travel-time occurs over a short lateral distance demonstrating the sharpness of the eastern LLSVP boundary. The position of the transition only moves along the profile slightly with changing turning point height indicating the steepness of the boundary.

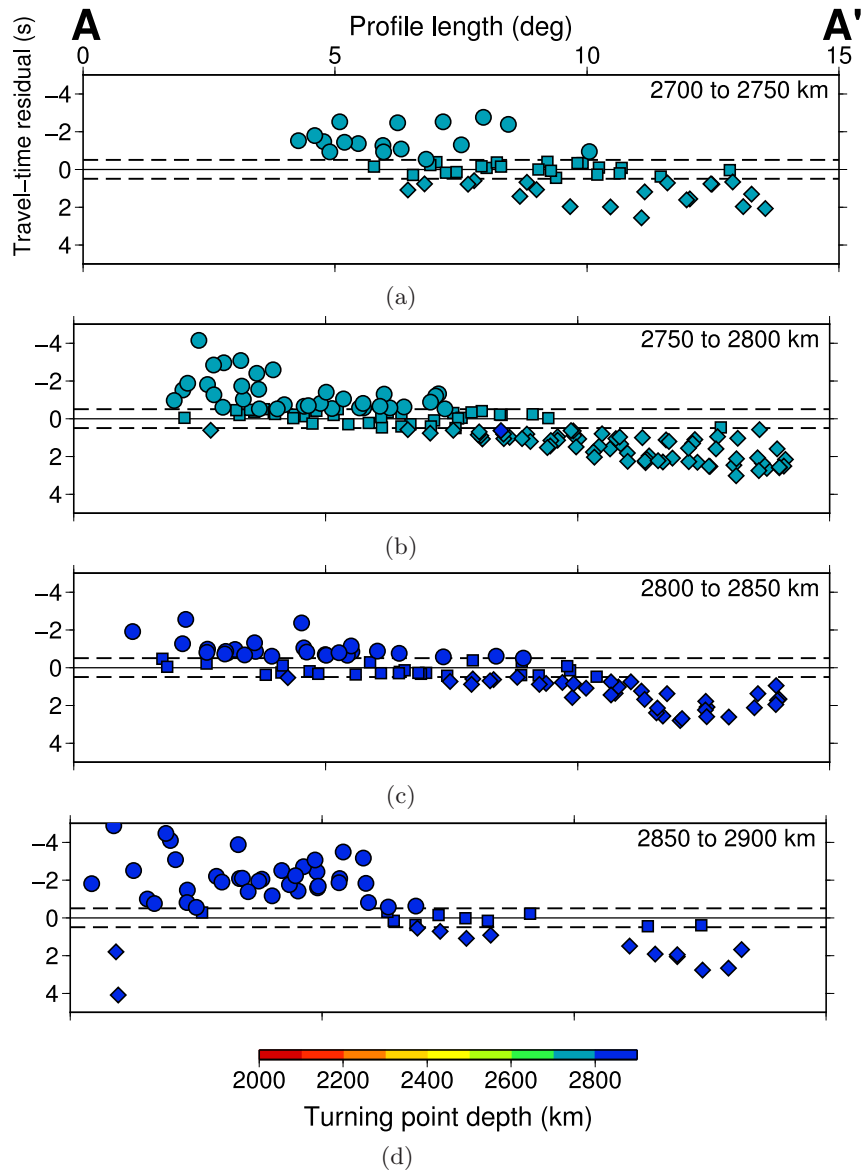


Figure 4.12: Residual travel-times plotted at the turning point distance along a profile transecting the northern boundary of the Pacific LLSVP (red dashed line in Figure 4.10b) for rays turning in 50 km thick height bins from 2700 km above down to the CMB. Diamonds denote early and circles show late arrivals while squares show low travel-time residuals (between  $-0.5$  to  $+0.5$  s, also indicated by the dashed line). In each height bin, the transition from positive to negative residual travel-time occurs over a relatively large lateral distance indicating that the boundary of the LLSVP is broader than on the eastern side (Figure 4.11) while the position of the transition from positive to negative residuals moves along the profile with changing turning point height suggesting that the boundary is also less steep than the eastern side, dipping at a shallower angle.

#### 4.4 Sources of Error

The boundaries of the LLSVP inferred by the P-wave data are very consistent and stable between events (Figure 4.5) and the crustal and mantle corrections for 3-D velocity heterogeneity correct for most structure along the path above the region of interest (the lower 1300 km of the mantle). Nonetheless, there are several potential sources of error that might affect the location of the detected boundary of the LLSVP.

Due to the source-receiver locations, there are dominant back-azimuths for individual events, which does not allow for crossing paths. The lack of crossing paths might lead to smearing of the travel-time anomaly along the raypath. Rays may encounter lower mantle velocity heterogeneity outside the LLSVP which is then mapped to the ray turning point (demonstrated in Figure 4.4a). There may be additional smearing caused by assuming that the turning point represents the main source of the travel-time anomalies, while in actuality the travel-time anomaly is accumulated along the path through the lowermost mantle. This could account for the northern edge of the LLSVP being traced  $\sim 10^\circ$  further north than the  $-0.4\%$  contour in the tomography model (Figure 4.6). The rays in this region will travel through material both slower and faster than PREM, inside and outside of the LLSVP, likely masking the precise point of transition by reducing its apparent magnitude. This problem also affected S-wave studies of the boundary [He & Wen, 2012], and is a possible reason for the good agreement between both studies in this region. Further studies using waveform modelling might help to alleviate the issue. However, the frequencies used here are currently inappropriate for full 3-D wavefield modelling. The boundaries defined using the gradient of the residuals agree well with those determined by the zero crossing of the travel-time residuals in regions where rays travel parallel to the boundary, but plot further towards the centre of the LLSVP than the zero crossing where the ray travels perpendicular to the boundary (Figures 4.6 and 4.7), possibly related to smearing.

The REB catalogue is used due to the high quality source locations reported (Appendix Table D.1). Event lateral location is, on average, defined to within  $\pm 10$  km of the published hypocentre. Depth, however, is often less well constrained: half of the events used do not have a published depth, and of those with depths the average errors are  $\pm 7$  km. Prior to processing, I assign a depth of 10 km for all events where the depth has not been reported in the catalogue. The extent to which these depth variations affect the resulting delay-time patterns is measured. For hypocentres within the upper crust, depth uncertainties affect the pattern considerably; for example, between a source at the surface and at 10 km depth, for a ray reaching the CMB, there is  $\sim 1$  s travel-time difference relative to the 1-dimensional model, once 3-dimensional corrections are taken into account. However, between sources at 10 km and 20 km depth there is only  $\sim 0.03$  s travel-time difference. There is a negligible variation in turning point locations in both circumstances. Therefore, source depth uncertainty is only significant for events shallower than 10 km depth. The travel-time shifts introduced by a source depth error would affect all stations equally and so change the location of the boundary laterally, but the resolved shape of the boundary would be unaltered. The amount by which the boundary would move laterally depends on the gradient of the velocity anomalies around the boundary.

The applied source-side crustal structure corrections are static and are not varied for ray paths of different distances or azimuths. I believe that this is suitable, given that the difference in the section of the crust sampled by two rays, even with vastly different take-off angles and back-azimuths, is negligible when compared to the  $1^\circ$  resolution of the crustal model used [Laske *et al.*, 2012]. Therefore, inaccuracies in the source depth will affect the delay-time for all stations in the same way, increasing or decreasing all delay-times as a DC shift. The transition from positive to negative delay times will be affected,

and so will the point at which the boundary is defined. However, the pattern of delays relative to each other will not change. In these situations, therefore, the magnitude of the gradient is a better measure of the location of the LLSVP boundary. Gradients can only be calculated where there are rays sampling adjacent locations. If sampling of the lower mantle is sparse then gradients cannot be determined. Also, care must be taken not to pick sharp changes in gradient resulting from lack of sampling as a boundary, a problem which can be easily avoided when using travel-time residuals.

Body-waves are sensitive to off-ray-path structure [Marquering *et al.*, 1998, 1999]. However, this is only significant for intermediate and long period waves. Using high-frequency P-waves ( $\sim 1$  Hz) with the related small Fresnel zone makes this irrelevant and approximation to ray theory allows good predictions of the sampling area. The width of the first Fresnel zone for P-waves sampling the lower mantle with a dominant frequency of 1 Hz is  $\sim 100$ -140 km [Sato & Fehler, 2008], equivalent to the distance between three stations of the Transportable Array. Therefore, finite-frequency effects may affect the exact location at which the LLSVP boundary is defined, but the location will still be accurate to within  $2^\circ$  orthogonal to the ray path at the turning point of the ray.

The velocity drops observed are likely sufficient to cause refraction of rays, thus affecting the region of the mantle sampled. However, I use a 2-dimensional ray-tracer which cannot account for this, therefore, it only provides an approximate location of the velocity changes. Using a 3-dimensional ray-tracer could resolve these issues although the tomographic models involved are of low resolution relative to the high-frequency waves used here and would not accurately represent the velocity structure on these scales.

Following crustal and mantle corrections, the remaining residual travel-times represent the deviation of the wave arrival time from that predicted by a 3-D tomography model. Any further errors are due to tomography models not sufficiently explaining Earth structure on the scales imaged here and are unavoidable in high frequency studies [Thorne *et al.*, 2013b].

## 4.5 Discussion

I map out spatially limited but detailed sections of the P-wave boundary between the Pacific LLSVP and the surrounding mantle. The boundary is resolved to be locally complex and of varying steepness. The location of the boundary generally agrees well with that determined using S-waves [He & Wen, 2012] (Figure 4.8), and no decorrelation of the structure for the different wave types is observed, except at the eastern end of the boundary. Local variations of the P-wave and S-wave boundaries do not allow the different resolution of these two probes to be compared.

In the north-west (Figures 4.6b and 4.7b) the LLSVP boundary slopes shallowly to the north-west. However, ray coverage in this location does not allow the boundary to be traced to depths less than  $\sim 2600$  km, 300 km above the CMB. At the CMB, the boundary is mapped further north than indicated by the 0.0 % or -0.4 %  $V_P$  contours in the tomography model. The high resolution S-wave study [He & Wen, 2012] does not have coverage of the boundary in this location and so the two studies cannot be compared. On the other hand, the boundary matches the -0.4 %  $V_S$  iso-velocity contour in the S-wave model S40RTS well (Figure 4.9). The difficulty of delineating a well defined boundary from the travel-times

in this region that is in agreement with tomographic models might stem from the broad band of low residual travel-times, which is possibly due to multipathing effects (Figure 4.10d). Alternatively, this may represent a region of material with transitional properties from the LLSVP to ambient mantle. This boundary shows further complexity with a 50 km thick layer of small amplitude positive and negative residual travel-times bounded above and below by negative residuals, within the region defined as the LLSVP (Figure 4.10h). While this could be the effect of faster material sampled outside of the LLSVP being smeared along the path it could also be the result of double-crossing of perovskite-post-perovskite transition [Hernlund *et al.*, 2005] from relatively slow perovskite above to faster post-perovskite and back again to perovskite close to the CMB (and possibly ULVZ material) as has been observed in a similar region near the edge of the Pacific LLSVP [Lay *et al.*, 2006]. Local vertical complexity on the LLSVP boundary, for example an embayment of faster material into the LLSVP, is another possible cause for this feature. However, I cannot test these possibilities further.

The north-eastern boundary determined here (Figures 4.6c and 4.7c) appears to show a steeper vertical dip than that observed in the north-west, and the position agrees well with that determined in the S-wave travel-time study [He & Wen, 2012], and also the -0.4 %  $V_S$  contour in the S-wave model (Figure 4.9). At this location, the boundary determined by the gradient method is mapped  $\sim 10^\circ$  further towards the centre of the LLSVP than the boundary from the travel-time residual method, possibly due to smearing of travel-time anomalies along the ray path (see Chapter 4.4).

At the eastern edge of the LLSVP the boundary becomes steeper and shows a sharp transition between fast and slow material. There is also good agreement between the boundaries determined with both the travel-time residual and gradient methods. At this boundary the study matches well with the S-wave study and also the 0.0 %  $V_P$  contour in the tomography model, but my boundary deviates significantly from the -0.4 %  $V_S$  contour (Figure 4.9). The boundary in this region is likely the best determined in the whole study as the raypaths travel parallel to it, hence there will be less contamination from other lower mantle structure, and residual times for rays just grazing the LLSVP will be strongly affected. In this region I observe the boundary up to the greatest height above the CMB ( $\sim 700$  km) at the northern tip of the eastern extension of the LLSVP. Further east of the LLSVP, close to South and Central America, the boundary begins to deviate more significantly from either the LLSVP as defined by the -0.4 % iso-velocity contour, or the boundary determined by S-waves [He & Wen, 2012]. The boundary in this region trends east-west along the equator, contrary to other models. Given the consistency of the results using both the travel-time residual and gradient methods in this location (Figures 4.6 and 4.7), it seems that the boundary is well defined. However, as the boundary close to South America can be traced to  $\sim 900$  km above the CMB (Figure 4.7), I conclude that this edge is likely not the eastern edge of the Pacific LLSVP but the transition to some other velocity structure and might be related to subduction structures in this region [Garnero & Lay, 2003; Thomas *et al.*, 2004a; Hutko *et al.*, 2006; Thorne *et al.*, 2007; Hutko *et al.*, 2009].

Knowledge of the sharpness of the transition will help to resolve arguments about the degree to which lower mantle anomalies are chemical, thermal, or thermo-chemical

in nature [Trampert *et al.*, 2004; Davies *et al.*, 2012]. The shape of the LLSVP and the steepness of the walls give constraints on the viscosity and convective support of these features [Tan & Gurnis, 2005; McNamara & Zhong, 2005; Tan & Gurnis, 2007]. Previous S-wave studies have used waveform modelling to comment on the dip of the boundary [He & Wen, 2009, 2012]. They show the Pacific LLSVP to have both steep and shallow sides on the east and north, respectively, but do not quantify the dip. They demonstrate that the western and eastern boundaries are steeper than those reported for the African LLSVP, and the northern boundary of the Pacific LLSVP is reported as shallowly dipping close to the CMB and steeper at greater heights above the CMB. The African LLSVP is shown to also have laterally varying boundary steepness [Ni & Helmberger, 2003a]. The northern edge of the African LLSVP is reported to be steeply overturned [Ni *et al.*, 2002], although other studies show that, despite the boundaries being steep, dipping at between 28 and 70°, they are not overturned [Wen, 2001; Wen *et al.*, 2001; Wang & Wen, 2004, 2007; Helmberger *et al.*, 2009]. In this study I too find boundaries dipping as steeply as that of the African LLSVP and also with lateral variation in the steepness (Figure 4.10). The eastern edge of the Pacific LLSVP shows an apparent dip of  $\sim 70^\circ$ , roughly to the north-east, whereas the northern edge is shallower, dipping at  $\sim 26^\circ$  towards the north-west. Dynamic models of meta-stable, buoyant plumes attempting to take-off from the CMB [Tan & Gurnis, 2005] or a dense, passive body constrained by subduction [McNamara & Zhong, 2005] can both replicate the narrow, curving, and steep-sided nature of the African LLSVP. The Pacific LLSVP's rounder, more dome-like shape, as seen in tomography models, can be generated either by different material properties, relative to the African LLSVP [Tan & Gurnis, 2007], or greater subduction control [McNamara & Zhong, 2005]. Using My technique I can track the LLSVP and the associated boundary up to  $\sim 700$  km above the CMB, matching the heights observed with S-waves [He & Wen, 2012]. However, the data coverage does not allow me to mark out the top of the anomaly and so the complete shape cannot be defined.

The boundaries selected in the cross-sections to determine the dip of the flanks of the LLSVP are drawn as straight lines for simplicity and in acknowledgement of the limited constraints. However, a complex, non-linear boundary may be necessary to separate all points. The profiles include points up to  $5^\circ$  either side of the section line hence 3-dimensional structure on the boundary may account for some faster points plotting on slow side of the boundary, and vice versa, when viewed in a 2-dimensional cross section through the middle of the group of points. The boundary selected is also dependent on the angle at which the cross section is determined across the data points, hence the values stated are apparent dips. The location of the boundary and the resulting steepness of the LLSVP should, therefore, be considered an approximation. Nonetheless, the differences observed between the northern and eastern boundaries of the LLSVP are striking and likely to be significant.

Dynamic models imply that active subduction zones could interact with LLSVP, forcing the less viscous thermo-chemical pile laterally, dictating its location and shape [McNamara & Zhong, 2005]. Therefore, actively subducting slabs may steepen the LLSVP boundary compared to regions where there is no active or recent subduction. I observe that the transition from positive to negative delay times is sharper on the eastern side of

the LLSVP than on the northern side (Figure 4.10), possibly owing to the closer proximity to an active subduction zone on the eastern side. The observation of a steeper eastern edge than northern edge agrees with previous S-wave studies [*He & Wen, 2012*], indicating that this is a robust observation.

Previously, some studies have reported the LLSVPs to show little to no P-wave velocity change in the lower mantle [*Masters et al., 2000; Helmberger & Ni, 2005; Helmberger et al., 2005*] while S-wave velocities change significantly. However, I find substantial P-wave velocity variations: waves with travel-time residuals commonly of 4 s relative to PREM (both slower and faster) but up to -6 s, with the travel-time perturbation being attributable to the lowermost 1300 km of the mantle. In a simple 1-D calculation of P-wave velocity anomaly, I assume that the Pacific LLSVP is constrained to the lower 500 or 700 km of the mantle (based both on observations by previous studies [*He & Wen, 2012*] and the overall maximum and local maximum boundary heights in this study, respectively) and that only part of the ray-path is contained in the LLSVP (as the turning points are often on the edge of the LLSVP) and has a constant velocity reduction with depth, in order to fit the observed -4 s travel-time residual. This can be matched with a 700 km thick layer with  $\Delta V_P$  of -1.5 to -2.5 %, relative to PREM, and a ray travelling through this reduced velocity model for 70 to 50 % of its total length. Alternatively, a 500 km thick layer would have to have  $\Delta V_P$  of -2.2 to -2.9 %, relative to PREM. However, I accept that this is a grossly simplified calculation and constraining the wavespeed deviation and velocity structure with waveform modelling would be preferable. Waveform modelling could also be compared to examples of wavelet broadening to determine how sharp or diffuse the boundaries are. This consideration notwithstanding, these values are similar to those observed in past studies using  $P_{diff}$  passing through the African LLSVP [*Wen, 2001; Wen et al., 2001*].

The relationship between the P- and S-wave boundaries can help determine the material properties. The ratio of S- to P-wave velocity variations ( $R_{S,P} = \frac{\delta \ln V_S}{\delta \ln V_P}$ ) is often used as a measure of the degree to which temperature controls the seismic velocities [*Robertson & Woodhouse, 1996a,b*]. A ratio of <2.5 implies that mantle velocity anomalies are dominated by thermal contributions [*Karato, 2003*], while ratios larger than this imply that chemical variations are also important. Results of comparing tomography models indicate that the seismic velocity of the mantle is dominantly controlled by chemical variations [*Robertson & Woodhouse, 1996a,b; Trampert et al., 2004; Della Mora et al., 2011*]. However, the validity of this method has been disputed [*Schuberth et al., 2009; Davies et al., 2012*]. Nonetheless, comparing my 1-D velocity calculations with  $\Delta V_S \sim -5$  % calculated for the Pacific LLSVP [*He & Wen, 2012*] translates to a  $R_{S,P}$  of 1.7 to 3.4. The median value of  $\sim 2.4$  is higher than other high-frequency lower mantle studies [*Wyssession et al., 1999; Sun et al., 2007b*], but agrees with large-scale studies [*Robertson & Woodhouse, 1996b; Mosca et al., 2012*]. Using this estimate indicates that the Pacific LLSVP, at least in this region, can be explained by a combination of chemical and thermal anomalies [*Karato, 2003*]. It should be said that this is a maximum estimate for the magnitude of  $\Delta V_P$ , hence a minimum value of  $R_{S,P}$ , and by using either a higher LLSVP height (>700 km) or a longer ray path through the anomaly (perhaps all of the lower mantle) would produce a smaller  $\Delta V_P$ . Additionally, this estimate relies on comparing two different studies

and using the maximum  $\Delta V_S$  reported. Using the S-wave information from my dataset processed in a similar way would allow more accurate constraints on the  $R_{S,P}$  value of the LLSVP.

Superimposed on the large-scale patterns in residual travel-times, I observe more rapid aberrations in seismic velocities on smaller scales. I see significantly slower seismic velocities in an area previously identified as containing an ULVZ [Luo *et al.*, 2001; Cottaar & Romanowicz, 2012]. This region is prominent due to the large magnitude gradient of the travel-time residuals between it and the surrounding slow velocities (Figures 4.7b and 4.10b). The strong gradient is in agreement with other core diffracted wave results [Rost & Garnero, 2006]. A simple 1-D calculation through a velocity model with two reduced velocity layers is used to determine the  $\Delta V_P$  of the ULVZ while the LLSVP is assigned a  $\Delta V_P$  of -2.7 %, calculated above. Residual travel-times increase from -3 s for a P wave travelling  $97^\circ$  to -6 s for a  $P_{diff}$  travelling  $99^\circ$  (Figure 4.10d). To account for this additional -3 s residual in the lowermost 35 km of the mantle (the thickness of the mantle that is unique to the second, deeper travelling wave) a velocity reduction of 15-25 % is required, very close to that of other ULVZ studies which often report values of  $\Delta V_P = -15\%$  using lower frequency  $SP_{diff}KS$  [Jensen *et al.*, 2013; Thorne *et al.*, 2013a] and using  $P_{diff}$  of a similar frequency to this study [Xu & Koper, 2009]. However, this calculation has the same limitation as the single layer model of under- or over-estimating the path length within the ULVZ due to not knowing the full lateral extent of the structure. The location of this ULVZ supports the hypothesis that ULVZs can often be found at the edges of, or just within, the LLSVPs [McNamara *et al.*, 2010].

In addition to low velocities (as indicated by negative residuals) I find consistent areas of faster velocities (positive residuals) within the lowermost mantle along the coast of Mexico and South America. This agrees well with many previous studies [Garnero & Lay, 2003; Thomas *et al.*, 2004a; Hutko *et al.*, 2006; Thorne *et al.*, 2007; Hutko *et al.*, 2009] showing faster velocities related to subduction of the Farallon slab. As subduction is a top down process it may explain why the transition between slow and fast residuals is detected at greater heights in this region than anywhere else in this study (Figure 4.7d). Subduction reconstructions suggest that slabs have been accumulating under Central America for at least 180 Ma [Lithgow-Bertelloni & Richards, 1998; Maruyama *et al.*, 2007] and tomography models show strong positive velocity anomalies in the lowermost mantle in this region suggesting the presence of slabs (Figures 4.6 and 4.9). This region also correlates with the location of scattering close to the CMB observed in Chapter 3, demonstrating that the subducted crust in this region likely reaches the lowermost mantle.

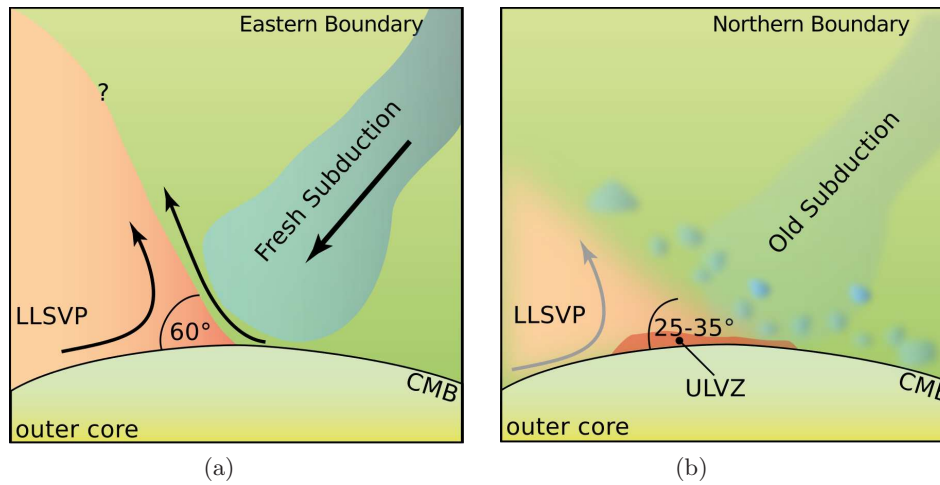


Figure 4.13: Conceptual relationship between LLSVP structure and subduction processes. (a) The observed steep ( $70^\circ$  dip), sharp ( $\sim 40$  km) LLSVP boundary in the east may be caused by recently subducted slab material increasing the thermal gradient and shaping the LLSVP. (b) The shallower ( $26^\circ$ ) and more diffuse ( $\sim 120$  km) northern boundary, by contrast, may be due to the absence of recent subduction. From Frost & Rost [2014, in press].

I speculate that the boundary width (sharpness) and steepness is related to mantle dynamics (Figure 4.13). In the eastern Pacific, where there are active subduction zones, the boundary is seismically sharp, occurring over 40 km or less, although resolution is limited by the size of the Fresnel zone. In contrast, the northern edge of the Pacific LLSVP has a broader seismic boundary and is further from an active subduction zone. Subducted material that has been present in the lower mantle for longer will have had longer to thermally, and possibly chemically, equilibrate with ambient conditions through conduction and mechanical mixing, respectively. This would result in a lower gradient (both thermal and compositional) across the boundary which may present as a lower seismic velocity gradient, hence a wider boundary. Conversely, regions of active subduction where crust has recently been subducted, such as the eastern edge of the Pacific LLSVP, would have higher thermal gradients and, therefore, higher seismic delay-time gradients.

## 4.6 Summary

P-wave travel-time delays relative to a tomography model are used to map out the northern and eastern edges of the Pacific LLSVP from the CMB to 700 km above, and other lower mantle structures up to 900 km above the CMB. The northern and eastern regions show contrasting structures: the northern boundary has a seismically broad transition with a shallow slope ( $\sim 120$  km wide and a dip of  $26^\circ$  relative to the horizontal), while the eastern boundary is sharper with a steep slope ( $\sim 40$  km wide and dipping at  $70^\circ$ ). I attribute this to the proximity of the eastern edge to active subduction, steepening and sharpening the boundary through viscous forcing and an increased thermal and/or compositional gradient. I observe smaller scale velocity variations linked to the larger scale structure in the form of a sharply defined low velocity region, which is correlated with observations of an ULVZ. Calculation of  $R_{S,P}$  to explore the thermal or compositional origin of the LLSVP is complicated by limited data and the result is inconclusive. Contrary to patterns observed

in P-wave and bulk-sound tomography models, the P-wave boundary closely matches that determined with S-wave travel times and the 0.0 %  $V_P$  and -0.4 %  $V_S$  iso-velocity contours in the GyPSuM and S40RTS models, respectively. The shape, sharpness, and location of LLSVPs and their relationship with small scale structure demonstrates their involvement with the whole dynamic mantle system.



## Chapter 5

---

# Discussion

---

There is growing evidence from geochemistry, mineral physics, and seismology that the Earth's mantle is poorly mixed and in chemical disequilibrium. Pronounced geochemical differences between Mid-Ocean Ridge Basalts, sourced from the shallow mantle, and Ocean Island Basalts, which are likely sourced from deeper in the mantle, demonstrate the variability of the chemical structure of the Earth, although the specific source regions of the samples is unclear [*Dupre & Allegre, 1983; Hart, 1984; Castillo, 1988; Cabral et al., 2013*]. Seismic studies resolve variations in velocity ranging from 1000s to 10s km in size, which can be interpreted as resulting from changes in chemistry or temperature (or both) of the material sampled. As such, the mantle contains chemical and thermal aberrations of various sizes. All scales of structure are governed by the dynamic processes operating in the mantle, hence by observing, understanding, and tracking both the small-scale heterogeneities and larger-scale features we can learn what the mantle comprises and how it behaves.

Seismology allows us to study changes in velocity and density within the Earth. Different methods allow the resolution of a range of scales of structure. The broad scale structure is arguably better studied than the smaller length scales. However, larger scale tomographic studies still lack precision and cannot reliably resolve structure smaller than  $\sim 1000$  km [*Becker & Boschi, 2002*]. More detail about the lower mantle structures can be resolved through focussed (non-tomographic) studies using less data and higher wave frequencies. I demonstrate use of scattered waves (see Chapters 2 and 3) to study small chemical anomalies on the order of 10 km in size and smaller, and direct wave travel-times (see Chapter 4) to study the fine scale aspects of the Pacific Large Low Shear Velocity Province with a resolution limit of  $\sim 100$  km. The accuracy of the results is controlled by the frequencies used, which affect both the sensitivity to structure of different sizes and the resolution limit in terms of the Fresnel zone (discussed in Chapter 1.5.3); the noise levels, which can distort and mask signals leading to misidentifications; and errors inherent in the processing techniques (discussed in Chapters 2.7, 3.7, and 4.4).

In this thesis, I analyse new data and apply procedures from forensic seismology to improve the resolution of my processing (described in Chapter 1.4.7). Application of the F-statistic to a standard beam-pack to create F-packs (as in Chapter 2) and also in the frequency domain to the fk process (as in Chapter 3) dramatically increases the accuracy to which the slowness, back-azimuth, and time of incoming scattered waves can be measured

(by factors of 9 and 6, for back-azimuth and slowness resolution, respectively, for an example event. Figure 1.17). This process was tested at small and medium aperture arrays. This improves the accuracy of locations of scattering heterogeneities over previous studies. Using the F-pack and ray-tracing, scattering heterogeneities related to PKP precursors can be located to within  $\pm 2^\circ$  laterally and  $\pm 25$  km vertically (Figure 2.10). Using the fk F-statistic and ray-tracing, heterogeneities are located to within  $\pm 2.5^\circ$  laterally and  $\pm 30$  km (Figure 3.15). Improved detection limits also allow study of events with smaller magnitudes than has previously been possible. Useful observations can be derived using PKP data from events with magnitudes as low as  $m_b = 3.2$  (described in Chapter 2.3). In addition to using novel processing techniques, new data are analysed to make new observations. Data from 16 IMS arrays are used to create a near-global study of PK•KP scattering in the lower mantle and data from USArray are analysed to study the P-wave boundary of the Pacific LLSVP in unprecedented detail. By precise study of both the large scale LLSVPs and small scale scattering heterogeneities, I aim to bridge the gap between these two areas and determine the degree of interaction between mantle structure and processes of different scales.

## 5.1 Summary of Observations

A range of lower mantle structures are studied using various data and processing techniques. I observe high amplitude precursors to PKP<sub>df</sub> from low magnitude events related to mining in South Africa (see Chapter 2). The sources of the scattered energy are determined to be locally distributed heterogeneities in the lower mantle beneath South Africa, which, based on the observed frequencies of scattering, are inferred to be  $\sim 10$  km in size. These heterogeneities vary in both height above the CMB and scattering strength. The heterogeneities form a strongly scattering ridge approximately 80 km tall [Frost *et al.*, 2013]. The ridge is surrounded by scattering of lower amplitudes close to the CMB, although on the north side coverage is limited by the ray geometry and so no conclusions can be drawn. Although modelling using phonon scattering methods proves inconclusive, the aspect ratio of the ridge implies that the heterogeneities are  $\sim 5$ -10 % denser than the surrounding mantle (for a given viscosity structure) and, therefore, must be dynamically supported [Bower *et al.*, 2011] (for greater discussion see Chapter 2.9). Scattering heterogeneities in an adjacent area have been modelled as having a  $V_P$  anomaly of 8 % [Wen, 2000] and other similar observations of precursors to PKP<sub>df</sub> were modelled to result from heterogeneities with a P-wave velocity drop of 5-15 % [Thomas *et al.*, 2000]. Therefore, I consider the heterogeneities observed in this study as volumes with anomalously low velocities, similar to that of ULVZs. The ridge is located close to south-eastern edge of the African LLSVP. The unusually large height of the low velocity zone, combined with the position close to the margin of the LLSVP is suggestive of dynamic processes supporting this structure, providing a link between small and large scale mantle structures.

I detect anomalous phases related to scattering of PKKP to PK•KP in a global dataset of events with magnitudes greater than 6 (see Chapter 3). The directivity and time information suggests that these waves scatter from anomalies in the lowermost 300 km of the mantle and are globally, yet unevenly, distributed with scattering heterogeneities

showing significant grouping. Lateral clustering is particularly evident for heterogeneities located at greater heights above the CMB. Maximum scattering heights of 320 km are observed but might be limited by the time window analysed. Heterogeneities are seen close to, or at the CMB for nearly the entire area sampled by the PK•KP probe. The frequencies of the waves demonstrate that they are scattered by volumes between 1 and 10 km in size. The scattering heterogeneities appear to be preferentially located close to the inside edges of the LLSVPs (defined by low velocity anomalies in tomography models) and close to subduction related structures (high velocity anomalies in tomography models), and these patterns are often stronger with increasing height of scattering above the CMB. This correlation implies that dynamic processes are dictating the heights of locations of scattering, supported by the observation that high scattering heights are co-located with regions of strong lower mantle upwelling and downwelling calculated from tomography models [Forte *et al.*, 2013].

Travel-time variations detected in deep penetrating P and  $P_{diff}$  waves from events with magnitudes greater than 5 in South America and Tonga-Fiji demonstrate consistent fluctuations correlating with the edge of the Pacific LLSVP in the lower mantle (see Chapter 4). The edge of the LLSVP is accurately and precisely traced at various heights above the CMB. The boundary of the LLSVP is seismically sharp and steep in the east, and the transition from positive to negative time residuals occurs over  $\sim 60$  km with a slope of  $\sim 70^\circ$ . The boundary is broader and shallower in the north, transitioning over  $\sim 120$  km with a slope of  $\sim 30^\circ$ . The steeper eastern boundary is close to a region of active subduction while there is no current or recent subduction near the shallower boundary at the north of the LLSVP. Following from dynamic models demonstrating that subduction can shape LLSVPs [McNamara & Zhong, 2005; McNamara *et al.*, 2010; Tan *et al.*, 2011], I hypothesise that interaction with cold slabs steepens and sharpens the LLSVP boundary that would otherwise be more gently sloped and diffuse. This method also resolves strong velocity gradients indicative of an ULVZ in the north of the LLSVP in a location where an ULVZ has previously been resolved by other methods [Cottaar & Romanowicz, 2012], further suggesting a link between small and large scale structure.

The results of each of these studies indicates a connection between the small-scale and large-scale structures within the lower mantle. Many of these patterns can be replicated by dynamic models of mantle processes [Tan & Gurnis, 2005; McNamara & Zhong, 2005; Tan & Gurnis, 2007; McNamara *et al.*, 2010; Bower *et al.*, 2011; Tackley, 2011; Tan *et al.*, 2011; Li & McNamara, 2013; Li *et al.*, 2014] and there are geochemical and physical mechanisms by which these structures could be explained as partial melt, iron-enrichment of lower mantle perovskite, or assimilation of subducted basaltic crust [Manga & Jeanloz, 1996; Williams & Garnero, 1996; Hirose *et al.*, 1999; Wicks *et al.*, 2010; Deschamps *et al.*, 2011; Kudo *et al.*, 2012; Deschamps *et al.*, 2012]. Since global wave propagation modelling of these scattered waves is currently almost impossible due to the high frequencies required, no further insight into the detailed origin of the heterogeneities seems feasible. Further modelling approaches and further observations of these interactions will help to constrain the models, leading to a more complete understanding of Earth mechanics.

## 5.2 Integration of Observations

Convergent observations between different mantle probes not only increase the reliability of the results, but also help to reveal different aspects and properties of the structure. Through comparing results of my large and small-scale studies, and past studies of all scales of mantle structure, I intend to draw conclusions about how different aspects of mantle structure are related and interact.

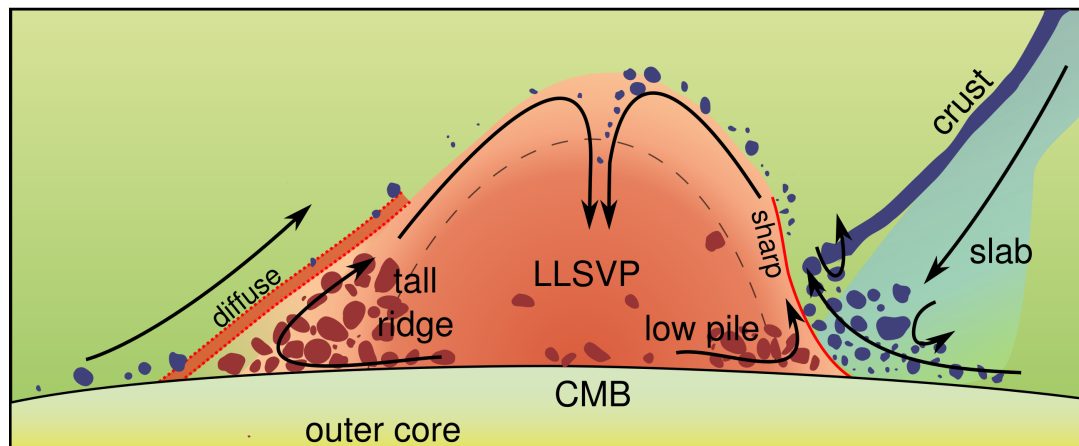


Figure 5.1: Lower mantle structures interacting on both large and small scales demonstrating features similar to those resolved in this study. Subducting slabs may introduce chemically anomalous basaltic crustal material to the lower mantle which can cause scattering, while also sharpening and steepening the edges of LLSVP (thin red line) on which they may impinge, similar to that observed under Central America and the Pacific LLSVP. Internal convection within LLSVPs may drive dense compositional anomalies to the margins (the region of strongest velocity contrast is shown by the dashed black line). Weak convection may be unable to entrain heterogeneities resulting in low piles of scatterers. In contrast, stronger internal convection may more fully entrain heterogeneities and create tall piles close to the edge of the LLSVP, similar to that seen under South Africa. Without interaction with subducting slabs, the margin of the LLSVP may be diffuse (region of dashed red lines) and shallowly sloping, similar to the northern edge of the Pacific LLSVP. Regions of the lower mantle without either LLSVPs or subducting slabs may contain relatively few scattering heterogeneities, such as under the Indian and southern Atlantic Oceans. Not to scale.

Observations of PKP and PK•KP scattering in the lower mantle indicate the locations of small volumes with anomalous velocities and/or densities with respect to the ambient lower mantle. The results of these two probes agree incredibly well where their sampling overlaps. The heterogeneities resolved are unevenly distributed throughout the lower mantle and comprise piles of various heights and shapes, up to 320 km tall relative to the CMB (Figures 3.9). Heterogeneities are observed forming an 80 km tall ridge under the eastern edge of the African LLSVP (Figure 2.22) with other peaks of equal or greater heights under eastern Africa, and Central and South America. Many of the heterogeneities detected at large heights above the CMB are located either at the inside edges of the LLSVPs, or close to the termination of subduction zones, also correlating with regions of upwelling and downwelling, respectively, calculated from tomography models [Forte *et al.*, 2013]. Dynamic models of a convecting mantle have demonstrated that the location of

small scale anomalies can be influenced by mantle flow [McNamara *et al.*, 2010]. Dense heterogeneities are likely to remain in the lowermost mantle and be swept by the motion of subduction towards the edges of the LLSVP where they will reside, while less dense heterogeneities will be entrained into mantle upwellings and possibly return to the surface [Li & McNamara, 2013; Li *et al.*, 2014]. The small scale structure of the mantle is heavily influenced by the large scale processes operating (Figure 5.1).

The frequencies of the scattered PKP and PK•KP waves are suggestive of heterogeneities between 1 and 10 km in size, although the strongest scattering may be from volumes  $\sim 6$  km in size. Scattering heterogeneities of a similar range of sizes have previously been observed [Ansell, 1973; Haddon & Cleary, 1974; Bataille & Lund, 1996; Wen & Helmberger, 1998; Thomas *et al.*, 1999; Wen, 2000; Braña & Helffrich, 2004; Thomas *et al.*, 2009; Rost & Earle, 2010; Ivan & Cormier, 2011; Frost *et al.*, 2013], although these studies involve multiple probes of lower mantle structure, while the size range is resolved here with a single probe. Velocity contrasts can result from chemical or thermal deviations. However, due to their small size and the likelihood that purely thermal structures would quickly diffuse away, scattering heterogeneities are most probably predominantly chemical anomalies [Becker *et al.*, 1999; Turcotte & Schubert, 2002; Gonnermann *et al.*, 2002]. Some previous studies of scattering heterogeneities used modelling to determine the properties of the heterogeneities and determined P-wave velocity contrasts of 5-15 % relative to the ambient mantle [Vidale & Hedlin, 1998; Thomas *et al.*, 2000; Wen, 2000], and density anomalies of up to 10 % have been calculated through seismic and geodynamic modelling [Wen & Helmberger, 1998; Cao & Romanowicz, 2007; Thomas *et al.*, 2009; McNamara *et al.*, 2010; Bower *et al.*, 2011; Frost *et al.*, 2013]. These observations support a compositional origin for the small scale heterogeneities detected here.

A combination of viscous coupling with the overall mantle convection and internal convection due to heating from below have been suggested to drive convection within the LLSVPs [Tan & Gurnis, 2007; McNamara *et al.*, 2010]. Dense compositional anomalies entrained within this convection may collect towards the upwelling edges. Heterogeneities with lower density contrasts will be entrained and possibly extracted from the LLSVPs while denser material, above the entrainment threshold of  $\sim 5$  % [McNamara *et al.*, 2010], will likely remain in the LLSVPs and pool at the margins. Scattering heterogeneities associated with the LLSVPs display a strong preference towards the inside edges of the LLSVPs. Scatterers are also frequently observed at large heights above the CMB close to the LLSVP edges. Therefore, it is likely that the heterogeneities resolved are dense anomalies that are influenced by the mantle convection. Regions of stronger convection, higher concentrations of heterogeneities, or lower density anomalies may allow scatterers to be drawn to exceptionally large heights above the CMB, as is seen in South Africa. The unusual shape (an embayed region) of the LLSVP in this area may affect mantle flow causing greater entrainment. Scattering heterogeneities may make up ULVZs which are often associated with the LLSVP edges and have similar velocity contrasts [Williams & Garnero, 1996; Revenaugh & Meyer, 1997; Rost *et al.*, 2005]. LLSVPs are often thought to be hot, thermo-chemical anomalies [Williams *et al.*, 1998; Trampert *et al.*, 2004; Thorne *et al.*, 2004; McNamara & Zhong, 2005; Helmberger & Ni, 2005; Wen, 2006; Torsvik *et al.*, 2006]. Scattering heterogeneities associated with LLSVPs may, therefore, be composi-

tional structures, or possibly partial melt as a result of the higher ambient temperature. Partial melting of the lowermost mantle would reduce seismic velocities with a  $R_{S,P}$  value of approximately three to one, a relationship commonly observed seismically for ULVZs [Williams & Garnero, 1996; Berryman, 2000; Lay et al., 2004; Beuchert & Schmeling, 2013]. However, maintaining a coherent volume of negatively buoyant partial melt and preventing percolation at great heights above the CMB (where density contrasts would likely be larger) may be difficult although it may be possible if small quantities of melt were restricted to grain boundaries [Rost et al., 2005; Hernlund & Tackley, 2007; McNamara et al., 2010; Hernlund & Jellinek, 2010; Thomas et al., 2012; Wimert & Hier-Majumder, 2012]. Solid-state compositional changes may be more consistent with observations of scattering heterogeneities. Enrichment of mantle perovskite with iron from a primordial source [Labrosse et al., 2007] or core-mantle interaction [Knittle & Jeanloz, 1986; Mao et al., 2006] would be able to strongly reduce seismic velocities, however, this may result in partial melting also [Garnero & Jeanloz, 2000; Rost et al., 2006a; Mao et al., 2006; Wicks et al., 2010]. Although the actual chemistry of scattering heterogeneities is, as yet, unknown, it is clear that they are indicative of the larger scale mantle processes and so their study is important for understanding the mantle as a whole.

Subduction zones introduce material into the lower mantle that is both thermally and chemically distinct. The lithospheric portion of the slab will likely be in chemical equilibrium with the ambient lower mantle as it forms directly from upwelling mantle without melting, but it will not be in thermal equilibrium [Kito et al., 2008; Stixrude & Lithgow-Bertelloni, 2012]. The basaltic crust will neither be chemically similar to the lower mantle due to partial melting at the mid-ocean ridges, nor thermally similar, although as the crust is thin (approximately 7 km) it may thermally equilibrate more quickly than the thicker lithosphere. The crust is likely to separate from the downgoing lithosphere [Tackley, 2011] and, dependent upon its physical properties, remain in the lower mantle or be entrained back into convection [Li et al., 2014]. Mineral physics experiments imply that basalt in the lower mantle will be both denser than the ambient mantle [Hirose et al., 1999, 2005] and show a significant positive velocity contrast [Karato & Karki, 2001; Kudo et al., 2012]. Therefore, it is likely that the scattering heterogeneities that are spatially associated with regions of subduction (high seismic velocities in tomography models) are related to the basaltic crust contaminating the lower mantle. Brittle fracturing of the crust at subduction zones and break up due to internal convection as the slab travels into the mantle may result in a greater concentration of scatterers higher above the CMB, while progressive mechanical mixing may disperse the volumes throughout the lower mantle resulting in a wider spread of scatterers closer to the CMB, as seen under South America. Further mixing may disaggregate the crust until it is too small to be resolved by scattering probes, or mantle flow may entrain the anomalies into the overall convection [Tackley, 2011; Li et al., 2014]. It is also possible that this crustal material may be included into the LLSVP convection cycle [Li et al., 2014], further linking both these two structures and the small scale features of the mantle.

Regions of non-observations of scattering heterogeneities are likely real observations, given that other regions with similar levels of sampling do show scattering. However, they may still result from detection problems due to noise or weak signals. Alternatively, these

regions of fewer detected heterogeneities may be true representations of the structure of the lower mantle, indicative of mantle processes. Many of the regions that display little scattering or scattering predominantly near to the CMB are not close either to LLSVPs, or present or past subduction. If lateral mantle flow sweeps heterogeneities into areas of stagnant or vertical flow [McNamara *et al.*, 2010; Forte *et al.*, 2013] then it is feasible that some patches would contain fewer small scale structures.

The large scale structure is also affected by mantle dynamics. LLSVPs are often considered to be viscous upwellings, but also fairly passive and ductile [Tan & Gurnis, 2005; McNamara & Zhong, 2005; Tan & Gurnis, 2007]. Subducting slabs are contrastingly stiff. Slabs may force and shape LLSVPs, a process which has been invoked to explain the relationship between the location of current subduction and the antipodal locations of the LLSVPs [McNamara & Zhong, 2005; Trønnes, 2010; Tan *et al.*, 2011]. The character of the boundary between the LLSVP and the surrounding mantle is also likely influenced by subducting slabs. Even if the LLSVP is the result of both thermal and chemical deviations from the ambient mantle [Trampert *et al.*, 2004], the velocity contrast between cold slab material and a hot LLSVP will appear sharper to seismic waves than the contrast between ambient mantle and a hot LLSVP. Using P-wave travel times, the eastern edge of the Pacific LLSVP is observed to be seismically sharp and steep. In this area subduction is currently active and past and present slabs have previously been imaged in the deep mantle [Lithgow-Bertelloni & Richards, 1998; Fukao *et al.*, 2001; Hutko *et al.*, 2006]. Furthermore, the northern edge of the Pacific LLSVP is distant from present subduction, and the boundary between the LLSVP and the mantle is observed to be both seismically diffuse and more gently sloping than the eastern edge. Both seismic observations and dynamic models of mantle convection imply that subduction processes and LLSVP behaviour are closely related [Tan & Gurnis, 2007; Tan *et al.*, 2011].

Considering all observations together, it is clear that the broad and finer dynamic processes within the Earth influence all scales of chemical and thermal structure within the mantle. Seismic probes utilising scattered energy can resolve and locate detailed structure of the mantle, which wavefield modelling can be used to characterise. These observations can then be integrated with those from broader scale seismic and dynamic studies. The thermal and chemical complexities observed throughout the mantle highlight the differing levels of complication and interaction that arise from a poorly mixed Earth.

### 5.3 Concluding Statement

The internal structure of the Earth varies both in terms of composition and temperature on all scales. Geophysical, geodynamic, and geochemical study can identify and explain specific aspects of this heterogeneity. Combining the observations of different methodologies is necessary to fully understand the processes involved. Although this seismic study has been able to identify locations of complexity and interaction within different aspects of Earth processes, the precise mechanisms of mantle dynamics and compositions involved are still unknown. Further work utilising more sophisticated seismic modelling and involving dynamic calculations will help to more fully describe the observations, while inclusion of more mineral physics results is necessary to explain the detections. Nonetheless, this work demonstrates the many scales on which internal Earth processes operate.

Overlooking either the broad or fine scale structure vastly limits the extent to which we are able to understand the intricacy of processes in the interior in our planet.

## Appendix A

# Introduction Appendix

### A.1 Arrays

Station configurations and Array Response Functions (ARFs) for the other IMS arrays used that are not otherwise displayed in the text. Only the stations at each array that were used in processing are displayed.

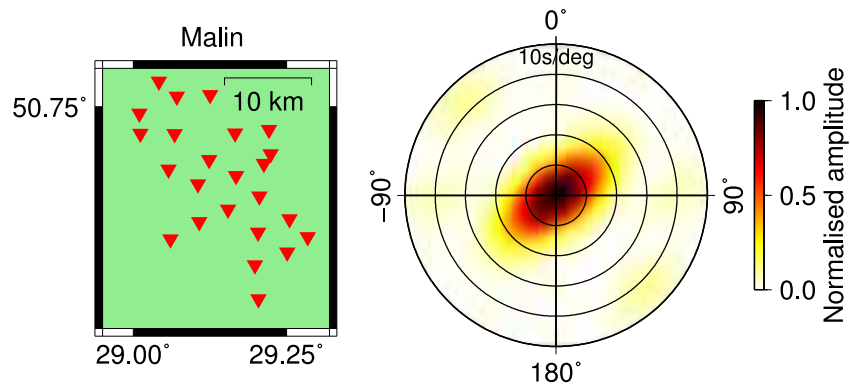


Figure A.1: Array configuration and array response function computed at 1 Hz and 0 s/deg slowness for AK array in Ukraine. ARF is displayed between slownesses of 0 to 10 s/deg and back-azimuths of 0 to 360°).

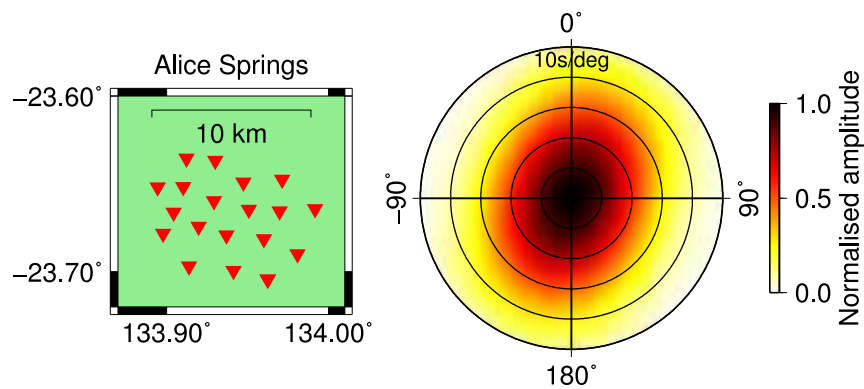


Figure A.2: Array configuration and array response function for AS array in Australia. Calculated as in Figure A.1.

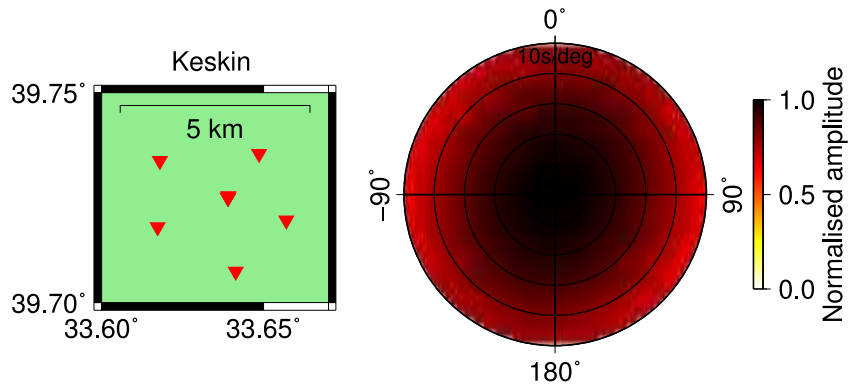


Figure A.3: Array configuration and array response function for BR array in Turkey. Calculated as in Figure A.3.

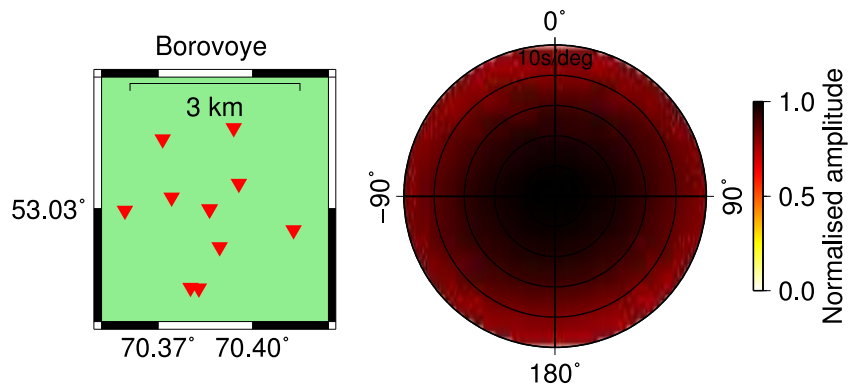


Figure A.4: Array configuration and array response function for BV array in Kazakhstan. Calculated as in Figure A.4.

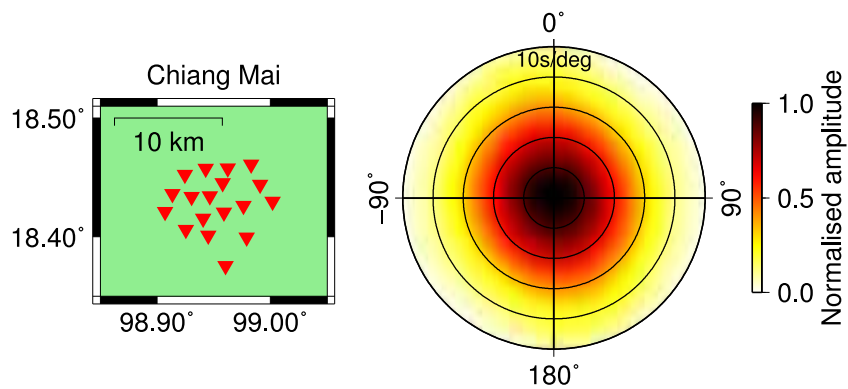


Figure A.5: Array configuration and array response function for CM array in Thailand. Calculated as in Figure A.5.

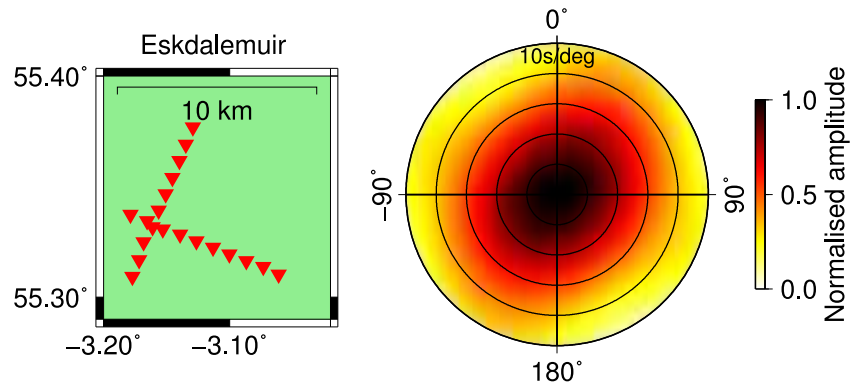


Figure A.6: Array configuration and array response function for EK array in Scotland. Calculated as in Figure A.6.

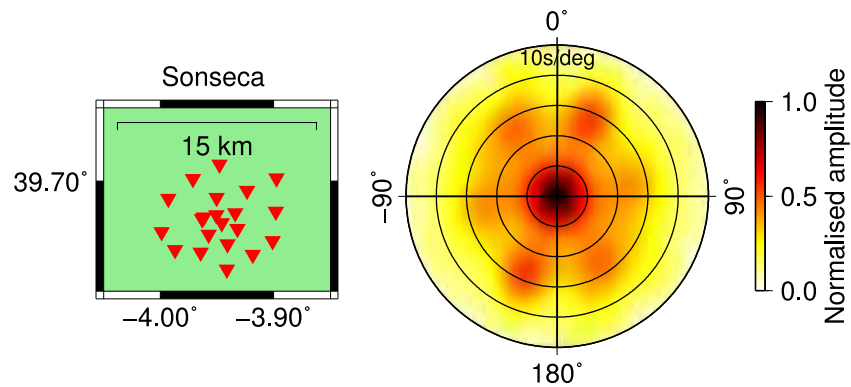


Figure A.7: Array configuration and array response function for ES array in Spain. Calculated as in Figure A.7.

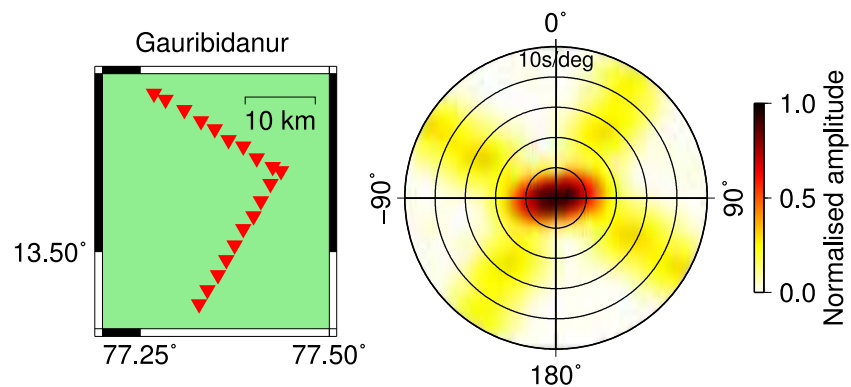


Figure A.8: Array configuration and array response function for GB array in India. Calculated as in Figure A.8.

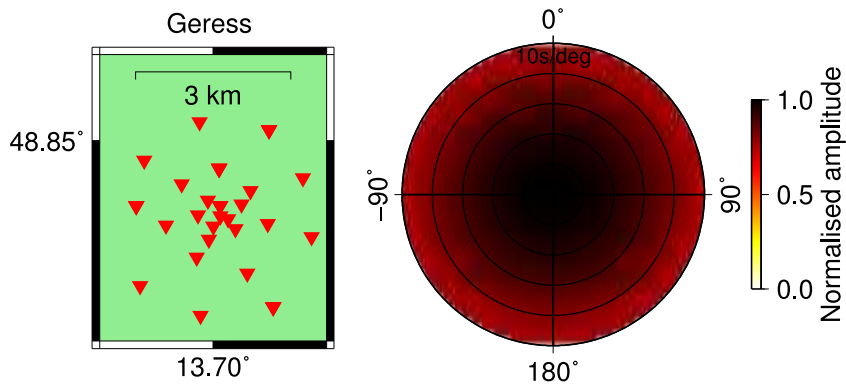


Figure A.9: Array configuration and array response function for GE array in Germany. Calculated as in Figure A.9.

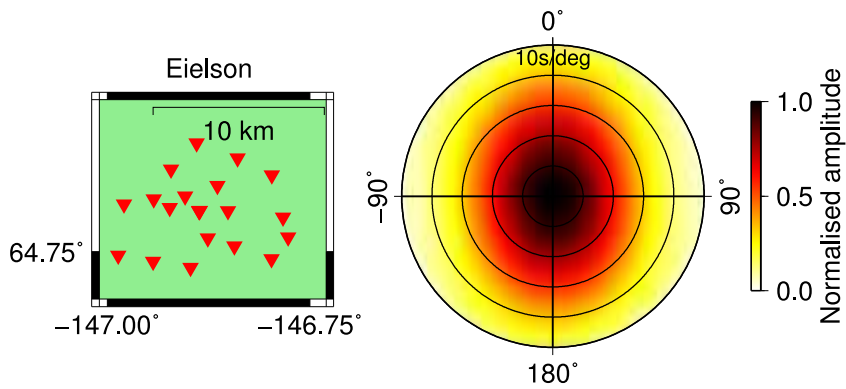


Figure A.10: Array configuration and array response function for IL array in Canada. Calculated as in Figure A.10.

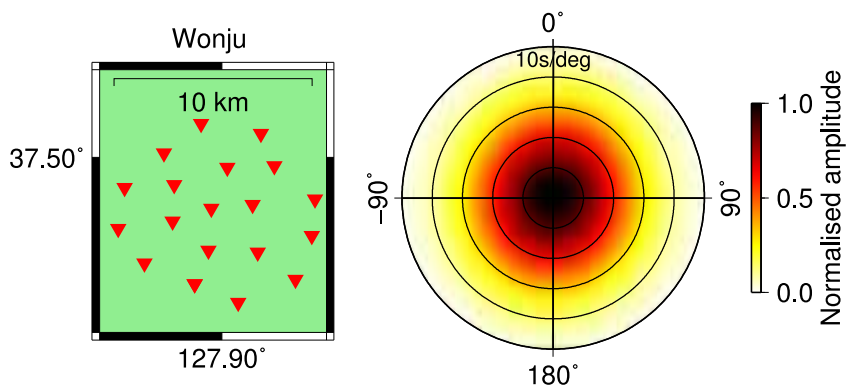


Figure A.11: Array configuration and array response function for KS array in South Korea. Calculated as in Figure A.11.

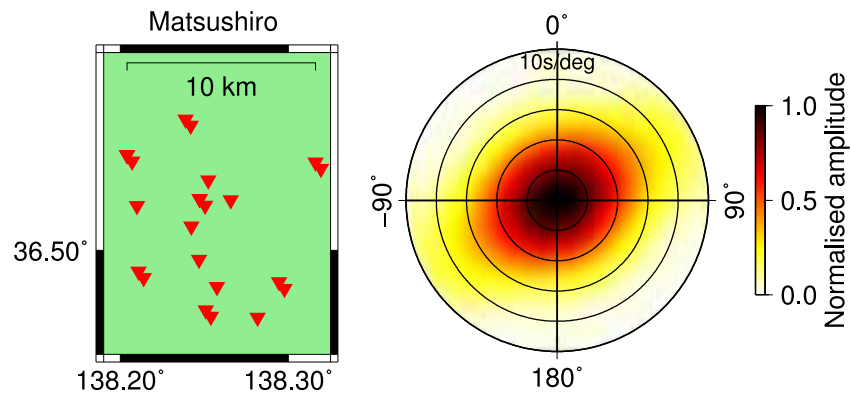


Figure A.12: Array configuration and array response function for MJ array in Japan. Calculated as in Figure A.12.

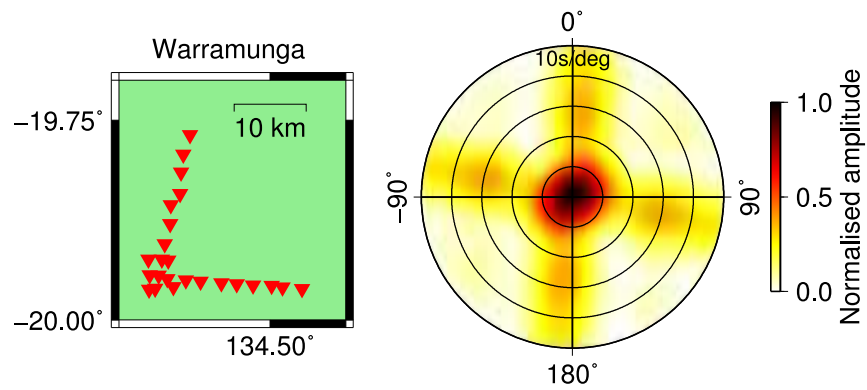


Figure A.13: Array configuration and array response function for WR array in Australia. Calculated as in Figure A.13.



## Appendix B

# PKP Scattering Appendix

### B.1 Event Data

A total of 153 events from southern Africa over the time period from 1978 to 2011 recorded at YK are selected the International Seismological Centre (ISC) catalogues and Comprehensive Nuclear Test Ban Treaty Organisation Reviewed Event Bulletins (REB).

Table B.1: Events in PKP dataset. Dates are given in day/month/year format.

Date	Origin time	Latitude	Longitude	Magnitude (mb)
08/01/1978	06:31:48.03	-12.0151	34.2369	5.2
24/01/1979	10:54:40.44	-26.8525	26.6475	4.7
06/04/1979	05:33:10.17	-26.8548	26.7330	4.9
20/06/1979	16:08:03.71	-26.3223	27.3851	4.5
15/08/1979	13:18:29.69	-26.2837	27.3891	4.5
28/01/1980	06:30:57.07	-26.3965	27.4634	4.5
09/02/1980	13:51:10.25	-27.8029	26.2358	5.2
17/02/1980	21:01:21.94	-27.6272	26.8651	4.7
22/03/1980	02:14:09.63	-26.1209	27.7521	5.2
03/04/1980	22:45:38.45	-26.0819	27.7038	4.8
06/05/1980	21:07:25.42	-26.9261	26.9981	4.6
12/06/1980	03:03:41.93	-26.9514	26.9918	4.8
13/06/1980	21:15:02.57	-26.8454	26.7690	4.8
30/08/1980	10:36:05.66	-26.1984	28.1691	4.7
28/01/1981	16:20:28.94	-26.3362	27.4091	4.5
18/02/1981	08:28:15.12	-26.7906	26.6465	4.7
17/04/1981	07:07:03.49	-28.0104	26.9001	4.5
21/05/1981	16:15:05.54	-26.3887	27.3369	4.6
07/09/1981	15:55:25.15	-26.3039	27.1768	4.9
08/10/1981	00:00:25.45	-26.8883	26.7596	4.8
22/11/1981	03:31:26.89	-26.3815	27.5445	4.5
17/02/1982	18:11:25.68	-26.1236	28.1272	4.5
11/12/1982	22:03:57.86	-26.8703	26.6709	4.5
03/01/1983	22:29:37.03	-26.8166	26.6576	4.5
17/01/1983	04:18:16.80	-18.4062	34.7300	4.7
22/02/1983	16:26:18.05	-29.1871	27.9266	4.9
06/06/1983	10:48:51.15	-26.8771	26.7460	5.1
07/12/1983	20:04:50.63	-26.8778	26.6168	4.6
25/12/1983	07:51:01.84	-26.3475	27.3801	4.6
27/12/1983	07:38:24.55	-26.3912	27.4155	4.8
28/01/1984	14:40:13.91	-26.8954	26.6298	4.8
07/04/1984	21:42:44.64	-28.0577	26.8716	4.6
18/04/1984	12:48:38.97	-27.9948	26.8623	4.8
04/05/1984	06:17:40.52	-26.8341	26.6301	4.6
20/06/1984	04:49:35.77	-28.1286	26.8944	4.7
26/10/1984	07:44:28.20	-16.4516	28.7166	5.3
21/11/1984	20:28:13.22	-26.1904	28.1997	4.5
24/04/1985	02:48:56.34	-26.8010	26.6068	4.7
08/05/1985	11:35:43.27	-29.3541	24.7016	4.6
10/02/1986	20:45:01.37	-28.0371	26.7102	4.9
15/03/1986	18:50:47.70	-27.7726	26.7115	4.7
22/04/1986	07:33:45.75	-26.3872	27.2511	4.7
03/07/1986	15:37:36.55	-26.3258	27.2594	4.5
11/08/1986	04:59:10.50	-26.9078	26.5957	4.9

Date	Origin time	Latitude	Longitude	Magnitude (mb)
15/09/1986	07:06:30.24	-26.2730	27.4154	4.7
28/10/1986	15:04:21.66	-26.9342	26.7179	5.1
13/11/1986	11:11:18.35	-26.9014	26.7509	5.0
29/12/1986	20:41:59.07	-26.3547	27.4444	4.7
17/02/1987	11:00:22.89	-17.2236	24.9746	4.8
29/05/1987	11:35:53.94	-26.8407	26.6620	4.8
30/07/1987	12:46:27.25	-26.7753	26.6886	4.9
30/09/1987	07:37:36.37	-26.7833	26.6986	4.8
12/09/1988	02:32:20.68	-26.8932	26.6510	4.6
07/10/1988	20:59:12.28	-26.0983	27.9895	4.7
15/12/1988	14:31:53.15	-26.8261	26.7859	4.7
22/12/1988	12:23:43.34	-26.9460	26.6485	4.5
31/12/1988	12:49:59.19	-26.8815	26.6406	4.9
09/03/1989	02:37:00.21	-13.7377	34.4147	5.6
10/03/1989	21:49:45.80	-13.6965	34.4452	6.0
23/07/1989	08:57:54.87	-26.8589	26.7594	4.6
03/03/1990	07:29:17.79	-26.9543	26.7200	5.0
17/03/1990	00:41:04.73	-27.9958	26.7886	4.3
26/09/1990	23:08:23.08	-28.0960	26.7722	5.5
03/11/1990	00:31:28.89	-21.3451	33.2846	4.8
14/11/1990	00:31:42.74	-28.1954	26.8107	4.8
24/01/1991	12:55:51.43	-13.1283	23.1763	4.9
10/05/1991	01:12:38.49	-17.3484	24.9820	4.8
01/12/1991	20:03:10.37	-26.8915	26.6727	4.8
02/12/1991	14:37:58.61	-19.5974	23.5408	4.0
18/01/1992	23:51:51.16	-26.8918	26.7305	4.4
10/02/1992	15:47:22.80	-27.9966	26.6474	4.2
07/03/1992	00:43:04.08	-26.4414	27.3387	4.8
11/03/1992	18:00:29.97	-26.3835	27.2822	3.7
07/04/1992	12:55:03.59	-26.2067	27.7028	3.7
15/04/1992	13:09:10.04	-26.4692	27.3728	4.1
06/06/1992	18:33:59.63	-27.9762	26.7805	5.2
23/12/1992	10:54:52.36	-23.8258	17.3111	4.8
10/02/1993	05:01:00.18	-23.8278	26.0791	4.1
23/02/1993	05:12:44.89	-26.3566	27.3881	4.5
06/04/1993	17:23:47.66	-26.3474	27.3639	4.5
14/04/1993	08:05:49.43	-26.3138	27.2434	3.8
28/04/1993	12:52:14.00	-26.9112	26.6645	4.2
30/10/1994	06:06:27.09	-28.0213	26.7184	5.5
18/01/1995	15:06:19.98	-26.4133	27.2471	4.4
10/02/1995	01:56:24.10	-26.8338	26.6690	4.9
20/05/1995	04:19:00.43	-26.9223	26.6724	4.4
30/06/1995	16:58:29.50	-26.3853	27.4054	3.9
25/11/1995	04:05:02.61	-26.9224	26.6805	4.9
17/12/1995	22:31:33.46	-27.9673	26.6594	4.5
25/02/1996	06:18:16.07	-26.9418	26.6131	4.3
01/03/1996	05:34:27.06	-26.2167	28.0917	4.3
12/03/1996	18:49:00.78	-26.8172	26.6571	4.6
05/05/1996	01:14:37.23	-26.3916	27.2790	4.3
16/05/1996	22:09:01.70	-26.9145	16.9014	4.0
09/06/1996	20:12:33.66	-12.5624	26.2036	4.9
04/12/1996	00:09:10.59	-26.9569	26.5007	4.2
11/12/1996	12:50:07.03	-27.8959	26.7290	4.7
25/12/1996	12:20:46.39	-26.8640	26.5876	4.6
25/12/1996	18:23:41.18	-26.7991	26.5448	4.2
03/01/1997	03:23:25.91	-26.4785	27.6260	4.4
20/01/1997	06:47:14.10	-26.7500	26.3700	4.1
10/02/1997	16:10:28.58	-26.9330	26.7087	5.1
20/03/1997	07:44:59.66	-26.7831	26.4111	4.5
21/07/1997	08:45:49.05	-26.8706	26.7773	4.7
21/09/1997	18:13:22.95	-7.3604	30.3214	5.5
25/09/1997	00:05:23.49	-26.3720	27.3481	4.7
11/12/1997	05:29:45.83	-26.8974	26.6575	4.5
12/12/1997	16:42:46.96	-26.9542	26.6804	4.5
06/02/1998	07:52:38.09	-26.9433	26.6900	4.4
18/02/1998	07:47:16.08	-26.9103	26.5786	4.3
26/04/1998	00:50:24.72	-26.2812	27.4491	4.4
19/06/1998	11:47:42.70	-28.3446	27.8996	4.3
12/01/1999	02:50:22.29	-26.3770	27.3010	4.5
23/01/1999	08:47:33.16	-26.9180	26.6300	4.2
02/02/1999	10:33:19.38	-26.5010	27.7380	4.1
22/04/1999	22:19:36.77	-27.9390	26.6750	5.5

Date	Origin time	Latitude	Longitude	Magnitude (mb)
07/05/1999	02:10:42.20	-7.4860	31.6140	5.2
30/12/1999	00:19:23.82	-26.0700	35.1970	3.9
08/02/2000	13:30:23.53	-26.3517	27.3784	4.4
07/04/2000	18:29:43.14	-26.8493	26.6424	4.2
25/01/2001	09:20:46.76	-26.9029	26.6819	4.3
31/03/2001	05:09:04.49	-26.9152	26.4649	4.1
31/07/2001	22:22:23.33	-26.8672	26.6178	4.6
23/02/2002	03:28:47.29	-26.8799	26.5439	4.3
21/03/2002	16:05:32.68	-26.4706	27.3193	4.3
23/03/2002	00:52:08.42	-26.9227	26.6767	4.4
30/03/2002	02:10:47.25	-26.8630	26.5842	4.3
09/06/2002	09:40:04.43	-26.3002	27.0767	3.9
12/07/2002	03:16:56.57	-26.4327	29.0719	4.5
05/04/2003	14:46:56.78	-27.8300	27.2276	4.1
19/04/2003	08:20:15.10	-26.5789	26.1209	3.2
18/03/2004	14:23:11.17	-25.7690	27.6790	3.9
23/03/2004	20:54:58.54	-26.9786	26.7415	4.2
30/04/2004	19:47:38.32	-27.8427	26.3546	3.9
08/01/2005	04:01:22.99	-28.1098	26.7843	4.0
25/01/2005	18:10:34.74	-26.8907	26.5572	4.0
09/03/2005	10:15:31.41	-26.8981	26.6674	4.6
09/03/2005	16:47:26.73	-26.8300	26.6638	4.2
22/02/2006	22:19:05.86	-21.1788	33.5083	5.8
28/04/2006	10:50:02.27	-26.2420	28.2452	3.8
29/04/2006	20:57:37.22	-26.9517	26.6530	4.3
10/04/2007	08:43:13.93	-26.9330	26.6609	4.1
28/12/2007	05:59:40.38	-26.8934	26.6654	4.1
08/03/2008	04:20:12.27	-26.4056	27.4386	4.1
15/12/2008	01:34:40.97	-26.9086	26.6960	3.9
13/03/2009	07:51:29.92	-26.9268	26.7129	4.1
16/03/2009	14:05:43.17	-26.9406	26.6715	4.3
29/11/2009	01:04:48.48	-26.9275	26.7202	4.2
05/12/2010	14:13:30.15	-20.7572	33.7592	4.1
12/01/2011	06:14:21.04	-28.6544	20.3038	4.2
25/01/2011	02:39:54.12	-28.4301	20.5803	4.0
21/02/2011	21:19:11.81	-28.6636	20.3087	4.2
06/04/2011	23:34:52.69	-28.7036	20.2286	4.0

## B.2 Phonon Scattering Model Parameters

Phonon scattering synthetics are run for a range of models in attempt to simulate the precursors to PKP<sub>df</sub> observed in the data. The scattering layer is altered in terms of: thickness, height above the CMB, number of scattering layers, RMS velocity perturbation of the heterogeneities, density scaling factor, and heterogeneity scale length. The model parameters used are given below.

Table B.2: Phonon scattering model parameters for single layer models. The height of the upper and lower bounds of the scattering layer above the CMB are shown in columns “Bottom” and “Top”. The velocity/density scaling factor is in column “Density scaling”, RMS velocity perturbation is in column “RMS %”, and scatterer length scale is in column “Scale (km)”.

Bottom	Top	Density scaling	RMS (%)	Scale (km)
<b>Layer Height</b>				
CMB	50	0.8	2	8.0
100	150	0.8	2	8.0
150	200	0.8	2	8.0
200	250	0.8	2	8.0
250	300	0.8	2	8.0
300	350	0.8	2	8.0
350	400	0.8	2	8.0
400	450	0.8	2	8.0
50	100	0.8	2	8.0
500	550	0.8	2	8.0
600	650	0.8	2	8.0
700	750	0.8	2	8.0
800	850	0.8	2	8.0
900	950	0.8	2	8.0
1000	1050	0.8	2	8.0
1100	1150	0.8	2	8.0
1200	1250	0.8	2	8.0
<b>Density Scaling</b>				
CMB	50	0.7	2	8.0
CMB	50	0.75	2	8.0
CMB	50	0.8	2	8.0
CMB	50	0.85	2	8.0
CMB	50	0.9	2	8.0
CMB	50	0.95	2	8.0
CMB	50	1.0	2	8.0
<b>RMS</b>				
CMB	50	0.8	1	8.0
CMB	50	0.8	1	8.0
CMB	50	0.8	1	8.0
CMB	50	0.8	2	8.0
CMB	50	0.8	3	8.0
CMB	50	0.8	3	8.0
CMB	50	0.8	4	8.0
CMB	50	0.8	4	8.0
CMB	50	0.8	4	8.0
<b>Scale length</b>				
CMB	50	0.8	2	2.0
CMB	50	0.8	2	4.0
CMB	50	0.8	2	6.0
CMB	50	0.8	2	8.0
CMB	50	0.8	2	10.0
CMB	50	0.8	2	12.0
CMB	50	0.8	2	14.0
CMB	50	0.8	2	16.0
CMB	50	0.8	2	32.0
<b>Thickness</b>				
CMB	10	0.8	2	8.0
CMB	20	0.8	2	8.0
CMB	30	0.8	2	8.0
CMB	40	0.8	2	8.0
CMB	50	0.8	2	8.0
CMB	60	0.8	2	8.0
CMB	70	0.8	2	8.0
CMB	80	0.8	2	8.0
CMB	90	0.8	2	8.0
CMB	100	0.8	2	8.0

Bottom	Top	Density scaling	RMS (%)	Scale (km)
CMB	150	0.8	2	8.0
CMB	150	0.8	2	8.0
CMB	200	0.8	2	8.0
<b>Thickness+RMS</b>				
CMB	70	0.8	3	8.0
CMB	70	0.8	4	8.0
CMB	70	0.8	2	4.0
CMB	80	0.8	2	4.0
CMB	80	0.8	3	4.0
CMB	80	0.8	4	4.0
CMB	80	0.8	3	8.0
CMB	80	0.8	4	8.0

Models were also run with two independent layers of scattering heterogeneities. Parameters are given below.

Table B.3: Phonon scattering model parameters for double layer models. Parameters are listed as in Appendix Table B.2. The lower and upper of the two layers in the model are labelled “Layer 1” and “Layer 2”, respectively.

Layer 1					Layer 2				
Bot.	Top	Den.	RMS (%)	Sca. (km)	Bot.	Top	Den.	RMS (%)	Sca. (km)
CMB	20	0.8	2	8.0	20	40	0.8	2	8.0
CMB	25	0.8	2	8.0	25	50	0.8	1	8.0
CMB	25	0.8	3	8.0	25	50	0.8	1	8.0
CMB	25	0.8	4	8.0	25	50	0.8	1	8.0
CMB	25	0.8	4	8.0	25	75	0.8	1	8.0
CMB	50	0.8	2	8.0	50	100	0.8	1	8.0
CMB	50	0.8	4	8.0	50	100	0.8	1	8.0
CMB	50	0.8	4	8.0	50	100	0.8	2	8.0
CMB	20	0.8	2	8.0	22	42	0.8	2	8.0
CMB	20	0.8	2	8.0	24	44	0.8	2	8.0
CMB	20	0.8	2	8.0	26	46	0.8	2	8.0
CMB	20	0.8	2	8.0	28	48	0.8	2	8.0
CMB	20	0.8	2	8.0	30	50	0.8	2	8.0
CMB	20	0.8	2	8.0	40	60	0.8	2	8.0
CMB	20	0.8	2	8.0	50	70	0.8	2	8.0
CMB	20	0.8	2	8.0	60	80	0.8	2	8.0
CMB	20	0.8	2	8.0	70	90	0.8	2	8.0
CMB	20	0.8	2	8.0	80	100	0.8	2	8.0
CMB	20	0.8	2	8.0	90	110	0.8	2	8.0
CMB	20	0.8	2	8.0	100	120	0.8	2	8.0
CMB	20	0.8	2	8.0	100	130	0.8	2	8.0
CMB	20	0.8	2	8.0	110	130	0.8	2	8.0
CMB	20	0.8	2	8.0	120	140	0.8	2	8.0
CMB	20	0.8	2	8.0	520	540	0.8	2	8.0



## Appendix C

# PKKP Scattering Appendix

### C.1 PK•KP Scattering Regions

The region of the Earth that the PK•KP probe can sample varies with scattering height above the CMB. At greater heights the scattering region is smaller than at the CMB.

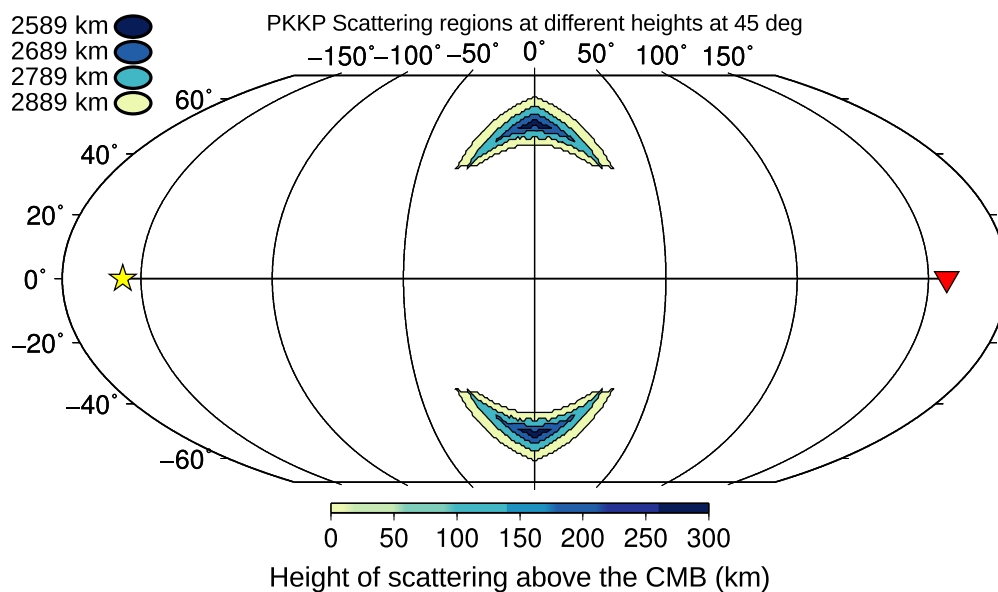


Figure C.1: Regions of potential scattering for a surface focus event (yellow star) to a receiver (red triangle) for scattering at depths from 2889 km (at the CMB) to 2589 km (300 km above the CMB) in 100 km increments. As Figure 3.4.

## C.2 Scattering Results

Scattering heterogeneities detected at all arrays are ray-traced to locations in the lowermost mantle. I observe strong lateral variation in the height of scattering at the CMB. Scattering points are grouped into  $10^\circ \times 10^\circ$  cells and plotted in Figure 3.9, and shown here in larger figures, Figure C.2.

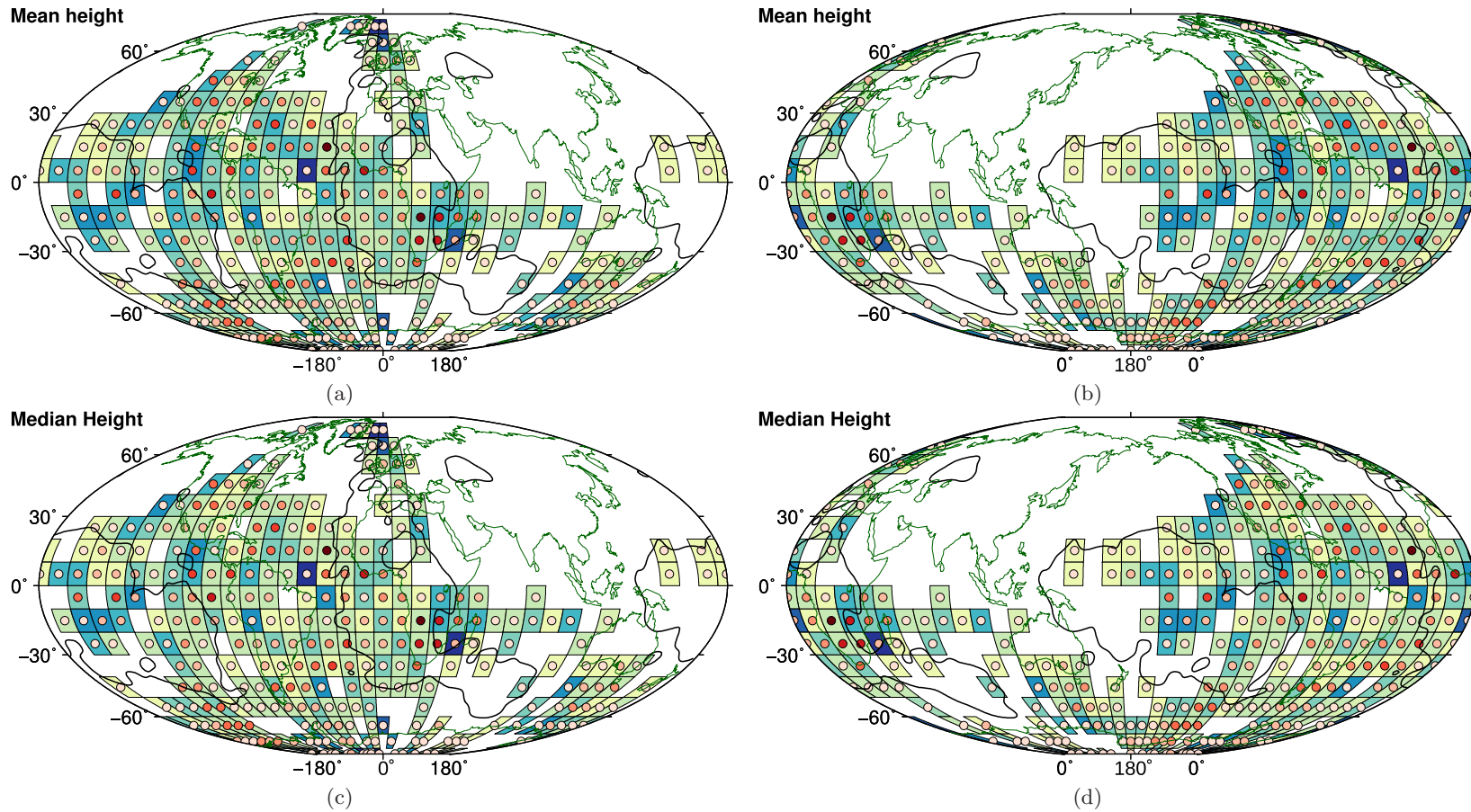


Figure C.2: Continues on to next page.

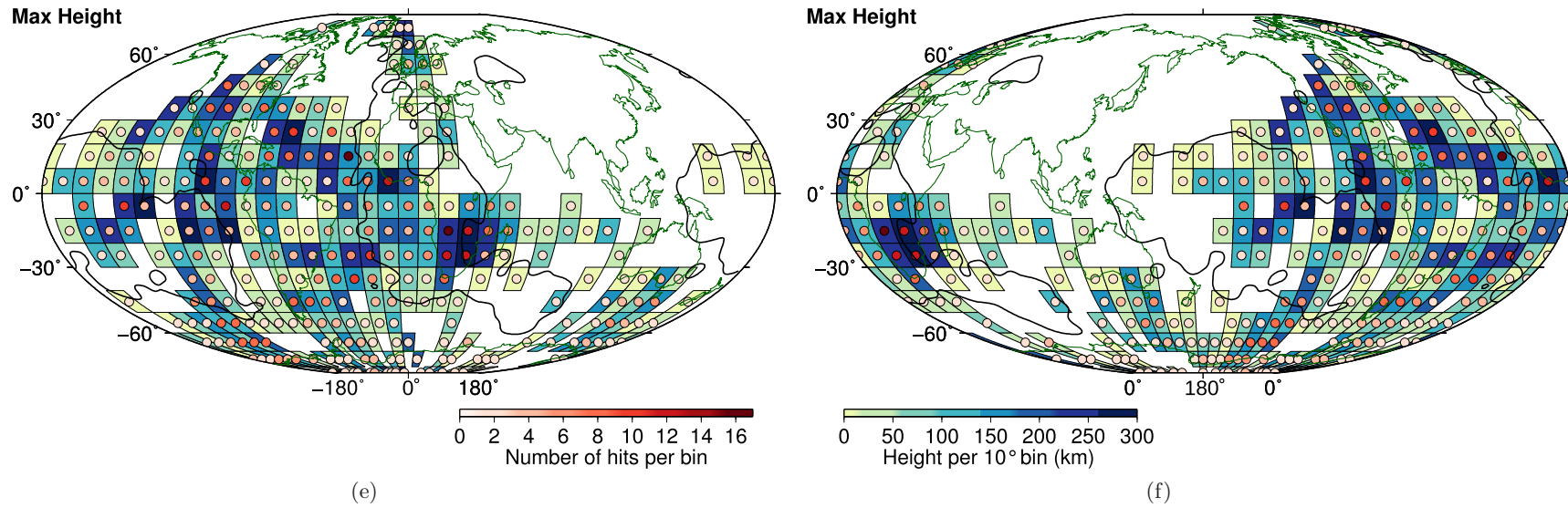


Figure C.2: Scattering heterogeneity heights above the CMB, centred at  $0^\circ$  (left) and  $180^\circ$  (right) longitude, displayed in  $10^\circ$  by  $10^\circ$  cells as (a and b) mean scattering height in each cell, (c and d) median scattering height, (e and f) maximum scattering height. The height of each cell is shown by the tile colour and the number of scattering locations in each cell is shown by the colour of the inset circle. The  $-0.4\%$   $V_S$  contour from S40RTS is shown as the black line to represent the extent of the LLSVPs.

Array by array error testing (Section 3.7) demonstrates that arrays BV and BR have lateral and vertical errors when ray-tracing scattering points. Results maps (Figure 3.9) are replotted excluding these data.

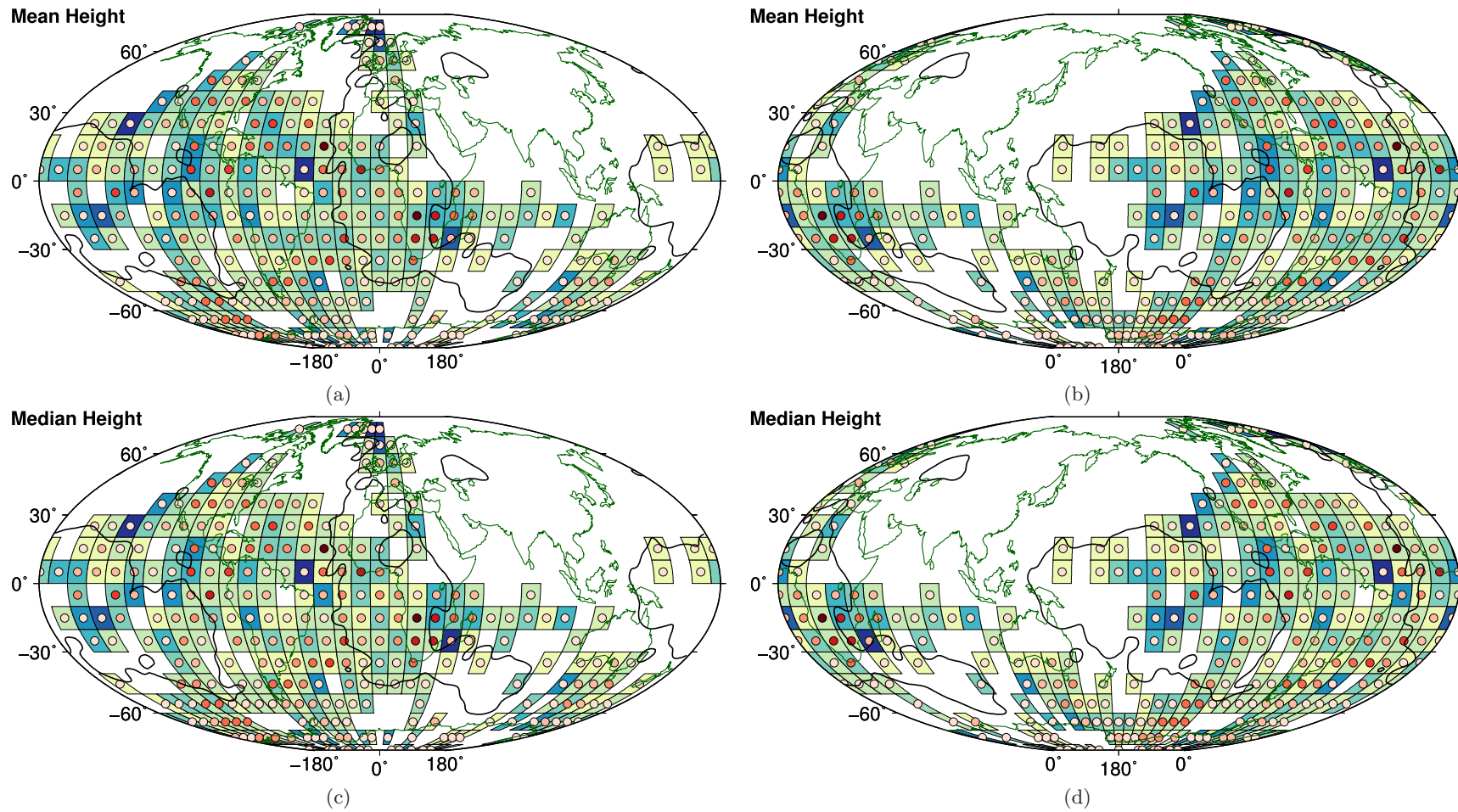
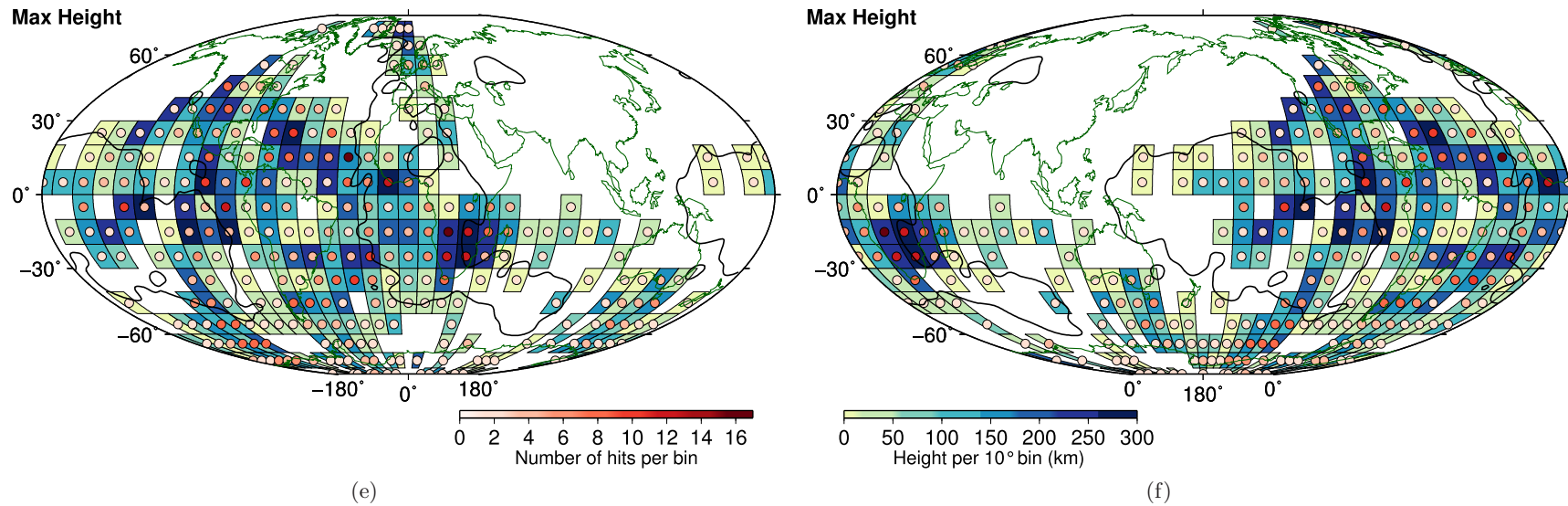


Figure C.3: Continues on to next page.



(e)

(f)

Figure C.3: Scattering heterogeneity heights above the CMB as in Figure 3.9 but excluding scattering from arrays BV and BR, centred at  $0^\circ$  (left) and  $180^\circ$  (right) longitude, displayed in  $10^\circ$  by  $10^\circ$  cells as (a and b) mean scattering height in each bin, (c and d) median scattering height, (e and f) maximum scattering height. The height of each bin is shown by the tile colour and the number of scattering locations in each bin is shown by the colour of the inset circle. The  $-0.4\%$   $V_S$  contour from S40RTS is shown as the black line to represent the extent of the LLSVPs.

## C.3 Directivity Error Testing

### C.3.1 Array Specific Errors

The accuracy of each array used is analysed by using the fk-F-trace process to identify synthetic signals created for a range of slownesses and back-azimuths. Noise of the character and relative amplitude (SNR) for that array is added to the synthetic signal. The directivity residuals (difference between the slowness and back-azimuth of the input signal and those measured by the fk-F-trace process) are then used to perturb a test signal which is then ray-traced. The differences in the ray-traced locations from that of the test signal indicate the accuracy to which each array can locate scattering heterogeneities in the lower mantle.

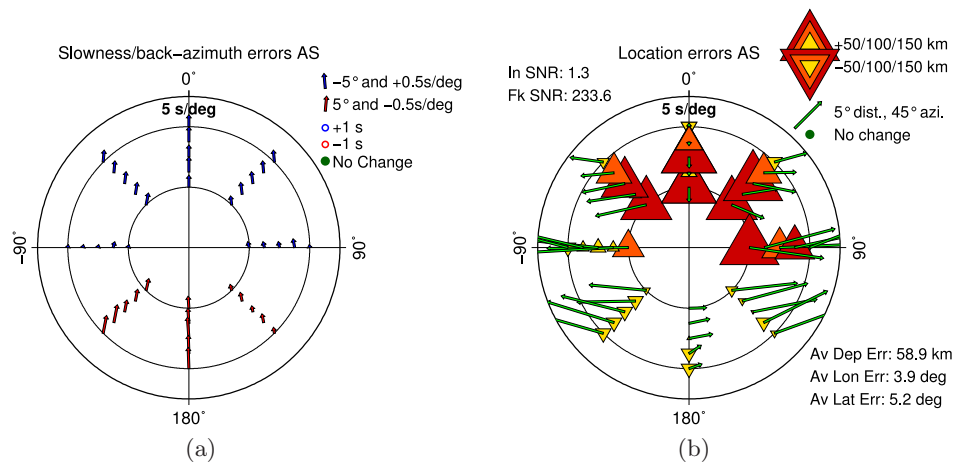


Figure C.4: Array specific errors of signal measurements and ray-traced locations for AS array for a range of input directions, as in Figure 3.14. (a) Errors in directivity values measured using the fk F-statistic are shown at the input slowness and back-azimuth of the synthetic signal as deviations in back-azimuth from north and arrow length. Time errors are shown as coloured circles. (b) Scattering point mislocations resulting from ray-tracing shown at the input slowness and back-azimuth of the synthetic signal displayed in terms of distance and direction (green arrow) and depth (triangles). Triangles and inverted triangles indicate the the scattering point is moved shallower and deeper, respectively, by the directivity error.

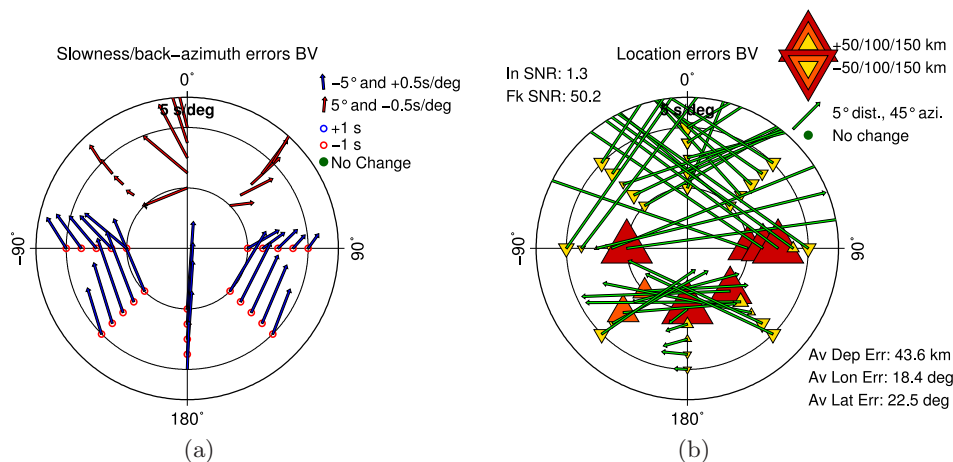


Figure C.5: Array specific errors of signal measurements and ray-traced locations for BV array for a range of input directions as Figure C.4.

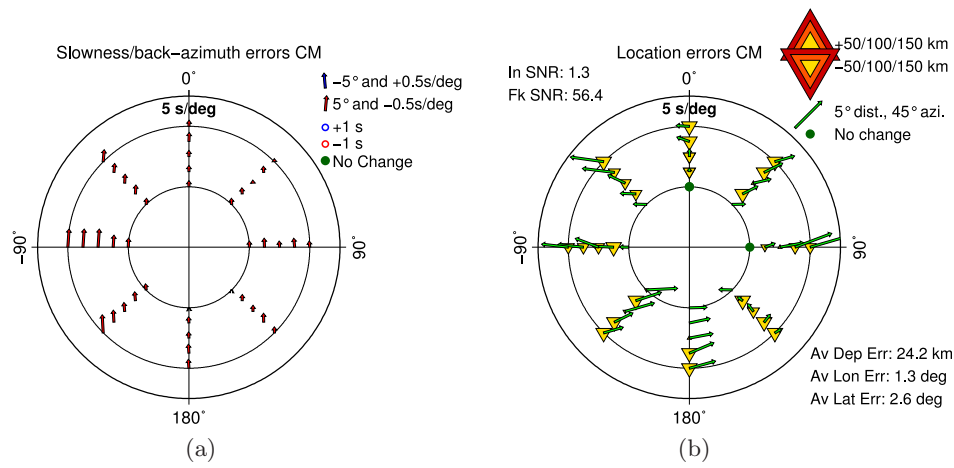


Figure C.6: Array specific errors of signal measurements and ray-traced locations for CM array for a range of input directions as Figure C.4.

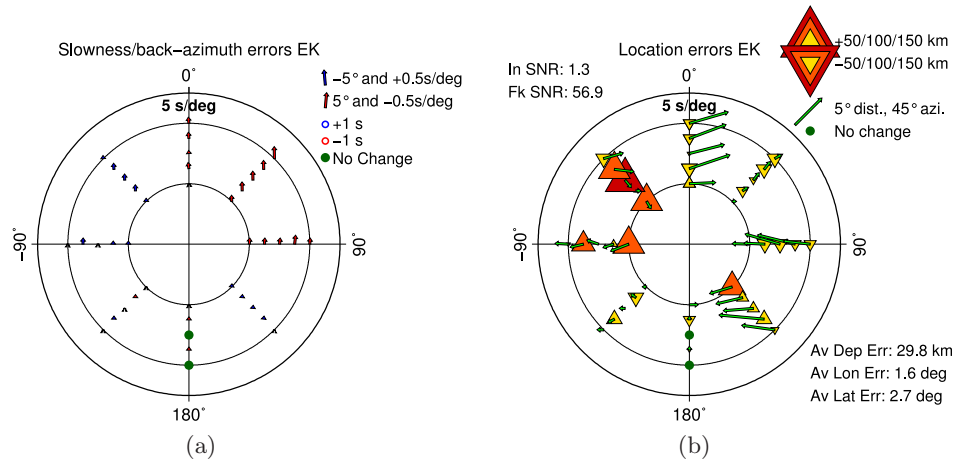


Figure C.7: Array specific errors of signal measurements and ray-traced locations for EK array for a range of input directions as Figure C.4.

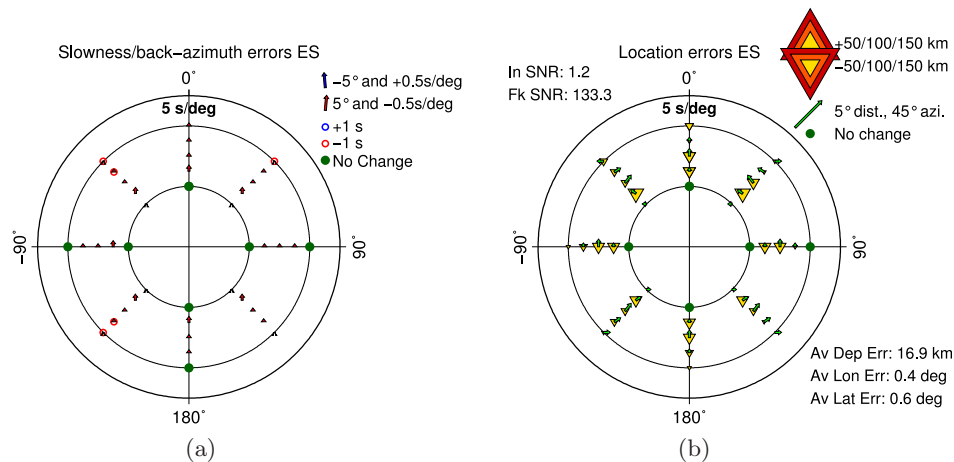


Figure C.8: Array specific errors of signal measurements and ray-traced locations for ES array for a range of input directions as Figure C.4.

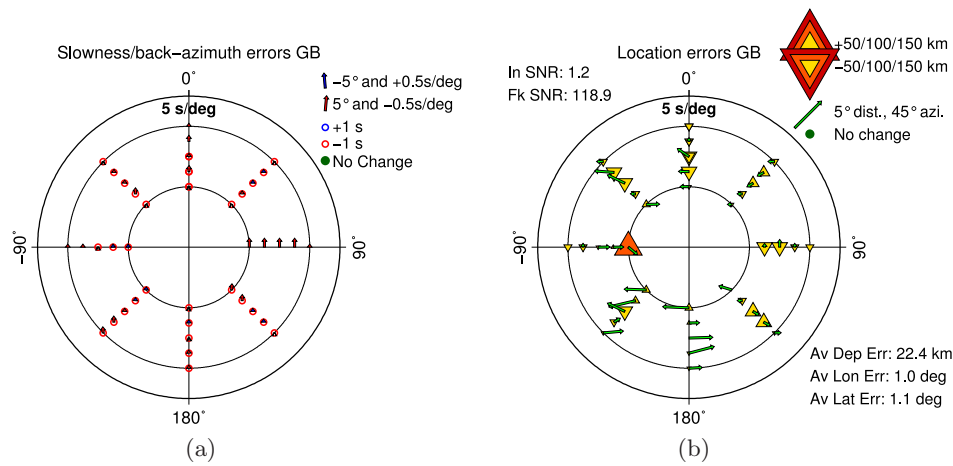


Figure C.9: Array specific errors of signal measurements and ray-traced locations for GB array for a range of input directions as Figure C.4.

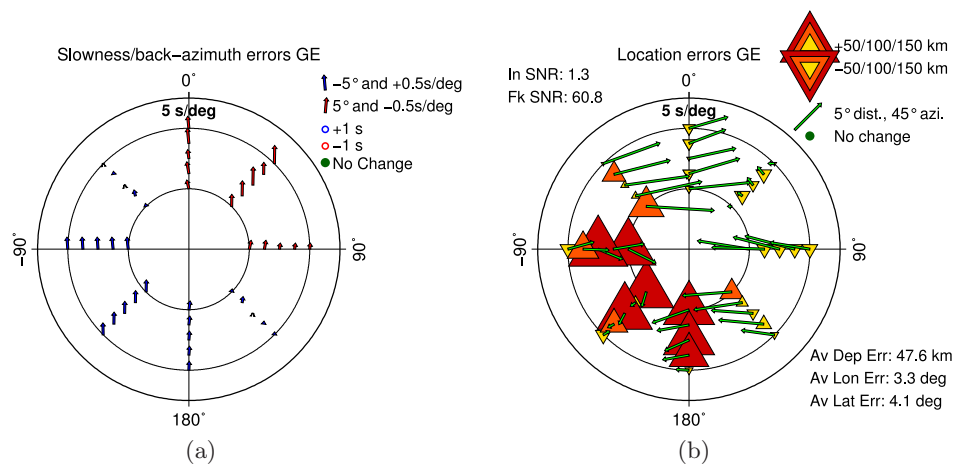


Figure C.10: Array specific errors of signal measurements and ray-traced locations for GE array for a range of input directions as Figure C.4.

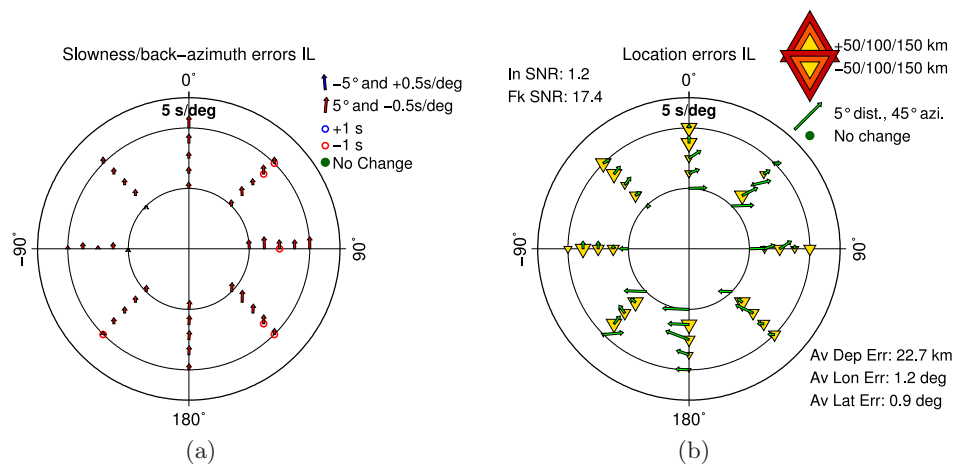


Figure C.11: Array specific errors of signal measurements and ray-traced locations for IL array for a range of input directions as Figure C.4.

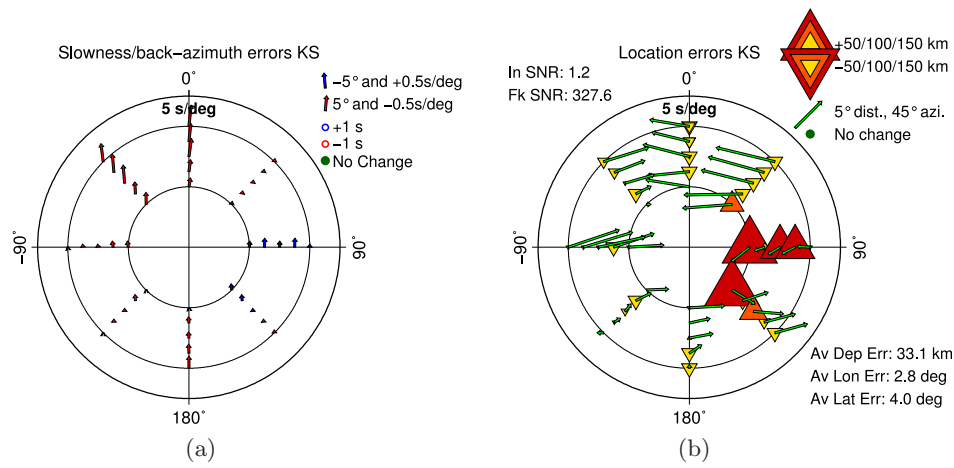


Figure C.12: Array specific errors of signal measurements and ray-traced locations for KS array for a range of input directions as Figure C.4.

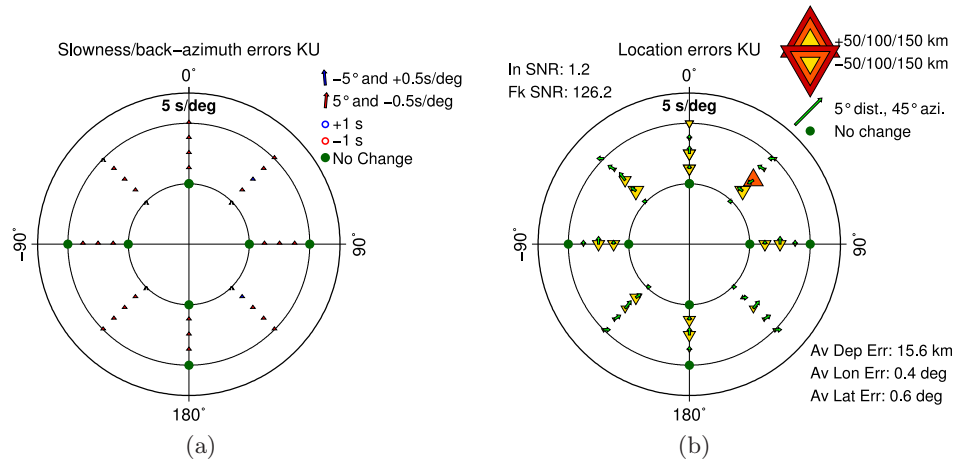


Figure C.13: Array specific errors of signal measurements and ray-traced locations for KU array for a range of input directions as Figure C.4.

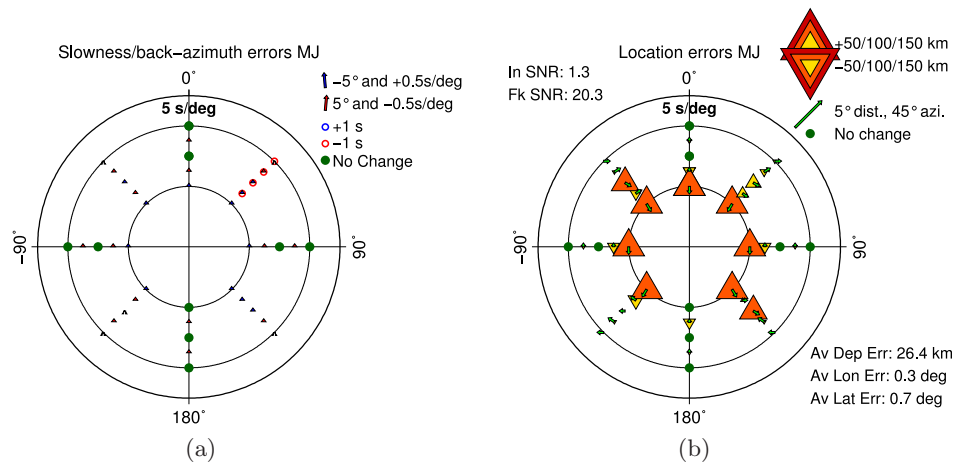


Figure C.14: Array specific errors of signal measurements and ray-traced locations for MJ array for a range of input directions as Figure C.4.

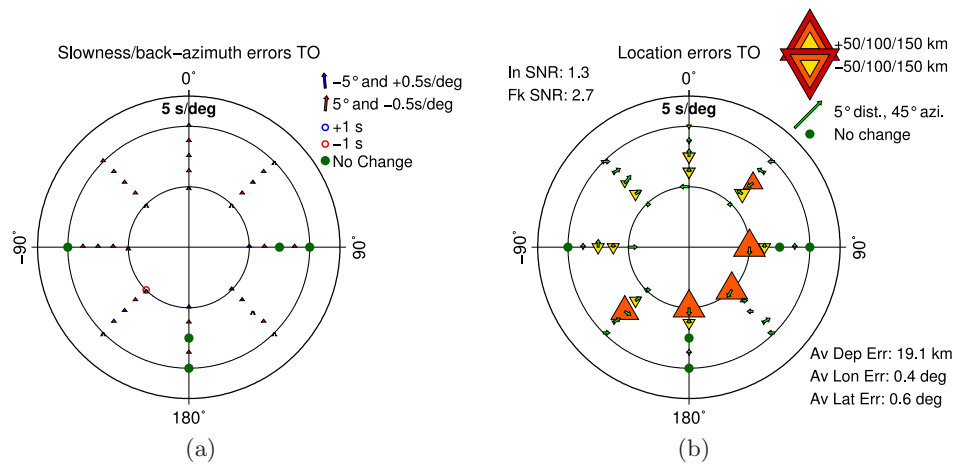


Figure C.15: Array specific errors of signal measurements and ray-traced locations for TO array for a range of input directions as Figure C.4.

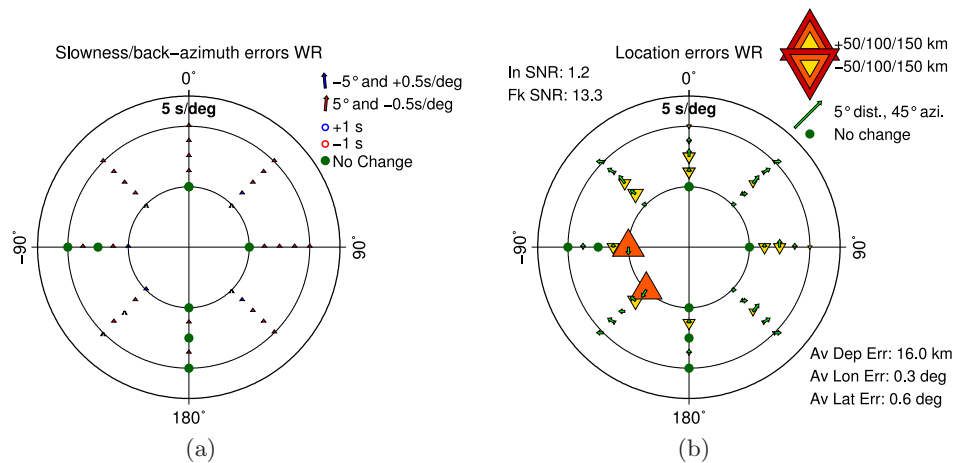


Figure C.16: Array specific errors of signal measurements and ray-traced locations for WR array for a range of input directions as Figure C.4.

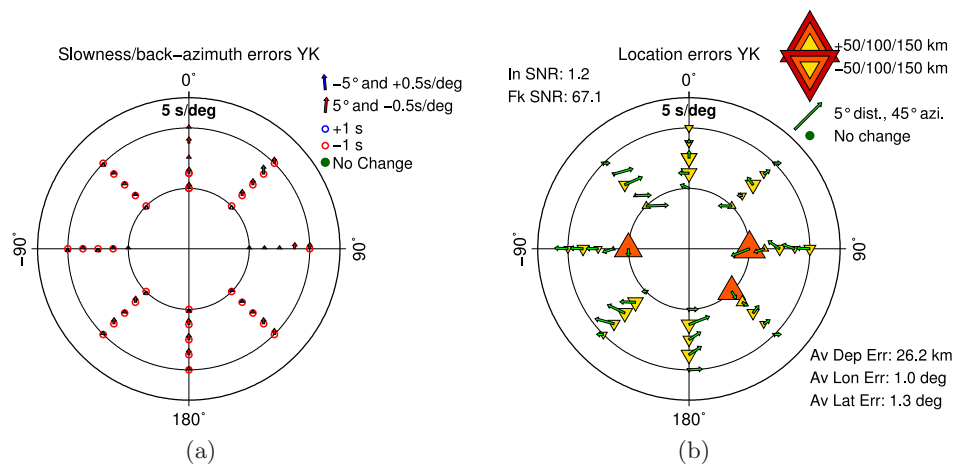


Figure C.17: Array specific errors of signal measurements and ray-traced locations for YK array for a range of input directions as Figure C.4.

### C.3.2 Average Array Errors

Synthetic waves with incident slownesses of 2.0 s/deg are found to be poorly fit as the PK ray path has a minimum slowness of 2.1 s/deg. Average scattering point mislocations are recalculated for each array disregarding the results of signals with a slowness of 2.0 s/deg.

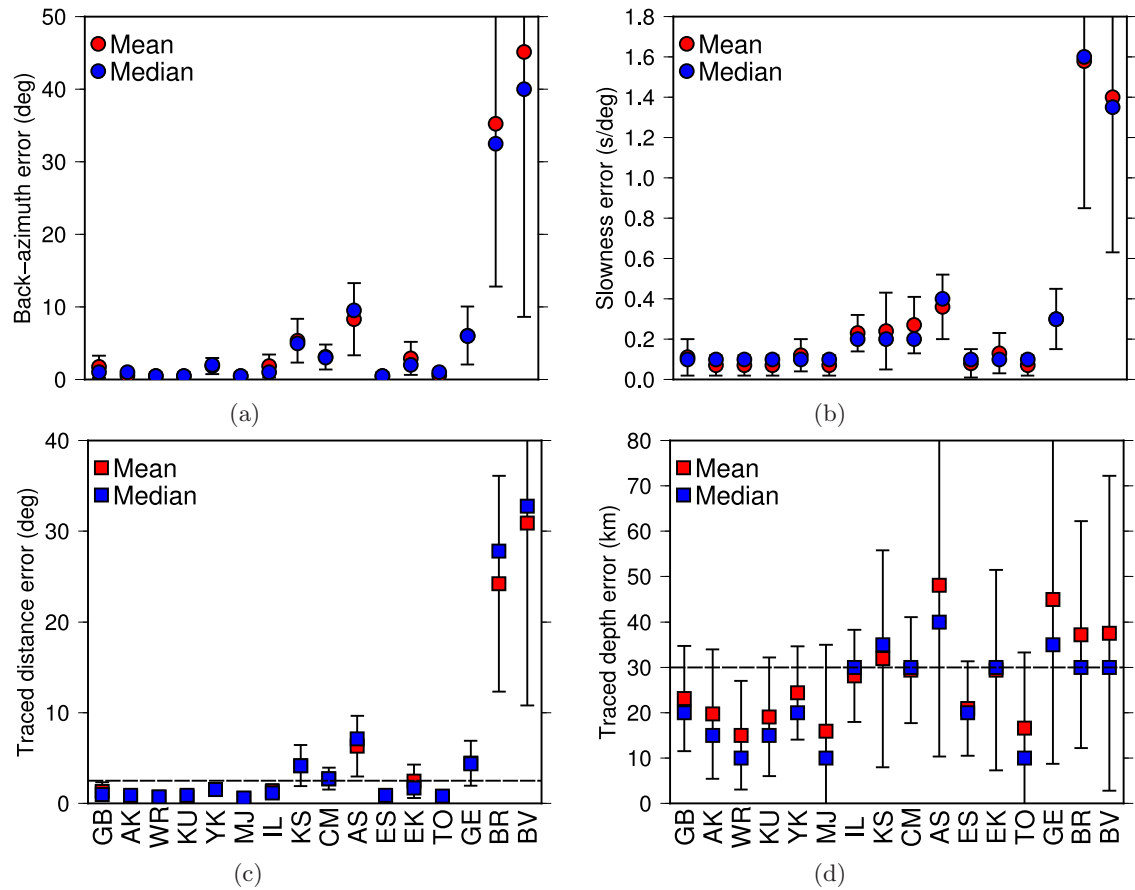


Figure C.18: Magnitude of errors of directivity values measured using the  $fk$   $F$ -statistic (a and b) and the scattering point mislocations resulting from ray-tracing (c and d) for each array, as in Figure 3.15 but excluding errors calculated for signals with input slownesses of 2.0 s/deg. Values are displayed as the mean (red) with 1-standard deviation error bars and the median (blue), the latter is considered more robust. Arrays are ordered by decreasing aperture from left to right. Measured (a) back-azimuth and (b) slowness errors for synthetic signals from a range of incoming directions with noise and noise levels typical of the array using values in Figure 3.13. Errors are dependent on incoming noise levels and the array configuration. (c) Lateral and (d) vertical mislocations for a typical scattering point ray-traced with the slowness and back-azimuth errors determined for that array.

### C.3.3 Correlation With Large Scale Features

The locations of scattering heterogeneities in the lower mantle are compared with the locations of large scale structures, the LLSVPs and high velocity anomalies associated with subduction. Here I reproduce Figures 3.18 and 3.19 as Figures C.19 and C.20, respectively, for easier viewing.

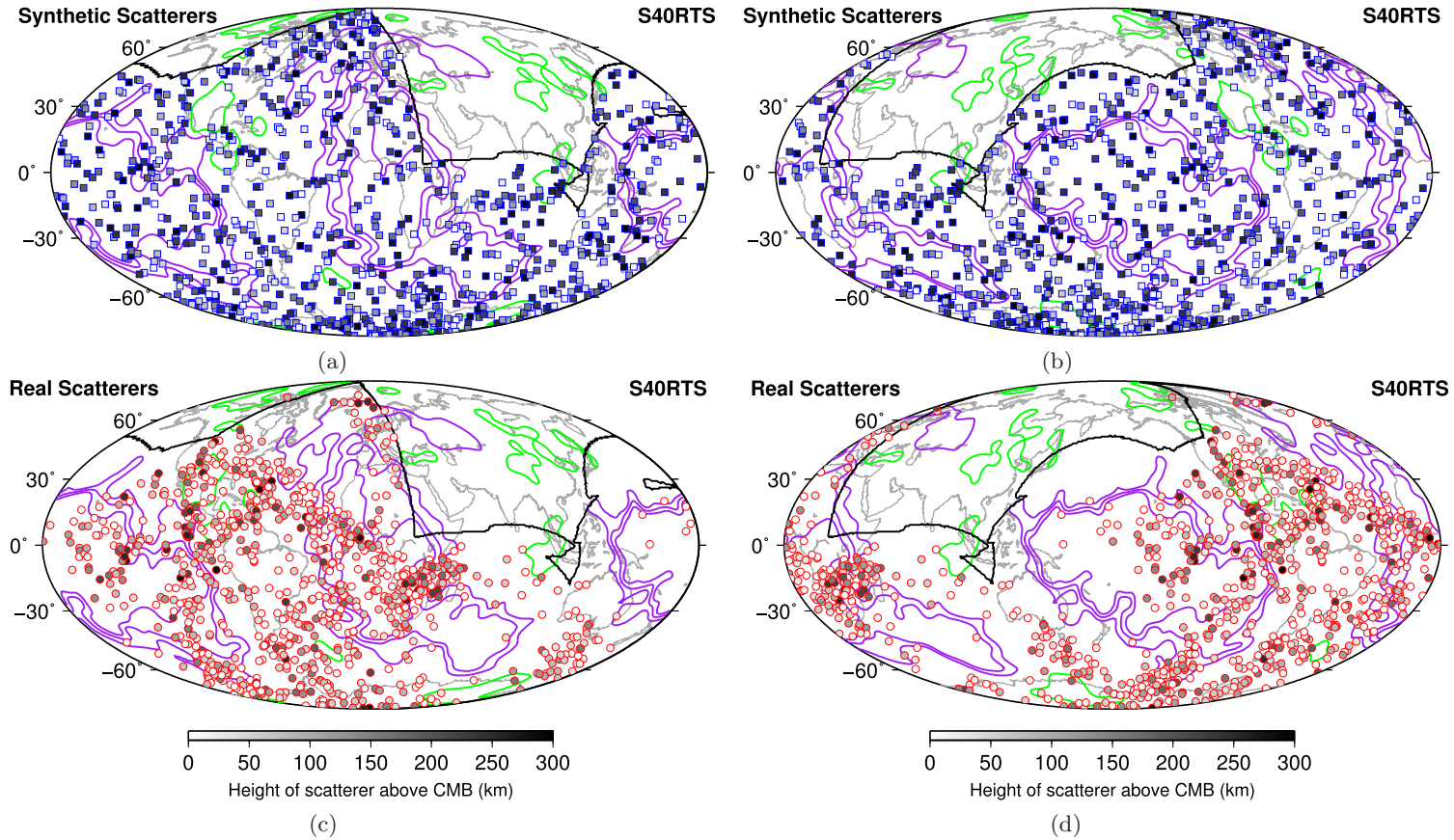


Figure C.19: Continues on to next page.

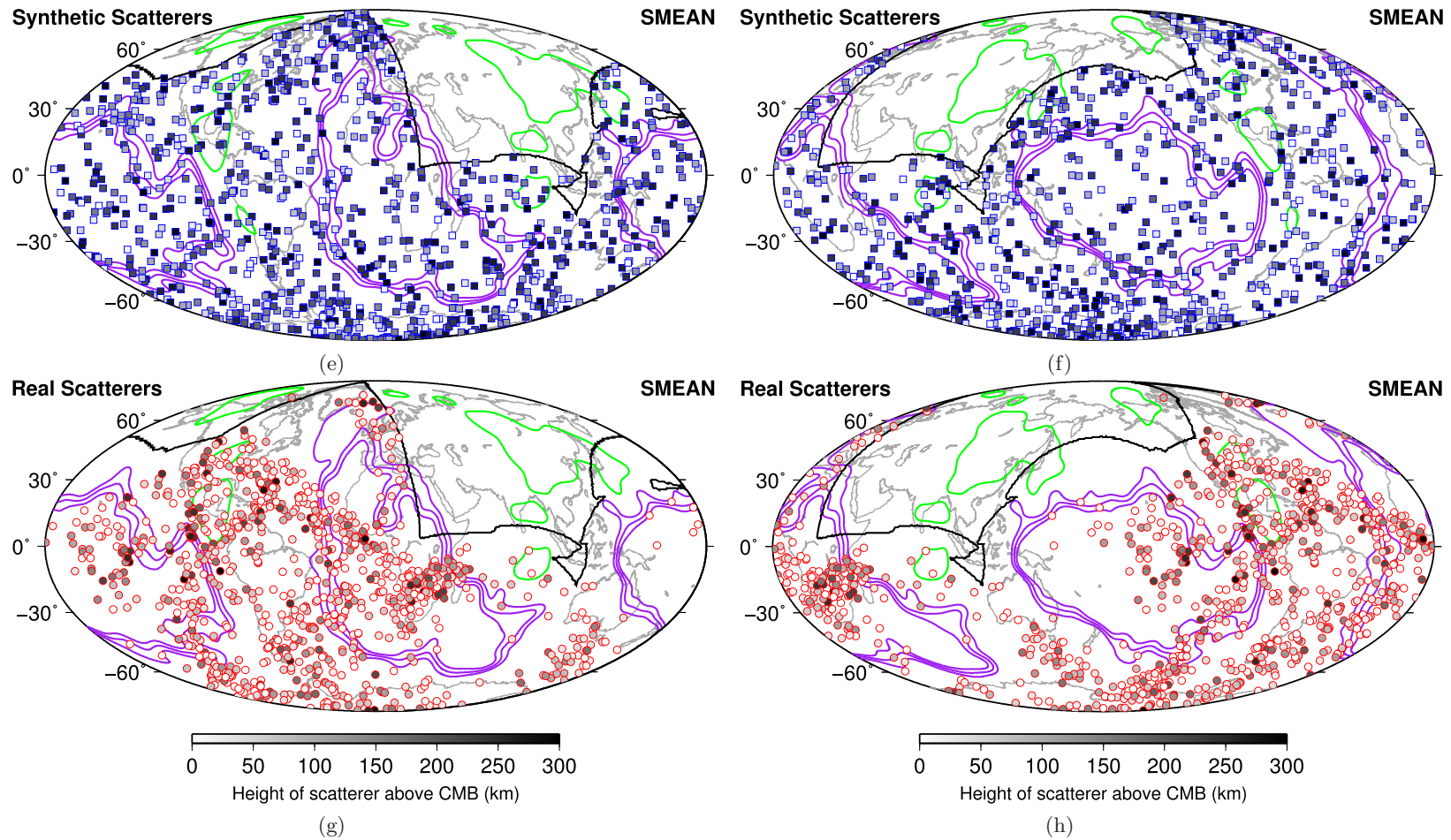


Figure C.19: Scattering heterogeneities relative to tomography models S40RTS (a-d) and SMEAN (e-h) [Ritsema et al., 2011; Becker & Boschi, 2002]. Location and height of scattering points above the CMB compared with S40RTS for synthetic (a and b) and real (c and d) data. LLSVP iso-velocity contours (0.0, -0.4, and -0.8 %  $V_S$ ) and faster velocity contours (+0.9 %  $V_S$ ) at 2800 km from S40RTS [Ritsema et al., 2011] are shown as purple and green lines, respectively. Location and height of scattering points above the CMB compared with SMEAN for synthetic (e and f) and real (g and h) data. LLSVP iso-velocity contours (0.0, -0.4, and -0.8 %  $V_S$ ) and faster velocity contours (+1.3 %  $V_S$ ) at 2850 km from SMEAN [Becker & Boschi, 2002] are shown as purple and green lines, respectively. The limit of the sampling area (Figure 3.6) is shown by the black line.

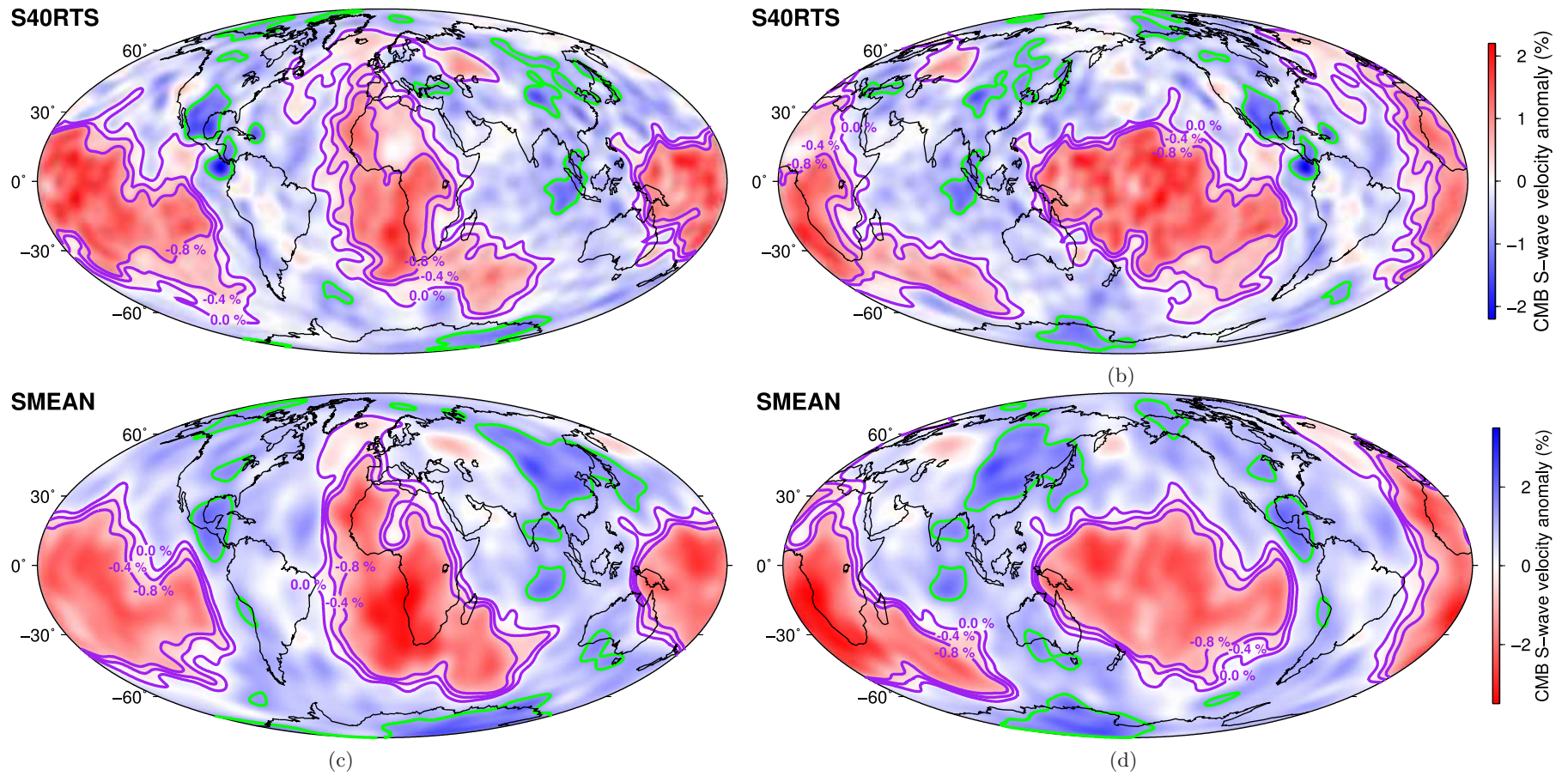


Figure C.20: Tomography models overlaid with the contours used to represent the low and high velocity anomalies to which distances from scatterers are measured for S40RTS (a and b) and SMEAN (c and d). Low velocity anomalies, LLSVPs, are defined by the 0.0, -0.4, and -0.8 %  $V_S$  iso-velocity contours for both models (purple lines) and high velocity anomalies are defined by the +0.9 and +1.3 %  $V_S$  contours for S40RTS and SMEAN, respectively (green lines). All contours are taken from the lowermost depth slice of each model: 2800 km for S40RTS and 2850 km SMEAN.

## C.4 Event Data

The NEIC PDE catalogue is search for events from 01/05/1985 (matching the earliest available GBA data) to 31/12/2011 for events with magnitude  $>6$ . A total of 1097 events with accessible data are found.

Table C.1: Events in PKKP dataset reported in the NEIC PDE catalogue. Dates are given in day/month/year format.

Date	Origin Time	Latitude	Longitude	Depth (km)	Mag.
14/05/1985	13:24:57.83	-10.61	41.42	10.0	6.0
14/05/1985	18:11:08.95	-10.56	41.42	10.0	6.4
16/05/1985	14:20:25.16	-29.08	77.74	10.0	6.1
20/05/1985	15:11:40.68	35.49	87.17	33.0	6.1
31/05/1985	07:24:34.12	12.25	144.28	31.0	6.0
04/06/1985	03:56:27.06	4.87	127.48	94.0	6.0
15/06/1985	00:57:00.79	49.89	78.88	0.0	6.0
30/06/1985	02:39:02.79	49.86	78.70	0.0	6.0
29/07/1985	07:54:44.07	36.19	70.90	98.0	6.6
02/08/1985	07:46:53.30	36.17	70.78	120.0	6.5
04/08/1985	02:36:23.87	7.50	123.50	35.0	6.2
09/08/1985	19:59:44.07	16.90	120.19	21.0	6.1
12/08/1985	03:49:18.09	37.77	141.77	51.0	6.3
23/08/1985	12:41:56.16	39.43	75.22	6.0	7.5
10/09/1985	06:39:01.74	27.21	139.85	501.0	6.1
11/09/1985	20:45:49.54	39.36	75.41	15.0	6.5
15/09/1985	01:29:23.31	-4.09	136.24	10.0	6.3
15/09/1985	02:42:54.89	-4.13	136.05	10.0	6.3
04/10/1985	12:25:51.86	35.82	140.09	84.0	6.2
23/10/1985	00:49:11.17	-11.11	125.16	13.0	6.0
29/10/1985	13:13:44.62	36.68	54.75	52.0	6.0
08/11/1985	18:40:24.85	27.96	140.61	41.0	6.1
16/11/1985	04:12:18.83	-38.58	78.37	10.0	6.6
17/11/1985	09:40:21.29	-1.64	134.91	10.0	7.1
14/12/1985	06:46:11.78	3.68	126.60	22.0	6.1
24/12/1985	04:09:41.27	-35.09	54.27	10.0	6.0
03/02/1986	20:47:35.34	27.79	139.55	508.0	6.5
12/02/1986	02:59:30.42	36.38	141.13	30.0	6.1
06/03/1986	00:05:38.35	40.37	51.56	33.0	6.6
24/03/1986	19:31:39.34	-2.49	138.70	29.0	6.8
17/06/1986	18:13:11.55	5.64	125.26	31.0	6.4
20/06/1986	17:12:46.94	31.24	86.85	33.0	6.1
06/07/1986	19:24:22.99	34.42	80.16	9.0	6.1
07/07/1986	16:26:56.61	10.39	56.83	7.0	6.4
09/07/1986	23:10:53.10	1.90	126.53	27.0	6.5
25/07/1986	23:41:08.64	26.38	125.92	21.0	6.2
10/08/1986	04:40:49.77	1.99	128.27	104.0	6.1
14/08/1986	19:39:13.67	1.79	126.52	33.0	7.4
17/08/1986	15:27:41.26	2.28	126.96	30.0	6.3
17/08/1986	15:31:19.08	2.16	127.11	33.0	6.3
20/08/1986	21:23:54.88	34.57	91.63	33.0	6.5
26/08/1986	09:43:00.39	37.72	101.50	8.0	6.2
30/08/1986	21:28:35.45	45.55	26.32	132.0	6.9
13/09/1986	17:24:31.49	37.01	22.18	11.0	6.0
17/09/1986	21:25:15.06	10.50	56.98	10.0	6.0
17/10/1986	07:32:51.30	-5.27	131.43	67.0	6.3
14/11/1986	21:20:10.55	23.90	121.57	33.0	7.8
14/11/1986	23:04:37.09	23.87	121.71	33.0	6.3
30/11/1986	20:15:30.32	38.85	141.95	36.0	6.0
19/12/1986	03:41:55.31	-9.92	119.20	24.0	6.2
28/12/1986	20:04:35.13	-38.78	78.69	10.0	6.1
29/12/1986	15:49:59.19	15.22	119.88	53.0	6.0
09/01/1987	06:14:44.87	39.90	141.68	67.0	6.8
14/01/1987	11:03:48.75	42.56	142.85	102.0	6.6
06/02/1987	12:23:48.02	36.99	141.79	35.0	6.1
06/02/1987	13:16:17.89	36.99	141.69	47.0	6.5
13/02/1987	07:18:29.09	0.67	126.17	32.0	6.5
02/03/1987	05:57:43.56	-45.71	96.21	10.0	6.2
18/03/1987	03:36:30.33	32.03	131.84	54.0	6.7
03/04/1987	01:17:08.08	49.93	78.83	0.0	6.2
09/04/1987	00:48:55.51	1.24	128.43	45.0	6.1
17/04/1987	01:03:04.81	49.89	78.69	0.0	6.0

Date	Origin Time	Latitude	Longitude	Depth (km)	Mag.
22/04/1987	20:13:23.15	37.15	141.57	30.0	6.6
25/04/1987	12:16:52.44	16.07	120.30	107.0	6.3
25/04/1987	19:22:07.20	2.24	98.87	11.0	6.6
07/05/1987	03:05:49.17	46.74	139.23	430.0	6.6
11/05/1987	09:59:34.12	4.47	127.71	94.0	6.3
12/05/1987	01:30:25.03	7.09	126.70	24.0	6.5
18/05/1987	07:23:24.15	-2.23	100.03	33.0	6.0
05/06/1987	04:59:58.39	41.58	88.74	0.0	6.2
06/06/1987	18:40:27.48	10.67	126.11	14.0	6.3
07/06/1987	05:49:43.63	20.43	121.37	14.0	6.1
17/06/1987	01:32:53.72	-5.58	130.79	67.0	6.8
18/06/1987	10:01:07.30	17.29	121.36	42.0	6.0
20/06/1987	00:53:04.83	49.91	78.74	0.0	6.1
27/06/1987	00:17:04.61	-2.16	138.17	20.0	6.5
03/07/1987	10:10:43.78	31.20	130.32	168.0	6.1
03/10/1987	10:16:26.27	-5.45	131.01	73.0	6.4
29/10/1987	20:23:41	4.82	127.69	152.0	6.1
07/11/1987	16:23:55.90	5.63	126.61	80.0	6.2
15/11/1987	03:31:06.70	49.87	78.79	0.0	6.0
18/11/1987	16:27:05.27	12.85	124.77	22.0	6.3
26/11/1987	01:43:14.05	-8.25	124.15	33.0	6.5
12/12/1987	04:51:50.51	29.69	140.02	164.0	6.3
13/12/1987	03:21:04.89	49.99	78.84	0.0	6.1
15/12/1987	14:57:40.17	23.43	142.91	39.0	6.1
17/12/1987	02:08:19.92	35.36	140.21	62.0	6.4
02/01/1988	12:42:02.52	43.29	142.42	177.0	6.4
22/01/1988	12:04:57.88	-19.83	133.88	5.0	6.9
13/02/1988	03:05:05.98	49.95	78.91	0.0	6.1
24/02/1988	03:52:03.29	13.48	124.62	24.0	7.1
26/02/1988	06:17:31.53	-37.32	47.99	10.0	6.7
03/04/1988	01:33:05.85	49.92	78.94	0.0	6.1
04/04/1988	15:43:04.03	30.40	131.08	39.0	6.0
04/05/1988	00:57:06.83	49.93	78.77	0.0	6.1
07/05/1988	01:59:26.24	42.60	143.75	72.0	6.1
19/06/1988	20:19:52.69	12.38	121.07	16.0	6.4
03/07/1988	11:43:12.67	8.92	137.90	14.0	6.3
06/07/1988	15:54:19.14	41.74	144.20	30.0	6.3
25/07/1988	06:46:06.69	-6.08	133.67	27.0	6.9
06/08/1988	00:36:24.65	25.15	95.13	90.0	7.3
06/08/1988	09:03:21.95	36.46	71.04	195.0	6.1
11/08/1988	16:04:45.61	29.97	51.68	33.0	6.1
17/08/1988	01:59:07.71	-7.70	107.15	27.0	6.1
20/08/1988	23:09:09.56	26.75	86.62	57.0	6.8
07/09/1988	11:53:24.13	30.25	137.43	485.0	6.1
14/09/1988	03:59:57.45	49.83	78.81	0.0	6.1
05/11/1988	02:14:30.30	34.35	91.88	7.0	6.3
06/11/1988	13:03:19.34	22.79	99.61	17.0	7.3
06/11/1988	13:15:43.38	23.18	99.44	10.0	6.4
07/11/1988	23:15:41.75	1.53	126.36	65.0	6.2
17/11/1988	06:55:46.06	12.40	124.54	19.0	6.6
07/12/1988	07:41:24.20	40.99	44.19	5.0	7.0
10/01/1989	05:55:01.45	-3.16	130.56	46.0	6.7
20/01/1989	02:03:54.69	-41.91	79.93	10.0	6.1
22/01/1989	22:20:17.97	41.81	144.28	25.0	6.3
10/02/1989	11:15:24.68	2.31	126.76	44.0	6.8
27/02/1989	23:39:10.82	2.30	128.01	53.0	6.2
10/03/1989	21:49:45.86	-13.70	34.42	30.0	6.6
20/04/1989	22:59:54.07	57.17	121.98	26.0	6.5
25/04/1989	02:13:20.83	30.05	99.42	7.0	6.2
12/06/1989	00:04:09.76	21.86	89.76	5.0	6.1
16/06/1989	23:42:35.12	31.81	137.98	359.0	6.2
14/07/1989	20:42:40.06	-8.08	125.13	9.0	6.4
22/07/1989	05:02:11.51	2.30	128.14	141.0	6.4
31/07/1989	17:07:27.87	-8.05	121.38	13.0	6.4
03/08/1989	11:31:20.43	23.04	121.96	10.0	6.4
20/08/1989	11:16:56.51	11.77	41.94	11.0	6.3
20/08/1989	11:46:28.07	11.88	41.81	10.0	6.1
20/08/1989	13:26:19.43	11.88	41.88	10.0	6.1
20/08/1989	19:25:56.51	11.90	41.82	11.0	6.2
21/08/1989	23:12:41.44	24.09	122.48	42.0	6.3
04/09/1989	05:20:55.93	-4.22	136.67	9.0	6.0
22/09/1989	02:25:50.88	31.58	102.43	14.0	6.1

Date	Origin Time	Latitude	Longitude	Depth (km)	Mag.
19/10/1989	09:49:57.28	49.94	78.97	0.0	6.0
29/10/1989	05:25:38.27	39.57	143.33	9.0	6.6
01/11/1989	18:25:34.94	39.84	142.76	28.0	7.4
01/11/1989	18:36:33.89	39.64	143.14	30.0	6.0
09/12/1989	20:38:08.59	0.14	123.34	151.0	6.8
15/12/1989	18:43:45.03	8.34	126.73	24.0	7.4
20/12/1989	00:08:20.61	8.09	126.83	21.0	6.3
09/01/1990	18:51:29.21	24.75	95.24	119.0	6.1
14/01/1990	03:03:19.23	37.82	91.97	12.0	6.1
05/02/1990	05:16:46.15	37.05	71.25	109.0	6.1
08/02/1990	07:15:32.23	9.76	124.69	25.0	6.8
08/02/1990	07:46:59.78	9.73	124.62	30.0	6.6
20/02/1990	06:53:39.89	34.71	139.25	14.0	6.4
04/03/1990	19:46:19.67	28.92	66.33	10.0	6.1
05/03/1990	20:47:00.76	36.91	73.02	12.0	6.0
25/03/1990	14:17:18.82	37.03	72.94	33.0	6.3
17/04/1990	01:59:33.40	39.44	74.90	33.0	6.2
18/04/1990	13:39:19.01	1.19	122.86	25.0	7.6
18/04/1990	18:32:59.98	1.32	123.02	19.0	6.2
19/04/1990	12:40:38.69	1.11	123.43	23.0	6.2
26/04/1990	09:37:15.04	35.99	100.25	8.0	6.9
11/05/1990	13:10:20.29	41.82	130.86	578.0	6.3
12/05/1990	04:50:08.71	49.04	141.85	605.0	7.2
17/05/1990	23:28:00.12	26.62	127.85	32.0	6.0
20/05/1990	02:22:01.62	5.12	32.15	14.0	7.4
24/05/1990	20:00:08.19	5.36	31.85	16.0	7.1
24/05/1990	20:09:23.24	-7.36	120.36	588.0	7.1
14/06/1990	07:40:56.21	11.76	121.90	18.0	7.1
14/06/1990	12:47:28.82	47.87	85.08	57.0	6.8
17/06/1990	04:51:45.51	27.40	65.72	14.0	6.4
20/06/1990	21:00:09.98	36.96	49.41	18.0	7.7
09/07/1990	15:11:20.38	5.39	31.65	12.0	6.6
13/07/1990	14:20:43.47	36.42	70.79	216.0	6.4
16/07/1990	07:26:34.61	15.68	121.17	25.0	7.8
17/07/1990	18:06:35.33	16.43	120.84	18.0	6.0
17/07/1990	21:14:43.86	16.50	120.98	23.0	6.6
03/08/1990	09:15:06.15	47.96	84.96	33.0	6.2
16/08/1990	04:59:57.69	41.56	88.77	0.0	6.2
23/09/1990	21:13:07.46	33.27	138.64	10.0	6.5
23/09/1990	22:09:04.27	33.19	138.68	10.0	6.2
30/09/1990	19:05:02.46	24.25	125.21	35.0	6.2
15/10/1990	01:35:44.56	-2.21	92.25	32.0	6.8
25/10/1990	11:01:38.72	8.31	126.46	44.0	6.1
06/11/1990	18:45:52.23	28.25	55.46	10.0	6.7
12/11/1990	12:28:51.52	42.96	78.07	19.0	6.3
13/11/1990	02:35:07.87	46.10	138.64	14.0	6.2
15/11/1990	02:34:32.40	3.91	97.46	48.0	6.8
13/12/1990	03:01:48.05	23.92	121.64	12.0	6.7
13/12/1990	12:26:40.75	1.12	124.03	33.0	6.0
21/12/1990	06:57:42.99	41.00	22.30	13.0	6.1
28/12/1990	22:32:17.27	-14.88	66.78	17.0	6.0
29/12/1990	13:23:54.32	8.26	94.06	18.0	6.0
05/01/1991	14:57:11.59	23.61	95.90	19.0	7.3
25/01/1991	17:38:36.51	-2.15	139.02	22.0	6.2
25/01/1991	17:40:16.45	-2.28	139.21	33.0	6.4
31/01/1991	23:03:33.67	35.99	70.42	142.0	6.9
18/02/1991	02:37:25.12	8.87	126.48	23.0	7.0
25/02/1991	14:30:27.62	40.39	78.96	20.0	6.1
26/03/1991	03:58:23.26	21.70	121.79	17.0	6.3
14/04/1991	08:08:55.70	27.16	127.42	83.0	6.2
24/04/1991	04:57:14.89	9.04	126.74	13.0	6.0
29/04/1991	09:12:48.10	42.45	43.67	17.0	7.3
29/04/1991	18:30:41.52	42.50	43.90	14.0	6.0
03/05/1991	02:14:14.43	28.08	139.59	433.0	6.0
19/05/1991	00:58:01.73	1.16	122.96	33.0	7.0
21/05/1991	11:00:19.08	-7.52	126.54	18.0	6.3
31/05/1991	05:28:02.67	-6.05	130.60	33.0	6.0
07/06/1991	11:51:25.97	-7.20	122.53	536.0	6.2
15/06/1991	00:59:20.31	42.46	44.01	9.0	6.5
15/06/1991	23:02:14.37	10.10	125.86	71.0	6.0
02/07/1991	05:14:30.19	-1.07	99.84	53.0	6.2
04/07/1991	11:43:10.49	-8.10	124.68	28.0	6.9

Date	Origin Time	Latitude	Longitude	Depth (km)	Mag.
08/08/1991	02:09:44.71	0.97	122.63	12.0	6.4
03/09/1991	08:44:48.60	33.65	138.78	27.0	6.4
19/10/1991	21:23:14.30	30.78	78.77	10.0	7.0
21/11/1991	12:38:28.57	5.78	126.83	73.0	6.0
26/11/1991	19:40:48.57	42.05	142.52	56.0	6.1
27/12/1991	09:09:37.50	51.02	98.15	13.0	6.4
13/01/1992	11:58:23.14	1.34	127.37	112.0	6.1
20/01/1992	13:37:03.08	27.98	139.40	498.0	6.7
06/02/1992	01:12:38.55	-5.72	103.16	36.0	6.5
26/02/1992	03:45:19.78	11.80	57.76	10.0	6.0
05/03/1992	08:55:05.60	11.51	42.81	7.0	6.2
19/03/1992	06:34:25.86	17.16	120.83	15.0	6.3
07/04/1992	03:37:02.92	-4.17	131.01	52.0	6.2
18/04/1992	09:16:52.85	-5.45	103.00	29.0	6.6
19/04/1992	18:32:19	23.86	121.59	15.0	6.2
15/05/1992	08:08:02.99	41.02	72.43	49.0	6.2
17/05/1992	09:49:19.11	7.24	126.64	32.0	7.1
17/05/1992	10:15:31.31	7.19	126.76	33.0	7.5
20/05/1992	12:20:32.85	33.38	71.32	16.0	6.3
21/05/1992	04:59:57.57	41.60	88.81	0.0	6.5
30/05/1992	12:42:03.52	30.69	141.59	20.0	6.0
02/06/1992	21:05:00.83	-16.14	92.84	13.0	6.2
04/06/1992	04:04:03.56	28.02	128.05	17.0	6.0
06/06/1992	21:40:40.81	1.07	124.04	17.0	6.0
09/06/1992	00:31:56.31	-8.47	111.10	63.0	6.1
10/06/1992	02:13:45.46	1.08	124.09	30.0	6.0
15/06/1992	02:48:56.25	24.03	95.93	17.0	6.3
16/06/1992	05:51:03.74	45.70	142.26	316.0	6.0
12/07/1992	11:08:55.36	41.46	142.03	63.0	6.2
14/07/1992	07:03:09.57	-4.72	125.46	465.0	6.0
18/07/1992	08:36:58.70	39.42	143.33	28.0	7.0
18/07/1992	08:39:05.79	39.67	143.03	34.0	6.1
18/07/1992	10:20:11.94	39.44	143.03	26.0	6.4
18/07/1992	13:56:54.48	39.48	142.96	27.0	6.1
18/07/1992	21:18:57.48	39.32	143.01	36.0	6.0
29/07/1992	04:30:47.72	39.49	143.50	15.0	6.2
30/07/1992	08:24:46.65	29.58	90.16	14.0	6.1
09/08/1992	19:49:44.13	4.01	126.36	73.0	6.1
11/08/1992	15:14:55.13	32.54	141.64	15.0	6.4
19/08/1992	02:04:37.41	42.14	73.57	27.0	7.5
19/08/1992	02:12:57.48	42.10	73.54	33.0	6.1
19/08/1992	03:12:04.97	42.11	73.26	21.0	6.3
19/08/1992	03:20:27.94	42.10	73.24	18.0	6.6
24/08/1992	06:59:39.91	41.98	140.66	120.0	6.3
29/08/1992	19:19:05.59	33.19	137.98	289.0	6.3
01/09/1992	16:41:13.35	23.75	121.68	54.0	6.0
11/09/1992	03:57:26.50	-6.09	26.65	10.0	7.0
26/09/1992	22:15:57.51	1.29	129.12	27.0	6.7
28/09/1992	14:06:02.64	24.12	122.65	29.0	6.4
18/10/1992	13:08:54.74	-6.28	130.21	118.0	6.2
23/10/1992	21:24:36.14	-9.47	122.56	33.0	6.1
23/10/1992	23:19:45.20	42.59	45.10	16.0	6.8
29/10/1992	07:29:57.64	6.83	124.01	33.0	6.2
30/10/1992	02:49:48.17	29.94	138.98	393.0	6.5
06/11/1992	19:08:09.25	38.16	27.00	17.0	6.1
18/11/1992	21:10:41.49	38.31	22.45	14.0	6.1
08/12/1992	07:08:39.92	9.29	93.48	66.0	6.0
12/12/1992	05:29:26.35	-8.48	121.90	27.0	7.8
12/12/1992	06:38:29.49	-8.52	121.93	20.0	6.1
20/12/1992	20:52:47.28	-6.58	130.39	77.0	7.3
23/12/1992	03:00:44.98	-6.54	130.42	101.0	6.1
27/12/1992	21:49:04.47	-6.09	113.05	600.0	6.0
15/01/1993	11:06:01.96	42.98	144.16	112.0	6.1
19/01/1993	14:39:26.17	38.65	133.46	448.0	6.6
20/01/1993	02:30:54.73	3.14	97.63	67.0	6.2
20/01/1993	17:31:15.57	-7.20	128.57	33.0	6.4
01/03/1993	01:39:27.88	-3.74	138.54	88.0	6.2
25/03/1993	07:08:18.93	41.80	143.47	33.0	6.0
19/04/1993	21:01:48.94	4.01	128.20	23.0	6.8
11/05/1993	18:26:51.32	7.22	126.57	58.0	7.0
18/05/1993	10:19:33.78	19.91	122.45	168.0	6.8
30/05/1993	17:08:53.95	1.55	127.21	80.0	6.1

Date	Origin Time	Latitude	Longitude	Depth (km)	Mag.
04/06/1993	10:49:33.65	3.73	128.50	20.0	6.0
12/06/1993	18:26:42.22	-4.38	135.12	9.0	6.2
12/07/1993	13:17:11.96	42.85	139.20	16.0	7.7
03/08/1993	12:43:05.36	28.73	34.55	10.0	6.1
04/08/1993	11:31:18.03	-1.63	99.61	31.0	6.5
07/08/1993	00:00:37.07	26.58	125.61	155.0	6.4
07/08/1993	19:42:41.91	41.99	139.84	13.0	6.5
09/08/1993	11:38:30.53	36.44	70.71	204.0	6.4
01/09/1993	14:03:19.16	2.99	96.12	34.0	6.3
04/09/1993	11:38:38.93	36.43	70.81	194.0	6.0
04/09/1993	21:39:33.84	-9.57	122.53	32.0	6.2
18/09/1993	05:02:27.01	36.42	71.59	112.0	6.3
26/09/1993	03:31:14.63	10.00	138.22	10.0	6.3
29/09/1993	11:16:03.54	0.49	121.53	96.0	6.4
02/10/1993	08:42:32.71	38.19	88.66	14.0	6.3
11/10/1993	15:54:21.24	32.02	137.83	350.0	6.9
09/12/1993	04:32:19.52	0.49	126.00	14.0	6.9
09/12/1993	11:38:27.96	0.43	125.89	15.0	6.8
10/12/1993	08:59:35.82	20.91	121.28	12.0	6.1
20/12/1993	13:56:14.87	-6.88	131.34	7.0	6.4
04/01/1994	19:31:59.88	-4.30	135.15	11.0	6.0
11/01/1994	00:51:56.38	25.23	97.20	9.0	6.1
19/01/1994	01:53:34.90	-3.18	135.97	23.0	6.8
21/01/1994	02:24:29.96	1.01	127.73	19.0	7.3
21/01/1994	18:00:17.67	-4.86	103.66	89.0	6.1
15/02/1994	17:07:43.80	-4.97	104.30	23.0	7.0
18/02/1994	04:19:07.57	-45.33	96.23	10.0	6.3
20/02/1994	01:54:35.76	2.06	126.47	28.0	6.0
23/02/1994	08:02:04.72	30.85	60.60	6.0	6.1
24/02/1994	00:11:12.32	30.77	60.49	9.0	6.3
26/02/1994	02:31:11.09	30.90	60.55	9.0	6.1
01/03/1994	03:49:00.83	29.10	52.62	12.0	6.1
08/04/1994	01:10:40.84	40.61	143.68	13.0	6.4
13/04/1994	22:22:29.90	-3.14	135.97	28.0	6.5
27/04/1994	14:11:45.15	13.07	119.54	9.0	6.0
01/05/1994	12:00:35.76	36.90	67.16	18.0	6.3
02/05/1994	17:14:00.88	-1.12	97.49	15.0	6.2
09/05/1994	12:36:37.26	-2.06	99.73	27.0	6.0
11/05/1994	08:18:15.67	-2.01	99.77	20.0	6.5
11/05/1994	21:14:33.76	-2.06	99.67	28.0	6.1
23/05/1994	06:46:16.12	35.56	24.73	76.0	6.1
23/05/1994	15:16:57.16	24.07	122.56	25.0	6.0
25/05/1994	04:03:41.26	-4.20	135.49	33.0	6.6
29/05/1994	14:11:50.96	20.56	94.16	35.0	6.5
02/06/1994	18:17:34.02	-10.48	112.83	18.0	7.8
03/06/1994	21:06:59.88	-10.36	112.89	25.0	6.6
04/06/1994	00:57:50.66	-10.78	113.37	11.0	6.5
05/06/1994	01:09:30.15	24.51	121.90	11.0	6.6
05/06/1994	01:45:02.16	-10.35	113.40	25.0	6.1
09/06/1994	16:22:22.09	13.26	124.28	75.0	6.2
15/06/1994	09:22:57.22	-10.34	113.66	19.0	6.2
15/06/1994	10:28:50.60	-10.17	113.75	28.0	6.1
16/06/1994	10:12:46.92	-7.39	128.12	108.0	6.0
30/06/1994	09:23:21.35	36.33	71.13	226.0	6.5
01/07/1994	10:12:41.21	40.23	53.38	40.0	6.0
13/07/1994	11:45:23.36	-7.53	127.77	158.0	6.8
21/07/1994	18:36:31.74	42.34	132.87	471.0	7.3
24/07/1994	21:57:27.40	-10.65	113.27	34.0	6.0
04/08/1994	22:15:37.77	-6.34	131.57	33.0	6.2
30/08/1994	19:42:46.51	-6.97	124.11	595.0	6.2
13/09/1994	04:28:01.02	29.29	129.91	34.0	6.2
16/09/1994	06:20:18.74	22.53	118.71	13.0	6.8
28/09/1994	16:39:51.67	-5.79	110.35	637.0	6.6
28/09/1994	17:33:58.21	-5.73	110.36	628.0	6.0
07/10/1994	03:25:58.12	41.66	88.75	0.0	6.0
08/10/1994	21:44:07.21	-1.26	127.98	16.0	6.8
12/10/1994	06:43:39.73	13.77	124.53	15.0	6.4
13/10/1994	05:04:24.98	-1.21	127.91	10.0	6.4
25/10/1994	00:54:34.30	36.36	70.96	238.0	6.2
31/10/1994	11:48:13.92	3.02	96.19	29.0	6.2
14/11/1994	19:15:30.66	13.52	121.07	31.0	7.1
15/11/1994	20:18:11.31	-5.59	110.19	560.0	6.5

Date	Origin Time	Latitude	Longitude	Depth (km)	Mag.
20/11/1994	16:59:05.63	-2.00	135.93	16.0	6.3
20/11/1994	18:34:34.49	4.33	97.59	153.0	6.1
28/12/1994	12:19:23.03	40.53	143.42	26.0	7.8
28/12/1994	20:52:25.83	40.09	142.69	21.0	6.2
28/12/1994	22:37:46.34	40.38	143.64	10.0	6.4
31/12/1994	13:50:23.70	40.22	142.55	43.0	6.0
23/02/1995	05:01:22.57	39.75	143.66	9.0	6.2
23/02/1995	05:19:01.99	24.14	121.61	40.0	6.2
23/02/1995	05:27:39.88	39.79	143.57	33.0	6.1
06/03/1995	18:43:40.15	2.69	118.23	16.0	6.1
19/03/1995	18:34:04.48	-4.23	135.01	19.0	6.1
19/03/1995	23:53:14.92	-4.18	135.11	33.0	6.9
31/03/1995	14:01:40.08	38.21	135.01	354.0	6.2
08/04/1995	17:45:12.92	21.83	142.69	267.0	6.2
18/04/1995	03:49:37.07	-2.06	140.46	20.0	6.1
20/04/1995	08:45:11.67	6.28	126.78	94.0	6.6
21/04/1995	00:02:48.41	11.97	125.69	27.0	6.0
21/04/1995	00:09:54.36	12.01	125.66	20.0	6.9
21/04/1995	00:30:10.82	11.93	125.56	17.0	6.8
21/04/1995	00:34:46.09	12.06	125.58	20.0	7.2
21/04/1995	05:17:01.33	12.05	125.92	27.0	6.8
23/04/1995	05:08:01.97	12.39	125.40	24.0	6.8
23/04/1995	06:38:11.20	5.95	123.82	530.0	6.1
29/04/1995	09:43:57.77	11.85	125.98	15.0	6.1
02/05/1995	11:48:11.65	43.78	84.66	33.0	6.0
04/05/1995	02:18:47.92	1.89	128.48	23.0	6.1
05/05/1995	04:39:10.63	12.64	125.24	33.0	6.1
06/05/1995	01:59:07.13	24.99	95.29	117.0	6.4
13/05/1995	08:47:12.73	40.15	21.69	14.0	6.6
14/05/1995	11:33:18.87	-8.38	125.13	11.0	6.9
15/05/1995	04:05:57.83	41.60	88.82	0.0	6.1
16/05/1995	21:48:05.83	17.90	96.46	11.0	6.1
26/05/1995	03:11:17.18	12.11	57.94	62.0	6.5
15/06/1995	00:15:48.73	38.40	22.28	14.0	6.5
25/06/1995	06:59:06.24	24.60	121.70	52.0	6.0
07/07/1995	21:15:19.70	33.97	137.13	333.0	6.0
08/07/1995	05:42:53.09	39.68	143.35	11.0	6.0
11/07/1995	21:46:39.78	21.97	99.20	12.0	6.8
26/07/1995	23:42:02.78	2.53	127.68	65.0	6.4
27/07/1995	05:51:18.94	-12.59	79.23	16.0	6.0
17/08/1995	00:59:57.73	41.56	88.80	0.0	6.0
23/08/1995	07:06:02.76	18.86	145.22	594.0	7.1
24/08/1995	01:55:34.63	18.90	145.05	587.0	6.2
24/08/1995	07:54:42.97	18.82	145.04	612.0	6.1
24/08/1995	07:55:26.24	18.85	145.09	585.0	6.2
29/08/1995	07:25:49.25	-47.94	99.47	10.0	6.4
17/09/1995	17:09:20.62	-17.09	66.71	8.0	6.5
01/10/1995	15:57:16.20	38.06	30.13	33.0	6.4
01/10/1995	17:06:03.45	29.31	139.04	430.0	6.1
06/10/1995	18:09:45.90	-2.05	101.44	33.0	6.8
18/10/1995	09:30:38.50	36.43	70.39	222.0	6.3
18/10/1995	10:37:26.38	27.93	130.18	28.0	7.1
18/10/1995	23:25:58.77	28.20	130.21	27.0	6.1
19/10/1995	00:32:06.44	28.16	130.16	33.0	6.3
19/10/1995	02:41:36.19	28.09	130.15	19.0	6.8
23/10/1995	22:46:50.81	26.00	102.23	10.0	6.2
29/10/1995	18:44:21.18	0.86	125.98	33.0	6.1
29/10/1995	19:24:33.60	0.86	125.89	68.0	6.0
02/11/1995	22:13:46.05	-6.73	130.29	104.0	6.0
05/11/1995	16:29:58.35	-4.92	103.22	36.0	6.3
08/11/1995	07:14:18.61	1.83	95.05	33.0	6.9
08/11/1995	16:01:19.16	1.29	121.68	19.0	6.0
13/11/1995	02:17:51.08	3.59	126.65	33.0	6.3
22/11/1995	04:15:11.94	28.83	34.80	10.0	7.2
05/12/1995	06:32:06.10	-9.03	124.67	33.0	6.4
19/12/1995	23:28:12.18	-3.70	140.23	63.0	6.5
25/12/1995	04:43:24.46	-6.90	129.15	141.0	7.1
17/01/1996	10:06:46.71	-4.40	140.07	109.0	6.1
27/01/1996	17:48:09.38	9.19	126.42	33.0	6.0
03/02/1996	11:14:20.12	27.29	100.28	11.0	6.6
07/02/1996	07:57:18.11	1.02	120.19	13.0	6.1
12/02/1996	09:08:07.99	-11.04	118.67	8.0	6.1

Date	Origin Time	Latitude	Longitude	Depth (km)	Mag.
14/02/1996	21:26:56.30	29.25	140.45	141.0	6.0
16/02/1996	15:22:58.83	37.35	142.38	40.0	6.7
17/02/1996	05:59:30.55	-0.89	136.95	33.0	8.2
17/02/1996	14:21:22.35	-0.57	135.84	19.0	6.5
17/02/1996	20:18:07.02	-0.92	136.23	31.0	6.5
18/02/1996	02:25:33.35	-1.34	136.46	10.0	6.4
24/02/1996	15:52:59.10	-0.87	137.35	33.0	6.2
28/02/1996	09:44:10.92	1.76	126.05	115.0	6.4
05/03/1996	14:52:28.68	24.09	122.21	29.0	6.3
16/03/1996	22:04:06.24	28.98	138.94	477.0	6.7
19/03/1996	15:00:26.09	39.99	76.70	28.0	6.3
28/03/1996	07:28:28.12	11.92	57.81	10.0	6.1
03/05/1996	03:32:47.11	40.77	109.66	26.0	6.0
07/05/1996	08:44:36.61	1.62	126.56	33.0	6.0
06/06/1996	17:35:38.19	-41.33	80.67	20.0	6.3
11/06/1996	18:22:55.73	12.61	125.15	33.0	7.1
14/06/1996	15:04:40.74	12.81	125.06	28.0	6.1
17/06/1996	11:22:18.54	-7.14	122.59	587.0	7.9
26/06/1996	03:22:03.14	27.73	139.75	468.0	6.3
06/07/1996	21:36:28.72	21.97	142.83	241.0	6.2
16/07/1996	10:07:36.65	1.02	120.25	33.0	6.6
20/07/1996	00:00:41.88	36.15	27.10	33.0	6.2
05/06/2001	10:00:9.74	-6.87	146.55	0.0	6.3
02/08/2001	23:41:06.17	56.26	163.79	14.0	6.3
13/08/2001	20:11:23.40	41.05	142.31	38.0	6.4
21/08/2001	06:52:06.25	-36.81	-179.57	33.0	7.1
11/09/2001	14:56:50.92	-0.58	133.13	33.0	6.5
29/09/2001	02:40:07.38	-18.50	168.16	33.0	6.4
08/10/2001	18:14:26.44	52.59	160.32	48.0	6.5
12/10/2001	15:02:16.84	12.69	144.98	37.0	7.0
19/10/2001	03:31:22.28	-9.14	124.77	0.0	6.6
21/10/2001	00:29:21.49	-37.14	178.98	18.0	6.7
31/10/2001	09:10:20	-5.91	150.20	33.0	7.0
22/11/2001	23:22:20.44	-16.25	178.02	10.0	6.3
03/12/2001	11:32:29.80	-16.50	-177.54	10.0	6.4
12/12/2001	14:02:35.04	-42.81	124.69	10.0	7.1
18/12/2001	04:03:0.11	24.10	122.91	15.0	7.1
23/12/2001	22:52:54.33	-9.61	159.53	16.0	6.8
03/01/2002	10:17:36.30	-17.66	168.00	10.0	6.6
10/01/2002	11:14:56.93	-3.21	142.43	11.0	6.7
13/01/2002	14:10:56.52	-5.65	151.07	43.0	6.4
15/01/2002	07:13:0.92	-6.35	105.22	20.0	6.1
03/02/2002	07:11:28.41	38.57	31.27	5.0	6.5
05/02/2002	13:27:24.67	-5.34	151.25	39.0	6.6
03/03/2002	12:08:07.81	36.43	70.44	209.0	6.3
05/03/2002	21:16:09.13	6.03	124.25	31.0	7.5
25/03/2002	14:56:33.82	36.06	69.32	8.0	6.1
26/03/2002	03:45:48.70	23.35	124.09	33.0	6.4
31/03/2002	06:52:50.49	24.28	122.18	32.0	7.1
08/04/2002	03:48:55.24	-51.07	139.27	10.0	6.2
18/04/2002	05:02:46.19	16.99	-100.86	24.0	6.8
26/04/2002	16:06:07	13.09	144.62	85.0	7.1
14/05/2002	16:56:10.42	-36.52	78.93	10.0	6.2
15/05/2002	03:46:05.76	24.64	121.92	10.0	6.2
25/05/2002	05:36:31.97	53.81	-161.12	33.0	6.4
28/05/2002	16:45:17.10	24.07	122.26	33.0	6.1
13/06/2002	01:27:19.47	-47.80	99.75	10.0	6.6
16/06/2002	02:46:14.03	8.78	-83.99	35.0	6.4
17/06/2002	21:26:22.92	-12.59	166.38	33.0	6.7
22/06/2002	02:58:21.30	35.63	49.05	10.0	6.5
27/06/2002	05:50:35.11	-6.96	104.18	11.0	6.5
31/07/2002	00:16:44.61	7.93	-82.79	10.0	6.5
14/08/2002	13:12:39.88	7.83	136.88	10.0	6.3
14/08/2002	13:57:52.11	14.10	146.20	30.0	6.5
19/08/2002	11:01:01.19	-21.70	-179.51	580.0	7.7
19/08/2002	11:08:24.31	-23.88	178.49	675.0	7.7
20/08/2002	10:59:32.02	30.99	141.97	9.0	6.3
08/09/2002	18:44:23.71	-3.30	142.95	13.0	7.6
13/09/2002	22:28:29.46	13.04	93.07	21.0	6.5
20/09/2002	15:43:35.46	-1.68	134.23	10.0	6.4
03/10/2002	16:08:29.62	23.32	-108.53	10.0	6.5
06/10/2002	15:46:33.01	-8.20	118.34	10.0	6.3

Date	Origin Time	Latitude	Longitude	Depth (km)	Mag.
10/10/2002	10:50:20.57	-1.76	134.30	10.0	7.6
19/10/2002	12:09:05.38	44.30	149.96	33.0	6.3
23/10/2002	11:27:19.43	63.51	-147.91	4.0	6.7
02/11/2002	01:26:10.70	2.82	96.08	30.0	7.4
02/11/2002	09:46:46.70	2.95	96.39	27.0	6.3
03/11/2002	03:37:42.07	38.89	141.98	39.0	6.4
03/11/2002	22:12:41	63.52	-147.44	4.0	7.9
03/11/2002	23:11:48.87	63.05	-143.64	0.0	6.5
07/11/2002	15:14:06.76	51.20	179.33	33.0	6.6
17/11/2002	04:53:53.54	47.82	146.21	459.0	7.3
20/11/2002	21:32:30.81	35.41	74.51	33.0	6.3
12/12/2002	08:30:42.77	-4.79	153.27	34.0	6.7
20/12/2002	14:14:42.05	-3.08	147.94	33.0	6.3
30/12/2002	04:49:08.69	7.47	123.41	10.0	6.3
10/01/2003	13:11:56.91	-5.31	153.70	71.0	6.7
16/01/2003	00:53:15.72	44.28	-129.02	10.0	6.3
20/01/2003	08:43:06.07	-10.49	160.77	33.0	7.3
21/01/2003	02:46:47.74	13.63	-90.77	24.0	6.5
22/01/2003	02:06:34.61	18.77	-104.10	24.0	7.6
10/02/2003	04:49:31.12	-6.01	149.79	33.0	6.3
19/02/2003	03:32:36.36	53.65	-164.64	19.0	6.6
24/02/2003	02:03:41.45	39.61	77.23	11.0	6.3
11/03/2003	07:27:32.65	-4.69	153.24	40.0	6.8
12/03/2003	23:41:32.92	26.56	-110.59	10.0	6.4
17/03/2003	16:36:17.31	51.27	177.98	33.0	7.1
25/03/2003	02:53:25.03	-8.29	120.74	33.0	6.5
17/04/2003	00:48:38.58	37.53	96.48	14.0	6.4
01/05/2003	00:27:04.70	39.01	40.46	10.0	6.4
04/05/2003	13:15:18.66	-30.53	-178.23	62.0	6.7
13/05/2003	21:21:14.05	-17.29	167.74	33.0	6.3
14/05/2003	06:03:35.86	18.27	-58.63	41.0	6.7
21/05/2003	18:44:20.10	36.96	3.63	12.0	6.8
26/05/2003	09:24:33.40	38.85	141.57	68.0	7.0
26/05/2003	19:23:27.94	2.35	128.85	31.0	7.0
07/06/2003	00:32:45.57	-5.09	152.50	33.0	6.6
15/06/2003	19:24:33.15	51.55	176.92	20.0	6.5
16/06/2003	22:08:02.14	55.49	160.00	174.0	6.9
23/06/2003	12:12:34.47	51.44	176.78	20.0	6.9
28/06/2003	15:29:42.26	-3.33	146.15	10.0	6.3
15/07/2003	18:46:38.12	-3.83	152.17	33.0	6.5
15/07/2003	20:27:50.53	-2.60	68.38	10.0	7.6
25/07/2003	09:37:45.84	-1.53	149.69	24.0	6.4
14/08/2003	05:14:54.76	39.16	20.60	10.0	6.3
21/08/2003	12:12:49.79	-45.10	167.14	28.0	7.2
02/09/2003	18:28:00.33	-15.23	-173.22	10.0	6.4
21/09/2003	18:16:13.41	19.92	95.67	10.0	6.6
22/09/2003	04:45:36.24	19.78	-70.67	10.0	6.4
25/09/2003	19:50:06.36	41.81	143.91	27.0	8.3
27/09/2003	11:33:25.08	50.04	87.81	16.0	7.3
27/09/2003	11:50:56.67	49.96	88.10	0.0	6.0
27/09/2003	18:52:46.98	50.09	87.76	10.0	6.4
29/09/2003	02:36:53.14	42.45	144.38	25.0	6.5
29/09/2003	21:33:16.74	41.45	143.98	0.0	6.0
30/09/2003	14:08:37.74	-30.44	-177.40	10.0	6.4
01/10/2003	01:03:25.24	50.21	87.72	10.0	6.7
08/10/2003	09:07:0.44	42.61	144.50	68.0	6.5
17/10/2003	10:19:06.82	-5.47	154.15	133.0	6.4
22/10/2003	11:45:30.84	-6.06	147.73	53.0	6.3
31/10/2003	01:06:28.28	37.81	142.62	10.0	7.0
02/11/2003	05:32:15.72	-45.19	166.54	10.0	6.4
09/11/2003	19:52:36.82	-0.67	-19.69	10.0	6.6
17/11/2003	06:43:06.80	51.15	178.65	33.0	7.8
18/11/2003	17:14:22.62	12.02	125.42	35.0	6.5
25/11/2003	20:19:46.29	-5.58	150.88	35.0	6.6
05/12/2003	21:26:09.48	55.54	165.78	10.0	6.7
10/12/2003	04:38:11.59	23.04	121.36	10.0	6.8
22/12/2003	19:15:56	35.71	-121.10	7.0	6.6
25/12/2003	07:11:11.59	8.42	-82.82	33.0	6.5
25/12/2003	20:42:33.72	-22.25	169.49	10.0	6.5
26/12/2003	01:56:52.44	29.00	58.31	10.0	6.6
26/12/2003	21:26:04.10	-22.27	169.31	10.0	6.8
27/12/2003	16:00:59.45	-22.01	169.77	10.0	7.3

Date	Origin Time	Latitude	Longitude	Depth (km)	Mag.
27/12/2003	22:38:01.88	-21.67	169.84	10.0	6.7
27/12/2003	22:55:01.28	-21.65	169.77	10.0	6.3
03/01/2004	08:07:34.22	-22.38	169.73	10.0	6.0
03/01/2004	08:09:03.81	-22.16	169.55	10.0	6.1
03/01/2004	08:21:48.40	-22.32	169.62	10.0	6.4
03/01/2004	16:23:21.02	-22.25	169.68	22.0	7.1
03/01/2004	16:38:27.80	-22.12	169.92	0.0	6.2
16/01/2004	18:07:55.66	7.64	-37.70	10.0	6.2
28/01/2004	22:15:30.70	-3.12	127.40	17.0	6.7
05/02/2004	21:05:02.84	-3.62	135.54	16.0	7.0
07/02/2004	02:42:35.21	-4.00	135.02	10.0	7.3
08/02/2004	08:58:51.80	-3.66	135.34	25.0	6.7
23/02/2004	16:04:49.44	-14.74	-175.63	31.0	6.3
24/02/2004	02:27:46.23	35.14	-4.00	0.0	6.4
09/03/2004	22:56:42.51	-32.26	-178.36	18.0	6.2
09/03/2004	22:58:29.14	-32.40	-178.08	0.0	6.0
23/04/2004	01:50:30.22	-9.36	122.84	65.0	6.7
29/04/2004	00:57:21.08	10.81	-86.00	10.0	6.2
03/05/2004	05:12:39.95	14.50	-90.57	120.0	6.0
07/05/2004	01:26:42.20	-21.99	170.28	14.0	6.3
13/05/2004	09:58:43.45	-3.58	150.73	10.0	6.4
19/05/2004	07:04:11.71	22.66	121.50	20.0	6.2
28/05/2004	12:38:44.47	36.29	51.61	17.0	6.3
29/05/2004	20:56:09.60	34.25	141.41	16.0	6.5
09/06/2004	22:49:43.45	-51.48	139.74	0.0	6.5
09/06/2004	22:52:08.80	-51.60	139.62	10.0	6.4
10/06/2004	15:19:57.75	55.68	160.00	188.0	6.9
28/06/2004	09:49:47	54.80	-134.25	20.0	6.8
19/07/2004	08:01:49.46	49.62	-126.97	23.0	6.4
28/07/2004	03:56:28.60	-0.44	133.09	13.0	6.5
05/09/2004	10:07:07.82	33.07	136.62	14.0	7.2
05/09/2004	14:57:18.61	33.18	137.07	10.0	7.4
06/09/2004	23:29:35.09	33.21	137.23	10.0	6.6
08/09/2004	14:58:25.83	33.14	137.20	21.0	6.1
08/10/2004	08:27:53.54	-10.95	162.16	36.0	6.8
09/10/2004	21:26:53.69	11.42	-86.67	35.0	7.0
15/10/2004	04:08:50.24	24.53	122.69	94.0	6.7
23/10/2004	08:55:57.84	37.28	138.74	0.0	6.4
02/11/2004	10:02:12.82	49.28	-128.77	10.0	6.7
08/11/2004	15:54:56.23	24.06	122.61	0.0	6.1
11/11/2004	17:34:52.05	-11.13	162.21	10.0	6.7
11/11/2004	21:26:41.15	-8.15	124.87	10.0	7.5
11/11/2004	22:49:48.14	-8.26	124.93	10.0	6.4
20/11/2004	08:07:22.08	9.60	-84.17	16.0	6.4
21/11/2004	11:41:07.76	15.68	-61.71	14.0	6.3
26/11/2004	02:25:03.31	-3.61	135.40	10.0	7.1
28/11/2004	07:36:45.40	-3.64	135.45	23.0	6.2
06/12/2004	14:15:11.89	42.90	145.23	35.0	6.8
14/12/2004	23:20:13.36	18.96	-81.41	10.0	6.8
18/12/2004	06:46:19.87	48.84	156.31	11.0	6.2
23/12/2004	14:58:59.78	-49.95	161.17	0.0	7.6
26/12/2004	00:58:53.45	3.30	95.98	30.0	9.1
26/12/2004	01:06:10.87	9.84	94.11	0.0	8.6
26/12/2004	01:25:48.76	5.50	94.21	30.0	6.1
26/12/2004	03:08:44.40	13.75	93.08	29.0	6.9
26/12/2004	04:21:29.81	6.91	92.96	39.0	7.2
26/12/2004	05:01:16.95	9.41	92.13	0.0	6.1
29/12/2004	05:56:47.54	8.79	93.20	12.0	6.2
31/12/2004	02:24:00.52	7.12	92.53	14.0	6.1
12/01/2005	08:40:03.65	-0.88	-21.19	10.0	6.8
16/01/2005	08:25:04.47	-25.53	-176.30	16.0	6.2
16/01/2005	20:17:52.76	10.93	140.84	24.0	6.6
19/01/2005	06:11:36.40	34.06	141.49	27.0	6.6
22/01/2005	20:30:17.35	-7.73	159.48	29.0	6.4
24/01/2005	04:16:47.44	7.33	92.48	30.0	6.3
22/02/2005	02:25:22.92	30.75	56.82	14.0	6.4
26/02/2005	12:56:52.62	2.91	95.59	36.0	6.8
06/03/2005	05:21:43.43	84.95	99.39	10.0	6.3
20/03/2005	01:53:41.83	33.81	130.13	10.0	6.6
28/03/2005	16:09:36.53	2.09	97.11	30.0	8.6
30/03/2005	16:19:41.10	2.99	95.41	22.0	6.3
07/04/2005	20:04:41.06	30.49	83.66	11.0	6.3

Date	Origin Time	Latitude	Longitude	Depth (km)	Mag.
10/04/2005	11:14:19.62	-1.71	99.78	30.0	6.5
10/04/2005	17:24:39.40	-1.59	99.72	30.0	6.4
11/04/2005	12:20:05.96	-3.48	145.91	11.0	6.6
16/04/2005	16:38:03.90	1.81	97.66	31.0	6.4
28/04/2005	14:07:33.70	2.13	96.80	22.0	6.2
10/05/2005	01:09:05.10	-6.23	103.14	17.0	6.3
14/05/2005	05:05:18.48	0.59	98.46	34.0	6.7
16/05/2005	03:54:14.62	-32.59	-179.35	34.0	6.6
19/05/2005	01:54:52.85	1.99	97.04	30.0	6.9
08/06/2005	06:28:10.92	2.17	96.72	23.0	6.1
14/06/2005	17:10:12.28	51.24	179.31	17.0	6.8
15/06/2005	02:50:54.19	41.29	-125.95	16.0	7.2
27/06/2005	11:35:45.60	18.78	-107.30	20.0	6.2
02/07/2005	02:16:43.70	11.24	-86.17	27.0	6.6
05/07/2005	01:52:02.95	1.82	97.08	21.0	6.7
24/07/2005	15:42:06.21	7.92	92.19	16.0	7.2
03/08/2005	11:03:15.13	11.25	-85.54	14.0	6.3
16/08/2005	02:46:28.40	38.28	142.04	36.0	7.2
09/09/2005	07:26:43.73	-4.54	153.47	90.0	7.6
29/09/2005	15:50:24.03	-5.44	151.84	25.0	6.6
08/10/2005	03:50:40.80	34.54	73.59	26.0	7.6
08/10/2005	05:26:3.90	34.80	73.19	0.0	6.2
08/10/2005	10:46:28.79	34.73	73.10	8.0	6.4
19/10/2005	11:44:42.79	36.40	140.84	32.0	6.3
05/11/2005	10:48:21.22	-3.15	148.14	25.0	6.4
14/11/2005	21:38:51.42	38.11	144.90	11.0	7.0
19/11/2005	14:10:13.03	2.16	96.79	21.0	6.5
30/11/2005	16:53:42.47	6.27	124.03	13.0	6.4
02/12/2005	13:13:09.52	38.09	142.12	29.0	6.5
05/12/2005	12:19:56.62	-6.22	29.83	22.0	6.8
11/12/2005	14:20:45	-6.58	152.22	17.0	6.6
04/01/2006	08:32:32.40	28.16	-112.12	14.0	6.6
08/01/2006	11:34:55.64	36.31	23.21	66.0	6.7
23/01/2006	06:02:58.14	-17.39	167.71	23.0	6.4
27/01/2006	16:58:53.67	-5.47	128.13	397.0	7.6
22/02/2006	22:19:07.80	-21.32	33.58	11.0	7.0
28/02/2006	07:31:02.65	28.12	56.87	18.0	6.0
14/03/2006	06:57:33.86	-3.60	127.21	30.0	6.7
31/03/2006	13:20:58.12	-29.49	-176.82	0.0	6.5
07/04/2006	08:30:44.63	-16.53	176.99	14.0	6.5
20/04/2006	23:24:58.39	60.93	167.02	0.0	7.5
20/04/2006	23:28:03.90	60.87	167.01	10.0	6.1
25/04/2006	18:26:17.15	1.99	97.00	21.0	6.3
29/04/2006	16:58:06.32	60.49	167.52	11.0	6.6
03/05/2006	15:26:40.29	-20.19	-174.12	55.0	8.0
03/05/2006	15:42:20.92	-19.54	-175.05	0.0	6.7
03/05/2006	15:43:31.65	-19.14	-174.42	0.0	6.4
10/05/2006	02:42:51.03	52.51	-169.26	18.0	6.4
16/05/2006	10:39:23.34	-31.81	-179.31	152.0	7.4
16/05/2006	15:28:25.92	0.09	97.05	12.0	6.8
22/05/2006	11:11:57.47	60.79	165.71	0.0	6.7
26/05/2006	22:53:58.92	-7.96	110.45	12.0	6.3
28/05/2006	03:12:08.76	-5.72	151.13	34.0	6.5
14/06/2006	04:18:42.51	51.75	177.08	14.0	6.5
08/07/2006	20:40:00.98	51.21	-179.31	22.0	6.6
08/07/2006	20:41:47.66	51.40	-179.22	0.0	6.5
17/07/2006	08:19:26.68	-9.28	107.42	20.0	7.7
17/07/2006	09:13:04.96	-9.09	107.76	10.0	6.0
17/07/2006	15:49:55.37	-9.54	109.22	0.0	6.0
19/07/2006	11:48:58.29	-5.47	150.68	28.0	6.4
07/08/2006	22:18:55.09	-15.80	167.79	150.0	6.8
11/08/2006	20:54:14.37	2.40	96.35	22.0	6.2
24/08/2006	21:50:36.65	51.15	157.52	43.0	6.5
01/09/2006	10:18:51.60	-6.76	155.51	38.0	6.8
16/09/2006	09:45:23.91	-3.08	129.44	17.0	6.3
28/09/2006	06:22:09.73	-16.59	-172.03	28.0	6.9
30/09/2006	17:50:23.05	46.35	153.17	11.0	6.6
01/10/2006	09:06:02.32	46.47	153.24	19.0	6.5
01/10/2006	09:09:57.97	46.45	153.16	0.0	6.8
15/10/2006	17:07:49.25	19.88	-155.93	38.0	6.7
17/10/2006	01:25:12.23	-5.88	150.98	32.0	6.7
22/10/2006	08:55:16.76	-45.73	95.99	10.0	6.1

Date	Origin Time	Latitude	Longitude	Depth (km)	Mag.
23/10/2006	21:17:19.98	29.35	140.27	11.0	6.4
07/11/2006	17:38:33.80	-6.48	151.20	11.0	6.6
15/11/2006	11:14:13.57	46.59	153.27	10.0	8.3
15/11/2006	11:29:22.79	46.37	154.48	10.0	6.2
15/11/2006	11:40:55.05	46.48	154.73	10.0	6.7
07/12/2006	19:10:21.85	46.15	154.39	16.0	6.4
26/12/2006	12:26:21.14	21.80	120.55	10.0	7.1
26/12/2006	12:34:13.80	21.97	120.49	10.0	6.9
30/12/2006	08:30:49.79	13.31	51.37	15.0	6.6
08/01/2007	12:48:40.51	8.08	92.44	11.0	6.1
13/01/2007	04:23:21.16	46.24	154.52	10.0	8.1
21/01/2007	11:27:45.06	1.07	126.28	22.0	7.5
21/01/2007	11:44:52.86	-11.40	166.41	94.0	6.3
21/01/2007	12:02:6.81	1.16	126.14	0.0	6.1
21/01/2007	12:08:22.42	1.13	126.16	0.0	6.1
30/01/2007	04:54:50.57	-54.74	146.30	11.0	6.9
30/01/2007	21:37:44.37	20.98	144.71	20.0	6.6
31/01/2007	03:15:52.29	-29.78	-178.00	34.0	6.5
20/02/2007	08:04:25.28	-1.03	126.98	12.0	6.7
06/03/2007	03:49:38.90	-0.49	100.50	19.0	6.4
06/03/2007	05:49:25.43	-0.49	100.53	11.0	6.3
25/03/2007	00:40:01.61	-20.62	169.36	34.0	7.1
25/03/2007	00:41:57.82	37.34	136.59	8.0	6.7
25/03/2007	01:08:19.05	-20.75	169.35	35.0	6.9
01/04/2007	20:39:58.71	-8.47	157.04	24.0	8.1
01/04/2007	20:47:31.31	-7.17	155.78	10.0	6.6
01/04/2007	21:11:33.15	-7.31	155.74	10.0	6.9
01/04/2007	21:24:53.51	-7.06	155.45	0.0	6.5
01/04/2007	22:57:20.99	-7.51	156.18	0.0	6.1
04/04/2007	06:34:35.96	-7.76	156.49	17.0	6.4
04/04/2007	11:00:27.94	-20.72	168.83	13.0	6.2
04/04/2007	11:02:29.62	-20.69	169.06	10.0	6.5
05/04/2007	03:56:50.48	37.31	-24.62	14.0	6.3
16/04/2007	13:20:38.23	-58.01	147.96	10.0	6.4
20/04/2007	00:26:40.60	25.72	125.09	10.0	6.1
20/04/2007	01:45:56.11	25.71	125.11	9.0	6.3
20/04/2007	02:11:6.07	0.99	126.17	0.0	6.3
16/05/2007	08:56:14.12	20.50	100.73	9.0	6.3
02/06/2007	21:34:57.78	23.03	101.05	5.0	6.1
07/06/2007	00:40:38.13	-3.32	146.76	4.0	6.2
13/06/2007	19:29:40.18	13.55	-90.62	23.0	6.7
28/06/2007	02:52:10.99	-7.98	154.63	18.0	6.7
16/07/2007	01:13:22.37	37.53	138.45	12.0	6.6
26/07/2007	05:40:16.10	2.87	127.46	25.0	6.9
01/08/2007	17:08:51.40	-15.60	167.68	120.0	7.2
02/08/2007	03:21:42.82	51.31	-179.97	21.0	6.7
15/08/2007	20:22:11.12	50.32	-177.55	9.0	6.5
16/08/2007	08:39:28.44	-9.83	159.46	15.0	6.5
17/08/2007	03:04:03.09	-5.26	129.43	10.0	6.4
20/08/2007	13:46:17.41	6.13	127.38	8.0	6.4
20/08/2007	22:42:28.53	8.04	-39.25	6.0	6.5
02/09/2007	01:05:18.15	-11.61	165.76	35.0	7.2
02/09/2007	02:34:5.89	-11.80	165.93	0.0	6.3
12/09/2007	11:10:26.83	-4.44	101.37	34.0	8.5
12/09/2007	23:48:58.30	-2.61	100.86	0.0	7.8
13/09/2007	01:26:36.13	-2.00	99.87	30.0	6.1
13/09/2007	02:30:03.30	-1.69	99.67	28.0	6.5
13/09/2007	03:35:28.72	-2.13	99.63	22.0	7.0
13/09/2007	09:48:45.13	3.80	126.34	26.0	6.3
14/09/2007	06:01:32.27	-4.07	101.17	23.0	6.4
14/09/2007	06:03:13.55	-4.35	101.02	0.0	6.1
20/09/2007	08:31:14.49	-2.00	100.14	30.0	6.7
26/09/2007	12:36:26.89	-4.99	153.50	40.0	6.8
27/09/2007	19:57:44	-21.10	169.28	9.0	6.1
28/09/2007	01:01:49.18	-21.21	169.36	12.0	6.3
28/09/2007	01:35:51.97	-21.13	169.37	10.0	6.5
28/09/2007	13:38:57.88	22.01	142.67	260.0	7.5
30/09/2007	02:08:30.17	10.45	145.72	14.0	6.9
30/09/2007	05:23:34.07	-49.27	164.12	10.0	7.4
30/09/2007	09:47:51.97	-49.14	164.11	18.0	6.6
02/10/2007	18:00:06.87	54.51	-161.71	32.0	6.3
15/10/2007	12:29:34.86	-44.80	167.55	18.0	6.8

Date	Origin Time	Latitude	Longitude	Depth (km)	Mag.
24/10/2007	21:02:50.61	-3.90	101.02	21.0	6.8
10/11/2007	01:13:29.35	-51.78	161.32	10.0	6.6
22/11/2007	08:48:27.53	-5.76	147.10	53.0	6.8
25/11/2007	16:02:15.75	-8.29	118.37	20.0	6.5
25/11/2007	19:53:05.47	-8.22	118.47	18.0	6.5
27/11/2007	11:50:2.54	-10.99	162.14	50.0	6.4
29/11/2007	19:00:20.42	14.94	-61.27	156.0	7.4
09/12/2007	07:28:20.82	-26.00	-177.51	152.0	7.8
19/12/2007	09:30:27.93	51.36	-179.51	34.0	7.2
19/12/2007	09:35:13.87	51.07	-179.16	0.0	7.1
20/12/2007	07:55:15.84	-39.01	178.29	20.0	6.6
21/12/2007	07:24:34.03	51.37	-178.98	25.0	6.3
22/12/2007	07:11:08.10	-2.41	139.07	20.0	6.2
26/12/2007	22:04:54.67	52.56	-168.22	25.0	6.4
05/01/2008	11:01:06.11	51.25	-130.75	15.0	6.6
05/01/2008	11:44:48.17	51.16	-130.54	10.0	6.4
09/01/2008	08:26:45.49	32.29	85.17	10.0	6.4
22/01/2008	17:14:57.95	1.01	97.44	20.0	6.2
08/02/2008	09:38:14.10	10.67	-41.90	9.0	6.9
14/02/2008	10:09:22.72	36.50	21.67	29.0	6.9
14/02/2008	12:08:55.79	36.35	21.86	28.0	6.5
20/02/2008	08:08:30.52	2.77	95.96	26.0	7.4
20/02/2008	08:12:20.22	3.08	96.15	0.0	7.0
20/02/2008	18:27:06	36.29	21.77	9.0	6.2
24/02/2008	14:46:21.47	-2.40	99.93	22.0	6.5
25/02/2008	08:36:33.03	-2.49	99.97	25.0	7.2
25/02/2008	08:47:2.43	-2.65	99.79	0.0	6.0
25/02/2008	18:06:03.90	-2.33	99.89	25.0	6.6
25/02/2008	21:02:18.42	-2.24	99.81	25.0	6.7
27/02/2008	06:54:20.61	26.82	142.44	15.0	6.2
03/03/2008	02:37:27.12	-2.18	99.82	25.0	6.2
03/03/2008	09:31:02.50	46.41	153.18	10.0	6.5
03/03/2008	14:11:14.62	13.35	125.63	24.0	6.9
12/03/2008	11:23:34.06	-16.57	167.34	13.0	6.4
12/03/2008	11:36:55.28	-16.49	167.18	10.0	6.3
29/03/2008	17:30:50.15	2.86	95.30	20.0	6.3
09/04/2008	11:13:17.69	-20.17	168.86	16.0	6.4
09/04/2008	11:23:40.35	-20.18	168.90	35.0	6.3
09/04/2008	12:46:12.72	-20.07	168.89	33.0	7.3
09/04/2008	14:47:50.51	-20.00	168.87	35.0	6.3
12/04/2008	00:30:12.60	-55.66	158.45	16.0	7.1
12/04/2008	00:46:28.17	43.91	147.55	66.0	6.1
15/04/2008	22:59:51.50	51.86	-179.36	11.0	6.4
16/04/2008	00:35:48.87	-18.61	-175.70	10.0	6.3
16/04/2008	05:54:19.69	51.88	-179.16	13.0	6.6
19/04/2008	05:58:42.25	-20.27	168.80	14.0	6.3
26/04/2008	23:34:49.39	-49.09	164.12	10.0	6.1
28/04/2008	18:33:34.20	-19.94	168.95	32.0	6.4
02/05/2008	01:33:37.24	51.86	-177.53	14.0	6.6
07/05/2008	16:01:59.22	36.19	141.66	0.0	6.1
07/05/2008	16:45:18.70	36.16	141.53	27.0	6.9
09/05/2008	21:51:29.73	12.52	143.18	76.0	6.8
12/05/2008	06:27:57.46	31.00	103.35	0.0	7.9
12/05/2008	06:50:35.07	31.93	104.53	0.0	6.4
12/05/2008	07:00:41.25	32.25	104.99	0.0	6.6
12/05/2008	07:07:30.04	32.23	104.94	0.0	6.3
23/05/2008	19:35:34.78	7.31	-34.90	8.0	6.5
29/05/2008	15:45:59.37	64.01	-21.11	0.0	6.2
31/05/2008	04:37:56.01	-41.20	80.48	9.0	6.4
01/06/2008	01:57:23.69	20.12	121.35	31.0	6.3
08/06/2008	12:25:29.71	37.96	21.52	16.0	6.4
13/06/2008	23:43:45.36	39.03	140.88	7.0	6.9
27/06/2008	11:40:13.99	11.01	91.82	17.0	6.6
13/07/2008	14:58:33.01	21.01	121.15	14.0	6.2
15/07/2008	03:26:34.70	35.80	27.86	52.0	6.4
19/07/2008	02:39:28.70	37.55	142.21	22.0	7.0
19/07/2008	09:27:01.46	-11.04	164.49	11.0	6.6
23/07/2008	15:26:19.95	39.80	141.46	108.0	6.8
25/08/2008	13:21:58.82	30.90	83.52	12.0	6.7
25/08/2008	13:29:21.15	30.65	83.41	0.0	6.4
27/08/2008	01:35:32.15	51.61	104.16	16.0	6.3
08/09/2008	18:52:06.97	-13.50	166.97	110.0	6.9

Date	Origin Time	Latitude	Longitude	Depth (km)	Mag.
10/09/2008	13:08:14.69	8.09	-38.71	9.0	6.6
11/09/2008	00:20:50.92	41.89	143.75	25.0	6.8
24/09/2008	02:33:05.56	17.61	-105.50	12.0	6.4
29/09/2008	15:19:31.59	-29.76	-177.68	36.0	7.0
05/10/2008	09:12:36.07	-30.18	-177.18	10.0	6.1
05/10/2008	15:52:49.40	39.53	73.82	27.0	6.7
06/10/2008	08:30:45.57	29.81	90.35	12.0	6.3
16/10/2008	19:41:25.72	14.42	-92.36	24.0	6.7
16/10/2008	19:43:34.32	14.38	-92.28	0.0	6.4
19/10/2008	05:10:33.91	-21.86	-173.82	29.0	6.9
23/10/2008	10:04:35.04	-2.63	145.57	10.0	6.3
28/10/2008	23:09:57.65	30.64	67.35	15.0	6.4
29/10/2008	11:32:43.13	30.60	67.46	14.0	6.4
07/11/2008	07:19:35.71	-14.83	168.03	13.0	6.4
07/11/2008	16:04:23.35	-6.71	129.07	10.0	6.2
10/11/2008	01:21:58.93	37.59	95.97	0.0	6.3
16/11/2008	17:02:32.70	1.27	122.09	30.0	7.4
22/11/2008	16:00:58.43	-4.25	101.28	0.0	6.4
22/11/2008	16:01:01.70	-4.35	101.26	24.0	6.3
09/12/2008	06:23:59.75	-31.23	-176.92	18.0	6.8
20/12/2008	10:29:23.10	36.54	142.43	19.0	6.3
03/01/2009	19:43:50.65	-0.41	132.88	17.0	7.7
03/01/2009	20:08:55.44	0.22	132.25	0.0	6.1
03/01/2009	20:18:37.66	0.07	132.18	0.0	6.3
03/01/2009	22:33:40.29	-0.69	133.30	23.0	7.4
15/01/2009	07:27:20.29	-22.35	170.63	27.0	6.7
15/01/2009	17:49:39.07	46.86	155.15	36.0	7.4
19/01/2009	03:35:18.84	-22.60	170.91	12.0	6.6
11/02/2009	17:34:50.49	3.89	126.39	20.0	7.2
12/02/2009	13:15:06.28	4.03	126.55	27.0	6.3
18/02/2009	21:53:45.16	-27.42	-176.33	25.0	7.0
06/03/2009	10:50:29.41	80.32	-1.85	9.0	6.5
19/03/2009	18:17:40.47	-23.04	-174.66	31.0	7.6
01/04/2009	03:54:58.77	-3.52	144.10	10.0	6.4
06/04/2009	01:32:39	42.33	13.33	8.0	6.3
07/04/2009	04:23:33.15	46.05	151.55	31.0	6.9
15/04/2009	20:01:34.68	-3.12	100.47	22.0	6.3
18/04/2009	19:18:0.11	46.04	151.46	42.0	6.4
16/05/2009	00:53:51.25	-31.55	-178.83	43.0	6.5
28/05/2009	08:24:46.56	16.73	-86.22	19.0	7.3
02/06/2009	02:17:03.51	-17.76	167.95	15.0	6.3
05/06/2009	03:30:33.06	41.82	143.45	29.0	6.4
23/06/2009	14:19:22.35	-5.16	153.78	64.0	6.7
01/07/2009	09:30:10.41	34.16	25.47	19.0	6.4
13/07/2009	18:04:58.96	24.21	122.30	0.0	6.1
15/07/2009	09:22:29.03	-45.76	166.56	12.0	7.8
15/07/2009	10:04:1.42	-46.20	165.80	0.0	6.5
03/08/2009	17:59:56.17	29.04	-112.90	10.0	6.9
03/08/2009	18:40:50.10	29.31	-113.73	10.0	6.2
09/08/2009	10:55:55.11	33.17	137.94	292.0	7.1
10/08/2009	04:06:31	-11.61	166.09	35.0	6.6
10/08/2009	19:55:38.73	14.10	92.90	24.0	7.5
10/08/2009	20:07:09.11	34.74	138.26	40.0	6.2
12/08/2009	22:48:51.42	32.82	140.40	53.0	6.6
16/08/2009	07:38:21.70	-1.48	99.49	20.0	6.7
17/08/2009	00:05:49.03	23.50	123.50	20.0	6.7
17/08/2009	10:10:56.50	23.43	123.52	15.0	6.1
28/08/2009	01:52:06.64	37.70	95.72	13.0	6.3
30/08/2009	14:51:32.89	-15.22	-172.57	11.0	6.6
02/09/2009	07:54:58.99	-7.71	107.41	31.0	6.8
24/09/2009	07:16:20.26	18.83	-107.34	13.0	6.4
29/09/2009	17:48:10.99	-15.49	-172.10	18.0	8.1
29/09/2009	18:22:11.59	-16.10	-173.23	0.0	8.7
29/09/2009	18:40:10.14	-15.33	-173.25	0.0	6.6
29/09/2009	19:19:58.11	-15.66	-172.75	0.0	6.3
30/09/2009	10:16:09.25	-0.72	99.87	81.0	7.6
01/10/2009	01:52:27.32	-2.48	101.52	9.0	6.6
07/10/2009	22:03:14.47	-13.01	166.51	45.0	7.7
07/10/2009	22:18:51.24	-12.52	166.38	35.0	7.8
07/10/2009	22:38:17.19	-12.82	166.05	0.0	6.1
07/10/2009	22:50:15.78	-12.39	166.09	21.0	6.8
07/10/2009	23:13:48.16	-13.09	166.50	31.0	7.4

Date	Origin Time	Latitude	Longitude	Depth (km)	Mag.
07/10/2009	23:54:10.29	-13.23	166.50	0.0	6.4
08/10/2009	02:12:33.81	-11.64	166.20	0.0	6.2
08/10/2009	08:28:47.97	-13.30	165.91	35.0	6.8
13/10/2009	05:37:23.69	52.75	-167.00	24.0	6.5
13/10/2009	20:21:53.20	52.60	-167.12	14.0	6.4
24/10/2009	14:40:43.72	-6.13	130.38	130.0	6.9
30/10/2009	07:03:39.12	29.22	129.78	34.0	6.8
02/11/2009	10:47:13.24	-24.12	-175.17	9.0	6.2
08/11/2009	19:41:43.36	-8.21	118.63	18.0	6.6
17/11/2009	15:30:47.44	52.12	-131.40	17.0	6.6
24/11/2009	12:47:15.66	-20.71	-174.04	18.0	6.8
09/12/2009	09:46:03.30	-22.15	170.96	45.0	6.4
19/12/2009	13:02:15.57	23.80	121.61	43.0	6.4
03/01/2010	21:48:02.87	-8.73	157.49	10.0	6.6
03/01/2010	22:36:25.64	-8.78	157.35	10.0	7.1
05/01/2010	12:15:32.21	-9.02	157.55	15.0	6.8
05/01/2010	12:25:25.15	-9.04	157.91	0.0	6.0
09/01/2010	05:51:30.47	-9.13	157.63	12.0	6.2
10/01/2010	00:27:39.32	40.65	-124.69	29.0	6.5
12/01/2010	21:53:10.06	18.44	-72.57	13.0	7.0
05/02/2010	06:59:05.50	-47.91	99.59	1.0	6.2
07/02/2010	06:09:56.94	23.47	123.70	0.0	6.1
13/02/2010	02:34:28.86	-21.90	-174.77	11.0	6.1
26/02/2010	20:31:26.97	25.93	128.43	25.0	7.0
04/03/2010	00:18:51.29	22.92	120.79	21.0	6.3
05/03/2010	16:06:56.23	-3.74	101.03	0.0	6.5
05/03/2010	16:09:24.97	-3.73	100.90	0.0	6.8
14/03/2010	08:08:03.96	37.74	141.59	32.0	6.5
30/03/2010	16:54:46.73	13.67	92.83	34.0	6.6
04/04/2010	22:40:43.10	32.30	-115.28	4.0	7.2
04/04/2010	23:15:13.89	32.33	-115.02	0.0	6.2
06/04/2010	22:14:57.27	2.47	97.18	0.0	7.7
11/04/2010	09:40:25.60	-10.88	161.12	21.0	6.9
13/04/2010	23:49:38.33	33.17	96.55	17.0	6.9
26/04/2010	02:59:52.15	22.18	123.62	22.0	6.5
05/05/2010	16:28:58.76	-4.06	101.10	0.0	6.3
09/05/2010	05:59:41.62	3.75	96.02	38.0	7.2
26/05/2010	08:53:08.03	25.77	129.94	10.0	6.5
27/05/2010	17:14:46.57	-13.70	166.64	31.0	7.2
12/06/2010	19:26:50.46	7.88	91.94	35.0	7.5
16/06/2010	03:05:59.07	-2.36	136.56	0.0	6.6
16/06/2010	03:16:27.55	-2.17	136.54	18.0	7.0
16/06/2010	03:58:08.48	-2.33	136.48	10.0	6.6
18/06/2010	02:23:05.58	44.45	148.69	28.0	6.2
26/06/2010	05:30:19.49	-10.63	161.45	35.0	6.7
02/07/2010	06:04:03.13	-13.64	166.49	29.0	6.3
04/07/2010	21:55:51.98	39.70	142.37	27.0	6.3
18/07/2010	05:56:44.93	52.88	-169.85	14.0	6.7
18/07/2010	13:04:09.41	-5.97	150.43	28.0	6.9
18/07/2010	13:34:59.36	-5.93	150.59	35.0	7.3
20/07/2010	19:18:20.37	-5.90	150.71	24.0	6.3
23/07/2010	23:10:10.70	6.32	121.62	0.0	6.3
30/07/2010	03:56:13.71	52.50	159.84	23.0	6.3
04/08/2010	12:58:24.20	51.42	-178.65	27.0	6.4
04/08/2010	22:01:43.62	-5.75	150.76	44.0	7.0
10/08/2010	05:23:44.98	-17.54	168.07	25.0	7.3
10/08/2010	05:50:33.27	39.41	143.32	0.0	6.4
13/08/2010	21:19:34.09	12.49	141.47	16.0	6.9
20/08/2010	17:56:14.15	-6.57	154.25	19.0	6.1
03/09/2010	11:16:06.60	51.45	-175.87	23.0	6.5
03/09/2010	16:35:47.77	-43.52	171.83	12.0	7.0
03/09/2010	17:06:51.67	-3.61	102.08	80.0	6.3
08/09/2010	11:37:31.89	-20.67	169.82	10.0	6.3
29/09/2010	17:11:25.94	-4.96	133.76	26.0	7.0
04/10/2010	13:28:38.86	24.27	125.15	32.0	6.3
08/10/2010	03:26:13.71	51.37	-175.36	19.0	6.4
21/10/2010	17:53:13.57	24.70	-109.16	13.0	6.7
25/10/2010	14:42:22.46	-3.49	100.08	20.0	7.8
25/10/2010	19:37:31.15	-2.96	100.37	26.0	6.3
10/11/2010	04:05:24.41	-45.46	96.39	10.0	6.5
02/12/2010	03:12:09.82	-6.00	149.98	33.0	6.6
20/12/2010	18:42:1.38	28.38	59.18	32.0	6.5

Date	Origin Time	Latitude	Longitude	Depth (km)	Mag.
21/12/2010	17:19:40.66	26.90	143.70	14.0	7.4
22/12/2010	21:49:40.08	26.81	143.60	18.0	6.4
23/12/2010	14:00:32.33	53.13	171.16	18.0	6.4
25/12/2010	13:16:37	-19.70	167.95	16.0	7.3
29/12/2010	06:54:19.64	-19.66	168.14	16.0	6.4
09/01/2011	10:03:43.99	-19.16	168.31	22.0	6.5
13/01/2011	16:16:41.54	-20.63	168.47	9.0	7.0
18/01/2011	20:23:23.48	28.78	63.95	68.0	7.2
27/01/2011	08:38:28.34	28.19	59.01	10.0	6.2
04/02/2011	13:53:46.26	24.62	94.68	85.0	6.2
21/02/2011	23:51:42.35	-43.58	172.68	5.0	6.1
07/03/2011	00:09:36.45	-10.35	160.77	22.0	6.3
09/03/2011	02:45:20.33	38.44	142.84	32.0	7.3
09/03/2011	02:58:8.90	38.27	143.13	0.0	6.3
09/03/2011	04:36:59.11	38.63	143.11	0.0	6.0
09/03/2011	18:16:16.44	38.31	142.43	22.0	6.0
09/03/2011	21:23:59.39	38.32	142.79	0.0	6.6
09/03/2011	21:24:01.68	38.30	142.81	15.0	6.4
11/03/2011	05:46:24.12	38.30	142.37	29.0	9.0
11/03/2011	06:08:29.66	38.97	143.37	2.0	6.7
11/03/2011	06:11:10.93	36.08	141.83	0.0	7.0
11/03/2011	06:12:36.36	37.79	144.23	25.0	6.2
11/03/2011	06:15:23.12	37.93	143.80	35.0	6.3
11/03/2011	06:23:09.48	39.03	142.28	56.0	6.2
11/03/2011	06:25:50.30	38.06	144.59	18.0	7.7
11/03/2011	06:29:15.99	37.81	144.23	40.0	6.1
11/03/2011	06:48:45.59	37.96	142.72	11.0	6.2
11/03/2011	06:49:16.61	37.34	144.24	47.0	6.1
11/03/2011	06:55:27.28	37.55	142.90	0.0	6.9
11/03/2011	06:58:53.69	37.23	144.76	0.0	6.7
11/03/2011	07:14:58.82	36.59	141.82	24.0	6.3
11/03/2011	07:28:12.36	36.82	141.82	28.0	6.1
11/03/2011	08:19:24.38	36.17	141.56	6.0	6.5
11/03/2011	08:27:51.60	38.02	142.66	42.0	6.0
11/03/2011	08:39:6.06	37.67	142.94	0.0	6.5
11/03/2011	08:40:49.79	37.44	141.11	0.0	6.3
11/03/2011	08:48:19.28	36.43	142.18	0.0	6.3
11/03/2011	09:27:43.39	38.28	142.14	79.0	6.1
11/03/2011	10:10:34.22	39.19	142.76	26.0	6.0
11/03/2011	11:36:40.92	39.24	142.46	25.0	6.6
11/03/2011	11:49:19.00	37.88	144.47	0.0	6.1
11/03/2011	18:59:16.54	37.01	138.38	9.0	6.2
11/03/2011	19:02:59.17	39.34	142.87	27.0	6.0
11/03/2011	19:45:19.36	37.50	141.61	0.0	6.0
12/03/2011	01:35:25.26	39.18	142.97	0.0	6.0
12/03/2011	01:43:21.02	36.37	141.62	38.0	6.3
12/03/2011	01:47:15.40	37.59	142.65	20.0	6.5
13/03/2011	01:26:04.25	35.72	141.64	8.0	6.1
14/03/2011	06:12:36.06	37.78	142.46	14.0	6.0
15/03/2011	15:23:54.13	40.33	143.29	19.0	6.1
22/03/2011	07:18:45.38	37.24	144.00	11.0	6.4
22/03/2011	09:19:06.23	37.33	141.79	31.0	6.1
22/03/2011	09:44:28.42	39.85	143.44	7.0	6.4
24/03/2011	13:55:12.01	20.69	99.82	8.0	6.9
25/03/2011	11:36:24.49	38.77	141.88	39.0	6.2
27/03/2011	22:23:58.80	38.42	142.01	19.0	6.2
29/03/2011	10:54:33.20	37.40	142.29	15.0	6.1
31/03/2011	00:11:58.30	-16.54	-177.52	15.0	6.3
03/04/2011	20:06:40.39	-9.85	107.69	14.0	6.7
07/04/2011	14:32:43.29	38.28	141.59	42.0	7.1
11/04/2011	08:16:12.73	37.00	140.40	11.0	6.6
11/04/2011	23:08:16.87	35.42	140.57	15.0	6.2
13/04/2011	19:57:25.42	39.58	143.34	22.0	6.0
23/04/2011	04:16:54.72	-10.38	161.20	79.0	6.8
10/05/2011	08:55:08.93	-20.24	168.23	11.0	6.8
05/06/2011	11:51:12.01	-55.84	146.62	3.0	6.4
16/06/2011	00:03:35.79	-5.93	151.04	16.0	6.4
22/06/2011	21:50:52.35	39.96	142.21	33.0	6.7
24/06/2011	03:09:39.47	52.05	-171.84	52.0	7.3
26/06/2011	12:16:38.60	-2.38	136.63	17.0	6.3
26/06/2011	12:19:13.69	-2.45	136.56	0.0	6.2
06/07/2011	19:03:18.26	-29.54	-176.34	17.0	7.6

Date	Origin Time	Latitude	Longitude	Depth (km)	Mag.
09/07/2011	19:35:18.75	-29.44	-177.01	15.0	6.0
10/07/2011	00:57:10.80	38.03	143.26	23.0	7.0
11/07/2011	20:47:04.30	9.51	122.18	19.0	6.4
19/07/2011	19:35:43.48	40.08	71.41	20.0	6.1
23/07/2011	04:34:24.18	38.90	141.82	41.0	6.3
25/07/2011	00:50:47.59	-3.18	150.61	10.0	6.3
30/07/2011	18:53:49.68	36.94	140.96	30.0	6.3
31/07/2011	23:38:56.61	-3.52	144.83	10.0	6.6
20/08/2011	16:54:58.61	-18.32	168.12	0.0	6.9
20/08/2011	17:13:06.38	-18.31	168.16	35.0	6.5
20/08/2011	18:01:55.37	-18.57	168.07	0.0	6.3
20/08/2011	18:19:23.55	-18.31	168.22	28.0	7.1
22/08/2011	11:23:32.75	36.10	141.79	0.0	6.0
02/09/2011	10:55:53.59	52.17	-171.71	32.0	6.9
03/09/2011	22:55:40.92	-20.67	169.72	185.0	7.0
05/09/2011	17:55:11.22	2.96	97.89	91.0	6.7
09/09/2011	19:41:34.15	49.53	-126.89	22.0	6.4
15/09/2011	08:00:09.64	36.26	141.34	28.0	6.1
16/09/2011	19:26:40.97	40.27	142.78	35.0	6.7
18/09/2011	12:40:51.83	27.73	88.15	50.0	6.9
22/09/2011	23:07:03.57	-15.44	-175.31	10.0	6.4
14/10/2011	03:35:14.81	-6.57	147.88	37.0	6.5
21/10/2011	17:57:16.10	-28.99	-176.24	33.0	7.4
23/10/2011	10:41:22.93	38.72	43.51	16.0	7.1
11/12/2011	01:47:25.90	17.84	-99.96	54.0	6.5
14/12/2011	05:04:59.27	-7.56	146.80	140.0	7.1
27/12/2011	15:21:56.84	51.84	95.91	15.0	6.6

## Appendix D

# P-wave Travel Times Appendix

### D.1 Event Data

Events with magnitude  $>5.0$  within  $\sim 85^\circ$  to  $\sim 95^\circ$  from USArray are selected from the Reviewed Events Bulletin from when USArray started operating in 01/01/2004 to 31/07/2013. Events picked are primarily from the Indonesian Arc, Tonga Trench, south-eastern Pacific, and South-American Trench and preferentially from depths  $\geq 30$  km. All events used are listed below.

Table D.1: Events in dataset reported in the REB catalogue. Events at 0 km depth are assigned a depth of 10 km before being processed. Dates are given in day/month/year format.

Date	Origin Time	Latitude	Longitude	Depth (km)	Error (km)	Mag.	Mag. Type
29/01/2004	03:52:50.60	-50.2311	-114.5760	0.0	0.0	5.9	Ms1
03/05/2004	04:36:46.17	-37.6975	-73.4590	0.0	0.0	6.7	Ms1
02/06/2004	08:50:38.58	-32.8080	-179.2670	50.7	17.3	5.7	Ms1
15/06/2004	11:16:32.16	-38.7379	-73.0550	40.8	4.0	5.6	Ms1
28/08/2004	13:41:33.01	-35.0085	-70.5490	32.1	16.4	6.5	Ms
28/11/2004	02:35:11.03	-26.6375	-113.8760	0.0	0.0	6.2	Ms1
23/12/2004	14:59:03.00	-49.9522	161.1740	0.0	0.0	7.7	Ms1
16/01/2005	20:17:48.72	10.8665	140.8750	0.0	0.0	6.5	Ms1
22/01/2005	20:30:17.20	-7.8927	159.4700	24.9	9.1	6.4	Ms1
02/03/2005	10:42:11.08	-6.5018	129.8800	196.9	4.0	6.9	mbtmp
21/03/2005	12:23:54.22	-24.8201	-63.4030	580.4	3.9	6.4	mbtmp
12/05/2005	11:15:33.11	-57.3256	-139.1500	0.0	0.0	6.3	Ms1
02/06/2005	10:56:00.50	-24.0577	-66.8760	185.6	3.3	5.8	mbtmp
04/06/2005	14:50:48.66	-6.3735	146.8450	39.4	9.2	5.8	Ms1
13/06/2005	22:44:32.79	-19.9043	-69.1240	109.6	2.3	7.2	Ms1
15/06/2005	10:13:55.10	-4.5417	153.2100	37.2	7.1	5.7	mbtmp
15/06/2005	19:52:22.86	-44.9612	-80.6860	0.0	0.0	5.9	Ms1
10/07/2005	04:46:29.50	-36.3517	-97.3350	0.0	0.0	5.7	Ms
07/08/2005	11:35:24.31	-14.4012	-177.1970	0.0	0.0	5.7	Ms1
05/09/2005	07:37:28.13	-56.5051	-142.2550	0.0	0.0	5.8	Ms1
09/09/2005	07:26:43.76	-4.5031	153.3150	95.6	20.1	7.0	Ms1
29/09/2005	15:50:20.47	-5.3781	151.8760	0.0	0.0	6.5	Ms1
17/11/2005	19:26:55.32	-22.2588	-67.6840	151.4	2.6	6.2	mbtmp
22/11/2005	15:11:33.18	-5.1855	145.3930	82.6	19.4	5.7	mbtmp
11/12/2005	14:20:46.41	-6.5837	152.1870	24.6	10.0	6.2	Ms1
11/12/2005	14:20:46.41	-6.5837	152.1870	24.6	10.0	6.2	Ms1
27/01/2006	16:58:51.75	-5.4244	128.1500	378.0	3.3	7.0	mbtmp
05/03/2006	08:07:55.27	-20.1441	-175.7220	195.5	8.1	6.1	mbtmp
10/03/2006	10:12:17.18	-60.4068	-46.5340	0.0	0.0	5.4	Ms1
16/05/2006	10:39:20.74	-31.5728	-179.1710	122.0	6.9	6.8	Ms1
07/08/2006	22:18:56.53	-15.7922	167.7890	161.8	5.3	6.5	mbtmp
01/09/2006	10:18:55.21	-6.7815	155.4540	70.1	10.0	6.5	Ms1
01/09/2006	10:18:55.21	-6.7815	155.4540	70.1	10.0	6.5	Ms1
17/09/2006	09:34:13.04	-31.7291	-67.1010	136.4	1.8	5.7	mbtmp
10/10/2006	08:02:49.82	-56.1238	-122.5430	0.0	0.0	5.8	Ms1
17/10/2006	01:25:17.62	-5.9881	151.0560	77.4	9.0	6.7	Ms1
17/10/2006	01:25:17.62	-5.9881	151.0560	77.4	9.0	6.7	Ms1
07/11/2006	17:38:31.75	-6.4324	151.2520	0.0	0.0	6.2	Ms1
27/12/2006	20:15:39.64	-5.8304	154.3310	361.8	6.3	5.4	mb1
31/12/2006	14:55:05.96	-37.9745	-71.2400	47.0	17.1	5.0	mb1mx

Date	Origin Time	Latitude	Longitude	Depth (km)	Error (km)	Mag.	Mag. Type
17/01/2007	18:34:13.73	-57.9826	-64.4700	0.0	0.0	5.7	ML
04/02/2007	21:17:42.58	-55.6693	-123.5230	0.0	0.0	5.9	Msl
10/02/2007	06:03:02.85	-43.0439	-71.7370	160.2	3.8	4.8	mb1
31/03/2007	12:49:01.60	-55.8618	-123.4770	0.0	0.0	6.1	Msl
01/04/2007	20:39:55.04	-8.4009	156.9350	0.0	0.0	7.5	Msl
01/04/2007	20:39:55.04	-8.4009	156.9350	0.0	0.0	7.5	Msl
01/04/2007	20:47:29.24	-7.1990	156.0660	0.0	0.0	7.4	Msl
01/04/2007	21:11:31.75	-7.3166	155.8140	0.0	0.0	7.0	Msl
02/04/2007	02:49:39.75	-45.3134	-72.6630	25.7	15.5	5.7	Msl
13/04/2007	18:24:17.83	-34.9579	-108.9980	0.0	0.0	5.7	Msl
21/04/2007	17:53:42.31	-45.2236	-72.6390	10.8	7.0	6.2	Msl
07/05/2007	11:15:14.23	-44.9415	-80.7710	0.0	0.0	5.7	ML
29/05/2007	01:03:27.43	-4.6293	151.7550	128.9	2.5	5.3	mb1mx
07/06/2007	00:40:39.05	-3.3887	146.7150	8.2	10.5	6.0	Msl
28/06/2007	02:52:07.64	-8.0099	154.5230	0.0	0.0	6.4	Msl
16/08/2007	08:39:25.68	-9.8066	159.5920	0.0	0.0	6.4	Msl
07/09/2007	04:46:44.38	-56.0433	-124.0470	0.0	0.0	5.0	Ms
26/09/2007	12:36:20.67	-4.8338	153.6490	0.0	0.0	6.1	Msl
30/09/2007	02:08:28.01	10.4573	145.7800	0.0	0.0	6.9	Msl
05/10/2007	07:17:51.80	-25.1189	179.4870	497.7	5.0	5.3	mb1mx
22/11/2007	08:48:30.51	-5.7972	147.0560	74.8	18.2	6.4	Msl
29/11/2007	03:26:21.83	-36.3826	-97.5820	0.0	0.0	5.5	Ms
09/12/2007	07:28:14.43	-25.8822	-177.6450	89.9	11.0	6.9	Msl
11/12/2007	17:20:54.17	-61.8796	-65.2910	0.0	0.0	5.6	ML
15/01/2008	17:52:16.89	-21.8985	-179.5820	601.9	2.6	5.4	mb1
09/05/2008	21:51:31.73	12.5419	143.2430	92.9	3.3	6.2	Msl
20/05/2008	15:16:04.88	-44.7011	-77.5730	0.0	0.0	5.0	Ms
03/06/2008	16:20:51.58	-10.4437	161.3370	91.6	3.6	5.7	mb1
15/06/2008	08:37:15.97	-36.4449	-107.6950	0.0	0.0	5.3	Ms
26/06/2008	21:19:15.71	-20.8343	-173.2930	38.3	3.7	6.2	ML
19/07/2008	22:39:52.68	-17.2961	-177.3120	387.0	2.9	5.6	mb1
22/10/2008	12:55:57.80	-18.5290	-175.5300	233.1	4.5	5.7	mb1
04/11/2008	18:35:45.24	-17.1211	168.4500	202.9	4.7	5.3	mb
09/12/2008	06:24:01.42	-30.9751	-176.8570	0.0	0.0	6.6	Msl
03/01/2009	19:43:48.91	-0.4922	132.7570	0.0	0.0	7.3	Msl
03/01/2009	22:33:36.40	-0.7239	133.1330	0.0	0.0	7.2	Msl
18/02/2009	21:53:41.29	-27.3387	-176.3580	0.0	0.0	7.1	Msl
19/03/2009	18:17:35.76	-23.0141	-174.7350	0.0	0.0	7.4	Msl
12/05/2009	01:26:27.11	-5.6724	149.4650	96.3	2.5	5.5	mb1
23/06/2009	14:19:22.02	-5.2054	153.7170	96.2	3.4	6.2	Msl
08/07/2009	19:23:35.97	-35.9498	-102.8730	0.0	0.0	5.3	mb1
15/07/2009	20:10:39.80	-3.3882	150.6430	0.0	0.0	5.9	Msl
01/08/2009	13:33:27.99	-56.2785	-124.2160	0.0	0.0	5.4	Ms
17/09/2009	23:21:38.15	-28.9814	-112.5610	0.0	0.0	6.0	Msl
29/09/2009	17:48:08.06	-15.5716	-172.0830	0.0	0.0	8.0	Msl
14/10/2009	18:00:22.01	-14.5033	-174.9490	0.0	0.0	5.9	Msl
24/10/2009	14:40:46.23	-6.0643	130.4240	151.0	7.0	6.3	Msl
27/10/2009	00:04:44.61	-59.9575	-65.1980	0.0	0.0	5.6	ML
09/11/2009	10:44:53.17	-17.2944	178.4080	571.8	6.1	5.8	mb1
22/11/2009	22:47:28.62	-31.4545	179.5500	440.8	3.5	5.9	mbtmp
03/12/2009	06:12:30.93	-56.0247	-122.7040	0.0	0.0	5.7	Msl
03/01/2010	21:48:01.74	-8.6247	157.3590	0.0	0.0	6.1	Msl
03/01/2010	22:36:25.04	-8.6752	157.2140	0.0	0.0	6.8	Msl
05/01/2010	12:15:29.80	-8.9872	157.4440	0.0	0.0	6.4	Msl
05/01/2010	13:11:37.71	-8.9551	157.8000	0.0	0.0	5.7	Msl
17/01/2010	12:00:00.45	-57.6703	-65.7130	0.0	0.0	5.8	Msl
27/02/2010	06:51:11.48	-31.7032	-69.3140	0.0	0.0	6.3	ML
27/02/2010	07:37:17.99	-36.9396	-72.8060	34.5	3.1	5.7	mbtmp
27/02/2010	08:01:17.05	-37.9535	-75.3880	0.0	0.0	7.3	Msl
27/02/2010	19:00:02.08	-33.3888	-71.8960	0.0	0.0	5.9	Msl
27/02/2010	23:12:29.89	-34.7288	-71.8660	0.0	0.0	5.5	mb1
28/02/2010	11:25:35.88	-34.9714	-71.6710	46.5	4.6	5.8	mbtmp
03/03/2010	17:44:21.89	-36.6233	-73.3770	0.0	0.0	5.8	Msl
20/03/2010	14:00:52.76	-3.4000	152.1700	437.8	10.4	6.2	mbtmp
20/03/2010	14:00:52.76	-3.4000	152.1700	437.8	10.4	6.2	mbtmp
17/04/2010	23:15:26.20	-6.6419	147.2790	87.4	7.3	5.9	mbtmp
23/04/2010	10:03:07.76	-37.5376	-72.9210	43.1	18.3	5.6	Msl
19/05/2010	10:30:08.40	-54.5737	-135.5050	0.0	0.0	5.5	Ms
19/05/2010	10:51:01.58	-54.6125	-135.4730	0.0	0.0	5.7	Msl
16/06/2010	03:16:25.82	-2.1010	136.4420	0.0	0.0	6.9	Msl
16/06/2010	03:58:06.35	-2.2787	136.6280	0.0	0.0	6.4	Msl
17/06/2010	13:06:53.26	-32.9068	179.8190	222.6	7.7	5.9	mbtmp

Date	Origin Time	Latitude	Longitude	Depth (km)	Error (km)	Mag.	Mag. Type
14/07/2010	08:32:17.61	-38.1215	-73.4290	0.0	0.0	6.5	Ms1
18/07/2010	13:04:11.14	-5.9808	150.5960	35.9	6.2	6.8	Ms1
18/07/2010	13:35:00.00	-5.9208	150.8270	0.0	0.0	7.0	Ms1
04/08/2010	07:15:33.19	-5.5067	146.8260	217.4	4.2	6.1	mbtmp
04/08/2010	07:15:33.19	-5.5067	146.8260	217.4	4.2	6.1	mbtmp
04/08/2010	22:01:36.91	-5.7719	150.7910	0.0	0.0	6.4	Ms1
13/08/2010	21:19:30.54	12.5029	141.7080	0.0	0.0	6.8	Ms1
15/08/2010	15:09:29.23	-5.7334	148.3550	174.2	2.1	6.1	mbtmp
29/09/2010	17:11:20.53	-4.9226	133.7800	0.0	0.0	6.7	Ms1
30/10/2010	15:18:28.87	-56.4651	-142.8330	0.0	0.0	5.5	Ms
21/11/2010	04:36:29.26	-54.7245	-131.6020	0.0	0.0	5.5	Ms1
02/12/2010	03:12:11.68	-5.9849	149.8600	43.8	5.7	6.3	Ms1
01/01/2011	09:56:59.13	-26.8215	-63.2420	587.1	2.3	6.8	mbtmp
02/01/2011	20:20:13.41	-38.4370	-73.2710	0.0	0.0	7.0	Ms1
12/02/2011	17:57:56.56	-20.8429	-175.6110	86.8	9.4	5.8	mbtmp
01/03/2011	00:53:44.52	-29.5026	-111.9880	0.0	0.0	5.8	Ms1
15/05/2011	18:37:11.44	-6.0992	154.4540	49.0	12.7	5.9	mbtmp
01/06/2011	12:55:18.92	-37.6025	-73.6960	0.0	0.0	6.3	Ms1
31/07/2011	23:38:54.94	-3.4978	144.7360	0.0	0.0	6.6	Ms1
28/08/2011	10:10:17.17	-24.3776	-115.9510	0.0	0.0	5.2	Ms1
02/09/2011	13:47:11.06	-28.4251	-63.1350	590.8	2.6	6.5	mbtmp
14/10/2011	03:35:14.46	-6.5551	147.9330	37.1	8.4	6.2	Ms1
11/11/2011	10:41:34.34	-55.4129	-125.0210	0.0	0.0	5.2	Ms1
14/12/2011	05:04:59.64	-7.5434	146.8700	142.1	4.0	6.6	mbtmp
15/01/2012	13:40:19.50	-60.9176	-55.9400	0.0	0.0	5.6	mb1
21/03/2012	22:15:07.78	-6.2051	146.0330	132.8	9.0	6.2	mbtmp
14/04/2012	10:56:16.88	-57.5568	-65.4750	0.0	0.0	6.0	Ms1
17/04/2012	07:13:50.83	-5.5176	147.1360	209.6	3.2	6.5	mbtmp
28/04/2012	10:08:08.02	-18.6560	-174.7240	128.6	3.8	6.2	mbtmp
18/05/2012	02:00:36.02	-44.9077	-80.6110	0.0	0.0	6.0	ML
28/07/2012	20:03:56.36	-4.6632	153.2280	33.6	4.5	6.0	mbtmp
13/11/2012	04:31:24.84	-45.7464	-77.2260	0.0	0.0	5.7	Ms1
29/12/2012	07:59:14.00	-3.2956	148.8270	0.0	0.0	5.4	Ms
23/01/2013	07:42:56.12	-44.6692	-79.5140	0.0	0.0	4.6	ms1mx
10/03/2013	22:51:52.87	-6.7060	148.2180	53.9	8.0	6.3	Ms1
14/04/2013	01:32:22.04	-6.4404	154.6930	26.7	8.1	6.2	Ms1
16/04/2013	22:55:25.38	-3.2048	142.5110	0.0	0.0	6.1	Ms1
23/04/2013	23:14:37.91	-3.8833	152.2390	0.0	0.0	6.0	Ms1
20/05/2013	09:49:01.19	-44.9980	-80.7190	0.0	0.0	5.6	Ms1
07/07/2013	18:35:31.48	-3.9861	153.8650	394.0	2.9	6.0	mbtmp
07/07/2013	18:35:31.48	-3.9861	153.8650	394.0	2.9	6.0	mbtmp
07/07/2013	20:30:07.45	-6.0104	149.8370	62.4	2.3	5.9	Ms1
16/07/2013	19:41:51.99	-63.3242	-62.3530	0.0	0.0	5.3	mb1mx

## D.2 Results

Travel-time residuals are calculated for P-waves turning at a range of distances and depths from events on 31/12/2006 at  $37.97^\circ$  S,  $71.24^\circ$  W at  $47 \pm 17.1$  km depth and 28/06/2007 at  $8.01^\circ$  S,  $154.52^\circ$  E at 10 km depth, sampling the eastern and northern edges of the Pacific LLSVP, respectively. Cross-sections are calculated through these turning points to determine the shape of the LLSVP boundary. Here I replot the cross-sections from Figure 4.10 for easier viewing.

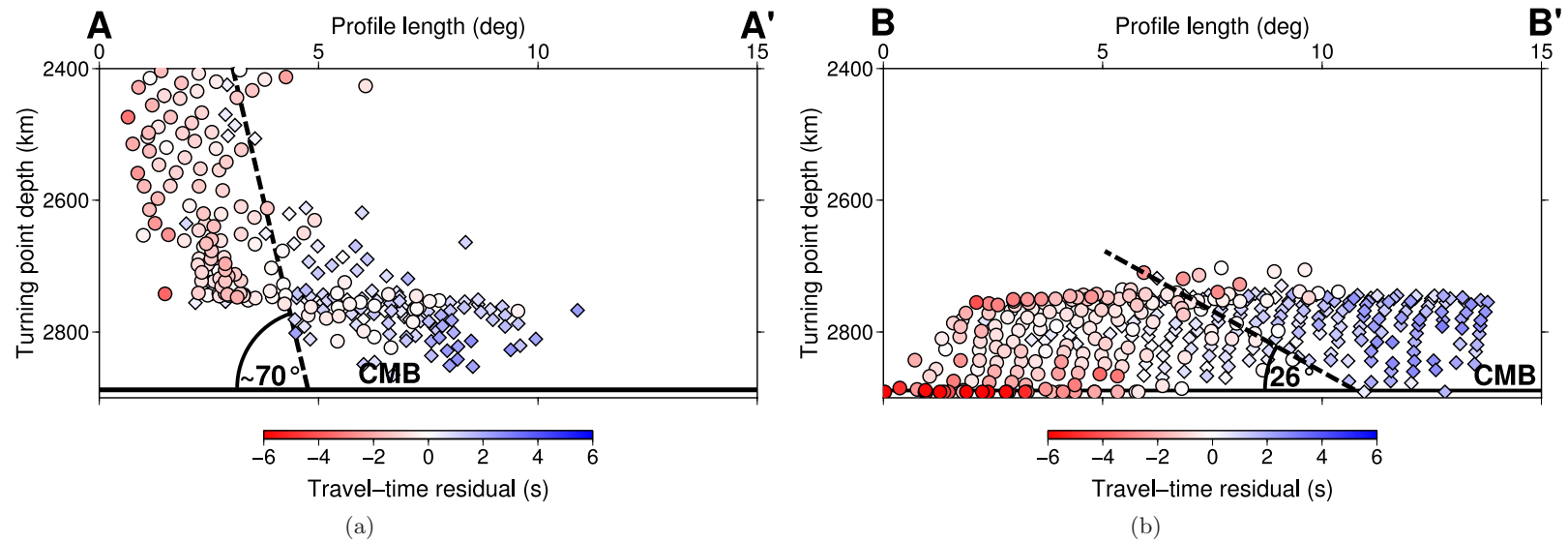


Figure D.1: Figure continues on to next page.

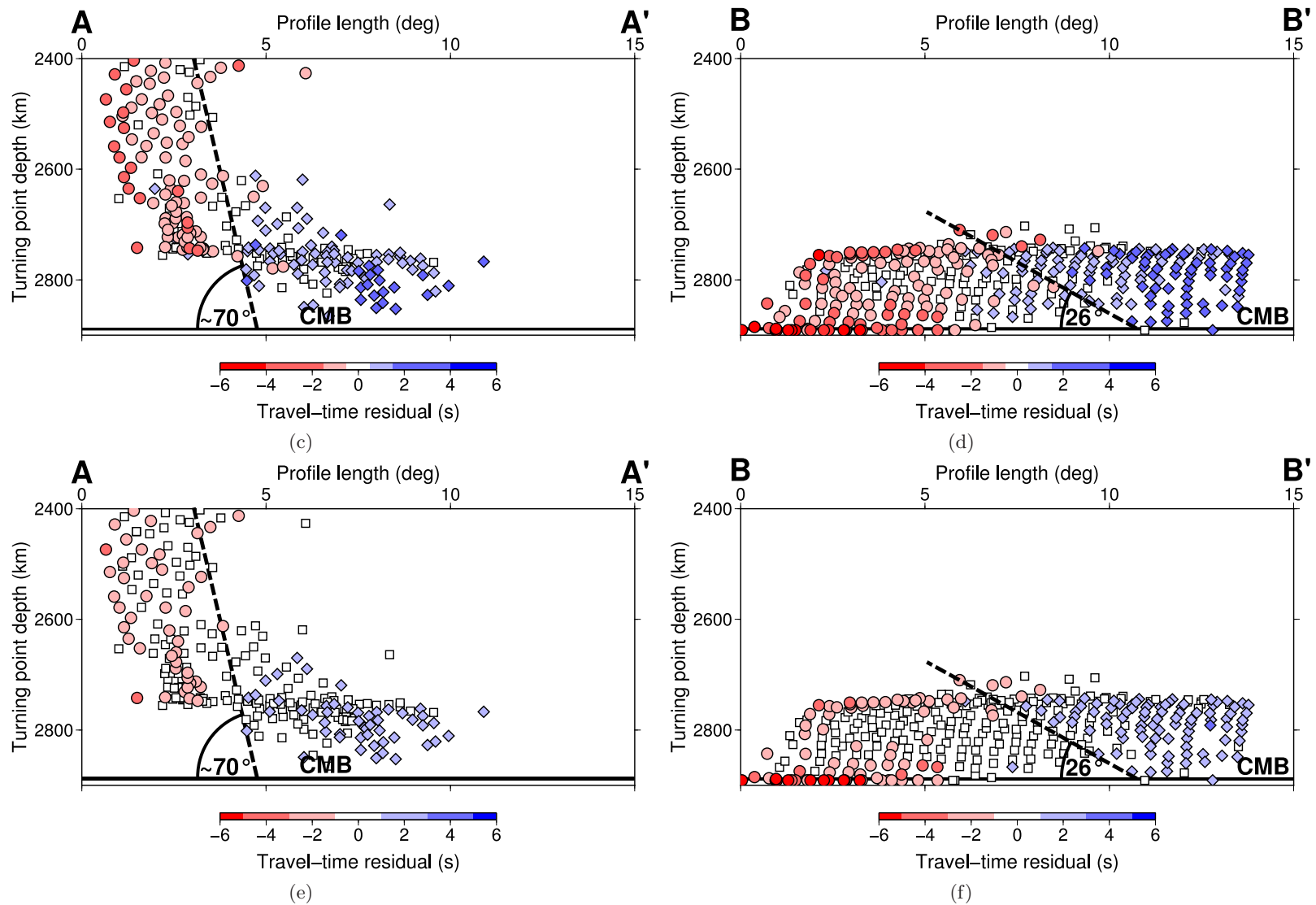


Figure D.1: Cross sections through P-wave travel-time residuals sampling the (left) eastern and (right) northern edges of the Pacific LLSVP. Caption as Figure 4.10.



# Bibliography

---

- Adams, D., 1979. *The Hitchhiker's Guide to the Galaxy*, Pan Books.
- Aki, K., 1969. Analysis of the Seismic Coda of Local Earthquakes as Scattered Waves, *Journal of Geophysical Research*, **74**, 615–631.
- Aki, K., 1973. Scattering of P Waves under the Montana Lasa, *J. Geophys. Res.*, **78**, 1334–1346.
- Aki, K. & Chouet, B., 1975. Origin of Coda Waves: Source, Attenuation, and Scattering Effects, *Journal of Geophysical Research*, **80**, 3322–3342.
- Aki, K. & Richards, P. G., 2002. *Quantitative Seismology*, University Science Books.
- Anderson, T. W., 1962. On the Distribution of the Two-Sample Cramer-von Mises Criterion, *Annals of Mathematical Statistics*, pp. 1148–1159.
- Ansell, J. H., 1973. Precursors to PKP: Seismic Wave Scattering and Spectral Data, *Geophys. J. R. astr. Soc.*, **35**, 487–489.
- Avants, M., Lay, T., & Garnero, E. J., 2006a. A new probe of ULVZ S-wave velocity structure: Array stacking of ScS waveforms, *Geophysical Research Letters*, **33**(7), 2–5.
- Avants, M., Lay, T., Russell, S. A., & Garnero, E. J., 2006b. Shear velocity variation within the D region beneath the central Pacific, *Journal of Geophysical Research*, **111**(B5), 1–10.
- Babu, G. J. & Feigelson, E. D., 2006. Astrostatistics: Goodness-of-Fit and All That!, in *Astronomical Data Analysis Software and Systems XV*, vol. 351, pp. 127–136.
- Barber, N., 1957. Timing errors in an equilateral array of receivers, *Journal of Atmospheric and Terrestrial Physics*, (June), 299–300.
- Bataille, K. & Flatte, S. M., 1988. Inhomogeneities Near the Core-Mantle Boundary Inferred from at the Global Digital Seismograph Network, *J. Geophys. Res.*, **93**(88), 15,057–15064.
- Bataille, K. & Lund, F., 1996. Strong scattering of short-period seismic waves by the core-mantle boundary and the P-diffracted Wave, *Geophys. Res. Lett.*, **23**(18), 2413–2416.
- Bataille, K., Wu, R. S., & Flatte, S. M., 1990. Inhomogeneities near the core-mantle boundary evidenced from scattered waves: A review, *Pure appl. Geophys.*, **132**, 151–173.
- Becker, T. W. & Boschi, L., 2002. A comparison of tomographic and geodynamic mantle models, *Geochem. Geophys. Geosyst.*, **3**.
- Becker, T. W., Kellogg, J. B., & Connell, R. J. O., 1999. Thermal constraints on the survival of primitive blobs in the lower mantle, *Earth Planet. Sci. Lett.*, **171**, 351–365.
- Bennett, T. J., Marshall, M. E., McLaughlin, K. L., Barker, B. W., & Murphy, J. R., 1996. Seismic Characteristics and Mechanisms of Rockbursts, *S-Cubed*, pp. 542–551.
- Berryman, J. G., 2000. Seismic velocity decrement ratios for regions of partial melt in the lower mantle, *Geophys. Res. Lett.*, **27**(3), 421–424.
- Beuchert, M. J. & Schmeling, H., 2013. A melting model for the lowermost mantle using Clapeyron slopes derived from experimental data: Consequences for the thickness of ultralow velocity zones (ULVZs), *Geochemistry, Geophysics, Geosystems*, **14**(1), 197–208.

- Bhattacharyya, J., Masters, G., & Shearer, P., 1996. Global Lateral Variations of Shear Wave Attenuation in the Upper Mantle, *J. Geophys. Res.*, **101**, 22,273–22,289.
- Birtill, J. W. & Whiteway, F. E., 1965. The application of phase arrays to the analysis of seismic body waves, *Philosophical Transactions of the Royal Society of London*, **258**(1091), 421–493.
- Blandford, R. R., 1974. An automatic event detector at the Tonto Forest seismic observatory, *Geophysics*, **39**, 633–643.
- Bolt, B. A., 1962. Gutenberg's early PKP observations, *Nature*, **196**, 122–124.
- Bondár, I., North, R. G., & Beall, G., 1999. Teleseismic slowness-azimuth station corrections for the International Monitoring System seismic network, *Bull. seism. Soc. Am.*, **89**, 989–1003.
- Bormann, P., 2002. *IASPEI New Manual of Seismological Observatory Practice*, vol. 1.
- Boschi, L. & Dziewonski, A. M., 1999. High- and low-resolution images of the Earth's mantle: Implications of different approaches to tomographic modeling, *J. Geophys. Res.*, **104**, 25,567–25,594.
- Bower, D. J., Wicks, J. K., Gurnis, M., & Jackson, J. M., 2011. A geodynamic and mineral physics model of a solid-state ultralow-velocity zone, *Earth Planet. Sci. Lett.*, **303**, 193–202.
- Bowers, D., 1997. The October 30, 1994, seismic disturbance in South Africa: Earthquake or large rock burst?, *J. Geophys. Res.*, **102**, 9843–9857.
- Bowers, D., 2000. Using the F-detector to help interpret P-seismograms recorded by seismometer arrays, in *Proceedings of the 22nd Annual DoD/DOE Seismic Research Symposium*.
- Boyet, M. & Carlson, R. W., 2005. <sup>142</sup>Nd evidence for early (4.53 Ga) global differentiation of the silicate Earth., *Science*, **309**(5734), 576–81.
- Braña, L. & Helffrich, G., 2004. A scattering region near the core-mantle boundary under the North Atlantic, *Geophysical Journal International*, **158**(2), 625–636.
- Brandenburg, J. P. & van Keken, P. E., 2007. Deep storage of oceanic crust in a vigorously convecting mantle, *Journal of Geophysical Research*, **112**(B6), B06403.
- Brodholt, J., Ammann, M., Hunt, S., Walker, A., & Dobson, D., 2009. The rheological properties of post-perovskite and implications for D, *Goldschmidt Conference Abstracts*, p. 162.
- Buffett, B. A., Garnero, E. J., & Jeanloz, R., 2000. Sediments at the Top of Earth's Core, *Science*, **290**, 1338–1342.
- Bullen, K. E., 1942. The density variation of the Earth's central core, *Bull. seism. Soc. Am.*, **32**, 19–29.
- Bullen, K. E., 1949. Compressibility-pressure hypothesis and the Earth's interior, *Science*, **5**, 355–368.
- Burke, K., Steinberger, B., Torsvik, T. H., & Smethurst, M. A., 2008. Plume Generation Zones at the margins of Large Low Shear Velocity Provinces on the core-mantle boundary, *Earth and Planetary Science Letters*, **265**(1-2), 49–60.
- Cabral, R. a., Jackson, M. G., Rose-Koga, E. F., Koga, K. T., Whitehouse, M. J., Antonelli, M. a., Farquhar, J., Day, J. M. D., & Hauri, E. H., 2013. Anomalous sulphur isotopes in plume lavas reveal deep mantle storage of Archaean crust, *Nature*, **496**(7446), 490–493.
- Cao, A. & Romanowicz, B., 2007. Locating scatterers in the mantle using array analysis of PKP precursors from an earthquake doublet, *Earth Planet. Sci. Lett.*, **255**, 22–31.
- Capon, J., 1969. High-Resolution Frequency-Wavenumber Spectrum Analysis, *Proceedings of the IEEE*, **57**, 1408–1418.
- Capon, J., Greenfield, R., & Kolker, R., 1967. Multidimensional maximum-likelihood processing of a large aperture seismic array, *Proceedings of the IEEE*, **55**(2), 192–211.

- Carlson, R. & Boyet, M., 2006. Long-term consequences of early Earth differentiation, *Geochimica et Cosmochimica Acta*, **70**(18), A84.
- Castillo, P., 1988. The Dupal anomaly as a trace of the upwelling lower mantle, *Nature*, **336**, 667–670.
- Castle, J. C. & van der Hilst, R. D., 2000. The core-mantle boundary under the Gulf of Alaska : No ULVZ for shear waves, *Earth Planet. Sci. Lett.*, **176**, 311–321.
- Castle, J. C. & van der Hilst, R. D., 2003. Searching for seismic scattering off mantle interfaces between 800 km and 2000 km depth, *J. Geophys. Res.*, **108**.
- Castle, J. C., Creager, K. C., Winchester, J. P., & van der Hilst, R. D., 2000. Shear wave speeds at the base of the mantle, *J. Geophys. Res.*, **105**(B9), 21543–21557.
- Catalli, K., Shim, S.-H., & Prakapenka, V., 2009. Thickness and Clapeyron slope of the post-perovskite boundary., *Nature*, **462**(7274), 782–5.
- Chaloner, J. W., Thomas, C., & Rietbrock, A., 2009. P - and S -wave reflectors in D beneath southeast Asia, *Geophysical Journal International*, **179**(2), 1080–1092.
- Chang, A. C. & Cleary, J. R., 1981. Scattered PKKP: Futher evidence for scattering at a rough core-mantle boundary, *Phys. Earth planet. Int.*, **24**, 15–29.
- Chang, B. Y. A. C. & Cleary, J. R., 1978. Precursors to PKKP, *Bull. seism. Soc. Am.*, **68**(4), 1059–1079.
- Chernov, L. A., 1960. *Wave propagation in a random medium*, McGraw-Hill Book Company, New York.
- Christensen, U. R. & Hofmann, A. W., 1994. Segregation of subducted oceanic crust in the convecting mantle, *J. Geophys. Res.*, **99**, 19,867–19,844.
- Cleary, J. R. & Haddon, R. A. W., 1972. Seismic Wave Scattering near the Core-Mantle Boundary: a New Interpretation of Precursors to PKP, *Nature*, **240**, 549–551.
- Cobden, L. & Thomas, C., 2013. The origin of D” reflections: a systematic study of seismic array data sets, *Geophysical Journal International*, **194**(2), 1091–1118.
- Cormier, V. F., 1999. Anisotropy of heterogeneity scale lengths in the lower mantle from PKIKP precursors Precursors to PKIKP, *Geophys. J. Int.*, **136**, 373–384.
- Cottaar, S. & Romanowicz, B., 2012. An unusually large ULVZ at the base of the mantle near Hawaii, *Earth and Planetary Science Letters*, **355-356**, 213–222.
- Creager, K. C. & Jordan, T. H., 1986. Slab Penetration Into the Lower Mantle Beneath the Mariana and Other Island Arcs of the Northwest Pacific, *J*, **91**, 3573–3589.
- Davies, D. & Sheppard, R. M., 1972. Lateral Heterogeneity in the Earth’s Mantle, *Nature*, **239**, 318–323.
- Davies, D., Kelly, E. J., & Filson, J. R., 1971. Vespa Process for Analysis of Seismic Signals, *Nat. Phys. Sci.*, **232**, 8–13.
- Davies, D. R., Goes, S., Davies, J. H., Schuberth, B. S. A., Bunge, H., & Ritsema, J., 2012. Reconciling dynamic and seismic models of Earth’s lower mantle: The dominant role of thermal heterogeneity, *Earth and Planetary Science Letters*, **353-354**, 253–269.
- Della Mora, S., Boschi, L., Tackley, P. J., Nakagawa, T., & Giardini, D., 2011. Low seismic resolution cannot explain S/P decorrelation in the lower mantle, *Geophysical Research Letters*, **38**, L12303.
- DeMets, C., Gordon, R. G., Argus, D. F., & Stein, S., 1990. Current plate motions, *Geophys. J. Int.*, (101), 425–478.
- Deschamps, F., Kaminski, E., & Tackley, P. J., 2011. A deep mantle origin for the primitive signature of ocean island basalt, *Nature Geoscience*, **4**(12), 879–882.

- Deschamps, F., Cobden, L., & Tackley, P. J., 2012. The primitive nature of large low shear-wave velocity provinces, *Earth and Planetary Science Letters*, **349-350**, 198–208.
- Dobson, D. P. & Brodholt, J. P., 2005. Subducted banded iron formations as a source of ultralow-velocity zones at the core–mantle boundary, *Nature*, **434**, 371–374.
- Dobson, D. P., Miyajima, N., Nestola, F., Alvaro, M., Casati, N., Liebske, C., Wood, I. G., & Walker, A. M., 2013. Strong inheritance of texture between perovskite and post-perovskite in the D layer, *Nature Geosci.*, **6**(7), 575–578.
- Doornbos, D. J., 1974. Seismic Wave Scattering Near Caustics: Observations of PKKP Precursors, *Nature*, **247**, 352–353.
- Doornbos, D. J., 1976. Characteristics of Lower Mantle Inhomogeneities from Scattered Waves, *Geophys. J. R. astr. Soc.*, **44**, 447–470.
- Doornbos, D. J., 1978. On seismic-wave scattering by a rough core-mantle boundary, *Geophys. J. R. astr. Soc.*, **53**, 643–662.
- Doornbos, D. J., 1980. The effect of a rough core-mantle boundary on PKKP, *Phys. Earth planet. Int.*, **21**, 351–358.
- Doornbos, D. J. & Husebye, E. S., 1972. Array analysis of PKP phases and their precursors, *Phys. Earth planet. Int.*, **5**, 387–399.
- Doornbos, D. J. & Vlaar, N. J., 1973. Regions of Seismic Wave Scattering in the Earth’s Mantle and Precursors to PKP, *Nat. Phys. Sci.*, **243**, 58–61.
- Dupre, B. & Allegre, C. J., 1983. Pb-Sr isotope variation in Indian Ocean basalts and mixing phenomena, *Nature*, **303**, 142–146.
- Dziewonski, A. M., 1984. Mapping the Lower Mantle : Determination of Lateral Heterogeneity in P Velocity up to Degree and Order 6, *J. Geophys. Res.*, **89**, 5929–5952.
- Dziewonski, A. M. & Anderson, D. L., 1981. Preliminary reference Earth model, *Physics of the Earth and Planetary Interiors*, **25**(4), 297–356.
- Dziewonski, A. M., Lekic, V., & Romanowicz, B. a., 2010. Mantle Anchor Structure: An argument for bottom up tectonics, *Earth Planet. Sci. Lett.*, **299**, 69–79.
- Earle, P. S., 2002. Origins of High-Frequency Scattered Waves near PKKP from Large Aperture Seismic Array Data, *Bull. seism. Soc. Am.*, **92**, 751–760.
- Earle, P. S. & Shearer, P. M., 1997. Observations of PKKP Precursors Used to Estimate Small-Scale Topography on the Core-Mantle Boundary, *Science*, **277**, 667–670.
- Earle, P. S. & Shearer, P. M., 1998. Observations of high-frequency scattered energy associated with the core phase PKKP, *Geophys. Res. Lett.*, **25**(3), 405–408.
- Earle, P. S. & Shearer, P. M., 2001. Distribution of Fine-Scale Mantle Heterogeneity from Observations of P diff Coda, (December), 1875–1881.
- Earle, P. S., Rost, S., Shearer, P. M., & Thomas, C., 2011. Scattered P’P’ Waves Observed at Short Distances, *Bull. seism. Soc. Am.*, **101**, 2843–2854.
- Efron, B., 1979. Bootstrap Methods: Another Look at the Jackknife, *Annals of Statistics*, **7**, 1–26.
- Efron, B. & Tibshirani, R., 1991. Statistical Data Analysis in the Computer Age, *Science*, **253**(5018), 390–395.
- Engmann, S. & Cousineau, D., 2011. Comparing Distributions: The two-sample Anderson-Darling test as an alternative to the Kolmogorov-Smirnoff test, *Journal of Applied Quantitative Methods*, **6**, 1–17.
- Ford, S. R., Garnero, E. J., & McNamara, A. K., 2006. A strong lateral shear velocity gradient and anisotropy heterogeneity in the lowermost mantle beneath the southern Pacific, *Journal of Geophysical Research*, **111**(B3), 1–14.

- Ford, S. R., Garnero, E. J., & Thorne, M. S., 2012. Differential t\* measurements via instantaneous frequency matching: observations of lower mantle shear attenuation heterogeneity beneath western Central America, *Geophysical Journal International*, **189**(1), 513–523.
- Forte, A. M., Simmons, N. A., & Grand, S. P., 2013. Constraints on 3-D Seismic Models from Global Geodynamic Observables: Implications for the Global Mantle Convective Flow, in *Treatise on Geophysics: Seismology and the Structure of the Earth*, pp. 805–858, eds Romanwicz, B. & Dziewonski, A. M., Elsevier, 2nd edn.
- Fowler, C., 1993. Boundary Layer Theory and Subduction, *J. Geophys. Res.*, **98**, 21,997–22,005.
- Frost, D. A. & Rost, S., 2014. The P-wave Boundary of the Large-Low Shear Velocity Province beneath the Pacific, *Earth Planet. Sci. Lett. (in press)*.
- Frost, D. A., Rost, S., Selby, N. D., & Stuart, G. W., 2013. Detection of a tall ridge at the core-mantle boundary from scattered PKP energy, *Geophysical Journal International*.
- Fukao, Y., Obayashi, M., Inoue, H., & Nenbai, M., 1992. Subducting slabs stagnant in the mantle transition zone, *Journal of Geophysical Research*, **97**(B4), 4809.
- Fukao, Y., Widiyantoro, S., & Obayashi, M., 2001. Stagnant slabs in the upper and lower mantle transition region, *Reviews of Geophysics*, **39**(3), 291–323.
- Garnero, E. J., 2000. Heterogeneity of the lowermost mantle, *Ann. Rev. Earth planet. Sci.*, **28**, 509–537.
- Garnero, E. J. & Helmberger, D. V., 1995. A very slow basal layer underlying large-scale low-velocity anomalies in the lower mantle beneath the Pacific : evidence from core phases, *Phys. Earth Planet. Int.*, **9201**, 161–176.
- Garnero, E. J. & Helmberger, D. V., 1996. Seismic detection of a thin laterally varying boundary layer at the base of the mantle beneath the central-Pacific, *Geophys. Res. Lett.*, **23**(9), 977–980.
- Garnero, E. J. & Helmberger, D. V., 1998. Further structural constraints and uncertainties of a thin laterally varying ultralow-velocity layer at the base of the mantle, *J. Geophys. Res.*, **103**, 12495–12509.
- Garnero, E. J. & Jeanloz, R., 2000. Fuzzy Patches on the Earth’s Core-Mantle Boundary?, *Geophys. Res. Lett.*, **27**, 2777–2780.
- Garnero, E. J. & Lay, T., 2003. D shear velocity heterogeneity, anisotropy and discontinuity structure beneath the Caribbean and Central America, *Physics of the Earth and Planetary Interiors*, **140**(1-3), 219–242.
- Garnero, E. J. & McNamara, A. K., 2008. Structure and dynamics of Earth’s lower mantle, *Science*, **320**, 626–628.
- Gonnermann, H. M., Manga, M., & Jellinek, M. A., 2002. Dynamics and longevity of an initially stratified mantle, *Geophys. Res. Lett.*, **29**(1399).
- Gutenberg, B., 1958. Caustics Produced by Waves Through the Earth’s Core, *Geophys. J. R. astr. Soc.*, **1**, 238–248.
- Haddon, R. A. W. & Cleary, J. R., 1974. Evidence for scattering of seismic PKP waves near the mantle-core boundary, *Phys. Earth planet. Int.*, **8**, 211–234.
- Harjes, H. P. & Henger, M., 1973. Array-Seismologie, *Z. Geophys.*, **39**, 865–905.
- Hart, S. R., 1984. A large-scale isotope anomaly in the Southern Hemisphere mantle, *Nature*, **309**, 753–757.
- Hasegawa, S. & Gendzwil, N. J., 1989. Induced Seismicity in Mines in Canada - An Overview, *Pure appl. Geophys.*, **129**, 423–453.
- Haubrich, R. A., 1968. Array Design, *Bull. seism. Soc. Am.*, **58**(3), 977–991.

- Havens, E. & Revenaugh, J., 2001. A broadband seismic study of the lowermost mantle beneath Mexico: Constrains on ultralow velocity zone elasticity and density, *J. Geophys. Res.*, **106**, 30,809–30,820.
- He, Y. & Wen, L., 2009. Structural features and shear-velocity structure of the Pacific Anomaly, *J. Geophys. Res.*, **114**, 1–17.
- He, Y. & Wen, L., 2012. Geographic boundary of the Pacific Anomaly and its geometry and transitional structure in the north, *J. Geophys. Res.*, **117**(B9), 1–16.
- Hedlin, M. A. H. & Shearer, P. M., 2000. An analysis of large-scale variations in small-scale mantle heterogeneity using Global Seismographic Network recordings of precursors to PKP, *J. Geophys. Res.*, **105**(B6), 13655–13673.
- Hedlin, M. A. H. & Shearer, P. M., 2002. Probing mid-mantle heterogeneity using PKP coda waves, *Phys. Earth Planet. Int.*, **130**, 195–208.
- Hedlin, M. A. H., Shearer, P. M., & Earle, P. S., 1997. Seismic evidence for small-scale heterogeneity throughout the Earth's mantle, *Nature*, **387**, 145–150.
- Helfrich, G., 2014. Outer core compositional layering and constraints on core liquid transport properties, *Earth and Planetary Science Letters*, **391**, 256–262.
- Helmberger, D., Ni, S., Wen, L., & Ritsema, J., 2000. Seismic evidence for ultralow-velocity zones beneath African and eastern Atlantic, *J. Geophys. Res.*, **105**, 865–878.
- Helmberger, D. V. & Ni, S., 2005. Seismic Modeling Constraints on the South African Super Plume, in *Earth's Deep Mantle: Structure, Composition, and Evolution*, pp. 63–81, American Geophysical Union.
- Helmberger, D. V., Wen, L., & Ding, X., 1998. Seismic evidence that the source of the Iceland hotspot lies at the core-mantle boundary, *Nature*, **396**, 251–255.
- Helmberger, D. V., Lay, T., Ni, S., Gurnis, M., & Hemley, R. J., 2005. Deep Mantle Structure and the Postperovskite Phase Transition, *Proceedings of the National Academy of Sciences of the United States of America*, **102**, 17257–17263.
- Helmberger, D. V., Sun, D., Liu, L., Tan, E., & Gurnis, M., 2009. Review of large low shear velocity provinces in the lower mantle, *Geochimica et Cosmochimica Acta*, **73**, 520.
- Hernlund, J. W. & Jellinek, a. M., 2010. Dynamics and structure of a stirred partially molten ultralow-velocity zone, *Earth and Planetary Science Letters*, **296**(1-2), 1–8.
- Hernlund, J. W. & Tackley, P. J., 2007. Some dynamical consequences of partial melting in Earth's deep mantle, *Phys. Earth planet. Int.*, **162**, 149–163.
- Hernlund, J. W., Thomas, C., & Tackley, P. J., 2005. A doubling of the post-perovskite phase boundary and structure of the Earth's lowermost mantle, *Nature*, **434**, 882–886.
- Heyburn, R. & Bowers, D., 2008. Earthquake Depth Estimation Using the F Trace and Associated Probability, *Bull. seism. Soc. Am.*, **98**, 18–35.
- Hirose, K., Fei, Y., Ma, Y., & Mao, H., 1999. The fate of subducted basaltic crust in the Earth's lower mantle, *Nature*, **397**, 53–56.
- Hirose, K., Takafuji, N., Sata, N., & Ohishi, Y., 2005. Phase transition and density of subducted MORB crust in the lower mantle, *Earth Planet. Sci. Lett.*, **237**, 239–251.
- Hock, S., Korn, M., Ritter, J. R. R., & Rothert, E., 2004. Mapping random lithospheric heterogeneities in northern and central Europe, *Geophysical Journal International*, **157**(1), 251–264.
- Husebye, E. S. & Ruud, B. O., 1989. Array Seismology - Past, Present and Future Developments, in *Observatory Seismology*, chap. 8, pp. 123–153, ed. Litchiser, J. J., University of California Press, Berkeley.

- Husebye, E. S., King, D. W., & Haddon, R. A. W., 1976. Precursors to PKIKP and Seismic Wave Scattering Near the Mantle-Core Boundary, *J. Geophys. Res.*, **81**(11), 1870–1882.
- Hutko, A. R., Lay, T., Garnero, E. J., & Revenaugh, J., 2006. Seismic detection of folded, subducted lithosphere at the core-mantle boundary., *Nature*, **441**, 333–6.
- Hutko, A. R., Lay, T., & Revenaugh, J., 2009. Localized double-array stacking analysis of PcP: D and ULVZ structure beneath the Cocos plate, Mexico, central Pacific, and north Pacific, *Phys. Earth Planet. Int.*, **173**, 60–74.
- Ishii, M. & Tromp, J., 1999. Normal-Mode and Free-Air Gravity Constraints on Lateral Variations in Velocity and Density of Earth's Mantle, *Science*, **285**, 1231–1236.
- Ivan, M. & Cormier, V. F., 2011. High Frequency PKKPBC Around 2.5 Hz Recorded Globally, *Pure and Applied Geophysics*, **168**(10), 1759–1768.
- Jeffreys, H., 1939. The times of core waves, *Monthly Notices Roy. Astron. Soc., Geophys. Suppl.*, **4**, 548–561.
- Jeffreys, H. & Bullen, K. E., 1958. Seismological Tables, *British Association for the Advancement of Science*.
- Jensen, K. J., Thorne, M. S., & Rost, S., 2013. SPdKS analysis of ultra-low velocity zones beneath the western Pacific, *Geophysical Research Letters*, **40**(August), 4574–4578.
- Julia, J., Nyblade, a. a., Durrheim, R., Linzer, L., Gok, R., Dirks, P., & Walter, W., 2009. Source Mechanisms of Mine-Related Seismicity, Savuka Mine, South Africa, *Bull. seism. Soc. Am.*, **99**, 2801–2814.
- Julian, B. R., Miller, D., & Foulger, G. R., 1998. Non-double-couple earthquakes 1. Theory, *Reviews of Geophysics*, (98), 525–549.
- Kanasewich, E. R., Hemmings, C. D., & Alpaslan, T., 1973. Nth-Root Stack Nonlinear Multichannel Filter, *Geophysics*, **38**, 327–338.
- Kaneshima, S. & Helffrich, G., 2013. Vp structure of the outermost core derived from analysing large-scale array data of SmKS waves, *Geophysical Journal International*, **193**(3), 1537–1555.
- Karato, S. I., 2003. *The Dynamic Structure of the Deep Earth: An Interdisciplinary Approach*, Princeton University Press, Princeton, NJ.
- Karato, S.-i. & Karki, B. B., 2001. Origin of lateral variation of seismic wave velocities and density in the deep mantle, *J. Geophys. Res.*, **106**, 21,771–21,783.
- Kennett, B. L. N. & Engdahl, E. R., 1991. Traveltimes for global earthquake location and phase identification, *Geophys. J. Int.*, **105**, 429–465.
- King, D. W. & Cleary, J. R., 1974. A note on the interpretation of precursors to PKPPKP, *Bull. seism. Soc. Am.*, **64**, 721–723.
- King, D. W., Haddon, R. A. W., & Cleary, J. R., 1973. Evidence for seismic scattering in the D'' Layer, *Earth Planet. Sci. Lett.*, **20**, 353–356.
- King, D. W., Haddon, R. A. W., & Cleary, J. R., 1974. Array analysis of precursors to PKIKP in the distance range 128 to 142, *Geophys. J. R. astr. Soc.*, **37**, 157–173.
- King, D. W., Husebye, E. S., & Haddon, R. A. W., 1976. Processing of seismic precursor data, *Phys. Earth planet. Int.*, **12**, 128–134.
- Kito, T., Rost, S., Thomas, C., & Garnero, E. J., 2007. New insights into the P - and S - wave velocity structure of the D discontinuity beneath the Cocos plate, *Geophysical Journal International*, **169**(2), 631–645.
- Kito, T., Thomas, C., Rietbrock, A., Garnero, E. J., Nippres, S. E. J., & Heath, A. E., 2008. Seismic evidence for a sharp lithospheric base persisting to the lowermost mantle beneath the Caribbean, *Geophysical Journal International*, **174**(3), 1019–1028.

- Knittle, E. & Jeanloz, R., 1986. High-pressure metallization of FeO and implications for the Earth's core, *Geophys. Res. Lett.*, **13**, 1541–1544.
- Knittle, E. & Jeanloz, R., 1989. Simulating the core-mantle boundary: An experimental study of high pressure reactions between silicates and liquid iron, *Geophys. Res. Lett.*, **16**(7), 609–612.
- Knittle, E. & Jeanloz, R., 1991. Earth's core-mantle boundary: results of experiments at high pressures and temperatures, *Science*, **251**, 1438–1443.
- Knopoff, L. & Hudson, J. A., 1964. Scattering of Elastic Waves by Small Inhomogeneities, *The Journal of the Acoustical Society of America*, **36**, 338–343.
- Knott, C. G., 1899. Reflexion and Refraction of Elastic Waves, with Seismological Applications, *Philosophical Magazine*, **48**, 64–97.
- Koper, K. D., Foy, B. D., & Benz, H., 2009. Composition and variation of noise recorded at the Yellowstone Seismic Array, 1991–2007, *J. Geophys. Res.*, **114**, 1–13.
- Koper, K. D., Seats, K., & Benz, H., 2010. On the Composition of Earth's Short-Period Seismic Noise Field, *Bulletin of the Seismological Society of America*, **100**(2), 606–617.
- Korn, M., 1997. Modelling the teleseismic P coda envelope: depth dependent scattering and deterministic structure, *Phys. Earth planet. Int.*, **104**, 23–36.
- Krüger, F. & Weber, M., 1992. The effect of low-velocity sediments on the mislocation vectors, *Geophys. J. Int.*, **108**, 387–393.
- Krüger, F., Weber, M., Scherbaum, F., & Schlittenhardt, J., 1995. Evidence for normal and inhomogeneous lowermost mantle and core-mantle boundary structure under the Arctic and northern Canada, *Geophys. J. Int.*, **122**, 637–657.
- Kudo, Y., Hirose, K., Murakami, M., Asahara, Y., Ozawa, H., Ohishi, Y., & Hirao, N., 2012. Sound velocity measurements of CaSiO<sub>3</sub> perovskite to 133GPa and implications for lowermost mantle seismic anomalies, *Earth and Planetary Science Letters*, **349–350**, 1–7.
- Labrosse, S., Hernlund, J. W., & Coltice, N., 2007. A crystallizing dense magma ocean at the base of the Earth's mantle, *Nature*, **450**, 4–7.
- Laske, G., Masters, G., Ma, Z., & Pasyanos, M. E., 2012. CRUST1.0: An Updated Global Model of Earth's Crust, *Geophysical Research Abstracts*, **14**.
- Laske, G., Masters, G., Ma, Z., & Pasyanos, M., 2013. Update on CRUST1.0 - A 1-degree Global Model of Earth's Crust, *Geophys. Res. Abstracts*, (15).
- Lassak, T. M., McNamara, A. K., Garnero, E. J., & Zhong, S., 2010. Core-mantle boundary topography as a possible constraint on lower mantle chemistry and dynamics, *Earth Planet. Sci. Lett.*, **289**, 232–241.
- Lay, T. & Garnero, E. J., 2007. Reconciling the Post-Perovskite Phase With Seismological Observations of Lowermost Mantle Structure, pp. 129–154.
- Lay, T. & Garnero, E. J., 2011. Deep Mantle Seismic Modeling and Imaging, *Ann. Rev. Earth planet. Sci.*, **39**, 91–123.
- Lay, T., Garnero, E. J., & Williams, Q., 2004. Partial melting in a thermo-chemical boundary layer at the base of the mantle, *Phys. Earth planet. Int.*, **146**, 441–467.
- Lay, T., Hernlund, J., Garnero, E. J., & Thorne, M. S., 2006. A post-perovskite lens and D'' heat flux beneath the central Pacific, *Science*, **314**, 1272–6.
- Lee, C.-T. a., Luffi, P., Höink, T., Li, J., Dasgupta, R., & Hernlund, J., 2010. Upside-down differentiation and generation of a 'primordial' lower mantle., *Nature*, **463**(7283), 930–3.
- Lekic, V., Cottaar, S., Dziewonski, A., & Romanowicz, B., 2012. Cluster analysis of global lower mantle tomography: A new class of structure and implications for chemical heterogeneity, *Earth and Planetary Science Letters*, **357–358**, 68–77.

- Li, C., van der Hilst, R. D., Engdahl, E. R., & Burdick, S., 2008. A new global model for P wave speed variations in Earth's mantle, *Geochem. Geophys. Geosyst.*, **9**.
- Li, L. & Weidner, D. J., 2013. Effect of dynamic melting on acoustic velocities in a partially molten peridotite, *Physics of the Earth and Planetary Interiors*, **222**, 1–7.
- Li, M. & McNamara, A. K., 2013. The difficulty for subducted oceanic crust to accumulate at the Earth's core-mantle boundary, *J. Geophys. Res.*, **118**, 1807–1816.
- Li, M., Mcnamara, A. K., & Garnero, E. J., 2014. Chemical complexity of hotspots caused by cycling oceanic crust through mantle reservoirs, *Nature Geosci.*, (March), 1–5.
- Lithgow-Bertelloni, C. & Richards, M. A., 1998. The Dynamics of Cenozoic and Mesozoic Plate Motions, *Reviews of Geophysics*, **36**, 27–78.
- Liu, L., Tan, Y., Sun, D., Chen, M., & Helmberger, D., 2011. Trans-Pacific whole mantle structure, *J. Geophys. Res.*, **116**, 1–14.
- Liu, Q. & Tromp, J., 2006. Finite-Frequency Kernels Based on Adjoint Methods, *Bulletin of the Seismological Society of America*, **96**(6), 2383–2397.
- Luo, S.-N., Ni, S., & Helmberger, D. V., 2001. Evidence for a sharp lateral variation of velocity at the coremantle boundary from multipathed PKPab, *Earth Planet. Sci. Lett.*, **189**, 155–164.
- Mancinelli, N. J. & Shearer, P. M., 2013. Reconciling discrepancies among estimates of small-scale mantle heterogeneity from PKP precursors, *Geophysical Journal International*, **195**(3), 1721–1729.
- Manga, M. & Jeanloz, R., 1996. Implications of a metal-bearing chemical boundary layer in D'' for mantle dynamics, *Geophys. Res. Lett.*, **23**, 3091–3094.
- Mao, W. L., Shen, G., Prakapenka, V. B., Meng, Y., Campbell, A. J., Heinz, D. L., Shu, J., Hemley, R. J., & Mao, H.-k., 2004. Ferromagnesian postperovskite silicates in the D'' layer of the Earth., *Proceedings of the National Academy of Sciences of the United States of America*, **101**, 15867–9.
- Mao, W. L., Mao, H.-K., Sturhahn, W., Zhao, J., Prakapenka, V. B., Meng, Y., Shu, J., Fei, Y., & Hemley, R. J., 2006. Iron-rich post-perovskite and the origin of ultralow-velocity zones., *Science*, **312**, 564–5.
- Margerin, L., 2003. Multiple scattering of high-frequency seismic waves in the deep Earth: PKP precursor analysis and inversion for mantle granularity, *Journal of Geophysical Research*, **108**(B11), 2514.
- Marquering, H., Nolet, G., & Dahlen, F., 1998. Three-dimensional waveform sensitivity kernels, *Geophysical Journal International*, **132**(3), 521–534.
- Marquering, H., Dahlen, F. A., & Nolet, G., 1999. Three-dimensional sensitivity kernels for finite-frequency traveltimes: the banana-doughnut paradox, *Geophys. J. Int.*, **137**, 805–815.
- Maruyama, S., Santosh, M., & Zhao, D., 2007. Superplume, supercontinent, and post-perovskite: Mantle dynamics and anti-plate tectonics on the CoreMantle Boundary, *Gondwana Research*, **11**, 7–37.
- Masters, G., Laske, G., Bolton, H., & Dziewonski, A., 2000. The Relative Behaviour of Shear Velocity, Bulk Sound Speed, and Compressional Velocity in the Mantle: Implications for Chemical and Thermal Structure, in *Earth's Deep Interior: Mineral Physics and Tomography from the Atomic to the Global Scale*, *Geophysical Monograph 117*, pp. 63–87, American Geophysical Union.
- McGarr, A., 1992. Moment Tensors of Ten Witwatersrand Mine Tremors, *Pure appl. Geophys.*, **139**(3), 781–800.
- McGarr, A., Bicknell, J., Sembera, E., & Green, R. W. E., 1989. Analysis of Exceptionally Large Tremors in Two Gold Mining Districts of South Africa, *Pure appl. Geophys.*, **129**, 295–307.

- McNamara, A. K. & Zhong, S., 2005. Thermochemical structures beneath Africa and the Pacific Ocean., *Nature*, **437**, 1136–9.
- McNamara, A. K., Garnero, E. J., & Rost, S., 2010. Tracking deep mantle reservoirs with ultra-low velocity zones, *Earth Planet. Sci. Lett.*, **299**, 1–9.
- Melton, B. & Bailey, L., 1957. Multiple Signal Correlators, *Geophysics*, **22**(3), 565–588.
- Meltzer, A. S., Rudnick, R., Zeitler, P., Levander, A., Humpheys, G., Karlstrom, K., Ekström, G., Carlson, R., Dixon, T., Gurnis, M., Shearer, P., & van der Hilst, R. D., 1999. USArray Initiative, *GSA Today*, pp. 8–10.
- Menke, W., 1986. Few 2-50 km corrugations on the core-mantle boundary, *Geophys. Res. Lett.*, **13**, 1501–1504.
- Miles, J. W., 1960. Scattering of elastic waves by small inhomogeneities, *Geophysics*, **15**, 642–648.
- Miller, D., Foulger, G. R., & Julian, B. R., 1998. Non-double-couple earthquakes 2. Observations, *Reviews of Geophysics*, (98), 551–568.
- Miller, M. & Niu, F., 2008. Bulldozing the coremantle boundary: Localized seismic scatterers beneath the Caribbean Sea, *Phys. Earth planet. Int.*, **170**, 89–94.
- Morelli, A. & Dziewonski, A. M., 1987. Topography of the core-mantle boundary and lateral homogeneity of the liquid core, *Nature*, **325**, 678–683.
- Moresi, L. & Solomatov, V. S., 1995. Numerical investigation of 2D convection with extremely large viscosity variations, *Physics of Fluids*, **7**(9), 2154–2162.
- Mosca, I., Cobden, L., Deuss, A., Ritsema, J., & Trampert, J., 2012. Seismic and mineralogical structures of the lower mantle from probabilistic tomography, *Journal of Geophysical Research*, **117**(B6), B06304.
- Murakami, M., Hirose, K., Kawamura, K., Sata, N., & Ohishi, Y., 2004. Post-perovskite phase transition in MgSiO<sub>3</sub>., *Science*, **304**, 855–8.
- Mykkeltveit, S., Astebol, K., Doornbos, D. J., & Husebye, E. S., 1983. Seismic Array Configuration Optimization, *Bull. seism. Soc. Am.*, **73**, 173–186.
- Neidell, N. S. & Turhan Taner, M., 1971. Semblance and other coherency measures for multichannel data, *Geophysics*, **36**, 482–497.
- Ni, S. & Helmberger, D. V., 2001. Probing an Ultra-low velocity zone at the Core Mantle Boundary with P and S Waves, *Geophys. Res. Lett.*, **28**, 2345–2348.
- Ni, S. & Helmberger, D. V., 2003a. Seismological constraints on the South African superplume; could be the oldest distinct structure on earth, *Earth Planet. Sci. Lett.*, **206**, 119–131.
- Ni, S. & Helmberger, D. V., 2003b. Ridge-like lower mantle structure beneath South Africa, *J. Geophys. Res.*, **108**, 1–14.
- Ni, S., Tan, E., Gurnis, M., & Helmberger, D., 2002. Sharp sides to the African superplume., *Science*, **296**, 1850–1852.
- Ni, S., V. Helmberger, D., & Tromp, J., 2005. Three-dimensional structure of the African superplume from waveform modelling, *Geophys. J. Int.*, **161**, 283–294.
- Niu, F. & Wen, L., 2001. Strong seismic scatterers near the core-mantle boundary west of Mexico, *Geophys. Res. Lett.*, **28**, 3557–3560.
- Niu, F., Kelly, C., & Huang, J., 2012. Constraints on rigid zones and other distinct layers at the top of the outer core using CMB underside reflected PKKP waves, *Earthquake Science*, **25**, 17–24.
- Nowacki, A., Wookey, J., & Kendall, J.-M., 2010. Deformation of the lowermost mantle from seismic anisotropy., *Nature*, **467**(7319), 1091–4.

- Nowacki, A., Walker, A. M., Wookey, J., & Kendall, J.-M., 2012. Evaluating post-perovskite as a cause of D" anisotropy in regions of palaeosubduction, *Geophysical Journal International*, **192**(3), 1085–1090.
- Oganov, A. R. & Ono, S., 2004. Theoretical and experimental evidence for a post-perovskite phase of MgSiO<sub>3</sub> in Earth's D" layer, *Nature*, **430**, 445–448.
- Olson, P., Yuen, D. A., & Balsiger, D., 1984. Mixing of passive heterogeneities by mantle convection, *J. geophys. Res.*, **89**, 425–436.
- Ouzounis, A. & Creager, K. C., 2001. Isotropy overlying anisotropy at the top of the inner core, *Geophys. Res. Lett.*, **28**(22), 4331–4334.
- Panning, M. & Romanowicz, B., 2006. A three-dimensional radially anisotropic model of shear velocity in the whole mantle, *Geophysical Journal International*, **167**(1), 361–379.
- Persh, S. E., Vidale, J. E., & Earle, P. S., 2001. Absence of short-period ULVZ precursors to PcP and ScP from two regions of the CMB, *Geophys. Res. Lett.*, **28**, 387–390.
- Pettitt, a. N., 1976. A Two-Sample Anderson-Darling Rank Statistic, *Biometrika*, **63**(1), 161.
- Poupinet, G., Souriau, A., & Jenatton, L., 1993. A test on the Earth's core-mantle boundary structure with antipodal data: example of Fiji-Tonga earthquakes recorded in Tamanrasset , Algeria, *Geophys. J. Int.*, **113**, 684–692.
- Rawlinson, N. & Kennett, B. L. N., 2004. Rapid estimation of relative and absolute delay times across a network by adaptive stacking, *Geophysical Journal International*, **157**(1), 332–340.
- Razali, N. M., Wah, Y. B., & Sciences, M., 2011. Power comparisons of Shapiro-Wilk , Kolmogorov-Smirnov , Lilliefors and Anderson-Darling tests, *Journal of Statistical Modeling and Analytics*, **2**(1), 21–33.
- Reasoner, C. & Revenaugh, J., 2000. ScP constraints on ultralow-velocity zone density and gradient thickness beneath the Pacific, *J. Geophys. Res.*, **105**, 28173–28182.
- Revenaugh, J. & Meyer, R., 1997. Seismic evidence of partial melt within a possibly ubiquitous low-velocity layer at the base of the mantle, *Science*, **277**, 670–673.
- Ritsema, J., Garnero, E. J., & Lay, T., 1997. A strongly negative shear velocity gradient and lateral variability in the lowermost mantle beneath the Pacific, *J. Geophys. Res.*, **102**, 20,395–20,411.
- Ritsema, J., Ni, S., Helmberger, D. V., & Crotwell, H. P., 1998. Evidence for strong shear velocity reductions and velocity gradients in the lower mantle beneath Africa, *Geophys. Res. Lett.*, **25**, 4245–4248.
- Ritsema, J., Deuss, A., van Heijst, H. J., & Woodhouse, J. H., 2011. S40RTS: a degree-40 shear-velocity model for the mantle from new Rayleigh wave dispersion, teleseismic traveltime and normal-mode splitting function measurements, *Geophysical Journal International*, **184**(3), 1223–1236.
- Robertson, G. S. & Woodhouse, J. H., 1996a. Constraints on lower mantle physical properties from seismology and mineral physics, *Earth Planet. Sci. Lett.*, **143**, 197–205.
- Robertson, G. S. & Woodhouse, J. H., 1996b. Ratio of relative S to P velocity heterogeneity in the lower mantle, *J. Geophys. Res.*, **101**, 20,041–20,052.
- Rondenay, S. & Fischer, K. M., 2003. Constraints on localized core-mantle boundary structure from multichannel, broadband SKS coda analysis, *J. Geophys. Res.*, **108**, 1–16.
- Rost, S., 2003. Detection of a D discontinuity in the south Atlantic using PKKP, *Geophysical Research Letters*, **30**(16), 1840.
- Rost, S. & Earle, P. S., 2010. Identifying regions of strong scattering at the core-mantle boundary from analysis of PKKP precursor energy, *Earth Planet. Sci. Lett.*, **297**, 616–626.

- Rost, S. & Garnero, E. J., 2004. A study of the uppermost inner core from PKKP and PP differential traveltimes, *Geophys. J. Int.*, **156**, 565–574.
- Rost, S. & Garnero, E. J., 2006. Detection of an ultralow velocity zone at the core-mantle boundary using diffracted PKKP ab waves, *J. Geophys. Res.*, **111**, 1–8.
- Rost, S. & Revenaugh, J., 2001. Seismic detection of rigid zones at the top of the core, *Science*, **294**, 1911–4.
- Rost, S. & Revenaugh, J., 2003. Small-scale ultralow-velocity zone structure imaged by ScP, *J. Geophys. Res.*, **108**, 1–10.
- Rost, S. & Thomas, C., 2002. Array seismology: Methods and applications, *Reviews of Geophysics*, **40**, 1–27.
- Rost, S. & Thomas, C., 2009. Improving seismic resolution through array processing techniques, *Surveys in Geophysics*, **30**, 271–299.
- Rost, S. & Thomas, C., 2010. High resolution CMB imaging from migration of short-period core reflected phases, *Phys. Earth Planet. Int.*, **183**, 143–150.
- Rost, S. & Weber, M., 2001. A reflector at 200 km depth beneath the northwest Pacific, *Geophys. J. Int.*, **147**, 12–28.
- Rost, S. & Weber, M., 2002. The upper mantle transition zone discontinuities in the Pacific as determined by short-period array data, *EPSL*, **204**, 347–361.
- Rost, S., Garnero, E. J., Williams, Q., & Manga, M., 2005. Seismological constraints on a possible plume root at the core-mantle boundary., *Nature*, **435**, 666–9.
- Rost, S., Garnero, E. J., & Williams, Q., 2006a. Fine-scale ultralow-velocity zone structure from high-frequency seismic array data, *J. Geophys. Res.*, **111**, 1–14.
- Rost, S., Thorne, M. S., & Garnero, E. J., 2006b. Imaging Global Seismic Phase Arrivals by Stacking Array Processed Short-Period Data, *Seismological Research Letters*, **77**(6), 697–707.
- Rost, S., Garnero, E. J., & Williams, Q., 2008. Seismic array detection of subducted oceanic crust in the lower mantle, *J. Geophys. Res.*, **113**, 1–11.
- Rost, S., Garnero, E. J., & Stefan, W., 2010a. Thin and intermittent ultralow-velocity zones, *J. Geophys. Res.*, **115**, 1–12.
- Rost, S., Garnero, E. J., Thorne, M. S., & Hutko, A. R., 2010b. On the absence of an ultralow-velocity zone in the North Pacific, *J. Geophys. Res.*, **115**, 1–12.
- Rost, S., Earle, P. S., Shearer, P. M., Frost, D. A., & Selby, N. D., 2014. Seismic Detections of small-scale heterogeneities in the deep Earth, *Springer Monograph (In press)*.
- Sato, H., 1991. Study of seismogram envelopes based on scattering by random inhomogeneities in the lithosphere: a review, *Physics of the Earth and Planetary Interiors*, **67**, 4–19.
- Sato, H. & Fehler, M. C., 2008. *Seismic Wave Propagation and Scattering in the Heterogeneous Earth*, Springer Verlag and AIP Press, New York, 2nd edn.
- Schimmel, M., 1999. Phase Cross-Correlations: Design, Comparisons, and Applications, *Bull. seism. Soc. Am.*, **89**, 1366–1378.
- Schimmel, M. & Paulssen, H., 1997. Noise reduction and detection of weak, coherent signals through phase-weighted stacks, *Geophys. J. Int.*, **130**, 497–505.
- Scholz, F. W. & Stephens, M. A., 1987. K-Sample Anderson-Darling Tests, *Journal of the American Statistical Association*, **82**(399), 918–924.
- Schuberth, B. S. A., Bunge, H.-P., & Ritsema, J., 2009. Tomographic filtering of high-resolution mantle circulation models: Can seismic heterogeneity be explained by temperature alone?, *Geochem. Geophys. Geosyst.*, **10**.

- Schweitzer, J., Fyen, J., Mykkeltveit, S., & Kvaerna, T., 2002. Seismic Arrays, in *New Manual of Seismological Observatory Practice*, vol. 1, pp. 481–532, ed. Bormann, P., IASPEI.
- Selby, N. D., 2008. Application of a Generalized F Detector at a Seismometer Array, *Bull. seism. Soc. Am.*, **98**, 2469–2481.
- Selby, N. D., 2011. Improved Teleseismic Signal Detection at Small-Aperture Arrays, *Bull. seism. Soc. Am.*, **101**, 1563–1575.
- Shapiro, S. S., Wilk, M. B., & Laboratories, B. T., 1965. An analysis of variance test for normality (complete samples), *Biometrika*, **52**, 591–611.
- Shearer, P. M. & Earle, P. S., 2004. The global short-period wavefield modelled with a Monte Carlo seismic phonon method, *Geophys. J. Int.*, pp. 1103–1117.
- Shearer, P. M., Hedlin, M. A. H., & Earle, P. S., 1998. PKP and PKKP Precursor Observations: Implications for the Small-scale Structure of the Deep Mantle and Core, in *Geodynamics*, chap. The Core-M, pp. 37–55, American Geophysical Union.
- Simmons, N. a., Forte, A. M., & Grand, S. P., 2009. Joint seismic, geodynamic and mineral physical constraints on three-dimensional mantle heterogeneity: Implications for the relative importance of thermal versus compositional heterogeneity, *Geophysical Journal International*, **177**(3), 1284–1304.
- Simmons, N. A., Forte, A. M., Boschi, L., & Grand, S. P., 2010. GyPSuM: A joint tomographic model of mantle density and seismic wave speeds, *Journal of Geophysical Research*, **115**(B12), B12310.
- Simmons, N. a., Myers, S. C., & Johannesson, G., 2011. Global-scale P wave tomography optimized for prediction of teleseismic and regional travel times for Middle East events: 2. Tomographic inversion, *J. Geophys. Res.*, **116**, 1–31.
- Simmons, N. A., Myers, S. C., Johannesson, G., & Matzel, E., 2012. LLNL-G3Dv3: Global P wave tomography model for improved regional and teleseismic travel time prediction, *Journal of Geophysical Research*, **117**(B10).
- Soldati, G., Boschi, L., & Forte, A. M., 2012. Tomography of core-mantle boundary and lowermost mantle coupled by geodynamics, *Geophys. J. Int.*, **189**, 730–746.
- Song, T.-R. A., Tanaka, S., & Takeuchi, N., 2010. PKP waveform complexity and its implications to fine structure near the edge of African Large Low Shear Velocity Province, *Geophysical Research Abstracts*, **12**, 5913–5913.
- Stixrude, L. & Lithgow-Bertelloni, C., 2012. Geophysics of Chemical Heterogeneity in the Mantle, *Ann. Rev. Earth planet. Sci.*, pp. 569–595.
- Sun, D., Tan, E., Helmberger, D., & Gurnis, M., 2007a. Seismological support for the metastable superplume model, sharp features, and phase changes within the lower mantle., *Proceedings of the National Academy of Sciences of the United States of America*, **104**(22), 9151–5.
- Sun, D., Helmberger, D., Ni, S., & Bower, D., 2009. Direct measures of lateral velocity variation in the deep Earth, *J. Geophys. Res.*, **114**, 1–18.
- Sun, D., Helmberger, D. V., Jackson, J. M., Clayton, R. W., & Bower, D. J., 2013. Rolling hills on the coremantle boundary, *Earth Planet. Sci. Lett. Letters*, **361**, 333–342.
- Sun, X., Song, X., Zheng, S., & Helmberger, D. V., 2007b. Evidence for a chemical-thermal structure at base of mantle from sharp lateral P-wave variations beneath Central America, *Proceedings of the National Academy of Sciences of the United States of America*, **104**, 26–30.
- Sze, E. K. M. & van der Hilst, R. D., 2003. Core mantle boundary topography from short period PcP, PKP, and PKKP data, *Phys. Earth Planet. Int.*, **135**, 27–46.
- Tackley, P. J., 2011. Living dead slabs in 3-D: The dynamics of compositionally-stratified slabs entering a slab graveyard above the core-mantle boundary, *Physics of the Earth and Planetary Interiors*, **188**(3-4), 150–162.

- Tan, E. & Gurnis, M., 2005. Metastable superplumes and mantle compressibility, *Geophys. Res. Lett.*, **32**, 1–4.
- Tan, E. & Gurnis, M., 2007. Compressible thermochemical convection and application to lower mantle structures, *Journal of Geophysical Research*, **112**(B6), B06304.
- Tan, E., Leng, W., Zhong, S., & Gurnis, M., 2011. On the location of plumes and lateral movement of thermochemical structures with high bulk modulus in the 3-D compressible mantle, *Geochem. Geophys. Geosyst.*, **12**, 1–13.
- Tanaka, S. & Hamaguchi, H., 1997. Degree one heterogeneity and hemispherical variation of anisotropy in the inner core from PKP(BC)-PKP(DF) times, *J. Geophys. Res.*, **102**(96), 2925–2938.
- Thomas, C., 2002. Investigating the heterogeneity of the D region beneath the northern Pacific using a seismic array, *Journal of Geophysical Research*, **107**(B11), 2274.
- Thomas, C., Weber, M., Wicks, C. W., & Scherbaum, F., 1999. Small scatterers in the lower mantle observed at German broadband arrays, *J. Geophys. Res.*, **104**(B7), 15073–15088.
- Thomas, C., Igel, H., Weber, M., & Scherbaum, F., 2000. Acoustic simulation of P-wave propagation in a heterogeneous spherical Earth: Numerical method and application to precursor waves to PKPpdf, *Geophys. J. Int.*, **141**, 307–320.
- Thomas, C., Kendall, J.-M., & Weber, M., 2002. The lowermost mantle beneath northern Asia-I. Multi-azimuth studies of a D heterogeneity, *Geophysical Journal International*, **151**(1), 279–295.
- Thomas, C., Garnero, E. J., & Lay, T., 2004a. High-resolution imaging of lowermost mantle structure under the Cocos plate, *J. Geophys. Res.*, **109**, 1–11.
- Thomas, C., Kendall, J.-M., & Lowman, J., 2004b. Lower-mantle seismic discontinuities and the thermal morphology of subducted slabs, *Earth Planet. Sci. Lett.*, **225**, 105–113.
- Thomas, C., Kendall, J.-M., & Helffrich, G., 2009. Probing two low-velocity regions with PKP b-caustic amplitudes and scattering, *Geophys. J. Int.*, **178**, 503–512.
- Thomas, C., Wookey, J., Brodholt, J., & Fieseler, T., 2011. Anisotropy as cause for polarity reversals of D reflections, *Earth and Planetary Science Letters*, **307**(3-4), 369–376.
- Thomas, C. W., Liu, Q., Agee, C. B., Asimow, P. D., & Lange, R. a., 2012. Multi-technique equation of state for Fe<sub>2</sub>SiO<sub>4</sub> melt and the density of Fe-bearing silicate melts from 0 to 161 GPa, *Journal of Geophysical Research*, **117**(B10), B10206.
- Thorne, M., Garnero, E. J., & Grand, S. P., 2004. Geographic correlation between hot spots and deep mantle lateral shear-wave velocity gradients, *Phys. Earth Planet. Int.*, **146**, 47–63.
- Thorne, M. S. & Garnero, E. J., 2004. Inferences on ultralow-velocity zone structure from a global analysis of SPdKS waves, *J. Geophys. Res.*, **109**, 1–22.
- Thorne, M. S., Lay, T., Garnero, E. J., Jahnke, G., & Igel, H., 2007. Seismic imaging of the laterally varying D region beneath the Cocos Plate, *Geophys. J. Int.*, **170**, 635–648.
- Thorne, M. S., Garnero, E. J., Jahnke, G., Igel, H., & McNamara, A. K., 2013a. Mega ultra low velocity zone and mantle flow, *Earth and Planetary Science Letters*, **364**, 59–67.
- Thorne, M. S., Zhang, Y., & Ritsema, J., 2013b. Evaluation of 1-D and 3-D seismic models of the Pacific lower mantle with S, SKS, and SKKS traveltimes and amplitudes, *Journal of Geophysical Research: Solid Earth*, **118**(3), 985–995.
- To, A., Romanowicz, B., Capdeville, Y., & Takeuchi, N., 2005. 3D effects of sharp boundaries at the borders of the African and Pacific Superplumes: Observation and modeling, *Earth planet. Sci. Lett.*, **233**, 137–153.
- To, A., Fukao, Y., & Tsuboi, S., 2011. Evidence for a thick and localized ultra low shear velocity zone at the base of the mantle beneath the central Pacific, *Phys. Earth planet. Int.*, **184**, 119–133.

- Torsvik, T. H., Smethurst, M. A., Burke, K., & Steinberger, B., 2006. Large igneous provinces generated from the margins of the large low-velocity provinces in the deep mantle, *Geophys. J. Int.*, **167**, 1447–1460.
- Torsvik, T. H., Burke, K., Steinberger, B., Webb, S. J., & Ashwal, L. D., 2010. Diamonds sampled by plumes from the core-mantle boundary., *Nature*, **466**, 352–5.
- Trampert, J., Deschamps, F., Resovsky, J., & Yuen, D., 2004. Probabilistic tomography maps chemical heterogeneities throughout the lower mantle, *Science*, **306**, 853–6.
- Trønnes, R. G., 2010. Structure, mineralogy and dynamics of the lowermost mantle, *Miner. Petrol.*, **99**, 243–261.
- Turcotte, D. L. & Schubert, G., 2002. *Geodynamics Applications of Continuum Physics to Geological Problems*, John Wiley & Sons, Inc, New York, 2nd edn.
- van Keken, P. E., Hauri, E. H., & Ballentine, C. J., 2002. Mantle Mixing: The Generation, Preservation, and Destruction of Chemical Heterogeneity, *Ann. Rev. Earth planet. Sci.*, **30**, 493–525.
- van Keken, P. E., Hauri, E. H., Brandenburg, J. P., & Ballentine, C. J., 2010. Generation of mantle heterogeneity by ocean crust recycling: Geophysical and geochemical constraints, *Geochimica et Cosmochimica Acta*, **74**, 1072.
- Vanacore, E. & Niu, F., 2011. Characterization of the D” beneath the Galapagos Islands using SKKS and SKS waveforms, *Earthq. Sci.*, **24**, 87–99.
- Vanacore, E., Niu, F., & Ma, Y., 2010. Large angle reflection from a dipping structure recorded as a PKIKP precursor: Evidence for a low velocity zone at the coremantle boundary beneath the Gulf of Mexico, *Earth Planet. Sci. Lett.*, **293**, 54–62.
- Vidale, J. E. & Benz, H. M., 1992. A sharp and flat section of the core-mantle boundary, *Nature*, **359**, 627–629.
- Vidale, J. E. & Hedlin, M. A. H., 1998. Evidence for partial melt at the coremantle boundary north of Tonga from the strong scattering of seismic waves, *Nature*, **391**, 682–685.
- Wallace, M. & Thomas, C., 2005. Investigating D structure beneath the North Atlantic, *Physics of the Earth and Planetary Interiors*, **151**(1-2), 115–127.
- Wang, Y. & Wen, L., 2004. Mapping the geometry and geographic distribution of a very low velocity province at the base of the Earth’s mantle, *J. Geophys. Res.*, **109**(B10), B10305.
- Wang, Y. & Wen, L., 2007. Geometry and P and S velocity structure of the African Anomaly, *J. Geophys. Res.*, **112**, 1–26.
- Weber, M., 1993. P- and S-wave reflections from anomalies in the lowermost mantle, *Geophysical Journal International*, **115**, 183–210.
- Weber, M., 1994. Lamellae in D””? An alternative model for lower mantle anomalies, *Geophys. Res. Lett.*, **21**, 2531–2534.
- Weber, M. & Davis, J. P., 1990. Evidence of a laterally variable lower mantle structure from P- and S-waves, *Geophys. J. Int.*, **102**, 231–255.
- Weber, M. & Körnig, M., 1990. Lower mantle inhomogeneities inferred from PcP precursors, *Geophys. Res. Lett.*, **17**(11), 1993–1996.
- Weber, M. & Körnig, M., 1992. A search for anomalies in the lowermost mantle using seismic bulletins, *Phys. Earth Planet. Int.*, **73**, 1–28.
- Weber, M. & Wicks, J. C. W., 1996. Reflections from a distant subduction zone, *Geophys. Res. Lett.*, **23**(12), 1453–1456.
- Weichert, D. H. & Whitham, K., 1969. Calibration of the Yellowstone Seismic Array with first zone explosions, *Geophys. J. R. astr. Soc.*, **18**, 461–476.

- Wen, L., 2000. Intense seismic scattering near the Earth's core-mantle boundary beneath the Comoros hotspot, *Geophys. Res. Lett.*, **27**(22), 3627–3630.
- Wen, L., 2001. Seismic evidence for a rapidly varying compositional anomaly at the base of the Earth's mantle beneath the Indian Ocean, *Earth Planet. Sci. Lett.*, **194**, 83–95.
- Wen, L., 2006. A compositional anomaly at the Earth's core-mantle boundary as an anchor to the relatively slowly moving surface hotspots and as source to the DUPAL anomaly, *Earth Planet. Sci. Lett.*, **246**, 138–148.
- Wen, L. & Helmberger, D. V., 1998. Ultra-Low Velocity Zones near the Core-Mantle Boundary from broadband PKP precursors, *Science*, **279**, 1701–1703.
- Wen, L., Silver, P., James, D., & Kuehnel, R., 2001. Seismic evidence for a thermo-chemical boundary at the base of the Earth's mantle, *Earth Planet. Sci. Lett.*, **189**, 141–153.
- Wicks, J. K., Jackson, J. M., & Sturhahn, W., 2010. Very low sound velocities in iron-rich (Mg,Fe)O: Implications for the core-mantle boundary region, *Geophys. Res. Lett.*, **37**, 1–5.
- Williams, Q. & Garnero, E. J., 1996. Seismic evidence for partial melt at the base of Earth's mantle, *Science*, **273**, 1528–1530.
- Williams, Q., Revenaugh, J., & Garnero, E. J., 1998. A Correlation Between Ultra-Low Basal Velocities in the Mantle and Hot Spots, *Science*, **281**, 546–549.
- Wimert, J. & Hier-Majumder, S., 2012. A three-dimensional microgeodynamic model of melt geometry in the Earth's deep interior, *Journal of Geophysical Research*, **117**(B4), B04203.
- Woodhouse, J. H. & Dziewonski, A. M., 1984. Mapping the upper mantle: Three-dimensional modeling of earth structure by inversion of seismic waveforms, *Journal of Geophysical Research*, **89**(B7), 5953.
- Wookey, J., Stackhouse, S., Kendall, J.-M., Brodholt, J., & Price, G. D., 2005. Efficacy of the post-perovskite phase as an explanation for lowermost-mantle seismic properties, *Nature*, **438**, 1004–1007.
- Wright, C., 1975. The origin of short-period precursors to PKP, *Bull. seism. Soc. Am.*, **65**, 765–786.
- Wright, C. & Cleary, J. R., 1974. The Effects of Local Structure and the Adjacent Upper Mantle on Short-Period P Wave Arrivals Recorded at the Warramunga Seismic Array, *Geophys. J. R. astr. Soc.*, **36**, 295–319.
- Wu, R. & Aki, K., 1988. Introduction: seismic wave scattering in three-dimensionally heterogeneous earth, *Pure appl. Geophys.*, **128**, 1–6.
- Wu, R.-S., 1984. *Seismic wave scattering and the small scale inhomogeneities in the lithosphere*, Ph.D. thesis, Massachusetts Institute of Technology.
- Wu, R.-S. & Aki, K., 1985a. Scattering characteristics of elastic waves by an elastic heterogeneity, *Geophysics*, **50**, 582–595.
- Wu, R.-S. & Aki, K., 1985b. Elastic Wave Scattering by a Random Medium and the Small-Scale Inhomogeneities in the Lithosphere, *J. Geophys. Res.*, **90**(12), 10261–10273.
- Wyssession, M. E., 1996. Large-scale structure at the core-mantle boundary from diffracted waves, *Nature*, **382**, 244–248.
- Wyssession, M. E., Okal, E. a., & Bina, C. R., 1992. The structure of the core-mantle boundary from diffracted waves, *Journal of Geophysical Research*, **97**(B6), 8749.
- Wyssession, M. E., Lay, T., Revenaugh, J., Williams, Q., Garnero, E. J., Jeanloz, R., & Kellogg, L. H., 1998. The D" discontinuity and its implications, in *The Core-Mantle Boundary Region*, pp. 273–298, ed. Gurnis, M., AGU, Washington D.C., geodynamic edn.
- Wyssession, M. E., Langenhorst, A., Fouch, M. J., Fischer, K. M., Al-eqabi, G. I., Shore, P. J., & Clarke, T. J., 1999. Lateral Variations in Compressional / Shear Velocities at the Base of the Mantle, *Science*, **284**, 120–125.

- Xu, Y. & Koper, K. D., 2009. Detection of a ULVZ at the base of the mantle beneath the northwest Pacific, *Geophys. Res. Lett.*, **36**, 1–5.
- Young, C. J. & Lay, T., 1987. Evidence for a shear velocity discontinuity in the lower mantle beneath India and the Indian Ocean, *Phys. Earth planet. Int.*, **49**, 37–53.
- Youngs, B. A. R. & Houseman, G. A., 2007. Topography on the D region from analysis of a thin dense layer beneath a convecting cell, *Phys. Earth Planet. Int.*, **160**, 60–74.
- Youngs, B. A. R. & Houseman, G. A., 2009. Formation of steep-sided topography from compositionally distinct dense material at the base of the mantle, *J. Geophys. Res.*, **114**, 1–11.
- Zhang, Y., Ritsema, J., & Thorne, M. S., 2009. Modeling the ratios of SKKS and SKS amplitudes with ultra-low velocity zones at the core-mantle boundary, *Geophys. Res. Lett.*, **36**, 1–5.